Thorsten M. Buzug
Dietrich Holz · Simone Weber
Jens Bongartz · Matthias Kohl-Bareis
Ulrich Hartmann *Editors*

SPRINGER PROCEEDINGS IN PHYSICS 114

Advances in Medical Engineering

Springer

SPRINGER PROCEEDINGS IN PHYSICS 114

SPRINGER PROCEEDINGS IN PHYSICS

92 **Beyond the Standard Model 2003**
Editor: H.V. Klapdor-Kleingrothaus

93 **ISSMGE**
Experimental Studies
Editor: T. Schanz

94 **ISSMGE**
Numerical and Theoretical Approaches
Editor: T. Schanz

95 **Computer Simulation Studies in Condensed-Matter Physics XVI**
Editors: D.P. Landau, S.P. Lewis, and H.-B. Schüttler

96 **Electromagnetics in a Complex World**
Editors: I.M. Pinto, V. Galdi, and L.B. Felsen

97 **Fields, Networks, Computational Methods and Systems in Modern Electrodynamics**
A Tribute to Leopold B. Felsen
Editors: P. Russer and M. Mongiardo

98 **Particle Physics and the Universe**
Proceedings of the 9th Adriatic Meeting, Sept. 2003, Dubrovnik
Editors: J. Trampetić and J. Wess

99 **Cosmic Explosions**
On the 10th Anniversary of SN1993J (IAU Colloquium 192)
Editors: J. M. Marcaide and K. W. Weiler

100 **Lasers in the Conservation of Artworks**
LACONA V Proceedings, Osnabrück, Germany, Sept. 15–18, 2003
Editors: K. Dickmann, C. Fotakis, and J.F. Asmus

101 **Progress in Turbulence**
Editors: J. Peinke, A. Kittel, S. Barth, and M. Oberlack

102 **Adaptive Optics for Industry and Medicine**
Proceedings of the 4th International Workshop
Editor: U. Wittrock

103 **Computer Simulation Studies in Condensed-Matter Physics XVII**
Editors: D.P. Landau, S.P. Lewis, and H.-B. Schüttler

104 **Complex Computing-Networks**
Brain-like and Wave-oriented Electrodynamic Algorithms
Editors: I.C. Göknar and L. Sevgi

105 **Computer Simulation Studies in Condensed-Matter Physics XVIII**
Editors: D.P. Landau, S.P. Lewis, and H.-B. Schüttler

106 **Modern Trends in Geomechanics**
Editors: W. Wu and H.S. Yu

107 **Microscopy of Semiconducting Materials**
Proceedings of the 14th Conference, April 11–14, 2005, Oxford, UK
Editors: A.G. Cullis and J.L. Hutchison

108 **Hadron Collider Physics 2005**
Proceedings of the iTi Conference in Turbulence 2005
Editors: M. Oberlack, S. Guenther, T. Weller, G. Khujadze, A. Osman, M. Frewer, J. Peinke

109 **Progress in Turbulence 2**
Proceedings of the 14th Conference, April 11–14, 2005, Oxford, UK
Editors: A.G. Cullis and J.L. Hutchison

110 **Titel: Nonequilibrium Carrier Dynamics in Semiconductors**
Untertitel: Proceedings of the 14th International Conference, July 25-29, 2005, Chicago, USA
Editors: M. Saraniti, U. Ravaioli

111 **Vibration Problems ICOVP 2005**
Editors: E. Inan, A. Kiris

112 **Experimental Unsaturated Soil Mechanics**
Editor: T. Schanz

113 **Theoretical and Numerical Unsaturated Soil Mechanics**
Editor: T. Schanz

114 **Advances in Medical Engineering**
Editors: T.M. Buzug

Volumes 67–91 are listed at the end of the book.

Thorsten M. Buzug (Ed.)

Advances in Medical Engineering

With 296 Figures

Springer

Professor Dr. Thorsten M. Buzug
Institute of Medical Engineering
University of Luebeck
Ratzeburger Allee 160
D-23538 Luebeck, Germany
buzug@imt.uni-luebeck.de

Professor Dr. Dietrich Holz
Professor Dr. Jens Bongartz
Professor Dr. Matthias Kohl-Bareis
Professor Dr. Ulrich Hartmann
Department of Mathematics and Technology
RheinAhrCampus Remagen, Germany

Dr. Simone Weber
Central Institute for Electronics
Research Centre Juelich, Germany

Library of Congress Control Number: 2007920044

ISSN 0930-8989

ISBN 978-3-540-68763-4 Springer Berlin Heidelberg New York

Typesetting: Digital data supplied by editor
Production: LE-TEX Jelonek, Schmidt & Vöckler GbR, Leipzig
Cover concept: Frido Steinen-Broo, eStudio Calamar S.L., Spain

Printed on acid-free paper SPIN: 11546115 7/3100/YL 5 4 3 2 1 0

Preface

Continuous improvements in medical imaging together with advanced image processing algorithms, biomechanical simulations and interventional monitoring strategies lead to significant progress in computer-aided diagnosis, treatment planning and therapy. Navigation in image-guided surgery provides significant advantages in accuracy due to today's sophisticated techniques of patient-data visualization in combination with the flexibility and precision of novel surgical tools like robots and laser scalpels. These tools give finer control over sensitive movements in diseased anatomical areas and therefore, allow more surgical procedures to be performed using minimally invasive techniques than ever before.

After successful launch in the years 2002 and 2004 the Third Physics Days Remagen (3rd RPT – *Remagener Physiktage*) together with the Second Scientific Workshop of Medical Robotics, Navigation and Visualization (2nd MRNV) is again a forum of current research and development trends in the fields of physics, engineering, mathematics and computer sciences in biomedical engineering. RheinAhrCampus Remagen, Research Centre Jülich and the University of Lübeck provide a platform for scientists from industry, clinics, universities and research labs to present the recent results of their projects. Additionally, we have encouraged students to present their diploma-, master- and PhD-projects.

Foci of the 2007 RPT – MRNV conference are **medical imaging** (CT, MRT, US, PET, SPECT etc.), **medical image processing** (segmentation, registration, visualization etc.), **computer-assisted surgery** (medical robotics, navigation – MRNV workshop), **biomechanics** (motion analysis, accident research, computer in sports, ergonomics etc.), **biomedical optics** (OCT, soft-tissue optics, optical monitoring etc.) and **laser medicine** (tissue ablation, gas analytics, topometry etc.). Additionally, clinical application studies and other interesting fields of biomedical engineering have been included as well.

As chair of the Third Physics Days Remagen (*Remagener Physiktage* – RPT 2007) and the Second Scientific Workshop of Medical Robotics, Navigation and Visualization (MRNV 2007) and on behalf of Karl Ziemons, Research Centre Jülich, and Dietrich Holz, RheinAhrCampus Remagen, I would like to thank the members of the program committee for the selection of works included in these proceedings.

The members of the RPT – MRNV 2007 program committee are:

Til Aach	RWTH Aachen
Jens Bongartz	RheinAhrCampus Remagen
Thorsten M. Buzug	University of Lübeck
Hartmut Dickhaus	FH Heilbronn/University of Heidelberg
Olaf Dössel	University of Karlsruhe
Jürgen Eichler	TFH Berlin
Rolf Ellegast	BGIA, Berufsgenossenschaft St. Augustin
Werner Falkenstein	StarMedTech GmbH
Karin Gruber	University of Koblenz
Heinz Handels	UKE University of Hamburg
Ulrich Hartmann	RheinAhrCampus Remagen
Stefan Haßfeld	University of Heidelberg
Wolfram Hell	University of Munich
Peter Hering	University of Düsseldorf
Gerd Hirzinger	DLR Oberpfaffenhofen
Dietrich Holz	RheinAhrCampus Remagen
Alwin Kienle	University of Ulm
Edmund Koch	TU Dresden
Matthias Kohl-Bareis	RheinAhrCampus Remagen
Steffen Leonhardt	Helmholtz Institute RWTH Aachen
Tim C. Lueth	Humboldt University of Berlin
Heinz-Otto Peitgen	University of Bremen, MeVis Bremen
Siegfried J. Pöppl	University of Lübeck
Robert Sader	University of Frankfurt
Georg Schmitz	RheinAhrCampus Remagen
Klaus-Peter Schmitz	University of Rostock
Herbert Schneckenburger	Hochschule Aalen
Jens Steinbrink	Charité, HU Berlin
Achim Schweikard	University of Lübeck
Gudrun Wagenknecht	Research Centre Jülich
Simone Weber	Research Centre Jülich
Thomas Wittenberg	Fraunhofer Institute IIS Erlangen
Heinz Wörn	University of Karlsruhe
Waldemar Zylka	University of Applied Science Gelsenkirchen

Additionally, I would like to thank the following colleagues for accepting our key talk invitations:

Dr. Jörn Borgert (Philips Research Europe - Hamburg)
Magnetic Particle Imaging

Prof. Dr. Wolfgang Demtröder (University of Kaiserslautern)
Laser Spectroscopy in Biology, Medicine und Environmental Sciences

Prof. Dr. Olaf Dössel (University of Karlsruhe)
Modelling and Imaging Electrophysiology and Contraction of the Heart

Prof. Dr. Heinz-Otto Peitgen (University of Bremen/MeVis)
Challenges and Problems of Quantitative Radiology

Prof. Dr. Dr. h.c. Peter M. Schlag (Clinics for Surgery and Oncology, Charité)
Duties of the Section CTAC of the German Society of Surgery

For financial support of the RPT and MRNV 2007 workshop I would like to thank the Research Centre Jülich.

Warm thanks go to the members of the local organization team: Tobias Bildhauer, Holger Dörle, Dimitri Geraskin, Anke Hülster, Marie-Sophie Lafontaine, Birgit Lentz, Dr. Kerstin Lüdtke-Buzug, Volker Luy, May Oehler, Gisela Niedzwetzki, Waltraud Ott and Dirk Thomsen. Without their help the conference and these proceedings would not have been possible.

Many thanks go to the following cooperating societies: DGBMT (German Society of Biomedical Engineering) of VDE, CTAC (Section for Minimally Invasive, Computer and Telematics Assisted Surgery of the German Society of Surgery), DPG (German Society of Physics) and EMB German section of IEEE.

On behalf of all authors I would also like to thank Eva Hestermann-Beyerle and Monika Lempe (Springer Publisher Heidelberg) for their help in the preparation of these proceedings.

Remagen/Lübeck, March 2007

Thorsten M. Buzug
Conference Chair

Contents

Part V Biomedical Optics

Invited Paper

Modelling and Imaging Electrophysiology and Contraction of the Heart

Olaf Dössel, Dima Farina, Matthias Mohr, Matthias Reumann, Gunnar Seemann and Daniel L. Weiss

Institute of Biomedical Engineering, Universität Karlsruhe (TH), Kaiserstr. 12,
76131 Karlsruhe, Germany
E-mail: olaf.doessel@ibt.uni-karlsruhe.de

Abstract. A computer model of the human heart is presented, that starts with the electrophysiology of single myocardial cells including all relevant ion channels, spans the de- and repolarization of the heart including the generation of the Electrocardiogram (ECG) and ends with the contraction of the heart that can be measured using 4D Magnetic Resonance Imaging (MRI). The model can be used to better understand physiology and pathophysiology of the heart, to improve diagnostics of infarction and arrhythmia and to enable quantitative therapy planning. It can also be used as a regularization tool to gain better solutions of the ill-posed inverse problem of ECG. Movies of the evolution of electrophysiology of the heart can be reconstructed from Body Surface Potential Maps (BSPM) and MRI, leading to a new non-invasive medical imaging technique.

1. Introduction

Computer modelling of the human heart gains considerable interest. In the beginning it was motivated by basic research in physiology. The Physiome-Project [1] covers various organs of the body but has a focus on the heart: the Cardiome-Project. The heart is characterized by a complex interplay between electrophysiology, elastomechanics, fluid dynamics, metabolism as well as hormonal and neural control. Mathematical modelling can reveal complex macroscopic and cellular control circuits. The mathematical models bridge the nanometer scale of ion channels to the meter scale of the organ and the body. A temporal resolution of milliseconds has to be applied to understand the cellular processes and a second or even a minute scale has to be chosen to understand the heart rhythm. Laboratory data gained with isolated cells (voltage clamp or patch clamp technique) have to be combined with clinical data like the ECG or MRI data. Meanwhile an amazing amount of comprehension about the healthy heart was achieved but also many open questions remain [2, 3].

A major next step is the understanding of the diseased heart. The most important two topics are the modelling of ischemia/infarction and the modelling of arrhythmias. A prerequisite is the knowledge of some hundred parameters like rate constants of ion channels, electric conductivities or elastic constants of tissue for the diseased heart. In this field of research some remarkable results have been published but many important aspects need further research.

The final goal of computer modelling of the heart will be the creation of a virtual heart of the individual patient that includes precisely the health problem of this patient. The very challenging task is to measure as many data of the patient as needed to adapt the standard model to the individual one. Achieving this goal will lead to an in-depth diagnosis that goes down to the cellular origin of a disease. It would enable the medical doctor to try out any type of therapy first with the virtual heart, to decide which therapy is best suited for the patient and then to transfer the virtual therapy into reality.

This article is a brief review of the results of the last 5 years in the field of electrophysiological and elastomechanical modelling of the healthy and diseased human heart. It discusses the impact on future diagnosis and therapy planning.

2. Computer Models of Myocardial Cells

The computational reconstruction of cellular electrophysiology started in 1949 by Hodgkin and Huxley, who described the dynamic electrophysiology of a giant squid axon [4]. They measured the active and passive electrical behavior and found a set of equations reconstructing the measured data.

Most of the cardiac electrophysiological models are based on the Hodgkin-Huxley formalisms. They consist of mathematical reconstructions of ionic currents through channels, pumps, and exchangers. These currents depend on time, on transmembrane voltage, and on the concentration of ions and other substances. They represent the ionic flow through the pores of the cellular membrane as well as through membranes of intracellular structures.

The cellular membrane is presented with an electrical equivalent circuit consisting of a capacitance, variable and static conductances, and voltage sources. The conductances depict the different ion channels and the voltage sources are the Nernst potentials building a selective permeable membrane. A simple model to describe the movement of charge through a membrane, which is selective for only the ion type X, is given by an ohmic conductor

$$I_X = g_{X,max}\, N\, (V_m - E_X) \tag{1}$$

The value $g_{X,max}$ is the maximum conductance of the channel and (V_m-E_X), with the Nernst potential E_X, is the driving electrical force for the ions. N represents the fraction of the maximum conductances actually valid at a specific time instant. This coeffient is described by multiplication of the state variables of several gates and varies between zero and 1. The voltage and time-dependent change of a gate is given by a first-order reaction, where the gating particles transit between the permissive and nonpermissive forms with voltage-dependent rate constants α_n and β_n. If the initial value of the gate n is known, subsequent values can be calculated by solving the differential equation

$$\frac{dn}{dt} = \alpha_n\,(1-n) - \beta_n\, n \tag{2}$$

The sum of the several membrane currents I_X combined with the intercellular stimulus current I_{stim} determines the temporal derivative of the transmembrane voltage V_m across the membrane with the capacitance C_m

$$\frac{dV_m}{dt} = -\frac{1}{C_m}\left(\sum I_X - I_{stim}\right) \tag{3}$$

With this approach, the value of the currents and of the transmembrane voltage can be calculated for every time step by solving the according set of differential equations. Recently published models consist of up to 60 equations describing the properties of the cell membrane, ionic concentrations, intracellular structures like the sarcoplasmic reticulum, and calcium buffering mechanisms and also consider the effects of mechanical stretch to the cell. During recent years specific cell models of atrial and ventricular tissue have been published (see section 3.and 4).

The conduction of the excitation in the heart is based on the electrical coupling between cells. Commonly, excitation conduction is calculated in tissue with a macroscopic approach. Using this, the tissue is described as a continuum. One computational node is reproducing the properties of several real myocytes. The macroscopic methods can be divided into three different types: Cellular automata being rule based systems (see section 5), simplified reaction-diffusion systems neglecting mainly the complex flow of ions through the cell membrane and through gap junctions (low resistance connection between cardiac cells) [5], and models of the electrical flow combined with detailed electrophysiological descriptions, i.e. monodomain and bidomain models [6].

3. Computer Models of Electrophysiology of Atria

The two atria form the upper part of the heart. Inside of the atrial tissue the cardiac pacemaker is located called as the sinoatrial node. The electrical activity is conducted from that structure all over the atrium along specialized conduction bundles and the atrial muscle towards a structure that allows the propagation from atrium to the ventricles.

Several different electrophysiological models exist describing properly different atrial myocytes like sinoatrial node and atrial working myocardium for different species like human and rabbit (for an overview see [7]). Recently, these models have been modified to reconstruct heterogeneity in atrial electrical activity, to describe the changes on protein level during atrial fibrillation and to investigate the influence of genetic defects in ion channels in the cell membrane on atrial activity [7].

Detailed anatomical structures combined with fast conducting bundles including the description of fibre orientation and electrical heterogeneity have to be considered in computer simulations of the whole atrium in order to reproduce the normal excitation pattern in the atrium seen experimentally. Several groups have modeled whole human atrial activity with varying detail of anatomical and electrophysiological information [7, 8, 9, 10]. These models reconstruct measured electrical data from inside the atrium appropriately. Some of the models were extended to investigate arrhythmia and their treatment with ablation therapy. Fig. 1 illustrates a physiological sequence of excitation in the human atrium. The

excitation is initiated in the sinoatrial node and conducted fastest in the right atrium and towards the left atrium along the conducting bundles. After the activation, repolarization occurs and the atrium is again in the resting phase.

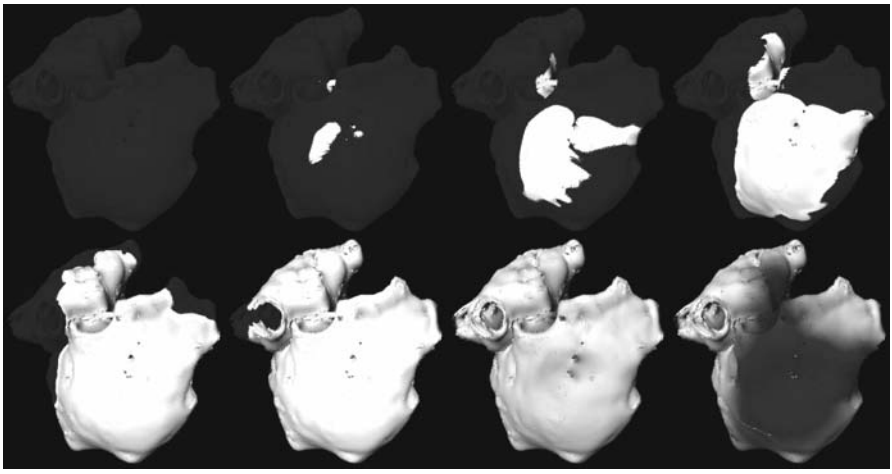

Fig. 1. Simulated excitation conduction in the atria in a frontal view at different time instances. The transmembrane voltage is illustrated color coded from blue V_m=-70mV to yellow V_m=10 mV [7]

4. Computer Models of Electrophysiology of Ventricles

Models describing the human ventricular electrophysiology have been published by Priebe and Beuckelmann [11], Bernus et al. [12], ten Tusscher et al. [13, 14] and by Iyer et al. [15].

Cells isolated from different regions of the ventricle display a characteristic response to pharmacological agents, expression of pathology, and their electrophysiological properties [16]. Thus, parameters of a ventricular model are determined by the position of the cell within the heart. In the heterogeneous ventricular myocardium, three principal cell types can be distinguished: subendocardial, subepicardial and M cells. The main distinctive feature is the variable action potential shape and duration.

Recently, formalisms were integrated into the models to represent the transmural electrophysiological heterogeneity [17]. Smooth gradients of maximum ion channel conductivity and kinetics across the virtual wall affect the distinctive properties of the transmurally varying cell types. The orientation of the muscle fibres was included in the underlying anatomical model allowing the incorporation of anisotropic electrical and mechanical properties. The fibre orientation was extracted from a Diffusion Tensor Magnetic Resonance Imaging (DTMRI) measurement of a human heart [18, 19].

Due to the resulting heterogeneous action potential duration (APD) a transmural dispersion of repolarization (TDR) is induced. M cells generating the longest APD were located near to the endocardium to obtain a realistic upright

positive T wave in the transmurally computed ECG [20]. Fig. 2 shows a simulation of the activation and repolarization of a healthy human ventricle.

With this framework the influence of drugs, medical treatment or mutations on the heart can be investigated by changing the properties of the underlying cellular models. Epicardial stimulation e. g. during biventricular pacing prolongs the QT interval and the TDR as an index of arrhythmogenicity. This has been shown in measurements as well as in simulations [21, 22, 23]. Pathological or mutant modifications of the models (e. g. long and short QT, Brugada-syndrome) can be used to investigate the influence of drugs or therapy to affected persons [24, 25, 26].

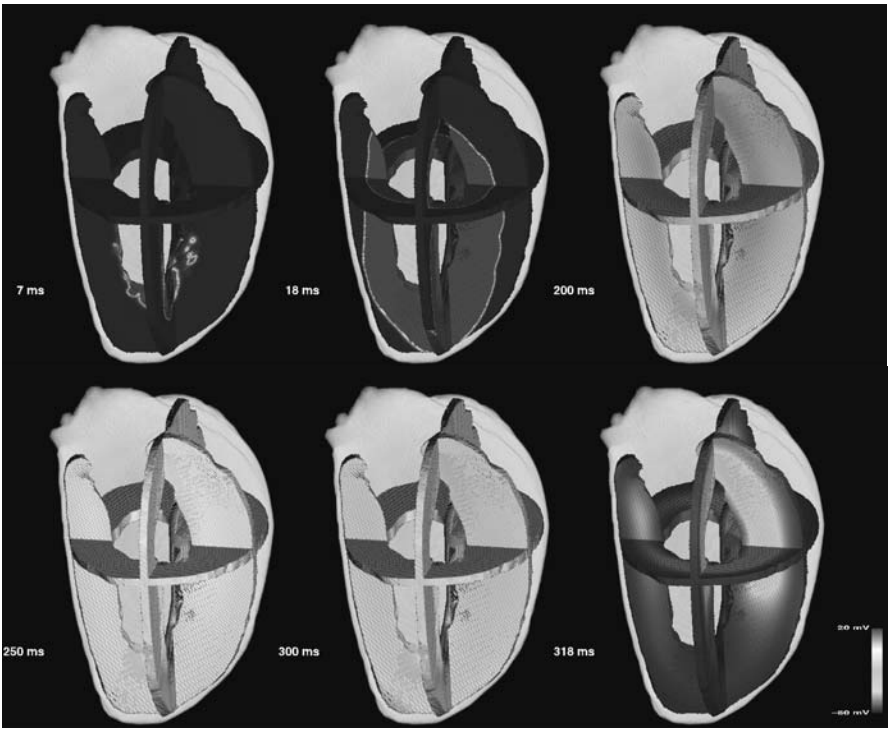

Fig. 2. Initiation, conduction and repolarization of excitation in a computational model of the human left ventricle. The transmembrane voltage is depicted color-coded at different time steps. Due to the prolonged APD of the M cells, the final repolarization vanished in this region leading to a positive T wave in the transmural ECG (adapted from [25])

5. Cellular Automaton Models

The cell models described in the previous sections provide an exact description of the electrophysiology of a single cardiac cell as well as of parts of the heart. Still the simulation of a de- and repolarization cycle for the whole heart with their means is a non-trivial task requiring a huge computational power.

The cellular automaton is a convenient mathematical model to describe the excitation propagation through the heart macroscopically. If the transmembrane voltage of a myocardial cell exceeds the threshold potential, the cell gets excited and triggers the excitation of the neighboring cells.

A typical anatomical model of the heart required for the cellular automaton is shown in Fig. 3. This model is based on the MEET Man data set [27]. It includes left and right ventricles, left and right atria as well as an automatically generated conduction system. The geometry of the heart is defined on a regular mesh with the resolution of $1\times1\times1$ mm^3. Also cellular automata based on irregular meshes were published [28].

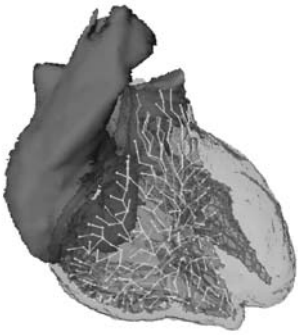

Fig. 3. The anatomical model of the heart used for the cellular automaton. Ventricles, atria and conduction system are shown

The voxels of the sinus node as well as of the AV-node are excited automatically with different frequencies. The excitation propagates from the sinus node over the atria and gets to the AV-node. Afterwards the conduction system carries the excitation to the ventricles. A typical excitation sequence is shown in Fig. 4. The cellular automaton generates the excitation times for each voxel; the time course of transmembrane voltage for each voxel has been previously generated using the ten Tusscher cell model [14].

The cellular automaton based cardiac model is able to simulate various cardiac diseases. For example, different bundle branch blocks can be introduced by slight changes in the conduction system. Decreasing the action potential amplitude and excitation propagation velocity in some regions of the myocard represents an ischemia or an infarction [29].

After the solution of the forward problem of electrocardiography, one obtains a simulated ECG, which can be compared with really measured Body Surface Potential Maps (BSPM). In case a measured ECG of a patient is provided, one can optimize the parameters of the cellular automaton in order to adapt the model to the individual BSPM [30].

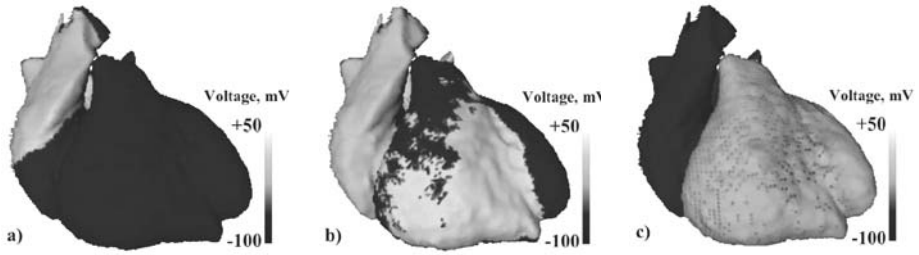

Fig. 4. A single heart cycle simulated with the cellular automaton. Depolarization of atria (a), depolarization of ventricles (b) and repolarization of ventricles (c) are shown

6. Computer Models of Tension Development

The mechanical function of a cardiomyocyte is initiated by electrical excitation. This process is called excitation contraction coupling (ECC). The electrical activation of the muscle cell is responsible for an increasing concentration of intracellular calcium, which, in turn, triggers the tension development in the force generating units by binding of calcium to intracellular proteins which then interact with each other to shorten the cell length. Several force generating units are combined into segments called sarcomeres and several lines of serial sarcomeres form the mechanical frame of a muscle cell.

Tension development is described in the models by different states, which are derived by physiological interactions between the intracellular proteins troponin, tropomyosin, actin, and myosin [31, 32]. The transition rates between these states are influenced by several parameters, e.g. the intracellular calcium concentration and the extent of stretch of the sarcomeres. The intracellular calcium concentration acts as an input for the models and is the mediator between electrophysiology and tension development.

The recent tension development model consists of 14 state variables incorporated in three coupled Markov chain models describing the three components troponin, tropomyosin, and actin-myosin interaction [33]. Cooperativity mechanisms are included in the model such that they influence specific transition probabilities between states depending on other states and transitions. To illustrate the high quality of the model a myofilament break up measurement performed by Peterson and co-workers [34] was reconstructed with the model. Figure 5 shows the result of the model and the experiment where the cell was stretched for 20 ms to an extent of 4.6 % and was relaxed afterwards.

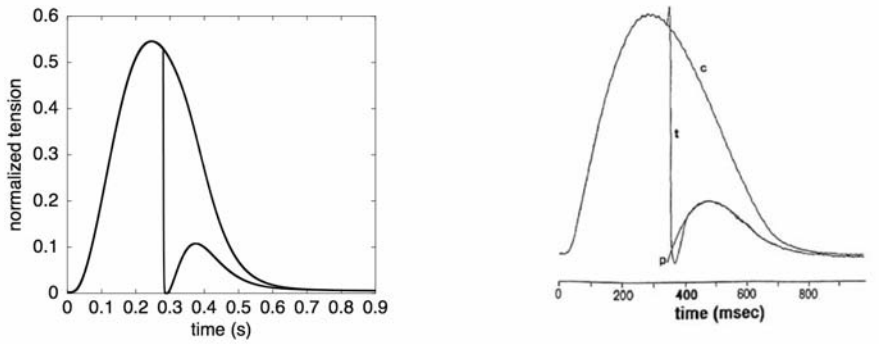

Fig. 5. Normalized tension during fast length changes achieved in intact cells that were electrically stimulated. Simulation (left), measured data (right) [7]

7. Computer Models of Contraction

The objective of this section is to illustrate how to calculate the time course of contraction from the tension developed in the myocardium cells. Ingredients are the anisotropic and nonlinear passive elastic properties of the heart. In addition reasonable assumptions have to be made about the boundary conditions: where and how is the heart fixed in the body, how is the heart contracting during the phase of closed valves (constant ventricular volume!), how is the blood ejected into the aorta (fluid dynamics!), how can we describe the relaxation and refilling through the atria?

Passive elastic properties of myocardial tissue have been measured and modelled by Guccione et al. [35] and Hunter et al. [36] leading to energy density functions with an appropriate choice of materials parameters.

Finite Element Method FEM has been employed by some groups to solve the elastomechanical problem. Sachse [37] developed a model based on finite deformations using the strain energy density function of Guccione et al. [35]. Hunter et al. established a biventricular model, based on 3D continuum mechanics [38, 39]. The model was further extended in the work of McCulloch [40]. Bourguignon [41] published a spring mass model of muscle tissue that included additional springs for anisotropy and incompressibility. Mohr [42] presented an extension of this spring mass model using the energy density function of Guccione [43] and Mooney Rivlin to adjust the springs according to the continuum mechanical models mentioned above. The heart is fixed at the apex, the outflow into the aorta is approximated by a Windkessel model, and for the relaxation a simple exponential pressure fall was assumed.

The model is used to describe the contraction and relaxation of the heart of a volunteer, for whom the real contraction was imaged using MRI. This way the results of the simulation can be compared to real data. The cellular automaton described in section 5 was used for propagation of depolarization and the model of Sachse et al. described in section 6. was used for tension development. The results (Fig. 6) show a very close similarity between simulation and MRI measurement during the contraction phase. Small differences can be explained by

the fact that only a left ventricle was simulated. The relaxation phase is much faster in reality as compared to simulation. Here a much faster refilling from the atria has to be considered.

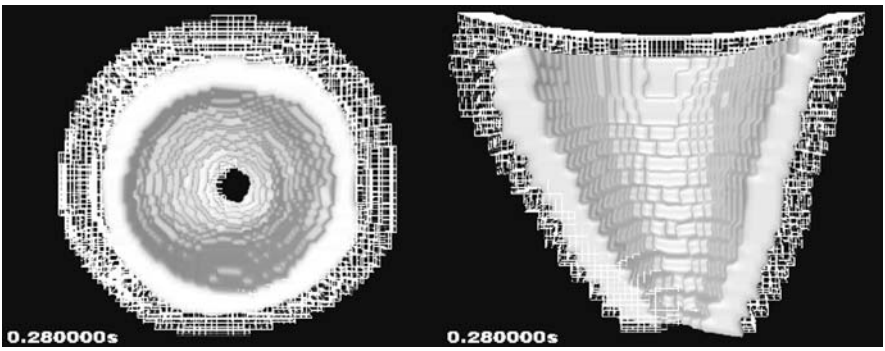

Fig. 6. Simulated contraction of the left ventricle, unfilled grid: heart geometry of the volunteer in end-diastolic phase, filled grid: heart geometry in the diastolic phase [42]

8. Solving the Inverse Problem using Computer Models of the Heart

The inverse problem of electrocardiography consists in the reconstruction of the cardiac source distributions given the results of the ECG measurements. If the forward problem is formulated as:

$$A\mathbf{x} = \mathbf{b}, \tag{4}$$

where b is the measured ECG at some time instant, x is the unknown cardiac source distribution and A is the lead-field matrix, the task of the inverse problem solution is to find such x that best fits this equation.

This problem is ill-posed. In other words, arbitrary small changes of the ECG lead to arbitrary large fluctuations of the solution. Thus, some kind of regularization must be performed by introducing *a priori* information into the problem to stabilize the solution.

The cardiac model described in section 5 is an ideal source of the *a priori* information. The simplest way to apply these data is the Twomey regularization [44]. It consists in the minimization of the following functional:

$$\mathbf{x}_\lambda = \arg\min(||A\mathbf{x} - \mathbf{b}||_2^2 + ||L(\mathbf{x} - \tilde{\mathbf{x}})||_2^2), \tag{5}$$

where L is the regularization operator, and $\tilde{x}$ is the a priori estimation of the solution obtained from a heart model.

Another approach is called *minimum a posteriori* (MAP) method introduced in [45, 46]. An estimator H of the inverse matrix A^{-1} is defined as follows:

$$H = C_x A^T \left(A C_x A^T + C_e \right)^{-1}, \tag{6}$$

where C_x is the covariance matrix of the a priori estimations and C_e is the covariance matrix of errors. These covariances can be spatial [47] or spatiotemporal [48]. The matrices are built from the results of simulations performed with parameters of the cellular automaton model being varied. The method can be considered to select the best solution out of the provided set of estimations that fits the input ECG.

In order to prove the quality of reconstruction, following approach is used: First, a single simulation using the cellular automaton model is performed. Then the forward problem is solved. After the introduction of 1% noise into the resulting ECG, the inverse problem is solved. The correlation between original cardiac source distribution and the reconstructed one is computed for each time instant. The results obtained using spatial MAP, spatiotemporal MAP regularization methods employing the simulation data as well as Tikhonov regularization without the simulation data are compared in Fig. 7.

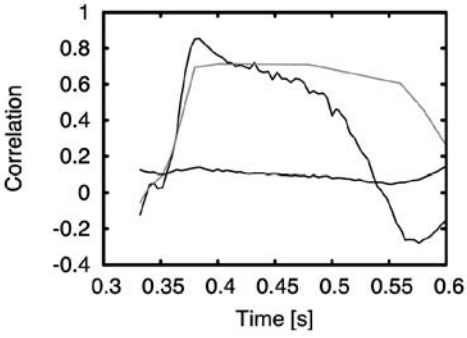

Fig. 7. The correlation between original and reconstructed epicardial potentials. Shown are the results obtained using spatiotemporal MAP (green line), spatial MAP (red line) and Tikhonov regularization methods

9. Clinical Applications

Clinical applications of computer models of the heart can be found in diagnosis and therapy of ischemia/infarction, aneurysms and arrhythmias. This section concentrates on arrhythmias, where the earliest applications are expected.

An optimal ablation therapy in atrial fibrillation (AF) is subject to current clinical research. While clinical studies can only investigate the outcome of a single ablation procedure to one patient, computer models bear the potential to investigate the effect of different ablation strategies with respect to each patients anatomy and electrophysiology prior to the interventional or surgical procedure. A

simulation study [49] of 23 different set–ups of ectopic beats in the pulmonary veins to generate AF showed the importance to guarantee transmural lesions: Only circumferential lesion sets with transmural lesions isolate the ectopic triggers and yield 100 % success rates. However, if the lesions had gaps, i. e. there was a bridge of active tissue between the pulmonary veins and the left atrium, AF could not be prevented in all cases. The success rate was increased if linear lesions were added (see fig. 8). Thus, the computer model gives an insight in AF initiation and maintenance as well as the effect of therapeutical strategies on a specific pathological set–up.

Optimization of cardiac resynchronization therapy (CRT) with respect to electrode position and optimal atrio-ventricular (AV) and interventricular (VV) delay is investigated these days [50, 51]. While the electrode position plays an important role for optimal cardiac output, the AV– and VV–delay is not adjusted to each patient in clinical practice since it is very time consuming. However, an optimal AV– and VV–delay increases the success rate of CRT.

By assuming that the physiological excitation of the heart yields the optimal cardiac output, a measure can be defined with which the electrode position as well as the AV– and VV–delay can be computed automatically by a computer model [52]. The root mean square error E_{RMS} between the electrical activation times of the ventricles in the physiological case and the pathology or therapy has to be minimized. The smaller the E_{RMS}, the closer the electrical activation times of the ventricles to its physiological behaviour. Simulating an AV and left bundle branch block with 100 %, 80 % and 60 % conduction velocity in the ventricular myocardium on different anatomical data-sets yields a significant reduction in the E_{RMS} for the optimal therapy.

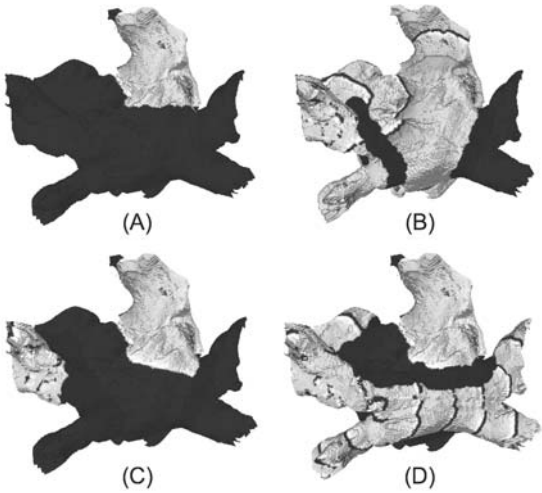

Fig. 8. The initial trigger was set at the left superior pulmonary vein. (A) The ablation strategy by Benussi et al. yielded the highest success rate in the first procedure with non–transmural lesions. The same ectopic trigger still caused fibrillatory conduction if the linear lesions were left out (B). If transmurality was achieved, the success rate was increased (C). However, fibrillation was observed in the isolated regions (C–D) [49]

The results of these studies show the potential role of computer models in therapy planning and optimization. Different ablation strategies can be evaluated for a specific patient. CRT can be automatically optimized with respect to electrode position and AV– and VV–delay. Future work will focus on clinical evaluation of the computer models and integration of patient data into the model for individualized therapy planning and optimization.

10. Conclusions and Outlook

The results demonstrate that mathematical modelling of electrophysiology and elastomechanics of the human heart is feasible, but also many open questions become visible. The description of heterogeneity of cells in various regions of the heart is not perfect. Intracellular and extracellular conductivities influence the results significantly but are not measured with sufficient accuracy. The influence of the autonomous nervous system, which is known to have a strong effect on the onset of arrhythmia is not included yet.

For genetic diseases like long QT syndroms the knowledge about the cellular data is quite extended so that a mathematical model of the whole heart of these patients becomes feasible. Other diseases like infarction or acquired arrhythmias are not well understood from the mathematical modelling point of view. The mathematical description of the process of "remodelling", in which the distribution of ion channels is modified due to an ongoing disease, will become a real challenge.

The adaptation of the standard model to the individual patient has just begun with only preliminary results. The benefit for the patient is only visible at the horizon.

Acknowledgements. The authors would like to thank David Keller for substantial contributions to fibre tracking, Julia Bohnert for substantial contributions to modelling of RF ablation and Yuan Jiang for substantial contributions to covariance matrix supported inverse problem solutions.

References

1 www.physiome.org.
2 P. J. Hunter, Modeling Human Physiology: The IUPS/EMBS Physiome Project, *Proceedings of the IEEE*, vol. 94, no. 4, 678-691, 2006.
3 D. Noble, Modeling the Heart: From genes to cells to the whole organ, *Science,* vol. 295, 1678-1682, 2002.
4 A. L. Hodgkin and A. F. Huxley, in *J. Physiol*., Vol. 177, pp. 500, 1952.
5 R. A. FitzHugh, in *Biophys J.*, Vol. 1, 445, 1961.
6 C. S. Henriquez, A. L. Muzikant and C. K. Smoak, in *J Cardiovasc Electrophysiol.*, Vol. 7, No. 5, 424, 1996.
7 G. Seemann, *Modeling of electrophysiology and tension development in the human heart*, Universitätsverlag Karlsruhe, http://www.uvka.de/univerlag/volltexte/2005/75/, 2006.

8 O. Blanc, N. Virag, J.-M. Vesin and L. Kappenberger, in *IEEE Transactions on Biomedical Engineering,* Vol. 48, No. 12, 1229, 2001.

9 C. W. Zemlin, H. Herzel, S. Y. Ho and A. Panfilov, in *Computer Simulation and Experimental Assessment of Cardiac Electrophysiology*, Futura, Edited by N. Virag, O. Blanc and L. Kappenberger, 29, 2001.

10 D. M. Harrild and C. S. Henriquez, in *Circ Res.*, Vol. 87, No. 7, e25, 2000.

11 L. Priebe and D. J. Beuckelmann, in *Circ. Res*., Vol. 82, 1206, 1998.

12 O. Bernus, R. Wilders, C. W. Zemlin, H. Verschelde and A. V. Panfilov, in *Am. J. Physiol.,* Vol. 282, H2296, 2002.

13 K. H. W. J. ten Tusscher, D. Noble, P. J. Noble and A. V. Panfilov, in *Am. J. Physiol.,* Vol. 286, H1573, 2004.

14 K. H. Ten Tusscher and A. V. Panfilov, in *Am J Physiol Heart Circ Physiol*., Vol. 291, No. 3, H1088, 2006.

15 V. Iyer, R. Mazhari and R. L. Winslow, in *Biophys. J.*, Vol. 87, No. 3, 1507, 2004.

16 C. Antzelevitch, G. Yan, W. Shimizu and A. Burashnikov, in *Cardiac Electrophysiology. From Cel l to Bedside*, Edited by. P. Zipes and J. Jalife,, Ch. 26, 222, Philadelphia: W. B. Saunders Company, 3 ed., 1999.

17 G. Seemann, F. B. Sachse, D. L. Weiß and O. Dössel, in *J. Cardiovasc. Electrophysiol.*, Vol. 14, 219, 2003.

18 http://www.ccbm.jhu.edu/research/DTMRIDS.php

19 D. U. J. Keller, *Detailed anatomical and electrophysiological modeling of human ventricles based on diffusion tensor MRI,* Diploma thesis, Institute of Biomedical Engineering, Universität Karlsruhe (TH), 2006.

20 D. L. Weiß, G. Seemann and O. Dössel, in *Proc. BMT*, Vol. 49-2/1, 364, 2004.

21 J. M. Fish, J. M. Di Diego, V. Nesterenko and C. Antzelevitch, in *Circulation*, Vol. 109, No. 17, 2136, 2004.

22 V. A. Medina-Ravell, R. S. Lankipalli, G.-X. Yan, C. Antzelevitch, N. A. Medina-Malpica, O. A. Medina- Malpica, C. Droogan and P. R. Kowey, in *Circ*ulation, Vol. 107, No. 5, 740, 2003.

23 D. L. Weiss, G. Seemann and O. Dössel, in *Proc. IFMBE / EMBEC*, Vol. 11, 2005.

24 G. Seemann, D. L. Weiß, F. B. Sachse and O. Dössel, in *Proc. Computers in Cardiology*, Vol. 30, 287, 2003.

25 D. L. Weiss, G. Seemann, F. B. Sachse and O. Dössel, *in Europace*, Vol. 7S2, 105, 2005.

26 D. L. Weiss, G. Seemann, F. B. Sachse and O. Dössel, in *Proc. Computers in Cardiology,* Vol. 32, 117, 2005.

27 F. Sachse, C. Werner, K. Meyer-Waarden and O. Dössel, in *Computerized Medical Imaging and Graphics,* Vol. 24, 165, 2000.

28 B. Messnarz, B. Tilg, G. Fischer and F. Hanser, in *IEEE Trans. Biomed. Eng*., Vol. 51, 273, 2004.

29 D. Farina, O. Skipa, C. Kaltwasser, O. Dössel and W. R. Bauer, in *Int. J. Bioelectromagn*., Vol. 7, No. 1, 2005.

30 D. Farina, O. Skipa, C. Kaltwasser, O. Dössel and W. R. Bauer, in *Proc. Computers in Cardiology*, Vol. 31, 129, 2004.

31 A. Landesberg and S. Sideman, in *J Physiol.*, Vol. 267, H779, 1994.

32 J. J. Rice, R. L. Winslow and W. C. Hunter, in *Am J Physiol.*, Vol. 276, H1734, 1999.

33 F. B. Sachse, K. Glänzel and G. Seemann, in *Int J Bifurc Chaos*, Vol. 13, No. 12, 3561, 2003.

34 J. N. Peterson, W. C. Hunter and M. R. Berman, in *Am J Physiol.*, Vol. 260, H1013, 1991.

35 J. M. Guccione, A. D. McCulloch and L. K. Waldman, in *J. Biomechanical Engineering,* Vol. 113, 42, 1991.

36 P. J. Hunter , A. D. McCulloch and. H. E. D. J. ter Keurs in *Prog. Biophys. Mol. Biol.*, Vol. 69, 289, 1998.

37 F. B. Sachse, in *Computational Cardiology: Modeling of Anatomy, Electrophysiology, and Mechanics,* LNCS 2966, Heidelberg: Springer Press, 2004

38 P. J. Hunter, in *Molecular and Subcellular Cardiology: Effects of Structure and Functions*, Edited by S. Sideman and R. Beyar, 303, Plenum Press, New York, 1995.

39 P. Hunter, M. P. Nash and G. P. Sands in *Computational Biology of the Heart*, Edited by A. V. Panfilov and A. V. Holden, 345, John Wiley & Sons, Chichester, 1997.

40 A. D. McCulloch, in *The Biomedical Engineering Handbook*, Edited by J. D. Bronzino, 28-1, CRC Press, 2000.

41 D. Bourguignon and M.-P. Cani, in *Computer Animation and Simulation, Proc. 11th Eurographics Workshop, Interlaken, Switzerland*, 113, Springer, 2000.

42 M. Mohr, A hybrid deformation model of ventricular myocardium, Thesis, Institute of Biomedical Engineering, University of Karlsruhe, 2006.

43 J. M. Guccione, in *Theory of Heart*, Edited by L. Glass, P. Hunter and A. McCulloch, 121, Springer, New York, 1991.

44 C. Hansen, *Rank-deficient and discrete ill-posed problems: numerical aspects of linear inversion* SIAM, Philadelphia, 1998.

45 D. Jackson, in *Geophys. J. R. astr. Soc*., Vol. 57, 137, 1979.

46 A. van Oosterom, in *IEEE Trans. Biomed. Eng*., Vol. 46, 778, 1999

47 D. Farina, Y. Jiang, O. Skipa, O. Dössel, C. Kaltwasser and W.R. Bauer, in *Proc. Computers in Cardiology*, Vol. 32, 571, 2005.

48 Y. Jiang, D. Farina, C. Kaltwasser, O. Dössel and W.R. Bauer, in *Proc. Gem. Jahrestagung für Biomed. Technik*, 2006

49 M. Reumann, J. Bohnert, G. Seemann, B. Osswald and O. Dössel, in *IEEE Transactions on Biomedical Engineering*, 2006. submitted October 10th.

50 L. C. M. van Campen, F. C: Visser, C. C. de Cock, D. h. S. Vos, O. Kamp and C. A. Visser.. in *Heart*, published online, Jun 2006.

51 Z. I. Whinnett, J. E. R. Davies, K. Willson, C. H. Manisty, A. W. Chow, R. A. Foale, D. W. Davies, A. D. Hughes, J. Mayet and D. P. Francis, in *Heart* published online 18 May, 2006.

52 M. Reumann, K. Nissen, G. Reinerth, G. Seemann, C. F. Vahl, S. Hagl and O. Dössel, in *Europace,* Vol. 8, Suppl. 1m 231/1, 2006.

Part I

Medical Imaging

Influence of Corrections During Image Reconstruction on the Spatial Resolution of ClearPET Neuro

Christine Steenkamp[1], Simone Weber[2], Brigitte Gundlich[2], Patrick Musmann[2] and Thosten M. Buzug[3]

[1] Department of Mathematics and Technology, RheinAhrCampus Remagen, Germany
E-mail: csteenka@rheinahrcampus.de
[2] Forschungszentrum Jülich, Zentralinstitut für Elektrotechnik, Germany
[3] Institute of Medical Engineering, University of Luebeck, Germany

Abstract. The small-animal PET scanner ClearPET Neuro developed at the Research Centre in Jülich is based on an unconventional scanner geometry. It represents axial and transaxial gaps that lead to sinograms with missing data. Images reconstructed from uncorrected data include artefacts and a high variation of spatial resolution between different slices. Methods to compensate these artefacts are applied by taking the geometrical sensitivity into account. In this work the effects of compensation strategies with regard to the slice by slice variation of spatial resolution are examined.

1. Introduction

The ClearPET [1] has a detector geometry of 20 modules, each consisting of 4 submodules (see Figure 1). Every 2nd module is axially shifted. The 8x8 crystal matrix is made of LSO and LuYAP [2] in phoswich technique. The rotation of the gantry is about 360°.

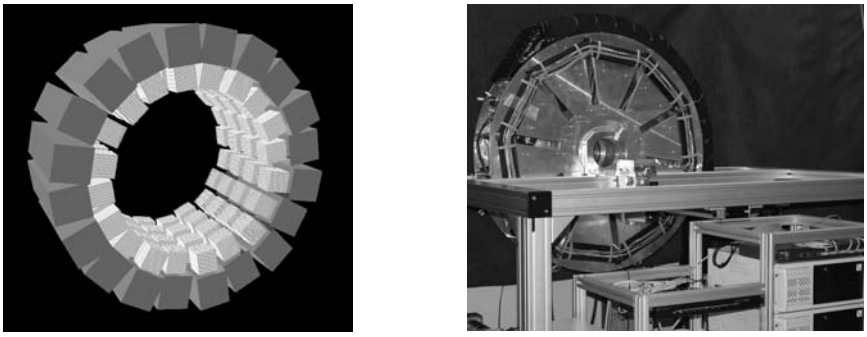

Fig. 1. Detector geometry of ClearPET Neuro

To obtain high quality images, the special detector sensitvity has to be considered during reconstruction or the gaps in the sinograms have to be filled. Therefore,

normalised sinograms have to be created. These data consists of every possible combination of detectors only once and describe the detector sensitivity with its gaps and inhomogeneity [3] (see Figure 2).

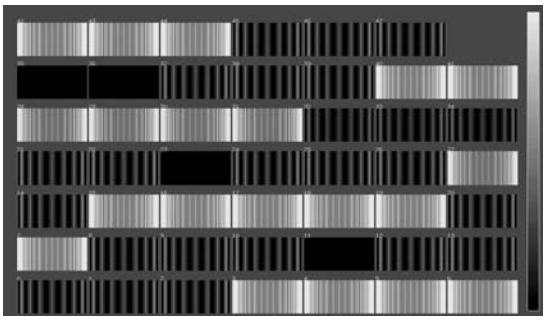

Fig. 2. Normalizing sinograms with gaps and inhomogeneity

Filtered Backprojection. When the filtered backprojection is used as the reconstruction algorithm, the gaps in the sinograms have to be compensated, because the method needs continuous data. In a first step the measured sinograms are compensated by the normalizing sinograms, for example per division. Then these data are forward projected to a provisional image [4] (see Figure 3).

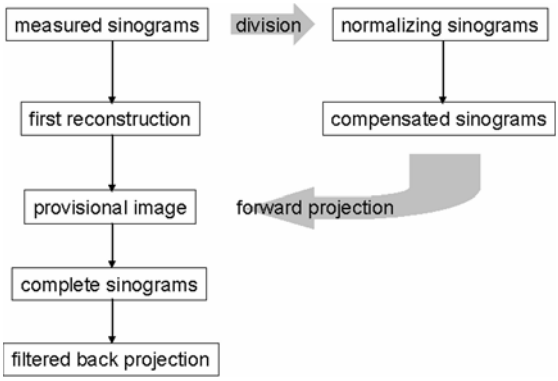

Fig. 3. Procedure of compensating during FBP

MLEM. When iterative reconstruction algorithms like the Maximum-Likelihood Expectation-Maximization are used, the geometrical sensitivity can be taken into account in the mathematical model.

$$f_i^{(k+1)} = \frac{f_i^k}{\sum_{j=1}^{m} a_{ji}} \sum_{j=1}^{m} a_{ji} \frac{p_j}{q_j^{(k)}}, q_j^{(k)} = \sum_{i=1}^{n} a_{ji} f_i^{(k)} \quad (1)$$

The system matrix a_{ji} connects the image values f_i $\{i = 1,....., n\}$ with the projecttions p_j, $\{j = 1,....., m\}$ and describes the probability of detecting a photon of voxel i in projection bin j.

The system matrix includes the sensitivity image

$$\sum_{j=1}^{m} a_{ji} \quad (2)$$

which characterizes the geometrical sensitivity. It is produced by the backprojection of a normalizing sinogram. These correction procedures suffer from very large differences in the correction factors. In this work, we examine the influence of the correction factor inhomogeneities on the spatial resolution over the Field-of-View.

2. Experimental Methods

A 2 mm diameter 18F filled line source with 11 cm length in a phantom of water of 5 mm diameter and 12 cm length was simulated using GATE [5]. Data are recorded with a maximum ring difference of 6 within an energy window of 350-650 keV, and are reconstructed using either 3D-OSEM or FBP. The spatial resolution for each slice is calculated by a polynomial-linear fitting, i.e. a polynomial is fitted to the maximum value and its two neighbors. Then the maximum of the fit is estimated, and a linear fitting is performed in the regions of the FWHM.

Line sources located with different radial offsets parallel to the scanner axis are used. With these data the radial and tangential resolution for each slice and for different positions with their specific detector sensitivity is calculated using different reconstruction parameters and corrections.

3. Results and Discussion

General Reconstruction Parameters. An adequate statistic is necessary to have a meaningful variation of the spatial resolution between the slices. If the statistic is too low, noise can appear and the resolution is highly over and underestimated, respectively. The noise increases when the source is positioned at a place with low detector sensitivity. At least around 2.2 million coincidences are needed at positions with low sensitivity.

With 3D-OSEM and correction for geometrical sensitivity a good image result is achieved with 20 iterations and 4 subsets. When 30 iterations are used the image is over-iterated. Then the peak splits into two parts and the resolution is underestimated. With a lower number than 20 iterations the slice by slice variation of resolution disappears and the image is blurred.

The zoom-factor (the division of one voxel into subvoxels) has a significant influence on the spatial resolution. 3D-OSEM and zoom factor 2 (the division of one voxel into 8 subvoxels) reveals an increasing of the resolution for each slice, (Table 1.). But with the use of a higher zoom-factor the resolution is overestimated in some slices. Otherwise, with zoom-factor 3 and FBP a continuous increasing of the resolution is achieved, (Table 2.).

Table 1. Effects of the zoom-factor on the radial resolution in the centre of the FOV. Images are reconstructed with 3D-OSEM. The individual detector sensitivity can be specified more detailed with zoom-factor 2, although this factor has almost no influence on the sensitivity profile with an odd number of tangential positions.

Zoom	Average FWHM [mm]	Standard deviation [mm]
1	2.81	0.01
2	2.45	0.03
3	1.54	0.04

Table 2. Effects of the zoom-factor on the radial resolution in the centre of the FOV. Images are reconstructed with FBP. Zoom-factor 2 has no influence to the sensitivity profile with an odd number of tangential positions, so the FWHM is not improved with FBP.

Zoom	Average FWHM [mm]	Standard deviation [mm]
1	2.68	0.01
2	2.68	0.01
3	2.27	0.01

Effect of Correction on Spatial Resolution. When a source is positioned with a radial offset to the scanner axis, the resolution decreases and the noise rises, because the detector sensitivity becomes lower (see Figure 4).

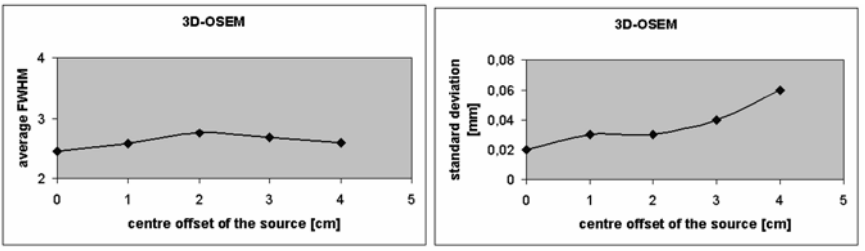

Fig. 4. Alteration of resolution and standard deviation concerning to centre offset (3D-OSEM). It seems that the average of the FWHM is not improved remarkable with a rising offset. This is only the case, because the noise increases with a rising offset and the FWHM is more and more underestimated.

With 3D-OSEM the deterioration of the radial resolution with a rising offset is higher than the deterioration of tangential resolution. Even the noise of radial resolution is higher.

With an offset of 1 cm and 3D-OSEM the gaps in the detector system have a strong influence when the correction for the geometrical sensitivity is missing (see Figure 5).

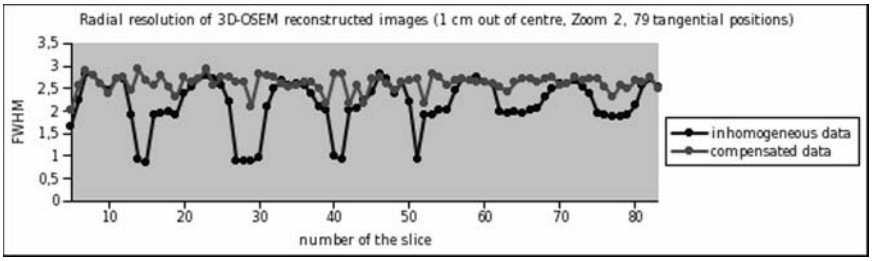

Fig. 5. FWHM with and without compensated data (1 cm centre offset and 3D-OSEM)

The resolution has highly under- and overestimated values in some slices. However, the resolution variation of the source with an offset of 1 cm is not remarkable, when the gaps are considered. Even the deterioration of the spatial resolution with a rising offset decreases when taking the detector sensitivity into account. But the noise is not improved, because the statistic becomes lower when the position of source approximates the end of the FOV.

The deterioration of the resolution is more continuous and equidistant when using FBP (see Figure 6).

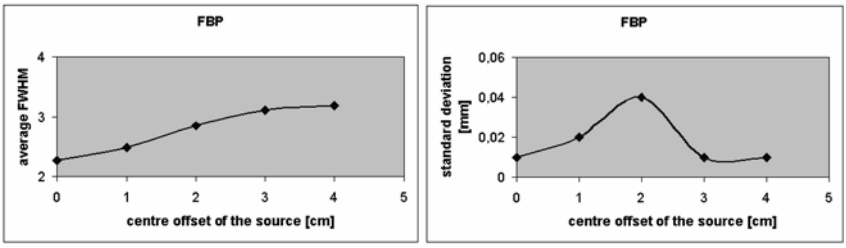

Fig. 6. Alteration of resolution and standard deviation concerning to centre offset (FBP)

The slice variation of the resolution is very high with a radial offset of 1 cm, too (see Figure 7). But this effect is well corrected when the gaps in the sinograms are filled.

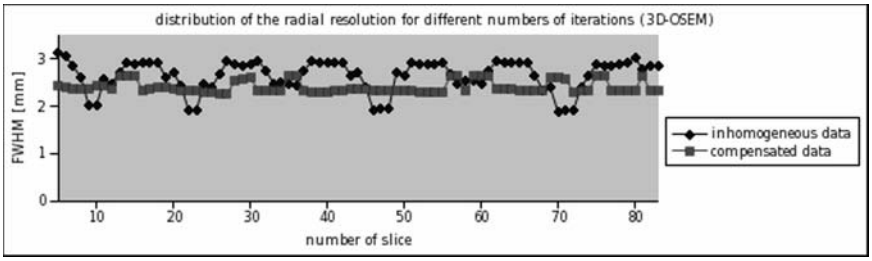

Fig. 7. FWHM with and without compensated data (1 cm centre offset and FBP)

4. Conclusions

The aim of this work was the examination of the influence of corrections during image reconstruction on the spatial resolution. Due to the unconventional scanner geometry of the ClearPET Neuro, for OSEM image reconstruction very large normalization factors have to be applied to correct for geometric effects, and for FBP some gap filling has to be performed. This work has shown that the spatial resolution variation is acceptable.

References

1 Ziemons K., Auffray E., Barbier R., et al., *The ClearPET^{TM} project: development of a 2nd generation high-performance small animal PET scanner*, Nucl. Instr. Meth. A 537 (2005) 307-311

2 Weber S., Christ D., Kurzeja M.,et al., 2003, *Comparison of LuYAP, LSO, and BGO as Scintillators for High Resolution PET Detectors*, IEEE Transaction on nuclear science, Vol. 50, No. 5 (2003) 1370-1372

3 Weber, S., Morel, C., Simon, L., et al., *Image reconstruction for the ClearPET Neuro*, 3rd International Conference on Imaging Technologies in Biomedical Sciences (ITBS 2005), Milos Island, Greece, 25.-28. Sep. 2005

4 Gundlich B., Weber S., Oehler M., *Compensation strategies for PET Scanners with unconventional Scanner geometry*, IEEE Nuclear Science Symposium & Medical Imaging Conference, Wyndham El Conquistador Resort, Puerto Rico, 23.- 29.10.2005

5 Jan S., Santin G., Strul D., et al., *GATE: a simulation toolkit for PET and SPECT*, Phys. Med. Biol. 49 (2004) 4543-4561

Dynamic Reconstruction for the ClearPET™ Neuro Using Temporal B-Splines

Brigitte Gundlich, Patrick Musmann and Simone Weber

Forschungszentrum Jülich GmbH, Central Institute for Electronics, 52425 Jülich, Germany
E-mail: b.gundlich@fz-juelich.de

Abstract. Dynamic reconstruction methods are studied for the small animal PET (positron emission tomography) scanner ClearPET™ Neuro. In dynamic reconstruction the data are usually sorted into timeframes and reconstructed independently of each other. Using this timeframe approach, an appropriate trade-off between time resolution and noise has to be found. A more advanced method is dynamic reconstruction with temporal basis functions, where voxel values are time dependent modeled as weighted sum of basis functions. In a simulated example list-mode data are generated for the ClearPET™ Neuro and reconstructed with timeframe reconstruction and with dynamic reconstruction using B-Splines as temporal basis functions. Time activity curves are computed for various reconstructions with different timeframes and B-Splines. The example demonstrates the potential of dynamic reconstruction with temporal B-Splines.

1. Introduction

The ClearPET™ Neuro [1], developed at the Research Center Jülich in cooperation with the Crystal Clear Collaboration, is a high performance small animal PET scanner dedicated for brain studies on rats and primates. Designed for receptor studies there is need for dynamic image reconstruction. The simplest way of dynamic reconstruction is timeframe reconstruction: the acquired data are sorted into a series of timeframes according to their detection time, then the data of each timeframe are reconstructed individually. Disadvantages of this simple method come from the underlying assumptions: first, the activity does not vary within a timeframe and, second, data of consecutive timeframes are completely independent of each other. To counteract the disadvantage arising from the first assumption, smaller timeframes and consequently a higher temporal sampling of the reconstructed images could be chosen, which on the other side reduces the number of counts per timeframe and increases the noise in the reconstructed images. The fact, that the data of different timeframes are processed completely independent of each other and information contained in the data of neighboring timeframes is ignored, is not plausible, as the metabolic processes should show some smoothness. To partially overcome the disadvantages of dynamic image reconstruction using timeframes, more sophisticated reconstruction algorithms, like dynamic reconstruction using temporal basis functions [2]-[4], are applied. The possibilities of B-Splines [5] as temporal basis functions are studied here for the ClearPET™ Neuro.

2. Dynamic Reconstruction

Time information plays an important role in image reconstruction with temporal basis functions. Therefore, list-mode reconstruction is predestinated as reconstruction method for dynamic processes. Compared to data representation with sinograms, list-mode data have the highest possible temporal resolution in data acquisition, as the corresponding timestamp can be stored for each detected event. The following reconstruction algorithms are applied to list-mode data.

Timeframe Reconstruction. The data of each timeframe are reconstructed. The iteration formula of the ML-EM (Maximum-Likelihood Expectation-Maximization) algorithm [6] for list-mode data [7], [8] is given by

$$x_{j,t}^{(k+1)} = \frac{x_{j,t}^{(k)}}{\sum_{i=1}^{I} a_{ij}} \sum_{i=1}^{N_t} \frac{a_{ij} y_{i,t}}{\sum_{l=1}^{M} a_{il} x_{l,t}^{(k)}} \tag{1}$$

with the activity distribution $x_{j,t}$ assigned to voxel j, j=1,...,M, in timeframe t at iteration (k) or (k+1), respectively. a_{ij} is the probability that an emission with origin in voxel j is detected in LOR (line of response) i. $y_{i,t}$ are the LORs observed in timeframe t with $y_{i,t}$=1 for list-mode reconstruction. I is the number of all different possible LORs in the scanner system and N_t the number of indeed detected coincident events in timeframe t.

Dynamic Reconstruction with Temporal Basis Functions. Applying dynamic reconstruction with temporal basis functions, a set of temporal basis function $b_c(t)$ c=1,...,C, has to be defined that enters into the reconstruction process [2]-[4]. Instead of estimating one activity value per voxel and timeframe, the activity value for a voxel $x_j(t)$ at time t is defined as a weighted sum of given temporal basis functions $b_c(t)$, whose weights $w_{j,c}$ refer to voxel j and basis function b_c

$$x_j(t) = \sum_{c=1}^{C} b_c(t) w_{j,c} \tag{2}$$

The weights $w_{j,c}$ at iteration (k+1) are estimated in analogy to the standard ML-EM algorithm

$$w_{j,c}^{(k+1))} = \frac{w_{j,c}^{(k)}}{\sum_{i=1}^{I} a_{ij}} \sum_{i=1}^{N} \frac{a_{ij} b_c(t_i) y_i}{\sum_{l=1}^{M} a_{il} x_l^{(k)}(t_i)} \tag{3}$$

with the observed coincident events y_i=1, i=1,…,N, detected at time t_i. According to equation (2), the activity value $x_j^{(k)}(t_i)$ can be computed for each iteration as linear combination of the weights and values of the temporal basis functions at the corresponding time.

3. Simulation and Image Reconstruction

To examine dynamic reconstruction, list-mode data sets were generated for the ClearPET^{TM} Neuro with the simulation toolkit GATE (Geant4 Application for Tomographic Emission [9]). A given time activity curve, see Figure 1., running over 60 minutes defines the input activity for a simulated sphere of 2.5 mm radius. The time activity curve is divided into time slices of 1 second, during this time period the simulation system is assumed to be static.

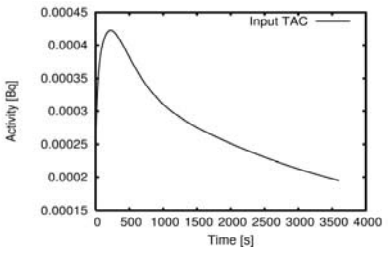

Fig. 1. Simulated time activity curve.

The simulated list-mode data are reconstructed using the ML-EM algorithm for timeframe reconstruction, equation (1), and its modified version for temporal basis functions, equation (2),(3), using B-Splines. B-Splines have shown to be suitable temporal basis functions. Due to their manifold versions - from simple rectangular functions that lead to timeframe reconstruction to overlapping temporal functions of higher order - they offer numerous possibilities in dynamic image reconstruction with temporal basis functions. Another advantage of B-Splines is their compact support in the time domain. Depending on the knots series and the order of the B-Splines, the modified version of the ML-EM algorithm with temporal basis functions costs much more calculating time than the common ML-EM algorithm operated for a series of timeframes. A tolerable computation time can be reached by using a simple Siddon algorithm [10] to compute entries of the design matrix, what has to be done on the fly, and distributing the computing tasks on several desktop PCs [11]. For that purpose LAM/MPI is used to operate on a heterogeneous cluster.

The generated list-mode data are reconstructed using different sets of timeframes or knots series for the B-Splines of different order:

a) Timeframes / knots series for B-Splines (6 x 10s, 3 x 20s, 8 x 60s, 4 x 300s, 3 x 600s), order 1 (timeframe reconstruction), order 5, order 9
b) Timeframes / knots series for B-Splines (4 x 72s, 3 x 144s, 4 x 360s, 2 x 720 s) , order 1 (timeframe reconstruction), order 5, order 9
c) knots series for B-Splines (0, 36, 108, 216, 360, 576, 936, 144, 2160, 3600 [s]), order 3
d) knots series for B-Splines (0, 72, 216, 432, 720, 1440, 3600 [s]), order 3

Whereas cases (a) and (b) are derived from a plausible subdivision into timeframes, a timeframe reconstruction corresponding to cases (c) and (d) makes no sense due to the rather small numbers of knots. The various methods of reconstruction differ also in the number of activity or weight image that have to be estimated (Table 1.) and therefore have a different noise behavior.

Table 1. Numbers of images that have to be estimated. () indicates that these reconstructions are not applied here.

	order 1	order 3	order 5	order 9
a)	24	(26)	28	32
b)	13	(15)	17	21
c)	(9)	11	(13)	(17)
d)	(6)	8	(11)	(15)

4. Results and Discussion

After image reconstruction time activity curves are computed and averaged over a region of interest consisting of 9 voxels. The results are scaled and compared to the input time activity curve of the GATE simulation (Figure 3.). The timeframe reconstruction (a) results in noisy data for small timeframes. Timeframe reconstruction (b) can reduce the noise on costs of temporal resolution. Continuous time activity curves are computed using timeframes (a) and (b) as knots series for dynamic reconstruction with B-Splines. The resulting time activity curves are smoother, but in case (a) still mirror the noise due to small timeframes or dense knots, respectively. B-Splines of higher order attenuate this effect. In both cases (a) and (b) many weight images have to be estimated (Table 1.), so that the computed time activity curves are susceptible to noise. They differ a little more from the simulated time activity curve at the end of the curve (second 3000-3600). This effect is removed, if less B-Splines (Figure 2.) are used in case (c) and (d). In less computing time the dynamic reconstruction with B-Splines of order 3 leads here to time activity curves that correspond very well to the simulated time activity curve, but show in some regions more discrepancies than in cases (a) and (b). Choosing too few basis functions can lead to underparametrization in the voxel model, see equation (2).

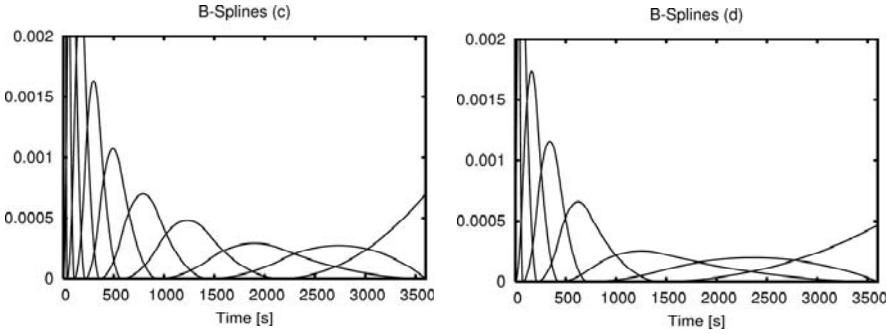

Fig. 2. B-Splines of order 3, case (c) and (d).

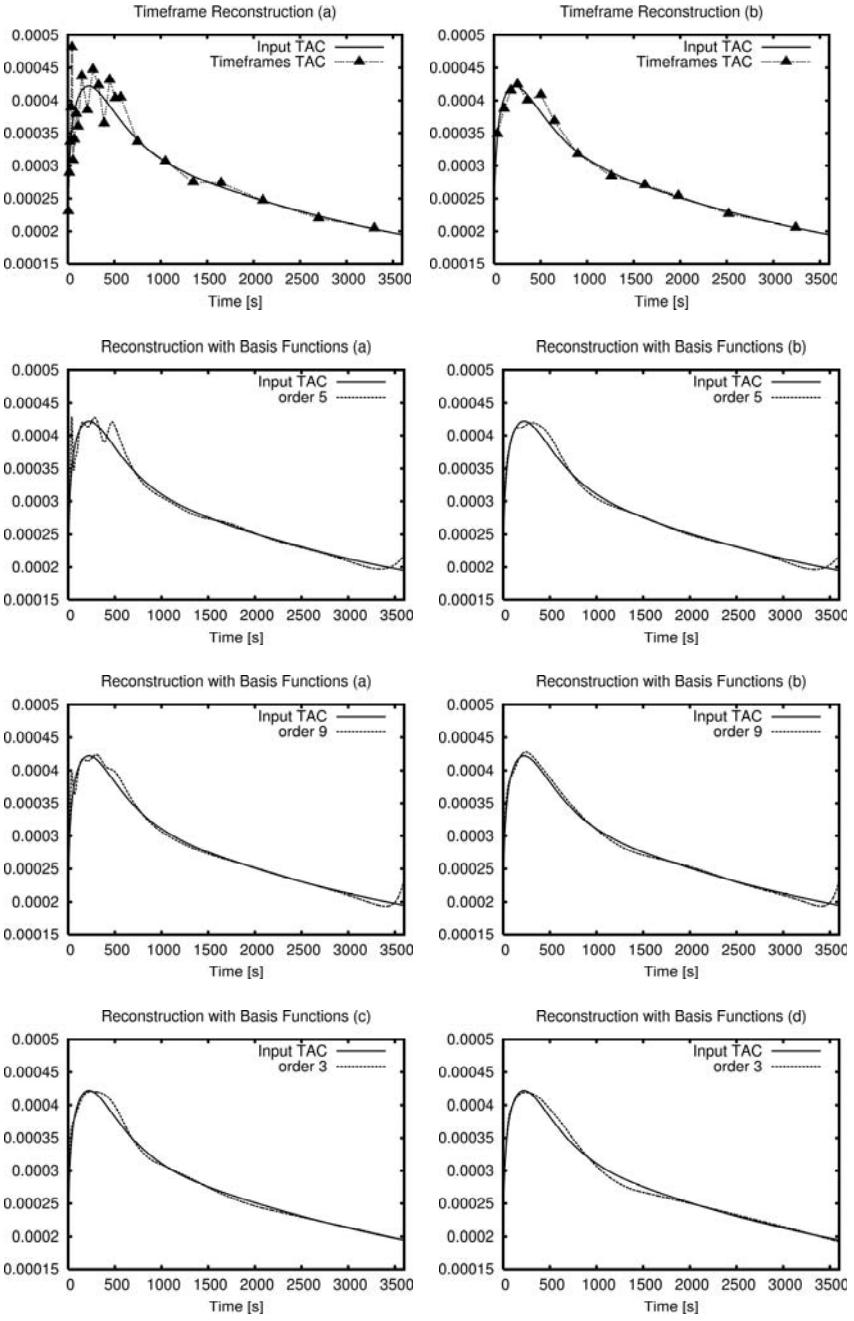

Fig. 3. Time activity curves (TAC) derived from various reconstructions, scaled and compared with simulated time activity curve

5. Conclusions

The potential of dynamic reconstruction using B-Splines as temporal basis functions is demonstrated for the ClearPET^{TM} Neuro. Due to their manifold variations, B-Splines offer many possibilities in dynamic image reconstruction, far beyond the limited possibilities of image reconstruction using timeframes. The use of B-Splines leads to smooth time activity curves, but can - in case of inappropriate knots series or order - also oversmooth the time activity curve. The practical question of parameter choice of the B-Splines is therefore still an issue. Concerning this aspect, an increasing computing time for a larger number of temporal basis functions and higher order has to be taken into consideration.

References

1 K. Ziemons, E. Auffrey, R. Barbier et al., Nuclear Instruments and Methods in Physics Research A **537**, 307, 2005.
2 T.E. Nichols, J. Qi, E. Asma, and R.M. Leahy, IEEE Transactions on Medical Imaging **21**, 396, 2002.
3 A.J. Reader, F.C. Sureau, C. Comtat, R. Trebossen, and I. Buvat, Physics in Medicine and Biology **51**, 5455, 2006.
4 J. Verhaeghe, Y. D'Asseler, S. Vandenberghe, S. Staelens, R. Van de Walle, and I. Lemahieu, in *Conference Record of the 2004 IEEE Nuclear Science Symposium and Medical Imaging Conference, October 16-22, Rome, Italy*, 5, 2004.
5 C. de Boor, *A Practical Guide to Splines*, Springer, New York, Berlin, Heidelberg, 1978.
6 L.A. Shepp and Y. Vardi, IEEE Transactions on Medical Imaging **MI-1**, 113, 1982.
7 H.H. Barrett, T. White, and L.C. Parra, Journal of the Optical Society of America A **14**, 2914, 1997.
8 A.J. Reader, K. Erlandsson, M.A. Flower, and R.J. Ott, IEEE Transactions on Nuclear Science, **45**, 1090, 1998.
9 S. Jan, G. Satin, D. Strul et al., Physics in Medicine and Biology **49**, 4543, 2004.
10 R.L. Siddon, Medical Physics 12, 252, 1985.
11 P. Musmann, U. Pietrzyk, N. Schramm, and S.Weber, in *Conference Record of the 2006 IEEE Nuclear Science Symposium and Medical Imaging Conference, October 29-November 4, San Diego, California,* to appear, 2006.

Local Compensation for Respiratory Motion in List-mode PET

Ralph Brinks and Marc Busch

Molecular Imaging Systems Group, Philips Research Europe – Aachen
Weisshausstrasse 2, 52066 Aachen, Germany
E-mail: <forename>.<lastname>@philips.com

Abstract. In this work we present a method to estimate and compensate the local motion of a hot region in a PET list-mode acquisition directly on the measured LORs. The method is applicable for arbitrary motion patterns. Different shapes of the hot regions, different contrast ratios and different count statistics are examined. In a simulated anatomical data set the algorithm has recovered 98% of the true activity in a lung lesion with respiratory motion.

1. Introduction

Respiratory motion is a serious problem in clinical emission imaging. Motion artifacts from patient motion degrade image quality and hamper accurate quantification in many clinical applications of positron emission tomography (PET). The consequence is a reduced ability of detecting lesions and a worse quantification of uptake values, such as the standardized uptake value (SUV). Different techniques have been proposed to compensate for respiratory motion: either using respiratory gating information or sinogram based [1]. The first needs an additional signal (e.g. chest belt) and leads to degraded images after reconstruction due to reduced count statistics in the individual gated frames. New PET scanners allow the acquisition of the measurements in list-mode, where the coincidence events are chronologically stored in a list. The high temporal resolution intrinsic in list-mode data can be used to compensate for respiratory motion leading to better lesion detectability and better quantification of the SUV.

In this work we describe a new method to estimate the local motion of a hot region in a PET study with high temporal resolution. The method is described in detail in the second section of this article. The third section describes the application and results of simulated geometrical data sets. The section ends with an examination of a simulated anatomical data set. The results are discussed in the fourth section and finally in the last section a conclusion is drawn and an outlook on future investigations is presented.

2. Local Motion Compensation

The three main sources of motion artifacts in medical imaging are respiratory motion, cardiac motion and patient motion. The relevance of each type of motion

clearly depends on the specific application. Cardiac motion and respiratory motion certainly pose no problem at all in brain imaging. Respiratory motion shows the biggest impact in lung imaging, and in cardiac imaging all three types of motion occur. There are different approaches to minimize motion in medical imaging. Patient motion can be reduced with positioning systems or by providing support for patient comfort. Instructions and audiovisual feedback that help the patient to breathe with a specific pattern are useful for respiratory gating. Cardiac imaging is especially difficult as both, respiratory and cardiac motion occur in combination.

Motion is complex and mostly too complicated to be described globally. There are large efforts made by many imaging companies to introduce technologies that acquire all kinds of information to help describing motion, e.g. breathing sensors, elastic belts, camera systems that visually track markers attached to the patient's body. All these devices complicate the workflow and do certainly not improve patient comfort. The ideal solution for motion would therefore be a correction method that works with the acquired PET data alone and requires no additional information at all. Even though this aim might be difficult to achieve for global motion, it appears feasible for local motion. Often, local structures of interest show no significant deformation. Compact tumors for example are relatively stiff objects without internal deformation during respiratory motion. This means that even if the overall movement and deformation of the lung are complex, the movement of a specific lesion or tumor in the lung is not.

Local motion compensation (LMC) is a method to select structures of interest and eliminate the motion in this selected region without changing the image globally. The LMC method can be separated into four steps:

1. VOI definition
2. Motion estimation
3. Data correction, and
4. Image reconstruction from the corrected data

Each step is described in the following.

VOI Definition. Our algorithm corrects motion locally, so it is necessary to define where in the image this correction should be applied. The easiest way to do this is to display a reconstructed (motion-blurred) PET image and let the clinician interactively define a volume of interest (VOI). It is important that the VOI contains the full trajectory of the object under consideration. Since nowadays PET/CT systems are common, the VOI can also be defined in the CT image. This sometimes is the case in PET/CT lung studies.

Motion Estimation. The acquired PET data is available in list-mode format, which means that for each coincidence the line of response (LOR) together with time information is available. We use this information to estimate the motion of the center of activity in the selected VOI over the course of time. This is done by generating intermediate VOI images for a number of short time frames. These small VOI images are generated with a simplified back projection algorithm. The simplification is that the exact overlap length of each LOR with each voxel is not calculated. Instead, voxel values inside the VOI are increased by 1 for each voxel that is intersected by the LOR. This simplified back projection is computationally

very efficient as the number of required divisions and multiplications is minimal. The time for generating a sufficient number of intermediate VOI images is in the order of a few seconds.

In a next step, the center of activity is determined for each intermediate VOI image. Here, it is important to note that coincidences from outside the VOI, which are associated with LORs that hit the selected VOI do also contribute to the intermediate images. This means, the locally constrained back projection described above has a considerable background from events outside the VOI. To minimize the impact of this background, only voxels with values above say 50% of the maximum VOI value are considered in the calculation of the center of activity. The results for all intermediate VOI images are combined to calculate the center of activity for the full time range of the acquisition. The difference to each of the centers of activity for the intermediate VOI images is also computed and stored in a vector array. This array is used to calculate an interpolated translation vector, see Figure 1.

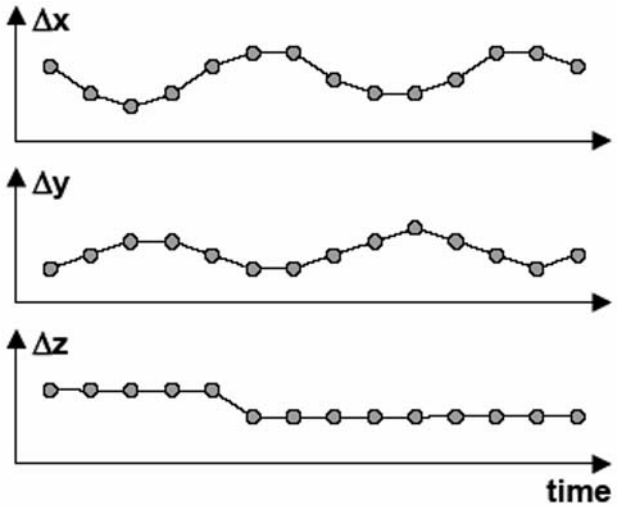

Fig. 1. The information about the position of the center of activity for each time bin and the overall center of activity for the full time range is used to calculate an interpolated translation vector.

Data Correction. Finally, shifting each LOR in the original dataset by the amount given by the translation vector generates a motion corrected list-mode dataset. This is done at the full timing resolution of the list-mode dataset, which is another advantage compared to gating where the data is still averaged or smeared over the duration of each time frame.

Image Reconstruction. The motion corrected list-mode dataset can be reconstructed with the same settings as in the initial motion-blurred reconstruction used for the VOI definition and can then be combined with the blurred image.

3. Application to Simulated Data Sets

The LMC implementation was evaluated and tested with different simulated datasets. The purpose was to test the validity of this approach for various imaging situations. The impact of three parameters was investigated:

- Shape of the object
- Different contrast levels
- Count statistics / image noise

Furthermore, LMC was tested with a realistic (anatomic) phantom to determine its impact on a typical clinical application, the SUV analysis of a lung lesion.
It shows that the algorithm works well for all tested types of shapes of the hot region. This is plausible since the shape of the object has no impact on the motion of the center of activity.

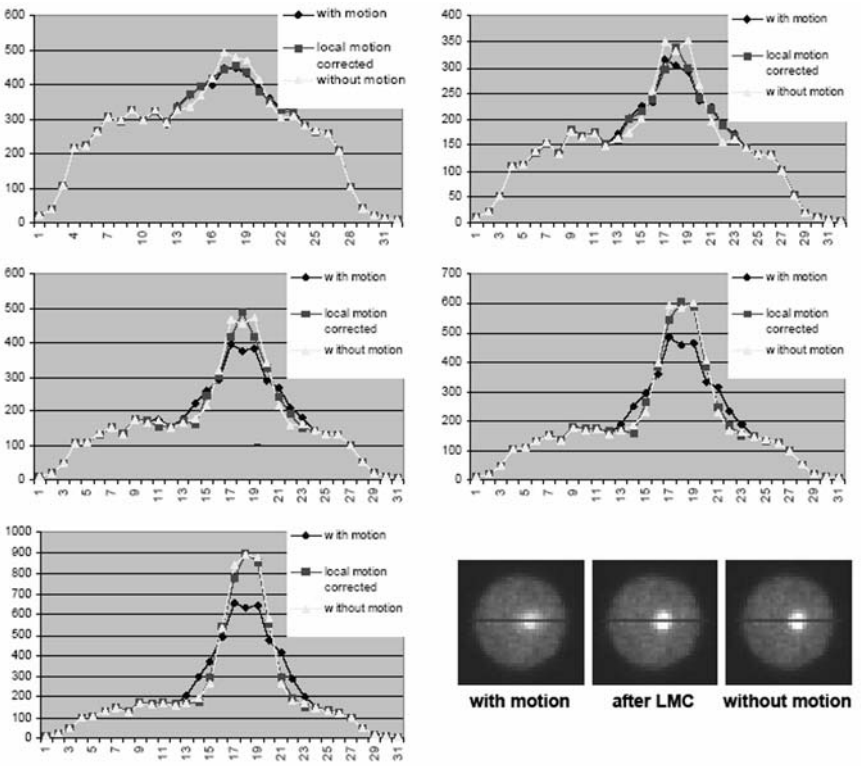

Fig. 2. A small moving sphere with background activity in different contrast rations is analyzed along a horizontal line in the direction of motion (bottom right) and compared to a non-moving sphere with the same activity.

The contrast between the object of interest and the surrounding background has great impact on the applicability of LMC. Small contrast levels mean that the contribution increases for LORs hitting the VOI that do not originate from the actual object of interest. This hampers the accurate determination of the center of activity on small time scales. The results are shown in the Figure 2, where a small moving hot sphere with background activity in different contrast ratios has been analyzed in terms of line profiles. The location of the line profile is indicated in the right part of the bottom row.

We have found that LMC shows no or only a very small effect for contrast levels below 2 : 1 and that motion is correctly compensated when the contrast is above 3 : 1.

For the examination of the impact of noise the contrast level is fixed to 6 : 1 and list-mode data sets were generated and analyzed for different count statistics. We have found that even for very low count statistics (a total number of counts of 50000) LMC compensates motion artifacts correctly, which means that the algorithm is quite insensitive to image noise.

NCAT Phantom. A digital phantom was utilized to test LMC under more realistic conditions. The "4D NURBS-based Cardiac-Torso" (NCAT, [2]) phantom realistically models the effect of respiratory and cardiac motion on the skeletal structure and all organs of the torso. The phantom and the position of the lesion is shown in the left part of Figure 3. This analytical phantom was used to generate voxelized activity distributions and emission images for 50 gates of the full respiratory cycle. The 50 activity distributions were then fed into an event generator that produced a list-mode dataset for the full cycle with a specified number of events.

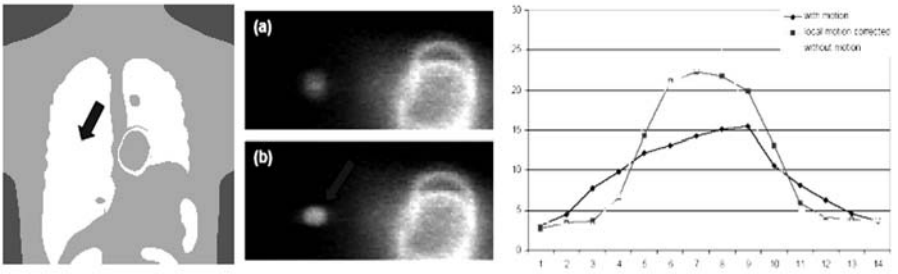

Fig. 3. The NCAT software phantom was used to simulate a realistic motion of a lung lesion (left). The middle part shows the lesion as it appears in sagital view (a) motion-blurred and (b) after application of LMC. The right part shows activity profiles along the main direction of movement with motion, after LMC and without motion.

It is obvious how good LMC reproduces the activity of the moving lesion. A region of interest (ROI) analysis shows that the true activity in the lesion is reproduced to 98%, while the uptake in the motion blurred case is only 72%.

4. Results

The geometrical phantoms were used to examine the impact of different physical settings such as different kinds of motion, different shapes of the lesion or different contrast ratios. The algorithm performs well in periodic and non-periodic motion and in arbitrary object shapes. Down to a contrast ratio of 2:1 (lesion vs. background) the algorithm yields a good match of motion-corrected and motion-free images.

With a view to clinical applications, the NCAT phantom was used to study the performance of the algorithm in improving quantification of a hot lesion near the diaphragm having realistic motion due to respiration. The analysis of the motion-corrected image is in 98% conformance with the theoretically expected value in terms of mean uptake of the lesion, while the motion blurred lesion only shows 72% of the true uptake.

5. Conclusions

We examined a local motion estimation and motion compensation algorithm for a PET acquisition in list-mode. The algorithm is based on estimating the center of gravity of a VOI with a high temporal resolution, and then correcting the corresponding LORs. The impact of different lesion shapes, contrast levels and count statistics has been considered. It shows that a contrast ratio of 2:1 (lesion : background) is sufficient, also in low count studies. The application and evaluation of LMC to real measurements, phantoms and clinical acquisitions is ongoing.

References

1 G. J. Klein, B. W. Reutter, E. H. Botvinick, T. F. Budinger, and R. H. Huesman, in *Proceedings of the 2001 IEEE Workshop on Mathematical Methods in Biomedical Image Analysis*, Edited by L. Staib L., 71, 2001.

2 W. P. Segars, Ph.D. Dissertation, University of North Carolina, 2001.

Hybrid Imaging with SPECT/CT - Presentation of 5 Cases

S. Berg[1], B.-I. Börner[2], H. Rasch[3], J. Müller-Brand[3] and G. Bongartz[1]

[1] Dept. of Radiology, University of Basel, Switzerland
[2] Dept. of Cranio-Maxillo-Facial Surgery, University of Basel, Switzerland
[3] Dept. of Nuclear Medicine, University of Basel, Switzerland

Abstract. Combined SPECT/CT imaging in one device is one of the latest developments in medical imaging. Performing SPECT (Single Photon Emission Computed Tomography) and CT (Computed Tomography) one after the other with a single machine can avoid many artifacts due to different patient positioning. To our experience an automatic and precise fusion of the images can be achieved in most cases. Tissue which is moving during the examination (e.g. lungs, heart) still causes artifacts when the data is fused.

1. Introduction

CT, a radiological imaging modality, depicts anatomy with high spatial resolution. Imaging techniques in nuclear medicine show the function and the biochemistry of the human body depending on the chosen radiopharmaceutical with poor spatial resolution.

Until a few years ago, the information of these two imaging modalities was evaluated by the clinician. Recently digital image fusion evolved, in order to reduce human error in image interpretation.

Unfortunately, artefacts caused by different patient positioning during these two subsequent examinations remained a core problem. Only those body parts could be fused accurately with provide fixed points of reference e.g. the brain.

In autumn 2006 our department bought a SPECT/CT machine - the second machine of this kind in Europe. With this machine it is possible to perform a SPECT and thereafter a CT examination without active patient movement.

2. Experimental Methods

We present 5 cases from our clinical routine in which we have used SPECT/CT imaging (Symbia T2®, Siemens). Depending on the type of examination (e.g. bone scan with ^{99m}Tc – dicarboxypropane-diphosphonate or receptor imaging with ^{111}In-DOTATOC) the interval between the injection of the radiopharmaceutical and the imaging varies between minutes and hours. For the examination the patient rests supine on the CT-table. Thereafter the table with the patient is positioned in a way that the area of interest comes to rest between the collimators. After positioning the collimators, the SPECT-scan starts. Depending on the

desired count rate, the SPECT imaging may take approximately 20 Minutes. After the SPECT-scan is completed, the table with the patient is re-positioned and the CT-scan is performed which, depending on the CT-machine, takes about 1 Minute.

3. Results

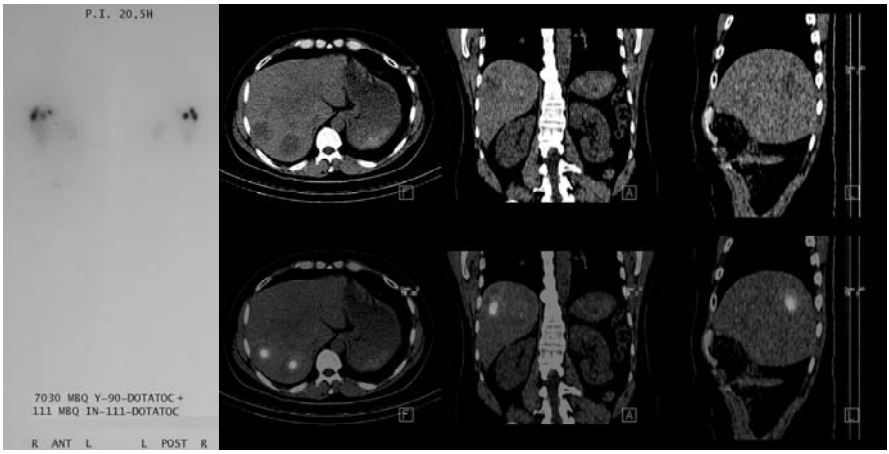

Fig. 1. Patient with neuroendocine tumor and liver metastasis. Irradiation with ^{111}In- / ^{90}Y-DOTATOC. Planar scintigraphic imaging on the left side, SPECT/CT fusion imaging on the right side of the picture.

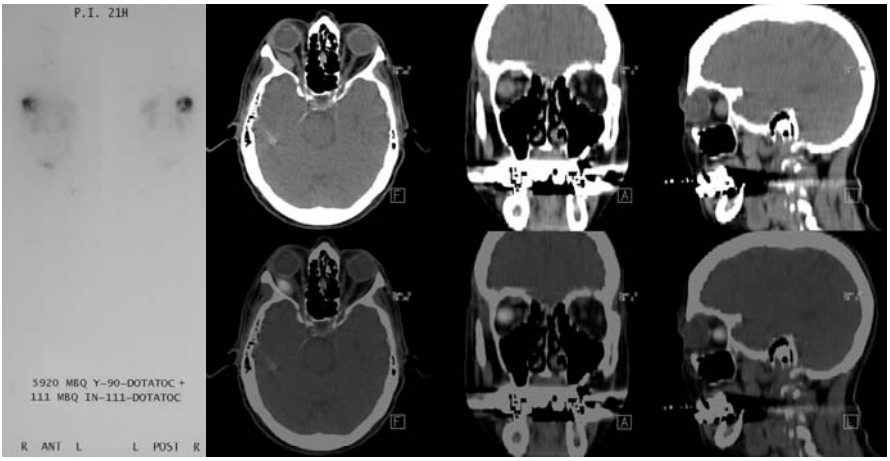

Fig. 2. Patient with neuroendocine and unusual single metastasis in the eye muscle. Irradiation with ^{111}In- / ^{90}Y-DOTATOC. Planar scintigraphic imaging on the left side, SPECT/CT fusion imaging on the right side of the picture.

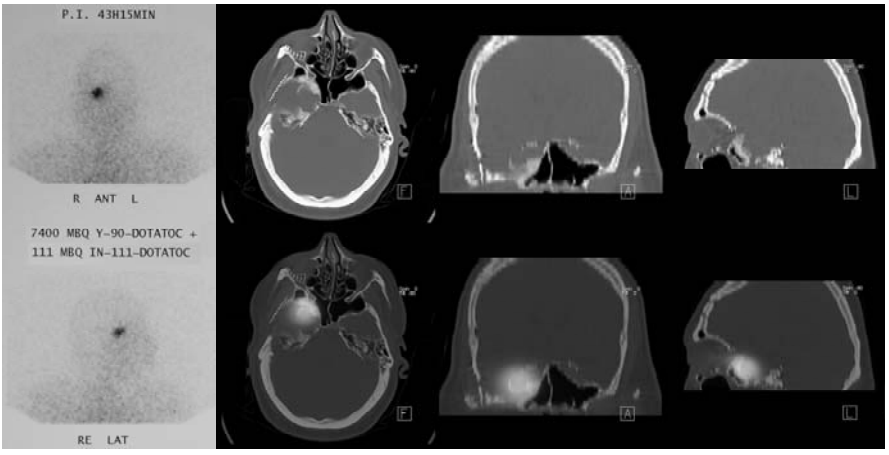

Fig. 3. Patient with meningioma. Irradiation with ^{111}In- / ^{90}Y-DOTATOC. Planar scintigraphic imaging on the left side, SPECT/CT fusion imaging on the right side of the picture.

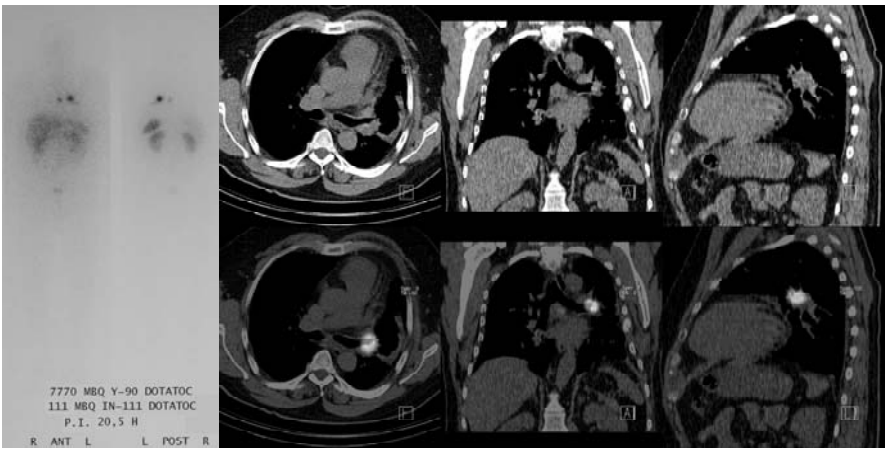

Fig. 4. Patient with lung tumor. Irradiation with ^{111}In- / ^{90}Y-DOTATOC. Planar scintigraphic imaging on the left side, SPECT/CT fusion imaging on the right side of the picture.

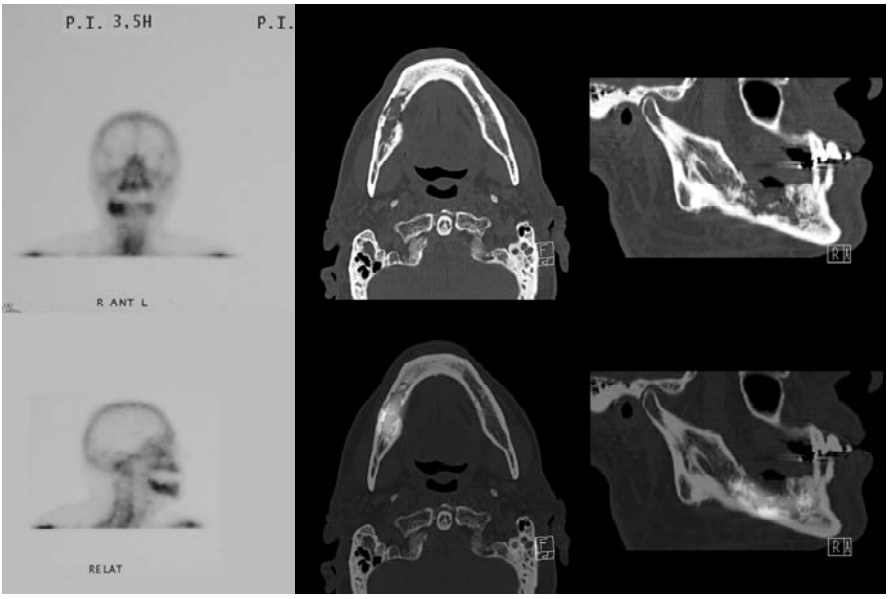

Fig. 5. Patient with pain in the jaw and proven osteomyelitis. Diagnostic scintigraphy with ^{99m}Tc-DPD to define the extension of the infectious bone changes. Planar scintigraphic imaging on the left side, SPECT/CT fusion imaging on the right side of the picture.

4. Conclusions

Automatic image fusion by SPECT/CT (Symbia T2®) works without problems if the patient has not been changing his position during the examination. Minor movement artifacts due to breathing can not be avoided.

Imaging of the lungs poses a problem, as the SPECT exam depicts the average size of the lungs (SPECT exam takes approx. 20 minutes), while the CT scan depicts the lung somewhere between in- and expiration (CT exam takes approx. 1 minute).

SPECT/CT has been shown to be a useful tool in addition to planar imaging if precise anatomical correlation is required.

The λ-MLEM Algorithm: An Iterative Reconstruction Technique for Metal Artifact Reduction in CT Images

May Oehler[1] and Thorsten M. Buzug[2]

[1] RheinAhrCampus Remagen, Department of Mathematics and Technology, Suedallee 2, 53424 Remagen, Germany
E-mail: oehler@rheinahrcampus.de
[2] Institute of Medical Engineering, University of Luebeck, Ratzeburger Allee 160, 23538 Luebeck, Germany
E-mail: buzug@imt.uni-luebeck.de

Abstract. Filtered backprojection (FBP) is an inadequate method to cope with inconsistencies in Radon space and, consequently, leads to artifacts in reconstructed CT images. A solution to this problem is given by statistical reconstruction methods like the Maximum-Likelihood Expectation-Maximization (MLEM) algorithm. The advantage of MLEM is that it allows to weight raw projection data during reconstruction. The method presented here consists of two steps. In a first step, inconsistent data in the Radon space were bridged using a directional interpolation scheme. Since these surrogate data are contaminated with residual inconsistencies, in a second step, the image is reconstructed using a weighted MLEM algorithm. In this work, the modified MLEM algorithm for metal artifact reduction in CT is presented for clinical hip prosthesis data. On the basis of image entropy the reconstruction success is evaluated.

1. Introduction

Beam hardening of X-rays leads to artifacts in reconstructed CT images especially in the presence of metal objects. Additionally, it has been demonstrated [1] that the exponential edge-gradient effect, object motion, detector under-sampling, view under-sampling and the axial partial volume effect are sources for metal artifacts in transmission CT images. Mathematically, these artifacts are caused by inconsistencies in the Radon space or sinogram, respectively. To reduce these artifacts the inconsistent metal data are bridged using interpolation. Since the repaired sinogram data consist of residual inconsistencies it can be demonstrated that a gradually weighted Maximum-Likelihood Expectation-Maximization (λ-MLEM) algorithm lead to a superior reconstruction quality compared with an ignoring data strategy or the interpolation step alone.

2. Materials and Methods

Preprocessing. Experiments were carried out on clinical hip prosthesis data provided by Philips Research Laboratories Hamburg (see Fig. 1a). The first step to reduce the existing metal artifacts consists of a pragmatic repair method applied

to raw data using an interpolation scheme. For this the metal object is labeled in a preliminary FBP reconstruction using simple threshold segmentation.

Then, a forward projection of the labeled marker image is calculated resulting in a metal-only sinogram (see Fig. 1b). All sinogram values which are different from zero are suspected to be inconsistent in the original sinogram and are therefore eliminated from the sinogram data (see Fig 1c).

Previous works [2,3] propose to replace these inconsistent data by linear or polynomial interpolation within a single projection view. However, in this work, a directional interpolation scheme based on the ideas of image inpainting [4] is proposed. The result of the directional interpolation is shown in Fig. 1d.

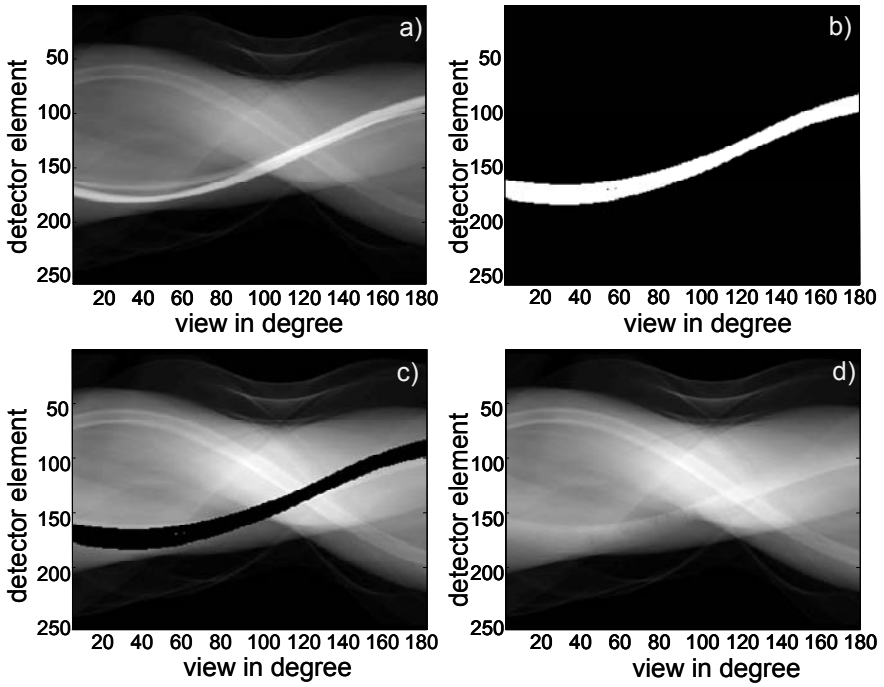

Fig. 1. (a) sinogram of the hip prosthesis data; (b) metal-only sinogram; (c) sinogram data without inconsistent projection data caused by the hip prosthesis; (d) sinogram data after directional interpolation.

The soft tissue absorption 'behind' the metal prosthesis is estimated more precisely by directional interpolation than through interpolation methods within one single projection view only. The directional interpolation follows the 'flow' of the raw data outside the metal projections. In the object domain the direction of this interpolation corresponds to the acquisition directions under slight angulations – able to squint behind the metal object.

Reconstruction: The λ-MLEM Algorithm. Subsequently, the data were reconstructed using the λ-MLEM algorithm which will be briefly explained in this subsection. As any surrogate data method, as described in the previous subsection, has a weak underlying physical model, it cannot be expected that the interpolated data perfectly fit imaginary projections measured without metal objects. Therefore, projections running through the metal object must be weighted by an appropriate confidence parameter λ. To be mathematically consistent, every row of the system matrix corresponding to those projection lines must be weighted as well. Hence, the λ-MLEM algorithm can be derived as follows.

The λ-MLEM algorithm is based on two changes of the original MLEM formula for transmission computed tomography [5]. In the first step, all rows of the system matrix $A = \{a_{ij}\}$ corresponding to projections running through a metal object are weighted with a confidence parameter $0 \le \lambda \le 1$. Hence, the new log-likelihood function for transmission computed tomography is given by

$$l(f^*) = \ln(L(f^*)) = \sum_{i=1}^{M} \left(-\tilde{n}_i \sum_{j=1}^{N} \lambda_i a_{ij} f_j^* - n_0 e^{-\sum_{j=1}^{N} \lambda_i a_{ij} f_j^*} \right) + \text{constant} \tag{1}$$

where n_0 is the number of photons leaving the x-ray source and $\tilde{n}_i$ is the modified number of detected photons. The original MLEM algorithm is a simple gradient based algorithm [5] and can be written, also after modification, as

$$f^{*(n+1)} = f^{*(n)} + \mathbf{D}\left(f^{*(n)}\right) grad\left(l\left(f^{'*}\right)\right). \tag{2}$$

Here, **D** denotes the diagonal matrix for transmission computed tomography

$$\mathbf{D}(f^{*(n)}) = diag\left(f_r^{*(n)} \Big/ \sum_{i=1}^{M} \tilde{n}_i \lambda_i a_{ir} \right). \tag{3}$$

Hence, eq. (2) can be expressed as

$$\begin{aligned} f_r^{*(n+1)} &= f_r^{*(n)} + \frac{f_r^{*(n)}}{\sum_{i=1}^{M} \tilde{n}_i \lambda_i a_{ir}} \left\{ \frac{\partial l(\boldsymbol{f}^*)}{\partial f_r^*} \right\} \\ &= f_r^{*(n)} + \frac{f_r^{*(n)}}{\sum_{i=1}^{M} \tilde{n}_i \lambda_i a_{ir}} \left\{ \sum_{i=1}^{M} n_0 \lambda_i a_{ir} e^{-\sum_{j=1}^{N} \lambda_i a_{ij} f_j^{*(n)}} - \sum_{i=1}^{M} \tilde{n}_i \lambda_i a_{ir} \right\}. \end{aligned} \tag{4}$$

The second modification takes into account that the number of detected x-ray quanta is proportional to the intensity of the x-rays. Therefore, the sum of all projections $p_j = \Sigma_{j=1,\ldots,M} a_{ij} f_j$, i.e. the projection values in the sinogram, must also be weighted adequately. So, the adapted number of x-rays is $\tilde{n}_i = n_0 \exp(-\lambda_i p_i)$ and the new fix-point iteration is

$$f_r^{*(n+1)} = f_r^{*(n)} \left(\sum_{i=1}^{M} \lambda_i a_{ir} e^{-\sum_{j=1}^{N} \lambda_i a_{ij} f_j^{*(n)}} \Big/ \sum_{i=1}^{M} \lambda_i a_{ir} e^{-\lambda_i p_i} \right). \quad (5)$$

Evaluation. To evaluate the quality of the metal artifact reduction the image entropy

$$h = \sum_{g \in G} q_g \log(q_g) \quad (6)$$

is calculated, where q_g is the fraction of pixels with gray value g. The entropy measure is applied on the processed clinical image. It measures additional gray value variations induced by image artifacts and is therefore maximized when gray value variations in the image are due to the anatomical content alone. By variation of the confidence parameter λ, the image with the smallest distance to the desired artifact-free target image can be found. An appropriate weighting is chosen that maximizes the entropy $h(\lambda)$. This principle works for any clinical data.

3. Results

Figure 2a shows the results of the classical MLEM reconstruction of the hip prosthesis data, which is equal to the λ-MLEM algorithm with a choice of $\lambda_i \equiv 1$ for all projections $i \in \{1,\ldots,M\}$. The metal artifacts caused by the steel hip prosthesis can clearly be seen. Figure 2b displays the results of the reconstruction with a choice of $\lambda = 0.0$ (in this case the inconsistent data are treated as missing data).

Rejecting the metal data obviously leads to new stripe artifacts in the image. Figure 2c shows the reconstruction based on directional interpolation data with consecutive λ-MLEM ($\lambda = 0.5$). As expected, artifact reduction is superior to the missing data concept. Visually, all diagnostically distorting stripes have been removed. In this case the best result is given by directional interpolation and λ-MLEM with a choice of $\lambda = 0.5$ (Fig. 2c).

The resulting curves of the entropy of the reconstructed λ-MLEM images in combination with the directional interpolation method (■) and the one without interpolation (○) show that best results are obtained with directional interpolation and a choice of $\lambda = 0.5$. The points a)-c) in Fig. 3 directly correspond to the image reconstructions presented in Fig. 2a-c.

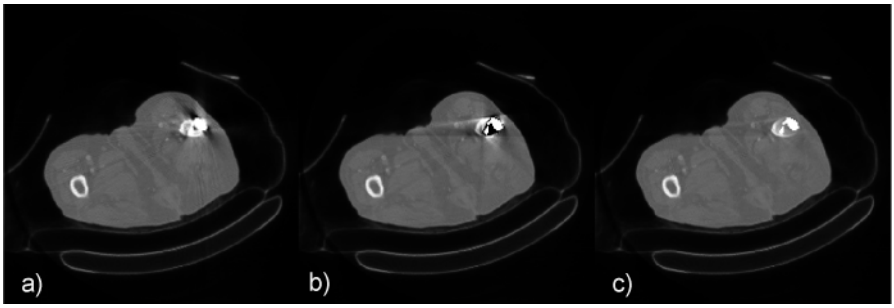

Fig. 2. Reconstruction of clinical hip prosthesis data. (a) classical MLEM reconstruction (λ-MLEM with $\lambda = 1.0$), (b) λ-MLEM reconstruction using $\lambda = 0.0$, (c) λ-MLEM reconstruction with directional interpolation and $\lambda = 0.5$. Figures b and c are overlaid with the metal-object image segmented from the initial FBP.

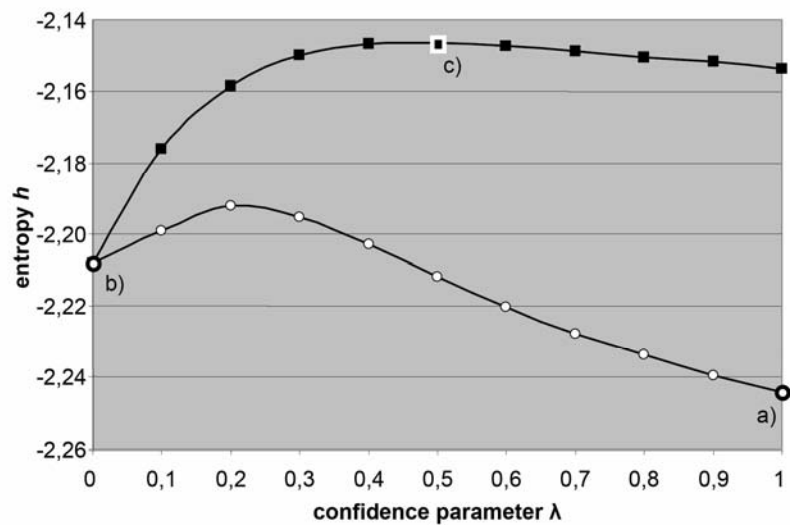

Fig. 3. Entropy h vs. confidence parameter λ; interpolation methods: ■ - directional interpolation; ○ - without interpolation (original hip prosthesis data). The points a)-c) in Fig. 3 directly correspond to the image reconstructions presented in Fig. 2a-c.

4. Conclusion

A novel metal artifact reduction for transmission computed tomography is presented. In a first step, inconsistent projection data caused by metal implants are bridged by directional interpolation, i.e. the interpolation follows the 'flow' of the adjacent projection data in the sinogram. In a second step, a weighted maximum-likelihood expectation maximization algorithm (λ-MLEM) is proposed. λ- MLEM

weights those projections running through a metal object and the corresponding rows of the system matrix with a certain confidence parameter λ.

The appropriate value for the confidence parameter in a clinical situation is a-priori not known. Therefore, an entropy quality criterion is proposed that estimates the amount of residuals artifacts in the reconstructed image. In our experiments [6-9] we found proper values for λ between 0.1 and 0.9 depending on poor or rich neighboring information, respectively, of the void data in the sinograms of different anatomical regions. However, all functions of entropy versus confidence parameter appear to be concave having a maximum in the range $0.1 \leq \lambda \leq 0.9$. Therefore, as practical rule of thumb, we recommend to set the parameter to $\lambda = 0.5$. This always improves image quality compared to pure interpolation and missing data concept, respectively.

Acknowledgements. The authors would like to thank Dr. Thomas Köhler, Philips Research Laboratories Hamburg, for providing the hip prosthesis data.

References

1. B. De Man, J. Nuyts, P. Dupont, G. Marchal and P. Suetens, *Metal Streak Artifacts in X-ray Computed Tomography: A Simulation Study*, IEEE Trans. Nucl. Sci. **46**, 691, 1999.
2. W. A. Kalender, R. Hebel, and J. Ebersberger, *Reduction of CT artifacts caused by metallic implants*, Radiology **164**, 576, 1987.
3. G. H. Glover and N. J. Pelc, *An algorithm for the reduction of metal clip artifacts in CT reconstructions*, Med. Phys. **8**, 799, 1981.
4. M. Bertalmio, G. Sapira, *Image Inpainting*, Computer Graphics SIGGRAPH2000, 417, 2000.
5. K. Lange, M. Bahn and R. Little, *A Theoretical Study of Some Maximum Likelihood Algorithms for Emission and Transmission Tomography*, IEEE Trans. Med. Imag. **6**, 106, 1987.
6. M. Oehler and T. M. Buzug, *CT Artifact Reduction with an Iterative Maximum Likelihood Approach*, in: S. Weber et al. (Eds.), Computer Aided Surgery around the Head, VDI Fortschritt-Bericht 17: Biotechnik/Medizintechnik **258**(17), (VDI-Verlag, Düsseldorf, 2005) 44.
7. M. Oehler, L. Pfaffmann and T. M. Buzug, *Artefact Suppression in Computed Tomography using Iterative Reconstruction Methods*, Biomedizinische Technik **50**, 1130, 2005.
8. M. Oehler and T. M. Buzug, *Gewichtete MLEM-Rekonstruktion zur Artefaktreduktion in der Transmissions-Computertomographie*, Proceedings of 37th Annual Meeting DGMP, Regensburg (2006) 345.
9. M. Oehler and T. M. Buzug, *Maximum-Likelihood-Ansatz zur Metallartefaktreduktion bei der Computertomographie*, BVM 2006 (Springer, Berlin, 2006) 36.

Quantification of Tissue Microcirculation by Dynamic MRI and CT: Comparative Analysis of Signal-Time Courses Measured in Muscle Tissue

G. Brix[1], J. Griebel[1], S. Delorme[2], F. Kiessling[2]

[1] Department of Medical Radiation Hygiene and Dosimetry, Federal Office for Radiation Protection, Oberschleissheim, Germany
E-mail: gbrix@bfs.de
[2] Research Program 'Innovative Diagnosis and Therapy', German Cancer Research Center (DKFZ), Heidelberg, Germany

Abstract. Quantitative analysis of microcirculatory parameters from dynamic MRI data is seriously hampered by the fact that the MR signal is not only affected by the local concentration of the contrast agent administered and the measurement sequence used but also by MR-specific processes, such as proton relaxation enhancement and water exchange between tissue compartments. It was thus the aim of our investigation to assess the reliability of an MRI approach developed by our group by comparing microcirculatory parameters estimated for muscle tissue with those determined from dynamic CT scans. The analysis yielded a good agreement between the tracer-independent parameters estimated from signal-time courses determined by both imaging modalities in muscle tissue.

1. Introduction

Estimation of well-defined physiological tissue parameters from dynamic contrast-enhanced MR image series makes it possible to perform quantitative comparisons between different patients as well as to monitor hemodynamic changes during therapy in individual patients in a quantitative manner. Due to the wide availability of MR systems and the fact that paramagnetic contrast media (CM) used for MRI are extremely safe it is likely that noninvasive dynamic MRI techniques will replace other approaches for assessing tissue microcirculation, such as CT or PET, that expose patients to ionizing radiation.

However, quantitative analysis of microcirculatory parameters from dynamic MRI data is hampered by the fact that the measured increase of the MRI signal after administration of a paramagnetic CM is not directly proportional to the local tissue concentration of the CM. In contrast to CT, there is a very complex non-linear relationship between the measured signal variation and the local CM concentration, which not only depends on the measurement sequence used and the tissue-specific transversal relaxation time, T_1, but also on two further assumptions: Firstly, that differences in the relaxivity of water protons in the different tissue compartments can be neglected. Secondly, that water diffusion within tissue compartments and water exchange between them is fast enough so that the relaxation of the bulk magnetization can be described by a single relaxation time.

Although recent studies provide evidence that both assumptions are not completely fulfilled in biological tissues [1,2,3], the error introduced by the idealized model assumptions cannot be evaluated at present due to the lack of tissue-specific data.

It was, thus, the aim of the present investigation to assess the reliability of an MRI approach developed by our group by comparing microcirculatory parameters estimated for muscle tissue with those determined from dynamic CT data. To this end, we re-evaluated dynamic MRI and CT data sets acquired in previous studies in patients with breast and head/neck cancer, respectively [4,5].

2. Experimental Methods

MRI measurements. In 8 patients with breast carcinoma, strongly T_1-weighted MR images were acquired at a 1.5-Tesla whole-body MR system (MAGNETOM Vision; Siemens, Erlangen, Germany) using a saturation-recovery-TurboFLASH (SRTF) sequence (*FOV* = 320 mm, *TH* = 6 mm, *TR* = 10 ms, *TE* = 4.1 ms, α = 12°). In order to estimate precontrast T_1 relaxation times, 7 T_1-weighted SRTF images were acquired with different recovery times, *TREC*, before CM administration. Subsequently, strongly T_1-weighted SRTF images (*TREC* = 125 ms) were acquired before, during, and after intravenous administration of 0.1 mmol Gd-DTPA (MAGNEVIST; Schering AG, Berlin, Germany) per kg-bw at a constant rate over 30 s. In each patient, 128 images were measured with a temporal resolution of 3.25 s. For quantitative analysis, SRTF signals were determined from the aorta and the pectoral muscle. Using the pre-contrast relaxation times, T_{10}, estimated for these tissues, concentration-time courses were computed from the measured signal-time courses under 'fast exchange' conditions [3] by

$$C_T(t) = \frac{-1}{T_{REC}\,\alpha} \cdot \ln\left[\frac{S_{CM}(t)}{S_0} - \exp(T_{REC}/T_{10}) \cdot \left(\frac{S_{CM}(t)}{S_0} - 1\right)\right] \qquad (1)$$

with α the relaxivity of the CM in blood and S_{CM}/S_0 the measured ratio between post- and pre-contrast SRTF signal.

CT Measurements. CT scanning was performed in six patients with squamous cell carcinoma of the oro- and/or hypopharyngeal region at a clinical CT scanner (SOMATOM Plus 4; Siemens AG, Erlangen, Germany; scan parameters: acquisition time, 0.5 s; tube voltage, 120 kV; tube current, 50 mA; slice collimation, 8 mm). Starting with the administration of 50 ml iopromide (Ultravist 300; Schering AG, Berlin, Germany), sequential CT scans were acquired with a repetition time of 5 s for a total of 90 s (18 scans) and a repetition time of 15 s up to a total scanning time of 6 min (18 additional scans). For quantitative analysis, density-time courses, $H(t)$, were evaluated from the carotid artery and neck muscles and converted into concentration-time courses according to the linear relationship

$$C_T(t) = k \cdot [H_{CM}(t) - H_0] \qquad (2)$$

where H_0 is the precontrast density and k a proportionality factor.

Pharmacokinetic Modeling. The pharmacokinetic model used to analyze the concentration-time courses determined by MRI and CT in muscle tissue is shown in Figure 1. It describes the transport of the CM through capillaries and its bi-directional transport between plasma (mean concentration, C_P; volume, V_P) and interstitial space (mean concentration, C_I; volume, V_I). $C_A(t)$ is the concentration in a tissue feeding artery, F the capillary plasma flow, and PS the permeability-surface area product. The following tissue-specific parameters were estimated from the measured concentration-time courses assuming a hematocrit of 0.45 and 0.25 in major vessels and capillaries, respectively: F/V_P and PS/V_P as well as the relative volume fractions f_P and f_I.

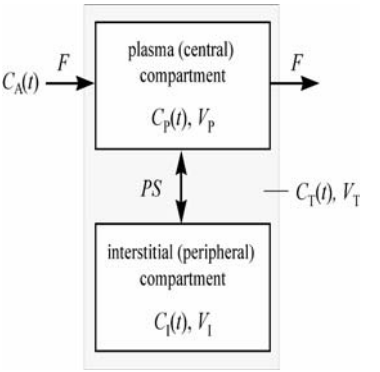

Fig. 1. Definition of tissue parameters characterizing the transport of an extracellular CM through capillaries and its bi-directional transport between the plasma and interstitial distribution space.

3. Results and Discussion

For blood and pectoral muscle, non-linear regression analysis yielded precontrast T_1 values of 1348 ± 94 ms and 607 ± 85 ms, respectively. Due to the low signal-to-noise ratio of the concentration-time courses measured by both imaging modalities in muscle tissue, the curves could not be analyzed on an individual basis with the proposed pharmacokinetic model. To overcome this limitation, individual concentration-time curves determined from blood and muscle tissue were averaged over the 8 MRI and the 6 CT patient examinations. The resulting curves are shown in Fig. 2.

The pharmacokinetic parameters estimated for muscle tissue are summarized in Tab. 1. The tracer-independent parameters f_P and F/V_P determined by dynamic MRI for pectoral muscle and by dynamic CT for neck muscles are nearly identical. Somewhat greater differences were observed for both the permeability-surface area product – which depends on the size and type of the CM used (Gd-

DTPA: ionic CM, 591 Dalton; ioprimide: non-ionic CM, 791 Dalton) – and the parameter f_P.

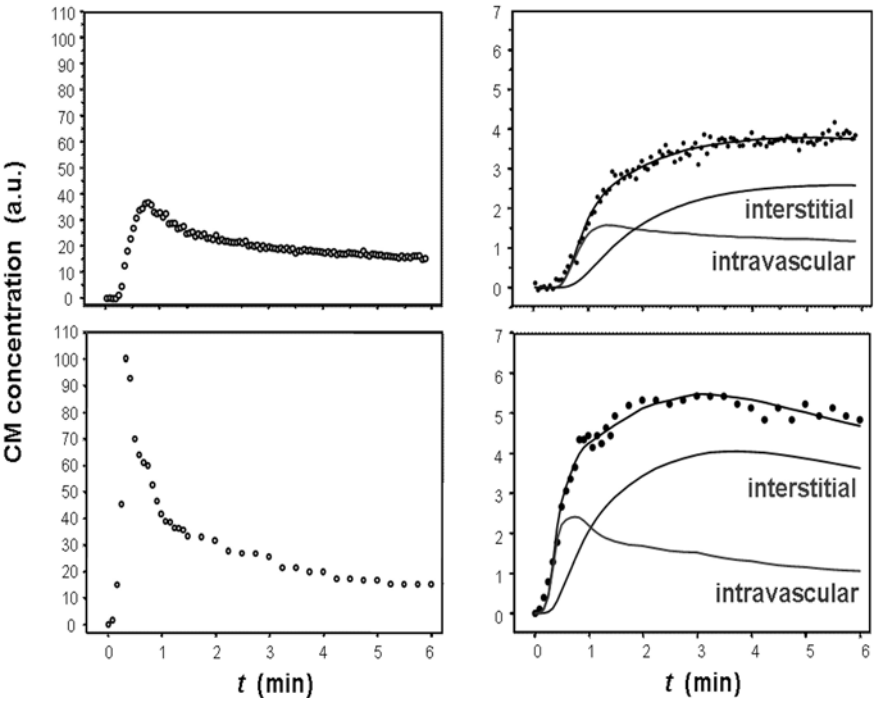

Fig. 2. Concentration-time courses determined from blood (left column) and muscle tissue (right column) by dynamic MRI (upper row) and CT (lower row) scanning upon administration of GD-DTPA over 30 s and iopromide over 15 s, respectively. To enable a visual comparison of the curves, they were normalized in such a way that the CM concentrations in blood were identical at the end of the measurement period.

Table 1. Microcirculatory parameters estimated from concentration-time courses measured in muscle tissue by dynamic MRI and CT.

Modality / CM	Muscle region	f_P	f_I	F/V_P (min^{-1})	PS/V_P (min^{-1})
MRI / Gd-DTPA	pectoral	0.04 ± 0.01	0.09 ± 0.01	2.4 ± 1.3	1.2 ± 0.6
CT / iopromide	neck	0.04 ± 0.01	0.12 ± 0.01	2.5 ± 0.9	1.6 ± 0.6

4. Conclusions

Since contrast-enhanced CT measurements are not affected by MR-specific processes, such as proton relaxation enhancement and water exchange, the good agreement between the tracer-independent parameters determined with dynamic CT and MRI for muscle tissue makes a strong argument that MRI data can be analyzed under the assumption of fast-exchange conditions and identical proton relaxivities in the different tissue compartments – at least for muscle tissue and the measurement conditions realized.

References

1 J. Mørkenborg, J. F. Taaghehøj, P. N. Væver, J. Frøkær, J. C. Djurhuus, H. Stødkilde-Jørgensen, Magnetic Resonance Imaging **16**, 933, 1998.
2 G. J. Stanisz, R. M. Henkelman, Magnetic Resonance in Medicine **44**, 665, 2000.
3 K. M. Donahue, R. M. Weisskoff, Journal of Magnetic Resonance Imaging **7**, 102, 1997
4 G. Brix. F. Kiessling, R. Lucht, S. Darai, K. Wasser, S. Delorme, J. Griebel, Magnetic Resonance in Medicine **52**, 420, 2004.
5 G. Brix, M. Bahner, U. Hoffmann, A. Horvath, W.G. Schreiber, Radiology **210**, 269, 19999

A Numerical Investigation of RF Heating Effects on Implants During MRI Compared to Experimental Measurements

Jens Stenschke[1,2], Dan Li[1], Maike Thomann[1], Gregor Schaefers[3] and Waldemar Zylka[1]

[1] Department Physical Engineering, University of Applied Sciences Gelsenkirchen, Neidenburger Str. 43, 45877 Gelsenkirchen, Germany
E-mail: waldemar.zylka@fh-gelsenkirchen.de
[2] Present address: Siemens AG Medical Solutions, Allee am Röthelheimpark 2, 91052 Erlangen, Germany
[3] mr:comp GmbH, Buschgrundstr. 33, 45894 Gelsenkirchen

Abstract. A numerical model was developed to examine relationships between energy absorption rate (SAR) and temperature distributions in of a phantom containing a hip prostheses implant during radio frequency deposition in MRI. Calculations of SAR and the resulting temperature increases were performed for different frequencies, i.e. B_0 values of 1T, 1.5T, and 3.0T. Experimental measurements at B_0=1.5T are compared to the numerical results yielding good qualitative agreement. Attempts to ensure RF safety in MRI often rely on assumptions about local temperature from local SAR levels. In case of patients with implants calculations of temperature may be preferable to calculations of SAR because of the more direct relationship between temperature and safety.

1. Introduction

When assessing the risk of RF power in an MR examination, the most important factor is the potential increase in core or local temperature. Due to the practical limitations of assessing local temperature enhancement, however, limits of power deposition are also expressed in SAR limits. The precise relationship between SAR and temperature is multifactorial. The effect of local SAR on local temperature depends on, among other things, the effects of thermal conduction, perfusion by blood, and the complex and heterogeneous geometry of human body. If the local or core temperature changes are high enough, there can be local and global physiological responses to maintain temperature stability.

More often patients who have had a total arthroplasty have an MR examination. A feeling of pain or heating during an MR scan is stated by some of the patients, with orthopedic implants [1]. Motivated by a FDA report of a patient with bilateral hip prosthesis who received burns on the inner thighs [2], we investigated RF heating within a phantom model of titanium hip prostheses (THP).

The aim of the present study was to model and calculate the SAR induced local temperature changes of different phantoms including a THP for different

frequencies, i.e. B_0 fields. The numerical results will be compared to an experimental assessment of temperature measured during a MR examination.

2. Materials and Methods

To estimate SAR, full-Maxwell equations calculations of absorbed power were performed for phantom models. A rectangular phantom was modeled according to the ASTM standard [3]. Experimental data were obtained with this phantom and a THP placed on a specific position. This setup also serves as a phantom for the numerical calculations. In addition a cylindrical phantom, shaped according to the human body torso, has been investigated numerically. Figure 1 shows the three dimensional representations of the phantoms which were filled with gel or a physiological saline solution of known electrical material properties.

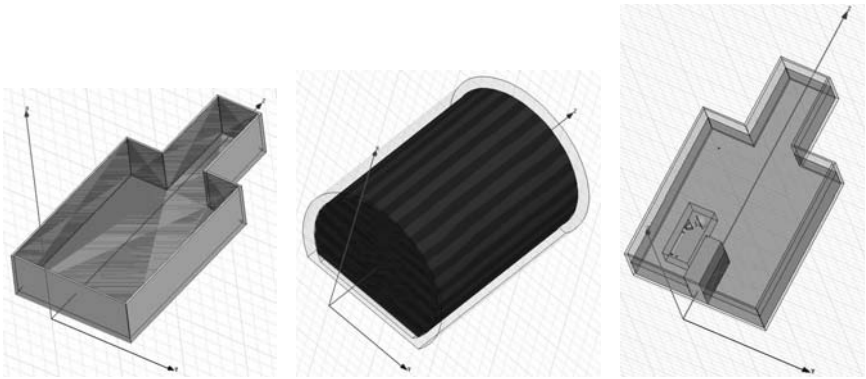

Fig. 1. Three-dimensional representations of phantoms. Left: rectangular ASTM phantom filled with gel (σ=0,27 S/m, ε_r=81). Middle: cylindrical phantom filled with physiological saline solution (σ=1,5S/m, ε_r=83). Right: ASTM phantom including the hip prosthesis filled with gel (σ=0,27S/m, ε_r=80) and with an integrated polystyrene block.

The numerical calculation of SAR levels and temperature fields requires a model of the RF coil and of the MR sequence. As the static field B_0 and the gradients are not expected to induce relevant deposition of energy in tissue, they have neglected. The RF coil was not modeled explicitly. Instead the B_1 field was assumed to be a circular-polarized wave. This corresponds to an ideal illumination of an ideal coil. The B_1 field is perpendicularly to the static B_0 of the MRI which determines the Larmor frequency of the wave. The circular polarization is achieved by superimposing two plane waves with 90° phase difference. The magnitude of the circularly polarized wave is determined from the maximum of the RF pulse of the MRI sequence used in the MR examination. For this turbo spin echo sequence B_1=12μT has been calculated. Only 180° pulses were considered in the numerical approach, because 90° pulses only deposits ¼ of the energy of a 180° pulse in the tissue. The total number of 180° pulses was 18240. The duration of a pulse equals to t=1ms, thus the effective RF exposition time is t=18.24s. For the delimitation of the environment in the model, a radiation

boundary was used which absorbs the wave, essentially ballooning the boundary infinitely far away from the phantom structure [4].

Numerical calculation of temperature changes are based on the bio-heat equation by Pennes [5]. Since the models are phantoms, perfusion by blood and heat generated by metabolism were be neglected. Thermal conductivity was assumed to be constant. Thermal source was modeled as the SAR value calculated by solving Maxwell equations. The exposure of the model to the electrical fields induced by the RF exposition was modeled as one continuous pulse. The pulse time was set to the effective RF exposition time. This approximates a pulsed MR sequence which is justified by different time scales for electromagnetic and thermal effects. All numerical investigations were performed using HFSS and ePhysics simulation software (Ansoft, USA). For the numerical calculation of the MR examination all data of the experimental setup were used as additional input. The relevant output of the calculation was the E field, the SAR values and temperature distribution.

The MR examination was done on a 1.5T MR-system (Intera, Philips Medical Systems) with body coil was used. Sequence protocol: Turbo Spin Echo, TE=60ms, TR=6190.6ms, FoV=530x530mm/416x416pixel, FA=90°, MTC=on resonance, slice thickness = 1.5 mm, slices 54, echoes (TSE) 22, TSE echo spacing 5.2ms, NSA=4, $SAR_{reported}$=3.9W/kg, max. B_1 amplitude 26.10μT, total duration 15:04minutes. A 4-channel fiber optic thermometer (Optocon, Germany) was utilized. A 40 kg human torso shaped gel phantom (114 mm gel depth) was used (dist. water; 0.8g/L NaCl; 5.85g/L poly(acrylic acid), Aldrich, USA) simulating the electrical and thermal properties of the human body. The upper thighs were separated by an inserted 'crotch' (60x173x200mm) of styrolene material (ε_r=2.6) fixed with silicone into the phantom. A total hip prosthesis (THP) (Plus Orthopedics, Switzerland), 185 mm total in length, each consisting of a titanium shaft and cup with polyethylene inlay and a stainless steel ball were inserted symmetrically at intended implant position into the gel fixed by a plastic holder system. Two temperature sensors were placed in the direct surrounding of the THP, a third one far away serving as a reference. A SAR pretest was performed without THP. Temperature was measured prior, during and after RF application.

3. Results and Discussion

The rectangular ASTM and the cylindrical phantom were numerically calculated for various field strengths in order to clarify changes of the energy deposition under the irradiated frequency. Figure 2 shows the local SAR distributions for the rectangular and cylindrical phantom. As expected, increasing the field strength (frequency) the local energy deposition increases. However, particular SAR distribution depends on the phantom geometry. The numerical calculations predict a typical structure of the local SAR distribution. The high SAR values in the neck of the rectangular phantom, especially in the corners, must be attributed to the phantom design. When placing instruments or implants at these points, the energy depositions due to geometry must be considered very carefully in order to avoid misinterpretations.

It is clearly recognized that the cylindrical phantom offers a larger volume with homogeneous SAR distribution contrary to the rectangular phantom. Primarily the

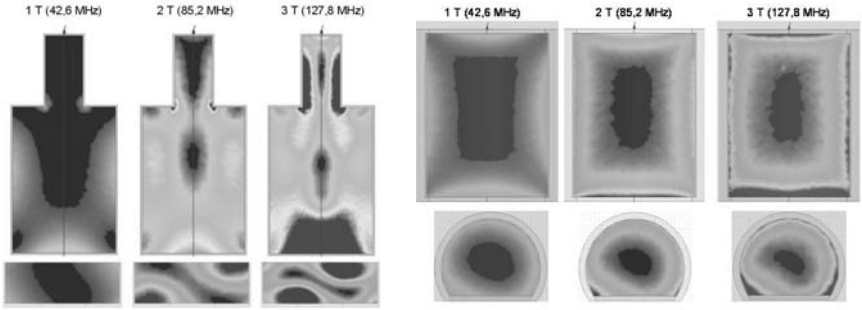

Fig. 2. Local SAR distributions in cross sections through the rectangular (left) and the cylindrical phantom at different frequencies, i.e. B_0 field strength. The linear scale ranges between 0W/kg on the left and 270W/kg and between 0W/kg and 140W/kg on the right.

energy deposition takes place at the edges. This is a result of the geometry of the phantom. In summary, the SAR distribution is a result of the irradiated frequency as well as the geometry, homogeneity, and material properties of the object, in which the energy deposition takes place.

Figure 3 shows the SAR and the temperature distribution in perpendicular cross sections for both phantom at B_0=1,5T. The SAR values at the sides are clearly increased. The higher SAR value at the lower end results from modelling the coil as a wave moving from infinity. If a bird cage coil would be used, this effect occurs only when the phantom is totally covered by the coil. The relationship between local SAR levels and local temperature is not, however, straightforward.

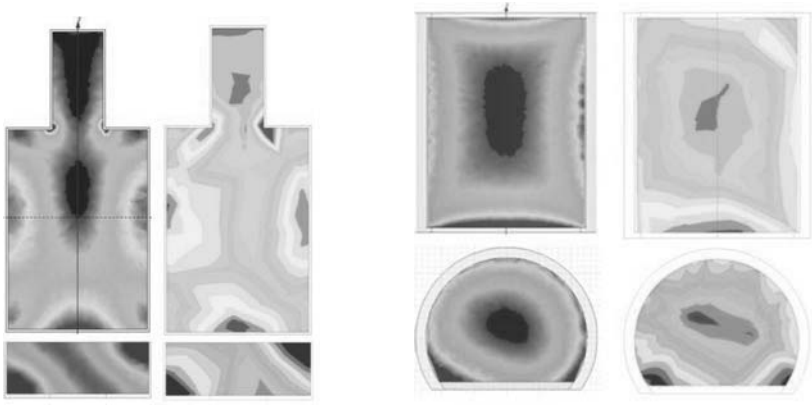

Fig. 3. Distribution of local SAR (left) and maximal local temperature (right) for $B_0 = 1.5$ T shown in cross sections through the rectangular (left) and the cylindrical phantom (right). The effective RF exposition is 18s. The temperature scale is linear between 25°C and 25,5°C on the left and 25,25°C on the right.

Numerical calculations confirms the theoretical power law $SAR \sim (B_0)^2$ but not $SAR \sim \Delta T$. Instead, in the local hot spot $SAR \sim \Delta T^{1.6}$ was observed.

Thus, calculations of temperature may be preferable to calculations of SAR as an expression of a more direct relationship between temperature and safety.

Clearly, the experiment is not able to provide a local temperature map.

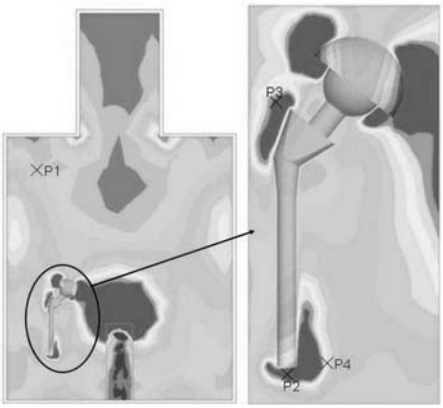

Fig. 4. Local temperature map shown in a cross section through the rectangular phantom with THP implant as used in a B_0=1,5T examination with effective RF exposition of 68,43s. The temperature is between 25°C and 27,5°C. On the implant the surface temperature is shown.

However, if taking the numerical solution maps into account, points of interest with a predicted significant change in temperature can be selected for measurements. In this manner, the numerical solutions guide and are beneficial for the experimental setup. In the present study there are four interesting measurements points as indicated in Fig. 4. To model the experimental setup numerically, the phantom were accomplished following the experimental setup. The magnitude of the RF wave was B_1=12μT. The effective duration of the RF exposure was 68.43s, only 180° pulses were taken into account. Figure 4 shows the temperature distribution within the phantom with integrated hip prostheses. It

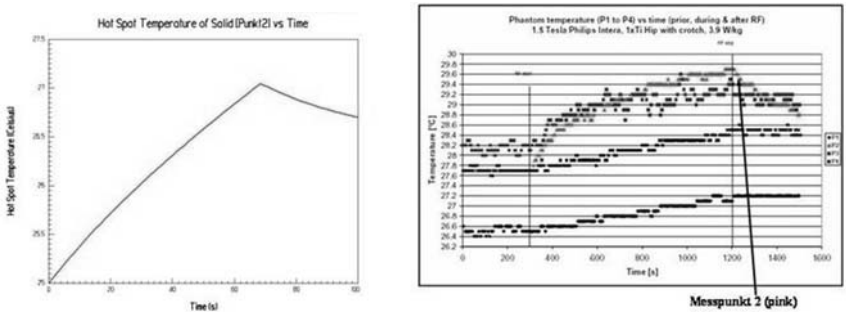

Fig. 5. Comparison of numerically calculated prediction and experimental measurement of the temperature as function of time at point P2 in a B_0=1,5T with effective RF exposition of 68,43s. Point P2 is the highest curve. Measurements of other points are shown too.

can be seen that the polystyrene block favours the energy deposition in the central part of the phantom. Thus a temperature increase at the hip prostheses pan

develops. Also a change of temperature at the shank ends is recognized. This is due to the edges of the prosthesis which are points of entrance for electromagnetic waves.

Figure 5 shows a direct comparison between the measurement and the numeric calculation for the measurement point P2, compare Fig. 4. The results are comparable qualitatively. In the present study the difference between numerical solution and experiment is between 2.25% and 81.33% depending on the point. The difference is a result of the simplified numerical model and not ideal experimental conditions.

4. Conclusions and Open Questions

SAR levels and temperature increases in phantoms are subject to phantom geometry, homogeneity and material. There is not good spatial correlation between SAR and temperature increase, the physiologically relevant parameter in evaluating risk of MR examinations. This is a result of the multifactorial relationship between SAR and temperature. It is apparent from numerical results and comparison to experimental results in this study that implants provide a relatively efficient conductive heat transfer to the surrounding tissue. Although this study exclude perfusion it is expected that in heterogeneous human body, the location of maxima of SAR levels and temperature will not totally coincide. Although global or local SAR levels may be a simple straight forward approach, predication of temperature increases remains more relevant in terms of safety.

It is noteworthy that all models presented here need a further refinement with respect to RF coil and MR sequence model; and a human body model instead of phantoms. The separation of solutions of Maxwell equations and governing temperature equations needs to be verified. Finally, the use of phantoms or special human body models is an intermediate step. A general approach addressing individual patient, potentially with implants, especially in high field MR examinations, remains an aim for the future.

Acknowledgements. The authors thank Markus Laudien from Ansoft Europe for continuing support and ePhysics license key.

References

1 FDA-Medical-Device-Reporting Database, ACCESS NUMBER: M375292.
2 FDA-MAUDE-Database, MDR Report Key 469680.
3 ASTM F2503-05 Standard Practice for Marking Medical Devices and Other Items for Safety in the MR Environment.
4 Ansoft Inc. HFSS V9.2 Online-Help.
5 H.H. Pennes, J. Appl. Physiol., **1**, 93, 1948.

Real Time Neuronavigation Using 3-D Ultrasound and MRI in Patients with Brain Tumor

Martin Engelhardt[1,4], Christian Hansen[2,4], Bernhard Brendel[4], Stephanie Hold[3,4], Christopher Brenke[1,4], Ioannis Pechlivanis[1,4], Albrecht Harders[1,4], Helmut Ermert[2,4] and Kirsten Schmieder[1,4]

[1] Department of Neurosurgery, Knappschaftskrankenhaus, Ruhr-University Bochum, In der Schornau 23-25, D-44892 Bochum, Germany
E-mail: martin.engelhardt@rub.de
[2] Institute of High Frequency Engineering, Ruhr-University Bochum, Universitätsstrasse 150, D-44801 Bochum, Germany
E-mail: christian.hansen@rub.de
[3] Institute of Medical Engineering, Ruhr-University Bochum, Universitätsstraße 150, D-44801 Bochum, Germany
[4] Ruhr Center of Excellence for Medical Engineering (KMR), Universitätsstraße 150, D-44801 Bochum, Germany

Abstract. The loss of accuracy during neuronavigation, caused by intraoperative changes of intracranial masses after trepanation, is one of the major problems in neurosurgery. It usually affects the planning and performing of surgery as both is conventionally based on preoperative patient data sets. Thus, an online acquisition and processing of data during surgery is needed to increase navigational accuracy. Beside cost-intensive solutions like intraoperative CT or MRI scanners, an ultrasound guided navigation is applicable and demonstrates online guidance in real-time. This study describes a development to provide the best possible support for neurosurgeons intraoperatively, concerning data presentation and ergonomic aspects in the operation theatre. Patients underwent MRI examination for a conventional neuronavigation preoperatively. Intraoperatively, ultrasound volume data sets were acquired by means of a tracked ultrasound probe and related to this preoperative MRI. The intraoperative ultrasound imaging was possible in all cases whereat ultrasound images were displayed beside the corresponding MRI images. Brain shift was presentable and the possibility of online navigation with ultrasound and preoperative MRI was helpful for the surgeon.

1. Introduction

As conventional neuronavigation systems usually incorporate preoperatively acquired volume data sets, such as CT or MRI, brain shift during surgery can lead to loss of accuracy [1]. Brain shift can be caused by swelling, loss of spinal fluid or tumor mass reduction and is usually present in brain surgery. In particular, in lesions which are located sub cortical, i.e. not directly visible, or which have greater dimensions, accurate neuronavigation is needed to achieve the best

possible resection and to avoid additional damage of brain tissue and neurological deficits due to the surgery. Hence, there is actual demand for an intraoperative update or re-acquisition of navigational volume data sets. Though, intraoperative CT- or MRI-scanner are already available, both are cost intensive and require extra time and laborious modifications during surgery and are mostly not used for this purpose.

The aim of the presented work was to develop a navigation system based on 3D ultrasound data for an intraoperative real-time navigation without loss of accuracy. Furthermore, the illustration of the ultrasound data during surgery was supposed to be optimized to develop an easy-to-use system applicable in the operation theatre. The aforementioned actual demand for this has also encouraged other groups to investigate on an intraoperative application of ultrasound [2,3] and even yield to commercial systems [4,5,6]. However, the application of ultrasound volume data for navigation is still not established. Neurosurgeons are often not familiar with ultrasound as an intraoperative imaging modality. An intraoperative orientation in ultrasound images as well as a cognitive transfer to the operation field and the anatomy are perceived to be difficult. Furthermore, the surgical workflow should be altered as low as possible to gain broad acceptance for a new online navigation system based on ultrasound data and the offered solution may not result in an overloading of visual information. Thus, the displaying of the ultrasound investigation during surgery was intended to be easy in orientation and reference to the preoperative MRI to access a save and easy planning of the surgical procedure.

2. Experimental Methods

Preoperatively acquired volume data sets of MRI were obtained of patients with brain tumor, planned for elective surgery. Common neuronavigation based on this data was implemented during surgery to compare the different navigational systems. With a Polaris Optical Tracking Camera System an intraoperative point-registration of the preoperative data to the patient's head was done using fiducials markers. For the intraoperative ultrasound investigation a Siemens Sonoline Elegra and an endocavity ultrasound probe with a small footprint (6.5EC10) armed with an active reference base were used. To improve coupling of ultrasound to tissue a stand-off gel pad was placed onto the dura after removal of the skull. Intraoperative ultrasound volume scans of the brain were acquired before opening the dura by scanning the region that was marked by trepanation. The volume data scans were matched and compared with the preoperative MRI data sets. For a better orientation of surgeons, corresponding cross-sections of the volume data set of the MRI and the ultrasound investigation were displayed side-by-side on one monitor (Fig.1,2). This process was performed repetitive during surgery. Ergonomic aspects concerning handling, visualization and accuracy of the different navigation systems were analyzed.

3. Results and Discussion

In 8 patients the intraoperative investigation was initially performed during surgery as described above. In all cases the referenziation and visualization of the tumor was possible with accurate online ultrasound data. The repetitive ultrasound investigations showed the progress of the surgical procedure in up-to-date ultrasound data, while corresponding preoperative MRI images contribute to a better orientation for the surgeon. The display of both data sets on an additional monitor provided for a precise further planning and performing of surgery. This advantage was obvious even if surgeons were not familiar with the use of intraoperative ultrasound. In contrast to common used neuronavigation systems based on preoperative volume data sets, the accuracy of an intraoperative online 3D ultrasound investigation stays unaffected by brain shift and tumor volume reduction (Fig.3).

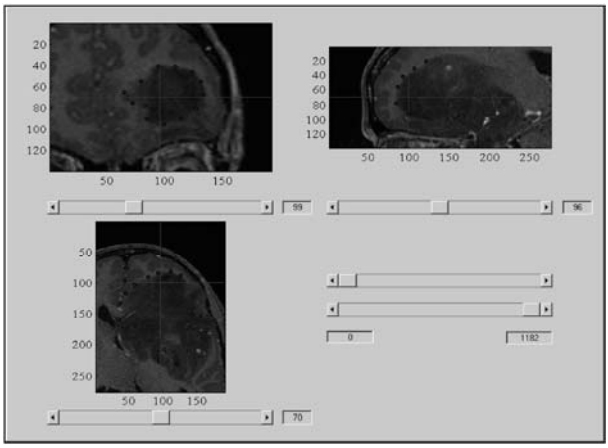

Fig. 1. Exemplary image planes (coronal, transverse and sagittal) of preoperative MRI. Female, 42 years with astrocytoma grade II. Intraoperative Illustration.

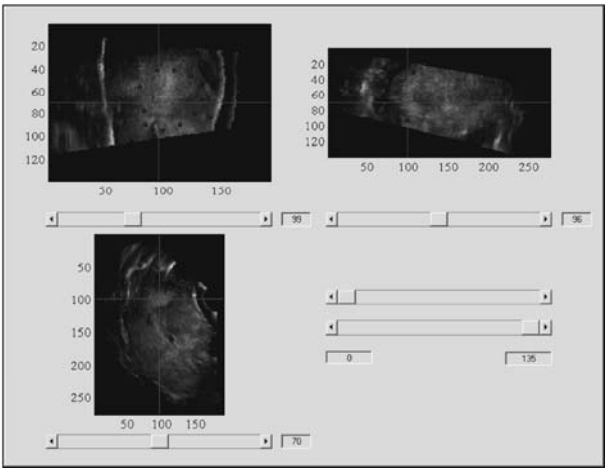

Fig. 2. Ultrasound image planes, position and orientation corresponding to Fig.1. Intraoperative ultrasound investigation in all orientations. Illustration corresponding to the preoperative MRI. Female, 42 years, astrocytoma grade II.

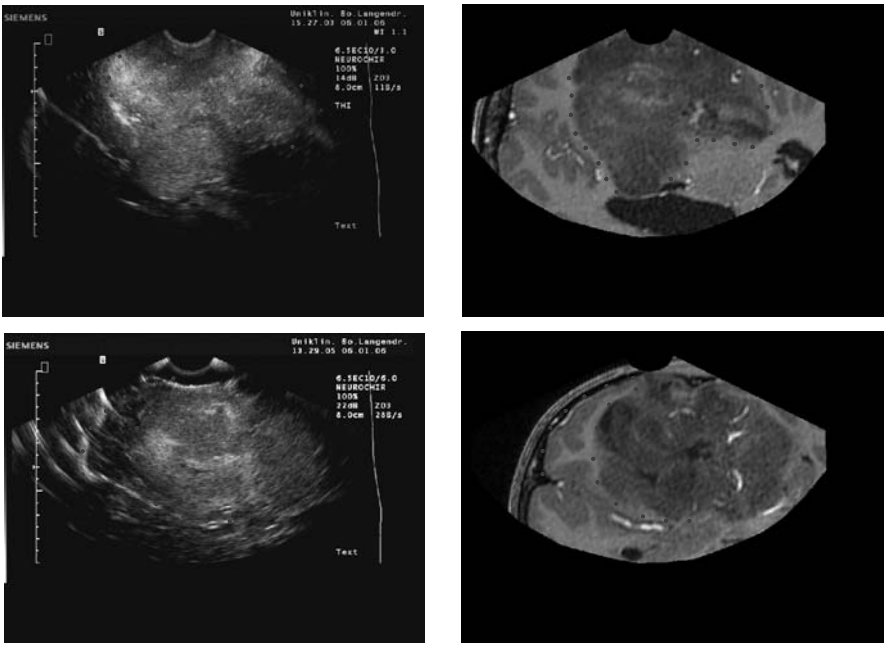

Fig. 3. Ultrasound image planes (left) and corresponding MRI image planes (right). Demonstration of tumor borders in relation to the brain to illustrate the brain shift.

4. Conclusions

In good correlation to the findings of other groups [4,5], the presented results show that the visualisation of anatomy using intraoperative 3D ultrasound and preoperative MRI is helpful for the planning and performing of brain surgery. Navigation, using accurate online data, is a reliable alternative to cost intensive solutions, even with the possibility of repetitive investigations and a commonly used illustration in three orientations, adapted to the preoperative MRI/CT scan. The online ultrasound navigation prevents the loss of accuracy caused by brain shift and the surgical workflow is not altered.

Furthermore, an additional depiction of preoperative MRI image planes might be totally redundant and the whole intraoperative navigation after trepanation might be conducted on ultrasound volume data sets.

Acknowledgements. This work is a project of the Ruhr Center of Excellence for Medical Engineering (Kompetenzzentrum Medizintechnik Ruhr, KMR), Bochum, Germany. It is funded by the Federal Ministry of Education and Research, Germany (BMBF, grant 13N8079) and supported by Siemens Medical Solutions.

References

1 M. M. J. Letteboer, P. W. A. Willems, M. A. Viergever, and W. J. Niessen, in *Brain Shift Estimation in Image-Guided Neurosurgery Using 3-D Ultrasound,* IEEE Trans Biomed Eng, 52(2), 268-76, 2005

2 A. Joedicke, T. Springer, and D.-K. Boeker, in *Real-time integration of ultrasound into neuronavigation: technical accuracy using a light-emitting-diode-based navigation system,* Acta Neuroch, 146, 1211-20, 2004

3 C. Trantakis, J. Meixensberger, D. Lindner, G. Strauß, G. Grunst, A. Schmidtgen, and S. Arnold, in *Iterative neuronavigation using 3D ultrasound. A feasibility study.* Neurological Research, Vol.24, 666-70, 2002

4 N. Shinoura, M. Takahashi, R. Yamada, in *Delineation of Brain Tumor Margins Using Intraoperative Sononavigation: Implications for Tumor Resection,* J Clin Ultrasound, Vol.34, No.4, 177-83, 2006

5 W. Tirakotai, D. Miller, S. Heinze, L. Benes, H. Bertalanffy, and U. Sure, in *A Novel Platform for Image-Guided Ultrasound,* Neurosurg, 58, 710-8, 2006

6 A. Gronningsaeter, A. Kleven, S. Ommedal, TE. Aarseth, T. Lie, F. Lindseth, T. Langø, G. Unsgård, in *SonoWand, An Ultrasound-Based Neuronavigation System*". Neurosurgery, 47:6: 1373-1380, 2000.

Vasodynamics of the Murine Arteria Saphena by Optical Coherence Tomography

Julia Walther[1], Sven Meißner[1], Gregor Müller[2], Alexander Krüger[1], Henning Morawietz[2] and Edmund Koch[1]

[1] Klinisches Sensoring und Monitoring, Medizinische Fakultät Carl Gustav Carus, Technische Universität Dresden, Fetscherstr. 74, 01307 Dresden
E-mail: edmund.koch@tu-dresden.de
[2] Gefäßendothel/Mikrozirkulation, Medizinische Fakultät Carl Gustav Carus, Technische Universität Dresden, Fetscherstr. 74, 01307 Dresden
E-mail: henning.morawietz@tu-dresden.de

Abstract. To investigate the pathogenesis of arteriosclerosis and its negative effects on the vasodynamics, *in vitro* experiments on isolated blood vessels as well as *in vivo* experiments are essential. The isometric force measurement commonly used to analyse the vasoconstriction of isolated blood vessels can not be applied in the *in vivo* situation. In contrast Optical Coherence Tomography (OCT) allows the acquisition of 2D cross sectional images und 3D cross sectional image stacks of vessel sections. We demonstrate that our two Fourier domain OCT-systems with their automated image analysis are suitable investigative tools for studying the stage of arteriosclerotic plaque formation as well as for examining the response of the blood vessel to vasomotor stimuli in the mouse model.

1. Introduction

In the industrialized world cardiovascular diseases have become the number one death cause. 46.8 % of all deaths can be ascribed to arteriosclerosis [1]. The disease is characterized by inflammatory changes of the inner (*intima*) and middle (*media*) blood vessel wall. These structural changes of the wall finally lead to arteriosclerotic plaque formation [2-4]. Even in an early stage the vasodilatation or -constriction can be negativelly affected due to an increased stiffness of the vessel wall [5, 6]. To analyse the pathogenesis of arteriosclerosis and its effects on the vasodynamics, *in vitro* experiments on isolated vessels as well as *in vivo* experiments are essential.

Optical Coherence Tomography (OCT) is a high resolution imaging technique, which allows non-invasive *in vivo* examinations of subsurface tissue [7]. With this technique it is possible to generate 2D cross sectional images of optical inhomogeneous biological tissue. In contrast to established *in vitro* techniques for the analysis of vasodynamics such as isometric force measurements the blood vessels remain in the surrounding tissue with blood flow and innervation [8]. Most reports dealing with vascular OCT imaging focus on intravascular catheter applications and characterization of arteriosclerotic plaques. We use high speed transluminal OCT in a mouse model to study the impaired vasodynamics during the early stage of arteriosclerosis. In comparison to intravascular OCT, the

transluminal approach has the advantage of avoiding micro traumata in the endothelium.

2. Experimental Methods

Examinations were carried out with two Fourier domain OCT-systems, which differ in the acquisition speed. Compared with Figure 1. both systems are based on short-coherence interferometry and consist of a broadband short-coherent light source, a 2D- or 3D-scanner, a spectrometer and a fiber coupling. The modified Michelson interferometer is integrated into the scanner head. In contrast to time domain OCT the output of the interferometer is measured with a spectrometer instead of one photodiode. Therefore this system uses the spectral analysis of the resulting interference signal. In one single spectrum the scatter amplitude a(z) with the path length z along an axis in the tissue is encoded. The depth information can be found out by a Fourier transformation of the interference spectrum. The advantage of the Fourier domain OCT (FD OCT) is the higher acquisition speed and the better signal to noise ratio to OCT with time domain detection [9, 10].

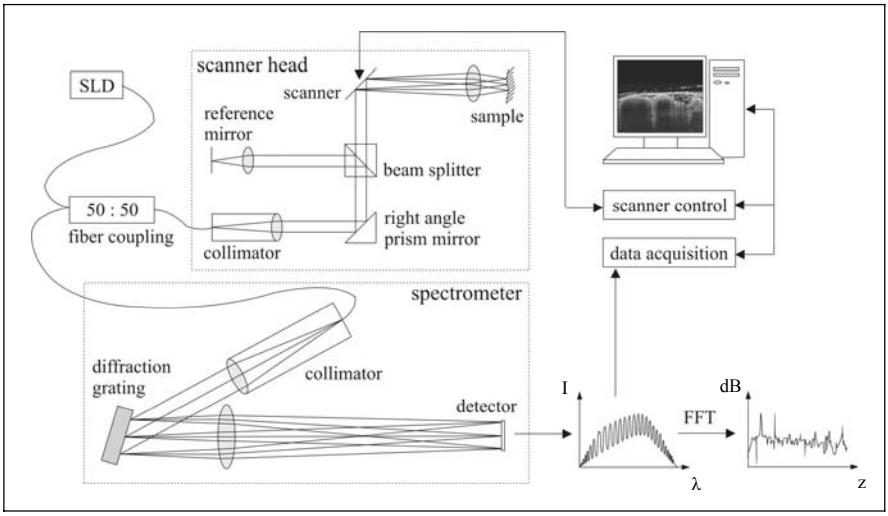

Fig. 1. Schematic of the principle of the FD OCT-system with 2D-scanner head.
Abbreviation: SLD – superluminescent diode; I – intensity; dB – Fourier amplitude in decibel; z – probe depth related to reference path length; FFT – Fast Fourier Transfomation

The first FD OCT-system has a read out rate of 1.25 kHz for one A-scan and the advantage, that it shows a high image quality due to the long integration time. The advantage of the second, fast FD OCT-system, is a tenfold higher read out rate compared to the first FD OCT-system. Because of the higher read out rate of 12.2 kHz it is possible to acquire 44 2D-images (B-scans) consisting of 256 A-

scans within one second. For this reason there is the possibility of an image acquisition with high temporal resolution.

For the analysis of the vasodynamics, the *arteria saphena* of the right leg of a wild type mouse (C57BL/6) was choosen. The murine *a. saphena* is suitable for the *in vivo* examination particularly due to the small diameter, the response of the blood vessel to vasomotor stimuli and the advantageous anatomical position. The reaction of the blood vessel is induced by dermal application of the vasodilator Sodium-Nitroprussid (SNP) with a concentration of 3 mM and the vasoconstrictor potassium K^+ in physiological saline solution containing 80 mM.

3. Results and Discussion

Our feasibility study has shown that OCT is very suitable for examining the vasodynamics of the murine *a. saphena*.

The first study was executed with the 1.25 kHz FD OCT-system. Time lapse series of 2D cross sectional images of the examined vessels as well as 3D cross sectional image stacks (300 B-scans) were acquired and analysed by automated image routines. The inner diameter of the blood vessel changed from 150±22 µm before to 86±6 µm after application of potassium. After application of SNP a vasodilatation of 124±2 % (185±25 µm) of the initial inner diameter was noticed.

The 2D cross sectional images, which were acquired with the 12.2 kHz FD OCT-system, had a higher temporal resolution. With the same expenditure of time it was possible to acquire the tenfold number of images. Because of the lower integration time, the detected amplitude of the back scattered intensity was reduced by a factor of ten. Figure 2. shows the 2D images of the vasodynamic measurement of a female wild type mouse.

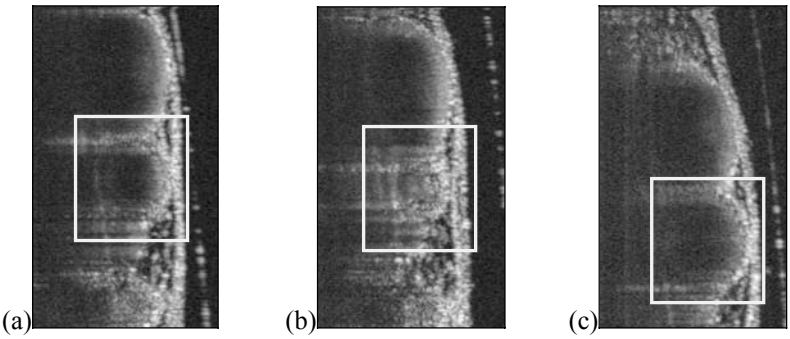

Fig. 2. Illustration of the vasodynamics on one example aquired with the 12.2 kHz FD OCT-system; (a) *a. saphena* after application of physiological saline solution (control condition); (b) vasoconstriction after application of 80 mM K^+ in physiological saline solution; (c) vasodilatation after application of 3 mM SNP; The range 140×240 pixel of a 1024×256 pixel 2D cross sectional image is shown.

With these acquired 2D cross sectional images it is possible to generate temporal resolved 3D image stacks in which the z-axis represents the time. By

automated image routines the diameter of the inner lumen of the a. saphena can be calculated depending on the time, compared to the following Figure 3. The diagramms in this Figure show the change of the inner diameter after application of vasomotor stimuli. These acquired values of the diameter of one examined wild type mouse lie approximately in the interval of our former feasibility study with the 1.25 kHz OCT-system. The inner diameter of the blood vessel changes from 190 µm before to 60 µm after application of potassium. After application of SNP a vasodilatation of 126 % (240 µm) of the initial inner diameter was noticed. For the evaluation of these values more in vivo examinations with the 12.2 kHz FD OCT-system at the murine a. saphena are essential.

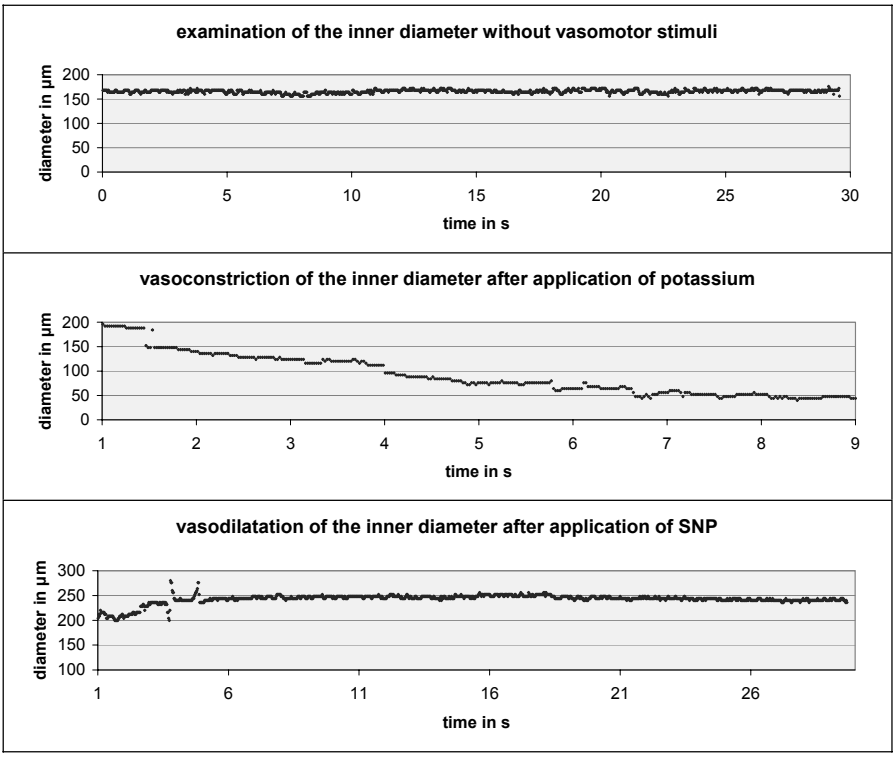

Fig. 3. Temporal characteristics of the diameter of the *a. saphena* after application of (a) physiological saline solution (control condition), (b) 80 mM K^+ in physiological saline solution and (c) 3 mM SNP; Scan rate: 44 B-scans consisting of 256 A-scans within one second

4. Conclusions

OCT is a suitable investigative tool for studying vasodynamics in the mouse model. It is possible to measure in vivo without preparation trauma which comes along with established methods such as isometric force measurements in organ chambers. In further experiments the results have to be evaluated in comparison to this standard technique. Knockout and transgenic mouse models will be used to examine the influence of genes during the development of early arteriosclerosis in vivo. Within following studies using the 12.2 kHz FD OCT-system the reliability on the examined results has to be proven.

References

1 Statistical Federal Office (Ger)
2 P. K. Shah, *Mechanisms of plaque vulnerability and rupture*, J Am Coll Cardiol, Vol. 41, 15-22, 2003
2 E. Falk, P. K. Shah, V. Fuster, *Coronary plaque disruption*, Circulation, Vol. 92, 657-71, 1995
4 P. Greenland, S. S. Gidding, r. P. Tracy, *Commentary: lifelong prevention of atherosclerosis: the critical importance of major risk factor exposures*, Int J Epidemiol, Vol. 31, 1129-34, 2002
5 J. P. Halcox, W. H. Schenke, G. Zalos, et al., *Prognostic value of coronary vascular endothelial dysfunction*, Circulation, Vol. 106, 653-8, 2002
6 J. E. Gage, O. M. Hess, T. Murakami, M. Ritter, J. Grimm, H. P. Krayenbuehl, *Vasoconstriction of stenotic coronary arteries during dynamic exercise in patients with classic angina pectoris: reversibility by nitroglycerin*, Circulation, Vol. 73, 865-76, 1986
7 D. Huang, E. A. Swanson, C. P. Lin, J. S. Schuman, W. G. Stinson, W. Chang, M. R. Hee, T. Flotte, K. Gregory, C. A. Puliafito, and J. G. Fujimoto, *Optical coherence tomography*, Science, Vol. 254, 1178-81, 1991
8 J. A. Angus, C. E. Wright, *Techniques to study the pharmacodynamics of isolated large and small blood vessels*, J Pharmacol Toxicol Meth., Vol. 44, 395-407, 2000
9 G. Häusler and M. W. Lindner, *Coherence Radar and Spectral Radar – New Tools for Dermatological Diagnosis*, Journal od Biomedical Optics, Vol. 3, 21-31, 1998
10 M. A. Chroma, M. V. Sarunic, C. Yang, and J. A. Izatt, *Sensitivity advantage of swept source and Fourier domain optical coherence tomography*, Optics Express, Vol. 11, 2183-89, 2003

An Imaging System in the Sub Millimeter Area

Christian Krebs[1], Thorsten M. Buzug[2] and Dirk Nüßler[3]

[1] RheinAhrCampus Remagen, Department of Mathematics and Technology, Suedallee 2, D-53424 Remagen, Germany
[2] Institute of Medical Engineering, University of Luebeck, Ratzeburger Allee 160, 23538 Luebeck, Germany
E-mail: buzug@imt.uni-luebeck.de
[3] FGAN, Research Institute for High Frequency Physics and Radar Techniques, Department MHS, Neuenahrerstraß2 20, D-53343 Wachtberg, Germany
E-mail: nuessler@fgan.de

Abstract. The millimeter wave frequency range was pushed through test systems for production lines in the last years. Non destructive test systems for quality control need more powerful sensors to detect non-metallic pollutions inside packages. The millimeter wave frequency range up to the lower terahertz frequencies (T-ray imaging) offers the opportunity to look through many packages. Alternative applications are the detection of non metallic and/or under cloth wearied weapons. Other fields of interest for this frequency range are medical applications, especially the detection of skin cancer.

1. Introduction

The majority of papers presenting terahertz scanners, based on pulsed systems which create the frequencies over mixing of two laser lines [1] [2]. Recent developments in laser technology allow the realization of sensor systems under 2 THz. In the frequency range between 100 GHz and 1 THz technologies for the frequency generation based on the mixing of laser lines and the multiplying from lower frequencies overlap. This frequency range is called terahertz gap. The terahertz gap (100 GHz–2 THz) could not be used in the past, due to the low availability of commercial components. Furthermore the higher atmospheric attenuation has prevented the use of this frequency range for many applications. Only astronomy research groups have used this frequency range intensively. Initiated by the technology evolution over the last years, more and more systems have been developed. The range of interest covers the region between the classic radar and communication bands (under 100 GHz) and the infrared band. It combines the features of both areas. THz waves offer less scattering in matter than the IR, because of the greater wavelength. It is capable of a better spatial resolution than radar frequencies as it has shorter wavelengths than classic radar. The development of compact frequency generators first allowed the assembly up to compact imaging systems, which show the potential of this unused frequency range.

Publications in the last years show a growing interest for millimeter and terahertz sensors for medical scenarios. Especially measurement systems which are using absorption lines and imaging systems for the detection of cancer are under development. A big drawback is the fact of high absorption of polar molecules

like water in this frequency range. Cause of this the typical range in dermal tissue is only about a few millimeters. For this reason in-vivo measurements are only useable for applications close to the surface.

One of the most important tissue anomalies is the malign melanoma. Skin cancer is very common, and one of the fastest growing types of cancer. The detection is difficult, because it often emerges beneath the skin. Nowadays the only approach to find melanomas is to operate the suspicious tissue and analyze it histological. Unfortunately most malign tissues are only visible in an advanced state. Therefore the risk for metastases is very high. A better way would be to detect melanomas in-vivo in an early state [3] [4].

It is suspected that the reflection properties are quite different between health and malign tissue. Due to the fact that for example the cell structure and/or the water consistent of skin anomalies are different. It is possible to detect skin anomalies in a 2D image based on differences in the reflection coefficients.
The characterization of the measurement system and the first laboratory results will be presented in this paper.

2. Frequency Generation and Detection

The measurement system consist of three several configurations to generate frequencies. At once a Synthesized Sweep generator from Agilent (Agilent 83650B) covers the frequency spectrum from 10 MHz through 50 GHz continuously. To generate frequencies from 75 GHz up to 110 GHz a mmW source module (Agilent 83550B) is used. The source module consists of an internal amplifier and a six time frequency multiplier (Figure 1 left). An internal feedback controls the amplifier and generates a leveled output of 1 mW.

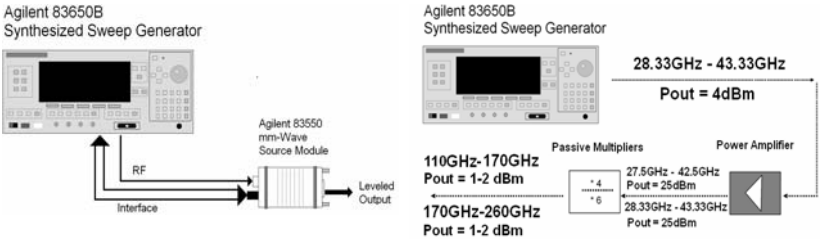

Fig. 1. Schemes of the frequency generation up to 110 GHz (left) and up to 260 GHz (right)

For higher frequencies up to 260 GHz, several external frequency multipliers from Vergina Diods are used. An additional external amplifier driver stage in the frequency range from 28.33 GHz to 43.33 GHz with an output power of 300 mW compensates the conversion loss. Figure 1 (right) shows a scheme of the of the frequency generation up to 260 GHz.

The detection of the signals will be done by a spectrum analyzer (Rhode&Schwarz FSEK30) with an external mixer. A PC received the measured data. In addition to the scalar measurement system a Vector Network Analyzer (VNA) is available and measures frequencies and phase up to 110 GHz.

3. Dielectrical Antennas

The antennas mounted in the system are dielectric waveguides with their tips cut in an appropriate angle [5]. The outer dimensions correspond to the inner dimensions of classical waveguides. For the W band (75 GHz - 110 GHz) frequencies the tip length amounts to 18 mm (asymmetric x-taper). Angle and length of the tips determine the gain of the waveguides, similar to horn-antennas. The advantage of this kind of antenna is the flexibility of the waveguide and the well-known location of the phase centre. As the wave is guided mostly outside the waveguides, the antennas are placed with spacer to avoid any contact with other parts of the measurement system.

The 3 dB bandwidth of the antenna is about 15° at 260 GHz. The difference in intensity between the main lobe and the first order maximum is around 25 dB. The distance between the antenna and the sample should be as small as possible. The measurement of the reflection intensity off a metallic surface shows a maximum at a distance of about 6 mm, which we chose as the standard distance for our measurements.

4. Scanning System

To realize a 2dimensional image two linear stages are used (x and y direction). The maximum scan area is about 2.5 cm by 2.5 cm with a velocity of 1.5 mm/s. The transmission and the reflection of the radiation can be measured with the antennas to both sides of the sample or under a specified angle on one side of the sample. Figure 2 shows the transmission configuration. The resolution of the scanning system is about 600 μm in transmission and about 450 μm in reflection at 260 GHz.

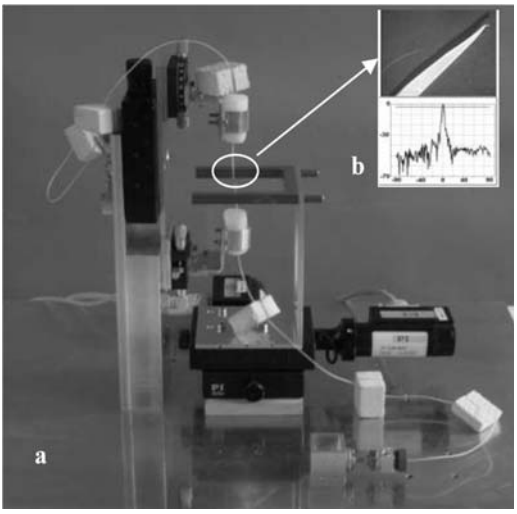

Fig. 2. Scanner in transmission configuration (a); Antenna diagram at 260GHz (b).

5. Test Measurements

The results presented in this chapter were measured in transmission and reflection. To compare the different frequencies and measurements, the color scale, which represents the amplitude, is the same in all pictures and not optimized for a single measurement. The first sample was a part of chocolate bar, polluted with a small piece of glass (Figure 3). This example shows the ability to detect non-metallic objects in a homogeneous sample. The amplitude varies over 10 dB in the presence of the glass. The structure of the glass can be clearly identified, as long as the chocolate is homogeneous. This method could be used in order to detect impurities in many different food-products, or other essential goods.

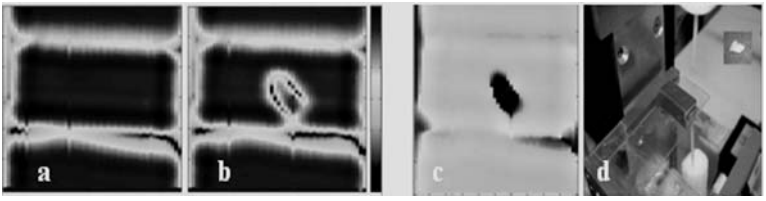

Fig. 3. Amplitude (in dB) and phase (in degree) of a chocolate bar a) Transmission without Glass (3 mm), b) Transmission with glass, c) measurement of the phase, d) measurement setup with chocolate.

The second sample is a leaf. It was measured at different frequencies from 94 GHz up to 260 GHz. Figure 4 shows the frequency range from 170 GHz to 260 GHz in 30 GHz steps. The higher the frequency the lower the transmission attenuation and consequently the dynamic range are increasing as shown in the measured leaf. The higher attenuation in parts of the structure of the leaf veins can be clearly identified. The transmission loss varies from 0 dB (red) to -30 dB (blue).

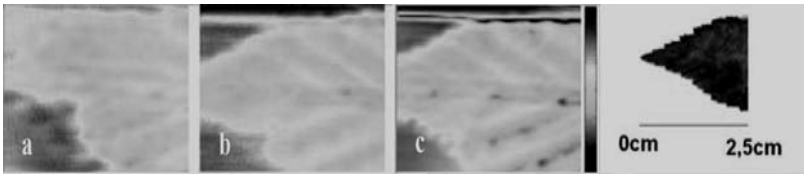

Fig. 4. Leaf at different frequencies scaled in dB a) 200 GHz, b) 230 GHz, c) 260 GHz.

To test the performance of the system a common floppy disc in transmission and a one euro coin in reflection was scanned at 260 GHz (Figure 5). The details of the disk can be clearly identified. Even the plastic pins and the guide of the data medium are visible. The transmission loss varies from 0 dB to -28 dB. The reflection of the euro coin shows the two different materials at the border and at the middle cause of the different reflection coefficient. Furthermore the cipher and parts of the structures around can be identified. The reflection varies from 0 dB to -15 dB.

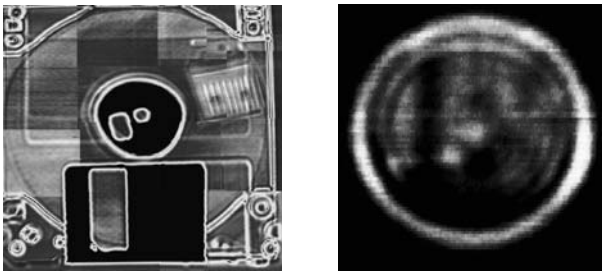

Fig. 5. Floppy in transmission at 260GHz (left) and Euro in reflection at 260GHz (right).

To analyze the reflection properties of water consistence in organic probes, a tip of a leaf was scanned at 260 GHz (Figure 6). The reflection in the veins is dispositional through the water allocation. From 0 dB (red) to -19dB (blue) the absorption increases.

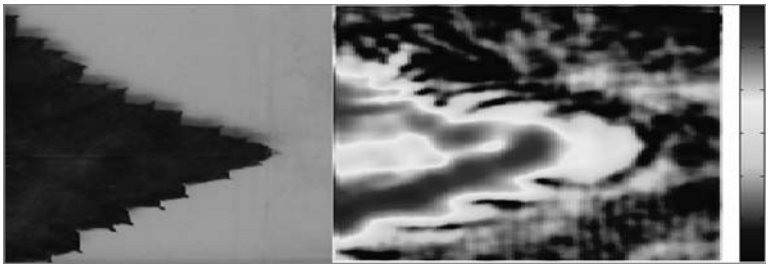

Fig. 6. Leaf in reflection configuration at 260 GHz (Scan area about 25 mm by 25 mm.

The next sample is a mole (Figure 7) at 94 GHz, measured in reflection, under an angle of 43°. It shows that the mole can be distinguished from the other tissue. The structure of the skin around can be clearly identified. This could be a method to locate skin cancer at an early stage. From 0 dB (red) to -35 dB, (blue) the absorption increases.

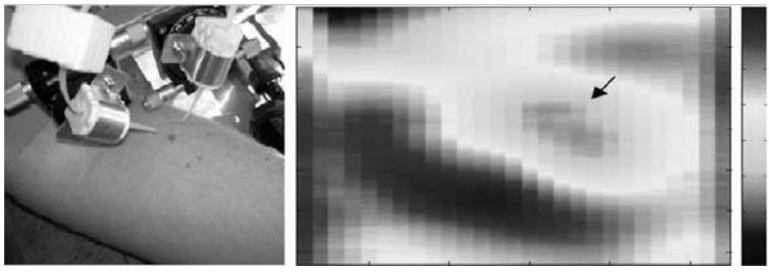

Fig. 7. A mole in reflection configuration at 260GHz.

6. Conclusions

The configuration of a scanner, which operates in the millimeter range, has been presented. Recapitulating, a vector measurement system can be accomplished up to 110 GHz while the measurement of the amplitude alone can be done up to 260 GHz.

A new VNA (Agilent PNA) in the range from 120 GHz to 220 GHz is available at the end of the year 2006 and the scalar frequency range will be up to 500 GHz in the next years.

Due to conversion losses, the signal output decreases at higher frequencies. To solve this problem, a different method for detecting and analyzing frequencies will be developed, using special probes with DAQ (data acquisition) devices. Therefore, the use of sub-harmonic mixers is no longer necessary.

The focus of the dielectric waveguides is about 8 mm in diameter at a distance of 10 mm (94 GHz). Lenses could help to bundle the power and lead to a higher spatial resolution. The present resolution is 600 μm at 260 GHz.

Till now, the measurement of a 25 mm by 25 mm area takes 15 minutes at minimum related to the chosen resolution cause of the old linear stages. So it was quite difficult to scan at a patient. The new scanner with the faster linear stages is under construction.

An application scenario of the mmW range in the medical field can not be answered at present. A skin cancer screening is the next step to analyze the frequency performance of infected and health tissue.

Acknowledgements. The authors would like to thank Lind™ Germany for the chocolate probes, Universitätsklinikum Bonn for the melanoma tissue and all colleagues who have been engaged in the realization of the scanner system.

References

1 Walker, G.C.: “Terahertz Imaging and International Safety Guidelines” Med. Imaging, SPIE 4682, 2002.
2 Woodward, R.M. et al.: “Terahertz pulse imaging in reflection geometry of human skin cancer and skin tissue”, Phys. Med. Biol. 47 3853-3863, 2002.
3 Zhang, X-C: “Terahertz wave imaging: horizons and hurdles”, Phys.Med.Biol. 47 3667-3677, 2002.
4 Terra View, Cambridge, UK.
5 Weinzierl, J. et al.: “Simulation and Measurement of Dielectric Antennas at 150GHz”, Proceedings of the 29th European Microwave Conference, 1999.

Mutual Attraction of Oscillating Microbubbles

Michiel Postema, Michał Mleczko and Georg Schmitz

Ruhr-Universität Bochum, Institute for Medical Engineering, Building IC, 6/144,
44780 Bochum, Germany
E-mail: michiel.postema@ruhr-uni-bochum.de

Abstract. The driving of contrast microbubbles towards a boundary by means of primary radiation forces has been of interest for ultrasound-assisted drug delivery. Secondary radiation forces, resulting from oscillating microbubbles under ultrasound insonification, may cause the mutual attraction and subsequent coalescence of contrast microbubbles. This phenomenon has been less studied. Microbubbles with a negligible shell can be forced to translate towards each other at relatively low mechanical indices (MI). Thick-shelled microbubbles would require a higher MI to be moved. However, at high MI, microbubble disruption is expected. We investigated if thick-shelled contrast agent microbubbles can be forced to cluster at high-MI. The thick-shelled contrast agent M1639, inserted through a cellulose capillary, was subjected to 3 MHz, high-MI pulsed ultrasound from a commercial ultrasound machine, and synchronously captured through a high numerical aperture microscope. The agent showed the ultrasound-induced formation of bubble clusters, and the translation thereof towards the capillary boundary. Hence, forced translation and clustering of thick-shelled contrast microbubbles is feasible. The phase difference between the excursion of the oscillating bubble and the incident sound field was computed for free and encapsulated bubbles. There is a transition in phase difference for encapsulated bubbles, owing to the friction of the shell. Therefore, approach velocities of encapsulated bubbles may not be comparable to those of free gas bubbles.

1. Introduction

Translations of ultrasound contrast agent microbubbles in the direction of a sound field and toward each other have been frequently optically observed [1,2]. The driving of contrast microbubbles towards a boundary has been of interest for ultrasound-assisted drug delivery [3]. Microbubble translation in the direction of the sound field has been attributed to a primary radiation force resulting from a pressure gradient across the bubble surface. The translation is maximal in contraction phase. The velocity v of a bubble in a steady fluid subjected to an ultrasound field can be expressed as [4]:

$$F_{\mathrm{r}} + F_{\mathrm{d}} - \frac{\mathrm{d}(mv)}{\mathrm{d}t} \approx 0, \tag{1}$$

where F_{r} is the primary radiation force, F_{d} is the drag force, $m=(2/3)\pi\rho r_0^3$ is the added mass of the translating bubble, equivalent to half the mass of the displaced surrounding fluid, in which r_0 is the ambient bubble radius and ρ is the density of the surrounding fluid. Averaging over one acoustic cycle, the primary radiation force is given by [1,4]:

$$F_{\mathrm{r}} = \frac{2\pi r_0 p_{\mathrm{a}}^2}{\omega\rho c} \frac{\delta\dfrac{\omega_0}{\omega}}{\left[\left(\dfrac{\omega_0}{\omega}\right)^2 - 1\right]^2 + \left(\delta\dfrac{\omega_0}{\omega}\right)^2}, \tag{2}$$

where c is the speed of sound, p_{a} is the peak rarefactional acoustic pressure, δ is the dimensionless total damping coefficient [5], ω is the angular driving frequency, and ω_0 is the angular bubble resonant frequency [5].

The drag force is given by [4]:

$$F_{\mathrm{d}} = -\frac{\pi\eta}{4} C_{\mathrm{d}}\,\mathrm{Re}\, r_0 \upsilon(t), \tag{3}$$

where η is the shear viscosity of the fluid, $\mathrm{Re}=2\rho r_0|\upsilon(t)|/\eta$ is the Reynolds number, and

$$C_{\mathrm{d}} = \frac{24}{\mathrm{Re}}\left(1 + 0.15\,\mathrm{Re}^{0.687}\right) \tag{4}$$

is the drag coefficient of a contaminated system [6], such as a contrast agent.

Secondary radiation forces, resulting from oscillating microbubbles under ultrasound insonification, may cause the mutual attraction and subsequent coalescence of contrast microbubbles. This phenomenon has been less studied [2]. Two bubbles that oscillate in phase approach each other, whereas two bubbles that oscillate out of phase recede from each other [7,8]. At low acoustic amplitudes, the phase angle difference ϕ between excursion of the oscillating bubble and the incident sound field is given by [7,8]:

$$\phi = \arctan\left(\frac{\delta\dfrac{\omega}{\omega_0}}{1 - \left(\dfrac{\omega}{\omega_0}\right)^2}\right) + \pi. \tag{5}$$

The presence of an encapsulating shell increases the damping coefficient by a term δ_{s} [9]

$$\delta_{\mathrm{s}} = \frac{S_{\mathrm{f}}}{m\omega}, \tag{6}$$

and the squared angular resonance frequency ω_0^2 by a term ω_{s}^2 [9]

$$\omega_{\mathrm{s}}^2 = \frac{2\chi}{r_0^3\rho}, \tag{7}$$

where χ is the shell stiffness parameter [8,9]

$$\chi = \frac{\mathrm{E}\varepsilon}{1-\nu}, \tag{8}$$

in which E is Young's modulus, ε is the shell thickness, and ν is the Poisson ratio. The mean approach velocity υ_{a} of two identical bubbles is given by [1]:

$$v_a = -\frac{(\omega p_a)^2}{27\eta}\rho\kappa^2\frac{r_0^5}{d_0^2}, \quad (9)$$

where κ is the compressibility of the bubble, and d_0 is the distance between the centers of the two bubbles.

Microbubbles with a negligible shell can be forced to translate towards each other at relatively low mechanical indices (MI). Thick-shelled microbubbles would require a higher MI to be moved. However, at high MI, microbubble disruption is expected. We investigated if thick-shelled contrast agent microbubbles can be forced to cluster at high-MI.

2. Experimental Methods

Setup. The experimental setup designed for simultaneous optical and acoustical observations of ultrasound contrast agents has been described in [10]. In short, the thick-shelled contrast agent M1639 (POINT Biomedical Corporation, San Carlos, CA), inserted through a cellulose capillary, was subjected to 3 MHz, high-MI pulsed ultrasound from a Toshiba SSA-770A CV ultrasound machine (Toshiba Medical Systems Europe, Zoetermeer, The Netherlands), and synchronously captured with a WAT-902DM monochrome CCD camera (Watec Co., Ltd., Tsuruoka-Shi, Yamagata-Ken, Japan) through a high numerical aperture microscope (Olympus Deutschland GmbH, Hamburg, Germany).

The agent M1639 consists of bilayered microspheres encapsulating nitrogen bubbles with a mean radius of 2 μm. The shell thickness is proportional to the bubble diameter.

Simulations. The phase angle differences ϕ were computed for free and encapsulated microbubbles, assuming low excursion amplitudes. Radii were chosen $0.5<r_0<5.0$ μm. Known shell stiffness and friction parameters of the ultrasound contrast agent Albunex® were included.

3. Results and Discussion

Figure 1 shows shows an image sequence of M1639 microbubbles under high-MI insonification. The direction of the ultrasound beam is right-to-left. In frame 1, the microbubbles are distributed unevenly on the right-hand side of the frame. In frame 10, two clusters have been formed. In the subsequent frames, these clusters travel in the direction of the ultrasound, owing to primary radiation forces.

The hexagons in frame 1 mark two microbubbles with 3 μm diameters. There approach has been measured and computed with equation (9), assuming $\kappa = 5\times10^{-7}$ m^2 N^{-1}. The result is shown in Figure 2.

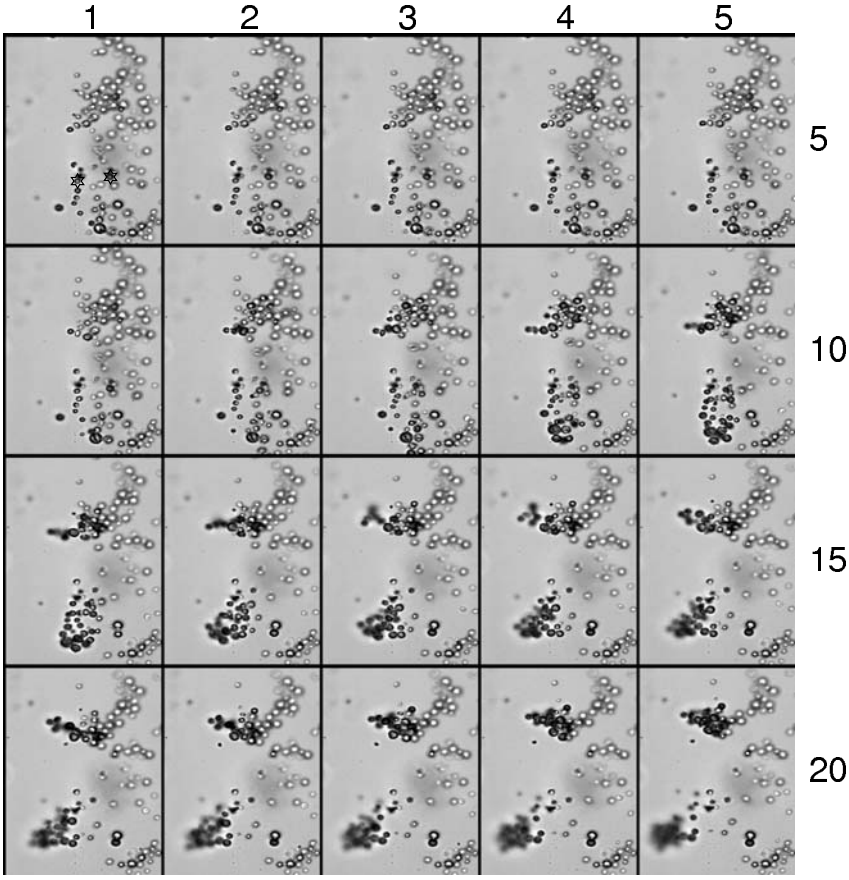

Fig. 1. M1639 microbubbles subjected to pulsed ultrasound from a commercial echo machine, operating at a 3 MHz center frequency and a mechanical index MI=1.3. Inter-frame time is 100 ms. The frame corresponds to a 94.4×70.8 μm^2 area. © 2006 IEEE. Reprinted with permission from [10].

The fact that the measured distances are lower than those computed has been attributed to the presence of surrounding bubbles.

It is remarkable that certain contrast agent microbubbles approach each other relatively quickly compared to others. Figure 3 offers a potential explanation. Free bubbles smaller than 1 μm (below resonance) oscillate out of phase with the sound field, but in phase with each other, whereas microbubbles larger than 2 μm (above resonance) oscillate in phase with the sound field and in phase with each other. For the contrast agent, the shell friction term causes a slow transition in phase difference, limiting the number of bubbles that oscillate exactly in or out of phase with each other. Identical bubbles, such as the bubbles indicated by the hexagons in Figure 1, therefore, may be expected to approach quickly, despite their distance.

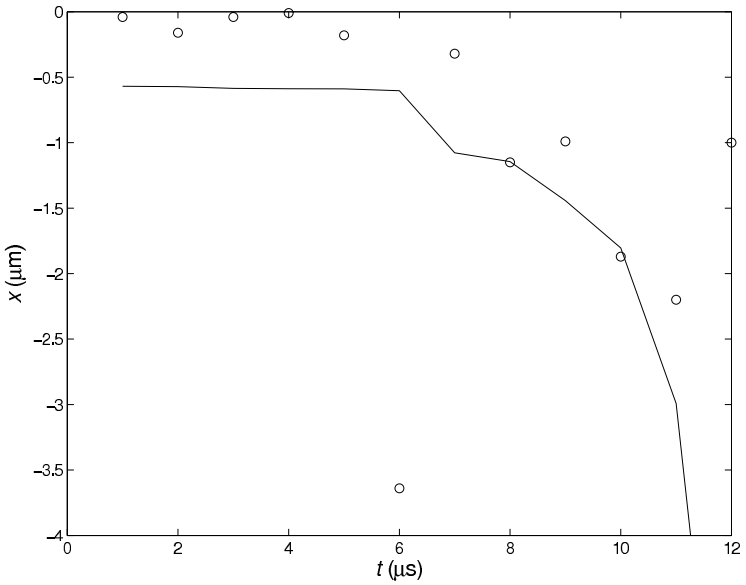

Fig. 2. Measured and computed traveled distances $x(t)$ of two identical r_0 = 1.5 μm M1639 microbubbles, assuming $\kappa = 5\times10^{-7}$ m^2 N^{-1}. © 2006 IEEE. Reprinted with permission from [10].

4. Conclusions

The agent M1639 showed the ultrasound-induced formation of bubble clusters, and the translation thereof towards the capillary boundary. It is concluded, that forced translation and clustering of thick-shelled contrast microbubbles is feasible at high MI.

The phase difference between the excursion of the oscillating bubble and the incident sound field was computed for free and encapsulated bubbles. There is a transition in phase difference for encapsulated bubbles, owing to the friction of the shell. Therefore, approach velocities of encapsulated bubbles may not be comparable to those of free gas bubbles.

Acknowledgements. The authors are grateful to POINT Biomedical Corporation, San Carlos, CA, for supplying the contrast agent M1639.

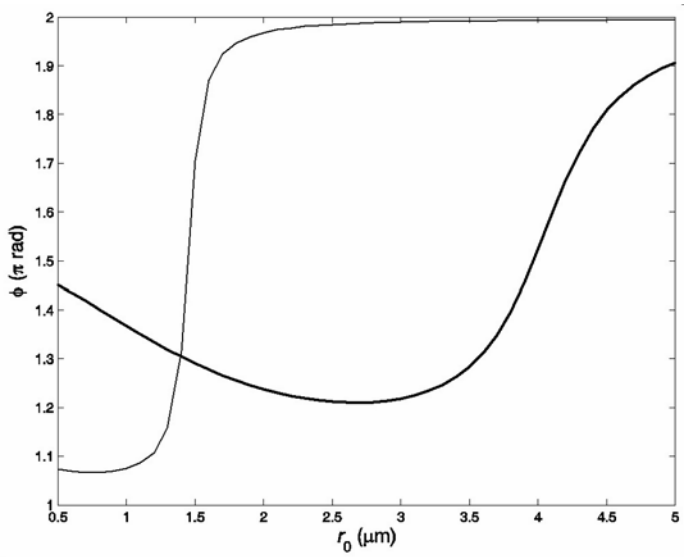

Fig. 3. Phase angle difference between a damped radially oscillating bubble and an incident 3 MHz sound field, as a function of equilibrium microbubble radius r_0. The thin line represents a free bubble: $\chi = 0$ kg s^{-2}, $S_f = 0$ kg s^{-1}, the bold line a hard-shelled microbubble: $\chi = 10$ kg s^{-2}, $S_f = 4\times10^{-6}$ kg s^{-1} [9].

References

1 P. A. Dayton, K. E. Morgan, A. L. Klibanov, G. Brandenburger, K. R. Nightingale, and K. W. Ferrara, IEEE Trans. Ultrason., Ferroelect., Freq. Contr. **44**, 1264, 1997.
2 M. Postema, A. van Wamel, C. T. Lancée, and N. de Jong, Ultrasound Med. Biol. **30**, 827, 2004.
3 M. J. Shortencarier, P. A. Dayton, S. H. Bloch, P. A. Schumann, T. O. Matsunaga, and K. W. Ferrara, IEEE Trans. Ultrason., Ferroelect., Freq. Contr. **51**, 822, 2004.
4 P. Tortoli, V. Michelassi, M. Corsi, D. Righi, and Y. Takeuchi, Ultrasound Med. Biol. **27**, 1265, 2001.
5 H. Medwin, Ultrasonics **15**, 7, 1977.
6 P. Di Marco, W. Grassi, and G. Memoli, Int. J. Therm. Sci. **42**, 435, 2003.
7 F. R. Young, *Cavitation*. McGraw-Hill, Maidenhead, 1989.
8 M. Postema and G. Schmitz, Ultrason. Sonochem., in press, 2006.
9 N. de Jong, R. Cornet, and C. T. Lancée, Ultrasonics **32**, 447, 1994.
10 M. Postema, M. Mleczko, and G. Schmitz, Proc. IEEE Ultrason. Symp., in press, 2006.

A new Imaging Data Fusion System for Application in Neurosurgery and Multimodality Phantoms for System Evaluation

Julia Oestreich[1], Falk Uhlemann[2], Tobias Meyer[1], Annett Werner[3], Matthias Kirsch[4] and Ute Morgenstern[1]

[1] Institut für Biomedizinische Technik, Technische Universität Dresden, Georg-Schumann-Straße 9, 01069 Dresden, Germany
[2] Department of Computer Science, University of Auckland, Private Bag 92019, Auckland, New Zealand
[3] Abteilung Neuroradiologie, Medizinische Fakultät Carl Gustav Carus, Technische Universität Dresden, Fetscherstr. 74, 01307 Dresden, Germany
[4] Klinik für Neurochirurgie, Medizinische Fakultät Carl Gustav Carus, Technische Universität Dresden, Fetscherstr. 74, 01307 Dresden, Germany

Abstract. A new system has been developed to register imaging data from different modalities (CT, MRI, ultrasound, angiography, DTI, fMRI, and others) and afterwards to process and to visualise these data on an autostereoscopic 3D-display with the possibility to navigate interactively with a 3D-mouse in the virtual data space. The system shall be used in operation planning and intraoperative navigation in neurosurgery. To determine the precision of the image processing, the visualisation and the navigation processes, a deformable head phantom with simulated tumour objects for multimodality imaging is developed.

1. Introduction

Three-dimensional multimodality imaging in medicine becomes more important today. The combination of different imaging modalities – such as X-ray computed tomography (CT), magnetic resonance imaging (MRI), functional MRI (fMRI), angiography (DSA, MRA), diffusion tensor imaging (DTI), ultrasound (US), emission tomography (PET, SPECT) and intraoperative optical imaging (OI) – offers the opportunity to improve tumour and aneurysm diagnostics and therapy. Especially in the field of neurosurgery the demands on the accuracy of the imaging data are very high because brain tumours are often located very close to functional active brain areas or they have infiltratively grown into the eloquent areas.

The aim of our research group is to create a new demonstrator system, which makes it possible to register all imaging data from different modalities and afterwards to process and to visualise these data in an accurate, well known and ergonomic way. The matched information of structural and functional datasets can be made available to the neuronavigation system and to postoperative evaluation of operation success. To create real three-dimensional information, the visualisation takes place on an autostereoscopic 3D-display, on which the three-dimensional images can be viewed without the need of any special eyeglasses. To navigate interactively in the virtual data space a 3D-mouse is used. The system can be used

in operation planning and intraoperative navigation in neurosurgery. A postoperative scientific analysis of the medical data will make it possible to draw conclusions for better operation planning and therefore reducing the patient's morbidity.

Working with such a system makes it necessary to know the precision of the image processing, the visualisation and the navigation processes. On the basis of patient data it is impossible to get this information because of the unknown internal geometry and structure of the alive person. Therefore a test object of a known morphology – a phantom – is required. This phantom must offer imaging properties equivalent to medical human head images. Until now no phantom exists which combines morphological and functional information for simulating a human head with anatomical structures, brain tissue, tumours and vessels. Existing multimodality phantoms (e. g. for MRI-CT [1], MRI-CT-PET [2], MRA-CTA-DSA-US [3]) also do not fit our application goal in neurosurgery: The phantom must be suitable to determine the application accuracy of the neuronavigation system and the precision of algorithms for image registration, fusion, visualisation, segmentation and compensation of deformations during the operating process.

2. Methods and Materials

For the import, processing and visualisation of the data the commercially available software Amira (Mercury Computer Systems GmbH Berlin; TGS Inc. San Diego) was used. The software offers many standard functions, which were used for our system; it also supports some autostereoscopic displays. With the developer tool AmiraDev additional functions, e. g. for semi-automatic segmentation within the brain area, were created and included. The used autostereoscopic 3D-displays are produced by SeeReal Technologies GmbH Dresden and by Sharp Inc. The integrated 3D-mouse (Spaceball 5000, 3Dconnexion) makes it possible to move objects with 6 degrees of freedom. Fig. 1 shows such a 3D work station.

For research purposes, there is a data base with multimodality pre-, intra-, and postoperative data from various patients documented also in a clearly arranged image catalogue. Amira Networks consisting of image processing and visualisation modules for special neurosurgical application tasks of segmentation or elastic

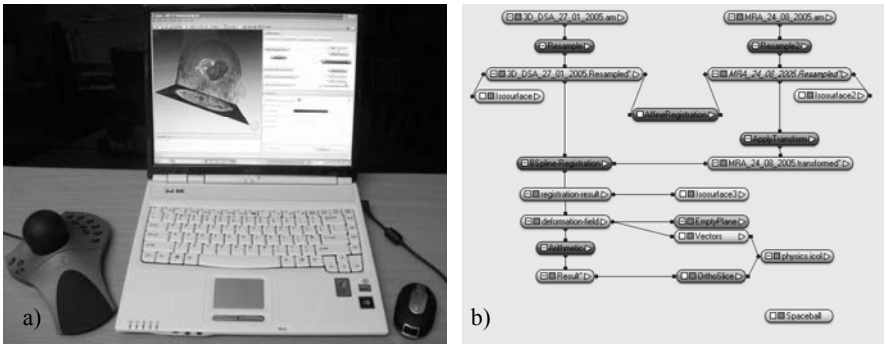

Fig. 1. a) Demonstrator system for clinical application: 3D-notebook, 3D-mouse and data connection to PACS, b) Network for elastic registration with B-spline algorithm module

registration were created (see Fig. 1b) and additionally a user-friendly interface between the physician and the complex Amira software system was implemented.

The phantom will be developed in two steps, first it should be useable for CT, MRI and US imaging of the brain region; in further development stages functional imaging modalities will be integrated. Because of partly contradicting requirements and size limit for the phantoms (acquisition like a human head, i. e. for example the phantoms must fit into a MRI head coil) we decided to develop different types of phantoms: An anatomical phantom, which simulates a realistic human head, including brain tumours, to evaluate interaction and visualisation under realistic conditions and technical phantoms to determine parameters like spatial solution, distortion, segmentation accuracy, etc. For the phantom development suitable materials are necessary. They must produce undisturbed images in all modalities and shall simulate physiological and pathological human brain tissue. The image properties depend on the acquisition settings, therefore parameters are necessary which are characteristic for the specific modalities. These parameters are for MRI the *T1* and *T2* values, for CT the *CT numbers* and for US the speed of sound *c* and the attenuation coefficient α. These parameters for brain tissue are partially known from different references (see Table 1). We examined some possible materials, e. g. gelatine, and compared the measured parameters with the target values. We were looking for a deformable base material and additives to influence each of the parameters separately so that we will be able to adjust any target value to simulate realistic brain tissues for imaging. Because in literature for the possibly suitable materials never all modality specific parameters for MRI, CT and US are provided we examined own series of measurements of varying material compositions.

Table 1. Target values for simulation of brain tissue (WM: white matter, GM: gray matter, TU: tumour) for MRI, CT and US, compiled from different references in [4]

	T1 in ms	*T2* in ms	*CT number* in HU	*c* in m/s	α in dB/MHz/cm
WM	787	92	25...35	1530...1560	0,85...1
GM	921	101	35...50		
TU	1073	124	17...53	no references	

For testing the suitability of the materials and the phantoms they were all imaged by MRI with a Siemens Sonata 1,5 T, by CT with a Siemens Sensation 16 and by US with a General Electric 3D/4D ultrasound system Voluson 730. The *T1* and *T2* values were determined by the software of the MRI system with an inversion recovery sequence (*TE* = 11 ms, *TR* = 10 s, *TI* between 50 ms and 2 s) and a multi-echo sequence (*TR* = 5 s, 32 echos with *TE* = 15 ms; 30 ms, 45 ms, ...) respectively. *CT numbers* were identified from the CT image. The acoustic velocity was calculated from measurements of the transmit time; therefore a send-receive transducer was put on a material sample of known height.

The chosen base material is gelatine (research grade, Serva Electrophoresis GmbH, Heidelberg, Germany / 240 Bloom, Carl Roth GmbH, Karlsruhe, Germany) with phenol as a preservative. Additives were for example graphite powder, flour type 405, $BaSO_4$, $CuSO_4$, Sab Simplex®, glycerol and n-propanol. Using the series of measurements material compositions for simulation of grey and white matter and brain tumour for MRI, CT and US imaging were derived.

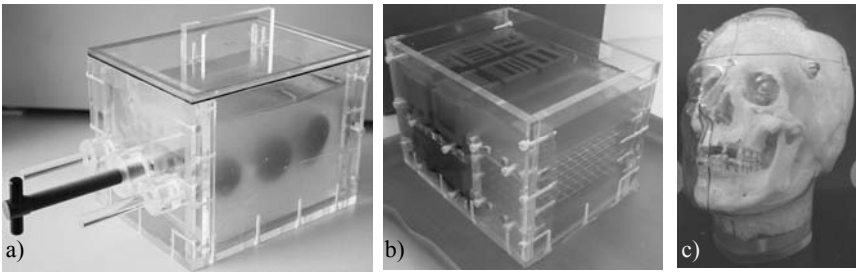

Fig. 2. a) deformable technical phantom, b) rigid technical phantom, c) head phantom

Later also different types of brain tumours will be simulated. The predicted modality specific parameters were checked by our own measurements. The experimental conditions were improved. To avoid influences from salts, aqua bidest was used instead of single distillated water.

The developed phantoms are shown in Fig. 2. Therefore a deformable base material and a contrast material, which produces high contrast in MRI, CT und US images, are used. The base material is made of 15 wt% gelatine, 0,1 wt% Sab Simplex® and 0,5 wt% phenol, the contrast material consists of 15 wt% gelatine, 0,5 wt% phenol, 3 wt% graphite and 0,3 wt% $BaSO_4$. The phantom in Fig. 2a) offers a defined deformation of the base material and embedded spherical and ovoid contrast objects. A second technical phantom (Fig. 2b) contains objects made of PVC to determine the spatial resolution and a grid for measurements of distortion and navigation accuracy. The anatomical phantom (Fig. 2c) consists of a head shaped membrane made of woblex; a human skull (released for research and education application) is positioned inside, and the brain region is filled with the base and contrast materials, thereby in a first step of modelling the contrast material forms spherical and ovoid tumour objects.

3. Results

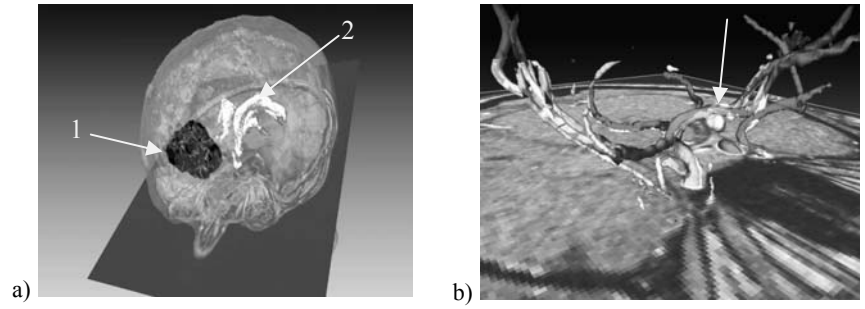

Fig. 3. Presentation of image processing results generated with implemented algorithms, a) segmentation of tumour (1) and ventricles (2) with semitransparent head surface, b) superposition of brain vessel data (bright: preoperative digital subtraction angiography with aneurysm (see arrow); dark-grey: postoperative magnetic resonance angiography)

The new system to register, process and visualise all imaging data from different modalities was realised and successfully tested using different patient imaging data. With the system it is for example possible to segment anatomical structures automatically after marking some points in the area of interest with the help of the 3D-mouse by using the Fast-Marching-Segmentation filter [5] and by using a B-Spline-Registration module two data sets can be elastically registered to each other, see Fig. 3. For intraoperative use of 3D-ultrasound data (GE / Kretz Technik Austria) for neuronavigation (Vektor Vision2, Brainlab AG Heimstetten, Germany) an implementation algorithm is written [6] and evaluated.

For simulating brain tissue material compositions were derived from the series of measurements; afterwards the predicted and the measured parameters were determined (see Table 2). The used contrast material for the phantoms produced high contrast to the used base material in MRI, CT and US, see Fig. 4. MR images from the deformable technical phantom in an undeformed and a deformed state are shown in Fig. 5a) and b). Fig. 5c) shows a CT image of the head phantom.

Table 2. Derived material compositions for simulating white matter (WM), gray matter (GM) and tumour (TU) in MRI, CT and US and predicted (aim) and measured parameters

	gela-tine in wt%	flour in wt%	gra-phite in wt%	$BaSO_4$ in wt%	Sab Simplex in wt%	*T1* in ms		*T2* in ms		*CT number* in HU		*c* in m/s (22°C)	
						aim	real	aim	real	aim	real	aim	real
WM	24,6	0	0	0	0,2	791	724	201	107	64	51	1552	1554
GM	21,3	0,4	0	0,12	0,4	913	822	221	125	85	66	1539	1536
TU	15	0	0,12	0,32	2	1067	1086	272	169	113	89	1517	1504

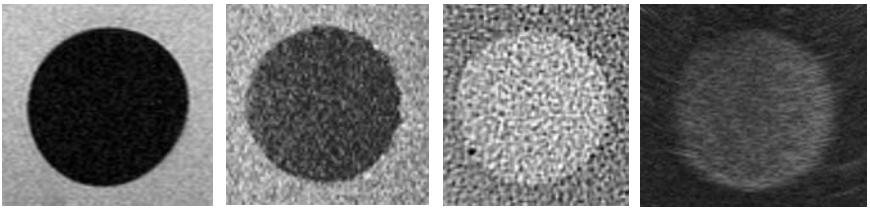

Fig. 4. Images of the contrast material (spherical) and base material used in the phantoms, from left to right: *T2* weighted MRI, *T1* weighted MRI, CT image, US image

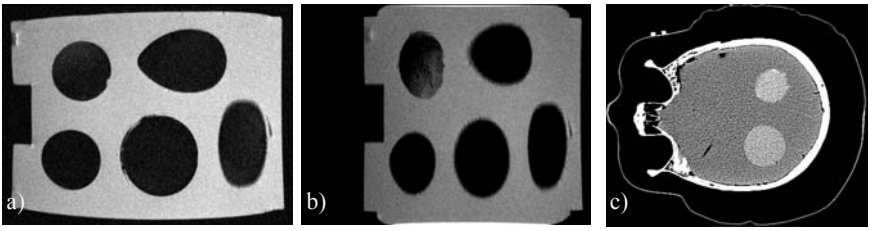

Fig. 5. a) and b) *T2* weighted MR images from the deformable technical phantom, a) undeformed, b) deformed (20 % compressed); c) CT image of the head phantom

4. Discussion

In future the new 3D demonstrator system has to be tested in the clinical routine in neurosurgery to evaluate the whole process from preoperative data acquisition till verification of operation success. Additionally, the system test with the phantom, which is still in process, will be continued. Therefore parameters to verify the system accuracy must be specified. For example such parameters could be the dimensions or the segmented volume of the phantom objects and the image.

After the first phantom material examinations it was impossible to reach the *T2* value of brain tissue and at the same time the other modality characteristic parameters for MRI, CT and US with one material composition. So first only the ratios for different human tissues were adjusted for the derived phantom materials. But by improving the experimental conditions also the *T2* values of brain tissue could be reached. Therefore now further series of measurements for determining the final composition of the phantom materials to simulate brain tissues are necessary. The long time stability of the parameters and different influences of the producing process of the gelatine to the measured parameters will be examined as well. After finishing this process the first used base and contrast materials in the phantoms will be replaced by the brain tissue simulating materials.

The images of the phantoms demonstrated, that the developed phantoms and the current base and contrast materials are suitable for multimodality imaging and fulfil our requirements for testing the demonstrator system. But the verification process is not finished yet and will be continued. Furthermore blood vessels will be integrated into the phantoms to use them with functional imaging modalities. Therefore further phantom investigations especially with DTI and fMRI are necessary.

Acknowledgements. We would like to thank the Wilhelm Sander Foundation, München, Germany, for the financial support.

References

1 R. Comeau: Intraoperative Ultrasound Imaging in Interactive Image Guided Neurosurgery. *Sample of the Ph.D. work*, McGill University, Montreal, 1998. URL: http://www.bic.mni.mcgill.ca/research/groups/igns/US/us_home.html

2 J.-F. Daisne et al: Evaluation of a multimodality image (CT, MRI and PET) coregistration procedure on phantom and head and neck cancer patients: accuracy, reproducibility and consistency. *Radiotherapy and Oncology*. 69: 237, 2003

3 G. Cloutier et al: A multimodality vascular imaging phantom with fiducial markers visible in DSA, CTA, MRA, and ultrasound. *Medical Physics*, 31(6): 1424, 2004

4 J. Oestreich: Entwicklung und Konstruktion multimodal nutzbarer Phantome für die Neurochirurgie. *Diploma thesis*. TU Dresden, 2005

5 J. A. Sethian: Level Set Methods and Fast Marching Methods. *Cambridge University Press*. 1996

6 O. Sergeeva, F. Uhlemann, G. Schackert, C. Hergeth, U. Morgenstern, R. Steinmeier: Integration of Intraoperative 3D Ultrasound in Commercial Navigation System. *Zentralblatt für Neurochirurgie*, 2006 (in press)

CCD-Video Endoscope Subjected to X-Ray

Lucas Pfaffmann[1], Ronny Hübl[2] and Thorsten M. Buzug[3]

[1] Department of Mathematics and Technology, RheinAhrCampus Remagen, Suedallee 2, D-53424 Remagen, Germany
[2] Olympus Winter & Ibe GmbH, Kuehnstrasse 61, D-22045 Hamburg, Germany
[3] Institute of Medical Engineering, University of Luebeck, Ratzeburger Allee 160, D-23538 Luebeck, Germany
E-mail: buzug@imt.uni-luebeck.de

Abstract. In minimally invasive surgery video endoscopes show salt-and-pepper artifacts when used together with an X-ray device. Since the semiconductor material of the CCD chip interacts with the X-ray photons via photoelectric absorption and Compton scattering, it is not clear if these interactions produce irreversible damages within a typical working window in all day use in a clinical environment. The present study was accomplished at the X-ray Lab of the RheinAhrCampus Remagen in the period between March and July 2006. It deals with the question if a CCD chip of a modern medical endoscope undergo irreversible alterations during a 28 hour radiation load using a commercial C-arm. The report describes the experimental set-up and the characteristic properties for CCD quality assessment, i.e. temporal behaviour of background noise and statistics of X-ray affected pixels of the CCD chip. We do not find any indication of a permanent quality degradation of the CCD chip after 28 hour X-ray exposure.

1. Introduction

If minimally invasive surgery is guided by an endoscope, images of constant high quality are required during the entire intervention. However, X-ray fluoroscopy imaging at the same time interferes with CCD-based endoscopic imaging. This effect is due to the nature of the CCD chip used in an endoscope. When the CCD chip is hit by a photon, a charge will be produced which is proportional to the energy of the incident photon. This effect is known as the inner photoelectric effect. During the readout process the charge of each pixel is shifted over the entire chip. Since the charge is typically very small a loss of charge is unacceptable, because it would change the image information significantly.

For a CCD chip loss of charge is a characteristic property, known as the **c**harge-**t**ransfer **e**fficiency (CTE), which essentially describes the quality of the device. CCD chips can be distinguished into two principal types that are defined by the way of their use. On the one hand, it is possible to use the chip in front direction. That means that the photon has to penetrate the entire chip before the charge is produced. In this case, there is a relatively high risk that the gate structure may be damaged. On the other hand, the device can be used from the back side. Here, a thin silicon layer is used and, obviously, the main advantage is that the photon must not penetrate the gate structure before it produces the charge. In that way, the path through the device is shorter, which reduces the probability

of undesired absorption resulting into image information degradation or even into irreversible damage.

Due to the fact that an X-ray photon has a much higher energy than a photon from the visible spectrum [1] the CCD chip is potentially damaged by known interactions between radiation and matter [2-4], i.e. the Compton effect and the photoelectric effect. Two forms of damage have been reported in literature. Due to ionization electron-hole pairs may be produced in the gate electric which carries the risk of producing malfunctions. It may also happen that such pairs are fixed in position. In that situation an unknown offset charge is produced.

The second effect is due to the high energy of the incident X-ray photons and results in so called shifting effects. When a photon of high energy strikes the atomic structure of the device, it may happen that a single atom is kicked away and a change in atomic structure appears. This typically results in a permanent malfunction of the device. Obviously, such an irreversible damage is unacceptable for CCD chips in daily used endoscopes of a medical environment.

2. Experimental Set-up

In a 28 hours long term stability test an Olympus endoscope (see Fig. 1 – left) has been irradiated with X-ray generated by a commercial C-arm. In the experimental set-up the endoscope with the CCD chip (placed directly behind the endoscope tip see Fig. 1 – right) was situated close to the focus spot of a C-arm X-ray tube.

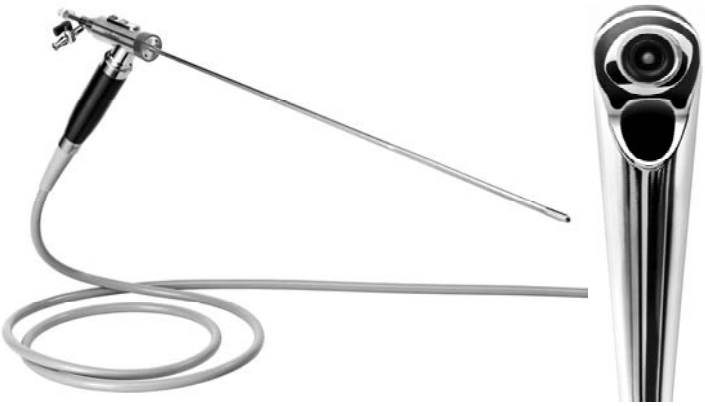

Fig. 1. CCD based endoscopic imaging device

In our experiments we used a Philips BV 25 and a Siemens SIREMOBIL 2000 C-arm. Since the radiation is emitted in cone-beam geometry the dose can be increased effectively by a decrease of the distance between X-ray focus and CCD chip. In that way, the chosen radiation parameters of 70-80 kV (X-ray tube acceleration voltage) and 2.6 mA (X-ray tube current) result in a higher dose compared to the clinical situation of the endoscope chip inside the patient. Figure 2 schematically shows the signal flow (left) of experimental set-up (right).

Every five seconds an endoscope image was acquired under radiation (Fig. 3) and subsequently stored in a data base. Alternating, an endoscope image without radiation was taken as well. This allows a direct comparison of the CCD chip status relative to the initial quality of the chip. During radiation no visible light reaches the CCD chip. In that way, an easy assessment of the photon statistics can be performed.

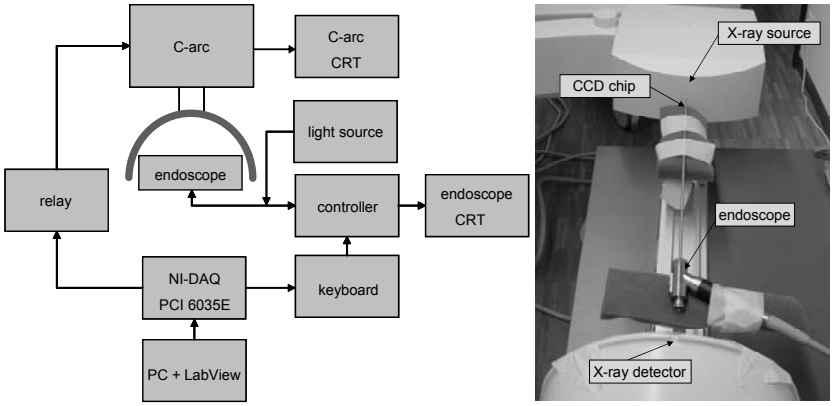

Fig. 2. Signal flow of experimental set-up for the long term test of the endoscopic imaging device

In the next section quality criteria for the CCD chip will be introduced. We decided to observe the temporal development of background noise and the number of pixels influenced by the X-ray photon absorption process to assess the long-term stability of the CCD chip subjected to X-ray.

3. Results of Quality Assessment

The video signal of the endoscope CCD chip is acquired via frame grabbing. Figure 3 shows the effect of X-ray photon interaction with the chip during the endoscopic imaging process. The noise peaks of the hitting X-ray photons are clearly visible. It is essentially salt and pepper noise. However, in this case it represents itself as randomly occurring bright colored spots. To simplify the analysis of strike statistics ambient light was blocked by a cover.

The left hand side of Fig. 3 represents the interaction pattern of a low dose situation (84 kV/1.8 mA). On the right hand side of Fig. 3 the interaction pattern at increasing X-ray parameters (110 kV/3.0 mA) is shown. Independent from the dose, it can be seen that incident photons affect more than one pixel per strike.

Background Noise. As mentioned above, one of the assessment parameters to estimate the long-term stability of the CCD chip is background noise. If an endoscope image is acquired from a dark scene, i.e. the endoscope light source is turned off and ambient light is blocked, variation in the image is caused by the

electronic noise of the used imaging device chain. In this situation defective pixels should affect the statistics of background noise significantly.

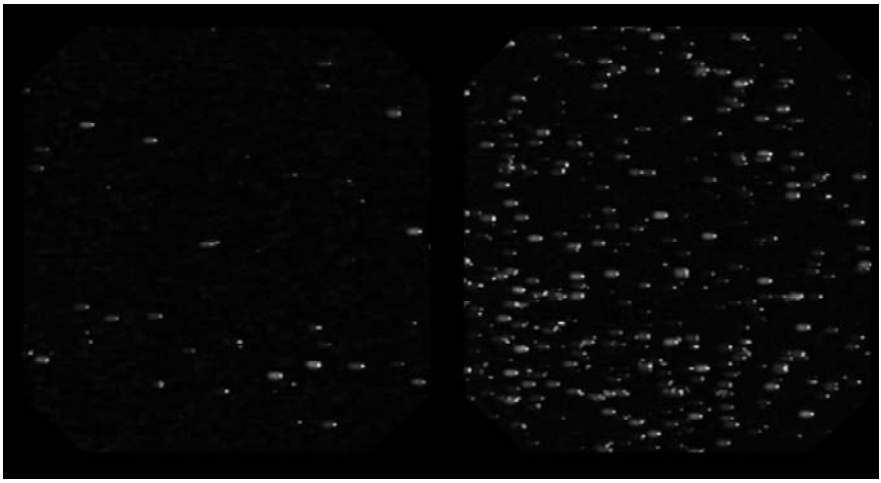

Fig. 3. Endoscope images are displayed which were acquired under radiation. Left: Radiation parameters of 84 kV and 1.8 mA were used. The imaging result of increasing X-ray generation parameters (110 kV and 3.0 mA) is shown on the right hand side

To analyze the impact of striking X-ray photons the trend of the temporal development of the background noise, i.e. the overall image standard deviation, is observed. It is assumed that CCD chip degradation due to X-ray load would lead to a significant trend of the background noise time series. In Fig. 4 the background signal versus time is shown for an interval of one hour (hour 16 of the 28 hours long-term test). In our experiments we do not see any changes of mean and standard deviation over the entire testing interval of 28 hours.

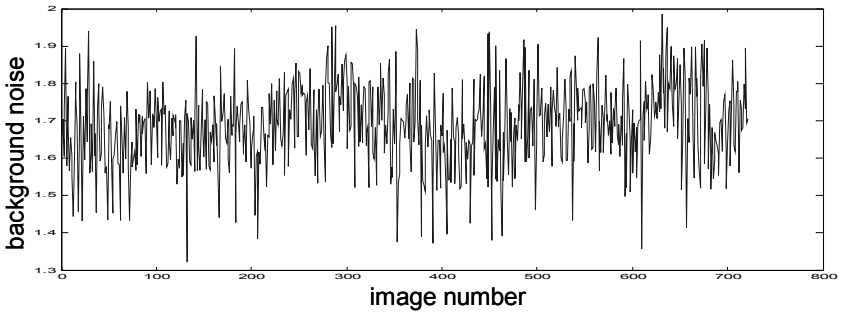

Fig. 4. Standard deviation versus time shown for an interval of one hour

Pixels Affected by X-Ray Photons. A second characteristic quality parameter is the temporal development of the number of pixels affected by X-ray photons. Due to the high energy of the incident X-ray photons those pixels that interact with the photons appear as flashing beacons in the endoscope image (compare Fig. 3). All other pixels have relatively low values represented by background noise as demonstrated in the previous subsection.

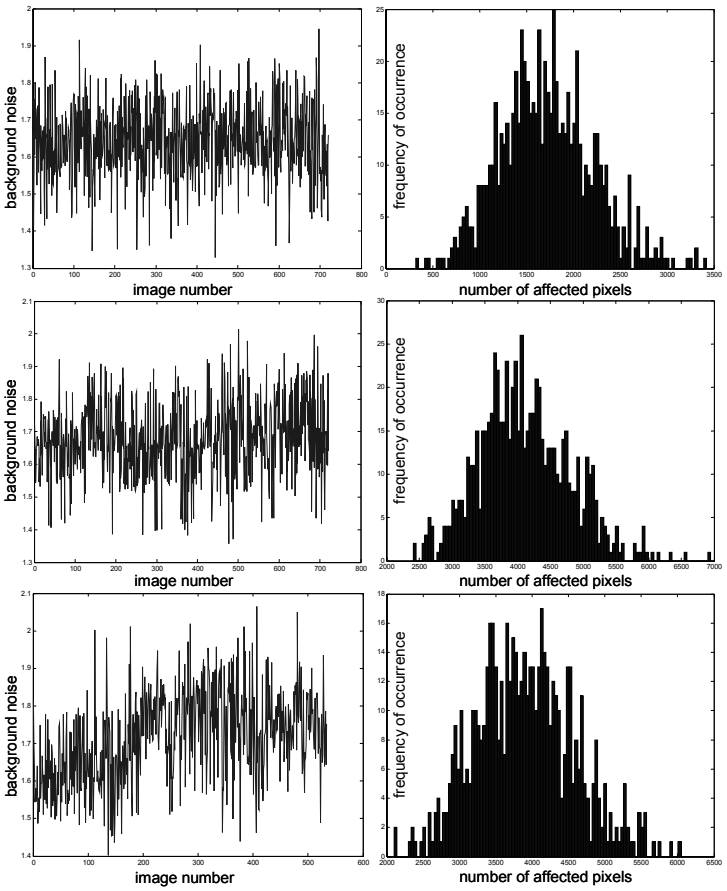

Fig. 5. The plots on the left represent the background noise time series each over an testing interval of one hour X-ray exposure time. The rows represent different stages of the long term test: First row – first hour; second row – 14th hour; last row – 28th hour. On the right, the corresponding distributions of the number of affected pixels of the CCD chip are presented

Figure 5 shows the background noise time series and the corresponding distributions of the number of affected CCD pixels for testing hours 1, 14 and 28, respectively. The X-ray generation parameters for the intervals were: Hour 1 – 70 kV/2,2mA; hours 14 and 28 – 84 kV/1,8mA. Our tests reveal that the background

noise is stationary over the entire testing interval of 28 hours. The distributions of the number of affected CCD pixels are sensitive to the X-ray dose. However, for constant dose – that has been applied for the testing interval between hour 9 and 28 – mean and standard deviation of the corresponding distributions are stationary as well.

4. Discussion and Conclusion

In our long-term test low C-arm image acquisition parameter are chosen. We set the tube voltage/current to 70 kV/2,2 mA in a first testing period and to 84 kV/1,8 mA in a second period. Compared to clinical settings these parameters are relatively low. However, the effective dose applied to the CCD chip is higher than in a clinical environment, because firstly, during exposure no anthropomorphic phantom is used and thus the device is directly exposed to the radiation and secondly, the CCD chip is placed directly in front or even close to the focus spot of the radiation source (source-device distance was chosen to approximately 1cm). Thanks to this set-up situation the radiation dose applied to the device is higher than in typically clinical applications. According to the defined CCD quality assessment parameters we do not find any indication of a permanent quality degradation of the CCD chip after 28 hour X-ray exposure.

References

1 S. R. Cherry, J. A. Sorenson,, and M. E. Phelps, *Physics in Nuclear Medicine*, Elsevier Science, Philadelphia, 2003.
2 J. R. Janesick, *Scientific Charged Coupled Devices*, in: SPIE Press, Bellington, 2001.
3 C. Clayes and E. Simoen, *Radiation Effects in Advanced Semiconductor Materials and Devices*, Springer, New York, 2002.
4 T. Wilhein, PhD Thesis, *Gedünnte CCDs: Charakterisierung und Anwendungen im Bereich weicher Röntgenstrahlung*, Shaker, Aachen, 1994.

MRI Based Attenuation Correction for Brain PET Images

Elena Rota Kops[1], Peng Qin[1,2], Mattea Müller-Veggian[2] and Hans Herzog[1]

[1] INB-Medicine, Forschungszentrum Juelich, D-52425 Juelich, Germany
E-mail: e.rota.kops@fz-juelich.de
[2] University of Applied Sciences Aachen, D-52428 Juelich, Germany

Abstract. This work describes a procedure to yield attenuation maps from MR images which are used for the absorption correction (AC) of brain PET data. Such an approach could be mandatory for future combined PET and MRI scanners, which probably do not include a transmission facility. T1-weighted MR images were segmented into brain tissue, bone, soft tissue, and sinus; attenuation coefficients corresponding to elemental composition and density as well as to 511 keV photon energy were respectively assigned. Attenuation maps containing up to four compartments were created and forward projected into sinograms with attenuation factors which then were used for AC during reconstruction of FDG-PET data. The commonly used AC based on a radioactive (^{68}Ge) transmission scan served as reference. The reconstructed radioactivity values obtained with the MRI-based AC were about 20% lower than those obtained with PET-based AC if the skull was not taken into account. Considering the skull the difference was still about 10%. Our investigations demonstrate the feasibility of a MRI-based AC, but revealed also the necessity of a satisfying delineation of bone thickness which tends to be underestimated in our first approach of T1-weighted MR image segmentation.

1. Introduction

The primary reason that PET is able to quantify radioactivity in vivo is the possibility to correct for attenuation explicitly in a satisfying way. The data on tissue attenuation is commonly derived from transmission measurements performed before or after injection of the radiotracer. For these measurements one or more line sources containing the positron emitter ^{68}Ge and rotating around the patient are used. Nowadays, many PET-CT scanners allow to derive the attenuation data from the CT-scan so that these scanners do not need and therefore do not offer a radionuclide based transmission scan. Furthermore, there are first developments to join PET and MRI for simultaneous scanning. Such combined scanners will probably not contain any facility to measure the tissue attenuation as we know from pure PET and PET/CT scanners. One way to get attenuation factors necessary for the attenuation correction of the acquired PET emission scan is to derive them from the anatomical MR images [1]. In this preliminary report we describe such a procedure realized in our laboratory and compare the original PET-based attenuation correction with the MRI-based attenuation correction for which different segmentations of the anatomical images have been used.

2. Materials and Methods

FDG scans of three normal volunteers who had been investigated with both PET and MRI in the context of a clinical study were utilized for the approach described in this report. The PET scans were recorded with a Siemens ECAT HR+ scanner in 3D mode for 60 min after injection of about 200 MBq FDG. Prior to the tracer injection a transmission scan of 10 min was acquired for which three rods of ^{68}Ge were used as transmission sources. The PET emission data were summed into a single frame ranging from 30 to 60 min after injection, Fourier rebinned and reconstructed with filtered back-projection (DIFT) into 63 images with 128x128 voxels of 2x2x2.45 mm^3. Corrections for randoms, scatter and attenuation were applied. High-resolution 3D T1-weighted volumetric MRI data were acquired with a Siemens 1.5-Tesla Sonata Vision scanner using an MP-RAGE sequence. The volumetric data included 160 sagittal images by 256×256 voxels of 1x1x1 mm^3.

Primarily, the attenuation correction was based on the transmission data measured with the PET scanner (PBA = PET-based attenuation correction). Secondly, the attenuation correction was derived from the MRI data (MBA = MRT-based attenuation correction) as described in the following. The MR images were co-registered to the PET images using the MPItool [2] and segmented into four different tissue compartments: brain tissue, bone, sinus and other (soft) tissue. All tissues within the image volume except brain tissue, bone and sinus area are considered as soft tissue. The segmentation was done with the software package BrainSuite2 [3] and, additionally, with some image processing of the MPItool. Next, attenuation coefficients valid for photon energy of 511 keV were assigned to the four compartments. For this purpose, the elemental compositions of the brain tissue, the bone, and the soft tissue were obtained from IRCU report 46 [4]. With these data and the values of the specific densities the attenuation coefficients could be determined using the Website XCOM of the National Institute of Standards and Technology (NIST) [5]: 0.099 1/cm for brain tissue, 0.146 1/cm for bone, and 0.095 1/cm for soft tissue. The attenuation coefficient of the sinus area was taken from [1] with a value of 0.054 1/cm. In order to examine the influence of choosing one, two, three, or all four compartments, four different attenuation maps were created: M1 refers to the whole head with a single attenuation coefficient (0.099 1/cm), M2 is divided into brain and soft tissue, M3 considers bone in addition to M2, and M4 comprises all four different compartments, i.e. the sinus area is included. These MRI-based attenuation maps were finally down-sampled into 3D attenuation maps with 128x128x63 voxels and a voxel size of 5.15x5.15x2.45 mm^3 as demanded by the ECAT 7.2 software. The resulting attenuation maps were forward projected and sinogram-like files with attenuation correction factors (ACF) were obtained which could directly be applied for correction of the PET emission scans.

Regions of interest were defined at several brain areas of the reconstructed FDG images for which either the PBA or MBA with its four different variations M1 to M4 had been used. The resulting activity concentrations were analyzed comparatively by calculating relative differences (%) between the values reconstructed with MBA (M1 to M4) and with PBA.

3. Results and Discussion

Figure 1 shows (A) an example of an attenuation map based on the measured transmission data with (B) the original T1-weighted MR image. The corresponding segmented MR image with all four assigned attenuation coefficients (M4) is shown in figure 1C, while figure 1D displays C after down-sampling into voxel size of 5.15x5.15x2.45 mm^3. A major feature of the MRI-based attenuation map is the absence of noise. It is generally known that PBA-corrected PET images suffer from statistical uncertainty derived e.g. from noisy transmission data. The MBA method of attenuation correction should thus reduce significantly this problem. On the other hand, in all three subjects examined the skull was thinner than known from brain CT scans. Since this was evident only in some part and not overall on the skull, e.g., a dilation operation as a possible correction could not be applied. The only way to overcome this problem is to find the right extension of the skull from the given T1-weighted MR images. Otherwise this is not very straightforward because of the low hydrogen concentration in the bone tissue resulting in a very low MR signal. An underestimated skull thickness leads to lower ACF which cause an underestimation of the reconstructed activity concentration of the PET images.

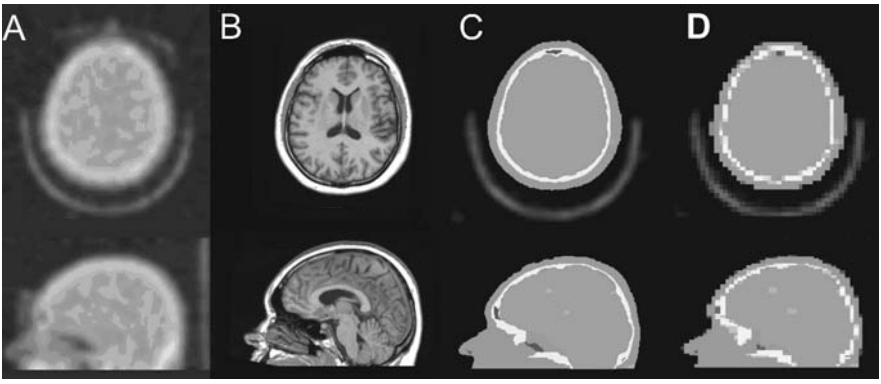

Fig. 1. Transaxial (top) and sagittal (bottom) images of (A) attenuation maps from the PBA, (B) the corresponding MRI data, (C) the attenuation map from the MBA (M4), (D) the data of C after being down-sampled to a voxel size of 5.15x5.15x2.45 mm^3

In figure 2 the relative differences (%) of the measured activity concentration of several brain regions in images reconstructed with MBA in respect to PBA are plotted. All PET images processed with MBA yielded lower values of activity concentration in all ROIs. Compared to PBA there was an underestimation of up to 20% when just one compartment (M1) was taken into account and the bone was neglected. The relative errors became smaller with values of about -10% when the bone tissue (M3 and M4) was considered.

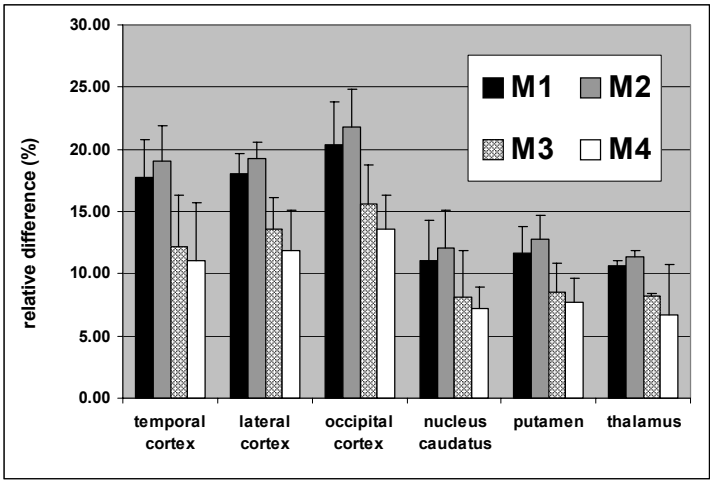

Fig. 2. Average (n=3) relative differences of the measured activity concentration in reconstructed images with MBA in respect to PBA. M1 to M4 indicate the use of different attenuation maps with 1 to 4 compartments

An example for cerebral FDG images obtained with PBA or MBA are displayed in figure 3. It shows the images of the same patient and the same cross-sections as in figure 1. Irrespective to the unequal scaling, one can observe the different activity distribution, e.g., in the frontal area as well as in the cerebellum of figure 3B and 3C (MBA with M1 and M4, respectively) compared to figure 3A (PBA).

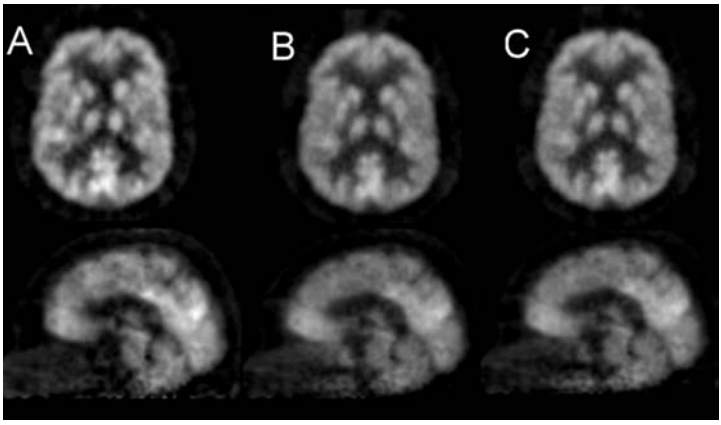

Fig. 3. Reconstructed FDG images of the same patient and same cross-sections as in figure 1 after correction for attenuation with PBA (A) and MBA using M1 (B) and M4 (C)

4. Conclusions

This work shows that attenuation correction of brain PET scans can be achieved by appropriate image processing of associated MRI data. The underestimation of the reconstructed radioactivity found here is related to an underestimated skull thickness which is clearly smaller than known from CT. This indicates the necessity of a satisfying definition of bone tissue which is difficult to delineate in the T1-weighted MRT images used for this report.

References

1 Zaidi H, Montandon ML, Slosman DO. Magnetic resonance imaging-guided attenuation and scatter corrections in three-dimensional brain positron emission tomography. Med. Phys., vol. 30, pp:937-948, 2003

2 Shattuck DW, Leahy RM. BrainSuite: an automated cortical surface identification tool. *Med. Image Anal*., vol. 6, pp:129-142., 2002 (see for BrainSuite2: http://brainsuite.usc.edu/index.php)

3 Pietrzyk U, Herholz K, Heiss WD. Three-dimensional alignment of functional and morphological tomograms. *J. Comput. Assist. Tomogr.*; vol. 14, pp:51–59, 1990

4 ICRU Report 46, Photon, electron, proton and neutron interaction data for body tissues. ICRU publications, Bethesda, 1992

5 http://physics.nist.gov/PhysRefData/Xcom/html/xcom1.html

Integration of Functional Data (PET) into Brain Surgery Planning and Neuronavigation

Stefan Vollmar[1], Jürgen A. Hampl[2], Lutz Kracht[1] and Karl Herholz[3]

[1] Max-Planck-Institute for Neurological Research, Cologne
Gleueler Str. 50, 50931 Köln, Germany
E-mail: vollmar@nf.mpg.de
[2] Department of Neurosurgery, University of Cologne, Germany
[3] Wolfson Molecular Imaging Centre, University of Manchester

Abstract. There are distinct advantages of including functional data from PET into surgery planning and neuronavigation: tumor delineation and localization of functional areas. Pre-operative intervention planning in brain tumours poses many additional challenges if the goal is to include functional data from PET for neuronavigation: co-registration of multimodal image data (MRI and PET) is conceptually the most demanding task. However, we find that associated problems of visualization, data transfer, documentation and, in general terms, quality assurance are often underestimated. We address some of these problems, including visual inspection of co-registration accuracy, preparation of image data, DICOM capabilities and "electronic documentation" [1].

1. Introduction

Functional imaging using O-15-water and PET can be used in order to localize the areas of language and motor skills. Specific PET tracers can be used to localize the most malignant parts of brain tumors, as well as the infiltration area at high sensitivity and specificity [2]. Suitable preprocessing of PET data often is required for accurate interpretation.

Including this information allows taking into account dynamic interactions between the natural history of the tumor and the reactive process of cerebral adaption which is required to maximise the quality of glioma resection while minimising the risk of irreversible postoperative deficits [3]. Ideally, the results from functional imaging should also be present during neuronavigation: this can be achieved by superimposing them on MRI data (image fusion), the representation of which can then be coupled with a virtual pointing device that reflects a hand-held pointer's position, e.g. BrainLAB's VectorVision [4].

We illustrate solutions to the challenges mentioned above using VINCI, our integrated software package for visualization, co-registration and analysis of image volumes [5, 6].

2. Methods

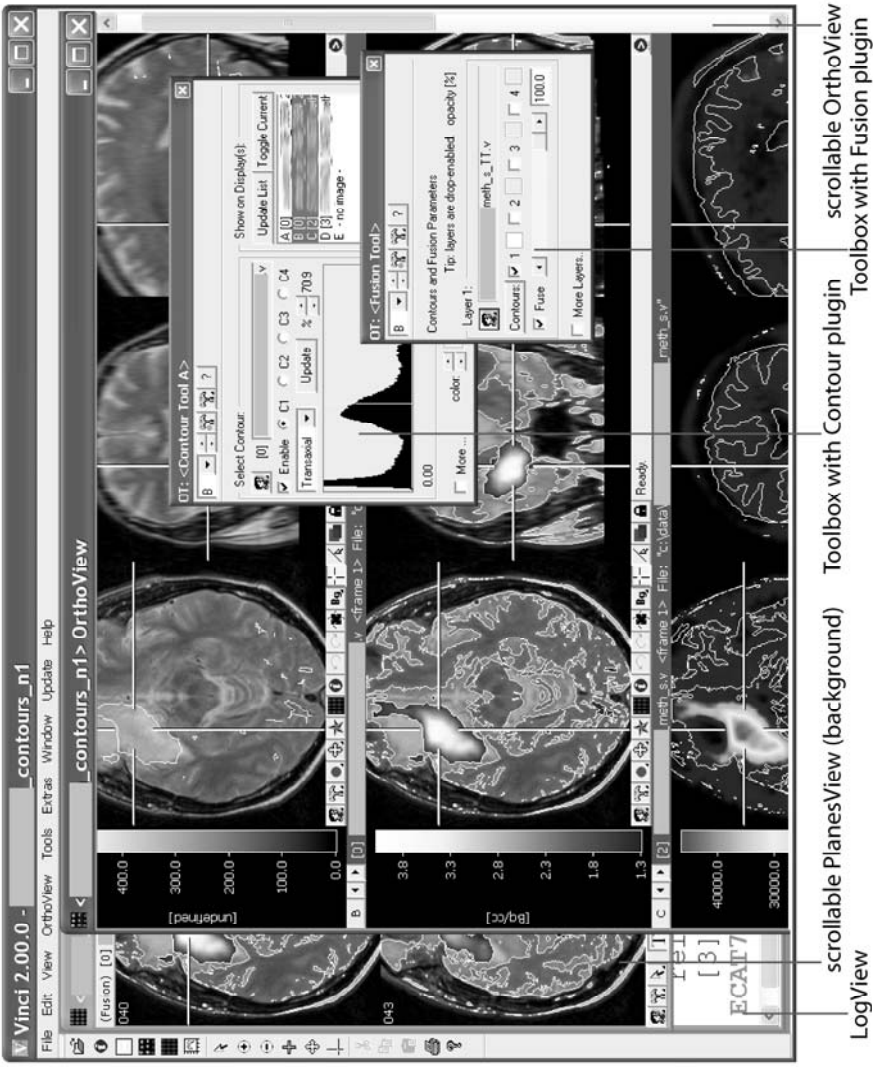

Fig. 1. Screenshot of VINCI presenting data for surgery planning. Here: full screen in projector resolution (1024 × 768 pixels). Observe that all major widgets are scrollable and that toolboxes can be positioned at arbitrary positions (or closed). VINCI projects can also be defined on much larger screens, e.g. in multi-display settings: if restored when running a different resolution (e.g. for projector presentation) widgets are resized and respositioned automatically. OrthoView top row: T2-MRI with contrast agent, bottom row: full range Methionine-PET (iso-contours defined on the MRI to validate registration accuracy), middle row: "tumor-normalized" (s.b.) Meth-PET fused with MRI.

Co-Registration. The algorithms and implementations for fully automatic co-registration of PET data to MRI studies are based on multiresolution coarse-to-fine optimisation of mutual information and also involve brain extraction, intensity threshold and masking as preprocessing steps, as described by Cizek et al. [5]. Registration time rarely exceeds 20 seconds on a 1.7 GHz Pentium M system for original clinical data (Siemens ECAT 961).

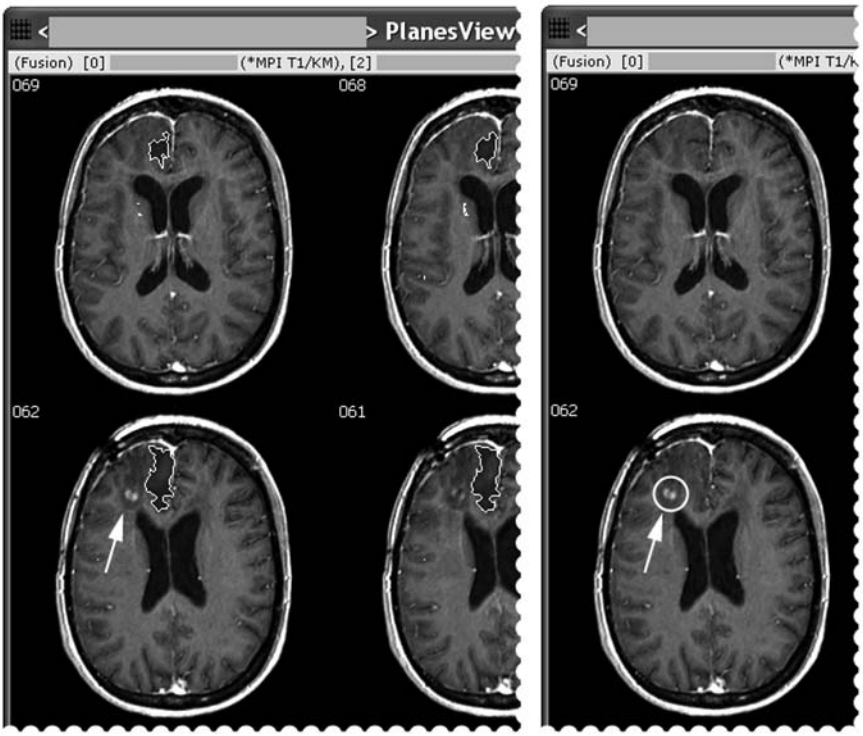

Fig. 2. VINCI's PlanesView widget. T1-MRI, left: fused with Meth-PET data. The iso-contour on the left-hand side marks the area of 1.3 fold normal Methionine uptake. VINCI's PlanesView mode allows to fuse this tumor-normalized Meth-PET image volume with varying degrees of opacity. Observe that MRI and Meth-PET show two distinct localizations of suspected tumor tissue (see arrow). PET-guided neuronavigation was performed and both tumor regions were resected. Histological investigation reported recurrent glioblastoma multiforme in both locations.

Visualization and Preparation of Image Data. Registration accuracy is checked visually using fusion overlay (of up to four image volumes) and an interactive tool for iso-contours. VINCI takes advantage of current high-resolution screens while retaining the option to run in standard projector resolution for presentations.

Presentations allow for online visualization (simultaneous display of several data sets, multi-slice views, realtime variations of fusion weights).

We have developed plugins to exploit the quantitative properties of C-11-methionine PET data ("Tumor Normalization") for PET-guided neuronavigation resulting in a robust data-reduction which is also suitable for systems with limited visualization capabilities: based on a reference region (a ROI is placed in the area of maximum Methionine uptake, the ROI is mirrored to the contralateral part of the brain) the image is scaled and automatically rendered with a special color palette (s.a. Fig. 1).

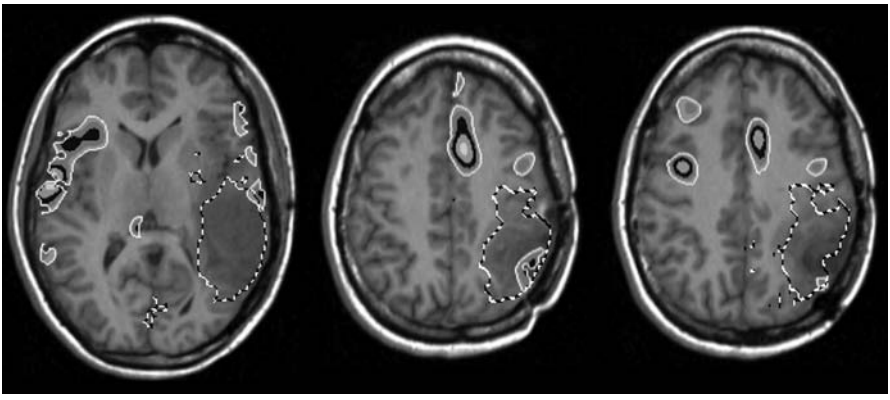

Fig. 3. T1-weighted MRI fused with ^{15}O-PET activation studies (z-scores) [7]. Speech repetition task (left), verb generation (centre), finger tapping (right-hand side). In addition, the area of increased Methionine uptake is shown (dotted-line iso-contour created from the tumor-normalized Meth-PET). We observed that this area is often significantly larger than any visible changes in the MRI study. Both activations for language and motor skills show signals in the area of increased Meth uptake and are consistent with a mild aphasia.

Furthermore, we have devised methods to document, log and gather all relevant image data and processing steps, resp., using "electronic fingerprints" (MD5 checksums) for quality assurance. This allows for online presentation of diagnostic findings during laptop-based presentations (independent of an institute's network).

Data Import and Export. Reading and writing native DICOM data [8] as image volumes is required to transfer data to a neuronavigation system (e.g. BrainLAB's VectorVision). We can read original data from most MRI-, CT-, PET- and PET-CT scanners and, in addition, have found a way to export any image data in DICOM-format using templates: from the BrainLAB system's point of view, the co-registered and resampled functional data appears as another MRI study with suitably changed header information (e.g. PET-specific descriptions). For each original slice of the reference volume we resample the corresponding slice of the co-registered PET volume (voxel-voxel-correspondence) and replicate the original slice's coordinate settings.

This general approach allows using the unmodified reference MRI and it does not require BrainLAB's optional module for importing PET data. In addition, it is highly portable: a large number of systems are able to read the co-registered and resampled functional data we can export, including other DICOM-based systems for neuronavigation, radiosurgery and radiotherapy planning.

Data Presentation. It is often difficult to present the multitude of relevant slices from multimodal imaging and the results of image fusion at clinical conferences. Computer-generated movies offer an easily portable electronic format for that. However, a surprising number of challenges need to be addressed first: evaluating suitable formats, lack of documentation and software development toolkits, finding suitable compression parameters, and, last but not least, creating a suitable user interface. We have created a method to create "Standard Movies": the animation is automatically generated by interpolating sequentially through transaxial, coronal and sagittal views of one configuration of orthogonal slices. It can be exported in several standard formats and viewed on all major platforms (WMV with codecs movie9 [9] and MP4a [10]; MOV with the PNG and RLE codecs [11]).

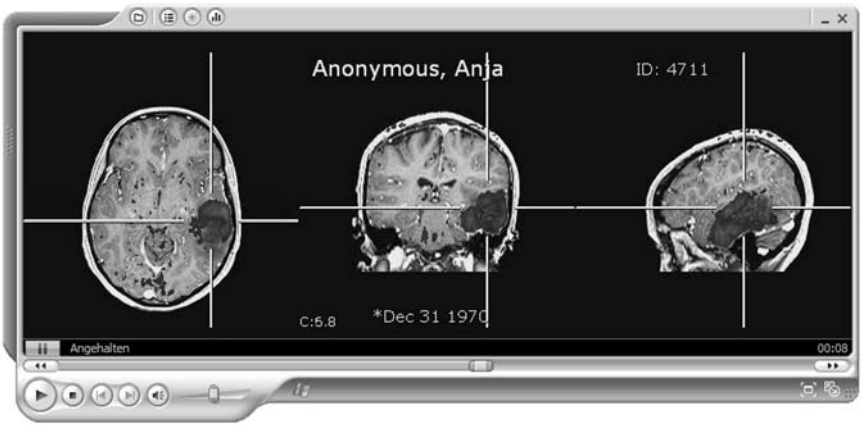

Fig. 4. Screenshot of a VINCI "Standard Movie", here a WMV movie9 format is being presented by Windows Media Player 10. A T1-weighted MRI is fused with a tumor-normalized Meth-PET data set (hot-metal color palette). Surgery was indicated due to tumor progression as documented by an increase in tumor volume on follow-up Meth-PET imaging. Partial resection of the tumor was performed taking into account functional data acquired with a PET stimulation study (speech activation). Histological assessment of the tumor tissue revealed an anaplastic oligodendroglioma WHO grade III.

Of the movie types mentioned above, the first two are "lossy" compression methods: for a given animation sequence, the movie's quality (in terms of artefacts and loss of detail) can vary considerably depending on the settings for the "frame rate" (more frames per second will make an animation "run more smoothly"), key frame spacing (the maximum number of delta frames between

two key frames) and the "bit rate". The latter is usually set to a comparatively small value to allow "streaming" of videos over low-bandwidth network connections, the major application of most current compression efforts. We have experimented with settings for unusually high quality which, in our experience, yield acceptable results for many clinical applications.

Electronic Documentation. PDF (Portable Document Format [12]) is an obvious choice for "static" documentation: its strong points include platform independence, support of vector graphics and meta-information, availability of readers. Unfortunately, few packages for scientific visualization use the more advanced options of this powerful and feature-rich format. We use PDF for documentation providing poster-quality printouts and take advantage of embedding meta-information (log file, searchable keywords) and its potential for archiving purposes [13].

References

1 S. Vollmar. Integration of Functional Imaging (PET) to Surgery Planning in Brain Tumors. Köln: (PhD thesis) University of Cologne/Max-Planck-Institute for Neurological Research; 2006.

2 L. W. Kracht, H. Miletic, S. Busch, A. H. Jacobs, J. Voges, M. Hoevels, et al. "Delineation of brain tumor extent with [11C]L-methionine positron emission tomography: local comparison with stereotactic histopathology". Clin Cancer Res. 2004 Nov 1;10(21):7163-70.

3 H. Duffau. "Lessons from brain mapping in surgery for low-grade glioma: insights into associations between tumour and brain plasticity". Lancet neurology. 2005 Aug;4(8):476-86.

4 BrainLAB GmbH. Heimstetten, Germany, http://www.brainlab.de.

5 J. Cizek, K. Herholz, S. Vollmar, R. Schrader, J. Klein, W. D. Heiss. "Fast and robust registration of PET and MR images of human brain". NeuroImage. 2004 May;22(1):434-42.

6 S. Vollmar, J. Cizek, M. Sue, J. Klein, A. H. Jacobs, K. Herholz. "VINCI - Volume Imaging in Neurological Research, Co-Registration and ROIs included". Forschung und wissenschaftliches Rechnen 2003 (Kremer K, Macho V, eds), Göttingen: Gesellschaft für wissenschaftliche Datenverarbeitung; 2004. p. 115-31.

7 A. Thiel, K. Herholz, A. Koyuncu, M. Ghaemi, L. W. Kracht, B. Habedank, et al. "Plasticity of language networks in patients with brain tumors: a positron emission tomography activation study". Annals of neurology. 2001 Nov;50(5):620-9.

8 National Electrical Manufacturers Association (NEMA). Digital Imaging and Communications in Medicine (DICOM) Part 1 http://dicom.nema.org.

9 Microsoft Inc. "Windows Media Format 9 Series SDK". 2005.

10 MPEG-4 Industry Forum. M4IF http://www.m4if.org.

11 Apple Computer Inc. QuickTime http://www.apple.com/quicktime.

12 Adobe Systems Incorporated. PDF Reference, fourth edition, Adobe Portable Document Format Version 1.5; 2003.

13 Adobe Systems Incorporated. PDF as a Standard for Archiving http://www.adobe.com/products/acrobat/pdfs/pdfarchiving.pdf.

Comparison of long-T_2 Suppression Techniques for 3D Ultrashort Echo-Time Imaging

Ulrike Blume[1], Jürgen Rahmer[2], Peter Börnert[2] and Dietrich Holz[1]

[1] RheinAhrCampus Remagen, Department of Mathematics and Technology,
Suedallee 2, 53424 Remagen, Germany
E-mail: holz@rheinahrcampus.de
[2] Philips Research Laboratories, Roentgenstraße 24-26, 22335 Hamburg, Germany
E-mail: Juergen.Rahmer@philips.com

Abstract. In this study two different approaches for long-T_2 component suppression in ultrashort TE (UTE) imaging haven been investigated. The aim was to improve depiction of short-T_2 components by means of the UTE technique.
A "dual-echo" and a magnetization-preparation technique were implemented on clinical scanners operating at 1.5T and 3.0T field strength. 3D images obtained in healthy volunteer examinations using both approaches were compared with respect to short-T_2 SNR, long-T_2 suppression quality as well as scan efficiency. A quantitative SNR evaluation was performed using ankle scans of six volunteers. T_2 suppression profiles were simulated for both approaches to facilitate interpretation of the observations.
Both techniques provide comparable results at 1.5T regarding the suppression of long-T_2 species and fat. At 3T however the magnetization preparation suffers from stronger off-resonance effects. The magnetization preparation approach is more sensitive to magnetic field inhomogeneities due to the application of narrow band RF pulses and requires more shimming effort. The "dual echo" approach needs an additional post-processing step to calculate the subtraction image of two data sets acquired with different echo times. The signal-to-noise ratio in image areas with short-T_2 components is superior in the "dual-echo" approach.
In conclusion, both techniques provide good suppression of long-T_2 species with comparable short-T_2 SNR. The "dual-echo" approach offers better scan efficiency and is less sensitive to field inhomogeneity.

1. Introduction

So far tissues with short T_2 relaxation times mainly found in the musculoskeletal system could hardly be assessed using MRI due to the rapidly decaying MR signal (T_2 decay) and hardware limitations. Recently ultrashort echo-time (UTE) imaging techniques have been developed that can be used to visualize short-T_2 species present in a variety of clinically interesting tissues having T_2 relaxations times in the sub-millisecond range, like tendons, ligaments, or cortical bone [1]. A considerable reduction in the echo time was achieved by using a combination of volume excitation and radial FID sampling. However, since also the long-T_2 tissue contributes to the MR signal, UTE images are often dominated by long-T_2 components or are almost proton density weighted. Hence those images are

characterized by low image contrast. To selectively show only the short-T_2 signal components, different approaches have been proposed using appropriate magnetization preparation [1,2] or multi-echo techniques subtracting the long-T_2 signal components [3]. In this work, 3D UTE imaging is performed with the main focus on musculoskeletal applications, to compare a magnetization preparation approach with the "dual echo" approach for long-T_2 suppression.

2. Experimental Methods

Imaging has been performed on a clinical 1.5 T scanner (Achieva, Philips Medical Systems) using a 3-element surface coil array (element diameter: 7.5 cm) with the aim to visualize short T2 components in the ankle of healthy volunteers. A software extension allowed very short echo times, which were limited by the tune delay of the employed coil to 70 µs.

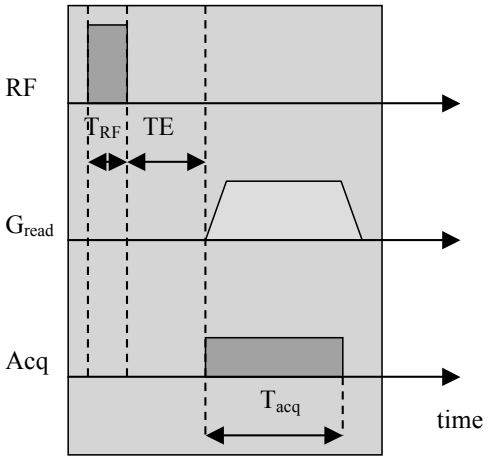

Fig. 1. Basic sampling scheme for UTE imaging

The basic signal sampling sequence consisted of a non-selective excitation pulse and a 3D radial free induction decay (FID) readout (cf. Fig.1). For all experiments, the same scan parameters have been used (128^3 matrix, FOV = 200 mm, excitation angle: 10°, angular sub-sampling: 50%, 24576 projections in total). The preparation sequence is illustrated in Fig. 2. Long-T2 species were flipped into the transverse plane by a 90° low amplitude, long duration symmetric Sinc-Gauss (40 ms, 2 side lobes on each side) or block pulse (10 ms, not shown) and dephased by a successive crusher gradient. Since short-T2 components lose coherence during the long preparation pulse, they are not affected and contribute to the MR signal after application of the subsequent excitation pulse. Both preparation pulses show good suppression of long T_2 components, with a T_2-cutoff of approximately 3.5 ms (Mz/M0 = ½). A fat suppression sequence was performed afterwards. To increase scan efficiency, compared to existing approaches [2], multiple ultrashort TE readouts (n=8) were performed after

magnetization preparation. A train of eight readouts has been found to be an optimal compromise between scan-acceleration and signal contamination caused by signal recovery (T_1) of the suppressed long T_2 components. In these experiments, TR was set to 4 ms, the preparation repetition interval to 250 ms, resulting in scan duration of 13 min for a 3D volume data set. For visualization, the reconstructed 3D image data was reformatted using the SoapBubble Tool [5].

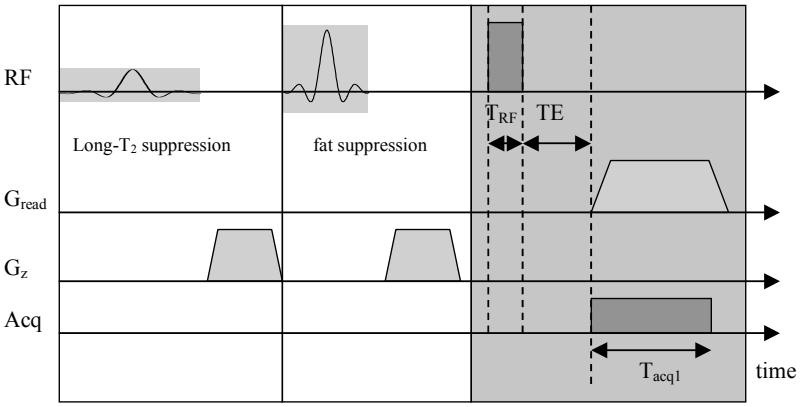

Fig. 2. Magnetization preparation with UTE sampling

For the "dual echo" approach (c.f. Fig. 3) no preparation was performed. In addition to the FID, a gradient echo was formed and sampled from the same transverse magnetization.

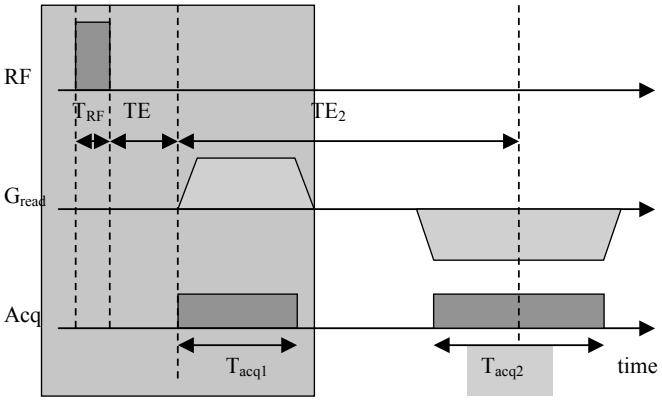

Fig. 3. Dual-Echo sampling scheme

The echo time TE_2 was set to 4.6 ms, where fat and water spins are in-phase at 1.5 T. Thus, for this sequence, TR increased to 7.3 ms resulting in a total scan time of 3 min. Subsequently, the FID and the echo images were subtracted to obtain an MR image that is dominated by short-T_2 species. In all experiments volume shimming was applied to reduce off-resonance related effects. SNR was assessed in the region of the extensor digitorum longus tendon and Achilles tendon.

3. Results and Discussion

Fig. 4 depicts a slice of a selected 3D "dual echo" data set of the right ankle (FID: Fig. 4a, echo: Fig. 4b). Fig. 4c shows the difference image of Fig. 4a and Fig. 4b, highlighting the fast T_2 components. Results of the long-T_2 magnetization

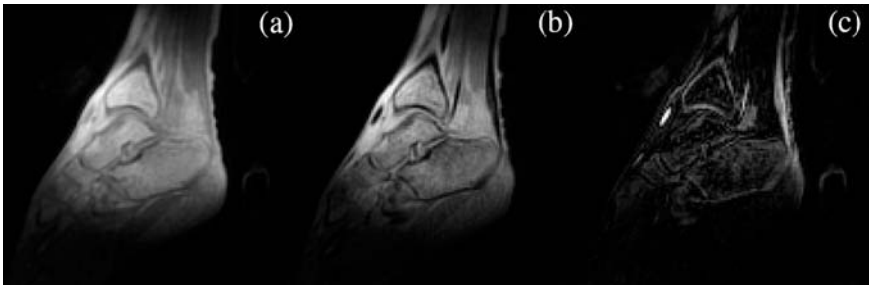

Fig. 4. Slice of a 3D data set of the right ankle acquired with the "dual echo" method. (a) FID image, TE = 70 µs. (b) Echo image, TE = 4.6 ms, (c) difference of (a) and (b).

preparation sequence are shown in Fig. 5. Fig. 5a shows data obtained employing only the T_2 preparation sequence. The remaining fat signal hampers the selective visualization of the short signal components. In Fig. 5b, fat suppression was applied additionally resulting in an excellent contrast underlining the necessity of

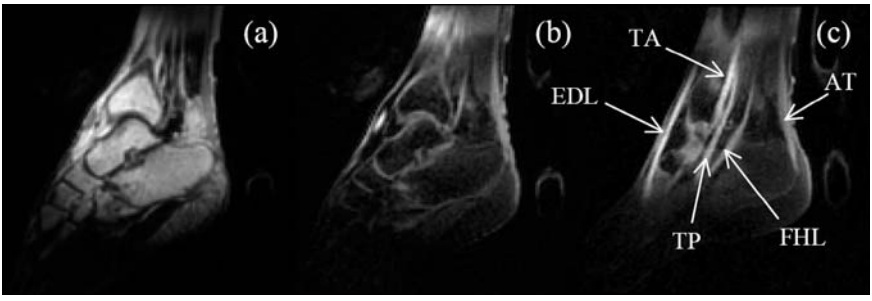

Fig. 5. Selected slice of 3D datasets of the right ankle acquired using (a) 40 ms Sinc-Gauss T2-preparation pulse, (b) T2-preparation and fat suppression. (c) Reformatted image of T2-prepared and fat suppressed data. Abbr.: TA: tibalis anterior tendon; TP: tibalis posterior tendon; EDL: extensor digitorum longus tendon; FHL: flexor hallucis longus tendon; AT: Achilles tendon.

the additional preparation. Tendons and periosteum become visible. Fig. 5c shows

a reformatted image of the 3D data set, visualizing main tendons along their path in the 3D volume. In contrast to the dual echo approach, applying long-T_2 and fat suppression yields the short-T_2 image without post-processing. However, off-resonance artifacts can degrade image quality, as visible at the top of Fig. 5b. The low bandwidth of the T_2 preparation pulse makes it sensitive to off-resonances, even though shimming was applied to reduce this complication. By using a block pulse of similar T_2-selectivity, off-resonance effects even increase. The difference images of the acquired dual echo data set show a better SNR of a factor of 2 in comparison to the magnetization prepared short-T_2 ones irrespective of using Sinc-Gauss or block pulses. This is contrary to the expectation that a difference image increases the noise level by a factor of sqrt(2) for the short T_2 components. We attribute this to the fact that preparation pulses have also an effect on short-T_2 components.

4. Conclusions

Two approaches to enhance short-T_2 signal in 3D UTE scans were compared: a "dual echo" technique and a magnetization preparation technique. While magnetization preparation directly yields the desired image contrast, the "dual echo" scanning requires the formation of a subtraction image as a post-processing step. However, since the magnetization preparation approach has to use rather long T_1-related shot intervals between preparations, the "dual echo" technique is more timeefficient with respect to the total scan time. It is furthermore less sensitive to off-resonance effects and, interestingly, in the demonstrated data shows better short- T_2 component SNR.

References

1 Robson MD, *et al*, J. Comp. Assist. Tomogr. **27**, 825-846 (2003);.
2 Larson PE, *et al*, Proc. ISMRM 13, 7861 (2005).
3 Rahmer J, *et al*, Proc. ISMRM 13, 1074 (2005).
4 Pauly JM, *et al*, Proc. SMRM 12, 145 (1992).
5 Etienne A, *et al*, MRM 48, 658 (2002).
6 Gurney P, et al, Proc. ISMRM 13, 787 (2005).

Scatter Analysis of the ClearPET™ Neuro Using Monte Carlo Simulations

Anna M. Fulterer[1,2], Stephan Schneider[2,3], Brigitte Gundlich[2], Patrick Musmann[2], Simone Weber[2] and Thorsten M. Buzug[4]

[1] Institute of Material Physics, TU Graz, A-8010, Austria
E-mail: fulterer@sbox.tugraz.at
[2] Zentralinstitut für Elektronik, Forschungszentrum Jülich GmbH, D-52425 Jülich, Germany
[3] RheinAhrCampus Remagen, Department of Mathematics and Technology, 53424 Remagen, Germany
[4] Institute of Medical Engineering, University of Luebeck, D-23538 Luebeck, Germany

Abstract. Scatter reduces the image quality in Positron Emission Tomography (PET). In this paper we discuss a) methods to estimate the scatter fraction in the raw data set as well as b) analysis of the different scatter components (e.g. phantom scatter, gantry scatter) arising from activity outside the field of view (OFOV). The PET detection system does not allow a discrimination of scattered events, thus Monte Carlo Simulations were used. The accuracy of the different scatter estimation methods was analyzed. Simulations with OFOV activity showed that small animal PET systems are indeed sensitive to random and scattered events from OFOV.

1. Introduction

Positron Emission Tomography bases on the coincident detection of two photons, which occur after an electron-positron annihilation. The thought line between the two detector elements is known as the line of response (LOR), the site of the annihilation should lie on the LOR. However, the photons may undergo Compton scattering within the object or the gantry of the scanner. This results in a displacement of the LOR from the real trajectories. Compton scattering is the most likely interaction between annihilation photons and tissue (water). The scatter fraction is defined as

$$SF = \frac{S}{S+T}, \tag{1}$$

where S is the amount of scatter and T the amount of unscattered coincidences in the raw dataset. In 3D mode the scatter fraction is often higher than 30%, for human scanners 50%. Correction for scatter is important to get a good image quality and high quantification accuracy.

The performance of PET scanners is characterized by several parameters (e.g. resolution, sensitivity & scatter fraction) For human systems two standards exist, NEMA NU-2 2001 and IEC 61675-1, in which the performance analysis is defined. For the small animal scanners up to date no standard was published.

Yang & Cherry proposed four different methods to estimate the scatter fraction [1]. Beside these methods, in this work two more are analyzed using Monte Carlo methods and phantom measurements. The shape of the projection profile can be used to get information about the amount of scatter in the dataset. Also the experimental parameters like the phantom geometry for this measurement influence the SF and have thus to be standardized.

Another important issue especially in small animal PET is the presence of activity outside the field of view. Activity accumulates not only in the brain, but also in heart and bladder, which are most often lying at the edges or outside the FOV. This is likely to cause additional scatter and random coincidences. In [2] the influence of these effects on slice dependent scatter fraction and noise equivalent count rate (NECR) was investigated. It was found that the scatter fraction increases considerably in slices near the OFOV activity. Moreover, apart from the object there may still be other material inside or next to the FOV e.g. animal bed, plexiglas screen and animal bed holder. Scattering in these materials can also result in detected events. To analyze this, the experimental setup was simulated using Monte Carlo methods. The advantage of Monte Carlo simulations over real experiments is that for each particle the complete history with all trajectories and interactions is available. In real experiments it is difficult to distinguish if a photon has undergone a scattering event, even for the inelastic scattering where the photon looses some energy. The reason is the scattering within the detector crystals and the poor energy resolution of the system (≈ 19%).

2. Experimental Methods

The small animal scanner ClearPET™ Neuro [3] is a high-resolution, high-sensitivity scanner dedicated to brain studies. One detector module of the ClearPET™ Neuro consists of a 8x8 dual layer LSO / LuYAP crystal matrix directly connected to a photomultiplier tube (PMT). Using the object oriented Simulation Toolkit GEANT4[1] a Monte Carlo Simulation reflecting an experiment with the ClearPET™ Neuro was programmed. It allows to define phantom size and position as well as activity distribution. The simulation program outputs data files with single and coincident events. For every event, time and position information e.g. crystal ID as well as scatter flags, describing where and how often Compton scattering occurred, can be recorded.

To estimate the scatter fraction from the raw dataset, the factors S and T from equation (1) have to be found. The NEMA scatter phantom is too large for small animal PET, thus, smaller phantoms are used. A line source with a known amount of activity is placed inside the phantom and the radiation is measured for a certain time. The dataset is represented as a 3D sinogram. The NEMA standard proposes that the sinogram is rebinned to 2D slices, so that for each ring the scatter fraction can be estimated separately and after a summation of all axial slices the total scatter fraction of the system can be calculated. The complete description of the algorithm can be found in the NEMA standard [4]. In Figure 1. the distributions from true, scattered and random events are shown in a projection. Unscattered

[1] Geant4 Website: http://geant4.web.cern.ch/geant4/

events (trues) are mainly found in the center of the profile. The distribution of the scattered radiation has a maximum in the center of the projection and falls of to the borders. The random coincidences are almost uniformly distributed across the whole projection.

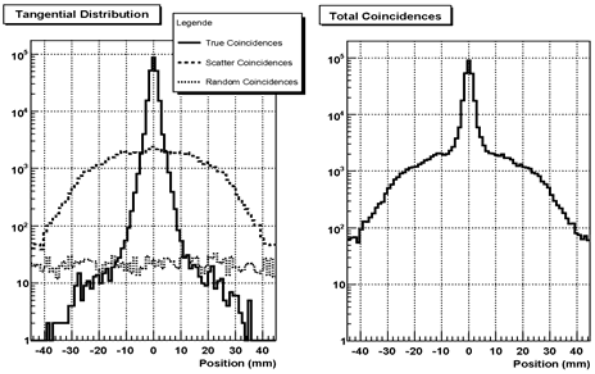

Fig. 1. (left) Distributions of true, scattered and random radiation, (right) Summed projection containing the different distributions.

Yang and Cherry discuss different methods to estimate the amount of scattered events. These are shown in Figure 2. The complete description of methods A to D can be found in [1].

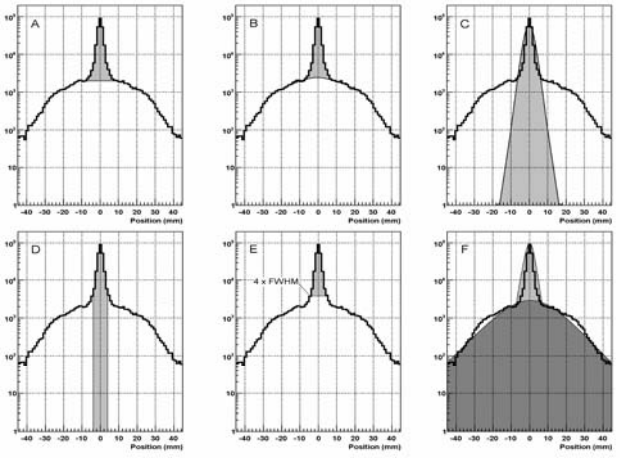

Fig. 2. Illustration of the different scatter estimation method A-F. (A) linear interpolation, (B) Gaussian approximation of the scatter tails, (C) Gaussian approximation of the peak, (D) integration over the peak area, (E) linear interpolation at 4 x FWHM, (F) combination of method (B) and (C)

Method E is an adaptation from the IEC standard. The approach is similar to method A, with the difference that the points for the linear interpolation depend on the shape of the maximum. A Gaussian function is fitted to the maximum like in method C. Afterwards the FWHM is computed for the fit result. The values at the points 4 x FWHM are used to interpolate the line. Like method A the area above the line are the unscattered events, the area below are the scattered events. The last method F uses the feature, that the measured projection is the superposition of the different distributions. In the first step the amount of scatter is estimated by a fit of a polynomial function to the projection. The result of the fit is subtracted from the projection; afterwards a fit of a Gaussian function to the maximum yields the quantity of unscattered events.

3. Results and Discussion

Scatter Estimation. Five phantom simulations of the ClearPET™ Neuro have been carried out. The mean value and the standard deviation of the scatter fraction were calculated directly from the Monte Carlo data. These values were used to compare the accuracy of the different methods.

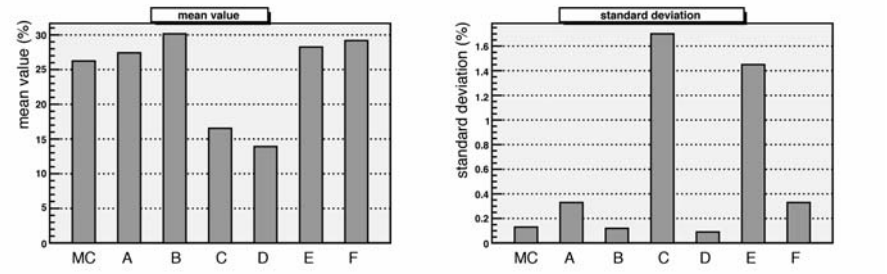

Fig. 3. Comparison of the accuracy of the different scatter estimation methods

In Figure 3 the results of the analysis are shown. The accuracy of method A is the best compared to all other methods. The result of method B lies over the reference value. The Gauss fit to the scatter distribution is not satisfying. Methods C and D underestimate the scatter fraction, because the maximum of the projection is a superposition of scattered and unscattered events. Method E overestimates the scatter fraction. In the IEC standard the calculations are done at 4 x FWHM, for the ClearPET Neuro the values at 5 x FWHM does better match the reference values. Like in method C the fit to the maximum of the projection results in unstable results, which can be seen in the higher standard deviation for both methods. Method F also overestimates the scatter fraction, but the standard deviation is much lower as for E. The overestimation results from inaccuracies during the fit of the different functions to the projection.

Impact of out Field of View Activity. For two different phantom sizes (rat phantom and small phantom) the number of scattered events accepted in the

scanner was determined for varying source positions outside the field of view (OFOV). The sensitivity for scattered events from annihilations OFOV decreases as the source is moved further away from the field of view, see Table 2. With a big phantom the number of scattered events is approximately doubled from the number accepted with a small phantom. Between about 20% (big phantom) and 50% (small phantom) of scattered events arise from gantry scatter.

Table 2. Sensitivity for OFOV activity at different source positions

Source distance	2 mm	7 mm	12 mm	17 mm
Sensitivity big phantom [%]	0.212	0.175	0.138	0.087
Fraction of gantry scatter [%]	20.51	19.72	18.19	21.03
Sensitivity small phantom [%]	0.1	0.078	0.062	0.046
Fraction of gantry scatter [%]	56.87	54.72	52.48	50.03

A look at the axial profiles of the scatter projections (Figure 4.) gave rise to the assumption that the distribution changes not so much with phantom shape or source position. Additional simulation series e.g. with varying phantom size confirmed the idea.

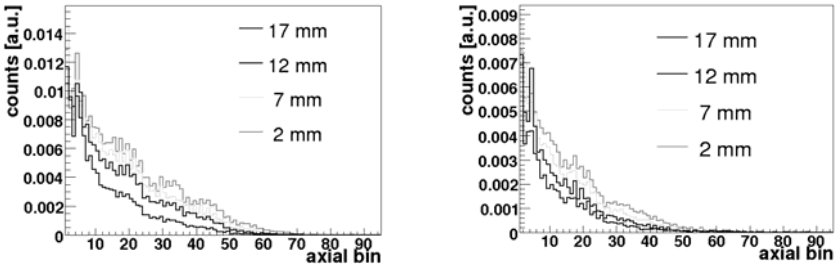

Phantom scatter Gantry scatter

Fig. 4. Axial profiles of the scatter projection for different source positions

In a next step the scattered events were sorted according to where scatter happened, to find out whether OFOV material or parts of the gantry influence the measurement. More than 95% of all gantry scatter events arise from the animal bed. Other parts of the gantry like electronics, a plexiglass screen that covers the scanner and the metal animal bed holder are only minor sources for gantry scatter.

From the results of the simulations it was inferred that OFOV activity causes both random and scattered events. Moreover, scattered photons that are accepted in coincidence detection have mostly undergone scatter in the phantom and the animal bed. Phantom and gantry scatter caused by OFOV activity result in similar projections. Therefore phantom and gantry scatter caused by OFOV activity are treated as one. Then it is possible to find a new classification for coincidences which reflects projection shapes and considers the source (Table 3.).

Activity in the FOV will result in true, scattered and random events, while OFOV activity can only be detected as scattered or random events. Moreover it is possible that random events are recorded where one photon comes from the FOV and the other one from outside (Mixed).

Table 3. Classification of coincidences in the presence of OFOV activity

Origin	FOV	Out FOV	Mixed
Trues	X		
Scatter	X	X	
Random	X	X	X

In order to find the percentage of coincidences lying in each of these categories in normal experiments with OFOV activity, a phantom with line source and OFOV depot was simulated (Table 4.).

Table 4. Coincidences arising from (long and short) line source and OFOV depot

		FOV	OFOV	Mixed		FOV	OFOV	Mixed
Trues	Long line	0.393			Short line	0.375		
scatter		0.131	0.076			0.133	0.079	
random		0.08	0.128	0.191		0.086	0.132	0.192

4. Conclusion

The scatter fraction highly depends on how the parameters *S* and *T* are estimated. The analysis showed that the result of method A is the most accurate of all methods compared. Beside the computational methods the study parameters influence the scatter fraction. To verify the results it could be interesting to apply the methods on more small animal scanners.

Out field of view activity contributes considerably to scattered and random events in small animal PET. With a rat phantom, only about 20% of scattered events arise from gantry scatter, mostly animal bed, the rest result from phantom scatter. Thus, it is not possible to reduce the impact of OFOV activity by shielding the detectors with end shields or by avoiding OFOV scattering material.

References

1 Y. Yang and S. R. Cherry, in *IEEE Trans. Nucl. Sci.*, Vol. 53, 127-132, 2006.
2 B. Gundlich et al., Poster at the 4. annual meeting of the SMI, Köln, 7.-10.09.2005
3 K. Ziemons et al., in *IEEE Nuclear Science Symposium Conference Record,* 1728-1732, 2003.
4 M.E Daube-Witherspoon et al., in *J. Nucl. Med. ,* Vol. 43, 1398-1409, 2002.

Multi-Modality-Imaging for Radiosurgery Planning of Arteriovenous Malformations

Klaus-D.Hamm[1], Cornelia Eger[2], Gunnar Surber[1], Gabriele Kleinert[1], Rene Aschenbach[2] and Joachim Klisch[2]

[1] Department for Stereotactic Neurosurgery and Radiosurgery, HELIOS Klinikum Erfurt, Germany
E-mail: stereotaxie@erfurt.helios-kliniken.de
[2] Institute for Radiology and Neuroradiology, HELIOS Klinikum Erfurt, Germany

Abstract. For arteriovenous malformations (AVMs) radiosurgery (RS) is a well-established treatment option. The needed high precise dose application is depending on the availability of imaging data sets with superior image quality that can be superimposed using an image fusion algorithm. Digital subtraction angiography (DSA) has to be integrated because it is a mandatory tool for RS planning procedure. In 34 patients suffering from an AVM various MR data sets including T1-weighted series and TOF angiographies (time of flight) were used together with the stereotactically localized CT and DSA data sets radiosurgery planning. All available image data sets were fused onto the CT data set using an automatic image fusion algorithm, in order to define the AVM nidus very precisely. The nidus was outlined in both localized DSA projections resulting in a DSA volume. Subsequently this DSA volume of the AVM has been adapted by inclusion of all available CT and MRI informations slice by slice resulting in the final target volume. We investigate in which cases the DSA volume and the finally treated target volume of the AVM were in agreement. The used thin-slice MR data sets (1-2 mm slice width) have been precisely fused onto the stereotactically localized treatment planning CT. The finally treated target volume was compared with the DSA volume of the AVM nidus as follows: In 19 cases the final target volume was larger than the DSA volume, in 6 it was smaller and 5 it was approximately equal. The difference was significant (Wilcoxon test: difference<0.0001; t-test: $t=3.01$, $p>0.005$). In 4 cases outlining the AVM was not possible without DSA. In 5 patients a two- or three-vessel DSA was needed, since there were different AVM compartments. In cases where previously a partial embolization had been undergone, the use of superimposed CT sets with, and without, contrast medium was important in order to define the completely embolized partial volumes that were not subject to treatment. The inclusion of the DSA images enabled a better identification of those arterialized veins that did not belong to the nidus. The exact 3-dimensional definition of the AVM nidus has been realized safely by integrating all available imaging modalities. The stereotactic DSA data acquisition remains a crucial tool for safe nidus definition in radiosurgery treatment planning.

1. Introduction

Radiosurgery (RS) is one of the therapeutic options for the management of arteriovenous malformations (AVMs), alone or combined with endovascular embolization and/or microsurgical resection, depending on localization and morphological characteristics of the AVM. The most important factor for RS is the AVM volume; therefore large AVMs (volume above 15 ccm or more than 4 cm in diameter) represent the

most challenging group[9,11]. The goal of RS is to obliterate the intracranial AVM with minimal injury to the surrounding normal brain and neural tissues using a sharply localized, single high radiation dose to cause a vascular response that ideally occludes the AVM nidus. This process lasts approximately 3 years; therefore RS cannot be the treatment of choice for AVM clinically presented with hemorrhage. But for properly selected AVMs, RS is an effective therapy option with published obliteration rates between 60% and 90%[9,10,11]. The treatment plan should offer the lowest risk, but the highest chance of complete AVM obliteration. As one of the most important factors, the exact definition of the three-dimensional (3D) shape of the AVM nidus is therefore required. Partial volume irradiation and a dose lower than 15 Gy are recognized to be associated with RS failures[4,9]. The precondition for an accurate delineation of lesion dimensions slice by slice is the availability of high quality images for the needed stereotactic 3D RS planning procedure [7]. Because of the superior spatial resolution and its dynamic demonstration, digital subtraction angiography (DSA) was the reference standard for RS of AVMs in the past and is the base of the published long-term results. But as a two-dimensional (2D) procedure DSA is proved to be unable to deliver the true 3D- volume configuration of the AVM nidus. 3D-radiation treatment planning systems have become available that offer more precise 3D-AVM definition by using thin-slice imaging systems, whether magnetic resonance imaging (MRI)-based or computed tomography (CT)-based. The spatial distortion in MRI-guided stereotaxy can be minimized using 3D- image acquisition sequences with high readout gradients of recent MRI scanners. The average difference between MRI and CT stereotactic coordinates was found to be 1-1.5 mm by Bednarz et al [1].

The advantages of using MRI and CT data sets are also shown by the fact that these procedures are less invasive and allow visualization of neurovascular structures, as well as the surrounding brain tissue and nerves as organs at risk. In order to provide more detailed information about angioarchitecture of the AVM that could possibly lead to a reduced target volume for RS, further 3D- examinations like magnetic resonance angiography (MRA) and computed tomography angiography (CTA) were used and evaluated for radiosurgery of AVMs[1,5,8,12]. The exact application of the therapeutic dose is based on the availability of imaging data sets with superior image quality that can be superimposed by an image fusion algorithm. The DSA is a mandatory tool for RS planning as well[3,6,10].

2. Methods

34 AVM patients treated with RS were analyzed in this report. Various MR data sets have been used together with the stereotactically localized CT and DSA data sets for the 3D-RS planning procedure. On a 1.5 T MR scanner (General Electrics, USA) the following MRI sequences were acquired: 3D-T1-SPGE (spoiled gradient echo) transversal data set with contrast medium (1 mm slice distance, 512^2 image matrix, resulting in approximately 0.5x0.5x1.0 mm voxel size that almost meets voxel isometry) and additional 2 mm transversal T2-SE (spin echo) slices. MRA as a non-invasive vascular diagnostic imaging has become a well-established procedure for RS

planning of AVMs. There are several techniques available for the exact characterization of the morphology. The MRA of choice for AVMs that was also used for our patients is a flood-based 3D- TOF (time-of-flight) technique without contrast medium. This technique is characterized by using the blood flow as an intrinsic contrast medium for differentiating vascular structures from brain tissue. The advantage of a 3D-acquisition is the high spatial image resolution enabling a high-quality image reformatting.

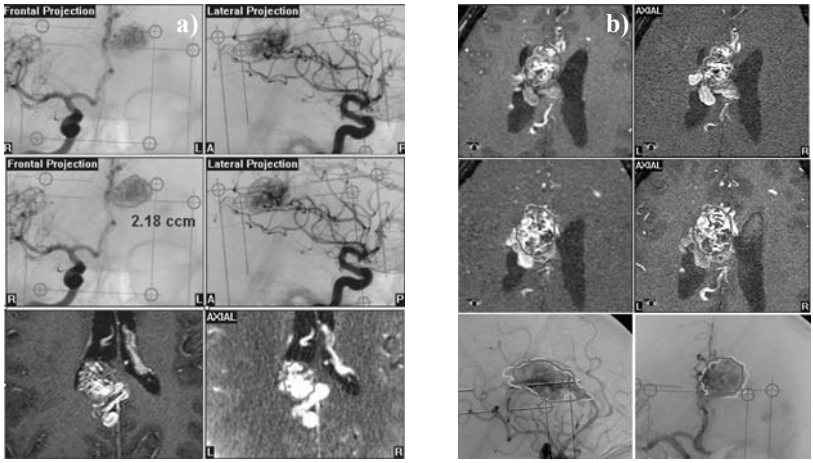

Fig. 1. a) Stereotactically performed DSA with a compact AVM nidus *(above left: anterior-posterior projection, above right: lateral projection)*, nidus delineated in both projections *(center left and right)* and integrated in an axial slice of MRI *(below left)* and CT *(below right)*. b) MRI, TOF-MRA and DSA of an AVM with the defined DSA target volume *(brown line)* and final target volume *(yellow line)*, overestimated DSA contour *(above left: MRI, above right: MRA)*, underestimated DSA contour *(center left: MRA, center right: MRI)*, both overlapping contours *(below left lateral and below right anterior-posterior projection of the DSA).*

The Linac-based RS was performed using the integrated Novalis Shaped Beam Surgery system including the 3D-treatment planning software BrainSCAN 5.31 (BrainLAB AG, Germany). On the treatment day the stereotactic frame was fixed to the patients' head under local anesthesia. The stereotactic CT acquisition (with localizer box attached) was performed without and with applied contrast medium using a standardized scan protocol (axial slice width: 1.25 mm, no gap, 512^2 image matrix)by a 16- or a 4-slice CT scanner (General Electrics, USA), followed by the needed stereotactic DSA imaging (with the head frame and a modified localizer box attached) of the involved intracranial vessels in anterior-posterior and lateral projection. The images with the suitable phase for AVM nidus definition were selected and all data transferred to the planning workstation. The CT data sets and both selected DSA projections were localized within the stereotactic space and all available MR data sets were fused onto the stereotactic CT using BrainLAB´s automatic image fusion software. The AVM nidus was delineated in both localized DSA projections resulting in the DSA volume to

superimpose the defined DSA contour onto the corresponding axial slices of the CT and MR data sets. Caused by the 2D-character of each projection, it is not possible to determine the true 3D shapes in this way (Fig. 1a). Subsequently, the DSA volume has been adapted by inclusion of all available CT/MR data sets slice by slice, resulting in the final target volume (Fig. 1b). The volume assessed by DSA only, and the final target volume, were evaluated to determine agreement between the volumes. The Wilcoxon test as a nonparametric analysis for the equality of co-variances and Student's t-test (for matched samples, comparison of differences) were used for the comparison of the two volumes. Statistical significance was determined as a probability value less than 0.05. All AVM nidi on DSA and on fused CT/MR were exclusively delineated by our interdisciplinary team (neurosurgeon, neuroradiologist, radiation oncologist).

3. Results and Discussion

The median AVM nidus volumes were 2.14 ccm (DSA volume) and 3.07 ccm (final volume). The comparison of the DSA volume with the final target volume resulted as follows: In 19 cases the final target volume was larger than the DSA volume, in 6 patients smaller and in 5 cases approximately equal, respectively. The differences of both volumes were assessed to be statistically significant (Wilcoxon test: Difference<0.0001; t-test: $t=3.01$, $p>0.005$). In the other 4 cases outlining of the AVM was not possible without DSA. There were 3 fistulous AVMs that were not precisely definable in fused CT/MR images. The fourth patient suffered from a residual AVM after microsurgical resection in 1984 – MRI was not available and the CT had restricted significance due to clip-artifacts. In 5 cases a two- or three-vessel DSA was needed since different AVM compartments were found. The use of superimposed CT sets without and with contrast medium was important in order to define the completely embolized partial volumes that were not subject to treatment, in cases where a partial embolization was previously undergone. The integration of the DSA images enabled us to better identify those arterialized veins that did not belong to the nidus.

Because of the low time-resolution of CT and MRI, RS planning without DSA is not accurate enough to determine the localization and volume of the AVM nidus. Differentiation between the AVMs arteriolar nidus, which must be obliterated, and normal vessels such as feeding arteries or draining veins, which should be spared, is clearly more possible on DSA that consists of a series of images obtained at different phases after contrast medium has been injected. Because of this dynamic demonstration by observing radiographic contrast flow and its superior spatial resolution, additional stereotactically performed DSA is still the standard for safe nidus definition in RS planning.[1,3,5,10] The goal is to obtain information about the right-left, anterior-posterior and inferior-superior extent of the AVM for each slice. The inability of DSA as a 2D procedure to determine the 3D shapes of the nidus (in particular in case of concave shapes) should result in a larger AVM volume. The modification of this volume using all additional information of the thin-slice 3D

imaging (CT, MR) aids in the precise estimation of the true nidus reducing the target volume for RS. Zhang et al[10] described a significant mean nidus volume reduction of 31.8% using 3D-DSA plans and further significant reduction of 9.8% using CT-DSA plans. Although we found a significant difference between the DSA assessed AVM volume and the final target volume, which was more often larger than the DSA volume (19/34). We were able to reduce the estimated nidus volume only in 6 cases and in 5 patients (with a compact AVM) both of the volumes were approximately equal. This is probably due to the special algorithm of the BrainSCAN software used to transfer the outlined AVM nidus from the two DSA projections into the 3D data base without rectangular edges.

Bednarz et al[1] reported MRA superior to MRI in defining the nidus, but in 10/22 cases both, MRA and MRI failed due to clip artifacts and embolization material. They concluded, that MRA could not be a sole imaging modality for AVM RS, at present time, but could be used alone for such patients who did not have prior embolization or surgery and have medium size compact nidi. We found the target definition improved by using all available information, but not with the TOF MRA as a static investigation alone. Compact nidi are well demarcated, in such cases both of the volumes were also approximately equally in the present report. DSA is definitively needed after surgery and/or partial embolizations and in case of special vascular anomalies like fistulous (micro) AVMs or associated aneurysms[1,3]. Nagaraja et al[8] measured the nidal volume using a combination of static and dynamic MRA procedures, which showed an excellent correlation between MRA and DSA. The development of dynamic 3D MRA techniques with short acquisition time and high spatial resolution (probably by using 3T MR scanners) or flow-based CTA will be the future in RS of AVMs.

The Amsterdam group[2] evaluated the well-known interobserver variation as an important factor when contouring AVMs for RS planning. We are trying to minimize this problem with our experienced interdisciplinary team (neurosurgeon, neuroradiologist, radiation oncologist) performing each AVM delineation slice by slice, using all imaging information directly at the workstation. For a well-circumscribed compact AVM nidus this fact is not so important, but a crucial step in case of intermediate nidi, with less clearly defined margins and presence of intervening brain tissue within the nidus, and especially in cases of diffuse nidi that are hard to distinguish from surrounding nutritive vessels[11]. Partial volume irradiation is recognized as an important fact, caused by inaccurate definition of the nidus[9]. The target volume error and a lower dose seem to be the most accepted facts for lower obliteration rates after RS of AVMs. The factors are combined and influence each other underlining the importance of using all available information of a high quality imaging to define the correct AVM nidus for RS.

4. Conclusions

Precisely-fused high quality image data sets are a very important precondition for target definition in RS because partial volume irradiation is the most important

failures for complete AVM obliteration. For all patients the accurate delineation of the 3D-shapes of the AVM nidus, slice by slice, by an interdisciplinary team has been realized safely by integrating all available information using different kinds of imaging. The stereotactic DSA data acquisition remains a crucial tool and should not be discarded at present, even in case of compact AVM nidi. To make RS procedure more comfortable for AVM patients, the development of dynamic 3D-MRA techniques with short acquisition times and high spatial resolution can probably replace the stereotactic DSA.

References

1 Bednarz G, Downes B, Werner-Wasik M, Rosenwasser RH: Combining stereotactic angiography and 3D time-of-flight magnetic resonance angiography in treatment planning for arteriovenous malformation radiosurgery. *Int J Radiat Oncol Biol Phys.46:1149-54,2000*

2 Buis DR, Lagerwaard FJ, Barkhof F, Dirven CM, Lycklama GJ, Meijer OW, van den Berg R, Langendijk HA, Slotman BJ, Vandertop WP: Stereotactic radiosurgery for AVMs: role of interobserver variation in target definition on digital subtraction angiography. *Int J Radiat Oncol Biol Phys.62:246-52,2005*

3 Colombo F, Cavedon C, Francescon P, Casentini L, Fornetta U, Castellan L, Causin F, Perini S: Three-dimensional angiography for radiosurgical treatment planning for arteriovenous malformations. *J Neurosurg 98:536-43,2003*

4 Ellis TL, Friedman WA, Bova FJ, Kubilis PS, Buatti JM: Analysis of treatment failure after radiosurgery for arteriovenous malformations. *J Neurosurg 89:104-10,1998*

5 Essig M, Engenhart R, Knopp MV, Bock M, Scharf J, Debus J, Wenz F, Hawighorst H, Schad LR, van Kaick G.: Cerebral arteriovenous malformations: improved nidus demarcation by means of dynamic tagging MR. *Magn Reson Imaging.14:227-33,1996*

6 Gauvrit JY, Oppenheim C, Nataf F, Naggara O, Trystram D, Munier T, Fredy D, Pruvo JP, Roux FX, Leclere X, Meder JF: Three-dimensional dynamic magnetic resonance angiography for the evaluation of radiosurgically treated cerebral arteriovenous malformations. *Eur Radiol.16:583-91,2006*

7 Hamm KD, Surber G, Schmücking M, Wurm RE, Aschenbach R, Kleinert G, Niesen A, Baum RP: Stereotactic radiation treatment planning and follow-up studies involving fused multimodality imaging. *J Neurosurg (Suppl 3) 101:325-333, 2004*

8 Nagaraja S, Capener D, Coley SC, Lee KJ, Wilkinson ID, Kemeny AA, Griffiths PD.: Brain arteriovenous malformations: measurement of nidal volume using a combination of static and dynamic magnetic resonance angiography techniques. *Neuroradiology.47:387-92,2005*

9 Pollock BE, Flickinger JC, Lunsford LD, et al: Factors associated with successful arteriovenous malformations radiosurgery. *Neurosurgery.42:1239-47,1998*

10 Zhang XQ, Shirato N, Aoyama H, Ushikoshi S, Nishioka T, Zhang DZ, Miyasaka K: Clinical significance of 3D reconstruction of arteriovenous malformation using digital subtraction angiography and its modification with CT information in stereotactic radiosurgery. *Int J Radiat Oncol Biol Phys.57:1392-9,2003*

11 Zipfel GJ, Bradshaw P, Bova FJ, Friedman WA: Do the morphological characteristics of arteriovenous malformations affect the results of radiosurgery? *J Neurosurg 101:393-401,2004*

12 Ziyeh S, Strecker R, Berlis A, Weber J, Klisch J, Mader I.: Dynamic 3D MR angiography of intra- and extracranial vascular malformations at 3T: a technical note. *AJNR Am J Neuroradiol.26:630-4,2005*

Image Based Analysis of Bone Graft Samples made by 3D Printing Using Conventional and Synchrotron-Radiation-Based Micro-Computed Tomography

S. H. Irsen[1], B. Leukers[1], C.Tille[1], F. Beckmann[2], B. Müller[3], T. M. Buzug[4] and H. Seitz[1]

[1] caesar research center, Ludwig-Erhard-Allee 2, 53175 Bonn,
[2] GKSS Forschungszentrum, Geesthacht, Germany,
[3] Computer Vision Laboratory, ETH Zürich, Switzerland
[4] Institute of Medical Engineering, University of Luebeck, Ratzeburger Allee 160, 23538 Luebeck, Germany
E-mail: buzug@imt.uni-luebeck.de

Abstract. Rapid Prototyping and especially the 3D printing, allows generating complex porous ceramic scaffolds directly from powders. Furthermore, these technologies allow manufacturing patient-specific implants of centimeter size with an internal pore network to mimic bony structures including vascularization. The non-destructive analysis of the internal structure of such 3D printed scaffolds provides important information. We used computed-microtomography as investigation method. Conventional and Synchrotron radiation based methods were tested and compared.

1. Introduction

The treatment of congenitally, traumatically or surgically caused bone defects is a major problem in reconstructive surgery [1]. Today autogenous materials are still used to fill larger cavities. These autologous implants need to be extracted and it is often difficult to find the suitable extraction site. Therefore, an urgent need exists for synthetic bone replacement with reasonable in-growth behavior and enhanced mechanical stability.

Rapid Prototyping (RP) technology provides a variety of generative fabrication techniques, which can produce real parts directly from computer data. In the last years RP-technologies have been used for medical purposes including the fabrication of anatomical models in oral and maxillofacial surgery. Such models play a crucial role in preoperative planning [2].

In RP-processes, models are built layer-by-layer based on a 3-dimensional (3D) dataset. Prior to fabrication the 3D dataset is sliced into a stack of layers to be processed by the RP machine. Depending on the used RP process, various materials can be used for fabrication.

For the production of ceramic parts, including bone grafts, 3D printing (3DP) is well suited. In 3DP, powder or granular material is selectively glued together layer by layer using ink jet printer technology [3]. Figure 1 shows an image of a Hydroxyapatite granulate, suitable for 3D printing.

Overall, RP-technology allows the fabrication of physical models with nearly no limitation in outer shape. Even more important, a great variety of internal structures can be realized. The data for the clinical morphology can be derived from computed tomography (CT) data, while the internal structure has to guarantee the cell in-growth and nutrition supply.

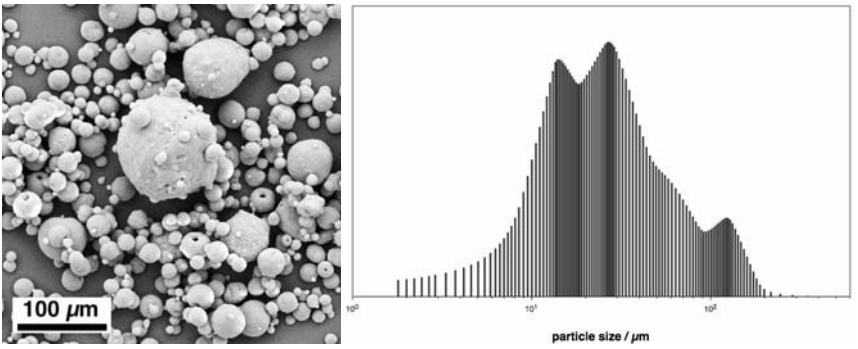

Fig. 1. Hydroxyapatite granulate for use in a 3 D printer and the corresponding particle size distribution. The multi modale size distribution of the grnaulate can easily be seen.

To optimize mechanical stability of 3DP scaffolds, the so-called green bodies undergo post processing, i.e. sintering or infiltration. It should be noted that Hydroxyapatite (HA) is a well-known synthetic biomaterial often used for bone replacement [4]. It provides a similar stoichiometry like the mineral phase of human bone. Beside the chemical and biological properties of the used building material, the internal structure of the scaffold is a key feature for a good bone graft. Interconnected pores having diameters between 100 and 500 µm are the prerequisite for the vascularization of an implanted scaffold [5]. Consequently, the internal structure of the scaffolds is one of the most important criteria for quality control as well as for design optimization.

The aim of this study is to analyze the internal structure of bone grafts fabricated by 3D printing using computer-micro-tomography. A comparison between conventional X-ray based and Synchrotron radiation based µCT is made and the limitation of the methods are discussed.

2. Materials and Methods

Scaffold Fabrication. Spray-dried Hydroxyapatite granules (HA) and a water based polymeric binder solution were chosen for this study [SPIE Paper]. These materials are specially conditioned for the use in a 3D printer. In this study we used simplified test geometries, which were constructed and prepared for 3D printing using the software tool Magics (Materialise, Belgium). The scaffolds had a diameter of 5 mm and a height of 9 mm and they posses internal channels with a diameter of about 1mm.

A 3D printing test setup [3] was used for scaffold fabrication. The flexibility of this 3D printing setup makes it possible to investigate both modified process techniques and different material combinations. Here, the 3D printer was used with a spatial resolution of 106 dpi and a slice thickness of 200 µm.

The 3D printed green bodies were freed from unglued granulate using an air blower. In this state the scaffolds are fragile and have to undergo a post processing procedure to obtain reasonably stable scaffolds. For final solidification the green bodies were sintered in air at 1250 °C for 3 hours.

X-Ray-Computed-Micro-Tomography. Micro focus Computed Tomography scans were done using an desktop µCT from Skyscan (model 1072).The voxel size of the reconstructed models (Feldkamp cone beam reconstruction) was 10.5 µm.

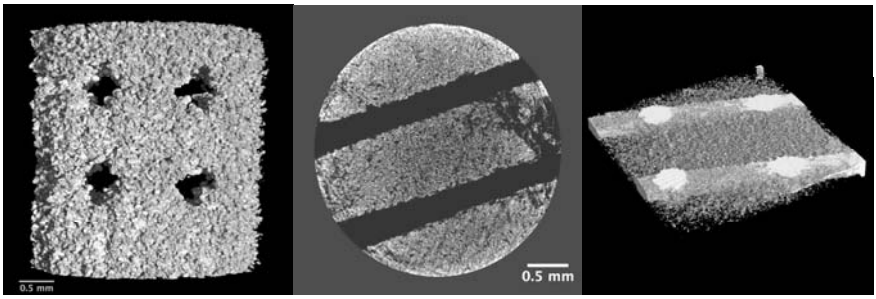

Fig. 2. 3D-visualisation of a µCT scan of a HA Scaffold (left image). The middle and right images illustrate segmentations of the scaffolds internal structure in 2D (middle) and 3D (right).

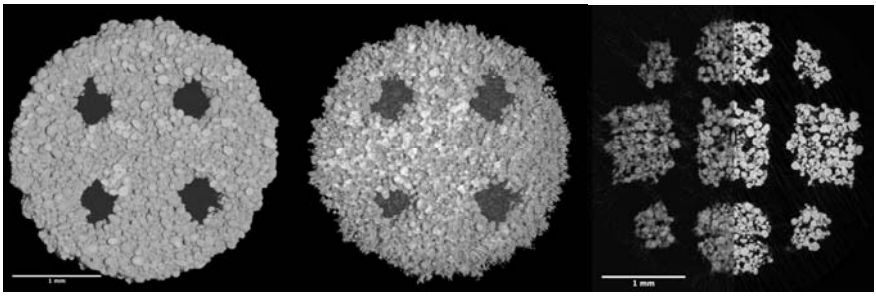

Fig. 3. 3D Visualisation of a sample scaffold based on SRµCT (left) and conventional µCT data (middle). The right image shows the resolution difference between both experiments using a slice image. For better illustration the image shows slices representing the same area of the scaffold.

Synchrotron Based Computed Micro Tomography. Synchrotron based computed-micro-tomography (SRµCT) was performed at the beamline BW 2 at HASYLAB (DESY, Hamburg, Germany) in absorption contrast mode [6] using the photon energy of 24 keV. The voxel length corresponds to 4.3 µm. The spatial resolution was determined using the modulated transfer function of a gold edge to

6.4 µm [7]. 3D data were reconstructed out of 720 projections by the filtered back-projection algorithm [8].

Image Analysis. For image analysis the slice images were cropped using the software AnalySIS (Soft imaging Systems, Münster, Germany). Line profiles for binarization were calculated using the same software package. The distance transforms for quantitative 3D porosity characterization were obtained by the means of the Gigatools software [9].

Results and Discussion

Qualitative Results. Figure 2 shows the visualization of a 3D-printed and sintered HA bone graft. The dataset was gathered using conventional X-ray µ-CT. The middle image of figure 2 shows a selected slice of the dataset while the left and right image represent 3D reconstructions of the dataset. The internal channel network as well as a structural defect of the scaffolds interior can easily be seen in the 2D representation. Furthermore the image allows a qualitative estimation of the scaffolds porosity. This is important to evaluate the influence of the size distribution of the granulates used for 3D printing. A bimodal or multimodal distribution of the granules is desirable to optimize the stability and the porosity of the 3D printed scaffolds.

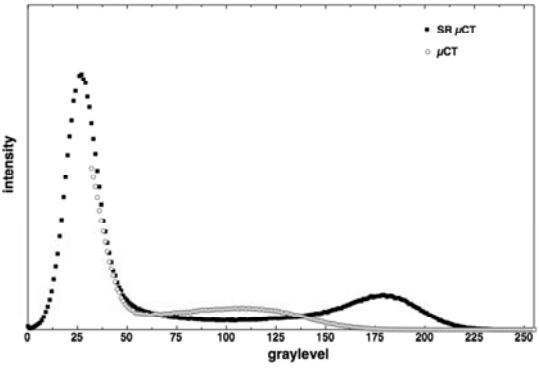

Fig 4. Histograms of one selected slice image. The circles represent the conventional µCT-scan while the filled squares are derived from the SRµCT dataset.

In summary conventional X-ray µCT is a versatile tool for nondestructive qualitative sample investigation, which allows the easy detection of structural failures in the µm scale caused by the 3D printing process or during the final sintering step.

Figure 3 and 4 on the other hand demonstrate the limits of conventional X-ray µCT for a quantitative porosity analysis. The left and middle image are 3D reconstructions of the same scaffold using synchrotron µCT (left) and conventional X-ray µCT (right) respectively. The enhanced contrast and resolution of the synchrotron based dataset resolves the single granules of the HA

building material down to their internal structures, which lie in an size range below 1 µm. The right image in figure 3 illustrates a direct comparison between the synchrotron and an X-ray based µCT scan of the same scaffold. Here the synchrotron data provide a much better density contrast and a higher detail resolution. The corresponding histograms are depicted in figure 4. In case of X-ray µCT a reliable separation of between material and air is not possible whereas in case of synchrotron µCT the two peaks for air and material is difficult but possible [10].

Quantitative Results. In order to quantify the effect of sintering on the internal scaffold structure, information about the porosity of the scaffolds is needed. To achieve the mean pore diameter the ratio of volume to surface has to be calculated. Since the extraction of the surface is hardly detectable for complex scaffolds like the ones used for this study, we calculated 3D distance transform, an alternative approach to gather porosity information. In this method the minimal distance of each voxel to material is determined [9].

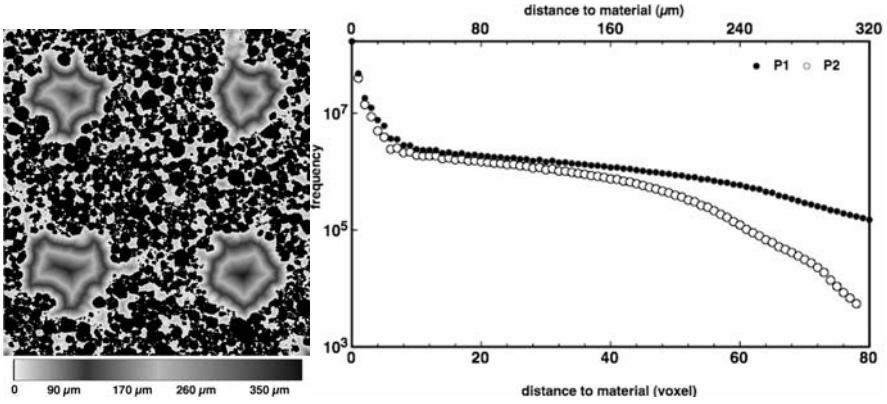

Fig. 5. 3D Distance transform map of a selected region of a sintered bone graft made by 3D printing. The right figure shows the distance to material distribution of the scaffold in before and after sintering.

Figure 5 shows the 3D distance map (left) of a representative slice and the distribution function (right). This demonstrates the effect of sintering on the internal structures. A significant difference between both samples is visible for distances above about 30 voxels (120 µm). The total porosity of both scaffolds is reduced from 52% to 49% during sintering.

Conclusion

In conclusion, image based analysis of the internals scaffold structure of 3D printed-printed bone grafts is a powerful too both in qualitative and quantitative means. Conventional X-ray based µCT can be used for the analysis in scale down to 100 µm or for the qualitative estimation of the porosity. So Conventional µCT

is ideal for every days quality analysis. Here the experimental effort of synchrotron-based measurements is overdone. For more sophisticated tasks like a quantitative interpretation of the results, synchrotron based experiments allow investigations on the µm scale. These results are important for the optimization of the scaffolds internal geometry as well as the optimization of the compromise between mechanical stability and porosity.

Acknowledgements. This study was funded through HASYLAB at DESY Hamburg, Germany (Proposal I-05-028). The authors gratefully acknowledge the Friedrich-Baur-Research Institute for Biomaterials (Bayreuth, Germany) for a generous donation of ceramic granulates and binder polymers.

References

1. S.M Schnürer,.U. Gopp, K. Kühn, S. J.Breusch, *Knochenersatzwerkstoffe*, *Orthopädie*, 32, 2003.
2. S. H. Irsen, H. Seitz,C. Tille, G. Bermes, E. Wolfinger, R. Sader, H.-F. Zeilhofer in *Technology and Health Care* Special Issue 12, 110-111, 2004.
3. Seitz, H.; Rieder, W.; Irsen, S.; Leukers, B.; Tille, C.: Three-dimensional printing of porous ceramic scaffolds for bone tissue engineering. *J Biomed Mater Res Part B: Appl Biomater*, 74B, 782–788, (2005).
4. S. V. Dorozhkin, M. Epple , Die biologische und medizinische Bedeutung von Calciumphosphaten, *Angew. Chem.* 114, 3260 – 3277, (2002).
5. O. Gaulthier, J.M. Boouler, E. Aguado, P. Pilet, G. Daculsi, *Biomater*. 19, 133-139 (1998).
6. F. Beckmann, in Developments in X-ray Tomography III, edited by U. Bonse (SPIE - The International Society for Optical Engineering, San Diego, USA, 2001), Vol. 4503, p. 34.
7. B. Müller, P. Thurner, F. Beckmann, T. Weitkamp, C. Rau, R. Bernhardt, E. Karamuk, L. Eckert, S. Buchloh, E. Wintermantel, D. Scharnweber, H. Worch: Three-dimensional evaluation of biocompatible materials by microtomography using synchrotron radiation, Proceedings of SPIE 4503 178-188, (2002).
8. T. M. Buzug, Computed Tomography: From Photon Statistics to Modern Cone-Beam Systems, Springer, Berlin (2007).
9. Müller, F. Beckmann, M. Huser, F. Maspero, G. Szekely, K. Ruffieux, P. Thurner, E. Winter¬mantel Biomol Engin 19:73-8, (2002).
10. S.H. Irsen, B. Leukers, B. Bruckschen, C. Tille, H. Seitz, F. Beckmann, B. Müller in Developments in X-Ray Tomography V, edited by U. Bonse, Proc. of SPIE Vol 6318, 631809 (2006).

SPECT-CT in Maxillofacial Surgery

B.-I. Boerner[1,2], S. Berg[3], P. Juergens[1,2], A. Robertson[2] and K. Schwenzer-Zimmerer[1,2]

[1] Hightech Research Center of Cranio-Maxillofacial Surgery, University Basel, Switzerland
[2] Dept. of Cranio-Maxillofacial Surgery, University Hospital Basel, Switzerland
[3] Institute and Clinic of Nuclear Medicine, University Hospital Basel, Switzerland

Abstract. Bone scintigraphy and SPECT (Single Photon Emission Computer Tomography) imaging with ^{99m}Tc-DPD (^{99m}Tc-dicarboxypropane-diphosphonate) is a routine procedure to detect Osteitis. Until now, the technique was of limited use in craniofacial surgery due to low spatial resolution and lack of anatomical detail. We present two cases in which bone scintigraphy with ^{99m}Tc-DPD and SPECT-CT imaging (Symbia®, Siemens) was performed. With SPECT/CT accurate image fusion is achieved automatically and complex anatomical regions can be investigated. Automatic image fusion matched precisely. The areas of increased bone turnover were clearly marked. No artefacts occurred due to patient's movement. SPECT/CT is a promising tool for the follow-up imaging of osteitis because of precise localisation and extension of the bone changes.

1. Introduction

In the field of Medical Imaging SPECT/CT is a modern imaging modality. SPECT-CT combines a radiological device (Computer Tomography) with a nuclear medicine technology (Single Photon Emission Computer Tomography) in one unit. The use of scintigraphy with ^{99m}Tc-DPD (dicarboxypropane-diphosphonate) for detecting osteitis is well known. Planar scintigraphic imaging was used in different aspects of skeletal imaging until the late 1960s. A few years later, the SPECT camera was developed. Different to the planar scintigraphic imaging the SPECT camera helps with anatomical locations and orientations because the information is displayed in a three dimensional way. Still detailed anatomical landmarks are not available due to the nature of the method. The next step is to generate images which are not so difficult to interpret: fused images (CT or MRI with SPECT). It is possible to fuse two different sets of data; however an anatomically correct and accurate image fusion is hard to achieve due to the patient positioning and patient motions. (In order to obtain the images the patients had to change the device. Sometimes there were even days between the SPECT image and the CT image.)

Therefore, a combination of both imaging modalities in one device is preferable. Symbia T2® (Siemens), a hybrid SPECT-CT, is such a device. We like to present two cases from this hybrid machine where one can see not only the location but also the extension of the infection.

2. Material and Methods

Two patients (age 36 and 70 years) received ^{99m}Tc-DPD scintigraphies of the mandible. The first aim was to locate increased osteoblastic activity due to the diagnosis osteitis (in these cases an infected bisphosphonate necrosis and an infection after tooth extraction) and the second aim was to assess the extension of the infection.

Planar scintigraphies were gained 3 min and approximately 3 hours after the injection of the radiopharmaceutical. A SPECT/CT was performed after approximately 3,5 hours. The diagnosis was correlated with microbiological and histological findings during the later course of treatment.

3. Results

Although the procedure took more than 20 minutes, it was well tolerated by all patients. No artefacts occurred due to patient's movement. The automatically fused images by Symbia T2® matched precisely. The areas of increased bone turnover were clearly visible and it was possible to see the extension of the increased bone turnover in a range of less than a centimetre.

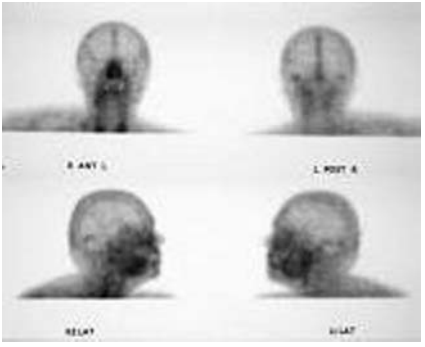

Fig. 1.

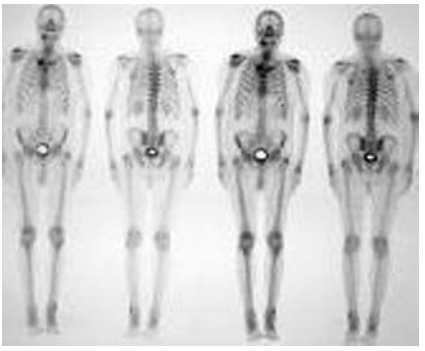

Fig. 2.

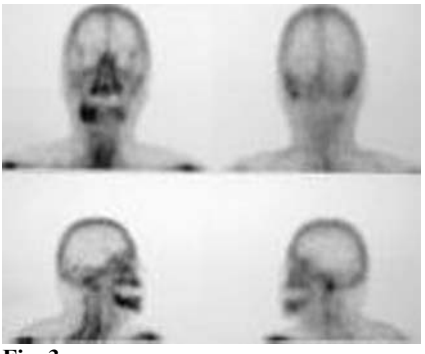

Fig. 3.

Planar Scintigraphies

70 Y old male patient
Infected bisphosphonate necrosis
Fig. 6: Bloodpool Phase (3 min)
Fig. 7 and 8: Mineral Phase (3,5 h)

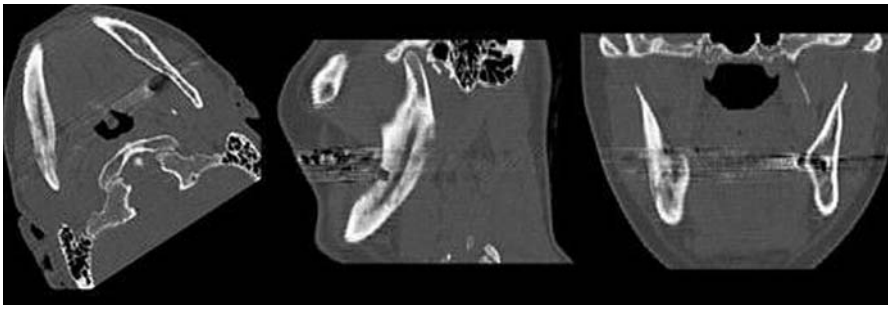

Fig. 4. and 5. SPECT-CT Imaging 3,5 hours after Injection of ^{99m}Tc-DPD.

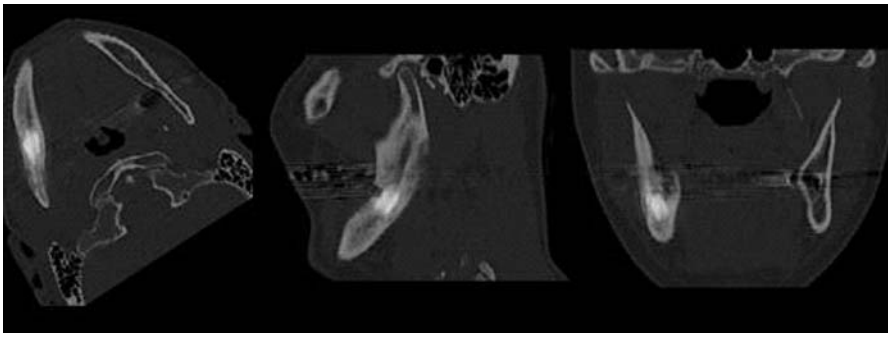

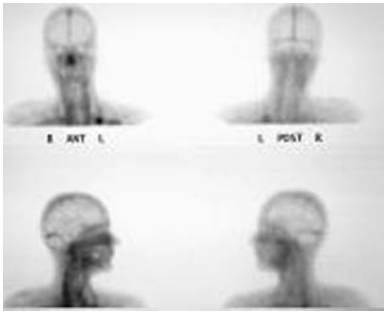

Fig. 6.

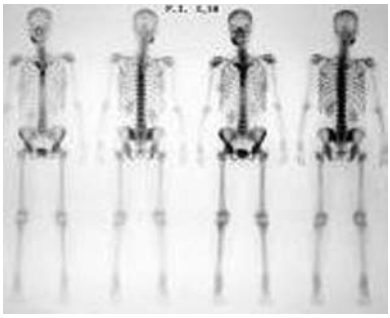

Fig. 7.

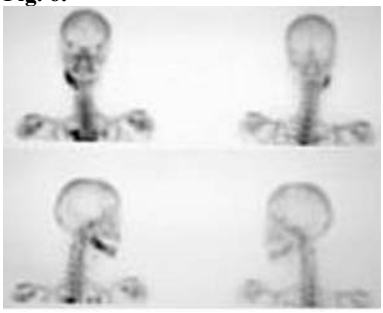

Fig. 8.

Planar Scintigraphies

36 Y old female patient
Osteitis of the Jaw
Fig. 6: Bloodpool Phase
(3 min)
Fig. 7 and 8: Mineral Phase
(3,5 h)

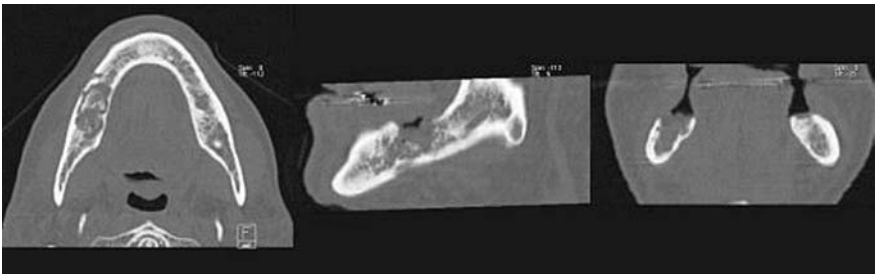

Fig. 9. and 10. SPECT-CT Imaging 3,5 hours after Injection of ^{99m}Tc-DPD.

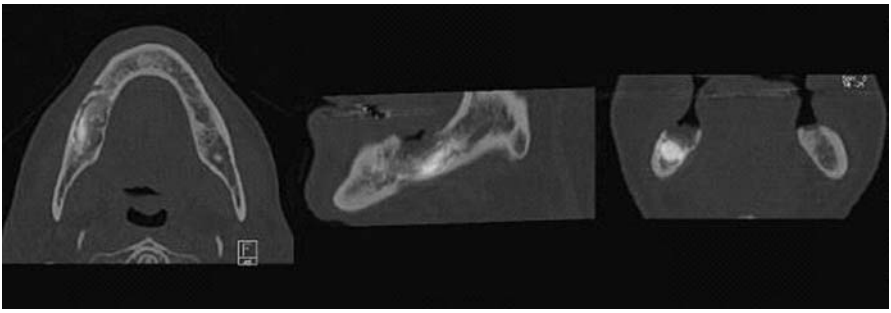

4. Discussion and Conclusion

SPECT/CT images gained and fused by the hybrid machine Symbia T2® relate facial skeletal anatomy and physiology in detail. Especially in the postoperative setting when the bone architecture has changed and causes an unusual pattern of nuclide uptake, the anatomical relations are crucial for an accurate diagnosis. In these situations the hybrid machine is superior to the SPECT camera because SPECT on its own is of limited use in craniofacial surgery due to low spatial resolution and lack of anatomical detail.

Other studies have shown that the fusion of SPECT and CT data, acquired by separate machines is possible but fused images show flaws due to different anatomical positions of the mandible and the fusion is far more time consuming. The precise localisation and extension gained by the hybrid machine will be especially useful for the follow-up diagnosis.

Part II

Medical Image Processing

High Performance 2D/3D-Registration for Patient Positioning in Radiotherapy

Frank Heinze[1], André Kupetz[2] and Jürgen Roßmann[3]

[1] Dortmunder Initiative zur rechnerintegrierten Fertigung (RIF) e.V.
Joseph-von-Frauenhofer-Str. 20, 44227 Dortmund , Germany
E-mail: heinze@rif.fuedo.de
[2] University of Dortmund, 44227 Dortmund, Germany
E-mail: kupetz@rif.fuedo.de
[3] Institute for Man Machine Interaction, RWTH Aachen
Ahornstraße 55, 52074 Aachen, Germany
E-mail: rossmann@mmi.rwth-aachen.de

Abstract. The precise and repeatable positioning of patients is one of the key elements of successful radiation therapy. Our aim is to develop an automated system, which determines the exact position of the patient. We use volume rendering based on 3D-textures to generate a 3D-model of the region of interest from pre-treatment CT-data. The idea is to generate before each treatment session additional x-ray images from orthogonal positions. These x-ray images represent the current position of the patient. With the help of projection images of the 3D-model, so-called digitally reconstructed radiographs (DRRs), we determine the rigid transformation between the 2D-x-ray images and the 3D CT data via an intensity based 2D/3D registration process. This represents the misalignment between the current position and the position in the treatment plan. For our simulation results we used as a first step ray-casting images instead of real x-ray images. Because of the high performance of our approach, we were able to investigate, which optimization methods and which number of orthogonal x-ray tubes give best results.

1. Introduction

Radiotherapy today is based on precise technologies like inverse treatment planning and precise apparatus like linear accelerators. The treatment is usually fractioned into multiple sessions. Thus, the precise and repeatable positioning of patients becomes the key element of successful radiotherapy treatment. Current techniques like the use of a stereo tactic frame pose an immense burden for the patient. But these techniques are necessary to precisely apply a sufficient dose of radiation to the target volume while simultaneously reducing the dose of radiation to healthy tissue [1].

The aim is to develop a system which determines the exact position of the patient in an automated, precise process with a low burden for the patient. The idea is to use the CT-data generated for the treatment planning to reconstruct a three dimensional (3D) model of the region of interest. Before each treatment session the therapist additionally generates x-ray images from orthogonal positions. These images represent the actual patient position. An iterative process determines the misalignment between the position in the planning CT and the

actual position represented by the x-ray images. The result is the difference of the position and orientation of the patient compared to the treatment plan. Other methods often use precalculated DRRs or are optimized for particular anatomical regions. We see our work as an enhancement of the work described in [2].

2. Methods

The explained procedure is divided into two parts: DRR generation and registration process.

DRR Generation. The very fast generation of DRRs is a key feature of a fast registration process and basis for comprehensive test series. We designed the DRR generation with the help of volume rendering based on 3D-textures [3].

The transfer function converts the pre-treatment CT-data, giving dark CT-values a high transparency and vice versa. The result is an abstract 3D point grid with luminance and alpha values. We load the point grid into the GPU memory and transform it rigidly according to the given geometry. Subsequently, we determine the bounding box of the grid and fill it with view aligned slices. These slices will be trilinear textured and alpha blended by the GPU. With the knowledge of the exact positions of the x-ray tubes we generate projection images of the 3D rendered CT-data that represent our digitally reconstructed radiographs (DRRs). We adapt the OpenGL frustum to the known geometry. The far-plane represents our DRR, the eye-point our simulated x-ray tube. Figure 1 shows this procedure.

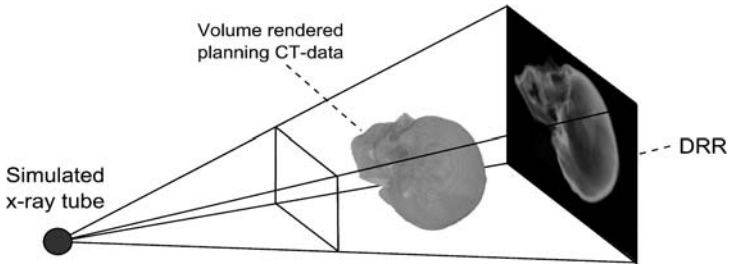

Fig. 1. Generating DRRs from the rendered planning CT-data.

Based on these principles we can generate DRRs from arbitrary positions on current graphic processors within milliseconds. The runtime of alternative approaches like ray-casting are often several orders of magnitude higher for generating DRRs in comparable resolutions.

Registration Process. The principle of the 2D/3D registration process is an iterative optimization process that translates and rotates the volume rendered 3D-model of the CT-data until it finds an optimum between DRRs and x-rays [4]. The rigid transformation that transfers the planning CT-Data into its final position is the difference matrix we are looking for.

The quality of the matching is determined by an intensity based approach. In fact we avoid segmentation in the start-up by using all gray value information in the images. As similarity measures for the image comparison itself we use normalized cross correlation (NCC) and mutual information (MI) [5].

The implemented optimization algorithms [6] can be divided into two categories: direction-set methods and methods, which use the complete search space at once, like Down Hill Simplex. For the direction-set-methods we use Brent's method and a brut force approach. These methods optimize along each degree of freedom successively. Further, we try to improve the optimization direction with the help of Powell's method. Figure 2 shows the basic concept.

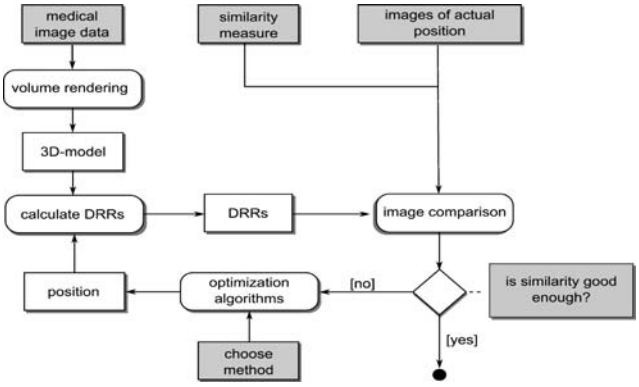

Fig. 2. Structural model of the registration process.

3. Experimental Setup

For our analysis we use a CT-data set of a human skull phantom. It consists of 128 slices with a distance of 2 mm each. Every slice has a resolution of 256 x 256 pixels with a distance of 0.98 mm x 0.98 mm each. The transfer function converts the Hounsfield value of each pixel into an 8 bit luminance and an 8 bit alpha value.

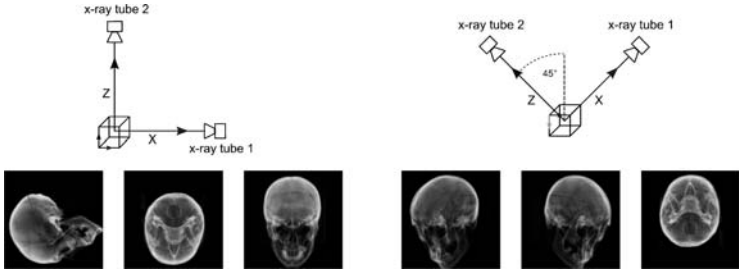

Fig. 3. On the left: 90°-configuration with sagital, axial and coronal DRRs. On the right: 45°-configurration with two DRRs that show a vertical symmetry. To give a better overview the y-axis is omitted.

We consider configurations with one, two or three x-ray tubes. For the optimization process we use either the single similarity measure of an image comparison or we sum up all three image comparisons as "accumulated approach".

Further, we examined how the arrangement of the x-ray tubes influences the registration process. We looked at two different configurations, the 90°-configuration and the 45°-configuration. Figure 3 illustrates these two configurations and shows typical sample DRRs for each configuration.

For our test cases we used 5 randomized defined positions that represent the actual patient position. For each of the 5 positions we use 10 different randomized starting positions of our CT-data, totalling 50 measurements.

We implemented these concepts as a modular and upgradeable framework and integrated it into the simulation environment COSIMIR® [7].

4. Results and Discussion

Performance Analysis. For our analysis we used two standard PC test configurations: one with a GeForce 4 and the other with a GeForce 7 graphics card. On both systems the creation of DRRs takes only milliseconds (170 ms for the GeForce 4 and 12 ms for the GeForce 7 system). Figure 4 subdivides the calculation process into the pure DRR calculation on the graphics card and the transfer of the data into system memory.

Compared to the ray-casting method in [2] our method takes less then 0.1% of the runtime. So we were able to run complete registration processes with up to 2000 DRRs in about 30 sec.

Accuracy Analysis. In the first step we tested the validity of the basic approach by registering images of the exact same modality. This means we generated volume rendered reference images from pre-defined positions. For each position the aim is to determine the six-dimensional rigid transformation matrix. In a second step we used DRRs that were generated by a ray-casting method. In that later case congruent images do not have to be identically, but identical regions might have different gray values. Thus, this second step poses a bigger challenge than the registration against the same modality.

Registration against volume rendered DRRs:
If we use at least two orthogonal x-ray tubes, we are able to determine exactly the rigid transformation matrix in all of our 50 test cases. If we are using only one x-ray tube we gain no satisfying results independent of the used optimization method, like table 1 illustrates. Table 1 shows the median and the standard deviation of the misalignment for each degree of freedom for the linear axis method and NCC as similarity measure. Miss registrations are defined by two different thresholds. Table 1 shows 21 discrepancies that are larger than 1mm for the x-axis from the target value.

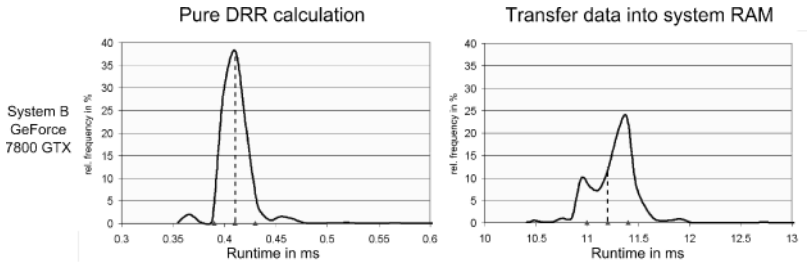

Fig. 4. Runtime analysis for 1000 measurements

Table 1. Registration results for the linear axis method with one x-ray tube and NCC as similarity measure.

Axis	x	y	z	roll	pitch	yaw	Σ
Median in mm/°	1.89	0.16	0.15	0.01	-0.13	-0.18	
Standard deviation in mm/°	3.84	0.12	0.16	0.19	0.14	0.06	
miss registrations ± 1 mm/°	21	0	0	0	0	0	21
miss registrations ± 0.5 mm/°	33	0	0	0	0	0	33

The reason is that a translation directly towards the camera, in our case the x-axis, is characterized by a scaling of the object, which is hardly recognizable for small translations. A second camera orthogonal to the first one can detect this movement as a translation e.g. from left to right. Consequently, two orthogonal cameras can detect all three translational degrees of freedom optimally.

If we compare the results of the 90°-configuration with the 45°-configuration, we recognized difficulties with the roll and yaw degree of freedom in the 45°-configuration. The reason is that the phantom skull DRRs show the described symmetry. Rotations about these axes are hardly detectable.

Registration against ray-casting DRRs:

Based on the former results of registration against volume rendered DRRs we now focus on the most promising methods, that use multiple x-ray tubes in the 90°-configuration. If we compare the different optimization algorithms, Brent's method is our first choice. The registration result for each degree of freedom is more precise than the linear axis method, so we gain a better starting condition for the next degree of freedom. In fact we can reach our target transformation more precisely. Compared to the Down Hill Simplex search strategy Brent's Method is more time-consuming, but shows a better robustness. Down Hill Simplex tends to converge to local optima.

Our results show no significant advantage for three single x-ray tubes versus two single x-ray tubes. However, the result with the smallest error is found by using the "accumulated approach". Although the summation triples the number of DRRs to create, it has the advantage, that it uses all possible given information, so that single outliers are balanced out and the variance in the result is minimized. Combined with Brent's method as optimization strategy we prefer this alternative. Table 2 shows the result for our 50 test cases. We were able to determine the rigid transformation with an accuracy of ±0.4 mm/° for each degree of freedom.

Table 2. Registration results for accumulated Brent's method and NCC as similarity measure.

Axis	x	y	z	roll	pitch	yaw	Σ
Median in mm/°	0.01	0.29	0.30	-0.04	-0.06	0.21	
Standard deviation in mm/°	0.03	0.02	0.05	0.07	0.08	0.10	
miss registrations ± 0.5 mm/°	0	0	0	0	0	0	0

5. Conclusions

We created a framework that allows us to determine the misalignment between the planning CT-data of a human skull phantom and the actual patient position simulated by ray-casting projection images. Our approach to generate volume rendered DRRs within milliseconds gives us the possibility to examine the influence of optimization methods, the number of orthogonal x-ray tubes and the arrangement of the tubes. Our preferred method is able to determine the rigid transformation matrix within 30 sec. with an accuracy of ±0.4 mm/° for each degree of freedom. The next step will be to use real patients x-ray data and analyze more clinical CT-data sets.

References

1 T. Feyerabend and E. Richter: *Grundlagen der Strahlentherapie*, 2.Auflage Springer, 2002.
2 E. Freund, F. Heinze and J. Rossmann: Robotic Simulation System for Precise Positioning in Medical Applications, in *Perspective in Image-Guided Surgery*, p. 270-277, MRNV 2004.
3 C. Rezek-Salma, *Volume Rendering Techniques for General Purpose Graphics Hardware*, Diss. University of Erlangen, 2001.
4 J. Flusser and B. Zitová: Image registration methods: a survey, in *Image and Vision Computing,* Vol. 21, p. 977-1000, 2003.
5 J. P. W. Pluim, A. J. B. Maintz and M. A. Viergever: Mutual information based registration of medical images: a survey, in *IEEE Transactions on Medical Imaging*, Vol. 22, p. 986-1004, 2003.
6 W. H. Press, A. S. Teukolsky, W. T. Vetterling and B. P. Nery, in *Numerical Recipes in C*, 2nd Edition, Cambridge Univ. Press, 1992.
7 E. Freund and J. Rossmann: Projective Virtual Reality: Bridging the gap between Virtual Reality and Robotics, in *IEEE Transactions on Robotics and Automation*, Vol. 15, p. 411-422, 1999.

Modelling Tumour Growth Patterns with Non-Rigid Image Registration

Andreas Mang[1,2], William R. Crum[2], Oscar Camara[2], Julia A. Schnabel[2], Gisele Brasil Caseiras[3], Thorsten M. Buzug[1], Hans R. Jäger[3], Tarek A. Yousry[3] and David J. Hawkes[2]

[1] Institute of Medical Engineering, University of Luebeck, 23538 Luebeck, Germany
E-mail: buzug@imt.uni-luebeck.de
[2] Centre for Medical Image Computing, Department of Medical Physics and Bioengineering, University College London, London WC1E 6BT, UK
E-mail: d.hawkes@ucl.ac.uk
[3] Institute of Neuroradiology, Lysholm Department of Neuroradiology, University College London, London WC1N 3BG, UK
E-mail: pa_yousry@ion.ucl.ac.uk

Abstract. We present a registration-based approach to model growth of glioma tumours seen in serial magnetic resonance imaging. Two state-of-the-art intensity-based non-rigid registration methods are investigated for their ability to compensate for the mass effect of the tumour. Both methods perform well and volume change estimates correlate well with manual delineation. However the complex structural and functional changes in glioma cannot be fully resolved by intensity-based methods due to the profound changes in morphology and appearance associated with glioma progression.

1. Introduction

Glioma is a common brain tumour with heterogeneous presentation and a poor prognosis. The growth of glioma tumours results from two mechanisms—proliferation of tumour cells, and infiltration of cells into surrounding healthy tissue. Multi-modal magnetic resonance imaging (MRI) is commonly used to non-invasively acquire information about the size, location, spread and functional state of the glioma and its surroundings [1][2]. This information is vital for the assessment of disease progression, surgical planning and monitoring the response to surgery or treatments such as chemotherapy and radiotherapy. Multi-modal MRI provides a useful snapshot of the current state of the tumour which aids diagnosis (but is not the diagnostic gold standard) and treatment planning. A potentially more powerful approach for learning about disease progression is to study temporal changes from series of images acquired at intervals of weeks or months. To enable the analysis of such changes, correspondence between features on scans acquired at different times must be found. Voxel-based image registration algorithms provide an automated solution to this correspondence problem.

In this study we are investigating whether well established intensity-based non-rigid image registration approaches can be used to determine correspondence between temporal series of images acquired from patients with glioma. This is a

difficult registration problem because of (i) gross volume change associated with tumour growth or therapeutic intervention; (ii) associated distortion of normal tissue distal to the primary tumour site; and (iii) intensity and textural changes within and in the neighbourhood of the tumour. In particular, local intensity variation of corresponding features, reflecting changes in tumour physiology over time, may adversely affect the performance of automated methods. We propose that consistent features such as the visible extent of the tumour boundary can be regarded as pseudo-correspondences; an accurate mapping between such correspondences will allow us to quantify the spread of the tumour.

The goals of this study are therefore (i) to assess the ability of established non-rigid registration methods to estimate local tumour volume change; and (ii) to compare automated volume change estimation with the clinical standard.

2. Experimental Methods

Longitudinal studies of different magnetic resonance (MR) images were acquired at 6 month intervals over a period of 2-5 years [3]. Patients who initially had a low grade glioma (WHO grade II) that progressed to a high-grade tumour (WHO grade III and IV) were imaged, not undergoing any treatment until the glioma tumours transformed from low- to high-grade. The imaging protocol includes conventional T1-weighted MRI (with and without contrast enhancement), T2-weighted MRI, and fluid attenuated inversion recovery (FLAIR) (Fig. 1). In the present study two patients have been included: patient 1, with five time points acquired over 30 months, patient 2, with two time points acquired over 24 months.

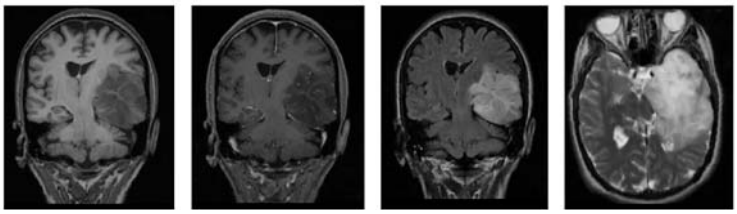

Fig. 1. Different imaging modalities for a patient diagnosed with a glioma tumour. From left to right, T1-weighted, T1-enhanced, FLAIR and T2-weighted MR image.

First a global aligment of all images to the baseline scan is performed via an established 9 degree of freedom (DOF) affine registration algorithm using normalized mutual information (NMI) as a voxel similarity measure [4]. This is motivated by the fact that NMI is known to be robust to large changes in intensity and texture and that 9 DOF are sufficient to compensate for gross differences in patient positioning and variations in voxel size due to scanner drifts. To model localized changes of tumour size and shape over time, non-rigid registration is required. Two independent and established methods were employed; a fluid registration [5] and a free-form deformation (FFD) method using B-splines [6]. Non-rigid registration is performed for the T1 structural volumes, since these images provide more consistent information about tumour morphology and are high resolution. For both non-rigid registration methods, a standard parameter

setup is used, including a multi-resolution scheme and NMI as a similarity measure. After non-rigid registration, volume change ΔV can be derived from the resulting deformation field by integrating the determinant of the Jacobian matrix $J(\mathbf{x})$ (Equation 1) over the the tumour. $|J(\mathbf{x})| < 1 / =1 / >1$ implies volume decrease / preservation / increase.

$$\det(J(\mathbf{x})) = \begin{vmatrix} \frac{\partial T_x(\mathbf{x})}{\partial x} & \frac{\partial T_x(\mathbf{x})}{\partial y} & \frac{\partial T_x(\mathbf{x})}{\partial z} \\ \frac{\partial T_y(\mathbf{x})}{\partial x} & \frac{\partial T_y(\mathbf{x})}{\partial y} & \frac{\partial T_y(\mathbf{x})}{\partial z} \\ \frac{\partial T_z(\mathbf{x})}{\partial x} & \frac{\partial T_z(\mathbf{x})}{\partial y} & \frac{\partial T_z(\mathbf{x})}{\partial z} \end{vmatrix} \quad (1)$$

Tumour outlines were also manually obtained by expert clinical observers from the T2-weighted/FLAIR images, (large enhancement of tumours and related features even for low-grade tumours). This is a challenging task, giving rise to large measurement variability [7]. For comparison with the registration results, these clinical outlines are transformed to the T1 images using shape-based interpolation to account for large differences in voxel size between FLAIR and T1-weighted images. The registration-based estimation of volume change ΔV between subsequent time points t_i is compared to that provided by the manual segmentation.

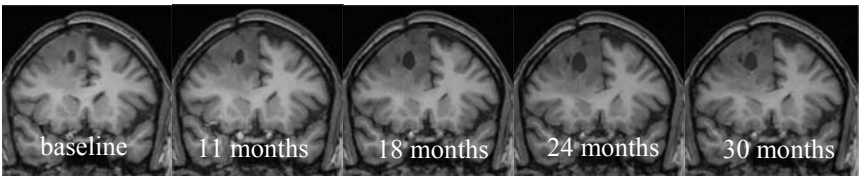

Fig. 2. T1 time series of a patient diagnosed with a glioma tumour. From the clinical course it is known that malignancy transformation was observed in the 4th image from left. Treatment (chemotherapy and radiotherapy) took then place so that the tumour decreases in size between the 4th and the 5th successive scans.

3. Results and Discussion

Careful visual inspection after affine registration suggests that images are well aligned. Fig. 2 shows the time-series of the T1 modalities of a patient diagnosed with a glioma tumour. Scanner-induced linear distortions were found to be small (scalings ~ [0.99, 1.01]). For the non-rigid registration we found that both algorithms are equally able to compensate for the coarse mass effect of the tumour. Qualitatively, the best results were obtained for patient 2 (Fig. 3). The

deformation within the ventricles has been recovered and the borders of the tumour are well aligned (red arrows in Fig. 3). Within the tumour, however, textural information differs considerably with respect to the baseline image. In contrast to that, deformations in areas not affected by the tumour are well recovered by the employed algorithms (white arrows in Fig. 3).

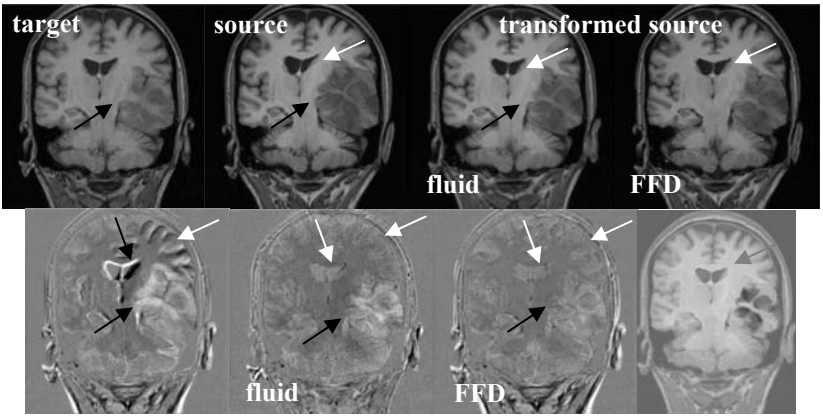

Fig. 3. Non-rigid registration results between two time-points for patient 2. Images on the top row with corresponding subtraction images on the bottom row. The rightmost image maps the Jacobian operator computed from the deformation field of the fluid registration, where black indicates large growth and gray indicates local shrinkage (ventricles, blue arrow).

For patient 1, large variances in glioma texture between successive scans can be seen (white arrows in Fig. 4) presenting a severe challenge for intensity based non-rigid registration algorithms. First visual inspection suggests that both algorithms provide quite similar results (Fig. 5) and recovered gross structural displacements but were not able to cope with significant changes within the glioma such as the appearance of cysts.

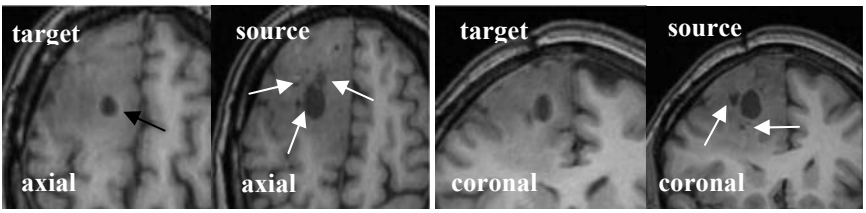

Fig. 4. Large differences in texture and structure in patient 1. Especially in the area around the cyst (black arrow) structures are visible that have no corresponding anatomical feature in the former image (white arrows).

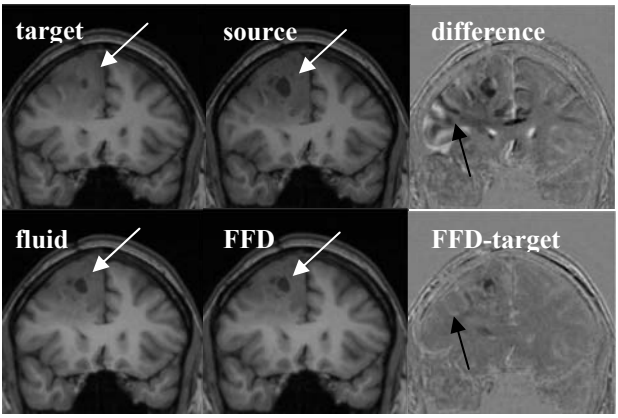

Fig. 5. Registration results for patient 1. Top row: before non-rigid registration. Bottom row: non-rigid registration results. White arrows show inconsistent features. The red arrow shows where the registration has compensated for the deformation due to tumour growth.

Even though that there are textural differences that the registration cannot pick up, both algorithms provide quite similar estimations of volume change (Fig. 6).

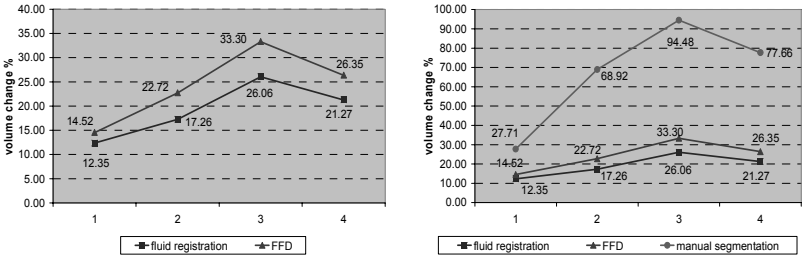

Fig. 6. Volume change estimation in patient 1. Left: by integrating the Jacobian determinant within the tumour using the registration results. Right: comparison of manual and registration volume changes.

The discrepancy between manual and registration volume change estimation seems large. However, the manual segmentation has been performed on FLAIR volumes which include features not visible in the T1 volumes, in particular signs of infiltration into surrounding tissue and oedema. Therefore, manual delineation on the FLAIR volume may overestimate the real volume of the tumour [8], compared with the apparent volume in T1 images. There remains a striking correlation between the time-course of the automatic estimations of volume change with those measured manually.

4. Conclusions

In this paper we have shown that state-of-the-art non-rigid image registration methods are to some extent able to compensate for the overall bulk effect of glioma tumour growth. However, problems due to ill-defined correspondence in textural information remain. The most obvious potential solution is to include both functional and structural information in the registration, an approach we are actively pursuing. The other obvious strategy is to inject anatomical knowledge by including feature, or shape information. This could be addressed by employing hybrid registration methods with an anatomical prior, which we are also investigating.

Acknowledgements. We acknowledge the support of the DAAD (German Academic Exchange Service) (AM), the EPSRC GR/N14248/01 and the UK Medical Research Council Grant No. D2025/31 (MIAS-IRC) (WRC), the EPSRC GR/S48844/01 (Modelling, Understanding and Predicting Structural Brain Change) (OC) and the EPSRC GR/S82503/01 (Integrated Brain Image Modelling) (JAS). We additionally want to thank Dr. J Rees (Neuro-Oncologist at the ION and Dr. J. Thornton (physicist at the ION).

References

1 E. Galanis et al., in *Neuro-Oncology*, Vol. 8, 2, 2006.
2 G. D. Shah, et al., in *Neuro-Oncology*, Vol. 8, 1, 2006.
3 H.R. Jäger, et al. in *Am J Neuroradiol*, Vol. 26, 2005.
4 C. Studholme, D. L. G. Hill and D. J. Hawkes, in *Medical Physics*, Vol. 24, 25, 1997.
5 W. R. Crum, C. Tanner and D. J. Hawkes, in *Physics in Medicine and Biology*, Vol. 50, 21, 2005.
6 D. Rueckert, L. I. Sonoda, C. Hayes, D. L. G. Hill, M. O. Leach and D. J. Hawkes, *IEEE Transactions on Medical Imaging*, Vol. 18, 8, 1999.
7 G. P. Mazzara, et al., *IEEE Transactions on Medical Imaging*, Vol. 18, 8, 1999.
8 Y. Cao and V. Nagesh and D. Hamstra et al., in *Cancer Research*, 66, 17, 2006.

Segmentation and Navigation Support of Clinical Data Sets to Simulate the Bronchoscopy and Rhinoscopy

Christian Dold[1,4], Ulrich Bockolt[1], Marcus Roth[1], Claus Peter Heussel[2], Jan Gosepath[3] and Georgios Sakas[1]

[1] Fraunhofer Institut für Graphische Datenverarbeitung (IGD), Cognitive Computing and Medical Imaging, Fraunhoferstr.5, D- 64283 Darmstadt
E-mail: Christian.Dold@igd.fraunhofer.de
[2] Thoraxklinik-Heidelberg gGmbH, Diagnostische und Interventionelle Radiologie, Amalienstraße 5, D-69126 Heidelberg
[3] Universität Mainz, HNO-Klinik, Langenbeckstraße 1, D- 55101 Mainz
[4] TU Graz, ComputerGraphik & WissensVisualisierung, Inffeldgasse 16c, A-8010 Graz

Abstract. A training and simulation system for therapy planning is developed based on patient specific imaging data. A real endoscope is used for navigation through the virtual patient. For this purpose sensors were built in the endoscope in order to track the translation, rotation and the angle of the distal end. Pre-processing (segmentation, tissue characterization) speeds-up the volume rendering up to real-time. Collision detection enables a realistic fly through the virtual patient.

1. Introduction

Endoscopic interventions are associated with a high risk of complication due to their invasive character and the limited field of view in poor orientation, especially for non-expert users. A main problem of all endoscopically interventions is that they are performed by the surgeon without direct sight control, that means quasi „blind“, as the interesting changes may lie either outside of the endoscopically visible antrum system or behind a narrowing, a bifurcation, pathology or behind the bronchial wall etc. Safer working can be assisted and improved by intensive training on the basis of individual patient data. In the context of the project VIVERA [1, 2, 3] corresponding simulators as operation-planning / training system are developed and tested for the domains rhinoscopy and bronchoscopy. Here we summarize mainly the results of the segmentation and the navigation.

2. Methods

The simulator is applying diagnostic imaging data (Multislice CT, MRI) and integrates simulation technologies as well as haptic interaction technologies. By using individual patient data, the anatomy and pathology of a present patient is

employed for preoperative individualized training. The individual image data of the patient are used to present the antrum system (bronchial tree, paranasal sinuses etc.) and further optional anatomic components (vessels, lymph system). These 3D data sets are then visualized in real-time when simulating the intervention by „Volume Rendering“ (Fig. 1).

Recording and Reconstruction of Data Sets. The majority of the used data were acquired with a four slice CT and a resolution of 0.57mm x 0.57mm x 1.25mm. The MRI data were acquired by 1.5 Tesla and highly resolving gradient sequences. Image artifacts through metals greatly disturb the segmentation result. It is advisable to choose a „flat reconstruction kernel“ at the location of such artifacts in order to be able to segment the data with reasonable effort.

Processing of Data Sets. Imaging preprocessing can be selected among a Mean, Median, Curvature Flow [4] or an Anisotropic Diffusion Filter [5]. In our experience edge preserving filters perform superior and minimize the distortions on the volume.

Isotropic voxels were generated by trilinear interpolation or a bispline algorithm [6] followed by a normalization (linear operation), which spread up the distribution of grey values to the totally available word length (16Bit).

Visualization of Data. Our rendering technique is based on direct volume rendering via 3D textures [7]. The latter are directly supported by graphics hardware and can be seen as a regular grid holding the scalar data. For visualizing this data, which usually is also pre-classified by applying a transfer function, an illumination model simulating the interaction with light is employed.

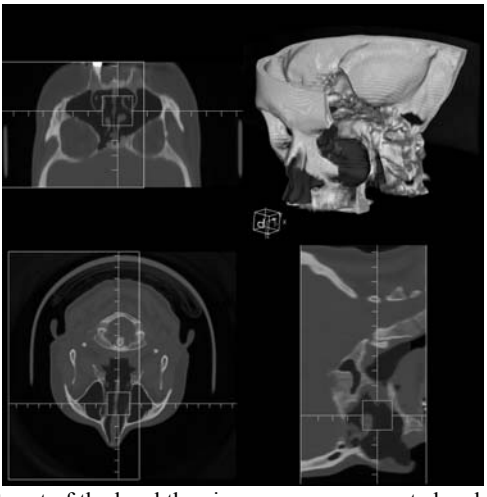

Fig. 1. At the CT data set of the head the airways were segmented and shown as red region. In the 3D-view (top right) the bony structures are emphasized and superposed with the segmentation result of the airways (red).

Especially in medical applications the data set contains semi-transparent material like tissue, fluids, mucus or other participating media, for which effects like absorption, attenuation and scattering have also to be taken into account. Rendering itself is generally done by slicing the texture block in back-to-front order with a set of view-aligned planes, which also has the advantage that alpha blending can be exploited for doing the (discrete) integration.

Modern graphics hardware, namely the GPU, is more and more replacing the fixed function rendering pipeline by means of vertex and fragment processing units. They operate on parallel streams of vertex and fragment data which can be transformed and lighted in a user-defined way with the help of shader routines. Therefore even quite complex algorithms can be implemented directly on the GPU. For platform independence we use the OpenGL Shading Language (GLSL), which is based on C and part of the core OpenGL specification since version 2.0 [8]. In the fragment shader first the scalar value and the corresponding normal are fetched and then the volumetric lighting calculations are performed as described in [7].

As a visual improvement the alpha value is modulated in our implementation with the slice distance for simulating depth queuing and attenuation effects. A label file is used for masking out areas that are out of interest in order to getting rid of bothering artefacts and to ensure a well distinguishable surface, which is quite essential for an interactive exploration of the segmented data set. The masking is also utilized for speed-up by discarding such fragments before doing complex calculations.

Segmentation Procedure. Obviously it is desired to have completely automatic segmentation procedures. This however is contradictory to achieving the best possible result during segmentation. Our experience with segmentation of the bronchial tree showed that even smallest movement artifacts and „partial volume effects“ can prevent a segmentation beyond the 5th bifurcation of the lung.

Therefore we used another approach for segmentation on which the user may select among various available methods and fine-tune the parameters of the segmentation pipeline interactively, based on the image quality. The procedures we used are based on Region Growing like Confidence Connected [9], Hojjatoleslami and Kittler [10] and Isolated Connected [9] to achieve reliable results. The algorithm of [10] was extended to 3D i.e. from slices to volumes. Furthermore we achieved very good segmentation results by employing adaptive thresholding in combination with the Hybrid Fuzzy Algorithm [11, 12].

Collision Detection for Navigation Support. The collision detection was implemented in order to navigate through the bronchial tubes like in real endoscopy. Thereby it is important to teach the learner how to navigate through the bronchus without hitting the bronchial walls and train him to recognize whether he can further navigate in the bronchial tubes without injuring the bronchus. For this purpose a point shell-based algorithm was implemented. Further on the endoscope tip has been modeled as an ellipsoid with a scalable size. This form is often chosen in order to navigate through „small passes“. The forces are determined by means of a distance function, depending on the diameter of bronchial access as well as the size and position of the endoscope tip, for the x, y, z axes and rotation/tilting of the tip (Fig. 2).

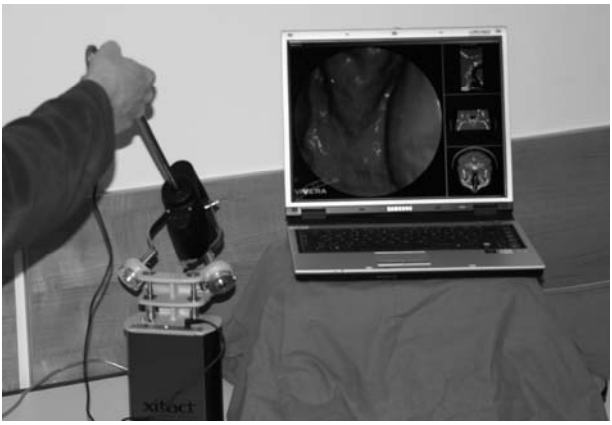

Fig. 2. When flying through the nose, the actual position in the 3 body axes is shown on the CT image in order to receive a better view in „blind“ regions and thus support the surgeon.

If a collision takes place, the real patient often reacts with tickle in his throat. This is simulated by jitter the virtual 3D image accordingly in order to receive a realistic impression. In case the bronchus is large enough, the endoscope slides after a collision along the bronchial wall. If the diameter is small, a further movement of the endoscope is prevented. So the user navigates within the phantom, or even the real patient data, with a real endoscope by performing the appropriate movements on the endoscope handle like in the real life as a surgeon (see Fig. 3).

Fig. 3. The user holds a real endoscope in his hand in order to „fly“ virtually through the original CT data. The position and orientation of the endoscope are tracked via potentiometer and used to render a 3D image during movement, thus generating a realistic impression. The prototype is ideal for learning purposes in order to find possible pathologies employing individual patient data. Exercising of taking a biopsy at critical locations or reaching tumors difficult to access can also be practiced by the specialist before operation.

4. Results and Discussion

The pre-processing and segmentation after reading in the data sets in DICOM format usually takes about 10 min. Bronchial trees up to the 5th, sometimes also down to the 7th bifurcation can usually be segmented from pathological data sets. Important difficulties requiring significant manual adjustment are caused by the presence of fluid, mucus or by movement artifacts. The current system already enables the simulation of endoscopy with clinical data sets. In addition to real endoscopy, the surgeon / learner can see regions which are invisible with a real endoscopy, i.e. behind a bronchial narrowing / wall or a pathologic occlusion.

It is also possible to set markers during "flying through" the airways. In case that a conspicuous region is visited, the actual position can be marked by pressing a key. Later on this region can be directly and autonomously re-loaded, by pressing this key again.

We discovered that a simultaneous display of the axial, sagital and coronal tomography slices at the location of the endoscope tip provides a very good aid for orientation (Fig. 4.). An even greater advantage is the possibility to look through and behind the bronchial wall in order to localize and / or avoid obscured structures such as lymph nodes, vessels or tumors. By means of virtual bronchoscopy and the facilitate navigation it will be possible to straightforward locate tumors or lymph nodes lying outside of the trachea lumen without injuring risk structures such as blood vessels.

Every possible complication and all kind of diseases should be simulated and shown during education to be prepared for the real surgery. When examining the bronchial tubes, the visual impression is mostly in the foreground. A biopsy probe at the corresponding location has to be done, if a lesion suspected in the lung. Knowing the individual physiology by taking these probes is very important to make a decision, if a biopsy probe is possible without injury risk. Such a risk is high in the upper bronchial tree, i.e. in areas close to large vessels or the heart. Displaying the hidden anatomy of the patient helps to become more familiar with the individual patient anatomy and to figure out the best solution.

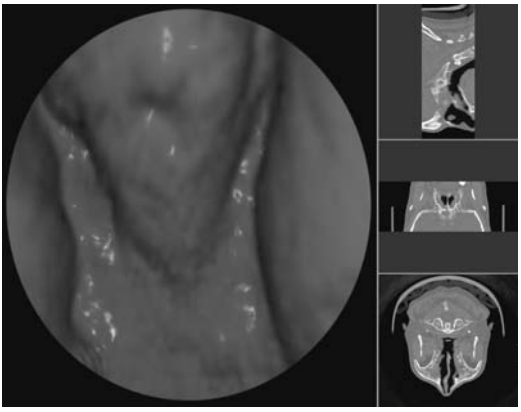

Fig. 4. The graphical user interface of the rhinoscopy simulator.

The resistance when moving the endoscope within the airways (bronchoscopy & rhinoscopy) is generally quite small and the existing mucus further reduces the friction forces. Therefore a haptic force feedback in such applications is in the general case not urgently necessary according to statements of the specialists. Nevertheless, we included haptic force feedback in our system in order to expand the application domain also to coloncospy and complex bronchoscopy procedures. In the near future such system will enable new standards for planning, medical education and quality assurance of endoscopic interventions.

Acknowledgment. The work has been supported by BMBF within the ViVera project. We cordially thank Mr. Barten (Schölly Fiberoptik GmbH) and his team for providing endoscopic hardware and technical assistance.

References

1 C. Dold, U. Bockolt, G. Sakas, M. Roth. Virtuelle Analyse und Simulation im Bereich der Bronchoskopie und Rhinoskopie mit echten Patientendaten. In: 9. IFF-Wissenschaftstage 2006. (2006), pp. 163-170.
2 G. Sakas, S. Stüring. Anwendungen der Virtuellen und erweiterten Realität in der Medizin. In: Schulze, T., Schlechtweg, S.; Hinz, V. (Hrsg.): Simulation und Visualisierung 2005. Erlangen/San Diego: SCS Publishing House (2005), ISBN 3-936150-40-0, S.383-392.
3 M. Schenk, E. Blümel, M. Schumann. ViVERA – Virtuelles Kompetenznetzwerk zur virtuellen und erweiterten Realität. In: Schulze, T., Schlechtweg, S.; Hinz, V. (Hrsg.): Simulation und Visualisierung 2005. Erlangen/San Diego: SCS Publishing House (2005), ISBN 3-936150-40-0, S.377-381.
4 J.A. Sethian et. al. Level Set Methods and Fast Marching Methods. In: Cambridge Press, Chapter 16 (1999), Second edition.
5 P. Perona and J. Maik. Scale-space and edge detection using anisotropic diffusion. In: IEEE Transactions on Pattern Analysis Machine Intelligence, volume 17 (1990), pp. 586–595.
6 M. Unser. Splines: A Perfect Fit for Signal and Image Processing. In: IEEE Signal Processing Magazine, volume 16 no. 6 (1999), pp. 22-38.
7 M. Ikits et al. Volume Rendering Techniques. In: GPU Gems. Addison-Wesley (2004), pp. 667 – 692.
8 J. Kessenich, D. Baldwin, R. Rost. The OpenGL Shading Language. In: OpenGL documentation (2006), pp 1- 93.
9 L. Ibanez, W. Schroeder, L. Ng, J. Cates and the Insight Software Consortium. The ITK Software Guide. URL http://www.itk.org/ItkSoftwareGuide.pdf, 2005.
10 S. A. Hojjatoleslami and J. Kittler. RegionGrowing: A New Approach. In: IEEE Transactions On Image Processing, volume 7 (1998), pp. 1079–1084.
11 A. Rosenfeld, “The fuzzy geometry of image subsets”, In: Pattern Recognition Letters 2 (1991), pp. 311-317.
12 J. Udupa and S. Samarasekara. Fuzzy Connectedness and Object Definition: Theory, Algorithms, and Applications in Image Segmentation. In: Graphical Models and Image Processing, volume 58, no.3 (1996), pp. 246-261.

Analysis of Body Surfaces in a Body-Fixed Coordinate System

Burkhard Drerup[1] and Stefan Kraneburg[2]

[1] Universitätsklinikum Münster, Klinik und Poliklinik für Technische Orthopädie und Rehabilitation, Robert-Koch-Str. 30, 48149 Münster, Germany
E-mail: drerup@uni-muenster.de.
[2] Kraneburg Productions, Am Helmerbach 12, 48308 Senden, www.kraneburg.de.

Abstract. Visualisation of shape and shape change e.g. by contour lines depends on the selection of the coordinate system of the contour levels. This is elucidated by using the plaster cast of a scoliotic back being rotated in front of a 3-D measurement and analysis system. Axial rotation through an axis parallel to the contour planes results in a dramatic change of the contour patterns on the back. This is in contrast to the expectation of the ingenuous viewer interpreting the contour line pattern like a fingerprint. To meet this attitude shape analysis must be referenced to a body fixed coordinate system, which may be defined by anatomical landmarks. It is shown, that vertebra prominens and the lumbar dimples provide anatomical landmarks capable for this purpose.

1. Introduction

A stereophotogrammetric measurement of the body surface typically provides measurement data in terms of 3-D coordinates of surface points. The medical interpretation of the data requires a presentation which is reliable and easy to understand. In particular it is necessary to be able to carry out an analysis and a comparison of a series of measurements of the same patient, whether they have been taken on the same day in the course of functional examinations or on several days as a follow-up. It is obvious, to use contours of elevation for this purpose [1]. Contour lines have proved to be perfectly suitable for this purpose in the domain of geographic range modelling.

The aim of this presentation is to point out a fundamental difference to the display of body surfaces. While the reference system in geographic representations is always given and well defined (i. e. by the vector of gravity and the north-south direction) there is no such a predefined coordinate system in medical representations. This is especially the case if the analysed body is not symmetrical. Here, one possible solution will be discussed, namely the construction of a body-fixed coordinate system by using anatomical landmarks and referencing the surface data to this system. This can be illustrated by the example of the plaster cast made of the back of a patient suffering from a scoliotic deformity of the spine. A scoliotic back generally features an obvious asymmetry and the diagnosis of this condition heavily depends on the assessment of the asymmetry.

2. Material and Methods

Anatomical landmarks in the domain of body shape measurement are defined as peculiarly shaped surface regions with a clear connection to the underlying skeletal structures. As the shape generally reflects the underlying structures the localisation of anatomical landmarks is usually not affected by displacements of the skin. Examples of anatomical landmarks are the elevation of the vertebra prominens in the region of the neck and the lumbar dimples indivating the posterior superior iliac spines. Due to their peculiar shape, anatomical landmarks can be mathematically localized on the surface by using established methods of differential geometry [2]. For reasons of simplicity, the anatomical landmarks have been localized in the following by markers attached to the plaster cast. All in all, 3 markers have been attached to indicate the vertebra prominens as well as the left and right lumbar dimple. Three further markers were used for mere checking purposes.

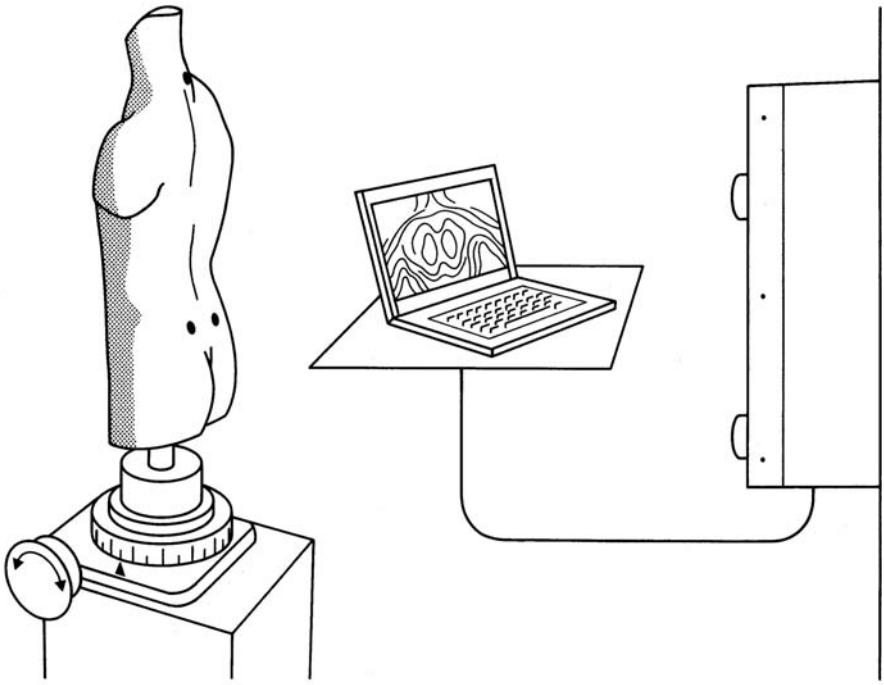

Fig. 1. Arrangement of rotatable plaster cast in front of the 3-D measurement system. To the plaster cast markers indicating the anatomical landmarks of vertebra prominens and left and right lumbar dimple are attached.

For the recording of the plaster cast, the MiniRot Kombi measurement system of ABW GmbH (Frickenhausen, Germany) was used. The plaster cast was positioned in front of the system at a distance of about 1 m and it was suspended in a way to allow controlled axial rotation. Figure 1. All in all, 6 records were taken, after each record the rotation was changed by 3°.

The automated evaluation provides 3-D coordinates of surface points and in addition the coordinates of the mar-ked landmarks. The surface points are distributed over the whole surface and amount to about 225.000 co-ordinate triples. All coordi-nates refer to the reference system of the measurement system (Fig. 2).

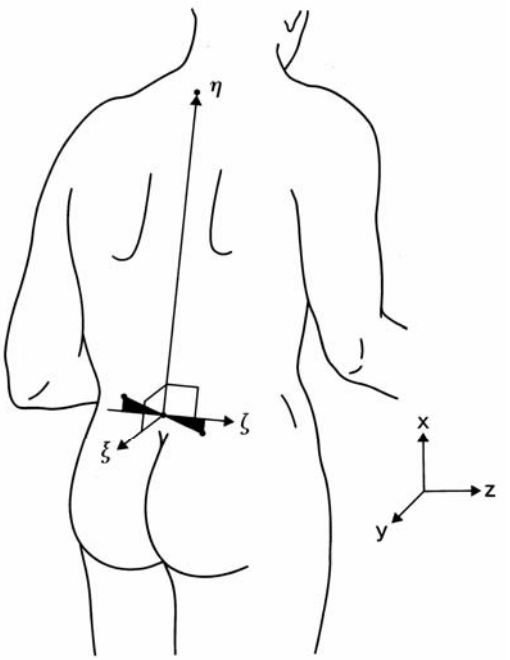

Fig. 2. Coordinate systems of the measurement system (latin letters) and of the body (greek letters).

The coordi-nates of the 3 landmarks are used to generate a body-fixed coordinate system into which all surface data are to be transformed. The centre point between the lumbar dimples is taken as the origin of the body-fixed coordinate system. The connection to the vertebra prominens land-mark provides the longit-udinal axis (η-axis). The ξ-axis is perpendicular to the η-axis and to the connecting line between the dimples. Then finally, the ζ-axis is perpendicular to the sagittal plane, which is spanned by the η-axis and ξ-axis.

3. Results

The 3-dimensional reconstruction of the surface is displayed by the system software as a countour map in two different rotational orientations differing by 3°. The software provides the contour maps in the coordinate system of the measurement system (Fig. 3). Using our own software, the contour lines in Figure 4 refer to the coordinate system defined by anatomical landmarks. In contrast to Fig. 3 any effects caused by rotation and the scoliotic back asymmetry are kept apart in Fig. 4.

4. Discussion

The results clearly show that the contour maps in the laboratory-fixed measurement system depend on the position and the orientation to the measurement system. This is of particular importance if the contour map is used for the assessment of asymmetries.

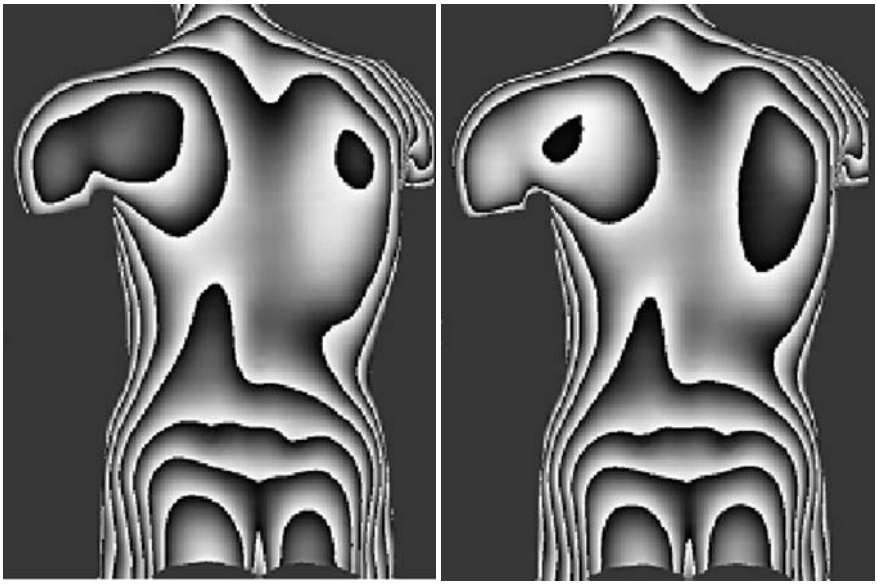

Fig. 3. Contour lines of a scoliotic back (plaster cast) in the laboratory fixed reference system (original plot). The two positions differ by a rotation through 3° with a dramatic effect on the contour pattern.

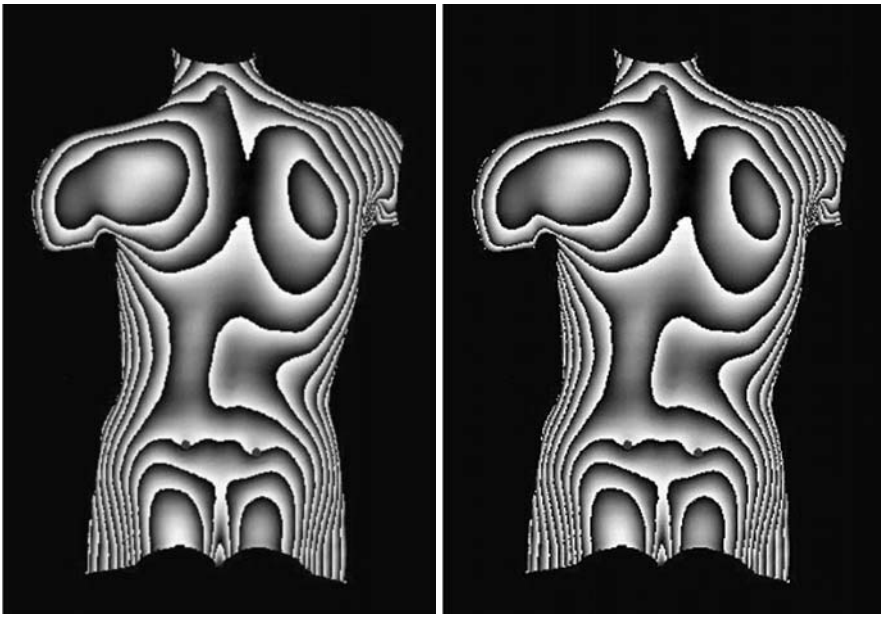

Fig. 4. Own calculation of contour lines of a scoliotic back in a body fixed reference system The two positions differ by a rotation through 3°. The anatomical landmarks (indicated by dots) are used as refence points – the contour patterns are body-fixed.

Nevertheless, different attempts have been made to utilize contour maps – such as the moire-topographic contours – for the assessment of back asymmetries and the diagnosis of scoliotic deformities without radiation exposure. To avoid artifacts by a misaligned positioning pelvic pads are utilized for positioning and fixing the patient during recording [1]. However, in this case a contact-free measurement is no longer carried out. One alternative is the representation of the data in a body-fixed coordinate system. The coordinate system can be defined by attached markers – implementing all sources of errors due to subjective attachment and skin movements. A better alternative is the automatic localization of anatomical landmarks analyzing the back shape in an invariant representation [3]. The localization of anatomical landmarks is achieved with a typical precision of ±2 mm [4].

The concept of referring a body-fixed coordinate system to anatomical landmarks can be applied to other body parts as well. In the case of lower limb measurements [5] in the foot region possible reference points for a body fixed coordinate system are the landmarks provided by the outer and inner malleola. In the knee region these are the condyles of the tibia and the fibula.

References

1 B. Drerup, Anwendungen der Moire-Topografie zur Diagnose und Dokumentation von Fehlbildungen des Rumpfes, Z. Orthop. **116**, 789, 1978.
2 B. Drerup, and E. Hierholzer, Objective Determination of anatomical landmarks on the body surface: Measurement of the vertebra prominens from surface curvature, J. Biomech. **18**, 467, 1985.
3 W. Frobin, and E. Hierholzer, Analysis of human back shape using surface curvatures, J. Biomech. **15**, 379, 1982.
4 E. Hierholzer, Valuation of body surface measurements: accuracy rating of anatomical landmarks, in *Research into spinal deformitie*s, Edited by IAF Stokes ED. IOS Press, Vol. 2, 25, 1999.
5 X. Liu, W. Kim, and B. Drerup, 3D characterization and localization of anatomical landmarks of the foot by FastSCAN, Real Time Imaging **10**, 217, 2004.

Deconvolution of Medical Ultrasound Data with Consideration of the Pressure Field, the Excitation Pulse and Focussing

Holger J. Hewener and Robert Lemor

Fraunhofer Institut für Biomedizinische Technik,
Ensheimer Strasse 48 D-66386 Sankt Ingbert
E-Mail: holger.hewener@ibmt.fraunhofer.de

Abstract. Medical ultrasound data suffers from blur caused by the volume expansion of the pressure field of the mechanical wave. This blur is dependent on the used excitation signal and focussing of the ultrasonic wave and can therefore be examined and manipulated to compute a set of better parameters for deconvolution on the data in order to improve overall system resolution. Looking at the ultrasound transfer function we can focus on the examination of the "point spread function" and ways to influence its size especially in the lateral and elevational direction. Furthermore the combination of several measurements from different directions is analyzed to compensate the worse elevational resolution with the lateral resolution of measurements from other directions.

1. Introduction

The use of ultrasound imaging for medical diagnosis and monitoring suffers from blur and the lack of details so that the user can have problems to identify and distinguish between objects. During an investigation the user can miss small structures that don't have hard boundaries and are blurred caused by the imaging properties of the ultrasound imaging modality.

Tumors and metastases are examples for such structures to identify and they have to be separated from the surroundings but are difficult to see in an image because they often look like scatters.

2. Resolution in Ultrasound Data

The resolution of ultrasonic data can be defined in several ways. On the one hand it can be defined as the minimum distance between objects that still can be distinguished and on the other hand the resolution is defined as the reciprocal of the image size of a point reflector. For the imaging and the measurements we take point reflectors or very small parallel wires with good acoustic properties.

The resolution depends on the used frequency of the mechanical wave and increases with higher frequencies in the axial direction because the length of the used ultrasound excitation pulse is defining the axial resolution. The width of the pressure field shows the resolution capabilities in the lateral and elevational

direction and gets smaller with higher frequencies and gives therefore a better lateral and elevational resolution.

In the beginning of medical ultrasound the data sets had a typical resolutions range from 4 to 6 millimeters [1] that was increased with the help of deconvolution techniques by the factor two [2]. The typical medical ultrasound device today has a better resolution so that objects can be distinguished that lie 1 millimeter or closer together. This results in a more detailed image that still can be improved with some knowledge about the details of the imaging modality.

3. Ultrasound Transfer Function and Point Spread Function

The cause for the blurry ultrasound imaging of in reality sharp structures like tissue boundaries can be explained by looking at the transfer function [3,4] of ultrasound systems.

$$p(p_{trans}, t) = ex(t) *_t f(p_{field}) *_s h(p_{trans}, p_{field}, t)$$

This function describes the imaging procedure as a convolution of the electrical excitation pulse *ex* with the impulse response *h* of the ultrasound transducer and the impulse response *f* of the target structures in a temporal and spatial way.

As one can see directly the transfer function is dependent on the impulse response of the transducer that itself is dependent on the position under the transducer inside the underlying pressure field because the pressure amplitude of the mechanical wave can be unique for different positions. This resulting pressure intensity field is a three-dimensional function that affects the „point spread function“ (PSF). This PSF is the image of a single point object and describes the impulse response of the ultrasound pulse in 3D and can be calculated looking at the pressure field.

In the transfer function the point spread function *h* is folded with the function representing the real objects *f*. Caused by the three-dimensional nature of the PSF the resulting data is also blurred in all three dimensions (axial, lateral and elevational). The degree of the width of the PSF is a measure for the quality of the ultrasound system for imaging.

To reduce the signal deterioration caused by this blurring we can use our knowledge of some properties of the transfer function for deconvolution. To quantify these properties we can measure on the one hand the impulse response using a steel reflector and a known excitation pulse or we can simulate it. This knowledge is important for the improvement of the analysis of the measured data in the axial direction.

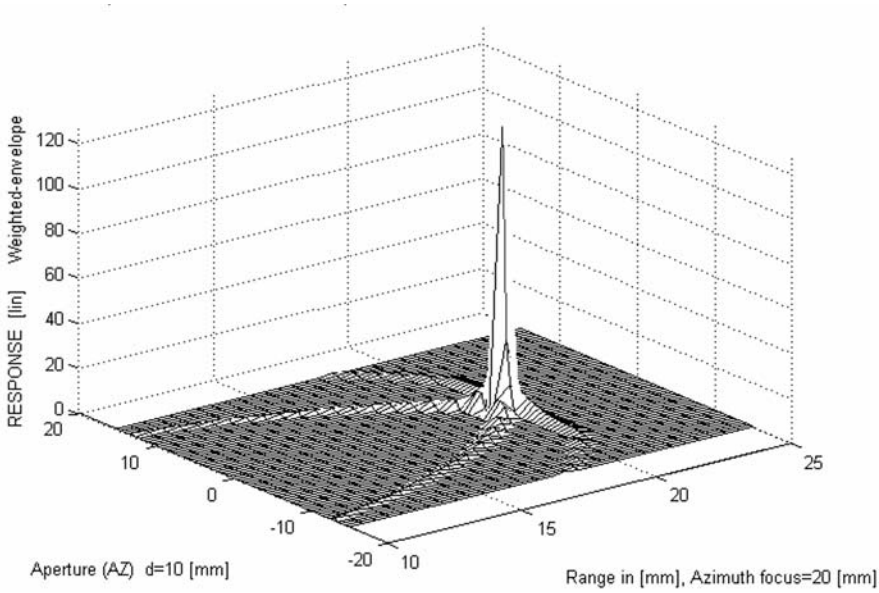

Fig. 1. Impulse response of a linear transducer (5 MHz) simulated by ultrasim

On the other hand we can measure the three dimensional pressure field using a PVDF hydrophone and scanning the area under the transducer in a water bath. The resulting beam profile and measurements of a point reflector can be used to determine the size of the PSF. The width of this beam profile in all dimensions is responsible for the blur and therefore determines the resolution directly. The knowledge of the PSF can be used for deconvolution particularly in the lateral and elevational direction because these are the main problems when looking at ultrasound resolution.

For simulation purposes we can use the approximation that the point spread function can be constructed by convolution of three gauss functions one in each direction. The function in axial direction has the smallest FWHM (full width half maximum) value followed by the lateral gauss function. This means that the resolution in axial direction is much higher than the one in lateral dimension. The worst resolution is available in the elevational direction caused by the mechanical properties (mechanical focusing) of the used transducers that are build for the two dimensional imaging.

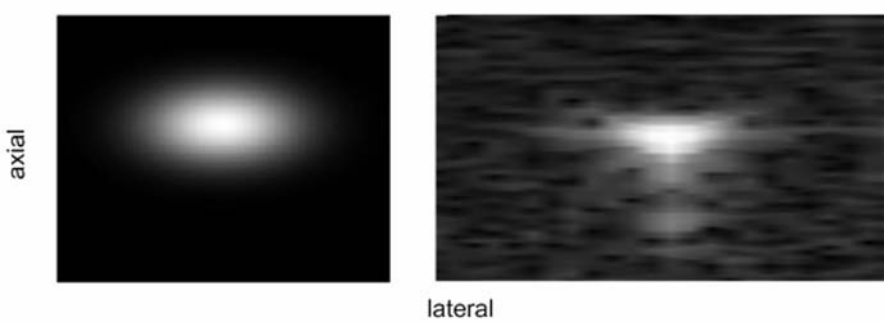

Fig. 2. Simulated point spread function and measured one used for deconvolution in 2D

The manipulation of the pressure field has the goal to enhance the FWHM and so to get a smaller PSF and is based mainly on approaches that change the excitation pulse or the electronically beamforming. With the DiPhAS system developed at Fraunhofer IBMT [5] it is possible to program free focusing in an unusual way so that several off-axis-measurements beside the acoustic axis can be used to manipulate the pressure field so that a special and improved PSF can be used for deconvolution later on. These changes will help to improve the resolution during image reconstruction for displaying the ultrasound data.

The future goal of the simulation of different beam profiles and PSF's is to find parameters for the beam forming process that can be used to improve the deconvolution process and increase the resolution of the image data to be computed.

4. Deconvolution and Multi-Direction Reconstruction

The simulation of the pressure field and the calculation of the PSF can be done using scripts implementing individual input parameters in tools like „Field II" [6] or „ultrasim" [7] based on MatLab.

The results of the simulation can then be compared to real data using phantom measurements to evaluate the changes of alternative focusing and excitation.

We look at our measured data set *g* as a convolution of the real structures *f* added with noise *n* with the kernel *h* that can be estimated:

$$g(t) = (f(t) + n(t)) *_s h(t)$$

The deconvolution itself can be done in several ways and based on different input data. The processing of video data is used for lateral deconvolution but the rf-data can be considered for axial deconvolution based on pulse estimation. The simplest approach is called „inverse filtering" that divides the Fourier transform of the measured data by the Fourier transform of the point spread function:

$$F(t) = G(t) / H(t)$$

This procedure works like a high pass filter that increases high frequency amplitudes where the amplitude of the PSF *H* is small. This results in much more noise than before and is undesirable.

Another approach is the wiener filter [8] that includes a noise modeling term *K* in the computation so that it is more robust and reduces noise in the resulting image but introduces ringing artifacts that have to be handled separately.

$$F(t) = G(t) * H(t)^2 / (H(t)^2 + K)$$

This approach is promising because it is noise robust and this is essential for ultrasound filtering.

Based on the high resolution of ultrasound imaging in the axial direction we focus mainly on deconvolution in lateral and elevational direction to improve the bad resolution of transducers used for two dimensional imaging on these axes.

The deconvolution is only one approach to improve the system resolution in elevational direction. Another way is the combination of different datasets taken from different directions. If the ultrasound transducer is rotated 90 degree between two measurements then the bad elevational resolution can be compensated with the better lateral resolution of the other data acquisition. The processing of several dataset of approximately 30, 60 and 90 degree into one single dataset can improve the overall resolution [9].

5. Conclusions

The simulation of different beam profiles and PSF can lead to a set of parameters that can be used to improve the deconvolution process and hereby increase the resolution of the whole image data to be computed. This enhanced deconvolution can be implemented in the Fraunhofer DiPhAS system and can be used for conventional ultrasound imaging.

The results then automatically improve even the resolution of three dimensional data sets that can be recorded using tracked freehand data acquisition like the data acquired with the SonoPilot thermo [10] device build for thermal therapy.

References

1 E.E. Hundt, E.A. Trautenberg, Digital Processing of Ultrasonic Data by Deconvolution, in IEEE Transactions on Sonics and Ultrasonics, Vol SU-27, No 5, 1980

2 W. Vollmann, Resolution Enhancement of Ultrasonic B-Scan Images by Deconvolution, in IEEE Transactions on Sonics and Ultrasonics, Vol. SU-29, No. 2, 1982

3 J.A. Jensen, N.B. Svendsen, Calculation of pressure fields from arbitrarily shaped, apodized and excited ultrasound transducers, in IEEE Transactions on Ultrasonics, Ferroeletrics and Frequency Control, 39(2): 262-267, 1992

4 J.A. Jensen, Deconvolution of Ultrasound Images, in Ultrasound Imaging Vol 14, pp 1-15, Academic Press, 1992
5 P. Weber et al, A Phased Array System for the Acquisition of ultrasonic RF-Data up to 20 MHz, in Acoustical Imaging, Vol. 27, pp25-33 2004
6 J.A. Jensen, Field: A Program for Simulating Ultrasound Systems, in Medical and Biological Engineering & Computing, Vol. 34, pp 351-353, 1996
7 S. Holm, Simulation of Acoustic Fields from Medical Ultrasound Transducers of Arbitrary Shape, in Nordric Symposium of Physical Acoustics, Norway, 1995
8 N. Wiener, Extrapolation, Interpolation and Smoothing of Stationary Time Series, New Yorl, Wiley, 1949
9 P. Soler et al., Comparison of Fusion Techniques for Spatial Compounding with Application to 3D Breast Ultrasound Imaging, to be published, SPIE 2006
10 H.J. Hewener, M. Hoss, S.H. Tretbar, C.G. Günther, R.M. Lemor, Diagnose und Therapiekontrolle – Ein System zur Aufnahme, Verarbeitung und Visualisierung von registrierten Freihand-3D-Ultraschall-Daten, in Bildverarbeitung für die Medizin, BVM 2005, pp 302-306

Evaluation and Enhancement of a Procedure for Generating a 3D Bone Model Using Radiographs

Sebastian Gollmer[1], Rainer Lachner[2] and Thorsten M. Buzug[1]

[1] Institute of Medical Engineering, University of Luebeck, Ratzeburger Allee 160, D-23538 Luebeck, Germany
[2] BrainLAB AG, Orthopedic Solutions, Kapellenstr. 12, D-85622 Feldkirchen, Germany

Abstract. Volumetric information about the patient's anatomy is quite valuable for medical diagnosis. Computed tomography (CT) is the common imaging modality for 3D visualization of bone tissue but rising costs in health care system demand for new approaches. A promising one is to use a 3D model being deformable under the constraint of statistical plausibility. The model is adapted to the patient's anatomy by extracting the specific bone features from several conventional radiographs (2D-3D registration). These have to be acquired under different angles thus providing the features' 3D position by means of which the model is deformed. The resulting bone representation may then be used for medical diagnosis instead of using CT data. Present work validates accuracy of the resulting bone shape and thus of the diagnosis relying thereon. Results are starting point for further implementations and modifications in order to reduce remaining errors.

1. Introduction

The reason for the recent interest on 2D-3D registration is the possibility of providing 3D information about the patient's anatomy without having to deal with drawbacks coming along with image acquisition using a CT scanner (high radiation dose, restricted availability, high costs concerning time, logistics and man-power). One target application of 2D-3D registration is to plan the replacement of an arthritic hip joint by an artificial one (total hip replacement, THR) more accurate thus reducing the current failure rate of approx. 15%.

Fleute et al. [1] propose to establish points on the projection rays of the bone contours corresponding to distinct model points. Minimizing the distance between the point pairs, the rigid registration parameters and the parameters for model deformation are optimized sequentially. Roth [2] refines how to extract the bone contours from the images. Additionally, he distinguishes the optimization method depending on the different parameters. A scheme for the scoliotic spine is presented by Benameur et al. [3]. An edge potential field is calculated for the bone contours and related to the silhouette of the statistical model. They use gradient descent technique for minimizing a cost function yielding both, rigid and elastic parameters. Lamecker et al. [4] are exerting a similar optimization method to calculate an individual pelvis model. But only for the elastic model parameters since the rigid registration is supposed to be known.

The to be evaluated 2D-3D registration algorithm was developed at the MEM Institute for Surgical Technology and Biomechanics (ISTB) at the University of

Bern [5] and will be introduced in section 3 after having outlined the subject of statistical modeling (section 2). Evaluation methods are discussed in section 4. Results and thereof following enhancement approaches are presented in section 5. Finally, conclusions and future prospects are given in section 6.

2. Statistical Modeling

The Point Distribution Model (PDM) enables individual representations of a patient's anatomy since it is a flexible shape [6]. It combines a set of representative, mutually aligned example shapes, each consisting out of n 3D points called vertices. The j^{th} out of m training shapes is expressed by the vector

$$\boldsymbol{x} = (x_{j1}, y_{j1}, z_{j1}, \ldots, x_{jn}, y_{jn}, z_{jn})^T \;, j = 1, 2, \ldots, m \;. \tag{1}$$

Principal component analysis (PCA) is used to build up the statistically deformable model, relying on the mean model $\bar{\boldsymbol{x}}$ and the covariance matrix $\boldsymbol{D}$:

$$\bar{\boldsymbol{x}} = \frac{1}{m}\sum_{j=1}^{m} \boldsymbol{x}_j \;,\; \boldsymbol{D} = \frac{1}{m}\sum_{j=1}^{m} (\boldsymbol{x}_j - \bar{\boldsymbol{x}}) \cdot (\boldsymbol{x}_j - \bar{\boldsymbol{x}})^T \;. \tag{2}$$

Diagonalizing of $\boldsymbol{D}$ yields the sorted eigenvalues λ_j and corresponding, orthonormal eigenvectors $\boldsymbol{p}_j$. Any patient specific surface is then defined as

$$\boldsymbol{x}' = \bar{\boldsymbol{x}} + \sum_{j=1}^{m} \alpha_j \boldsymbol{p}_j \;, \tag{3}$$

thus the weights $\alpha_j, j = 1, 2, \ldots, m$ have to be found.

3. Patient Specific Shape Reconstruction of the Femoral Bone

The 2D-3D registration algorithm strictly separates between the two stages rigid registration and elastic surface deformation. Input data are at least two localized and calibrated radiographs and a PDM, already pre-registered with the images.

Iterative Rigid 3D-3D Registration. The first stage is a modified ICP algorithm [7] since corresponding points are established in 2D image plane. The two point sets are the bone contour points $C^k = \{C_i^k; i = 1, 2, \ldots, M_k\}$, extracted from the k^{th} out of I images using a Canny edge detector [8], and the silhouette of the mean model. The vertices on the model surface contributing to its silhouette are $V^k = \{V_j^k; j = 1, 2, \ldots, N_k\}$, calculated with the fast illustrate library [9]. Projecting them into the k^{th} image plane yields the 2D point set $S^k = \{S_j^k; j = 1, 2, \ldots, N_k\}$.

$A^k = \{A_e^k; e = 1, 2, \ldots, L_k\}$ is the set of point pairs established between C^k and S^k using the SINMO (symmetric injective nearest-neighbor mapping operator) [5]. Interpolation between the point pairs using thin-plate splines (TPS) [10] allows increasing their number. The transformation f that describes how to align the set of silhouette points S^k with C^k is found by minimizing the cost function [5]

$$\Phi(f) = \sum_{e=1}^{L_k} \| C_e^k - f(S_e^k) \|_2 + \varpi_{2D} E_f \ , \tag{4}$$

where ω_{2D} is a regularization parameter and

$$E_f = \iint_{\Re^2} [(\frac{\partial^2 f}{\partial x^2})^2 + 2(\frac{\partial^2 f}{\partial x \partial y}) + (\frac{\partial^2 f}{\partial y^2})] dx dy \ . \tag{5}$$

The correspondence establishing is an iterative algorithm: The SINMO is applied again on the updated set of silhouette points and the TPS are calculated anew.

3D position is calculated for those contour points C_e^k for which corresponding silhouette points S_e^k are available after the last (e.g. 10th) 2D iteration (Fig. 1).

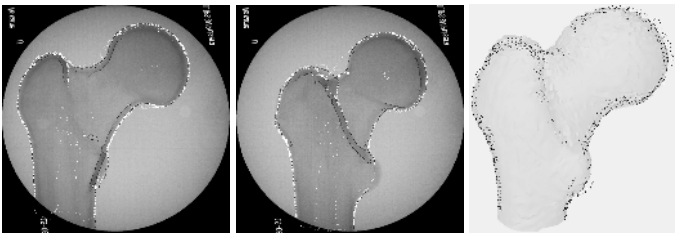

Fig. 1. Bone contour points (red) with correspondences (tagged green) are back projected from image planes to 3D (right) surrounding the mean model (blue: silhouette points)

The 3D positions of the silhouette points are already known being V_e^k. The 3D image points are W_e^k, whereas W_e^k is located on the ray between C_e^k and the focal point. Thus W_e^k is defined as the point on this ray closest to V_e^k. The set of *n'* 3D silhouette points $\boldsymbol{v} = \{V_d ; d = 1, 2, \ldots, n'\}$ and corresponding 3D image points $\boldsymbol{w} = \{W_d ; d = 1, 2, \ldots, n'\}$ result from merging the point pairs from *I* images. Rigid registration of $\boldsymbol{v}$ with $\boldsymbol{w}$ using e.g. least squares minimization updates the mean model's scale, position and orientation. The silhouette is calculated again for the updated model and projected into the image planes followed by an anew set of 2D iterations.

Elastic Surface Deformation. The 3D point pairs available after the last (e.g. 30th) 3D iteration are used as well for the following elastic deformation of the model surface. At first the weights α_j, in eq. (3) are determined by minimizing a joint cost function consisting out of two terms [11]: The likelihood energy term $E(\boldsymbol{x}, \boldsymbol{w}, \boldsymbol{x'})$ minimizes the distance of the points $\boldsymbol{v}$ on the model's surface to their corresponding image points $\boldsymbol{w}$ in the least squares sense. The prior energy term $E(\boldsymbol{x'})$ restricts the deviation of the deformed model from the mean shape due to the sparse point pairs $(n' << n)$.

Finally the patient specific shape that results according to eq. (3) is regularized by expanding the TPS scheme to 3D. The sought after mapping *g* is found by minimizing the cost function [11]

$$\Gamma(g) = \frac{1}{n'} \sum_{d=1}^{n'} \| V_d - g((X'_i)_d) \|_2 + \varpi_{3D} E_g \ . \quad (6)$$

Thereby $(X'_i)_d$ is the point on the already statistically (PCA-based) model corresponding to W_d and E_g is the 3D expansion of E_f in eq. (5).

4. Evaluation Methods

Single algorithm stages are evaluated separately. For the rigid registration the criteria are establishing point pairs, rate of convergence and robustness in the sense of reaching the global minimum. The resulting bone shape is evaluated by means of a reference surface S_R (gold-standard), build up from the CT data of the x-rayed bone using a marching cubes algorithm [12]. Mean error (ME) and root mean square error (RMSE) for any point $\boldsymbol{p}_M$ on the model surface S_M are defined:

$$d_{ME} = \frac{1}{|S_M|} \iint_{\boldsymbol{p}_M \in S_M} d_e(\boldsymbol{p}_M, S_R)\, dS_M \ , d_{RMSE} = \sqrt{\frac{1}{|S_M|} \iint_{\boldsymbol{p}_M \in S_M} d_e(\boldsymbol{p}_M, S_R)^2\, dS_M} \quad (7)$$

where $d_e(\boldsymbol{p}_M S_R) = \min \| \boldsymbol{p}_M - \boldsymbol{p}_R \|_2$ with $\boldsymbol{p}_R \in S_R$ and $|S_M|$ is the model's surface area. Secondary local triangle errors (TE) of the meshed surface are found using distinct sampling points, equally distributed over the particular triangle [13].

The complete surface evaluation scheme is characterized in Figure 2.

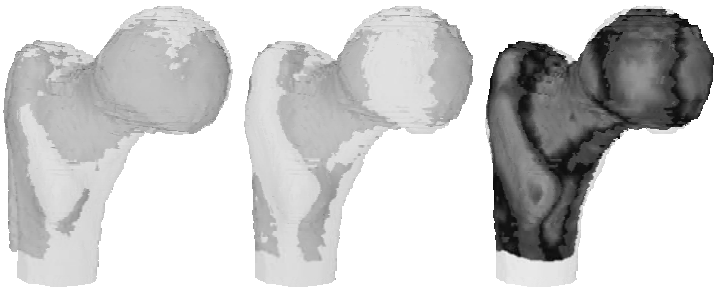

Fig. 2. Visualizing local TE (right) by mapping a distance map on the model's surface after minimizing the overall distance of S_M (blue) to S_R (red). An ICP algorithm is used for distance minimization (middle) after landmark-based initial alignment (left).

5. Evaluation Results and Enhancement Approaches

The correspondence establishing step is quite crucial for both, rigid registration and surface deformation. Despite the strict SINMO [5] anatomical non-reasonable point pairs may occur, only few of them corrupting the resulting bone shape significantly. Thus increasing their number without taking into account anatomical sensitivity should be avoided.

Pre-registration of the mean model with the radiographs is another decisive aspect. Crossover of bone contour and projected silhouette may occur from bad

initial alignment causing non-reasonable point pairs. Up to certain degree energy minimization using TPS [10] allows converging anyway iteratively towards the global minimum. But the number of 3D iterations to reach it increases.

Errors of the bone shape are determined after each elastic deformation scheme, the PCA-based and the final TPS kernel regularization (TPSK). Since applied directly in 3D space the latter is especially sensible against unevenly distributed or non-reasonable correspondences (Fig. 3).

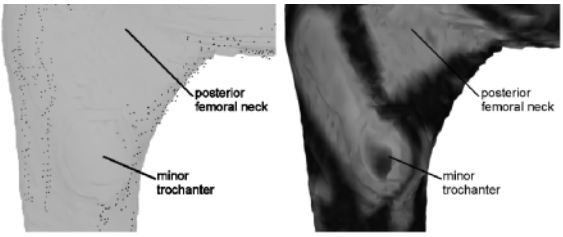

Fig. 3. Large local errors correlate with non-available point pairs (red: 3D image points)

As opposed deformation based on statistical knowledge performs robust even for less stable pre-registrations. On the other side restriction to m=23 example bones when building up the model prevents shaping of individual bone features for the well calculated pre-registration. These are covered better after the TPSK reducing the ME and median TE (MTE) to 1.0mm and 0.7mm, respectively (Table 1).
Results improve when eliminating anatomical non-reasonable point pairs appearing due to silhouette points associated with inner model structures (Fig. 1). Eliminating these structures prevents non-sensible point pairs, appreciating in turn the remaining ones. Rigid registration becomes faster and more robust for less stable pre-registrations. Moreover using 45 instead of 30 iterations, the bone shape is only little worse compared to the well calculated alignment (Table 1).

Table 1. Error values of resulting bone shape for different pre-registrations, 3D iterations (30 or 45 = values in parenthesis) and optimized model. Validation using a synthetic bone is separated after PCA-based deformation and TPSK regularization, all values in mm.

Model	original				optimized	
Pre-reg.	well calculated		less stable		less stable	
Deformation	PCA	TPSK	PCA	TPSK	PCA	TPS
ME	1.1	1.0	1.6 (1.6)	2.0 (1.8)	1.5 (1.4)	1.7 (1.3)
RMSE	1.4	1.3	2.0 (2.0)	2.6 (2.3)	1.9 (1.7)	2.2 (1.7)
Max. TE	4.8	5.0	7.0 (6.1)	10.0 (8.3)	6.1 (5.5)	8.9 (6.5)
Median TE	0.9	0.7	1.3 (1.3)	1.5 (1.5)	1.2 (1.1)	1.3 (1.0)

6. Conclusions and Future Prospects

Obtained results are promising facing the current project status. Initial alignment is crucial, influencing correspondences and in turn final results arbitrative. For reasonable input the combination of PCA-based and TPSK surface deformation provides satisfying ME and MTE but the max. TE needs to be improved. First approach is probably finding point pairs for these erroneous areas: A multi step procedure of rigid and elastic registration may allow establishing more point pairs for patient specific bone features. Finally, a general algorithm for localizing images is necessary to optimize parameters like the angle between the images.

References

1 M. Fleute, S. Lavallée: Nonrigid 3D/2D Registration of Images Using Statistical Models. In *MICCAI'99*, LNCS Vol. 1679, pp. 138-147, Cambridge, UK, 1999

2 M. Roth in *Intraoperative fluoroskopiebasierte Patientenlageerkennung zur präzisen Unterstützung chirurgischer Eingriffe*, Ph. D. Thesis, Institut für Informatik der Technischen Universität München, 2000

3 S. Benameur, M. Mignotte, S. Parent, H. Labelle, W. Skalli, J. De Guise: 3D/2D Registration and Segmentation of Scoliotic Vertebrae Using Statistical Models. In *Computerized Medical Imaging and Graphics*, Vol 27, 5, pp. 321-337, 2003

4 H. Lamecker, T. H. Wenckebach, H.-C. Hege, G. N. Duda, M. O. Heller: Atlas-basierte 3D-Rekonstruktion des Beckens aus 2D-Projektionsbildern. In *BVM2006*, pp 26-30, Hamburg, Germany, 2006

5 G. Zheng, M. A. Gonzalez Ballester, M. Styner, L. P. Nolte: Reconstruction of Patient-Specific 3D Bone Surface from 2D Calibrated Fluoroscopic Images and Point Distribution Model. In *MICCAI 2006*, LNCS Vol. 4190, pp. 25-32, Copenhagen, Denmark, 2006

6 T. F. Cootes, C. J. Taylor, D. H. Cooper, J. Graham: Active Shape Models - Their Training and Application. In *Computer Vision and Image Understanding*, Vol. 61, 1, pp: 38-59, 1995

7 P. J. Besl, N. D. McKay: A Method for Registration of 3-D Shapes. In *IEEE Transactions on Pattern Analysis and Machine Intelligence*, Vol. 14, 2, pp. 239-256, 1992

8 J. F. Canny: A Computational Approach to Edge Detection. In *IEEE Transactions on Pattern Analysis and Machine Intelligence*, Vol. 8, 6, pp. 679-698, 1986

9 A. Hertzmann, D. Zorin: Illustrating Smooth Surfaces. In *Siggraph 2000*, pp. 517-526, 2000

10 F. L. Bookstein: Principal Warps: Thin-Plate Splines and the Decomposition of Deformations. In *IEEE Transactions On Pattern Analysis and Machine Intelligence*, Vol. 11, 6, pp. 567-585, 1989

11 G. Zheng, K. T. Rajamani, L.-P. Nolte: Use of a Dense Surface Point Distribution Model in a three-stage Anatomical Shape Reconstruction from Sparse Information for Computer Assisted Orthopaedic Surgery: A Preliminary Study. In *ACCV'06*, LNCS Vol. 3852, pp. 52-60, 2006

12 W. E. Lorensen, H. E. Cline: Marching Cubes: A high Resolution 3D Surface Construction Algorithm. In *SIGGRAPH '87*, ACM Press, New York, USA, 1987

13 N. Aspert, D. Santa-Cruz, T. Ebrahimi: MESH: Measuring Error between Surfaces using the Hausdorff Distance. In *ICME*, Vol. 1, pp. 705-708. 2002

High-Speed-Camera Recordings and Image Sequence Analysis of Moving Heart-Valves: Experiments and First Results

Thomas Wittenberg[1], Robert Cesnjevar[3], Stephan Rupp[1], Michael Weyand [2] and Markus Kondruweit[2]

[1] Fraunhofer Institute for Integrated Circuits IIS, Am Wolfsmantel 33.
91058 Erlangen, Germany
E-mail: {wbg,rupp}@iis.fraunhofer.de
[2] Zentrum für Herzchirurgie der Universitätsklinik Erlangen, Krankenhausstrasse 12,
91054 Erlangen, Germany
E-mail: markus.kondruweit@herz.imed.uni-erlangen.de
[3] Kinderherzchirurgisches Zentrum der Universitären Herzchirurgie Hamburg

Abstract. Heart valve prosthesis and related reconstruction develop problems during clinical course in patients, due to calcification. To analyse and quantify these effects, heart valves of pigs are filmed during motion using a high-speed camera, whereas the resulting image sequences are analyzed by motion analysis methods based on dynamic active contours. In this contribution we present first experiments and results for both, recording and motion analysis. The far-goal of our work is an analysis and understanding of the heart valve motion in the context of automatic quality assurance for the production of heart valves.

1. Introduction

At the present state, heart valve prosthesis as well as the related heart valve reconstruction methods develop sever problems during clinical course in patients, as implanted bio prosthesis develop calcification with consecutive dysfunction of the prosthesis which can lead to re-operation. [1,2]. The causes of this process do not only physiological processes, but are also strongly related to stress forces against the leaflets with unphysiological flow. Furthermore, such force allocation can advance the calcification [3]. A re-operation rate after 15 years up to 70 % exists because of degenerative alteration of the leaflets in patients who received biological heart valve prosthesis [3].

While long time anticoagulation with according risks can be avoided, the structural degeneration with associated morbidity and mortality still are the main disadvantages for biological heart valve prosthesis [4]. Reasons for an accelerated structural degeneration have been variegated researched. Main factors which have been determinated, were the age of the patient, mitral valve replacement, bad left ventricular function and size and design of the heart valve prosthesis [5,6,7]. Another aspect of calcification is the kind of preservation of the valve to avoid intrusion respectively the generation of lime. The development of new chemical preservation methods already improved the durability of biological heart valve prosthesis [8]. But it should also be pointed out, that such changes of heart valve pros-

thesis are always caused by mechanical stress at the leaflets, which in turn damage the leaflet surface. Such alterations are then the origin for the process of calcification [9].

The main disadvantages of mechanical heart valve prosthesis – especially implantted in aortic valve position – are high transvalvular gradients which can constrain the aggrieved heart muscle to recover. This can limit the lifespan of the patient [10]. In our opinion, detailed high-speed cinematic recordings in combination with successive motion-analysis of the exact movements of such prosthesis can lead to optimizing and perfecting their design as well to modifications of the corresponding implantation techniques. Cinematic recordings and motion-analysis of prosthesis using a high speed camera system is capable to identify engineering and design deficiencies which could be corrected. These steps will lead to an improvement of the long time results and a decrease of re-operations with consecutive high morbidity and mortality [7].

Thus, the overall objective of this ongoing study will be the investigation of the heart valve movements. In this work, we will describe first experiments regarding the recording of native pig hearts in vitro as well as first results of motion analysis to detect and extract the changes of the orifice over time applying snakes.

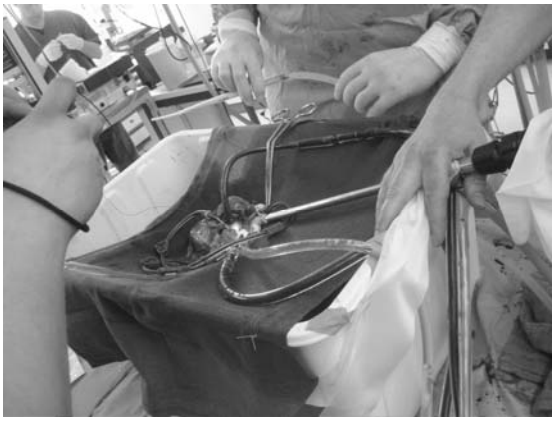

Fig. 1. Clinical set up for the recording of the heart valve motion. The rigid endoscope is (right) attached to the camera is moved into the heart.

2. Experimental Methods

This current work is a result of an ongoing cooperation between the Fraunhofer Institute for Integrated Circuits IIS with the center for heart surgery of the University Erlangen–Nuremberg. This study was performed on several pigs after heart explantation. For each pig's heart several high-speed recordings were made from different positions. In this work we report on the application of image processing algorithms to evaluate the shape of the orifice of the tricuspidal valve as a function of time.

Examination Technique. In order to acquire digital high speed recordings of native heart valves while the heart is beating, the heart of a pig is explanted for the experimental setup. From a narcotized pig (weight: 81 kg's) the heart is dissected via sternotomy, followed by a cardioplegic arrest. Then the heart is explanted using a technique just like for heart transplantation in man. Thereafter, the left and right coronary arteries are intubated directly and perfused via a heart lung machine in such way that the heart starts beating again. The optical system of the high speed camera (cf. section 2.2) is installed via the supraaortic branches for the examination of the aortic valve or alternatively via the left atrium to observe the mitral valve. The third postion to insert the optical system into the heart is via the apex of the left ventricle which allows to take pictures a well from the aortic as from the mitral valve. An example of the operation and recording set up is given in Figure 1.

Digital High-Speed Camera. Imaging of the native heart valves was performed with a digital high-speed camera (Richard Wolf, Knittlingen, Germany), which has been connected to a rigid 0^{o} laprascope endoscope. The camera system consists of (a) a camera head with a digital CMOS sensor chip, which has a spatial resolution of 256x256 pixel in color [11], (b) a controller unit with a capacity of 256 MByte digital storage, organized as a ring buffer, and (c) finally a standard personal computer for the archivation of the recorded images sequences as well as image processing and data handling.. The recording rate for was 2000 frames per second, enabling a sufficient oversampling with respect to the expected movements of the heart valves. During the recording each picture is written into the circular organized semiconductor memory. The recording were stopped by a manual posttrigger signal. By this procedure, all frames recorded during the preceding 2 seconds are held in the camera memory. For permanent storage and archivation all image sequences are copied onto secondary (hard-disc) or tertiary (CD-ROM, DVD, PACS) storage devices. All stored recordings can be replayed at any slow motion speed. As the high-speed recordings are available in a digital format, image processing methods can be applied on each frame of the recording. Figure 2 shows the tricuspidal valve at four different states of opening and closing and a different points of time.

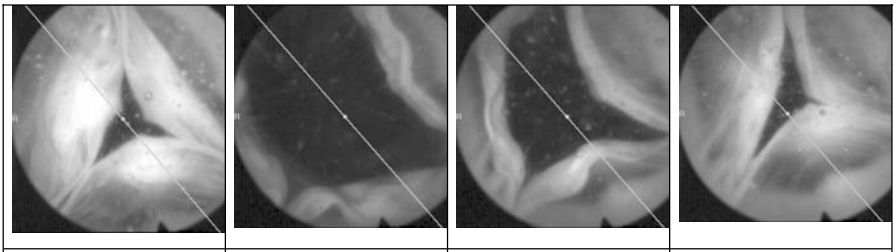

Fig. 2. Endoscopic view onto the native heart valve of a pig during an opening and closure process at four different point of time.

Motion Analysis. For the calculation of the orifice area of the heart valves and its geometric variation over time, contours (*snakes*) [12] were applied. Active contours are commonly used to compute and quantify motion and deformation of contiguous areas from digital image sequences. They have been studied extensively in recent years, particularly in biomedical image analysis, e.g. [13,14], with a number of different implementations described in literature.

In our case the contiguous area of interest is the orifice of the observed heart valve. The contour C of the orifice can formally be described as a set V of nodes $V = \{v_1, v_2, ..., v_n\}$, $n \in \mathbf{N}$, where each node v_i is connected via two edges to its neighboring nodes v_{i-1} and v_{i+1}. Each point v_i of a contour can be described non-ambiguously with regard to a defined origin of an image plane using a vector $v_i = (x_i, y_i)$. In our case a contour with $n = 51$ nodes was applied. In analogy to physical systems, a contour C owns an energy term $E = \alpha \cdot E_{elastic} + \beta \cdot E_{bend} + \gamma \cdot E_{image}$, consisting of the two terms $E_{elastic}$ and E_{bend} of internal energy and the external energy E_{image}. The terms $E_{elastic}$ and E_{bend} represent the internal properties of the contour such as elasticity, stiffness and curvature, in analogy to tension and rigidity of the snake. In contrast, the energy term E_{image} describes the external influence onto the contour from the gradient image, which in this case is the form and position of the border of the orifice in one single image of the sequence. The influence of each energy term, $E_{elastic}$, E_{bend} and, E_{image} can be weighted individually with parameters α, β and γ, respectively.

By using an energy-minimization algorithm, the position of each node of the contour is iteratively varied, until the total energy E of the contour is minimized with regard to the influence of the gradient image as well as the internal energy terms. The minimization process will stopped, when either the total energy E of the contour does not change significantly between two iteration steps or a predefined number of iteration steps have been applied. In our work, the dynamic programming algorithm as suggested by Amini et al has been used for the energy minimization [15]. Even though this algorithm is the extremely local nature of its decision criteria, the main advantages are its computational efficiency and its relative simplicity.

To obtain a good initial starting contour C_0 for the energy-minimization process, a freehand form is be drawn into an image of the sequence with an open orifice. Afterwards the starting contour is iteratively fitted to the real contour of the orifice using the optimization process. For all subsequent images of the sequence, the contour C_{t-1} of the preceding image is propagated from the previous image and used as starting contour. Furthermore, for this application local constraints are applied to three nodes of the contour, as suggested in the original work by Kass et al [12]. These three constrained nodes are marked manually in the first image and correspond anatomically to the commissions between the valve leaflets.

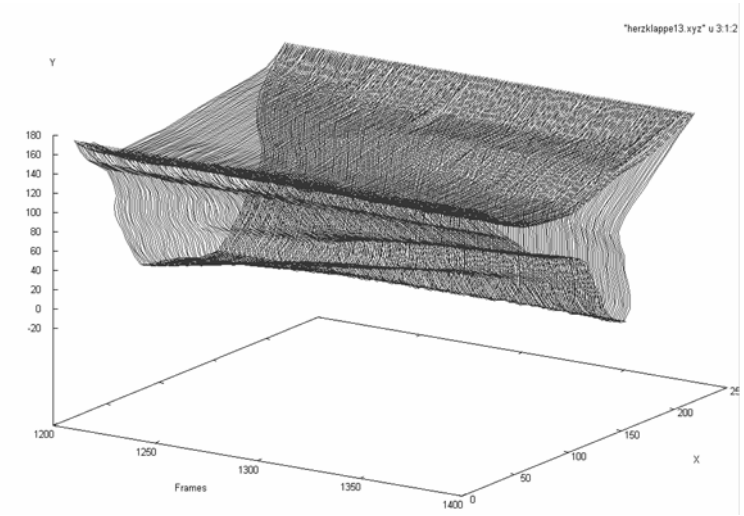

Fig. 3. Contours of the orifice during heart valve movement over a period of 50 ms.

3. Results and Discussion

In general, the movements of the heart valves over several periods of heart beats can be observed in full temporal and spatial detail using high-speed recordings. Due to limited memory capacity of 256 Megabyte or 2 seconds, only two or three heart beat cycles can be recorded at once. Nevertheless, in contrast to other experimental set-ups to observe the heart valve movement, the presented high-speed cinematography allows the observation of heart valve movements in vitro on native pig hearts. Using interactive contour-based motion-analysis methods such as active contours (snakes), the change of the orifice over time can be obtained as well as the related circumference and area. Fig. 3 shows a short sequence of computed contours of the heart valve orifice. In this example the heart valve leaflets depict the typical change of the orifice shape from a triangle-like to a wedge–like shape over a period of 50ms. Over the complete time span, the points of the commissions are kept constant at all time. Fig. 4 depicts the relative orifice area over four heart beats during a time span of 2 seconds.

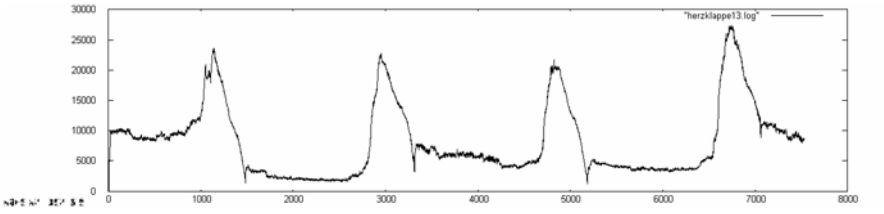

Fig. 4. Area of the orifice over time (time axis is labeled in frames).

4. Conclusions

Using a digital high-speed system allows a high resolution and temporal sampling of the heart valve dynamics in vitro. Subsequent image analysis tools like active contours allow the reduction of the generated data and the visualization of certain dynamics such as the relative area of the orifice. Future research will focus on different types of heart valve motions visible during the heart beat as well as a fully automatic image analysis, which allows automatic detection and initial delineation of the orifice. The far goal of this work will be the quality assurance for the production of artificial and native heart valves.

References

1 N.C. Poirer, et al: *15-year experience with the Carpentier-Edwards pericardial bio prosthesis.* Ann Thorac Surg 1998; 66 (Suppl 6): S57-S61.

2 W.R.E. Jamieson et al.: *Re-operation for bioprosthetic aortic valve structural failure-risk assessment*. Eur J Cardiothorac Surg., Dec 2003 ; 24 : 873-878.

3 F.J. Schoen, and R.J.Levy : Calcification of Tissue Heart Valve Substitutes: *Progress Toward Understanding and Prevention.* Ann Thorac Surg 2005;79:1972-80.

4 S.H. Ramitoola: *Choice of prosthetic heart valve for adult patients*. J Am Coll Cardiol 2003; 41(6): 893-904.

5 E.L. Jones et al.: Ten-year experience with the porcine bioprosthetic valve: interrelationship of valve survival and patient survival in 1050 valve replacements. Ann Thorac Surg 1990; 49(3): 370-383.

6 G.L. Grunkenheimer et al: *Actuarial versus actual risk of porcine structural valve deterioration.* J Thorac Cardiovasc Surg 1994; 108(4): 709-718.

7 G..J. Reul et al: *Valve failure with the Ionescu-Shiley bovine pericardial bio prosthesis: analysis of 2680 patients.* J Vasc Surg 1985;2(1):192–204.

8 F.J. Schoen, and C.E. Hobson: *Anatomic analysis of removed prosthetic heart valves: causes of failure of 33 mechanical valves and 58 bio prosthesis, 1980 to 1983*. Hum Pathol 1985;15:549

9 A.M. Borkon et al: *Aortic valve selection in the elderly patient.* Ann Thorac Surg 1988;46(3):270–7.

10 G. Tarantini et al.: Aortic valve replacement in severe aortic stenosis with left ventricular dysfunction: determinants of cardiac mortality and ventricular function recovery. Eur J Cardiothorac Surg., Dec. 2003 ; 24 :879-885.

11 T. Wittenberg et al. :Hochgeschwindigkeitskameras für die Stimmdiagnose-Status Quo und neue Perspektiven. Stimme - Sprache - Gehör, 29(1):29-34, 2005.

12 M Kass, A Witkin, D Terzopoulus, Snakes: *Active Contour Models*, Int.J.of Comp.Vision, 321--331, 1988.

13 K.R. Castleman, T.P. Riopka,Q Wu: *FISH Image Analysis*, IEEE Engineering in Medicine and Biology 15(1):67—75, Jan/Feb. 1996

14 F. Leymarie F,M Levine: *Tracking Deformable Objects in the Plane Using Active Contour Model*. IEEE Trans PAMI 15(6):617-634, 1993.

15 AA Amini, et al: Using Dynamic Programming for Solving Variational Problems in Vision. IEEE PAMI- 12(9):855–867, 1990.

Stereoscopic 4D-Visualization of Craniofacial Soft Tissue based on Dynamic MRI and 256 Row 4D-CT

Cornelia Kober[1,7], Britt-Isabelle Boerner[2], Shinichiro Mori[3], Carlos Buitrago Tellez[4], Markus Klarhöfer[5], Klaus Scheffler[5], Robert Sader[6,7] and Hans-Florian Zeilhofer[2,7]

[1] Faculty of Engineering and Computer Science, University of Applied Science Osnabrueck, D-49009 Osnabrueck, Germany
Email: c.kober@fh-osnabrueck.de
[2] University Hospital Basel, Switzerland
Email: iboerner@uhbs.ch
[3] National Institute of Radiological Sciences, Chiba 263-8555, Japan
Email: shinshin@nirs.go.jp
[4] Dept. of Neurology, University Hospital Basel / Radiological Center Aarau Zofingen, spitalzofingen AG, Switzerland
Email: cbuitrago@uhbs.ch
[5] MR Physics, University Hospital Basel, CH-4031 Basel, Switzerland,
Email: mklarhoefer@uhbs.ch
[6] Klinik für Mund-, Kiefer- und Plastische Gesichtschirurgie, University of Frankfurt, D- 60596 Frankfurt am Main, Germany
Email: r.sader@em.uni-frankfurt.de
[7] Center of Advanced Studies in Cranio-Maxillo-Facial Surgery, Munich University of Technology, D-81675 Munich, Germany

Abstract. For soft tissue organs, standard 3D-reconstructions can only provide a snapshot of a dynamically deforming structure. A reasonable possibility to overcome this drawback is the transition forward from 3D-reconstruction to 4D-visualization, i. e. rendering time dependent behavior based on dynamical radiological data sets. This article is dedicated to dynamical visualization of craniofacial soft tissue, namely human eye movement (MRI) and real time visualization of the downward movement of a volunteer's mandible (256 row 4D-CT, NIRS, Chiba, Japan). Within several considered approaches for presentation of the results, stereoscopic realization of the 4D-visualization was regarded as providing best diagnostic impact and acceptance.

1. Introduction

Based on dynamic sequences of radiological data sets, 4D-visualization is an extension of this research towards an analysis of the organs' functionality. Therefore, the step from 3D-reconstruction to 4D-visualization is expected to result in a significant progress in diagnostic imaging. This article is part of a detailed research project for dynamical radiology and visualization mainly in the craniofacial field [1].

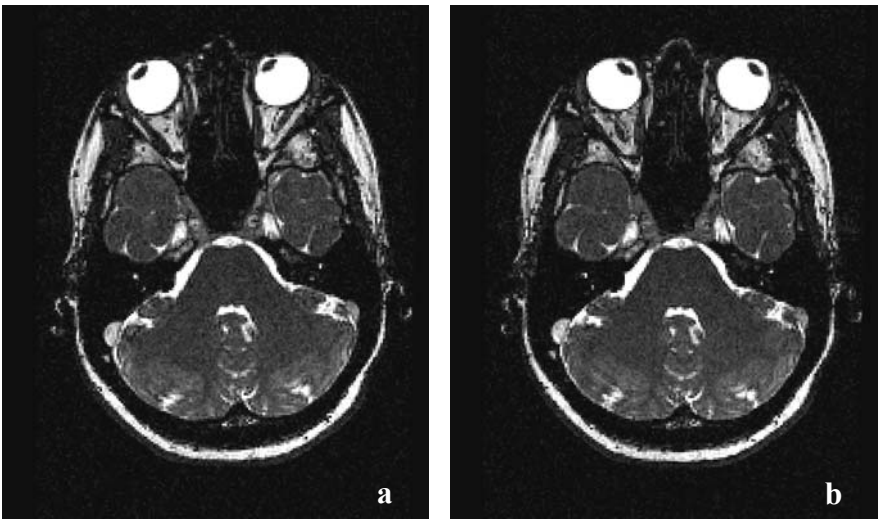

Fig. 1. Axial MRI-slices from the 4D-imaging series for the human eye movement, a: start, eyes oriented to the left, b: end, eyes oriented to the right

The actual stage of the project should be demonstrated by means of two examples. The first example refers to 4D-MRI of human organ of vision where the focus is on rendering the extraocular muscles and the optic nerve. The second approach is based on 256 row 4D-CT data stemming from NIRS, Chiba, Japan. For this case, the focus is on dynamic rendering of orofacial soft tissue, especially of the soft (and hard) palate. Finally, different ways of presentation of the visualization results were tested with regard to their diagnostic impact.

2. Patients and Methods

Radiological Data Acquisition. As regards the orbital example, several settings of continuous eye movement of a healthy volunteer (female, 28 Y) were recorded, see Figure 1. The acquisition time for each data set could be reduced to 1 minute. For each setting, 15-20 3D-MRI data sets (Siemens, 1.5 T, SE imaging sequence) were taken comprising 56 axial slices with isotropic voxel size of 1 mm in x, y, and z-direction.

By the means of the 256 row 4D-CT, located at NIRS, Chiba, Japan, dynamical data of a volunteer with 512x512 image matrix and 0.5 mm z-distance were provided [2]. Mouth opening was imaged over 4.9 seconds with a time increment of 0.05 seconds, see Figure 2. The sequence consisted in a total amount of data of more than 10 GB.

4D-Visualization Approach. For both cases, a combination of direct volume rendering and shaded surface reconstruction was applied. In order to allow a direct view into the optic cavity for the MRI case respectively to the soft and hard palate

for the 4D-CT data, the visualization had to be clipped which means that the visualization was cut by an axial (for the eyes) or sagittal (for the palate) “clipping” plane. This clipping plane could be scrolled by the user. For a comparison of the visualization results with the conventional diagnosis based on 2D grey images, a transparently rendered slice of the original MRI respectively CT data could be faded into the visualization, connected to the clipping plane and, by this, also scrollable. All image processing, visualization, and reconstruction steps were performed by means of Amira 4.1 [3, 4]. Due to the very high hardware requirements, a CELSIUS V-Serie Computer (Siemens-Fujitsu) was used equipped with a nVidia Quadro FX4000 graphics board.

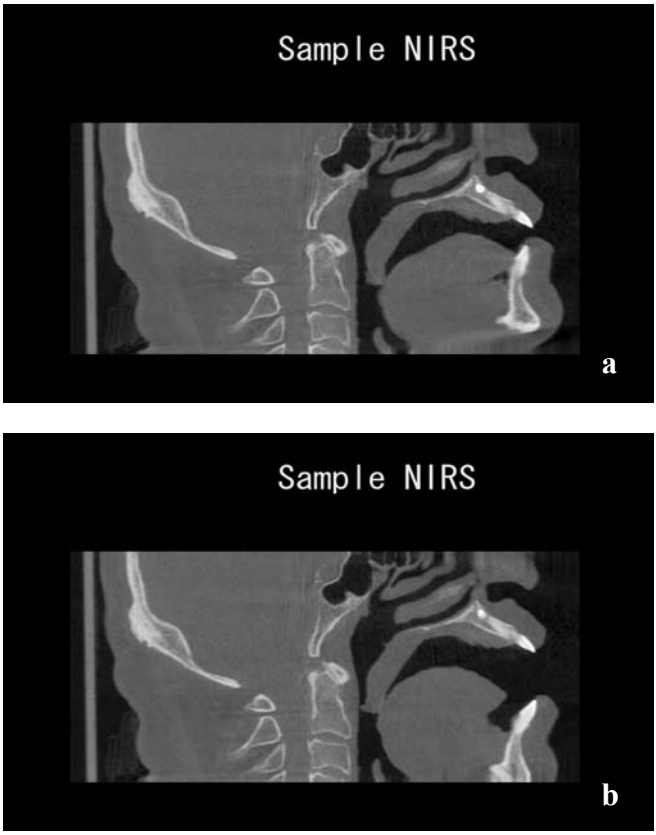

Fig. 2. Central sagittal cross sectional CT slices from 256 row 4D-CT, a: start, closed mouth, b: end, mouth opened

Significant Result Presentation. In order to get best possible diagnostic impact and acceptance different approaches for presentation of the visualization results were considered. Several observers, partially experienced craniomaxillofacial or oral surgeons, had the choice between stereoscopic and non-stereoscopic visualization. Motivated by easy feasibility and the availability of low cost paper glasses,

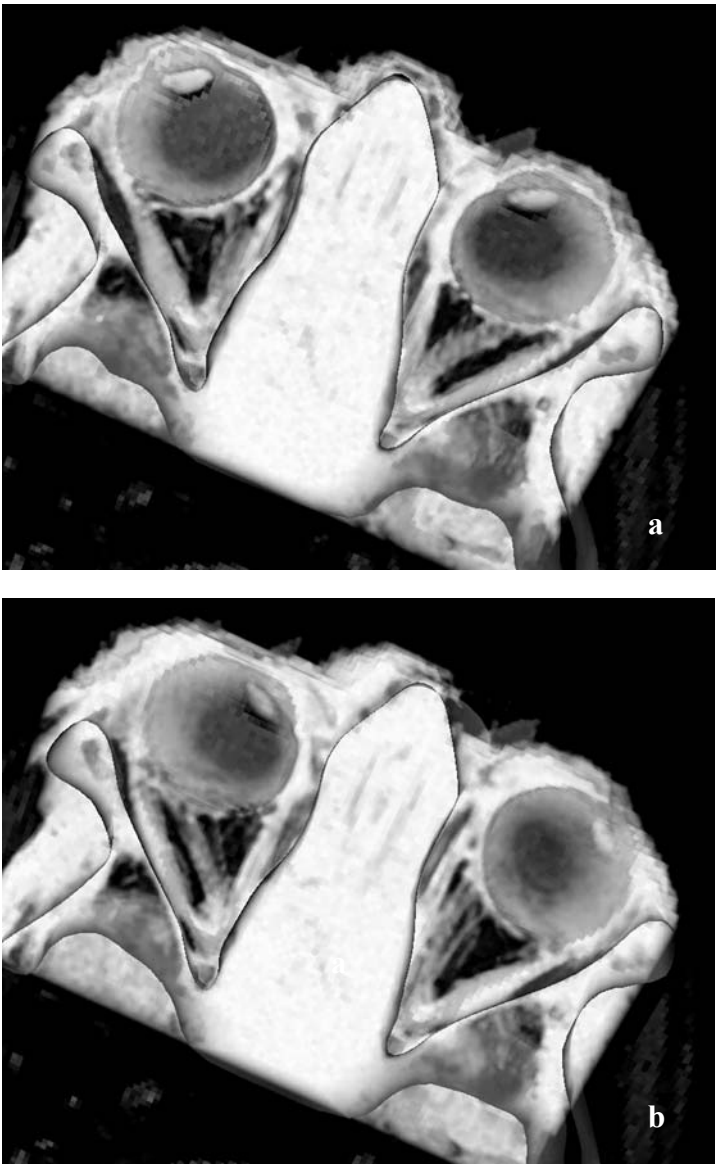

Fig. 3. 4D-visualization of human eye movement, red-cyan-stereo, a: start, eyes oriented to the left, b: end, eyes oriented to the right

at the actual stage of the project, red-cyan anaglyph images were chosen as means for stereoscopic visualization, see Figure 3 and 4. Further, the test persons could decide whether they prefer to interactively manipulate the dynamic visualization (rotation, translation, zooming in and out of the moving reconstruction) or to look at a previously recorded movie of the organ's dynamic behavior.

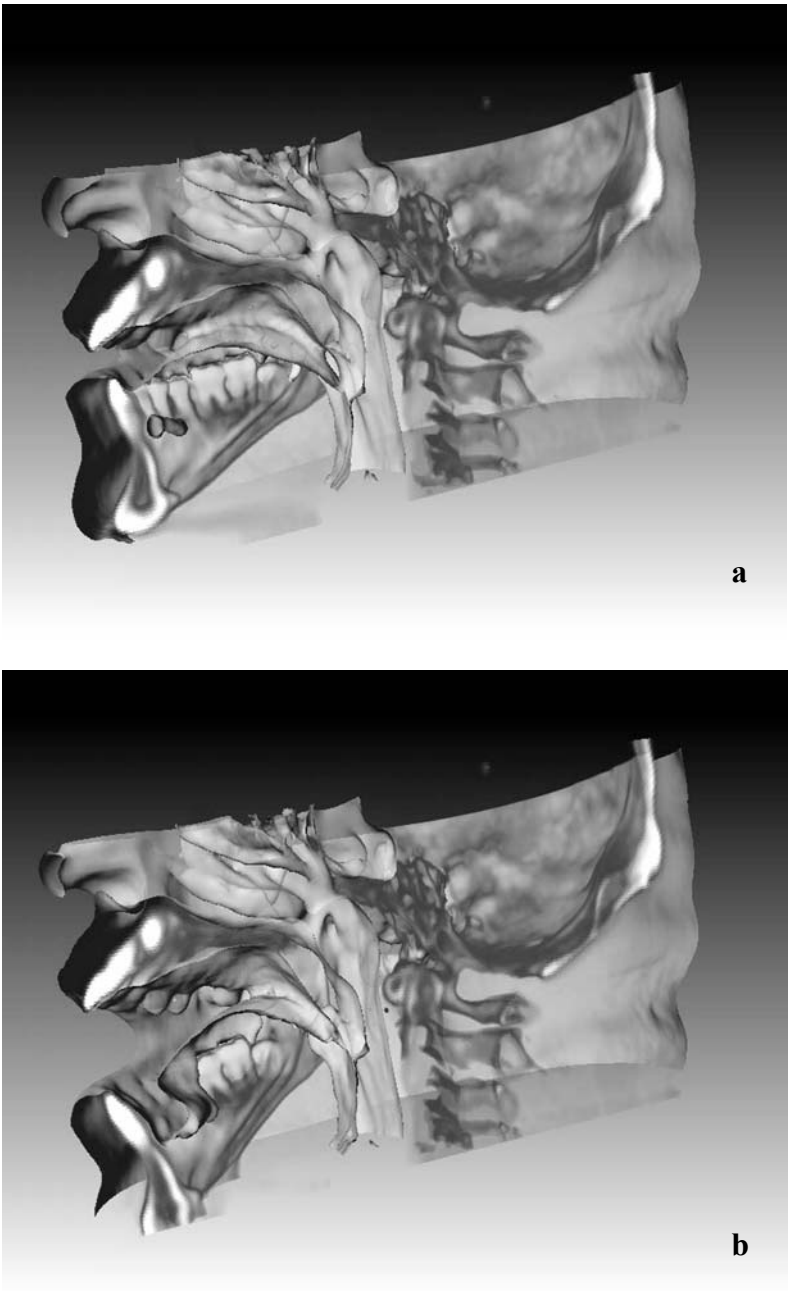

Fig. 4. 4D-visualization of orofacial soft tissue based on 256 row 4D-CT, red-cyan-stereo, a: start, b: end of movement

3. Results

By means of the described techniques, 4D-radiology and visualization of extraocular muscles and optical nerve as well as of deformation of orofacial tissue during mouth opening was possible, see Figure 3 and 4. The applied visualization approach revealed detailed anatomical features. At the actual stage of research, both approaches were very elaborate.

The medical observers voted clearly for the stereoscopic visualization as giving significantly better insight to the patient's functional anatomy. Additionally, interactive manipulation of the dynamic visualization which means rotation and translation of the moving organ was highly appreciated. The medical observers refrained from further operations as scrolling the clipping plane or changing the orientation of the clipping plane from an axial cut to a sagittal cut and left these actions to interested laypersons within the group of tested observers.

4. Discussion and conclusion

Though both examples were quite successful 4D-radiology and visualization are only in their early beginning. Acquisition of the radiological data as well as realization of the 4D-visualization is still very demanding. The hardware requirements are very high, especially with regard to the graphics board and the main memory. The huge amount of data needs careful interpretation. Nevertheless, 4D-radiology and visualization can be considered as a very promising field enabling new anatomical and clinical research about physiology and pathology of craniofacial and oral soft tissue organs.

Acknowledgements. The first author wants to acknowledge M. Melzig, Fujitsu Siemens Computers, and L. Eigenfeld, NVIDIA Corporation Germany, for supporting our research with computer equipment for effective 4D-Visualizations.

References

1 C. Kober, B.-I. Boerner, L. M. Gallo, S. Mori, C. Leiggener, C. Buitrago Tellez, R. Sader, and H.-F. Zeilhofer, to appear in *Proc. 24th CADFEM Users' Meeting* 2006.
2 S. Mori, M. Endo, T. Obata, T. Tsuno, K. Susumu, and S. Tanada, Eur Radiol. 2006 Mar 28.
3 Amira™ – Advanced 3D Visualization and Volume Modeling, www. Amira-vis.com.
4 D. Stalling, M. Westerhoff, and H.-C. Hege, in *The Visualization Handbook*, Edited by C. D. Hansen and C. R. Johnson, No. 38, 749-67, 2005.

Analysis of Tumor-Influenced Respiratory Dynamics Using Motion Artifact Reduced Thoracic 4D CT Images

René Werner[1], Jan Ehrhardt[1], Thorsten Frenzel[2], Wei Lu[3], Daniel Low[3] and Heinz Handels[1]

[1] Department of Medical Informatics, University Medical Center Hamburg-Eppendorf, Germany
E-mail: rwerner@uke.uni-hamburg.de
[2] Hermann-Holthusen Institute for Radiotherapy, AK St. Georg Hospital, Hamburg, Germany
[3] Department of Radiation Oncology, Washington University School of Medicine, St. Louis, MO 63110, USA

Abstract. Respiratory motion represents a major problem in radiation therapy of thoracic tumors. Methods for compensation require comprehensive knowledge of underlying dynamics. In this study, motion of thoracic anatomical and pathological structures in lung cancer patients was analyzed using motion artifact reduced 4D CT data sets of high temporal and spatial resolution. Motion artifact reduction was achieved by applying an optical flow based 4D CT reconstruction method. Motion analysis especially focuses on inner organ and tumor mobility and the interrelation between tumor / inner organ motion and chest wall motion. Trajectories of tumor mass centers and organ specific landmarks were determined and analyzed. To study chest wall motion a non-linear registration based point tracking scheme was applied to compute trajectories of points on the chest wall skin. The interrelation of chest wall and tumor / inner organ motion was investigated using methods of multivariate statistics. Results show that, for instance, tumor motion patterns differ noticeably between the patients; a dependency between tumor motion and tumor location seems apparent. The correlation of tumor motion and motion of chest wall points depends on the patient breathing pattern (e.g. abdominal or chest wall breathing). Thus, skin regions which are suitable for prediction of tumor motion differ between the patients.

1. Introduction

Radiation therapy aims at high tumor control and low normal tissue complication probabilities. Therefore, the dose distribution to be applied should be restricted to tumorous tissue as far as possible, avoiding especially organs at risk and hence minimizing treatment related complications. But, in current clinical practice radiation therapy is based on 3D imaging and consequently it suffers from missing information regarding organ and tumor mobility. According to international guidelines (ICRU reports [1]) motion related uncertainties in tumor shape and location shall be accounted for by adding safety margins to the Clinical Tumor Volume (i.e. the tissue volume that contains the demonstrable extent and location of the malignant growth and microscopic malignant disease [1]). Thus, the volume

to be irradiated is increased, which in turn increases the volume of normal tissue exposed to high dose. Consequently, the likelihood of normal tissue complications becomes larger.

In radiation therapy of thoracic tumors motion related uncertainties with respect to tumor shape and location are mainly caused by respiration. To overcome above-mentioned problem one has to explicitly account for respiratory motion. But, implementation and optimization of such techniques (e.g. real-time tumor tracking) require comprehensive knowledge of underlying dynamics. Accordingly, this paper deals with analysis and visualization of respiratory motion of anatomical and pathological thoracic structures (e.g. lungs and lung tumors). It especially aims at accurately modeling the spatiotemporal behavior of target volumes and organs of risk and finding reliable, easily observable biometric parameters which offer the opportunity to predict the tumor position with respect to the breathing phase. Therefore temporally and spatially high-resolved 4D CT data sets of lung cancer patients were generated. Data acquisition was done at the Department of Radiation Oncology, Washington University School of Medicine, St. Louis [2]. Resulting spatiotemporal CT segment sequences were reconstructed into the 4D CT images to be analyzed using a motion artifact reducing optical flow based reconstruction method developed at the Institute of Medical Informatics, Hamburg [3].

2. Materials and Methods

4D CT Data Acquisition and Reconstruction. Seven lung cancer patients were examined with a 16-slice CT scanner operated in cine-mode. The scanning of patients 1 to 4 was based on following protocol: The scanner was operated in 12-slice-mode. The scanning spatial resolution was between 0.78 x 0.78 x 1.5 mm and 0.98 x 0.98 x 1.5 mm. 16 to 19 couch positions were investigated to ensure adequate coverage of the thorax. For each couch position 15 scans were acquired continuously. Synchronized spirometry was used to assign each scan to a point of the breathing cycle. The patients were instructed to breathe naturally. The protocol for scanning patients 5 to 7 were modified slightly: The patients were scanned using 16-slice mode and acquiring 25 scans for each couch position. The scanning spatial resolution was chosen to be 0.98 x 0.98 x 1.5 mm. For further data acquisition details see [2, 4].

Resulting spatiotemporal series of CT data segments were reconstructed into high quality 4D CT images. A 4D CT image represents a series of 3D CT data sets, each of them covering the whole thorax and corresponding to a point of the patient's breathing cycle. Due to the different number of scans per couch position the 3D CT image series to reconstruct were chosen to consist of 10 images (patients 1 to 4) and 14 images (patients 5 to 7), respectively. In both cases the points of the patient breathing cycles corresponding to the 3D CT images were selected to sample the breathing cycle equidistantly in time. 4D CT reconstruction was accomplished by an optical flow based method. For further details with respect to the reconstruction method applied see [3]. In comparison to other reconstruction approaches [2] motion induced artifacts were reduced significantly, providing a better foundation for high-quality motion analysis.

Motion Analysis. To analyze and visualize respiratory dynamics, the skin, lungs, and lung tumors were segmented in the 4D CT images applying volume growing techniques, morphological operators and interactive correction. Lung segmentation results were used to perform a fractional air content analysis [4]: In order to validate the quality of the reconstructed 4D CT images the air volume in the lungs was calculated for each 3D image of the series. These values were correlated with the tidal volumes chosen for reconstruction of the 3D images considered. A strong correlation was seen as a prerequisite for high-quality motion analysis.

Given a strong correlation, organ motion was studied by tracking both organ specific landmarks and organ surface motion. Landmarks were determined interactively and resulting three dimensional trajectories were analyzed due to maximum excursion. Tracking organ surface motion was accomplished using an optical flow based point tracking scheme which consists of two main steps: First, a non-linear registration method [5] is applied to estimate the optical flow [6] between consecutive time frames of the 4D CT data set. The optical flow poses a dense vector field which establishes an approximation to the motion field. The second step consists of computing the trajectories of the points considered: Given a point $\boldsymbol{x}=\boldsymbol{x}_0$ of a 3D CT image at some initial time t=0, its position at the consecutive time step t=1 is assumed to be $\boldsymbol{x}_1=\boldsymbol{x}_0+\boldsymbol{u}_0(\boldsymbol{x}_0)$. Thereby, $\boldsymbol{u}_0$ represents the estimated motion field with respect to the 3D CT images corresponding to t=0 and t=1, which means $\boldsymbol{u}_0(\boldsymbol{x}_0)$ represents the displacement of the voxel containing $\boldsymbol{x}_0$ with respect to the temporal interval t=0..1. Iterating this procedure for following time steps results in the point trajectory $\boldsymbol{x}_0, \boldsymbol{x}_1, \ldots, \boldsymbol{x}_n$ searched for. Taking end-expiration as initial time frame, we applied this scheme to each point of a surface model of the organ considered which has been generated using segmentation results and Marching Cubes. Results were used, for instance, to identify organ surface regions of large motion.

Special attention was paid on studying tumor mobility and its interrelation to respiratory driven skin motion. The overall tumor mobility was visualized by computing 3D appearance probabilities: For each voxel the portion of the breathing cycle was determined during which the voxel was classified as tumorous tissue. Moreover, the trajectory of the tumor mass center was computed. Motion extent and hysteresis in craniocaudal (CC), anteroposterior (AP) and lateral (right-left, RL) directions were analyzed. Based on tumor mass center trajectories the interrelation between tumor motion and respiratory driven skin motion was investigated using methods of multivariate statistics: Assuming the trajectories of the points of the chest wall surface model to be regressors and the tumor mass center trajectory to be the regressand a multivariate regression was performed. Thus, for each point of the chest wall surface model the value of the minimized residual represents the summed squared difference (SSD) between the tumor trajectory observed (i.e. the tumor mass center trajectory) and the tumor trajectory predicted where the prediction is based on the trajectory of the point considered. Consequently, the value of the minimized residual was interpreted as a measure for appropriateness of the chest wall point considered in order to predict the tumor position with respect to the state of breathing of the patient. In this context, low residual values indicate high appropriateness.

Table 1. Maximum respiratory driven excursion of thoracic structures (right and left hemidiaphragm, lung tumor; additionally the tumor localizations are given) of the patient data sets considered.

data set	left hemidia-phragm motion	right hemidia-phragm motion	tumor motion	tumor location
#1	10.5 mm	19.0 mm	6.0 mm	left lung, near the heart
#2	17.1 mm	13.4 mm	12.0 mm	right lower lung lobe
#3	10.5 mm	20.8 mm	2.2 mm	right upper lung lobe
#4	19.4 mm	10.3 mm	6.7 mm	left upper lung lobe
#5	18.1 mm	22.8 mm	2.2 mm	right upper lung lobe
#6	24.0 mm	34.5 mm	19.5 mm	left lingual
#7	19.9 mm	22.8 mm	6.0 mm	near right hilum

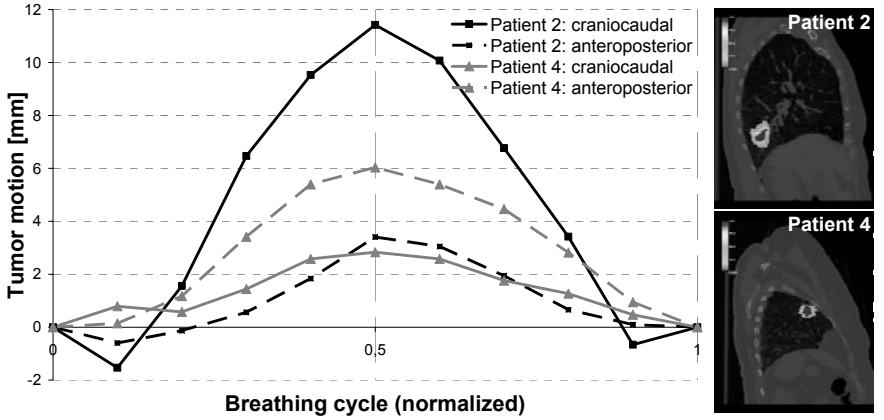

Fig. 1. Motion of the tumor mass center in patient data sets 2 and 4 in craniocaudal and anteroposterior direction. Right: Appearance probabilities of the tumors.

3. Results

For the patient data sets considered, air content analysis showed excellent correlation (Pearson's correlation coefficients from 0.960 to 0.991) between calculated air content in the lungs and spirometry values. This supports that the reconstructed 4D CT data sets are suitable for motion analysis of high accuracy.

Landmark motion amplitudes are similar with reported figures from other studies [7]. Exemplarily, maximum displacements of left and right hemidiaphragm are listed in table 1, showing values from 10.3 to 20.8 mm. Studying motion of organ surfaces and the chest wall skin, respectively, shows that respiratory driven motion is dominated mainly by diaphragmatic breathing. But, differences with respect to motion extent and motion patterns (e.g. the ratio of rib cage to diaphragmatic expansion) are noticeable (fig. 2). Analysis of tumor mobility yields that amount and direction of tumor motion differ obviously between the patients.

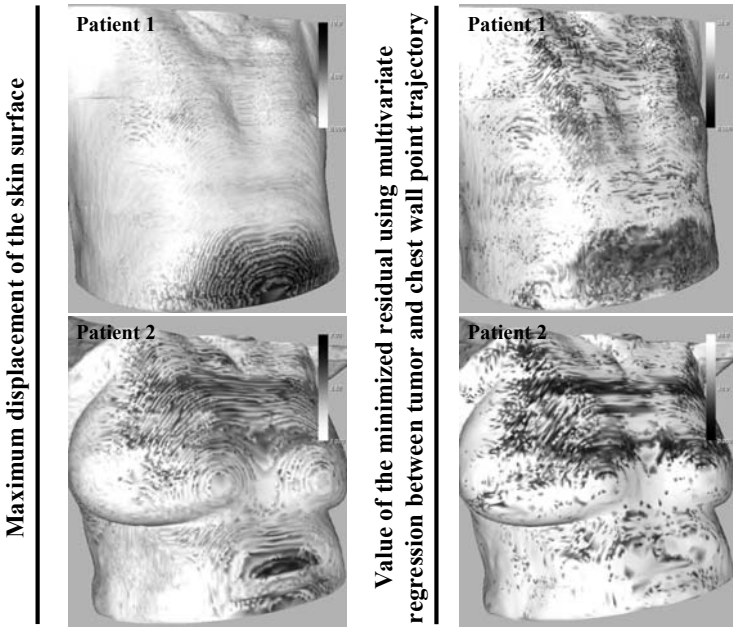

Fig. 2. Left: Visualization of the maximum displacement of the skin surface during the respiratory cycle for patients 1 (top) and 2 (bottom). Black: displacements >10 mm (patient 1) and >7 mm (patient 2). Right: Performing a multivariate regression (i.e. assuming a linear relationship) of tumor (regressor) and skin point trajectories (regressands) the SSD distance between the tumor trajectory observed and the tumor trajectory predicted is displayed. White: residual values >35 mm² (patient 1) and >80 mm² (patient 2).

A dependency between the motion of the tumor and its location seems apparent. Localization and maximum excursion of the tumors of the patients considered are listed in table 1. Furthermore, in fig. 1 3D tumor appearance probabilities and projections of the tumor trajectories in craniocaudal and anteroposterior directions are presented for patient data sets 2 and 4; lateral excursions are negligible small. The tumor location in these data sets varies noticeably – patient 2: tumor near the diaphragm, patient 4: tumor near the upper anterior chest wall – which holds for the tumor motion patterns, too. The tumor of patient 2 shows a motion amplitude of more than 12 mm in predominantly craniocaudal direction whereas the tumor of patient 4 moves predominantly in anteroposterior direction with a motion amplitude of about 7 mm. Thus, motion pattern of the tumor in patient 2 seems to be strongly influenced by movements of the nearby diaphragm whereas the motion pattern of the tumor in patient 4 seems to be driven especially by respiratory rib cage deformation.

Studying the interrelationship among tumor motion and skin movements mainly mirrors above results: Interpatient variations are apparent. Regions on the skin which are suitable to predict tumor motion differ between the patients. Thereby, it can be stated that large motion of the skin points poses a prerequisite for tumor motion prediction. Thus, areas which were identified as suitable for

tumor motion prediction widely agree with skin regions of large motion (fig. 2) – which vary among the patients as stated above. Among the data sets considered the suitability for tumor motion prediction does not depend on the tumor to surface point distance.

4. Discussion and Conclusions

Understanding respiratory motion of thoracic structures will valuably complement radiation therapy of thoracic tumors. We presented methods for the analysis of respiratory dynamics. The methods were applied to artifact reduced 4D CT data sets of high temporal and spatial resolution of lung cancer patients.
Tumor and organ displacements are similar to reported figures from other studies [7]. But, amount and direction of tumor motion differ strongly between the patients. A dependency of the tumor motion patterns on the tumor localizations and the patient's individual breathing patterns seems to be apparent. However, results are based on a data set of only seven patients and should be verified using an increased data set. Moreover, first steps were done to investigate the interrelation between tumor motion and respiratory driven skin motion. This especially aims at validating the possibility and accuracy of tumor motion prediction from external, non invasive tracking data. Therefore methods of multivariate statistics were used. Though still in a preliminary state of validation, this approach seems to be promising. In contrast to other approaches like computing correlation coefficients with respect to 1D signals (point excursions, displacements in AP, RL, CC direction, etc.; e.g. [8]) multivariate statistics take into consideration all three components of the point trajectories. Thus, thought is given to the nature of breathing caused motion of thoracic structures which generally occurs in all three spatial dimensions.

Further research especially aims at increasing the number of patient data sets. Based on the increased data set attention will be paid on identifying typical breathing patterns among the patients. Resulting information shall be used to develop a model for breathing motion which can be personalized easily with respect to patient-specific aspects like tumor localization and breathing pattern, and, hence, can be used for radiotherapy planning, delivery and verification.

References

1 International Commission on Radiation Units and Measurements (ICRU), *Prescribing, recording, and reporting photon beam therapy (supplement to ICRU report 50)*, Bethesda, Md., 1998.
2 D. A. Low et al., Medical Physics **30**, 1254, 2003.
3 J. Ehrhardt et al., Medical Physics, 2007 (accepted).
4 W. Lu et al., Medical Physics **32**, 890, 2005.
5 J. P. Thirion, Medical Image Analysis **2**, 243, 1998.
6 B. Horn and B. Schunck, Artif Intell **17**, 185, 1981.
7 K. Langen and D. Jones, Int J Radiat Oncol Biol Phys **50**, 265, 2001.
8 N. Koch et al., Int J Radiat Oncol Biol Phys **60**, 1459, 2004.

3D-CSC: A General Segmentation Technique for Voxel Images with Application in Medicine

Frank Schmitt, Patrick Sturm and Lutz Priese

University Koblenz-Landau, Campus Koblenz, D-56072 Koblenz, Germany
E-mail: {fschmitt, sturm, priese}@uni-koblenz.de

Abstract. The successful 2d segmentation method CSC has recently been generalized to 3d. We shortly introduce the concept of both 2D- and 3D-CSC and present two use cases (classification of MR brain data and CT bone data) which demonstrate that analysis of segments generated by the CSC allows high quality classification of 3d data by relatively easy means.

1. Introduction

Due to techniques like MRI, CT and PET real 3d images are available for diagnostics, but for physicians it is often still easier to do their diagnostic on 2d slices of a 3d image rather than to take the complete 3d information into account as visual analysis of 3d data is hard for humans. However, automatic segmentation methods don't have this restriction, they should use the 3d information to increase their segmentation quality.

The 2d color structure code (short CSC) invented by Rehrmann and Priese in 1993 [1] is a very fast and robust region-growing segmentation method steered by a hexagonal island hierarchy first introduced by Hartmann [2]. Because of its efficiency and quality, the University Koblenz and the research center Juelich generalized the CSC to 3d in a cooperated project[*]. This generalization is not trivial as it leads to some geometrical difficulties. In section 2 we give some further details of the 2d CSC and its generalization to 3d. In section 3 we present an MR brain image classifier and a CT bone classifier which are both based on the 3d CSC. Those two use cases show that high quality classification of 3d images can be achieved by relatively easy means if a robust segmentation method is applied beforehand.

2. The 2D and 3D CSC

The 2d CSC is a hierarchical region growing method for gray and color images. The region growing process is steered by a hierarchy of overlapping islands defined upon a hexagonal topology of pixels. Seven pixels, one center pixel and its six equidistant neighbors, form an island of level *0*. Each second pixel of each

[*] This work was supported by the BMBF Berlin under grant 01/IRC01B (research project 3D-RETISEG)

second row is chosen as a center pixel. Any island of level *0* overlaps exactly with six other island of level 0 within one common pixel. Assume that islands of level *n* are already defined. Two islands of level *n* are neighbors if they overlap in a common island of level *n*–1. An island *I* of level *n*+1 is formed by a center island I_0 of level *n* and its six neighbor islands $I_1,...,I_6$. *I* is the parent island of $I_1,...,I_6$ and $I_1,...,I_6$ are the sub-islands of *I*. Again each second island of level *n* of each second *macro island row* is chosen as a center. On each level of the hierarchy the overlapping pattern is the same. Figure 1a) illustrates that.

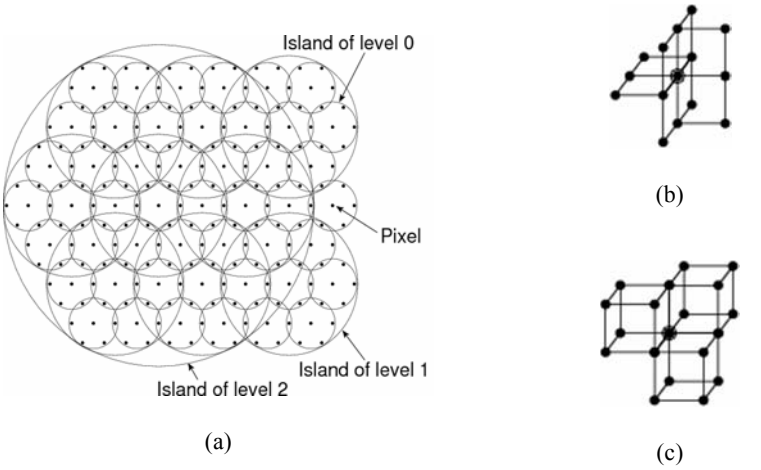

Fig. 1. The hexagonal island hierarchy (a) and two 3d cells S_{15} (b) and C_{19} (c)

The segmentation starts at level *0*. Within any island of level *0* small segments consisting of connected and color similar pixels are detected. Assume that segments of level *n* are already detected within islands of level *n*. All overlapping and similar segments of level *n* within an island of level *n*+1 are merged to a new segment of level *n*+1. In the case that overlapping segments of level *n*+1 are not color similar the common region is separated between the involved overlapping segments. In this paper two gray values are considered to be *(color) similar* if their distance is smaller than a certain similarity threshold *t*.

The first step in generalizing the CSC to 3d is to find a 3d structure which is similar to the hexagonal island hierarchy. The S_{15} structure (see figure 1b), as used in [3], builds up a cell hierarchy that covers nearly all properties of the hexagonal island hierarchy. Unfortunately, the S_{15} cell hierarchy does not fulfill the important density property, i.e. some overlapping cells will not have any common parent cell. Thus already detected segments cannot be merged. This will lead to an "artificial" over-segmented image. An alternative to S_{15} is the C_{19} structure (see figure 1c), proposed first by Sturm [4], which builds up a cell hierarchy that is dense but has more complex relationships between island levels which complicates implementation. Because of the density of the C_{19} cell hierarchy a segmentation will not lead to an artificial over-segmentation.

3. Applications of the 3D-CSC

As stated before, the 3D-CSC is an general segmentation method, applicable to 3d images from various sources. Here we want to present two use cases, where relatively easy post-processing steps allow us to transform the segmentation results of the CSC into robust and correct classifications.

3.1 MRI Brain Analysis

The first use case is the classification of T1-weighted MR brain images from healthy human brains into white matter, gray matter and non-brain. In recent years this task has been studied by different groups in detail. However we are able to compete with those methods [8], using our general CSC and some rather general and well know pre- and post-processing steps described below.

Preprocessing. To smooth the image within homogeneous regions and enhance the contrast at their borders, a single iteration of the 3D-Kuwahara filter [5] is applied. Also the so called bias field is corrected by applying a modified version [6] of the method presented in [7].

Histogram Analysis. The histogram of an MR brain image normally consists of 5 peaks representing the 5 tissue classes *background*, *CSF*, *gray matter*, *white matter* and *fat* (listed from dark to bright). We approximate the histogram by a sum of five weighted gaussian curves (gaussian mixture model). The intersection point of each two adjacent gaussian curves defines a threshold. The resulting 4 thresholds separates the gray value space into 4 disjoint classes.

CSC. We now apply the 3D-CSC on the corrected image. There is no static similarity threshold which works well for all MR images, instead it dependents on the gray value range in the image and the remaining intra-tissue intensity inhomogeneity after bias correction. We therefore automatically derive the similarity threshold from the mode representing the background peak as its standard deviation carries information about those image characteristics.

Morphology. The segments computed by the 3D-CSC are classified into gray matter, white matter and non-brain by classifying their mean gray value into the gray level classes estimated during histogram analysis. However, in MR brain images often small gray value bridges between anatomically different tissue classes occur. Because of this, the CSC normally generates some segments which include both gray matter and non-brain tissue. We break those bridges using binary morphology. A binary image B is generated where segments classified as either white or gray matter form the foreground and all others the background. On this image we apply an morphological erosion using a small ball structuring element SE to destroy the gray value bridges. The biggest connected component B' in the resulting binary image is an eroded brain mask. The conditional dilation $(B' \oplus SE) \cap B$ of B' with structure element SE restores the border of the brain which was lost during erosion. However, some smaller structures might still be missing. We reconstruct most of them by applying four conditional dilations with a ball structuring element of radius one. The results are binary masks of brain and non-

brain. The distinction between gray and white matter inside the brain is known from the histogram analysis before.

Evaluation. We classified images from eight healthy human brains using our methods and the publicly available state of the art brain analysis software package SPM [1]. The classification results have been evaluated by medical experts using a catalog of quality criteria for evaluation of MR brain images developed at the German Armed Forces Central Hospital (GAFCH), Koblenz. The results [8] of the evaluation show that our methods is able to compete with SPM which uses a priori knowledge about the anatomy of the human brain and which has been developed especially for this task.

3.2 CT Bone Classifier

The second use case is the classification of CT images [9] into the classes *background*, *soft tissue*, *enclosed air* and *bones*. Especially the automatic classification of bones from CT images is an important task in medical diagnostic, surgery planning and visualization. Often the classification of bones in CT images is done just by global or local thresholding methods. Such methods work well as the gray values of a CT image are calibrated (Hounsfield scale) and every tissue has a defined gray value range. Unfortunately, the gray level ranges of tissues may overlap. Thus some spatial and topological information should be used to distinguish different types of tissue.

Segmentation. One essential step of our CT bone classifier is the CSC segmentation. As CT images are calibrated we choose a fixed small similarity threshold. A preprocessing step like the Kuwahara filter may be used to reduce noise, but however this might destroy very thin bone structures especially in low resolution images. The segmentation results in many homogeneous segments which have to be classified by using topological information.

Topological Classifier. The histogram of a CT bone image has three significant peaks corresponding to the classes (from dark to bright) *air* (this means *background* and *enclosed air*), *soft tissue* and *bones*. By using the histogram analysis method from section 3.1 the histogram of the original CT image is approximated by a sum of three gaussian curves. The means of the 3 gaussians μ_{air}, μ_{soft}, μ_{bone} and the intersection points of two adjacent gaussians $\nu_{air,soft}$, $\nu_{soft,bone}$ are used in the classification. The classification starts with a first background classification. All dark segments, that touch the image border, are classified as *background*. We call a segment *dark* if its mean gray value is darker than $\nu_{air,soft}$. Small clusters of dark segments that are enclosed by only *background* segments are also classified as *background*. The largest segment with a mean gray $g \in [\nu_{air,bone}, \nu_{soft,bone}]$ is classified as *soft tissue* as in CT images the *soft tissue* is very homogeneous. According to their mean gray value all unclassified segments between background and soft tissue are clustered with the standard fuzzy C-Means technique into the classes *possibly background* and *possibly soft tissue*. All segments marked as *possibly background* (resp. *possibly soft tissue*) that have at least one already

classified *background* (resp. *soft tissue*) segment in their neighborhood are reclassified as *background* (resp. *soft tissue*). During this step, applied as often as possible, *background* and *soft tissue grow* toward each other. Sometimes there are segments that are marked as *possibly soft tissue* and that are surrounded completely by *background* segments. These segments will be classified as *background* as we assume that *soft tissue* is one connected region in the image. At this classification stage there are only unclassified segments left which are enclosed within the up to now classified soft tissue. These segments should be classified as bones if they are very bright or as enclosed air if they are very dark. Therefore a histogram over all voxels, that are either unclassified or classified as soft tissue, is computed. The histogram is divided up into a dark and bright part. Both parts are analyzed resulting in two thresholds separating soft tissue from bones (T_{bone}) resp. enclosed air (T_{encair}). All segments with a brighter (resp. darker) mean gray value than T_{bone} (resp. T_{encair}) are classified as bone (resp. enclosed air). All remaining segments are classified according to their neighbor segments. They will inherit the class of their most gray similar neighbor segment.

Evaluation. The method was quantitative evaluated on a CT image of rat. For this image a manual classification into the classes background, bone tissue and body (body=soft tissue+enclosed air) was done by the Research Center Juelich. The evaluation turned out that 95.97% (resp. 98.23%) of bone tissue (resp. body) was recognized correctly. Only 9.20% (resp. 1.17%) of the pixels classified as bones (resp. body) were misclassified.

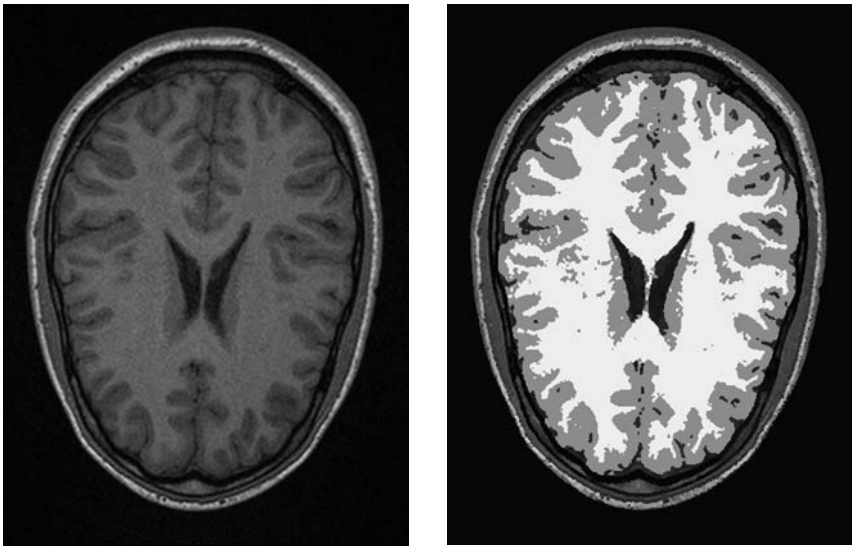

(a) (b)

Fig. 2. Classification result of MR brain image. (a) Slice of an 3d MR image. (b) Slice of the classification of the MR brain image. White Matter is represented in white and gray matter in gray.

4. Conclusion

We have shown that a high quality 3d segmentation allows high quality 3d classification in different application scenarios. The presented applications demonstrate that the task of assigning 3d data into several classes is simplified by applying a segmentation beforehand. After a segmentation we are able to work on relatively big, contiguous regions, which integrate voxels with a common property and don't have to examine each voxel on it's own. Even though we analyse medical data in both presented use cases, similar approaches can be carried out in other applications as well. For example we were able to adapt our CT classifier with extremely little effort to detection of enclosed air in 3d scans of plastic foil.

References

1 V. Rehrmann, and L. Priese. Fast and robust segmentation of natural color scenes, in *Proc. 3rd Asian Conference on Computer Vision (ACCV'98)*, LNCS 1351, 598–606, 1998.

2 G. Hartmann. Recognition of hierarchically encoded images by technical and biological systems. *Biological Cybernetics*, Vol. 57, 73–84, 1987.

3 J. Vogelbruch, P. Sturm, R. Patzak, L. Priese, and H. Halling. 3D Segmentierung mittels hierarchischer Inselstrukturen, in *Bildverarbeitung für die Medizin 2002*, 241, 2002.

4 L. Priese, P. Sturm, and H. Wang. Hierarchical cell structures for segmentation of voxel images, in *Image Analysis: 14th Scandinavian Conference (SCIA 2005)*, LNCS 3540, 6–16, 2005.

5 M. Kuwahara, K. Hachimura, S. Eiho, and M. Kinoshita. Processing of ri-angiocardiographic images, in *Digital Processing of Biomedical Images*, 187–202, 1976.

6 H. Wang, P. Sturm, F. Schmitt, and L. Priese. Improved Segmentation of MR Brain Images Including Bias Field Correction Based on 3D-CSC, in *VISAPP 2006 - First International Conference on Computer Vision Theory and Applications 25 - 28 February,* 2006.

7 U. Vovk, F. Pernus, and B. Likar. MRI intensity inhomogeneity correction by combining intensity and spatial information, in *Physics in Medicine and Biology*, Vol. 49, 4119–4113, 2004.

8 L. Priese, F. Schmitt, P. Sturm, H. Wang, R. Matern and R. Wickenhöfer. Analysis of Brain Images Using the 3D-CSC Segmentation Method, in *Medical Imaging 2006: Image Processing, 11-16 February 2006*, Vol. 6144 of Proceedings of SPIE, 1303–1313, 2006.

9 P. Sturm, L. Priese, and H. Wang. A CSC Based Classification Method for CT Bone Images, in *Third International Symposium on 3D Data Processing, Visualization and Transmission (3DPVT 2006)*, 2006.

An Algorithm for Automatic Stitching of CR X-ray Images

Markus Gramer[1], Wilfried Bohlken[2], Bernd Lundt[2], Thomas Pralow[2] and Thorsten M. Buzug[3]

[1] RheinAhrCampus Remagen, Department of Mathematics and Technology, Germany
[2] Philips Medical Systems, GXR-Development, Hamburg, Germany
[3] Institute of Medical Engineering, University of Luebeck, Germany

Abstract. Stitching of X-ray images is of interest in cases of disease patterns like scoliosis [1] or asymmetries in the structure of leg bones. Under those circumstances a measurement of the leg or the spine as a whole is necessary. As these objects of interest exceed the maximum size of the normal radiographic image recording device, two or three radiographs have to be joined. The manual procedure typically is very time consuming and needs training. Therefore, an algorithm has been developed that stitches the radiographs automatically. In the project presented here, it has been concentrated on CR images (CR = computed radiography).

1. Introduction

In CR-systems cassettes are used containing an X-ray sensitive imaging plate which consists of a phosphor film that can be stimulated by photons. To achieve the desired imaging size of the radiographs two or three cassettes are laid together such that the image plates overlap in a small area (Fig. 1.). Within the imaging procedure these plates are exposed at once and read out successively. In the end, two or three single digital images are obtained [2] (Fig. 2.).

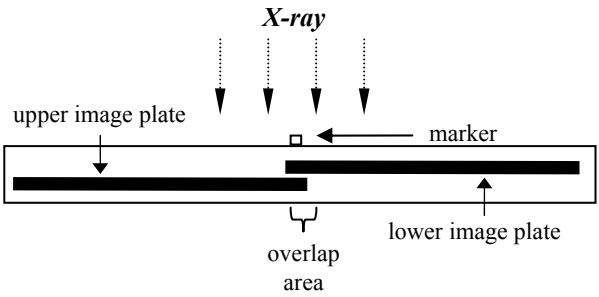

Fig. 1. Position of the image plates during exposure

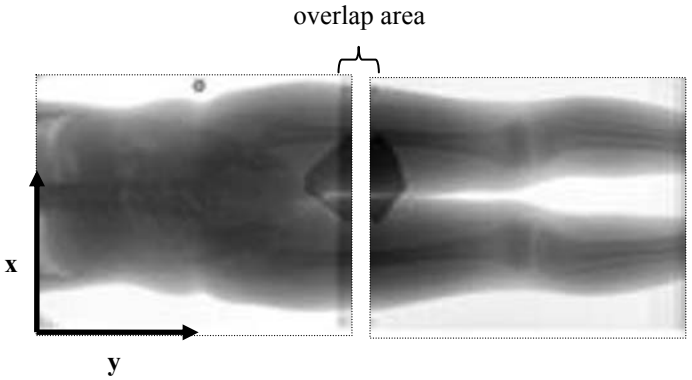

Fig. 2. Two digital images to be stitched

The overlap area is characterised by a grey-value step in one of the images to be stitched (Fig. 3.). This results from decreasing intensity in the image which is placed under the other during exposure. In both digital images cross-shaped markers can be found which are placed on the cassettes inside the overlap area. In that way, the border between the overlap and the remaining image is well defined. However, with this information only an approximate orientation of the two images can be obtained. This is due to e.g. mechanical tolerances of the reader device leading to cropped images and plates that are rotated against each other.

Fig. 3. Enlargement of the upper image containing the overlap

2. Experimental Methods

Edge Detection. In a first step of the edge detection, the area with the overlap edge is divided in *x*-direction in parts of constant size so called sub-views. The sub-views are summed up in *x*-direction and the resulting arrays are differentiated. The maximum of the derivative corresponds to the *y*-location of the desired edge in this sub-view.

Doing this for all sub-views, a set of (x,y) coordinates are obtained characterizing the edge. The edge line is calculated via an iterative weighted linear regression (Fig. 4.). To eliminate outliers - caused e.g. by implants - the points are weighted with the fourth root of the above received maximum. After each iteration the three points with the largest distance to the fit are rejected by weighting with zero.

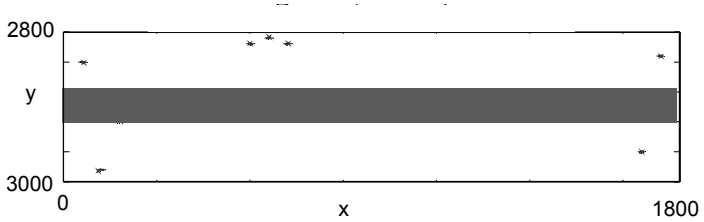

Fig. 4. Linear fit (straight line) to the detected edge points (stars). Points with large distance to the fit are rejected.

Rotation and Shift. In a next step the upper image is rotated in the way that the overlap edge becomes horizontal. As mentioned in the introduction this rotation probably does not correspond to the exact rotation angle, but for satisfying results of the following correlation it is necessary to minimize the rotation angle between the images. After this rotation the distance to the bottom of the image is defined as the temporary y-shift. To calculate the x-shift, sub-views extracted from the overlap area of the lower and upper image, respectively, are created. Note that the sub-view of the upper image should not contain the edge. The sub-views are summed up in y-direction and the resulting arrays are differentiated. The differentiation of the arrays is used because areas containing structure like bones or markers are shown more distinctively there and therefore lead to better results.

Finally, the arrays (shown in Fig. 5.) are correlated according to equation (1). The position of the correlation maximum [3] corresponds to the temporary x-shift.

$$c(x_0) = \frac{\sum_x \left[\left(i(x) - \bar{i}\right) \cdot \left(k(x - x_0) - \bar{k}\right)\right]}{\sum_x \left[i(x) - \bar{i}\right]^2 \cdot \sum_x \left[k(x - x_0) - \bar{k}\right]^2} \qquad (1)$$

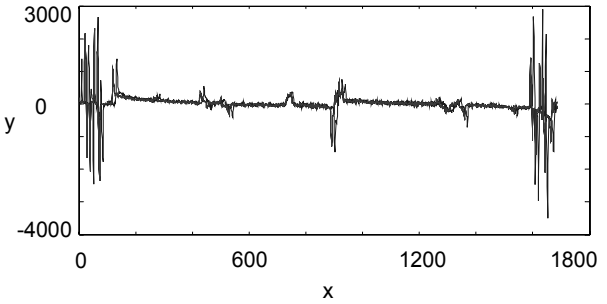

Fig. 5. Arrays of the upper and the lower sub-view that are correlated to determine the x-shift.

Correction of Rotation Angle and *y*-Shift. For re-adjustment fiducial markers or other structures are helpful. Therefore, both sub-views of the step before are divided in *x*-direction into parts with constant size. Each partition is summed up in *x*-direction and consecutively differentiated.

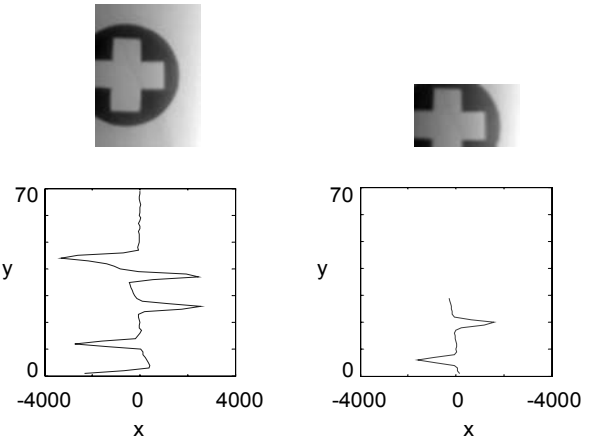

Fig. 6. Sub-view partition of the lower (left) and of the upper image (right) with their corresponding arrays that are correlated to determine the correction of the *y*-shift

Finally, each sub-view partition of the upper image is correlated with its corresponding part of the lower image sub-view. The location of the maximum correlation leads to the *y*-shift for this partition.

The received deviation results are sorted according to a quality measure which contains the corresponding correlation maximum and the *y*-energy. To obtain the *y*-energy the two sums of the squared arrays used for the correlation are multiplied. The deviation with highest quality is now compared to deviations whose quality measure is at least to a quarter of the highest one. To decide if the

images have to be corrected by another rotation two criteria are considered in the following: The first criterion is the difference between the deviations which must be at least two pixels to make sure that there still exists a rotation angle. The second criterion is the distance between the two parts of the deviations which must be at least the *x*-size of five parts by this way it is checked if the angle could be calculated with acceptable accuracy.

If these criteria are fulfilled the lower image is rotated by the arc tangent of the quotient of the deviation difference and the *x*-distance between the two parts. In both cases the image are shifted by the deviation with the highest quality.

Metric. To evaluate the results of this algorithm they are compared to a reference dataset. This is obtained with a program for manual stitching in which the user can shift one image in *x*- and *y*-direction until the outlines in the upper and lower image of a marker are lying upon each other. This has to be done for two different positions, so that the program can calculate a shifting vector including the rotation.

The elements of this vector are the *x*-shift, the *y*-shift and the α-shift, whereas the last one describes the maximum *y*-shift caused by the rotation angle.

A resulting image is evaluated as "good" when according to equation (2) the norm of the difference between the algorithm vector and the reference vector is smaller then ten pixels. With a pixel size of 150 µm this corresponds to a distance of 1.5 mm.

$$d = \sqrt{(\Delta x_{\text{Shift}})^2 + (\Delta y_{\text{Shift}})^2 + (\Delta \alpha_{\text{Shift}})^2} \tag{2}$$

3. Results and Discussion

Tested on a database of 342 pairs of images the algorithm presented here achieves a performance of about 85%. The as "good" declared images show no visible deviations as you can see in Fig. 7 exemplarily.

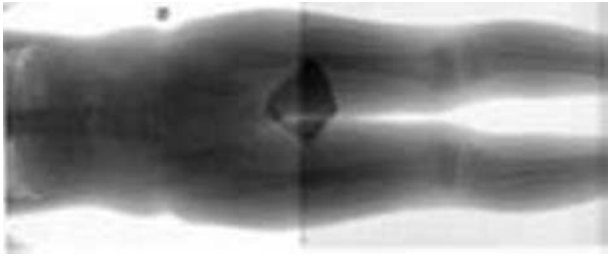

Fig. 7. Resulting image of the stitching algorithm

Regarding the single steps of the algorithm the edge detection and the *x*-shift calculation seem to be very robust and yield to insignificant small deviations. Tested on other datasets the algorithm sometimes shows larger deviations especially caused by a wrong rotation. Though the deviation of the rotation angle is comparable sized, the resulting deviations are dependent on varying image size and therefore worse in larger image dimensions.

In the case that a marker is positioned out of the exposed area, only one marker is visible. Then for manual stitching it often is difficult to find another distinctive structure especially in *y*-direction. The consequence is an imprecise angle, which has a significant effect on images with a large *x*-size.

4. Conclusions

As future improvement, the correction of the rotation angle may could be replaced by a more robust procedure. This could base on the correlation with a sub-view that rotates around the point with maximum quality.

A further point for improvements could be the software for manual stitching, this may could be realized by the opportunity to rotate one image around an arbitrary point. Consequently only one marker would be necessary. Also break conditions and a metric should be implemented that considers the size of the pixels and the images to make it independent from these dimensions.

References

1 L. Kaufman, L. Berliner and S. Kreang-Arekul, *Scoliosis evaluation by direct digital radiography and computerized post-processing*, Journal of Digital Imaging, 2002, pp. 270-274.

2 P. Dewaele, P. Vuylsteke, S. Van de Velde and E. Schoeters, *Full-leg/fullspine image stitching: a new and accurate CR-based imaging technique*, in: K. M. Hanson (ed.), Medical imaging 1999: Image Processing, SPIE **3661** (1999) pp. 131-138.

3 J. V. Hajnal, D. L. G. Hill and D. J. Hawkes (Eds.), *Medical Image Registration*, CRC-Press, 2001.

Topology Correction in Brain Segmentation Using a Multiscale Algorithm

Lin Chen and Gudrun Wagenknecht

Central Institute for Electronics, Research Center Juelich,
Juelich, Germany
E-mail: l.chen@fz-juelich.de
E-mail: g.wagenknecht@fz-juelich.de

Abstract. This is a new method for automatically correcting the spherical topology of a human brain segmentation under any digital connectivity. Topological correctness is important because it is an essential prerequisite for brain atlas deformation and surface flattening. A morphological multiscale approach which acts on foreground and background simultaneously divides the segmentation into several connected components, and subsequent region growing guarantees convergence to the correct spherical topology. In addition to existing graph-based procedures, this provides an alternate approach which has several advantages, including high speed and ease of operation without graph analysis and changing as few voxels as possible.

1. Introduction

Reconstruction of the shape of complex anatomical regions such as human brain structures has been a challenging problem. In the acquisition process, noise artifacts from imaging, partial volume effects and intensity inhomogeneities can lead to geometrical and topological errors. Thus, automatic extraction of topologically correct brain structures remains difficult, especially for regions in the cortex.

Several methods for correcting the topology of brain segmentations have recently been developed. Shattuck and Leahy [1] and Xiao Han et al. [2] introduced graph-based methods for topology correction. Shattuck and Leahy examined the connectivity of 2D segmentations between adjoining slices to detect topological defects and minimally correct them by changing as few voxels as possible. Building on their work, Han et al. developed an algorithm to remove all handles from a binary object under any connectivity. Successive morphological openings correct the segmentation at the smallest scale. This method is effective for small handles, but large handles such as ventricles may need to be edited manually. Wood et al. [3] proposed a different approach. Handles in the tessellation are located by simulating wavefront propagation on the tessellation and detected where the wavefronts meet twice. The size of a handle is the shortest non-separating cut along such a cycle, which helps retain as much fine geometrical detail of the model as possible. The region-growing models proposed by Kriegeskorte et al. [4] and Mangin et al. [5] are adopted as topology correction methods. These start from an initial point with the greatest distance from the surface, then grow the point by adding points which will not change the topology.

One drawback is that the result strongly depends on the order in which the points are grown from the set.

The method described here provides a fully automatic topology correction mechanism, thus avoiding tedious manual correction. This approach is novel in that it provides a very fast marching approach, which has several advantages over region growing and graph-based models [1-6], including corrections not being oriented along cardinal axes. It can thus be done under any connectivity in 3D (6, 18, 26) without graph analysis and changing as few voxels as possible.

2. Methods

Some basics of digital topology will be given here (see Bertrand [7] for details). The initial segmentation is a 3D binary digital image composed of a foreground object X and an inverse background object $\underline{X}$. Following the conventional definition of adjacency, three types of connectivity are considered: 6-, 18- and 26-connectivity. For example, two voxels are 6-adjacent if they share a face, 18-adjacent if they share at least an edge, and 26-adjacent if they share at least a corner. In order to avoid topological paradoxes, different connectivities n and $\underline{n}$ must be used for the foreground and background objects. This leaves four pairs of compatible connectivities: (6, 18), (6, 26), (18, 6) and (26, 6). Considering a digital object, the calculation of two numbers (criteria) is sufficient to check if the modification of one single point will affect the topology. These topological numbers introduced by Bertrand [7] are an elegant way to classify the topology type of a given voxel.

Definition 1 (topological numbers). The topological number of a point **x** relative to the foreground object **X** is the number of n-connected components in the corresponding geodesic neighborhood [7], termed $T_n(\mathbf{x}, \mathbf{X})$. The topological number of a point **x** relative to the background object $\underline{\mathbf{X}}$ is the number of $\underline{n}$-connected components in the corresponding geodesic neighborhood, termed $T_{\underline{n}}(\mathbf{x}, \underline{\mathbf{X}})$.

Definition 2 (simple point). For a point **x**, it is a simple point if and only if $T_n(\mathbf{x}, \mathbf{X}) = T_{\underline{n}}(\mathbf{x}, \underline{\mathbf{X}}) = 1$. Adding or removing a simple point will not change the topology of the object.

There are two types of filters which can be used to correct the topology of an input segmentation: foreground filters and background filters. Handles removed by a background filter correspond to tunnels filled in the foreground object. In the algorithm described here, both filters are applied at continuously increasing scales until all topology errors are fixed. Figure 1 shows the idea behind the development of each step. Morphological opening is used as a multiscale analyzer to detect handles at different scales. Figure 1b shows how the opening operation divides the foreground object into two classes.

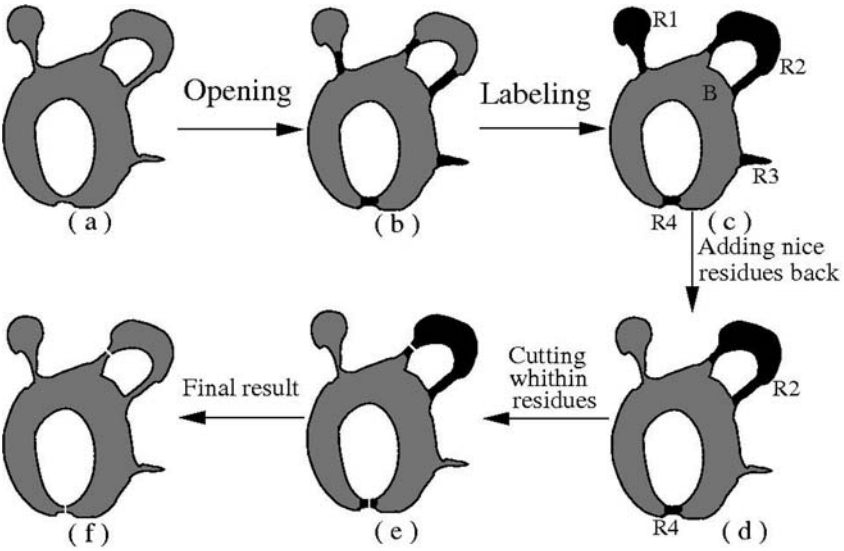

Fig. 1. Illustration of the basic idea behind the approach.

Points in the largest connected component of the opened object are called ***body*** points, and points in the residue of the original object and body set are called ***residue*** points (Fig. 1c). Thus, the body set consists of one and the residue set of many connected components. This method was designed to transfer as many points as possible from the residue back to the body component. Unfortunately, with complex shapes as in brain segmentations, opening can create "false" tunnels in the body component. Thus, the body set must be grown without introducing handles, but with filling the "false" tunnels. This can be done by only adding ***nice*** points [2] (Fig. 2a) from the residue set. The nice points can be detected like the ***simple*** points defined in [7].

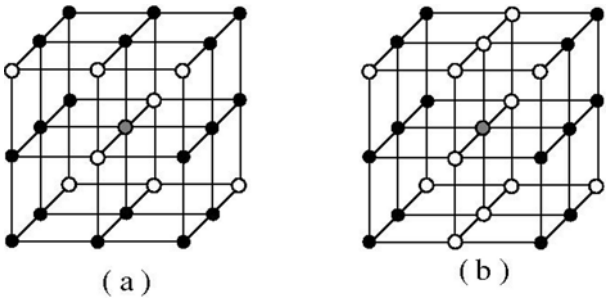

Fig. 2. Topological criterion of a nice point. In each figure, the gray point represents the residue point under consideration, the dark points body points, and the white points background points. Here, the gray point is a nice point in (a) but not in (b).

Definition 3 (nice point). If a point is added from background object $\underline{\mathbf{X}}$ to foreground object **X**, it is a nice point if and only if $T_{\mathbf{n}}(\mathbf{x}, \mathbf{X}) = 1$. In other words, the **n**-components of **X** are preserved and no handles/tunnels are created in **X**.

The concept of nice points is necessary because morphological opening can introduce tunnels in the body, and these should be filled. Since a simple point must satisfy two topological criteria – $T_{\mathbf{n}}(\mathbf{x}, \mathbf{X}) = T_{\underline{\mathbf{n}}}(\mathbf{x}, \underline{\mathbf{X}}) = 1$ – and a nice point only needs satisfy one, $T_{\mathbf{n}}(\mathbf{x}, \mathbf{X}) = 1$, adding a simple point to the body preserves the topology of the body, but adding a nice point allows a tunnel in the body to be filled.

Morphological opening was done by using a distance transform. The distance of a point within the object to its surface is the length of the shortest line to the surface. The chamfer distance transform is a quick way to calculate this distance. The morphological opening sequentially applies morphological eroding and morphological dilating: The erosion with a threshold **r** removes all points of the object with a distance less than or equal to **r**. This distance is the scale **r**. The dilation adds all points of the background with a distance $\leq \mathbf{r}$ to the surface after the erosion.

If there are regions within a handle which cannot fit a ball of radius **r**, then the handle can be broken into body and residue parts. However, on a complex shape like a brain segmentation, the opening cannot break all handles within the scale **r**. Figure 3a-b shows that the handle is not broken by the opening operation with the smallest radius 1. In order to break all handles within the scale **r,** erosion is followed by a special dilation procedure by adding only nice points with the background distance $\leq \mathbf{r}$**.** The breaks can then be preserved during the dilation (Fig. 3c).

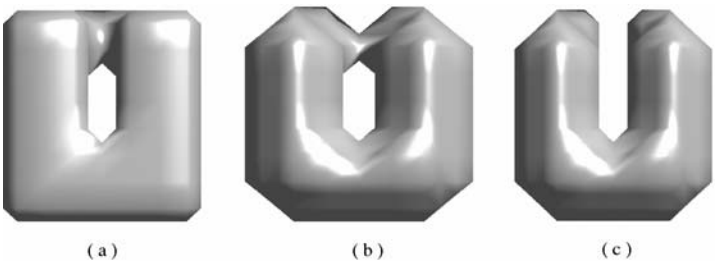

Fig. 3. Opening operation with preservation of breaks.

For each residue component **R**, we performed the following iterative procedure:

Residue Component Expansion (RCE).

1. Recursively add each point of **R** to the body set **B** if it is a nice point. If each point of **R** is added back, then stop; otherwise, go to step 2 (Fig 1d).

2. From **R**, find the set **S** of residue points that are adjacent to the body **B**.

3. Find and label all connected components in the set **S.**

4. Take the largest connected component **L**.

5. For each point of **L**, add it back to **B** if it is a nice point (Fig. 1d-f).

6. If no points can be added back, stop; otherwise, go to step 2.

Note that in steps 2-5, the largest set of border points (if there are nice points) is added to the body. The criterion of nice points ensures that the final residue points are not added back to the body and are positioned at the thinnest parts of the handles.

This method, after **RCE,** however, can result in unexpected large changes to the volume, as shown in Figure 4. Unfortunately, these steps cause a component to be disconnected from the body (Fig. 4b).

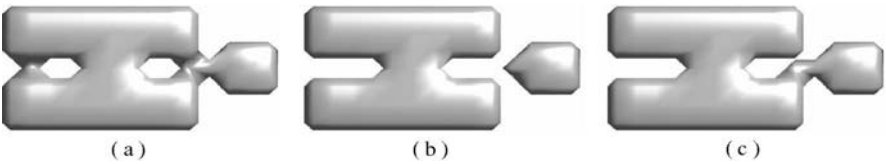

Fig. 4. Attachment of a disconnected component.

One way for attaching a disconnected component is dilating the component with the smallest radius to attach itself to the body, and doing the **RCE** again to find another correction (Fig. 4c). Disconnected components can be found by checking their topological criterion since they do not connect to the body.

3. Results and Discussion

This method was applied to the white matter segmentation of the ICBM-labeled anatomical template [8] and three white matter segmentations of the Brain Web data sets [9]. The volumes are defined on a 1 mm isotropic voxel grid in space, with dimensions 181x217x181.

Each segmentation thus labeled was tessellated after topology correction and the genus verified using the Euler formula. In each case, the method produced a final volume with a tessellation whose Euler characteristic equals 2, which is homeomorphic with a sphere. Figure 5 shows one part of a WM/GM surface before and after topology correction.

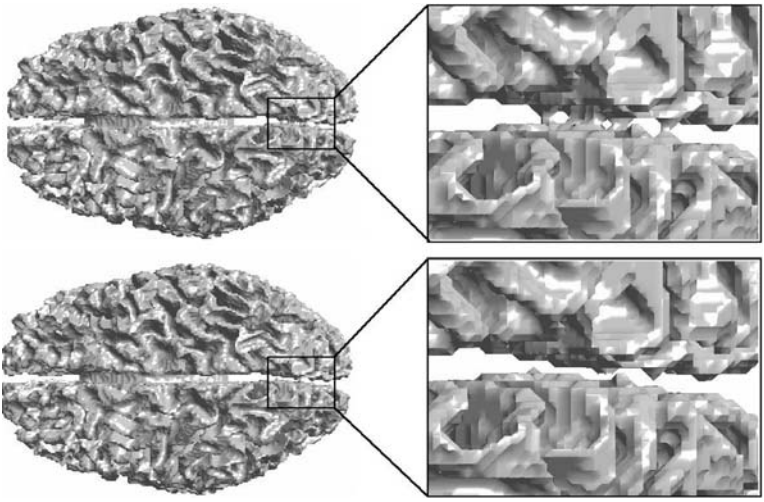

Fig. 5. WM/GM surface before and after topology correction.

Processing time for each segmentation was within 1 minute on an Intel Pentium IV 3 GHz CPU. This algorithm changed between 0.076% and 0.1% of the voxels for each of the 4 volumes, with an average of 0.09%.

4. Conclusions

It was experimentally shown that this topology correction algorithm works well on brain volumes with a large number of handles. It also works well with different connectivities (6, 18, 26).

References

1 Shattuck and Leahy, in *IEEE Trans. Med. Imag.,* Vol. 20, (11), 1167-1177, 2001.
2 X. Han, C. Xu, U. Neto, and J. L. Prince, in *IEEE Trans. Med. Imag.,* Vol. 21, (2), 109-121, 2002.
3 Z. Wood, H. Hoppe, M. Desbrun, and P. Schroeder, in *ACM Transactions on graphics.,* Vol. 23, 190-208, 2004.
4 Kriegeskorte and Goebel, in *NeuroImage,* Vol. 14, 329-346, 2001.
5 J.-F. Mangin, V. Frouin and I. Bloch and J. Regis and J. Lopez-Krahe, in *Journal of Mathematical Imaging and Vision,* Vol. 5, 287-318, 1995.
6 Lin Chen and Gudrun Wagenknecht, in *MICCAI 2006,* Vol. 2, 316-323, 2006.
7 G. Bertrand, in *Pattern Recognition Letters,,* Vol. 15, 1028-1032, 1994.
8 http://www.loni.ucla.edu/ICBM/ICBM_BrainTemplate.html
9 http://www.bic.mni.mcgill.ca/brainweb/

Intensity-Modulated Radiation Therapy – Quality Assurance with the Mutual Information Index (MI)

Astrid Brendemühl[1], Stefan Ostrowitzki[2], Uwe Altenburger[2], J. Christoph Haller[2], Jürgen Ruhlmann[1,2] and Thorsten M. Buzug[3]

[1] RheinAhrCampus Remagen, Department of Mathematics and Technology, Germany
E-mail: abrendem@rheinahrcampus.de
[2] Medizin Center Bonn, Germany
[3] Institute of Medical Engineering, University of Luebeck, Germany

Abstract. Radiation therapy is an important method of treating neoplastic diseases with ionizing radiation. For this treatment electromagnetic or corpuscular (electrons, protons, neutrons) radiation is used which causes ionization and excitation in the energy absorbing tissue [1]. The conventional radiation therapy applies beams with a homogeneous dose distribution or uses wedges to optimize the dose to the cancerous volume and prevents high doses in organs of risk (e.g. rectum, eye). The individual treatment plan is developed by the physicist who sets the beams in a treatment planning system which calculates the dose distribution. With the objective of ideal adjustment to the cancerous volume it is advantageous to use the "inverse treatment planning" and the intensity-modulated radiation therapy (IMRT) especially for concave volumes. Therefore, the dose distribution is designated by the physicist and the individual treatment plan is developed including the number and direction of beams and the multi-leaf collimators' position. Due to the fact that the leaf collimator conforms the dose to the tumor volume IMRT protects the adjacent tissue as good as possible. Before an application of IMRT starts a quality assurance is important. It is especially necessary to check the accuracy of the system including the data of the planning software.

1. Introduction

Intensity-modulated radiation therapy (IMRT) is a new method of radiation therapy. In contrast to the conventional radiation therapy the dose distribution is modulated. This means that a multi-leaf collimator (MLC) limits the beam and conforms it to the tumor volume. The leafs move through the beam and a different dose distribution results as shown in Fig.1.

Fig. 1. Schema of intensity modulated radiation therapy [1]

With IMRT an almost arbitrary dose distribution is available. In IMRT there are many influencing factors that may cause faults e.g. the MLC position accuracy or the algorithms for treatment calculation. The quality measurements for IMRT are performed with film dosimetry, a slab phantom and a self-designed prostate phantom. After matching the film data to the planning data a calculation of mutual information index (MI) is executed. The mutual information index expresses the relation between these two data sets. Valued at the MI you can make a statement about the conformance of the data sets.

2. Prostate Phantom

As mentioned is the section before a prostate phantom was constructed of acrylic glass. Its dimensions and physical properties are adapted to a real prostate patient. Especially the density (~1,1 g/cm³) and form are similar to an adult abdomen.

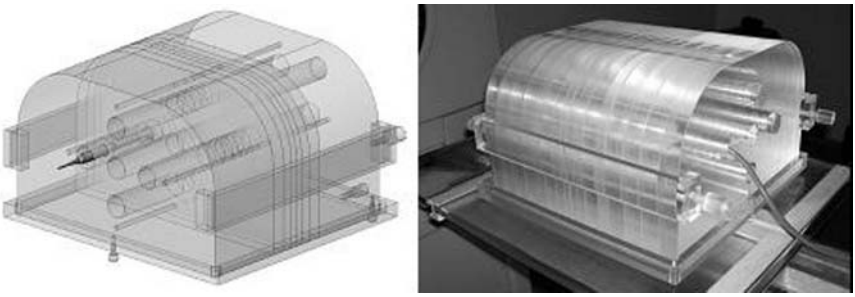

Fig. 2. Self-designed prostate phantom

Moreover it opens the opportunity to measure doses by film and ionization chamber. For film and ionization chamber measurements exist different phantom layers. The layers for using the film have only four bore holes to mark the film orientation. The layers for chamber measurements show five additional bore holes which are positioned near to a planned prostate volume. Thereby it is possible to measure explicit dose values in several positions. The bore holes which are not used during a measurement are compensated by pins.

3. Quality criteria

After matching the two data sets it is necessary to find criteria to evaluate the correspondence of film and plan. Additional to profiles, difference images and contours the mutual information index is used.

Mutual Information Index. One criterion to assess the accurateness of the dose distribution is the mutual information index *I*. It regards pixel values as stochastic variables.

The standardized histogram represents the probabilities $p\{i\}$ of the discrete pixel value *i*. This probability is directly related to the size of an image region. With these probabilities it is possible to calculate the marginal entropy which means the quantitative measure of uncertainty of an image, i.e.

$$H(M) = -\sum_{m \in M} p\{m\} \cdot \log(p\{m\})$$
$$H(N) = -\sum_{n \in N} p\{n\} \cdot \log(p\{n\}) \quad (1/2)$$

Matching two images and the regions that occur within is a tool to define how well those images match. To do so, it is necessary to calculate a 2D histogram and consequently the probabilities $p\{i,j\}$ of pixel value pair *i* and *j*. With $p\{i,j\}$ the joint entropy of the images can be evaluated straight forwardly

$$H(N) = -\sum_{n \in N} \sum_{m \in M} p\{m,n\} \cdot \log(p\{m,n\}) \quad (3)$$

The joint entropy is a minimum if both images are aligned optimally. However, the problem is that matching of two images cannot be done by using the joint entropy alone, because *H*(*N*) is minimized when the overlap contains least information. This occurs in case of the smallest overlap because only the overlapping information is used for calculation.

In this case the mutual information index must be used to solve the problem. It uses the marginal entropies of both images and the joint entropy to define the ideal matching.

$$I(M;N) = H(M) + H(N) - H(M,N) \quad (4)$$

The mutual information index (MI) must be maximized to achieve an ideal registration. The outcome of this is that the overlap of both images must be maximised which is in accordance with the marginal entropies. However, at the same time the joint entropy must be minimized which essentially indicates an optimal overlay.

The problem is that the MI is not independent of overlap. That means that overlapping irrelevant areas influence the match [3]. Therefore, a normalization of the MI is helpful. The result is called normalised mutual information index (*NMI*)

$$NMI(M;N) = \frac{H(M) + H(N) - H(M,N)}{H(M,N)} \tag{5}$$

The normalized mutual information index (5) is chosen as criterion to decide on the compliance of planning and measured film data. Measuring of conventional radiotherapy assess an $NMI \approx 0{,}3$ and it is estimated as a target value.

Profile. In addition to *NMI*, profiles are used to investigate the data compliance. First of all a calculation of usual profiles is applied to the data sets and the difference of plan and film profile.

However, a problem is that low dose areas point out higher deviations caused by dispersion and film sensitivity. Thus, a conventional calculation of deviation would lead to unacceptable values. Consequently, the dose deviation is estimated on the basis of percent profiles, which means that the plan matrix is normalized to the planned iso-centre dose and the film doses are standardized to the measured iso-centre dose. Then, the difference of percentage profiles is evaluated. The difference is independent of an exact match of the dose values. The ratio of the dose values to the iso-centre dose is crucial alone.

4. Results

First measurements are carried out with an Kodak EDR2 (sensitivity: 0,3 – 7 Gy) applying an irradiation dose of 1,8 Gy in the iso-centre. The irradiation setup and plan symbolizes a prostate patient. Especially the clinical volumes are adopted from a prostate patient. Hence, the gross tumor volume (GTV) corresponds to a prostate and the organ at risk (OAR) approximates the rectum. Both volumes are idealized.

The planning system calculation results in the following plan matrix. Additionally, the scanned film data is shown in Fig. 3.

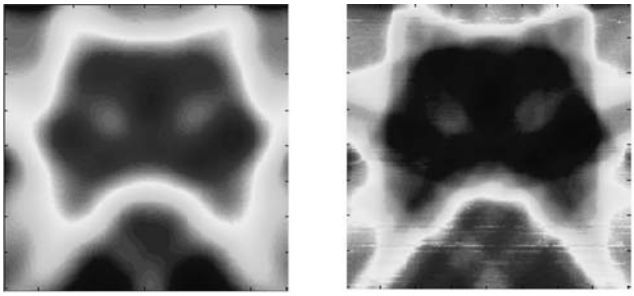

Fig. 3. Resulting images after matching both datasets a) planning data b) measured film

Subsequently the normalized mutual information index is calculated and results in *NMI* = 0,289. Due to the fact that the assessed value is close to the desired target value (NMI ≈ 0.3) the plan is acceptable.

The next step comprises calculating the film dose values. To do so, a grey value dose look-up table is used which is explicit applicable to Kodak EDR2. Furthermore, the planning data is normalized to the dose value of the iso-centre which is located in the middle of the planning data.

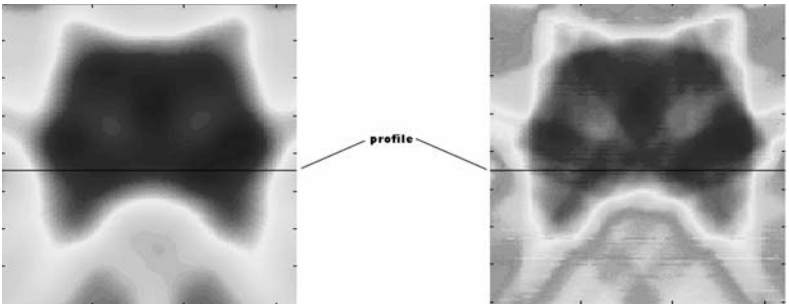

Fig. 4. Resulting images after dose calculation both datasets a) plan b) film

Additionally, profiles are calculated to evaluate the accurateness of the film data to the planning data. The dose values are normalized to the iso-centre dose (1,8 Gy) and afterwards the difference of the percents profiles is calculated. This difference is a percentage view based on the iso-centre dose. In Fig. 5 a typical profile – as indicated in Fig. 4 – is shown.

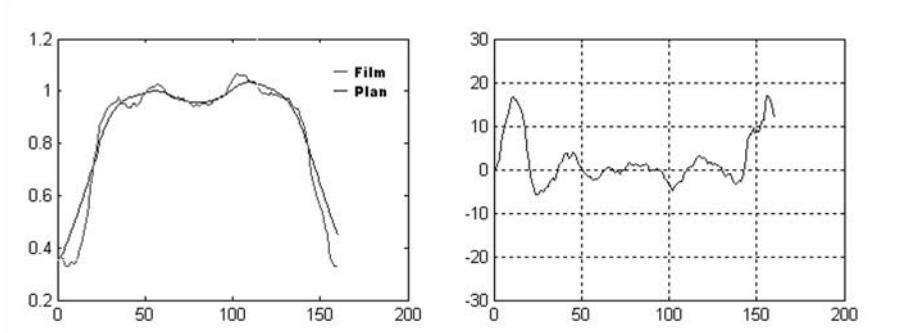

Fig. 5. a) Resulting profiles b) percentage difference based on iso-centre dose

As mentioned before, it is necessary to identify high deviations. In the case of Fig. 5 high positive deviations at the object boundaries are due to different boundary gradients of both images and can therefore be categorized as uncritical. A negative deviation, which means a higher irradiated dose than was planned, would be more relevant than a lower dose outside the gross tumor volume.

5. Conclusions

First measurements have shown that a quality assessment based of the normalized mutual information index (*NMI*) gives acceptable results. The prostate phantom opens the opportunity to verify the planning and film data in different layers. Various quality criteria are used to decide whether a planned irradiation is practicable or not. However, in our experiments a decision on the matching quality of the data sets could not be drawn on one criterion alone. At all times the irradiation plan should be adapted to the accelerator especially with reference to the number of segments per beam and minimum segment size.

References

1 J. Engler, G. Hartmann, R. Hofmann, J. R. Hörandel, *Flüssigkeitsionisationskammern in der Strahlentherapie*, Nachrichten Forschungszentrum Karlsruhe 2/2001, 201.

2 C. Studholme, D. L. G. Hill, D. J. Hawkes, *An ovelap invarant entropy measure of 3D medical image alignment*, Pattern Recognition 32 (1999), 71.

Image Registration of Structural and Physiological MR Images of Abnormal Anatomy

Andreas Mang[1,2], Oscar Camara[2], Gisele Brasil Caseiras[3], William R. Crum[2], Julia A. Schnabel[2], Thorsten M. Buzug[1], John Thornton[3], H. Rolf Jäger[3] and David J. Hawkes[2]

[1] Institute of Medical Engineering, University of Luebeck, 23538 Luebeck, Germany
E-mail: buzug@imt.uni-luebeck.de
[2] Center for Medical Image Computing, Department of Medical Physics and Bioengineering, University College London, London WC1E 6BT, UK
E-mail: d.hawkes@ucl.ac.uk
[3] Institute of Neuroradiology, Lysholm Department of Neuroradiology, University College London, London WC1N 3BG, UK
E-mail: pa_yousry@ion.ucl.ac.uk

Abstract. This study applies image registration techniques to combine functional and structural information derived from multi-modal magnetic resonance imaging in patients diagnosed with brain gliomas. The images vary substantially in resolution, signal-to-noise ratio, information content and field of view and therefore pose a challenging registration problem. Specific protocols have been designed for each registration task, with careful selection of critical parameters and appropriate pre-processing. In addition, we have developed a visual assessment protocol to evaluate the accuracy of the proposed methods. Preliminary results suggest that registrations errors are below the functional image resolutions, thus achieving sub-voxel accuracy.

1. Introduction

Perfusion weighted (PW) and diffusion-weighted (DW) magnetic resonance imaging (MRI) provide complementary information about physiological parameters of brain tumors such as glioma. The full assessment of glioma for staging, therapeutic planning and treatment response relies on such functional information in addition to traditional structural imaging. The use of DW- and PW MRI in tumor assessment is done on the basis of regional cerebral blood volume (rCBV) and apparent diffusion coefficient (ADC) maps [1], which represent functional information computed at each voxel. Combining these maps with the information from T1-weighted structural MRI is potentially very helpful since it localizes areas of high cellularity and vascularity which can be markers of high tumour activity. Potential applications are to improve the classification of gliomas; as an imaging marker for treatment response and also to guide biopsies.

Image registration is a powerful methodology which can be used to transform image data to a reference space, A variety of automated rigid and affine registration methods have been extensively studied in the past [2]. However, the

particular registration task of aligning images with glioma is very challenging since the images contain large areas of pathology, vary substantially in resolution, signal-to-noise ratio and information content, and are likely to contain motion artifacts and distortions. Although standard techniques may still be applicable, we would expect the results to be more sensitive to parameter choices than some simpler (eg. intra-modal) applications and that some pre-processing of the data may be necessary. The main contribution of this work is therefore the design/specification of a registration protocol for the alignment of rCBV and ADC maps with structural T1-enhanced MR images. In addition, we have developed a visual validation protocol to estimate the registration accuracy obtained with the presented methodologies.

2. Materials

At our institution, patients with glioma were followed, and radical intervention was usually delayed until the glioma transformed from low to high grade. Images of 14 patients who had initially low-grade glioma were acquired every 6 months within a period of 2-5 years [3]. For each patient, the following image volumes have been acquired (see Fig. 1): DW MRI 0.039± 0.005mm 0.039± 0.005mm, PW MRI, high-resolution coronal T1-weighted images, axial T2-weighted images, and fast fluid-attenuated inversion recovery (FLAIR) images, along with the derived rCBV and ADC maps. Voxel dimensions for the images used in this study were typically 0.9375mm x 0.9375mm x 1.5mm (T1 enhanced), 1.0156mm x 1.0156mm x 5.0mm (DW) and 2.0313mm x 2.0313mm x 5.0mm (PW).

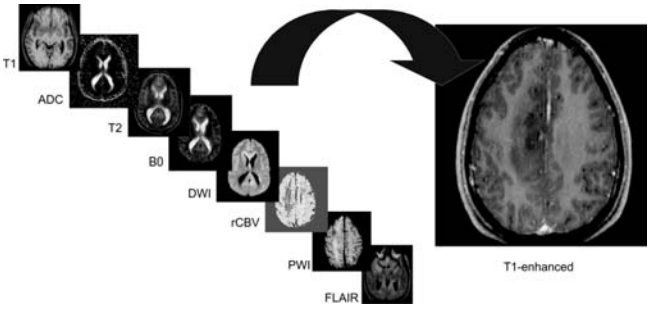

Fig. 1. Magnetic resonance images and derived maps (ADC, rCBV) used in this study.

3. Methods

Although the ultimate goal is to register rCBV and ADC maps, poor signal-to-noise ratio in these derived images makes this a challenging task. Nevertheless, we can take advantage of the inherently perfect registration between these maps and their corresponding PW and DW images (since one is derived voxel-by-voxel from the other) and register the PW and DW image volumes to the T1-enhanced MR volumes. Since images for each patient are acquired in the same session on

the same scanner, we assume that low degrees of freedom (DOF) transformations are sufficient. Such transformation can be rigid to correct for patient movement between scans, or affine to correct for additional geometrical distortions and scaling. Tackling the serial registration problem (across time-points) needs higher order methods and is described in a separate paper [4]. In both cases here, we have employed the linear registration method proposed by Studholme et al. [5], with 3 multi-resolution levels in order to extend the capture range; this is particularly critical in the PW to T1-enhanced registration as the PW data is acquired over a restricted field of view (a "slab") which dramatically affects the shape of the registration cost function. For the registration optimization, we have chosen a maximum of 100 iterations per step size, with 10 steps at each resolution level and an initial step size of 2mm. Normalized mutual information (NMI) is used as the registration cost function because the intensity relationship between registered images is probabilistic [6]. It is computed from a 2D joint intensity histogram with 64 bins in each dimension. Corresponding intensities between images are estimated using tri-linear interpolation. The functional data are the target (reference) images and the structural data are source images (transformed to target space). This approach reduces problems for the visual assessment related to the limited field of view of the PW images and the voxel anisotropy in the DW images. The inverse of the transformation obtained in each case can be applied to the relevant functional data to transform it into the space defined by the T1-enhanced MR image.

Further details on the registration applications, for the DW to T1-enhanced (Section 3.1) and the PW to T1-enhanced (Section 3.2) MRI registration protocols are given in the following.

Diffusion Weighted Data and T1-Enhanced MRI Registration. DW images are likely to contain acquisition-related distortions [7] and vary substantially in resolution with respect to the T1-enhanced datasets. Therefore, an affine registration approach is often used to compensate for some of these distortions. The DW imaging protocol includes a T2- ("B0") weighted MR image incorporated into the standard ADC calculation which we confirmed by experiment was inherently well-registered with the DW images. Therefore we used the T2-weighted image as a target and rigid registration. The images were first blurred with a Gaussian kernel of standard deviation (s.d.d) of half the voxel size in each direction in order to smooth the cost-function and to avoid aliasing effects in the intensity interpolation.

Perfusion Weighted Data and T1-Enhanced Registration. Identifying the optimal set of registration parameters in this registration scenario is more challenging since the PW-MR images have low resolution, poor signal-to-noise ratio and have been acquired within a limited field of view. Thus, they are substantially different from the high resolution volumetric MR data. We assume no change in shape and/or size of the brain and only minimal distortion between the two scans and use rigid transformations.

The PW-MR images are acquired as a dynamic series of transaxial slabs with time-varying information content and possible patient movement (fig. 2). This movement has been corrected by registering all remaining slabs to the first time-

point of the perfusion time series. Furthermore, each slab of this dynamically acquired data provides different information, as can be seen in Fig.2. Therefore, we have also tested the registration protocol using different combinations of acquired PW-MR images as target images. In particular, the analysis is performed on (i) the first acquired slab (before the contrast agent is applied), which contains the most anatomical information within the time-series; (ii) the slab corresponding to the time point of maximal arterial contrast since it represents the image that clinicians are mainly interested in; (iii) an averaged image over the whole time series in order to compensate for noise; (iv) and an averaged image of the slabs from the time of the contrast agent arrival in the artery until its drainage by a vein.

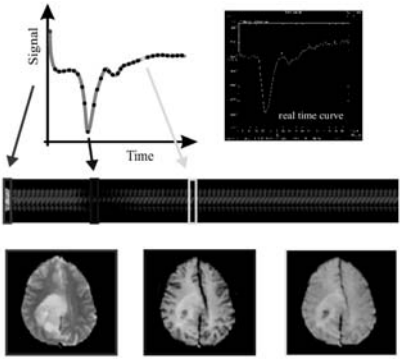

Fig. 2. Scheme representing the dynamic series of transaxial slabs of the perfusion data.

For registration, NMI is a function of voxel intensity probabilities which are approximated from discrete marginal and joint intensity histograms. Prior to the registration, a super-sampling procedure is applied in order to match the resolution of the PW-MR images to the resolution of the T1-enhanced MR images, there-by smoothing changes of the joint histogram with varying transformation parameters and therefore smoothing the registration cost function [6].

4. Visual assessment protocol

A visual assessment validation protocol was designed in which an expert clinical observer identifies a set of well-distributed corresponding anatomical landmarks in the registered images. For this purpose, we have used the 3D Slicer (http://www.slicer.org/). The main challenge in the visual assessment protocol has been to identify real 3D landmarks across all scans. This is particularly difficult in PW-MR images since they have coarse resolution and are acquired only over the locale of the glioma, limiting the possible landmarks. Therefore, it was not feasible to define consistent landmarks for all patients

We have applied the assessment protocol to both registered functional volumes, and to the T1 images, where the latter have been blurred and resampled to match

effective resolution of the functional data, considerably helping consistent landmark identification. Initially, the protocol has been applied for both, the DW and the PW images on a single patient. The number of landmarks found in the perfusion/diffusion data is 7/10 comprised of different sulci and, in the diffusion data, including the lateral ventricles and the middle cerebral artery.

5. Results

A visual inspection suggests a plausible registration in most cases. First quantitative validation results on one illustrative patient case give an average displacement of 1.82 ± 0.83 mm between the DW and T1-enhanced MR landmarks (with a minimum of 1.02 mm corresponding to the lateral intra-parietal and frontal sulci; and a maximum of 3.05 mm corresponding to the inferior segment of the lateral intra-parietal sulcus and the IV ventricle), mostly due to differences in the Z direction. These errors are below the voxel size of the functional images, suggesting sub-voxel accuracy. An example of the PW to T1-enhanced registration is shown in Fig. 3, where we can observe the large translation in the z-axis that has been successfully recovered by the registration algorithm. Applying the validation protocol to the same patient case gives an average displacement of 1.80 ± 0.84 mm between the functional and structural landmarks (with a minimum error of 0.6 mm corresponding to the superior sagital sinus; and a maximum error of 2.84 mm corresponding to the central portion of pars marginalis), again achieving sub-voxel accuracy.

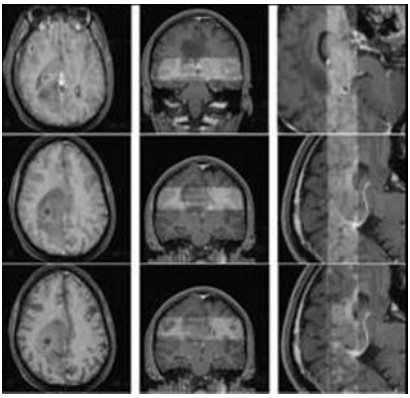

Fig. 3. Example of PW-T1-enhanced registration, showing the unregistered (first row) and the registered (PW images in the middle row and rCBV maps in the bottom row) data.

Visual assessment results show that registration of PW images performs more robustly when using the slab acquired before the application of the contrast agent. This was to be expected, since this dataset contains the most anatomical information in comparison to the rest of the time series. A final example combining the rCBV and ADC maps in the structural reference space is shown in Fig. 4, where features are well correlated.

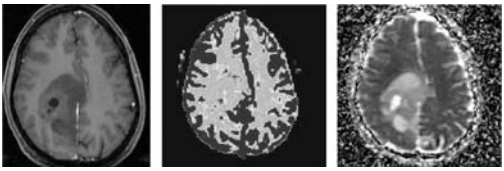

Fig. 4. Structural (left) and functional (rCBV map in the centre and ADC map in the right) data in the same reference space.

6. Conclusions and Future Work

We have presented a protocol for the registration of structural data and information given by the perfusion and diffusion images of glioma patients, which could give a new insight in critical tasks such as treatment response assessment. An initial qualitative assessment has shown good registration results supported by an indicative quantitative assessment in a single patient. Current efforts are focused on obtaining a full quantitative estimation of the registration accuracy applying the developed visual assessment protocol to the whole database of patients.

7. Acknowledgements

We acknowledge the support of the DAAD (AM), the EPSRC GR/N14248/01 and the UK MRC Grant No. D2025/31 (MIAS-IRC) (WRC), the EPSRC GR/S48844/01 (Modelling, Understanding and Predicting Structural Brain Change) (OC) and the EPSRC GR/S82503/01 (Integrated Brain Image Modelling) (JAS). We additionally want to thank Dr. J Rees (Neuro-Oncologist at the ION and Dr. J. Thornton (physicist at the ION).

References

1 S. Cha. in *Am J Neuroradiol*, Vol. 27, 3, 2006.
2 J. V. Hajnal and D. L. G. Hill and D. J. Hawkes, *Medical Image Registration*, CRC Press Inc., ISBN: 0849300649, 2001.
3 H.R. Jäger, et al. in *Am J Neuroradiol*, Vol. 26, 2005.
4 A. Mang et al., *Springer Proceedings in Physics*, 2007.
5 C. Studholme et al. in *Med Phys*, Vol. 24, 1, 1997.
6 J.P.W. Pluim et al. in *IEEE Trans Med Imaging*, Vol. 22, 8, 2003.
7 J.M. Provenzale et al. in *Radiology*, Vol. 239, 3, 2006.

Part III

Computer-Assisted Surgery (MRNV Workshop)

Video Camera Based Navigation of a Laser Beam for Micro Surgery Bone Ablation at the Skull Base – Setup and Initial Experiments

L. A. Kahrs[1], M. Werner[2], F. B. Knapp[3], S.-F. Lu[1,4], J. Raczkowsky[1], J. Schipper[3], M. Ivanenko[2], H. Wörn[1], P. Hering[2,5] and Th. Klenzner[6]

[1] Institute for Process Control and Robotics, Universität Karlsruhe (TH), Germany
[2] caesar (center of advanced european studies and research), Bonn, Germany
[3] Department of Oto-Rhino-Laryngology, Düsseldorf University Hospital, Germany
[4] School of Communication Engineering, Jilin University, China
[5] Institute of Laser Medicine, University of Düsseldorf, Germany
[6] Department of Oto-Rhino-Laryngology, University Hospital Freiburg, Germany

Abstract. The protection of soft tissue structures behind the ablated bone in skull base surgery is mandatory. As the destruction of the membrane lining the inner ear can lead to a damage of organ functions (e.g. deafness or vertigo) a precise bone tissue removal by a laser ablation setup is investigated. For the detection of the boundary between soft tissue and bone the ablation area and rate are monitored by a video camera. Through this the laser is guided across the ablation area by image processing technologies. An aim of this project is a defined, navigated-controlled and laser based bone removal for the future buildup of a robot based surgical laser instrument. This publication describes the setup of our video controlled laser ablation system, initial experiments and results.

1. Introduction

The authors are interested in precise bone cuts [1,2]. At the research center caesar a laser for bone ablation is developed. This technique has several advantages: noncontact cutting, no mechanical stress, no thermal tissue damages and self-stabilizing cutting geometry. In an in vivo study with canines it was shown that laser cuts without carbonization or necrosis are possible [3]. In cooperation with ENT surgeons and computer scientists a robotic system for high precision cochleostomy is established. A hexapod based platform is used for drilling experiments which were done in the designated, preplanned way [2]. These experiments used a conventional drilling tool for precise cochleostomy [4]. With a robot based approach it will be possible to advance the technique of laser bone ablation in a way that the integration into the operating room could be possible [5]. In industrial application coaxial monitoring is used to control laser processes [6]. In this paper our new concept is described to combine these techniques for a micro surgery bone ablation at the skull base.

2. Experimental Methods

The whole laser ablation system contains three main parts: a laser, a scan head and an image processing unit. The used CO_2-laser is a Rofin SC x10, has a wavelength of 10.6µm, an output power range of 5 - 100W, and a pulse frequency of 0 – 100kHz. The ablating micro explosions in the bone are caused by the absorption of the laser power by hydroxyapatite and water. The diameter of the laser beam is adjusted to around 200µm. We used a modified Arges COLIBRI scan head with a step resolution under 100µm covering a working area of 75x75mm² in a working distance of 100mm for positioning the laser beam. The scan head is controlled by a computer using a script language. The programmed pattern removes the bone in sequential scan cycles stepwise layer by layer. Due to the inter individual differences of the anatomic structures (e.g. bone thickness) an optical control of the area and an image processing is necessary. The detected spots where the boundary between soft tissue and bone is reached are excluded from the ablation process. To realize this optical controlled laser guidance a beam combiner enables simultaneously the view with the camera onto the bone and the ablation with the laser beam. We use the Mikrotron MC1303 color camera equipped with a Bayer filter and a resolution of 1280x1024 pixels. An Edmund Optics 7x Precision Zoom Lens is used as objective. With a working distance of 89mm this microscope lens offers a field of view with a diameter of 15mm. The microscope lens has a coaxial light adapter. This provides good light conditions for image processing. The 150W light source is connected to the objective by an optical fiber. The experimental setup is completed with a water spray to cool and to avoid tissue parching. In figure 1 the whole setup is illustrated with the optical paths of the laser and the camera. In industrial material treatments with laser an analogue setup is called coaxial process control [6]. Figure 2 shows the setup we build up in our lab.

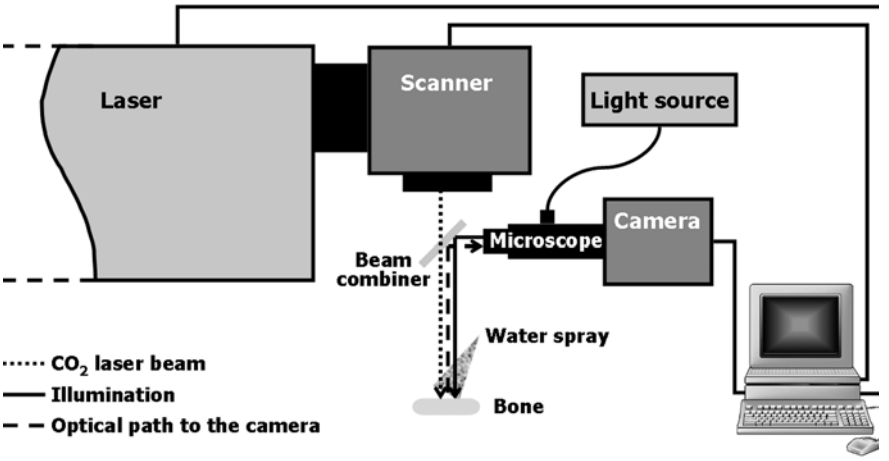

Fig. 1. Sketch of the video camera controlled laser ablation system

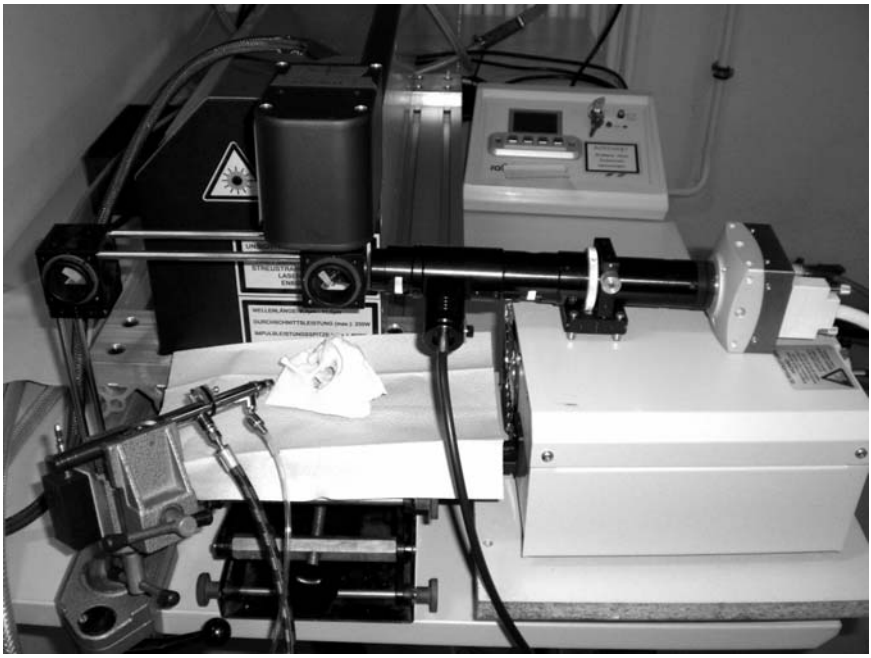

Fig. 2. Photograph of the system setup.

3. Results and Discussion

An experimental setup of the described system was built up. The laser parameters were initially optimized for the microsurgical bone ablation on the lateral skull base. The practically used laser power is in the range of 5 and 12W. The length of the single laser pulses can be set between 50 and 100µs. These parameters lead to an ablation diameter of around 200µm and a depth of around 100µm per pulse. In two initial experiments understanding the key problems of the image processing a series of images of one in vivo (with normal drilling tools) and one ex vivo (with laser osteotomy) human cochleostomy were analyzed. The ex vivo pictures show rough surfaces of the ablated bone (cp. fig. 3). That leads to less energy per laser pulse and more scan cycles and tight ablation paths. The used beam combiner in the ex vivo experiment was not optimal because of its strong wavelength dependency. Converting the in vivo pictures into separate images of the HSI color space (Hue, Saturation, Intensity [7]) shows distinctive areas on the human promontorium (cp. fig. 4).

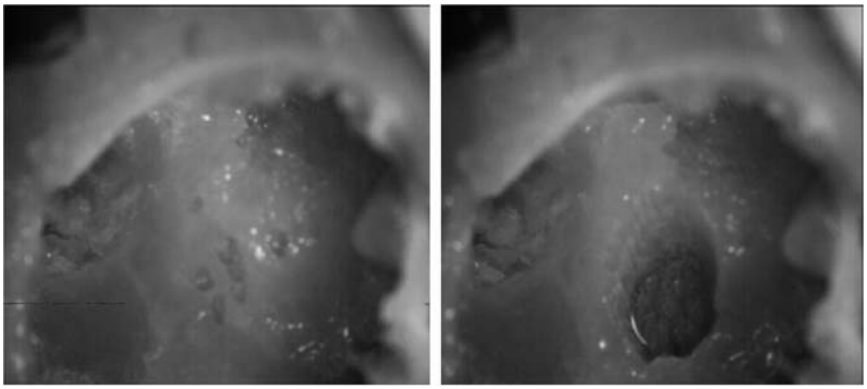

Fig. 3. Ex vivo laser ablation cochleostomy. At the left picture some small holes from single laser shoots can be detected. At the right picture a hole with the diameter of 2mm is ablated (drilled) by the laser.

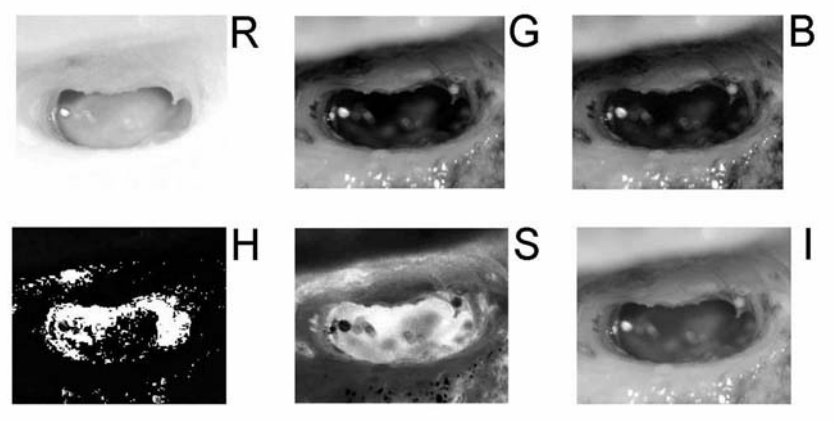

Fig. 4. Split-up into the RGB and HSI color space of a picture from a human promontorium at the skull base.

4. Conclusions

A new beam combiner out of gallium arsenide which fits optimal to the wavelengths of the color camera will be used. The described method of image processing will be the basis for further developments detecting the interface between soft tissue and bone. This technology could enable the development of a new robot based surgical laser instrument for skull base surgery.

Acknowledgements. We would like to thank the German Research Foundation, which supports this project in the frame of the Priority Program 1124 “Medical Navigation and Robotics”.

References

1 M. Ivanenko, M. Werner, S. Afilal, M. Klasing, and P. Hering, in *Medical Laser Application,* Vol. 20/1, 13, 2005.
2 T. Klenzner, C.C. Ngan, F. Knapp, J. Kromeier, K. Körner, A. Aschendorff, J. Raczkowsky, H. Wörn, and J. Schipper, in *Wiener Medizinische Wochenschrift*, Vol. 156/119, 27, 2006.
3 M. Ivanenko, R. Sader, S. Afilal, M. Werner, M. Hartstock, C. von Hänisch, S. Milz, W. Erhardt, H.-F. Zeilhofer, and P. Hering, in *Laser in Surgery and Medicine*, Vol. 37/2, 144, 2005.
4 J. Raczkowsky, J. Schipper, T. Klenzner, C.C. Ngan, K. Körner, and H. Wörn, in *Proceedings of the 20th International Congress and Exhibition Computer Assisted Radiology and Surgery*, 508, 2006.
5 H. Peters, H. Knoop, W. Korb, S. Ghanai, J. Raczkowsky, M. Werner, M. Klasing, M. Ivanenko, S. Hassfeld, P. Hering and H. Wörn, in *Proceedings of the 19th International Congress and Exhibition Computer Assisted Radiology and Surgery*, 1364, 2005.
6 J. Fang, Y. Chen, L. Li, and L. Wu, in *Advanced Materials and Devices for Sensing and Imaging II*, Vol. 5633, 101. 2005.
7 B.V. Dhandra, R. Hegadi, M. Hangarge, and V. S. Malemath, in *Proceedings of the 18th International Conference on Pattern Recognition*, 695, 2006.

Ultrasound Based Navigation System for Minimal Invasive Surgery at the Lumbar Spine within OrthoMIT

Karin Hensel[1], Stephanie Hold[1], Susanne Winter[2], Claudia Dekomien[2], Markus Mildenstein[2], Bernhard Brendel[3], Helmut Ermert[3] and Georg Schmitz[1]

[1] Institute of Medical Engineering, Ruhr-University Bochum, 44780 Bochum, Germany
E-mail: karin.hensel@rub.de
[2] Institut für Neuroinformatik, Ruhr-University Bochum, 44780 Bochum, Germany
[3] Institute of High Frequency Engineering, Ruhr-University Bochum, 44780 Bochum, Germany

Abstract. We present a system to register three-dimensional ultrasound datasets with preoperative CT datasets to support navigated surgery at the lumbar spine, using a registration algorithm based on bone structures. The registration of the coordinates of the patient and the image data is divided into two steps: a rough point-to-point pre-registration and an ultrasound based volume-surface registration. We evaluated three different methods for a pre-registration process in simulation and *in vitro*. The orthogonal *Procrustes* method was compared to the *Downhill Simplex method* with six and four degrees of freedom. The *Downhill Simplex method* with six degrees of freedom provided a precise and robust registration considering misplacements of landmarks on the phantom of up to 56 mm.

1. Introduction

Intraoperative imaging in navigated surgery supports the surgeon's orientation especially during minimally invasive procedures. The position of instruments can be displayed in the preoperative datasets (CT or MRI), and anatomical changes can be visualized during surgery.

Acquiring intraoperative CT or MRI datasets for the registration with preoperative datasets is often associated with high costs, difficult handling, and additional radiation exposure (CT). Due to real time capability and sufficient image quality, ultrasound can be considered as an alternative intraoperative imaging modality for registration.

A system to register three-dimensional ultrasound datasets with preoperative CT datasets to support navigated surgery at the lumbar spine was developed, with the use of a registration algorithm based on bone structures [1]. At first, bone structures are segmented from the preoperative data and fast image processing is applied to the intraoperative ultrasound data. The registration procedure is divided into two steps: a rough point-to-point pre-registration with four landmarks and a precise volume-surface registration (vs-registration) based on image information.

The pre-registration is necessary to find an initial position for the vs-registration, so that the algorithm can work as efficiently as possible. The point-

to-point method has to be performed intraoperatively, so it should be a fast and sufficiently precise process.

The vs-registration is realized by a Covariance Matrix Adaption evolution strategy, which is able to overcome local optima and which shows best results in comparison to other optimization methods [2]. *In vitro* accuracy measurements of the results of the ultrasound based navigation system were carried out by using a phantom consisting of three vertebrae in a water bath (fig. 1). The phantom's drill holes were used as reference points for the localization of the phantom with a conventional and precise point-to-point registration.

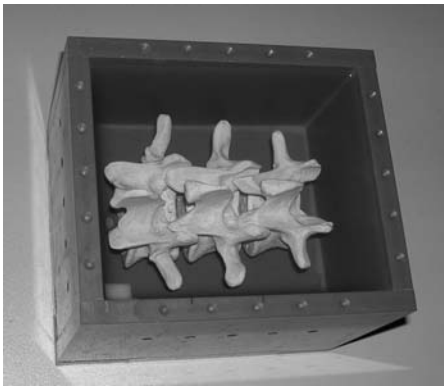

Fig. 1. Phantom for *in vitro* accuracy measurements and pre-registration experiments: three vertebrae in a water bath.

Ultrasound data of the vertebrae was acquired and point-to-point and vs-registrations were carried out. The registration results were compared. The measurements showed, that the registration error is less than 2 mm in all evaluated cases and less than 1.5 mm in 90 % of the cases. The RMSE is 0.9 mm [3].

An *in vivo* evaluation was accomplished by registering CT data of 12 patient vertebrae with the corresponding ultrasound data. For each vertebra the registration was repeated 1000 times with different starting positions. A vs-registration with precision better than 1 mm was considered as correct.

Assuming accuracy of the pre-registration between 0 and 15 mm and a rotation of the surface between 0 and 11°, 98.4% of the trials reached a correct position [2]. In these trials, high precision of the ultrasound registration with a mean error of less than 0.1 mm was measured.

In this paper, we concentrate on applications at the lumbar spine. Three point-to-point registration methods and their ability to provide a precise transformation as a pre-registration for the subsequent vs-registration are compared. In order to simulate a rough intraoperative point-to-point registration, four landmarks were misplaced on the phantom vertebra on purpose. The task for the registration algorithms was to compensate the incorrectly defined landmarks.

2. Experimental Methods

On the bone surface, strong reflection of ultrasound waves occurs. In B-Mode ultrasound the appearance of the bone surface is dependent on the incident angle. Structures below this surface are not visible. Therefore, a vs-registration method is an adequate solution when registering CT with ultrasound datasets. Preprocessing steps have to be carried out for the CT and ultrasound datasets.

Before surgery, the bone surface is extracted from the CT datasets by thresholding. The part of the bone surface visible in the ultrasound data, is estimated considering the restrictions of bone imaging with ultrasound. All surface elements, which are invisible due to specular reflection, are removed [1].

The extracted surface has to be registered intraoperatively with the patient's coordinate system in two steps: a rough point-to-point pre-registration using an infrared optical tracking system (NDI Polaris®) and a vs-registration with ultrasound data. Four landmarks were marked in the preoperative dataset and subsequently in the intraoperative dataset: two at the dorsal process and two on positions that accord with the skin surface above the superior articular processes, as displayed in figure 2.

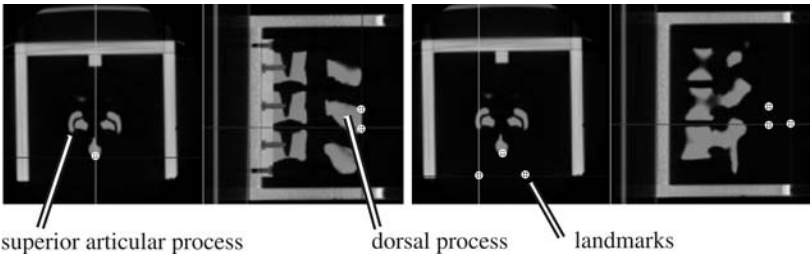

Fig. 2. Four landmarks (displayed white) are marked in the preoperative dataset and on the phantom: two at the dorsal process (left) and two above the superior articular processes (right).

These landmarks would be accessible with a pointer after preparing the patient for the surgery. Especially the landmarks on the dorsal process can be marked intraoperatively with a precision of approximately ± 1 mm. The landmarks on the skin surface have a larger range, since the patient is lying on the back for the CT data acquisition, but is turned around for the spine surgery. Furthermore, the superior articular processes are not visible and the surgeon has to estimate their positions.

Three pre-registration algorithms were evaluated: the orthogonal *Procrustes* method [4], the *Downhill Simplex method* [5] with six degrees of freedom (3 translation directions, 3 rotation angles) and the *Downhill Simplex method* with four degrees of freedom (3 translation directions, 1 rotation angle).

The solution of the orthogonal *Procrustes* problem is described in [4]. This method computes the centroids of two sets of points and overlays them (translation). In a second step, the rotation of one set of points towards the other is minimized, thus defining the transformation.

The *Downhill Simplex method* with six degrees of freedom (*DSm6*) simply searches for the minimum of the sum of the squared distances of the corresponding landmarks [5][6]. In this way, the optimal combination of three translation directions and three rotation angles is found on the basis of minimizing the landmark distances. The *Procrustes* and the *DSm6* algorithm weigh every landmark equally regardless the application.

The *Downhill Simplex method* with four degrees of freedom (*DSm4*) searches for the minimal sum of squared distances by changing one rotation angle and three translation directions. Here, it is assumed, that the two landmarks on the dorsal process are marked first, and with high precision. Thus, the axis between these landmarks defines the rotation axis, so that only one rotation angle is optimized.

A misplacement of some landmarks results in a deformation of the set of points. A perfect match with the landmarks in the preoperative dataset becomes impossible with a rigid transformation. A registration algorithm is only able to find the minimal error as the best fitting of the two sets of points.

Pre-registration experiments were performed. It was assumed, that the position of the two landmarks on the dorsal process can be defined with a pointer with high precision. The two landmarks on the skin surface above the superior articular processes are expected to be defined with a larger error. A misplacement of those landmarks along the anterior-posterior axis is supposable. For that reason, 14 misplacement positions between -13 and 56 mm along the anterior-posterior axis were simulated for the two landmarks on the skin surface. The two landmarks on the dorsal process were kept in their original positions.

This situation was also tested *in vitro* using the phantom in figure 1 and a freehand pointer to define the landmarks. A displacement of approximately ± 1 mm for each landmark is expected. The landmarks on the skin surface above the superior articular processes were defined equivalent to the simulation by 14 misplacement positions between -13 and 56 mm along the anterior-posterior axis

The ultrasound data acquisition was accomplished with a Toshiba Aplio (SSA-770A CV) ultrasound machine and a linear probe (PLT-704 AT) with a center frequency of 7.5 MHz. The tracking system was able to trace the probe's position, so three-dimensional ultrasound datasets for the vs-registration were reconstructed.

3. Results and Discussion

The registration of the ultrasound data with the CT data was considered as correct, if the position of the surface was transformed to the corresponding position in the ultrasound dataset. This was verified by a visual inspection. The pre-registration algorithms minimize the translation and the rotation, the vs-registration has to accomplish, in order to register the surface with the three-dimensional ultrasound data.

Figure 3 shows the results of the simulation: the translation and the rotation, the vs-registration has to accomplish after pre-registration. With no misplacement of the two landmarks on the skin surface, each algorithm delivers a perfect transformation. The vs-registration does not have to translate or rotate the surface

in the ultrasound dataset. That is only possible for a correct definition of each landmark, a situation that does not appear during surgery but during simulation. With a misplacement of the two landmarks on the skin surface, the pre-registration algorithms can only find the minimal error between the two sets of points.

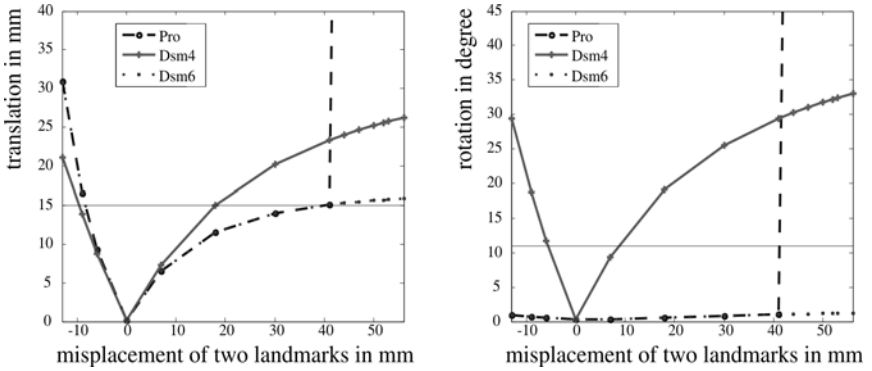

Fig. 3. The different pre-registration algorithms (*Procrustes* (Pro), *Downhill Simplex* with four degrees of freedom (*DSm4*) or *Downhill Simplex* with six degrees of freedom (*DSm6*)) provide different starting positions for the vs-registration. The vs-registration has to overcome a certain translation (left) and rotation (right) to reach the correct position of the surface within the ultrasound volume.

The orthogonal *Procrustes* method delivered the same transformation as the *DSm6* until a misplacement of the two landmarks on the skin surface above 40 mm. For larger misplacements, the vs-registration would have had to translate the set of points over more than 160 mm and rotate it more than 170° in order to carry out the registration.

The *Downhill Simplex methods* provided a robust transformation for landmark misplacements up to 56 mm. Since they search for the minimum error of the sum of the squared distances of the corresponding landmarks, every pre-registration provided a transformation, that demanded a translation less than 32 mm and a rotation less than 34° towards a correct registration. As expected, *DSm6* achieved a more precise pre-registration than *DSm4* in most cases.

In order to evaluate the success of each algorithm, a pre-registration and a vs-registration was carried out. The evolutionary vs-registration can overcome some local minima. The computing time decreases, if the pre-registration provides a starting position close to the correct position. The vs-registration was successful in combination with *DSm6* up to a 56 mm misplacement of two landmarks, with *DSm4* up to 50 mm and for the *Procrustes* method up to 41 mm.

In the *in vitro* tests on the phantom with the freehand pointer, the RMSE of marking the landmarks on the dorsal process was 0.58 mm. Still, *DSm4* and *DSm6* provided a robust pre-registration up to a misplacement of the two landmarks on the skin surface of 56 mm. The vs-registration was successful for the *DSm6* up to 56 mm misplacement, for *DSm4* up to 52 mm and for the *Procrustes* method up to

43 mm. The computation time for the *Procrustes* method was $0.188 \cdot 10^{-3}$ s, the *Downhill Simplex methods* needed 0.281 s for *DSm6* and 0.0781 s for *DSm4*.

4. Conclusions

Regarding results of prior *in vivo* evaluation, the vs-registration algorithm could find the correct surface position in an ultrasound volume data in 98.4% of all cases, if the initial translation does not exceed 15 mm and the initial rotation does not exceed 11°. Thus, the *DSm6* algorithm can provide a sufficiently precise pre-registration, even if the landmarks on the skin surface were misplaced between -6 and 40 mm along the anterior-posterior axis (vertical line in fig. 3).

Despite the fact, that the *Procrustes* method is a fast algorithm to find a transformation between two sets of points, it fails if the misplacement of some landmarks is too large. For the *Procrustes* point-to-point registration, this is the case, if two landmarks are misplaced more than 40 mm. A robust pre-registration algorithm should be preferred, since the computation time of these transformation algorithms can be ignored. This way, the precise *DSm6* should be implemented for the pre-registration.

The developed system for the registration of CT and ultrasound datasets allows a fast and robust registration of bone structures of the human lumbar spine. The easy handling and the *in vivo* accuracy measurements show that the achievable accuracy of the system is adequate for the application in surgical navigation.

Acknowledgements. This work was an activity of the OrthoMIT consortium. It was supported by the Bundesministerium für Bildung und Forschung (Az. 01EQ0424).

References

1 B. Brendel, S. Winter, A. Rick, M. Stockheim, and H. Ermert, *Registration of 3D CT- and ultrasound-datasets of the spine using bone structures*, Comput Aided Surg. Vol. 7, 3, 146-55, 2002.

2 S. Winter, B. Brendel, C. Igel, *Registration of bone structures in 3D ultrasound and CT data: Comparison of different optimization strategies*, In: Procs CARS, Vol. 1281, 242-247, 2005.

3 B. Brendel, J. Siepermann, S. Winter, and H. Ermert, *In vivo evaluation and in vitro accuracy measurements for an ultrasound-CT registration algorithm*, In: Procs CARS, Vol. 1281, 583-588, 2005

4 P.H. Schoenemann, *A generalized solution of the orthogonal Procrustes problem*, Psychometrika, Vol 31, 1, 1-10 1966.

5 W.H. Press, B.P. Flannery, S.A. Teukolsky, W.T. Vetterling, *Numerical Recipes in C,* Cambridge University Press, Cambridge, 305-309, 1988

6 J.C. Lagarias, J.A. Reed, M.H. Wright und P.E. Wright, *Convergence Properties of the Nelder Mead Simplex Method in low Dimensions*, SIAM J. Optimiz., Vol. 9, 1,114-147, 1998

Optimization and Quantification of Aaccuracy for Rigid Point Based Registration for Computer Aided Surgery

Philip Oberhammer[1], Urs Eisenmann[1], Roland Metzner[1],
Dimitrios Paraskevopoulos[2], Christian R. Wirtz[2] and Hartmut Dickhaus[1]

[1] Department of Medical Informatics, University of Heidelberg, Im Neuenheimer Feld 400, D-69120 Heidelberg, Germany
E-mail: hartmut.dickhaus@med.uni-heidelberg.de
[2] Neurosurgical Department, University of Heidelberg, Im Neuenheimer Feld 400, D-69120 Heidelberg, Germany
E-mail: rainer.wirtz@med.uni-heidelberg.de

Abstract. When conducting complex neurosurgical interventions on the brain, surgeons are often assisted by planning systems and neuronavigation. To position the instruments in relation to the preoperatively acquired image datasets, rigid registration between the coordination systems of the patient and the corresponding diagnostic images is performed using fiducial markers or screws attached to the patient's head. In this work a registration-framework was implemented, which allows the easy integration of different point based registration algorithms as well as the estimation of registration accuracy. To perform the registration, two algorithms were implemented and tested using simulation as well as real world measurements. The target registration error (TRE) is predicted by a method introduced from Fitzpatrick. Two different approaches were implemented and both achieve better results than the RMS Error ("Root Mean Square") widely used in clinical applications. To provide the surgeon with an intuitive understanding of the accuracy, a graphical representation of the estimator was developed and integrated into the existing MOPS 3D planning system. Additionally an iterative marker selection method was developed for identifying markers which would contribute to a higher registration error. The described registration framework is developed in C++ using MS Visual Studio and is easy to integrate in different medical applications.

1. Introduction

Complex surgical operations need to be thoroughly planned to guarantee a smooth progress of the interventions. Today, computer aided surgery (CAS) is widely used to facilitate the planning and conducting of surgical interventions. Preoperatively acquired datasets (i.e. CT, MRI) of the anatomical region of interest have to be processed to yield an intuitive 3D representation for the surgeon [1]. Especially in neurosurgery, where small mistakes may have a huge impact on neurological functions, accuracy is crucial [2]. Neuronavigation makes preoperative data available during the operation showing the current position of the instruments within the 3D dataset. For this purpose a registration between the patient during surgery and the preoperatively scanned patient data has to be

performed. In the case of the skull, rigid registration may be assumed to be sufficient which usually is achieved by using fiducials markers glued to the patients skin. As an estimator for the error of the registration occurring due to inaccurate measurements or accidentally displaced fiducial markers, the RMS-Error is widely used. This measure, however, neglects the geometric configuration of the fiducials and may thus lead to a misinterpretation of the situation. Therefore other more advanced estimators like the TRE (Target Registration Error) [3] have been described.

Our main goal was to achieve an accurate registration and an adequate estimation of the occurring error. We implemented a registration framework as an extension to a system for planning and carrying out neurosurgical interventions called MOPS 3D ("Multimodal Operation Planning System") [4]. The framework allows the integration of point based registration algorithms as well as the prediction of the registration error using a TRE estimator. To perform image registration, two algorithms were implemented. The rigid algorithm introduced by Horn et al. [5] reflects the behavior of several established rigid algorithms [6] as was shown by Eggert [7]. The algorithm introduced by Miller [8] is not strictly rigid and also supports dilation. Both algorithms have been tested for accuracy using measurements of a head phantom as well as simulated data. The impact of discarding markers suspicious of being accidentally moved is investigated by choosing different marker selection schemes. To estimate the registration error, the value of the TRE can be calculated independently of the used registration method.

2. Methods

To implement the registration algorithms, a C++ class structure was developed representing every algorithm as an independent class.

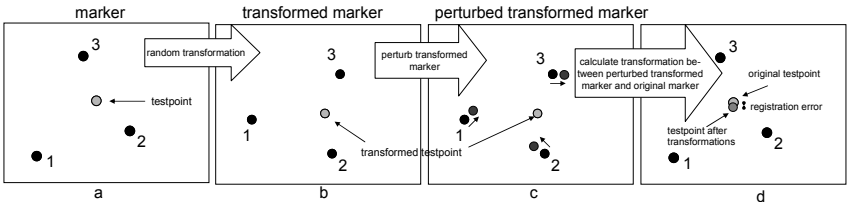

Fig. 1. 2D-schematic depiction of the simulation. A predefined number of fiducial markers is simulated by equally distributed points within a cubic space with an edge length of 255mm (Fig.1a). A rigid transformation is randomly generated and applied to the points (Fig.1b). The transformed points are then randomly perturbed by a normal distributed error (mean 0, standard deviation 1mm) to simulate measurement errors (Fig.1c). The implemented registration framework calculates a registration matrix using the original marker set and the transformed and perturbed marker set (Fig.1d). A random testpoint is generated and transformed by the known random rigid transformation and then transformed back by the calculated registration matrix (Fig.1a-d). The distance between the original testpoint and its transformed counterpart is the registration error at that specific point.

Communication between the framework and the calling program is handled by the class "PRegistration", which is the central class of the framework. The framework was tested for registration accuracy using the simulation described in Figure 1.

Based on the marker configuration the TRE estimator is calculated and compared to the registration error. Two different approaches were implemented to calculate the TRE estimator for the registration error, one in dependence of the previously measured accuracy of the navigation system and the second one depending on the RMS Error of the registration. The accuracy of the navigation system was estimated with the use of standard fiducial markers and fixed points, performing 200 measurements for each yielding 1.1mm and 0.6mm respectively. This will be referred to as "Fiducial Localisation Error" (FLE).

Target Registration Error. The Target Registration Error was calculated by equation (1) and (2). The first one is depending on the "Fiducial Localisation Error" (FLE) which is system dependent and must be previously obtained. Equation (2) is mainly dependent on the RMS error [3]. (d = distance between target point and principal axis k, f= RMS distance between fiducial markers and principal axis k)

$$TRE^2(r) \approx \frac{FLE^2}{N}\left(1+\frac{1}{3}\sum_{k=1}^{3}\frac{d_k^2}{f_k^2}\right) \tag{1}$$

$$TRE^2(r) \approx \frac{RMS^2}{(N-2)}\left(1+\frac{1}{3}\sum_{k=1}^{3}\frac{d_k^2}{f_k^2}\right) \tag{2}$$

In clinical practice the overall RMS error is frequently minimized by manually excluding presumably perturbed fiducials. To take that into consideration, different methods for selection of the markers were tested. Within a reference selection scheme, all markers with an aberration >1.5mm are discarded. One selection method uses an iterative leave-one-out algorithm to remove one marker at a time so that the resulting TRE at the centroid of the marker configuration is minimized. This is repeated until the resulting improvement comes to a halt. A third iterative algorithm removes the marker with the largest error after the registration, until the resulting overall RMS is below a certain threshold (0.4mm). The simulation was repeated 20.000 times, generating a new set of markers and testpoints in each case.

In addition to the simulation, the evaluation also included measurements with a phantom of the head which has 10 standard clinical fiducial markers as well as 10 fixed markers as reference points representing possible target points inside the brain. The positions of the fixed markers were quantified using a CNC system ("Computerized Numerical Control") as a gold standard. The real world coordinates were acquired by a Polaris Navigation System in combination with the MOPS System. The markers were also localized on CT images of the phantom, utilizing visualization and segmentation capabilities of MOPS 3D. With the markers identified, a registration between the real world and the CT dataset was performed using the standard clinical fiducial markers. The checkpoints are then transformed with the registration matrix, and the distances between the

transformed and the measured points are obtained. Again the different selection schemes are applied to the markers. The reference selection can not be implemented in this case, as the true aberration of the markers is unknown.

3. Results and Discussion

With 10 markers the mean simulated registration error using the algorithm derived by Horn [5] was 0.41mm (standard deviation 0.2mm), the mean simulated registration error using the algorithm derived by Miller [8] was 0.69mm (standard deviation 0.4mm). An overview of the results is given in Table 1.

Table 1. Simulated registration error of the two algorithms using 10 fiducials and applying different selections (all numbers given are in mm)

	Horn		Miller	
	mean	standard deviation	mean	standard deviation
all fiducials	0.42	0.21	0.69	0.40
reference selection	0.40	0.20	0.68	0.42
manual selection	0.59	0.29	0.90	0.54
leave-one-out selection	0.47	0.26	0.99	0.54

It is shown that the Horn algorithm yields smaller errors than the algorithm based on Miller [8]. Furthermore, all selection schemes, excluding the reference selection, result in an increasing error when removing fiducials from the original marker set. That is somehow contradictory to the subjective feeling that removing supposably "bad" markers should lead to a significantly higher accuracy. Even the reference-selection results in a slight improvement only.

The measurement results achieved at the phantom (Table 2) correspond to the results of the simulation.

Although the overall registration error was higher than for the simulations, the Horn algorithm still achieved better accuracy than the algorithm based on Miller [8]. Notably the leave-one-out selection does contribute to a slight improvement of accuracy, while the manual selection leads to higher registration errors.

Table 2. Registration error of the two algorithms using 10 fiducials and applying different selection schemes

	Horn		Miller	
	mean (mm)	standard deviation	mean (mm)	standard deviation
all fiducials	0.98	0.36	1.38	0.59
manual selection	1.02	0.50	1.42	0.86
leave-one-out selection	0.97	0.50	1.33	0.75

When comparing the estimated errors with the simulated registration errors, the results are dependent on the registration algorithm used. Applying the Horn algorithm, both TRE estimators achieve a better estimation than the RMS estimator as can be seen in Figure 2. When using the Miller algorithm [8], the RMS error shows better results. That can be explained with the fact, that the algorithm is not strictly rigid but also supports dilation and the TRE estimators on the other hand were designed for rigid transformations only [3].

Figure 3 shows the visualization of the TRE estimator in the MOPS system.

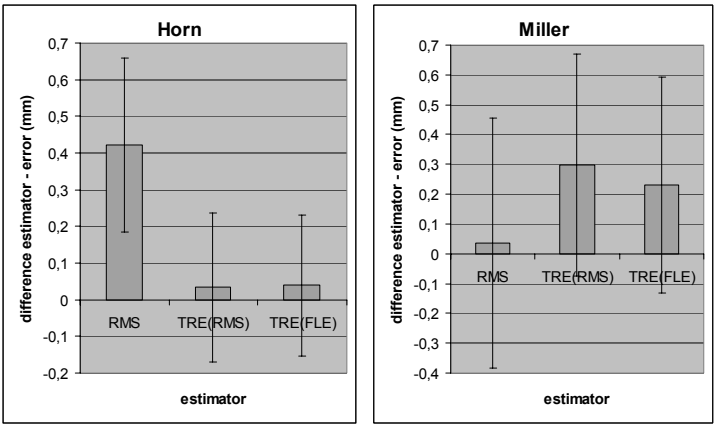

Fig. 2. Mean difference between the estimators and the simulated registration error

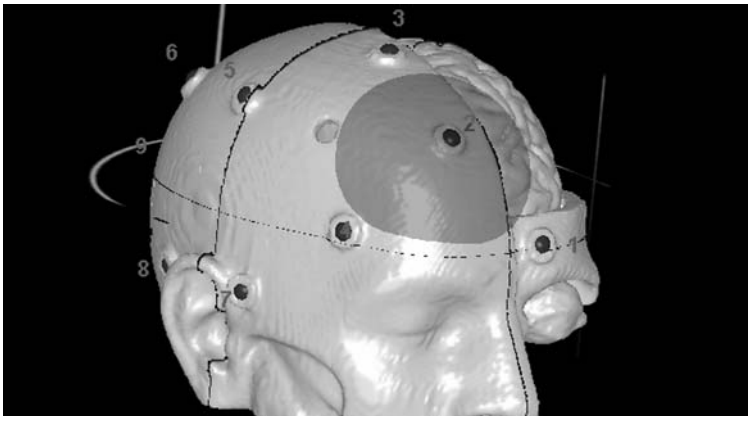

Fig. 3. CT Dataset of the phantom head with nine markers identified but only 1-4 used to calculate the registration. The transparent dark ellipsoid marks the area with an estimated registration error (TRE) below 1mm.

Table 3 demonstrates the results yielded for the measurements at the phantom. They show the same trend as for the simulated data.

Table 3. Mean differences between the estimator and the real (measured) registration error using the Horn algorithm

	Mean difference (mm)	standard-deviation
RMS	1,24	0,51
TRE(RMS)	0,03	0,38
TRE(FLE)	0,01	0,35

4. Conclusions

The implemented rigid Horn registration algorithm shows a higher accuracy than the Miller algorithm [8]. When using fiducial based registration of the head, rigid registration achieves better results than registrations also allowing dilation as long as brainshift and other elastic transformations of the head may be neglected.

The implemented TRE estimators prove to give a better approximation of the registration error than the widely used RMS estimator. To facilitate the understanding of the actual situation in terms of accuracy, an intuitive 3D representation of the estimator has been developed which is based on the distribution of the TRE [9] and depicts the area where the estimated registration error is beneath a certain threshold (Figure 3).

Considering the results for the marker selections, hardly any selection contributes to an improved registration accuracy but generally increases the resulting error.

Therefore no automatic selection was implemented. However, a semiautomatic leave-one-out algorithm is provided to help the surgeon to identify possible shifted markers, one at a time. Nevertheless, it is advised to be used very carefully.

References

1 C. R. Wirtz and S. Kunze, *Deutsches Ärzteblatt 95(39)*, 36-42, 1998.
2 P. Grunert, K. Darabi, J. Espinosa and R. Filippi, *Neurosurg Rev 26(2)*, 73-99, 2003.
3 J. M. Fitzpatrick, J. B. West and C. R. Maurer, Jr., *IEEE Transactions on Medical Imaging 17(5)*, 694-702, 1998.
4 U. Eisenmann, H. Dickhaus, R. Metzner and C. R. Wirtz, *Biomed Tech (Berl) 47,* Suppl 1 Pt 1, 49-52, 2002.
5 B. K. P. Horn, *Journal of the Optical Society of America A 4*, 629-642, 1987.
6 S. Umeyama, *IEEE Transactions on Pattern Analysis and Machine Intelligence 13(4)*, 376-380, 1991.
7 D. W. Eggert, A. Lorusso and R. B. Fisher, *Machine Vision and Applications 9*, 272-290, 1997.
8 R. D. Miller, in *Graphics Gems V,* Edited by A. Paeth, 111-120, 1995.
9 J. M. Fitzpatrick, and J. B. West, *IEEE Transactions on Medical Imaging 20(9)*, 917-927, 2001.

Virtual Reality Based Training of Lumbar Punctures Using a 6DOF Haptic Device

M. Färber[1], J. Heller[1], F. Hummel[2], C. Gerloff[2] and H. Handels[1]

[1] Department of Medical Informatics, University Medical Center Hamburg Eppendorf, Martinistraße 52, 20246 Hamburg, Germany
E-mail: mfaerber@uke.uni-hamburg.de
[2] Department of Neurology, University Medical Center Hamburg Eppendorf, Martinistraße 52, 20246 Hamburg, Germany

Abstract. The lumbar puncture is performed by inserting a needle into the spinal chord of the patient to inject medicaments or to extract liquor. This procedure is usually trained on the patient guided by experienced supervisors. A virtual reality lumbar puncture simulator has been developed in order to enhance the training by providing new insight into a virtual patient and in order to minimize the patient's risk. We use a haptic device with six degrees of freedom (6DOF) to feedback forces that resist needle insertion and rotation. An improved haptic volume rendering approach is used to calculate the forces for the haptic feedback. A real time 3D visualization with optional stereo view gives an overview of the punctured region. 2D visualizations of orthogonal slices enable a detailed impression of the anatomical context. In a first evaluation the visible human male data has been used to generate the virtual body. Several users with different medical experience tested the lumbar puncture trainer. The simulator gives a good haptic and visual impression of the needle insertion and the haptic volume rendering technique enables the feeling of segmented and unsegmented structures.

1. Introduction

Lumbar punctures are performed for diagnosis and therapy. The puncture is done by inserting a needle into the body to inject medicaments or to extract liquor. The puncture needle pierces structures like skin, fat or ligaments during the insertion. Experienced physicians obtain information about the needle position from the different haptic behavior of these structures. The training of lumbar punctures is usually done guided by experienced supervisors directly on the patient. The use of training dolls or cadavers is unusual. Recently the relevance of virtual reality based simulators is increasing. With the use of these simulators experience can be gained cheaply without risking the patient's health and a manifold of visualization techniques allow new insight into the human anatomy. Recent lumbar puncture simulators [1–3] use precompiled virtual haptic models generated from segmented image data. Haptic feedback from structures that have not been segmented or modeled can not be rendered. Our approach distinguishes from these systems since it combines original CT data with label data to facilitate the haptic feedback of structures that have not been segmented. Furthermore the use of a haptic device

with six degrees of freedom for puncture simulation is new and e.g. enables the haptic rendering of torques that resist needle rotation.

2. Methods

Our training system presents a virtual scene that consists of a user-steered virtual needle and a virtual body generated from segmented CT data. The simulation is split up into a haptic and a visual component. The haptic component renders the forces that affect the needle during the insertion. A force feedback device with six degrees of freedom (Sensable Phantom Premium 1.5) is used for the haptic I/O (Fig 1.). This device enables haptic feedback in three directions in space and in three rotation axes of the end-effector.

Fig. 1. Sensable Phantom Premium 1.5 haptic device with six degrees of freedom.

The forces are calculated in real-time depending on needle position, needle rotation, insertion angle and local tissue properties. The haptic device is then used to return the rendered forces to the user.

Different force components are considered (Fig. 2): Resisting force, surface friction and viscosity of medical structures are simulated based on a haptic volume rendering approach [4]. This proxy-based approach is generally used to navigate through volumetric medical data sets like CT data using haptic devices. The rendering algorithm has been improved to combine structure information extracted from original CT data with segmented data. This way the haptic rendering of small structures that have not been segmented is enabled and extends the haptic impression calculated from the skin, bone, muscle or fat label data.

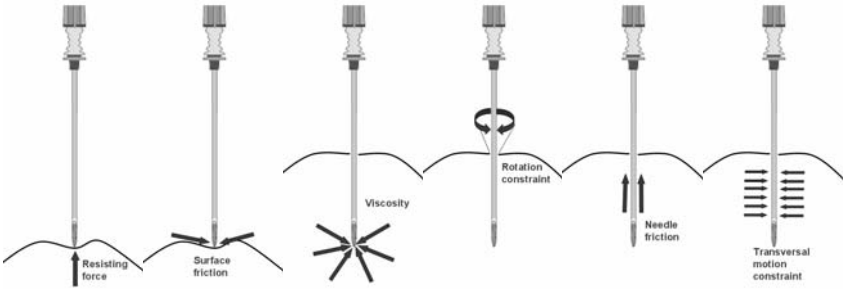

Fig. 2. Needle tip forces (a-c) and needle body forces (d-f) that build up the haptic component.

A friction force is increased depending on the penetration depth. The realistic behavior of the needle is improved by restricting rotation and transversal motion of the needle inside the body. For this purpose the needle position and needle direction vectors are stored at the moment the needle pierces the skin. Transversal motion of the needle is restricted using a spring force technique. The torque values that control the motors for the rotational axes of the 6DOF haptic device are calculated using a quaternion that transforms the current needle direction vector to the direction vector at the moment of insertion. The current penetration depth is used to compute an amplifying factor for the torque forces so that the restriction of needle rotation depends on the depth of needle insertion. 2D and 3D visualizations (Fig. 3) of the virtual body build up the visual component. The 3D scene shows a virtual representation of the needle and the surfaces of relevant medical structures. The whole scene can be rotated, panned and zoomed using the mouse. A stereo view improves the impression of depth in the virtual body. Three 2D views show orthogonal slices (sagital, coronal and axial) of the image data. The slice positions are defined by the current position of the needle tip. The alignment of the needle is shown by a projection into each orthogonal view.

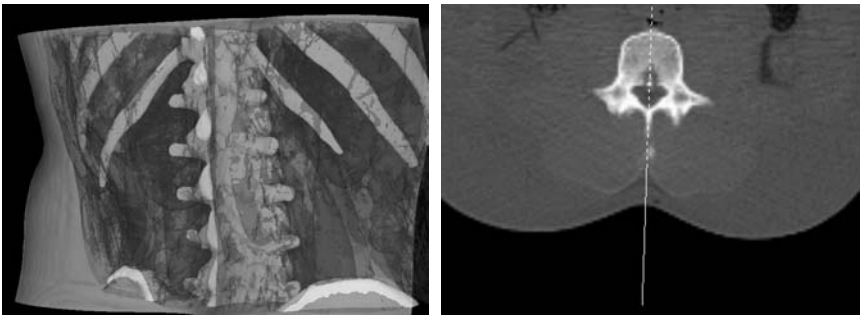

Fig. 3. a) Opaque illustration of skin, muscle and bone structures in 3D. b) Axial view showing a vertebral body. The needle position is indicated by a yellow line.

In a first step the input data for the lumbar puncture simulator has been generated based on the visible human male data set [5]. We used the CT data and the segmentations (label data) of skin, bone, muscles, ligaments, fat and target area. Surface models have been generated based on the label data to enable the 3D visualization. Parameters for the haptic and visual component and the definition of the input data are provided using an XML file.

3. Results

Several users with varying medical experience tested the simulation of lumbar puncture. The users were able to identify different tissues like muscles, fat, skin and bone by means of viscosity, resisting force and friction. The system is able to give a new insight into the body during needle insertion this can be used to enhance the training of lumbar punctures. The extended haptic volume rendering technique enables force feedback from labeled and unsegmented structures. The restriction of transversal needle movement together with the rotation constraints enabled by the 6DOF device facilitated a realistic needle behavior. The synchronization of force feedback and miscellaneous visualization techniques provided a realistic impression of the anatomy though most users were unfamiliar with the usage of a haptic device. The use of virtual reality techniques opens up new opportunities to support and improve the lumbar puncture training in medical education.

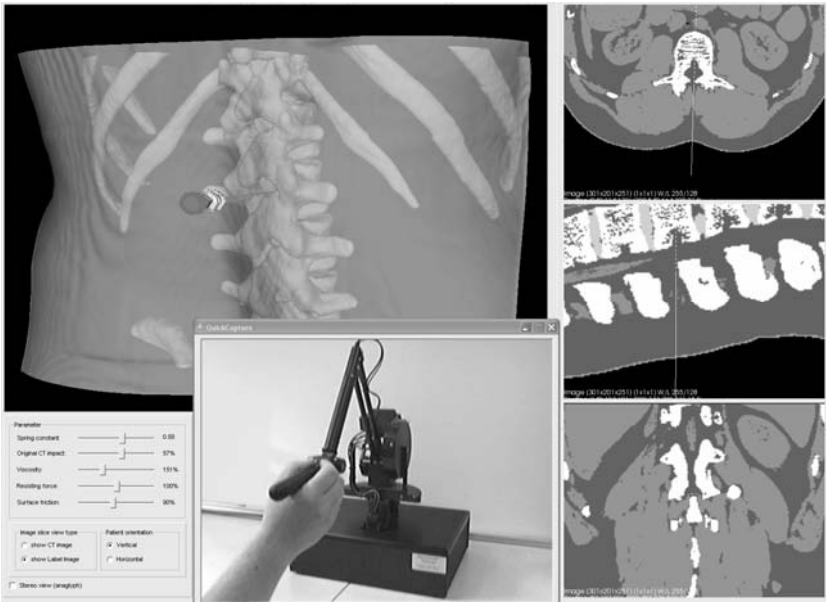

Fig. 4. The graphical user interface showing 3D and 2D visualizations as well as parameters for visualization and haptic feedback. The device position and orientation is illustrated by a webcam snapshot.

4. Conclusions and Future Work

The virtual reality simulator presented (Fig. 4) supports a realistic training of lumbar punctures in virtual bodies. The training method offers a new way to understand human anatomy and to gain experiences in using a puncture needle. The simulator is prepared to work with arbitrary patient data. We will exploit this feature by providing other lumbar puncture cases with different pathologies. Soft tissue deformation has been neglected in our system since only small deformations arise during the lumbar puncture. These tissue deformations are more relevant when other puncture interventions like lung or liver biopsy are considered. One of our next steps will be the simulation of these deformations to enable the training of other puncture interventions.

References

1 P. Gorman, T. Krummel, R. Webster, M. Smith, D. Hutchens: A prototype haptic lumbar puncture simulator, in *Stud Health Technol Inform*, Vol 70, 106, 2000.
2 J.B. Ra et al: Spine needle biopsy simulator using visual and force feedback, in *Comput Aided Surg,* Vol. 7, 353, 2002.
3 U. Dreifaldt, Z. Kulcsar, P. Gallagher: Exploring haptics as a tool to improve training of medical doctors in the procedure of spinal anaesthetics, in *Eurohaptics*, Paris 2006.
4 K. Lundin, A. Ynnerman, B. Gudmundsson: Proxy-based haptic feedback from volumetric density data, in *Eurohaptics Conference*, 104, 2002.
5 V.M. Spitzer, D.G. Whitlock: The Visible Human Dataset: the anatomical platform for human simulation, in *Anat Rec*, Vol 253, 49, 1998.

Robot-Assisted 3D-Ultrasound Volume Registration for Skull Bone Surgery

Philipp J. Stolka[1], Steffen H. Tretbar[2], Michel Waringo[1], Philipp A. Federspil[3], Peter K. Plinkert[3] and Dominik Henrich [1]

[1] Lehrstuhl für Angewandte Informatik III, Universität Bayreuth Robotik und Eingebettete Systeme, Bayreuth 95445, Germany
E-mail: {philipp.stolka, michel.waringo, dominik.henrich}@uni-bayreuth.de
[2] Fraunhofer IBMT, Department Ultrasound, St. Ingbert 66386, Germany
E-mail: steffen.tretbar@ibmt.fraunhofer.de
[3] University of Heidelberg, Department of Oto-Rhino-Laryngology, Heidelberg, Germany
E-mail: philippe.federspil@med.uni-heidelberg.de

Abstract. Surgical procedures with navigation or robot system support usually require some pre-operative planning data. This data can be acquired by traditional imaging modalities like e.g. computed tomography (CT), the current gold standard due to its high precision. With such imaging data, access trajectories, implant positions, individual milling paths etc. can be computed. We present an ultrasound-based method to generate 3D image data which is equally suited for many interventions, but less costly than CT and real time. The method's feasibility is demonstrated for robot-based implant bed milling in the lateral skull base.

1. Introduction

Performing surgical procedures with the assistance of navigation or robotic systems usually consists of several pre-operative steps during the preparation phase – imaging and planning – and several intra-operative steps during the execution phase – registration and actual plan execution. Those computer- or robot-assisted surgery (*CAS/RAS*) systems only fully exhibit their benefits when operating on high resolution imaging data and good quality registration, i.e. successful determination of the geometric relationship between planning data and execution site. Traditionally, this is achieved with the „gold standard“ procedures of performing a computed tomography (*CT*) scan of the patient and inclusion of some markers, implanted or temporary, for registration in the operating room (*OR*).

Addressing the most important drawbacks of this approach – time requirements, radiation exposure, and invasiveness – we present a robot-based 3D ultrasound scanning method to generate intra-operative global image data which is equally suited, but less costly than traditional CT, to perform both intervention planning and registration.

The scope of application for the presented system is the automated milling of cavities in the lateral skull bone for subdermal implantation of hearing aids, where one process step is the removal of bone material from the thin calotte in the shape of flat amplifier components [Henrich02]. Other applications can be any intervention where ultrasound data may take the place of imaging.

From an overview of the state of the art (Section 2), one can justify the development of a robot-based 3D ultrasound system and accompanying registration and

checking procedures (Section 3). The implementation for a specific application with a specific robot system (Section 4) is experimentally validated for the whole process on human preparations (Section 5). Finally, the outlined conclusions point to future work (Section 6).

2. State of the Art

Currently, the standard imaging modality for planning in autonomous RAS systems is global preoperative data from CT, with magnetic resonance imaging (*MRT*) closely behind, as in Robodoc [Taylor94] and CASPAR (orthopedic knee and hip interventions), the AcroBot (knee), or research systems like RobaCKa and CRANIO (orthopedic interventions on the skull).

The use of ultrasound (*US*) has been traditionally limited for CAS/RAS planning purposes due to its low resolution. However, its non-invasive nature makes it suitable for registration [Winter02, Tretbar04]. However, 3D ultrasound scanning can be found in only a small number of projects, e.g. scanning of the shoulder/elbow area [Jan04].

Finally, the combination of robot-based interventions with 3D ultrasound as planning basis (instead of CT) is not present in the literature yet, in spite of its potential advantageous properties like non-invasiveness of imaging and registration, no radiation exposure, and possible high axial resolution.

3. Registration and Surface Scanning

With the presented method, several implicitly registered image modalities are generated for navigation: First a skull surface representation generated by manual sampling of surface points with a hand-held IR pointer, and second a skull representation created by scanning the skull with a robot-held A-mode US probe, returning both outer and inner skull boundaries. Both representations can be used in addition to or as replacement of a CT scan. Their acquisition automatically registers the robot with the patient.

To achieve this, several registration relationships – between robot, optical tracking system, and IR pointers – need to be established first (Section A). Robot-based scanning relies on a manually defined path which has to be processed (smoothing, surface normals determination) (Section B). Finally, path planning for the robot may bring about kinematical problems that need to be addressed before actual execution (Section C).

Registration. The system is based on a process consisting of calibrating and registering the robot in optical tracking system (*OTS*) coordinates automatically, then calibrating hand-held pointers, sampling the skull surface and a US scan path, and finally automatic path refinement and execution of the robot-based US scan.

First, the robot performs calibration motions to calibrate the transformation between the miller tool and its rigidly attached IR marker and register both in OTS coordinates [Stolka06].

Second, the user calibrates a hand-held OTS pointer – determining the specific translation between pointer marker *A* and pointer tip *Z* (Figure 1) – by pivoting it around its tip. The user then samples a cloud of skull surface points by sliding the pointer over the exposed skull, thus creating a surface representation which is already registered with the OTS, and thus with the robot.

Third, the pointer is used to manually define the 3D positions making up the scan path on the skull surface to be followed by the robot-held US probe. Therefore, the sequence of 3D points thus acquired needs to be processed prior to path execution by path smoothing and surface normal determination procedures [Stolka07].

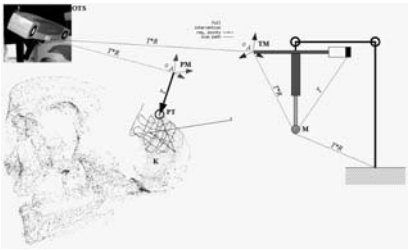

Fig. 1. Necessary registrations (3D – only translations T, 6D – translations T and rotations R) between robot and tool and US probe (tool tip M, tool infrared marker TM), the optical tracking system (OTS), patient skull surface and scan path (K) demonstrated by hand-held pointer (pointer tip PT, pointer infrared marker PM)

Path Processing. In order to allow faster and smoother processing, the scan path *P* is smoothed by successively removing points until the resulting path deviation exceeds an application-specific threshold [Waringo06].

In the next step, surface normals over a local sample neighbourhood are determined from the scan path and surface points. First, we need a point cloud *P* of surface points and the center $m = (m_x, m_y, m_z)$ indicating the point for which the normal vector on the surface should be determined. The next two steps consist in finding the relevant points $n_i \in Q \subseteq P$ in the proximity of m and in computing the normal vector on the surface defined by *Q*. The last two steps must be repeated for each normal vector. Finding the normal vector has asymptotic complexity $O(n)$.

Ultrasound Scan Execution. The procedure described so far yields a 5D path – a sequence of 3D positions with two rotational degrees of freedom (*DOF*) fixed. This leaves each point with one DOF open; in the presented system this is the roll parameter, i.e. rotation around the long tool axis. Since the US probe operates in A-mode, each single shot is rotationally invariant around this DOF, which can therefore be set to any value between 0° and 360° that is kinematically valid.

Arbitrarily selecting one orientation around the US sensor axis, the scan path can be followed, guiding the probe perpendicularly to the skull surface. However, since robots usually have limited DOF and joint ranges, not every orientation results in a valid executable path. In the presented case, the robot has six non-redundant DOF, and following the skull's curvature with the robot-held probe often leads to kinematic singularities and joint limit problems, which compromise safety and lead to the abortion of the current path execution. Therefore, the remaining DOF is used to offset those problems.

After registration of the robot, the patient, and the 5D path, a valid 6D path is searched from a set of paths generated with different roll values which are held constant over the whole path. First, a finite set V of roll values to be used is selected from a range that is (empirically) suspected to contain at least some values resulting in valid paths later on. Second, all paths P_v corresponding to roll values $v \in V$ are generated and interpolated densely with respect to Euclidean distance and orientation. Finally, each P_v is validated by applying the robot inverse kinematics to each interpolated path point and checking for joint limits, singularities, and discontinuities (Figure 2). In the current implementation, the first completely traversable path is selected for execution. In case no kinematically admissible path is found, the robot base location needs to be changed.

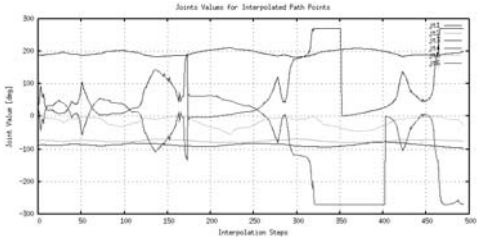

Fig. 2. Joint value graphs for the presented robot's six joints; for roll v = -10° (top), 0° (centre), and +10° (bottom) (the 0° path is invalid due to joint limit problems; and note the tightly counteracting elbow and wrist joints 4 and 6 for all paths)

The final scan path execution with concurrent ultrasound sampling returns a sequence of US A-scans, with the single upper and lower skull boundaries detectable by thresholding the filtered rf-signal. For better results, matched filtering is performed with coded excitation chirp signals, i.e. instead of single ultrasound pings a modulated waveform is emitted and cross-correlated with its echoes, improving detection in the face of bad signal-to-noise ratio [Tretbar04].

This creates two 2.5D skull boundary representations for implant position optimization [Waringo03]. As we now have two data sets describing the outer skull boundary – the US-based representation and the initial surface points which have been sampled manually with the IR pointer – they can be combined to create an improved outer boundary description.

4. Application and System

The system on which the presented method was implemented for validation performs automated milling of cavities in skull bone for subdermal implantation of hearing aids. (RONAF: *Robot-based Navigation for Milling at the Lateral Skull Base*, [Henrich02]).

The robot is an industrial model (Stäubli RX90, CASPAR, by Orto-Maquet). Sensors include – amongst others – a 6D force/torque (F/T) sensor (JR3 90M31A), an NDI Polaris infrared-optical tracking system (OTS; measured repeatability accuracy 0.05mm root-mean-square (RMS) after warm-up phase, specified absolute accuracy 0.35mm RMS, silo-shaped work volume

~(1000mm)³, data rate 20...60Hz), and a Transmit Receive Module II (US; by Fraunhofer IBMT, St. Ingbert/Germany). This US was integrated in a medically approved touch panel PC. It provided an ultrasonic transmitter with a free adjustable transmit frequency (0.5 – 40 MHz) and a integrated wave form generator (D/A-transducer 12 Bit / 100 MHz) to generate free programmable transmit forms (Chirps, Barker, Burst, Golay-Codes) with a transmit voltage of 0 – 160 Vpp (50 O). The receiver has an analogue bandwidth of 10 kHz - 40 MHz, a dynamic range of up to 80 dB with a free programmable time gain compensation unit (TGC). The received signals are digitized with a resolution of 12 Bit and a sample rate of 100 MHz. The US system PC is connected with the robot for position acquisition through a local network. Using two ultrasound probes (center frequency 2,25 MHz, diameter ¼" and 1 MHz, diameter ½") with flexible delay lines attached to the transducer, filtered and unfiltered radio frequency signals are available for signal processing.

5. Experiments and Results

We performed the whole described procedure on three human skull preparations , including pointer and robot calibration and registration, sampling of skull surface points, demonstration and processing of scan paths, and their execution with concurrent US scanning.

The manually generated surface point cloud is a 2.5D global map registered to the robot with a precision of <2.5mm RMS. Due to the flexible delay line attached to the front of the US probe, most scans could be completed successfully.

Secondly, the US scan generates a map consisting of two 2.5D skull surface point clouds, both of which are registered to the robot with a precision equal to the robot's absolute positioning accuracy (near to the robot's relative accuracy of 0.35mm) (Figure 3). Another factor in the scan map's precision is the accuracy of thickness detection in the single US shots, which is reported as 0.5mm, although this is highly patient-specific.

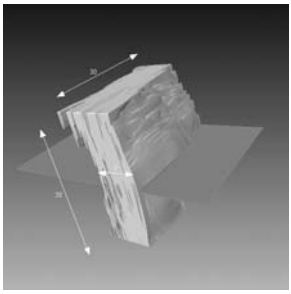

Fig. 3. 3D ultrasound volume reconstruction (skull sample, probe guided by μm 2D robot)

6. Conclusion

We have described an interface for bone surface and ultrasound scan path input using an IR pointer registered with a robot, resulting in two global maps: a

manually created, navigation system-based surface map and a robot-based 3D ultrasound map with extracted skull boundaries. These maps are created and registered non-invasively, thus representing an advance in planning data acquisition in RAS.

The created 3D ultrasound and surface maps can be used for CT-free implant position optimization and milling path planning [Waringo04]. The US system itself can be used as an IR-tracked manual standalone system as well (SonoPointer®, [Tretbar06]).

Future work includes force control of the contact between probe and skull to counteract bad tool-pointer registration quality and IR sensor noise as well as only partial probe-surface contact due to high surface curvature etc. Furthermore, optimization with variable probe orientations will be necessary as there may be paths which are not traversable with constant values for the open DOFs.

Acknowledgements. This work is a result of the project „Robot-based navigation for milling at the lateral skull base (RONAF)“ of the special research cluster „Medical navigation and robotics“ (SPP 1124) funded by the Deutsche Forschungsgemeinschaft (DFG), performed in cooperation with the Universitäts-HNO-Klinik (Abt. HNO-Heilkunde) in Heidelberg/Germany. Further information can be found at *http://ai3.inf.uni-bayreuth.de/projects/ronaf/*.

References

[Federspil05] P.A. Federspil, S.H. Tretbar, P.K. Plinkert, “Increase the Accuracy in Navigated Surgery by in site Measurement of individual Sound Velocity in Skull Bone”, CURAC 2005, Berlin/Germany, September 2005.

[Federspil06] P.A. Federspil, S.H. Tretbar, C. Sittel, P.K. Plinkert, “SonoPointer® - a prototype system for ultrasound scanning of skull bone thickness”, AORL 2006 (in Press).

[Henrich02] D. Henrich, “Robotergestütztes Fräsen an der lateralen Schädelbasis: Kraft-basierte lokale Navigation bei der Implantatbettanlage”, Robotik 2002, Ludwigsburg/Germany, June 2002.

[Henrich04] D. Henrich, Ph. Stolka, “Principles of Navigation in Surgical Robotics”, MRVN 2004, Remagen/Germany, March 2004.

[Jan04] U. v. Jan, D. Sandkühler, L. Kirsch, H.-M. Overhoff, „Definition of a humerus coordinate system from semiautomatically segmented 3-D ultrasound volumes“, Biomed. (49) Ergänzungsband., Schiele&Schön, Berlin, 2004.

[Stolka06] Ph. Stolka, D. Henrich, „Improving Navigation Precision of Milling Operations in Surgical Robotics“, IROS 2006, Beijing/China, 2006.

[Stolka07] Ph. Stolka, M. Waringo, D. Henrich, „Robot-Based 3D Ultrasound Scanning and Registration with Infrared Navigation Support“, submitted to ICRA 2007.

[Taylor94] R.H. Taylor et al, „An image-directed robotic system for precise orthopaedic surgery“, IEEE T-RA 10(3):261-275, June 1994.

[Taylor03] R. H. Taylor, D. Stoianovici, “Medical Robotics in Computer-Integrated Surgery”, IEEE T-RA, Vol. 19, No. 5, Oct. 2003.

[Tretbar04] S. H. Tretbar, Ph.A. Federspil, P.K. Plinkert, “Improved ultrasound based navigation for robotic drilling at the lateral skull base”, CARS 2004

[Waringo03] M. Waringo, Ph. Stolka, D. Henrich, “First System for Interactive Position Planning of Implant Components“, CURAC 2003, Nürnberg/Germany, 2003.

[Waringo04] M. Waringo, D. Henrich, „3-Dimensionale schichtweise Bahnplanung für Any-Time-Fräsanwendungen“, VDI Robotik 2004.

[Waringo06] M. Waringo, D. Henrich, „Efficient Smoothing of Piecewise Linear Paths with Minimal Deviation“, IROS 2006, Beijing/China, 2006.

[Winter02] S. Winter, B. Brendel, A. Rick, M. Stockheim, K. Schmieder, H. Ermert, „Registrierung 3-dimensionaler CT- und Ultraschalldaten anhand von Knochenstrukturen“, *CURAC*, Leipzig/Germany, 2002.

Recent Significance of Mechatronic Support Systems in General Surgery

Siegfried Beller[1] and Felix Härtl[2]

[1] Klinik für Chirurgie und Chirurgische Onkologie, Charitè Campus Buch
Robert-Rössle-Klinik am Helios-Klinikum Berlin-Buch, Berlin, Germany
E-mail: siegfried.beller@charite.de
[2] Chirurgische Klinik und Poliklinik, Klinikum rechts der Isar der TU München
Ismaningerstrasse 22, München, Germany
E-mail: haertl@lrz.tu-muenchen.de

Abstract. With an opinion and application poll in Swiss, Austria and Germany, the recent significance of mechatronic support systems was analyzed. Various advantages were reported by users. Advantages for surgery account for automation and limitation of surgical manipulations and increased instrumental skill, but the application of theses support systems are still very limited, due to negative cost-value ratio.

1. Introduction

More and more surgical procedures are performed using modern computer assisted systems. The abbreviations CAS and CIS mean “Computer assisted surgery” and “Computer integrated surgery” and are mainly used for these techniques. Various systems have established in neurosurgery and orthopedics and have proved advantages and validity in selected clinical applications. In general surgery minimally invasive surgery has established rapidly but the use of mechatronic systems is still in its infancy and its significance is not yet evident.

2. Methods

An opinion and application poll was performed in 980 hospitals in Germany, Austria and Swiss. A series of mechatronic systems (Acrobot, Aesop, Caspar, CyberKnife, DaVinci, EndoAssist, Hexapod, Laprotek, Naviot, NeuroMate, PahtFinder, Probot, Robodoc, Zeus) published in recent years were offered to mark with a cross. Other systems could be supplemented to this list. Questions dealt with the type and the frequency of its application, the evaluation of the systems and investigational activities.

3. Results and Discussion

89 standardizes questionnaires were answered and sent back for evaluation. Surgical departments with clinical application of systems were predominantly

from university hospitals. Applied systems were Aesop, DaVinci, Navitrac, Robodoc and other prototypes. Median application was 20 (range: 2-74) in one year. Reported investigational activities dealt with navigation, simulation, imaging and tracking.

Clinical applications were stopped in several departments due to bad reputations in the press and the solo-surgery principle anticipating surgical education in minimally invasive surgery. No application was argued with missing benefit and indications, and high costs.

4. Conclusions

Visualization and navigation technologies can be very helpful in surgery and have a future potential in minimal invasive and telerobotic surgery. Advantages for surgery account for automation and limitation of surgical manipulations. Increased instrumental skill is advantageous in particular in narrow limited surgical spaces. There is a negative cost-value ratio.

Table 1: Reports of tele-robotic systems applied in series of more than ten cases of surgical procedures.

Author	Clinic	Pub-year	Evidence	Surg. procedure
				Fundoplication
Cadiere et al.[1]	Saint-Pierre Hospital Brussels	2001	I	10
Chitwood et al.[2]	East Carolina University, Greenville	2001	III	14
Melvin et al.[3]	The Ohio State University, Columbus	2002	II-2	20
Gutt et al.[4]	Johann Wolfgang Goethe Universität Frankfurt	2002	III	11
Talamini et al.[5]	Johns Hopkins Med. Inst. Baltimore	2002/2003	III	25/69
Beninca et al.[6]	University of Torino	2003	III	13
Bodner et al.[7]	Medizinische Universität Innsbruck	2004	III	16
Knight et al.[8]	Children`s Hospital of Michigan	2004	III	14
Drasin et al.[9]	UCLA Los Angeles	2004	III	10
Ruurda et al.[10]	University Medical Center Utrecht	2005	III	41
				Heller-myotomy
Ruurda et al.[10,11]	University Medical Center Utrecht	2004/2005	III	14/24
				Gastric banding
Moser et al.[12]	University of Illinois	2004	III	32
				Gastric bypass
Moser et al.[12]	University of Illinois	2004	III	110
Mohr et al.[13]	Stanford Hospital, Stanford	2005	II-2	10
Ali et al.[14]	University of California, Sacramento	2005	III	50

Table 1 (cont'd): Reports of tele-robotic systems applied in series of more than ten cases of surgical procedures.

Author	Clinic	Pub-year	Evidence	Surg. procedure
				Cholezystectomy
Marescaux et al.[15]	Louis Pasteur University Strasbourg	2001	III	25
Ruurda et al.[16]	University Medical Center Utrecht	2002	III	35
Ruurda et al.[17]	University Medical Center Utrecht	2003	II-3	10
Talamini et al.[18]	Johns Hopkins Med. Inst. Baltimore	2003	III	36
Nio et al.[19]	Academic Medical Center Amsterdam	2004	I	10
Miller et al.[20]	Mayo Clinic College of Medicine, Scottsdale	2004	III	19
Corcione et al.[21]	AORN Monadi Hospital, Naples	2005	III	20
Bodner et al.[22]	Medizinische Universität Innsbruck	2005	III	23
Zhou et al.[23]	Shenzhen People`s Hospital, Jinan University	2006	I	20
Heemskerk et al.[24]	Maastricht University Hospital	2006	III	12
				Esophagectomy
Ruurda et al.[10]	University Medical Center Utrecht	2005	III	22
Espat et al.[25]	University of Illinois	2005	III	15
				Colonresection
Anvari et al.[26]	McMaster University, Hamilton - Ontario	2004	II-3	10
				Rektopexy
Ruurda et al.[10]	University Medical Center Utrecht	2005	III	16
				Adrenalektomy
Brunaud et al.[27]	University of Nancy	2003	II-2	14
Brunaud et al.[28]	University of Nancy	2004	II-2	19
Morino et al.[29]	University of Torino	2004	I	10
Winter et al.[30]	Johns Hopkins Med. Inst. Baltimore	2006	III	30

References

1. Cadiere GB, Himpens J, Vertruyen M et al. Evaluation of telesurgical (robotic) NISSEN fundoplication. Surg Endosc 2001; 15:918-923.
2. Chitwood WR, Jr., Nifong LW, Chapman WH et al. Robotic surgical training in an academic institution. Ann Surg 2001; 234:475-484.
3. Melvin WS, Needleman BJ, Krause KR et al. Computer-enhanced vs. standard laparoscopic antireflux surgery. J Gastrointest Surg 2002; 6:11-15.
4. Gutt CN, Markus B, Kim ZG et al. Early experiences of robotic surgery in children. Surg Endosc 2002; 16:1083-1086.

5. Talamini M, Campbell K, Stanfield C. Robotic gastrointestinal surgery: early experience and system description. J Laparoendosc Adv Surg Tech A 2002; 12:225-232.
6. Beninca G, Garrone C, Rebecchi F et al. [Robot-assisted laparoscopic surgery. Preliminary results at our Center]. Chir Ital 2003; 55:321-331.
7. Bodner J, Wykypiel H, Wetscher G et al. First experiences with the da Vinci operating robot in thoracic surgery. Eur J Cardiothorac Surg 2004; 25:844-851.
8. Knight CG, Lorincz A, Gidell KM et al. Computer-assisted robot-enhanced laparoscopic fundoplication in children. J Pediatr Surg 2004; 39:864-866.
9. Drasin T, Dutson E, Gracia C. Use of a robotic system as surgical first assistant in advanced laparoscopic surgery. J Am Coll Surg 2004; 199:368-373.
10. Ruurda JP, Draaisma WA, van HR et al. Robot-assisted endoscopic surgery: a four-year single-center experience. Dig Surg 2005; 22:313-320.
11. Ruurda JP, Gooszen HG, Broeders IA. Early experience in robot-assisted laparoscopic Heller myotomy. Scand J Gastroenterol Suppl 2004;4-8.
12. Moser F, Horgan S. Robotically assisted bariatric surgery. Am J Surg 2004; 188:38S-44S.
13. Mohr CJ, Nadzam GS, Curet MJ. Totally robotic Roux-en-Y gastric bypass. Arch Surg 2005; 140:779-786.
14. Ali MR, Bhaskerrao B, Wolfe BM. Robot-assisted laparoscopic Roux-en-Y gastric bypass. Surg Endosc 2005; 19:468-472.
15. Marescaux J, Smith MK, Folscher D et al. Telerobotic laparoscopic cholecystectomy: initial clinical experience with 25 patients. Ann Surg 2001; 234:1-7.
16. Ruurda JP, Broeders IA, Simmermacher RP et al. Feasibility of robot-assisted laparoscopic surgery: an evaluation of 35 robot-assisted laparoscopic cholecystectomies. Surg Laparosc Endosc Percutan Tech 2002; 12:41-45.
17. Ruurda JP, Visser PL, Broeders IA. Analysis of procedure time in robot-assisted surgery: comparative study in laparoscopic cholecystectomy. Comput Aided Surg 2003; 8:24-29.
18. Talamini MA, Chapman S, Horgan S et al. A prospective analysis of 211 robotic-assisted surgical procedures. Surg Endosc 2003; 17:1521-1524.
19. Nio D, Bemelman WA, Busch OR et al. Robot-assisted laparoscopic cholecystectomy versus conventional laparoscopic cholecystectomy: a comparative study. Surg Endosc 2004; 18:379-382.
20. Miller DW, Schlinkert RT, Schlinkert DK. Robot-assisted laparoscopic cholecystectomy: initial Mayo Clinic Scottsdale experience. Mayo Clin Proc 2004; 79:1132-1136.
21. Corcione F, Esposito C, Cuccurullo D et al. Advantages and limits of robot-assisted laparoscopic surgery: preliminary experience. Surg Endosc 2005; 19:117-119.
22. Bodner J, Hoeller E, Wykypiel H et al. Long-term follow-up after robotic cholecystectomy. Am Surg 2005; 71:281-285.
23. Zhou HX, Guo YH, Yu XF et al. Zeus robot-assisted laparoscopic cholecystectomy in comparison with conventional laparoscopic cholecystectomy. Hepatobiliary Pancreat Dis Int 2006; 5:115-118.
24. Heemskerk J, van DR, van Gemert WG et al. First Results after Introduction of the Four-Armed da Vinci Surgical System in Fully Robotic Laparoscopic Cholecystectomy. Dig Surg 2006; 22:426-431.

25. Espat NJ, Jacobsen G, Horgan S et al. Minimally invasive treatment of esophageal cancer: laparoscopic staging to robotic esophagectomy. Cancer J 2005; 11:10-17.
26. Anvari M, Birch DW, Bamehriz F et al. Robotic-assisted laparoscopic colorectal surgery. Surg Laparosc Endosc Percutan Tech 2004; 14:311-315.
27. Brunaud L, Bresler L, Ayav A et al. [Advantages of using robotic Da Vinci system for unilateral adrenalectomy: early results]. Ann Chir 2003; 128:530-535.
28. Brunaud L, Bresler L, Zarnegar R et al. Does robotic adrenalectomy improve patient quality of life when compared to laparoscopic adrenalectomy? World J Surg 2004; 28:1180-1185.
29. Morino M, Beninca G, Giraudo G et al. Robot-assisted vs laparoscopic adrenalectomy: a prospective randomized controlled trial. Surg Endosc 2004; 18:1742-1746.
30. Winter JM, Talamini MA, Stanfield CL et al. Thirty robotic adrenalectomies: a single institution's experience. Surg Endosc 2006; 20:119-124.

Registration of Intraoperative 3D Ultrasound with MR Data for the Navigated Computer Based Surgery

Claudia Dekomien[1], Markus Mildenstein[1], Karin Hensel[2], Stephanie Hold[2] and Susanne Winter[1]

[1] Institut für Neuroinformatik, Ruhr-Universität Bochum,
44801 Bochum, Germany
E-mail: claudia.dekomien@neuroinformatik.rub.de

[2] Lehrstuhl für Medizintechnik, Ruhr-Universität Bochum, 44801 Bochum, Germany
E-mail: karin.hensel@rub.de

Abstract. Computer based navigated surgery assists the spatial orientation of the surgeon. Our system registers preoperative data like CT or MR with intraoperative ultrasound data to get the coordinate transformation between the preoperative and the intraoperative data. With a surface volume registration we avoid a difficult surface segmentation in the ultrasound data. To prevent radial exposure and to get more details in the soft tissue the use of MR data for the operation planning is common. Extracting the bone surface in MR data is more difficult than in CT data because MR data has no normalized gray values. To register the ultrasound with the MR data at the knee we detected distinctive anatomic regions in the ultrasound data. We selected an adequate MR sequence in which we could segment the bone surface at the specific region. We evaluate the registration with 1000 random starting positions. 99.2% of the 1000 trails reached the optimum with an error less than 1 mm.

1. Introduction

Due to a trend towards minimal invasive surgery, there is an increasing demand for navigation systems. Image based navigation provides the surgeon a three dimensional orientation where he can control the position of his instruments within preoperative data of the patient.

Many of the commercial navigation systems utilize landmarks as reference for the registration of preoperative data within the coordinate system of the patient. Often these landmarks are difficult to define accurately, which makes them ineffective for procedures requiring a higher grade of accuracy. Using intraoperative imaging for registration yields a much higher accuracy. However, established systems based on intraoperative CT or MR are too expensive for common applications.

Additionally the registration procedure with the above mentioned systems is time-consuming. At this point intraoperative ultrasound is a reasonable alternative. The acquisition of ultrasound data is fast and easy, and leads to comparatively low purchasing and operating costs.

Because of these advantages the interest in using ultrasound as reference for bone surgery increased during the last years [1,2,3]. We developed an algorithm which is able to register bone structures in CT and ultrasound data [4,5]. Our surface volume registration method enables registration of intraoperative ultrasound with preoperatively acquired CT or MR data avoiding the error-prone task of directly segmenting ultrasound data. Our system showed a high accuracy in phantom data [6] and reliable results in registering patient data of the lumbar spine [7]. In this article, we applied our methods to register osseous structures of the knee. As MR data are frequently used for clinical diagnostics of the knee [8], we focused on the registration of MR and ultrasound data. The use of MR data for diagnostic reason especially at the knee is customary, because of the detail level in soft tissue. Furthermore, there is no radial exposure.

2. Experimental Methods

Our algorithm implements a surface volume registration [4, 5]. The bone surface is preoperatively segmented from a MR or CT dataset. As the scan path of the intraoperative ultrasound scan is defined preoperatively, we are able to eliminate surface points which do not get depicted in the ultrasound data.

A good spatial distribution of the surface points is a prerequisite for achieving good registration results.

Segmentation of bone structures in CT data was done by thresholding as they are represented by defined Hounsfield units. MR is different in this respect, since bone structures do not map to defined gray values. Therefore, we analyzed various MR sequences with respect to bone-tissue contrast. We used T2-weighted MR images for segmentation of bone structures, as this sequence proved to have the highest bone-tissue contrast among those tested (T1, T2, PD).

Several ultrasound datasets of the knee were recorded using various scan paths. All ultrasound datasets were visually inspected to assess if they were suitable for registration. Decision criterion at that point was the existence of clearly visible bone structures. In this respect the region posterior-caudal of the patella proved to be most suitable. The bone surface in the MR-data was extracted using a thresholding approach. Figure 1 shows the MR data of the knee. The surface was extracted by scanning from inside the bone along the rays (see Figure 1). A surface point was defined when the ray reaches a gray value greater than a selected threshold. To reduce the data, only every fourth of the surface points was taken. Thus, the extracted surface consisted of 1447 points.

For this purpose T2-weighted data was particularly suitable as osseous structures and synovial fluid showed a sharp contrast. The ultrasound data was pre-processed with an adaptive time gain correction algorithm to enhance the osseous

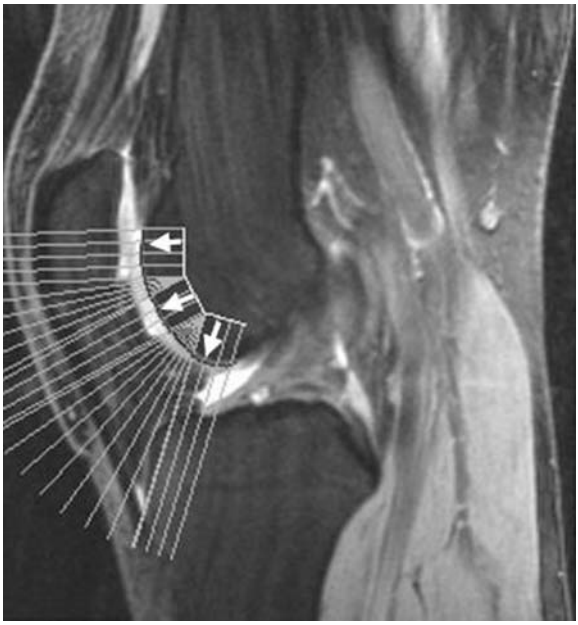

Fig. 1. T2-weighted MR data of a human knee. Extraction of the bone surface by scanning form inside the bone.

surfaces. For registration, the extracted surface was then projected into the ultrasound data.

The sum of gray values in the ultrasound data under the projected surface was used as optimization criterion. We applied a state of the art evolutionary algorithm (covariance matrix adaptation, CMA [9]) to this optimization problem [8].

3. Results and Discussion

For the evaluation a reference registration was defined by first manually pre-registering the surface and the ultrasound data as close to the optimum as possible and afterwards performing multiple local optimizations. The plausibility of the reference registration was verified by visual investigation of fused images of both volumes. The datasets were registered with 1000 different starting positions. The starting positions were generated by independent variation of translation (0 to 10 mm) and rotation (0 to 11 degrees).

To evaluate the registration results, we used the average distance between corresponding points of the registration result and the defined optimum. Within this metric, the starting distances (which were roughly uniformly distributed) ranged from 0 to 10 mm. We considered the registration successful if the average distance between corresponding points was below 1 mm. The results of the registration are shown in Figure 2.

The rate of correct registrations was 99.2%, and the mean precision of successful registrations was 0.096 mm (see Figure 3).Where about 80% of all trails registered with a misalignment of less than 0.01 mm. The average computing time for one registration was 3.7 seconds.

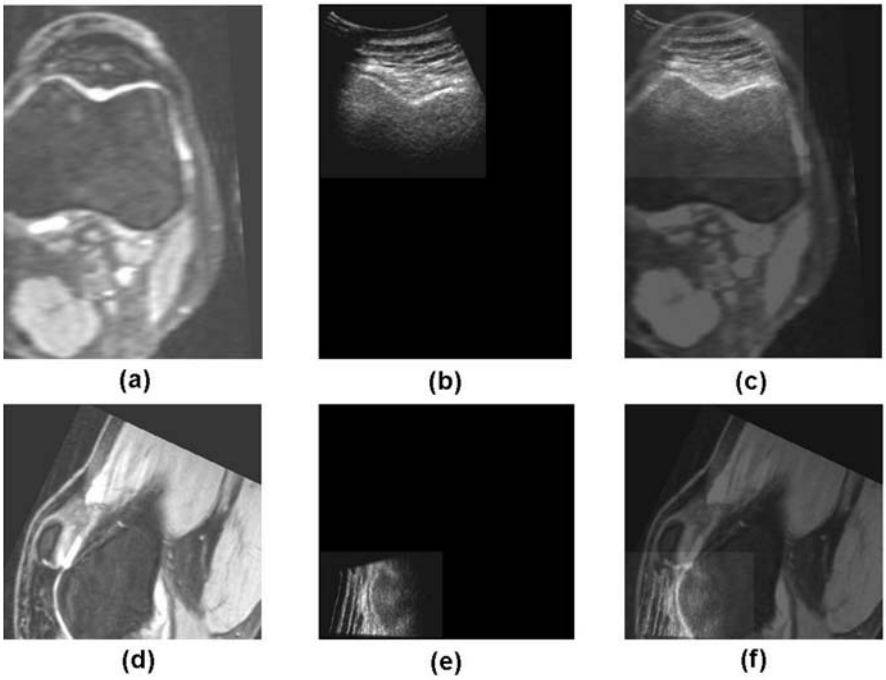

Fig. 2. Ultrasound-MR registration results (a) axial MR slice (b) corresponding axial ultrasound slice (c) axial MR-ultrasound fusion image (d) sagittal MR slice (e) corresponding sagittal ultrasound slice (f) sagittal MR-ultrasound fusion image.

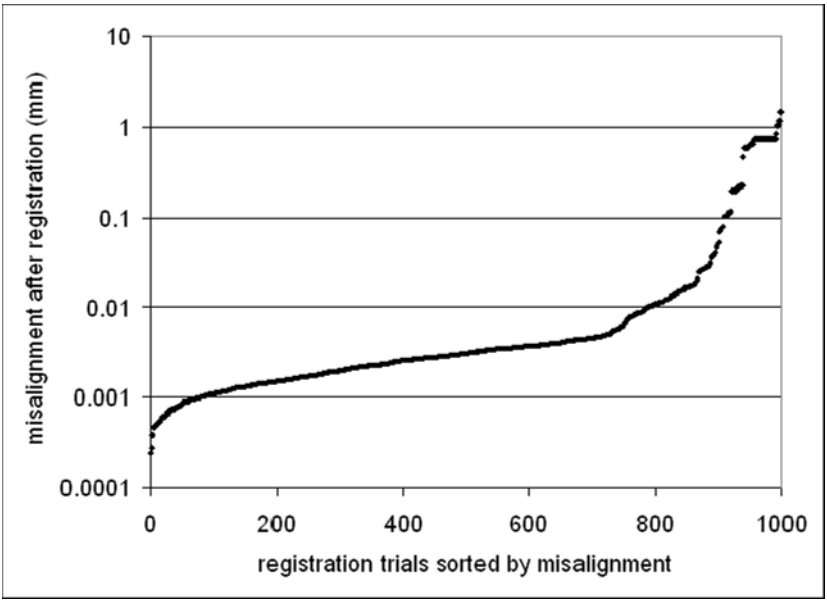

Fig. 3. Misalignment of 1000 registration trails with random starting positions between 0 and 10 mm and 0 and 11°.

4. Conclusions

The presented algorithm showed good performance registering MR and ultrasound data of the knee. We believe that it is well suited for navigated surgery because of its speed, precision and reliability.

The region posterior-caudal of the patella was particularly appropriate for registration as it featured a good spatial distribution of surface points. The computing time of just a few seconds was acceptable for intraoperative application. The high percentage of successful registrations was very promising and encourages us to carry out further experiments with additional anatomical regions and other MR-sequences.

Acknowledgements. This work was an activity of the OrthoMIT consortium. It was supported by the Bundesministerium für Bildung und Forschung (Az. 01EQ0424)

References

1 D. Amin, T. Kanade, A. DiGioia, B. Jaramaz, in *Ultrasound registration of bone surface for surgical navigation*, Comput Aided Surg 8, 1 - 16, 2003.

2 J. Tonetti, L. Carrat, S. Blendea, P. Merloz, J. Troccaz, S. Lavallee, J. Chirossel, *Vertebral surface extraction from ultrasound images for technology-guided therapy*, Computer Aided Surgery 4, Vol. 6, 204-211, 2001.
3 D. M. Muratore, B. M. Dawant, R. Ll. Galloway, *Clinical results of percutaneous pelvic surgery. Computer assisted surgery using ultrasound compared to standard fluoroscopy*, Proceedings of SPIE, Vol. 3661, 1499-1510, 1999.
4 B. Brendel, S. Winter, A. Rick, et al., *Registration of 3D CT- and ultrasounddatasets of the spine using bone structures*, Comput Aided Surg 7, 146-155, 2002.
5 S. Winter, B. Brendel, A. Rick, *Registration of bone surfaces, extracted from CT-datasets, with 3D-ultrasound*, Biomed Tech 47, 57-60, 2002.
6 B. Brendel, S. Winter, H. Ermert, et al., *In vivo Evaluierung und in vitro Genauigkeitsmessung für einen Algorithmus zur Registrierung von Ultraschall- und CT Datensätzen*, In: Procs BVM, 340-344, 2005.
7 S. Winter, B. Brendel, C. Igel, Registration of bone structures in 3D ultrasound and CT data: Comparison of different optimization strategies, Procs CARS, Vol. 1281, 242-247, 2005.
8 T. G. Sanders, M. D. Miller, *A Systematic Approach to Magnetic Resonance Imaging Interpretation of Sports Medicine Injuries of the Knee*, The American Journal of Sports Medicine, Vol. 33, No. 1, 2005
9 N. Hansen, A. Ostermeier, *Completely derandomized self-adaptation in evolution strategies*, Evol Comput 9, Vol. 2, 159-195, 2001.

Measuring the Fat Content of the Liver for Transplantation Medicine

Jörg Himmel [1], Manfred Nagelschmidt[2], Jürgen Treckmann[3], Christian Sehestedt[1], Sidi Mohamed Ait Sghir[1] and Stephan Sehestedt[4]

[1] RheinAhrCampus Remagen, Department of Measurement Engineering and Sensor Technology, Südallee 2, D-53424 Remagen, Germany
E-mail: himmel@rheinahrcampus.de
[2] Cologne University, Department of Surgery, D-51109 Köln, Ostmerheimer Str. 200, Germany
[3] Essen University, Department of Transplantation Surgery, D-45122 Essen, Huflandstraße 55, Germany
[4] The University of Technology, Faculty of Engineering, Sidney, PO Box 123, Broadway NSW 2007 Australia

Abstract. For a successful transplantation the fat content of the liver is an important parameter for the suitability of the graft. In a cooperation between the university hospitals Essen and Cologne and the RheinAhrCampus Remagen of the University of Applied Sciences Koblenz, the potentialities of electrical measurement of the liver fat content were investigated.

1. Introduction

The fat content of the liver is a crucial parameter for a transplantation to be successful. A fat content above 30% may result in strong rejection reactions and would even threaten the live of the patient. The determination of the fat content using tissue specimen in a pathologic laboratory is often problematic due to large distances. Thus, the specimen transport from the operating theatre to the laboratory cuts down the time in which the transplantation can be conducted. Especially in night time only a few laboratories in Germany are performing the examination.

In Cooperation between the university hospitals Essen and Cologne and the RheinAhrCampus of the University of Applied Sciences Koblenz, the possibility of measuring the fat content of the liver using the results of surveys on the interaction between electrical fields and biological tissue were examined.

2. Particularly Suitable Electrical Measurement Principles

In principle it is possible to use conductive, optical or electromagnetic active principles. However, because of the technical effort and applicability a measuring principle based on an optical spectroscopy was not considered any more.

Any biological tissue consists of living cells and extra cellular substances. Due to the structure of the tissue, the relative dielectric constant ε_r and the specific conductivity κ are highly dependent on the frequency [1,2,3,4]. The electrical behaviour of the liver can be described through the model of a suspension and its impedance property through an equivalent electrical circuit [1].

A measuring head was developed to conduct experiments based on a conductive active principle. Figure 1 illustrates the measuring head, which consists of two stainless steel needle laces, used as the electrodes, embedded in a plastics body. The distance between the electrodes is approximately 10mm.

Fig. 1. Conductive measuring head

To measure the impedance the Precision Impedance-Analyzer (type 4294A) from Agilent Technologies was used for the experiments in the frequency domain of 40Hz to 110MHz.

For the conduction measuring of the electrical impedance it is necessary to couple the electrodes to the tissue. Doing this, in general a barrier layer builds up between the metal and the electrolyte. The transition impedance is relatively unstable. For example, it varies through the contact pressure of the electrodes and the skins secretion. Therefore, the measuring of the impedance using two electrodes produces a large deviation [5]. The situation betters when using needle like electrodes that are plunged into the liver.

The impedance measuring using an electromagnetic stray field with a planar inductivity happens with only one coil, which is used to generate the field that we use to detect the backlash. Furthermore, the resonant frequency or the impedance of a parallel oscillating circuit consisting of a field generating inductivity and an in parallel connected capacitor can be analysed as a measurement signal. Inserting a tissue into the electromagnetic alternating field, both measurements vary depending on the composition of the tissue. For liver tissue, this happens mainly because of different dispersion impact from fat cells and body fluids based on water [1]. Figure 2 shows the measuring head with planar inductivity, which was

developed for the experiments. In the upper part of the illustration the convolution of the inductivity can be seen.

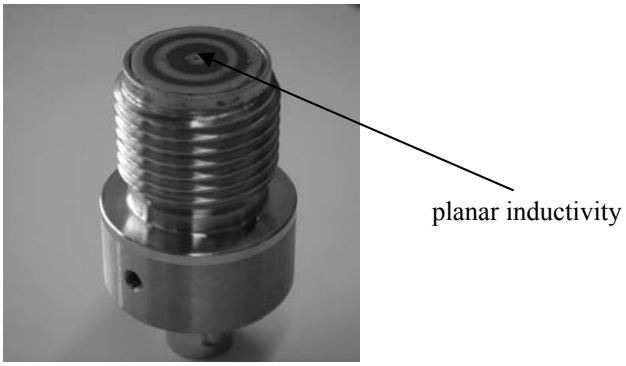

Fig. 2. Measuring head with planar inductivity

3. Measuring Results with Phantoms and Liver Tissue

For the experiments with prototypes of the sensor elements it was necessary to prepare a phantom, which has a similar behaviour as the liver. The chosen phantom consists of an emulsion of water and vegetable oil. Note that it is necessary to use emulsifier agents to compile a stable emulsion. These must not change the electrical impedance of the phantom. Such effects can occur when using emulsifier agents for cooling and lubrication purposes. Five phantoms were exclusively prepared for the experiments (Table 1).

Table 1. Phantoms

Number	1	2	3	4	5
Percentage Water/Oil	100/0	75/25	50/50	25/75	0/100
Emulsifying Agent	no	Lamesorb SMO20	Polymuls® PGPR	Polymuls® PGPR	no
Volume of the Emulsifying Agent	0%	<1,5%	<1.5%	<1,5%	0%
Agitation Time		1min	1min	1min	

The use of such a phantom is restricting in the meaning that the cellular structure cannot be reproduced. Moreover, locally varying concentrations are not feasible with these phantoms.

The aim of the experiments was to investigate how the impedance and resonant frequency vary with an increasing concentration of oil and where to find the greatest measurement effect. In figure 3 we present the results for the conductive measurement using plunged electrodes. As expected, we obtained good measurements in the lower frequency domain. A measurement of the impedance using alternate current in the domain of 1-5 kHz gives good results.

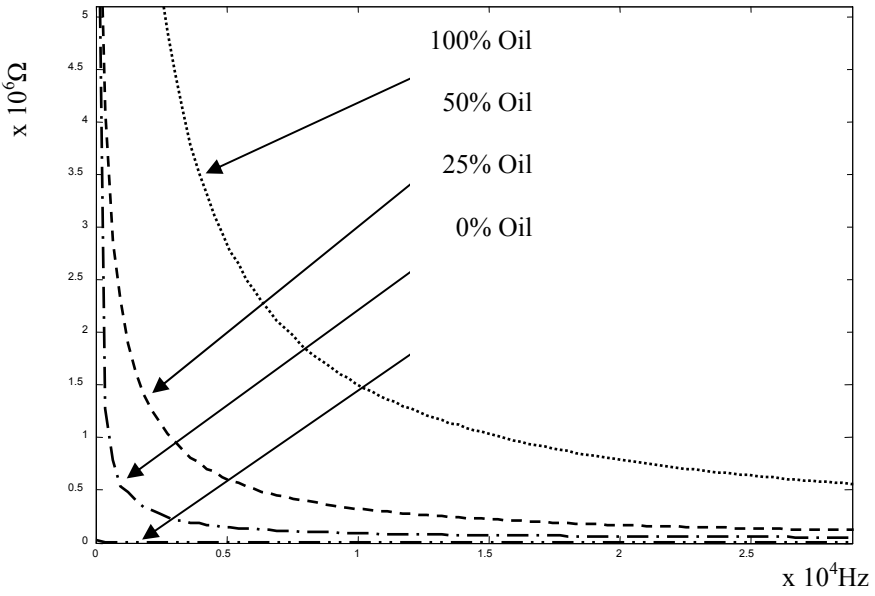

Fig. 3. Measuring results with the conductive Probe

The setup for the measurement using an electric stray field is comparably simpler. The measurement head only has to bear on the phantom and does not need to be plunged in. In the clinical every day live this is an easier to use method. An optimum of the measurement was found near 80 MHz. The according curves for the impedance in dependency on the concentration of oil are shown in figure 4.

Within the scope of first surveys using livers from pork and a first clinical trial, the measurement effect was approved. Caused by the locally different fat content, structural alteration of the tissue (carcinoma) and different moisture of the surface locally different measurements resulted

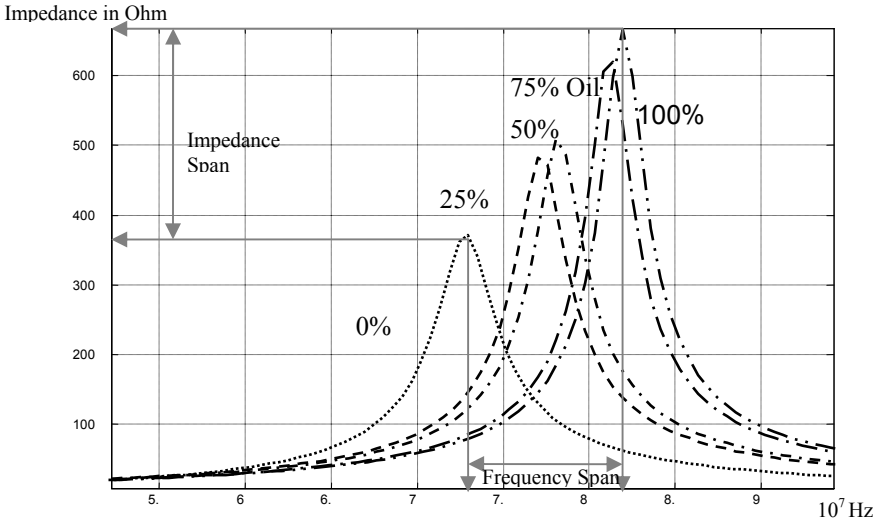

Fig. 4. Measuring results with the inductive Probe

4. Conclusion

For a transplantation to be successful, the fat content of the liver is a crucial parameter, which determines the suitability of a graft. Is this parameter above approximately 30%, a strong rejection reaction is likely and the transplantation cannot be conducted. With the presented method using measurements of the impedance based on an electromagnetic stray field, in many cases it will be possible to measure the fat content of a liver while the resection of the organ and thus, limiting the effort for examinations in pathological laboratories. In further clinical trials in the transplantation centre of the university hospital Essen, the accuracy of the measurements of the fat content are to be analysed and improved using human liver tissue.

References

1 Riedel, C. H.: Planare induktive Impedanzmessverfahren in der Medizintechnik. Dissertation, Universität Karlsruhe, Juli 2004.
2 Kaffanke, M.: Nichtinvasive Untersuchung von biologischem Gewebe mit Dielektrischer Hochfrequenz-Spektroskopie. Staatsexamensarbeit, Freie Universität Berlin, Juli 1996.
3 Netz, J., E. Forner, and S. Haagemann: Contact less impedance measurement by magnetic induction - a possible method for investigation of brain impedance. Physiological Measurement, vol. 14(4), pp. 463-471, 1993.
4 Foster, K. R. and H. P. Schwan: Dielectric properties of tissues and biological materials: A critical review. Rev. in Biomedical Engineering, vol. 17, no. 1, pp. 25-104, 1989.
5 http://www-ibt.etec.uni-karlsruhe.de/people/cr/forschung/forschung_de.htm (06.10.2006, 14:45)

Part IV

Biomechanics

Influence of Modern Above-Knee Prostheses on the Biomechanics of Gait

J. Wühr, U. Veltmann, L. Linkemeyer, B. Drerup and H. H. Wetz

Klinik und Poliklinik für Technische Orthopädie und Rehabilitation
Klinische Prüfstelle für Orthopädische Hilfsmittel, Robert-Koch Str. 30,
D-48149 Münster, Germany
E-mail: wuhr@uni-muenster.de

Abstract. The advent of modern knee prostheses has opened up a new quality in the provision of above-knee amputees. This can be demonstrated by means of kinetic and kinematic measurements. Amputees achieve significantly more security combined with sufficient dynamics.

1. Introduction

The provision of above-knee amputees with prostheses is in transition, especially the quantity and nature of prosthetic knees available has increased and thus became more and more complex. Meanwhile there are even more than those 219 prosthetic knees described by van de Veen [1] on the market. The demand on modern prosthetic knees is that they provide for maximum safety (prevention of fall) combined with high mobility [2]. In contrast to established prostheses the new generation of artificial knee joints should allow amputees a more physiological gait, which results in a higher level of safety and more dynamics but also in unloading of the contralateral side and a reduction of effort.

The advantage of modern prosthetic knee joints is the possibility of limited knee flexion under load (bouncing) or unlimited - but damped – knee flexion under load (yielding). This yielding and bouncing imitates properties of the natural gait i.e. the knee flexes throughout the loading phase at the beginning of the stance phase [3]. In this phase the vector of the ground reaction force is located behind the axis of the knee joint and determines a positive flexion moment.

At mid-stance of the gait cycle the prosthetic knee must be safe, but at the same time the amputee must able to unlock the knee easily and deliberately at roll-over when the weight is transferred to the contralateral side. There are basically two options for securing of the stance phase, one being the construction according to biomechanical principles - in this case the sagittal position of the knee joint – the other option the use of technical means [4]. Monocentric prosthetic knees without additional stance phase locking must be secured during loading by a strong hip extension moment exceeding physiological moments. Without this effort of the amputee the prosthetic knee would flex uncontrolled because the vector of the ground reaction force is located behind the joint axis at this stage. At the end of the stance phase a similar strong hip moment is needed to induce the necessary

knee flexion for the swing phase [5]. If the position of the axis of the knee joint is moved backwards, the amputee has more safety in the stance phase but needs more effort to unlock the prosthesis. Another consequence of this adjustment is the extension of the prosthesis in the swing phase. The amputee has to lift his body and so his gait becomes more unphysiological and, furthermore uneconomical.

Technical means, e.g. mechanical locking, load-dependent friction brakes or the use of hydraulic mechanisms, can help to reduce the unnatural strong extension moments in the hip joint.

The aim of our work still in progress is a classification of prosthetic knee joints by means of clinical and biomechanical aspects. We want to investigate the influence of the knee flexion under load on the biomechanics of gait. Special attention will be drawn to microprocessor controlled variable-damping knee prostheses.

2. Materials and Methods

So far 70 transfemoral amputees with mobility level 2-4 have taken part in our study. Altogether we investigated 21 different prosthetic knees. They range from the locked-knee type over mechanically passive prostheses to the microprocessor-controlled variable-damping knee. The amputees were aged between 17 and 91 years. As a prerequisite, optimum fitting of the socket had to be provided. The appropriate assembly guidelines for the joints were taken into consideration. This was supervised by a certified prosthetist-orthotist using the ***L.A.S.A.R. Posture*** (Otto Bock). This device combines a ground reaction force platform with an optometric laser system. It was used to control the statics of the prosthesis, especially the sagittal positioning of the prosthetic joint. After a medical examination by an orthopaedic surgeon, biomechanical and clinical measurements were taken using the optoelectronic gait analysis system ***(Vicon V460,*** 6 cameras, 50Hz) in combination with 2 ***Kistler*** force plates (9286 AA) to obtain kinetic and kinematic data.

3. Results and Discussion

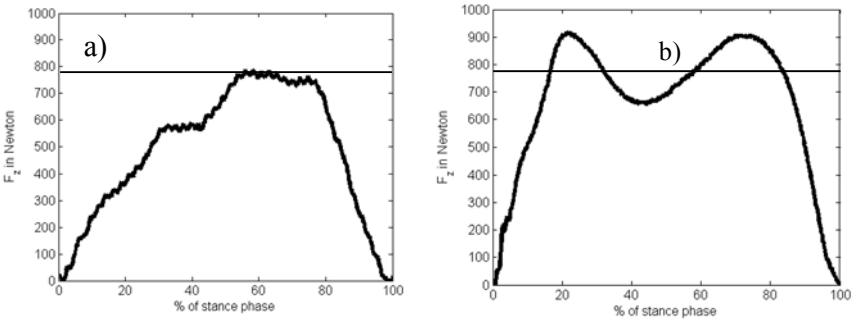

Fig. 1. a) prosthetic knee without flexion under load b) prosthetic knee with flexion under load.

The ground reaction force (Fig.1) shows the absorbing effect of prostheses with yealding and bouncing. In Fig 1b) one can clearly see the M-shape of the curve and the minimum which lies below the corresponding bodyweight of F_z /9.81. The curve looks like the ground reaction force of a healthy person. In Fig. 1a) this feature is completely missing.

If the prosthetic knee does not allow knee flexion in the beginning of the stance phase (Fig. 2a) – solid line) the corresponding joint moment is completely negative (extension moment). The dotted line of the healthy side shows the interrelation between knee flexion and flexion moment. At about 15 % of the gait cycle there is a clearly visible knee flexion of 20 degree at maximum and in the same region a positive flexion moment of the knee.

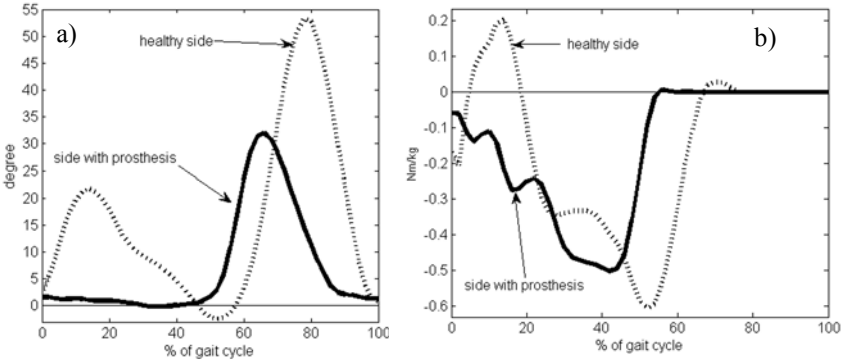

Fig. 2. Prosthetic knee without flexion under load: a) measured knee angle b) calculated knee moments - healthy side (dotted line), prosthetic side (solid line).

On the other hand already a slight bouncing or yealding can lead to positive flexion moments (Fig. 3). For the amputee this means not only comfort but also a reduction of effort because he does not need to secure the prosthesis with his

stump. Furthermore it implies that the amputee feels safe because he uses the full capacity of the prosthetic knee. If he tried or had to secure the prosthetic knee additionally with his stump, again a – sometimes strong – negative knee knee moment occurred.

The second advantage of modern prosthetic knees is the securing of the stance phase. All in all stance phase locking features and knee flexion under load lead to a more natural gait of the amputee. Especially the microprocessor-controlled variable-damping knees offer a high level of security and also sufficient dynamics at the same time. The gait of the amputee becomes more symmetric and thus physiological. Fig. 4 and Fig. 5 (same patient) show the difference between a prosthetic knee which secures the stance phase by mechanical means and a microprocessor-controlled variable-damping knee. Fig. 4 demonstrates that the asymmetry of the hip angle between the healthy side a) and prosthetic side b) becomes less.

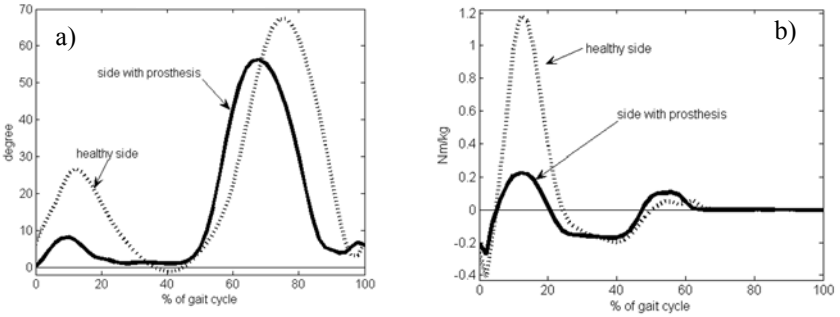

Fig. 3. Prosthetic knee with flexion under load: a) measured knee angle b) calculated knee moments - healthy side (dotted line), prosthetic side (solid line).

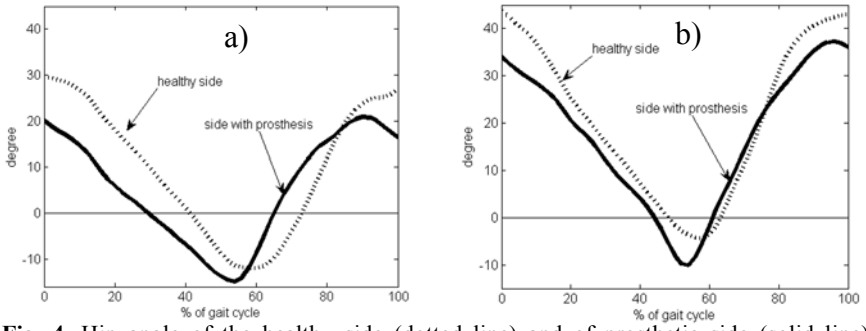

Fig. 4. Hip angle of the healthy side (dotted line) and of prosthetic side (solid line). a) mechanical passive knee: b) microprocessor-controlled knee.

In Fig. 5a) the amputee secures the prosthesis additionally using using his stump: At the beginning of the stance phase the flexion moment on the prosthetic side is low in comparison to the healthy side. The hip moment of the prosthetic side also changes much earlier from flexion to extension than the corresponding moment of the healthy side.

In Fig. 5b) the difference between the two prosthetic knees is evident. Most importantly, the microprocessor controlled prosthesis shows an increased flexion moment with a longer duration. This leads to a significantly improved symmetry between healthy and prosthetic side.

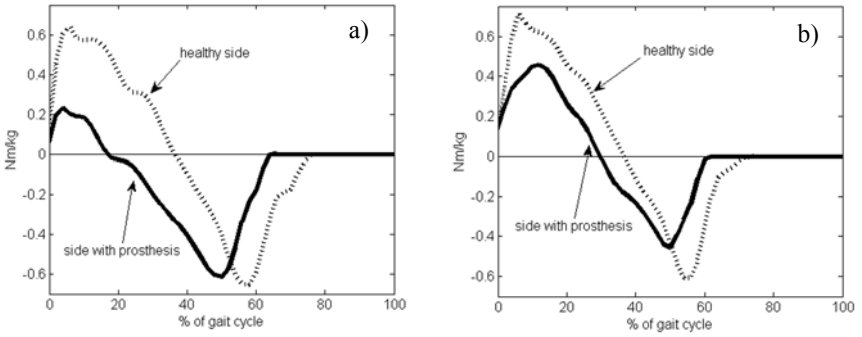

Fig. 5. Calculated hip moments on the healthy side (dotted line) and on the prosthetic side (solid line). a) mechanical passive knee: b) micorprocessor-controlled knee.

Overall the benefit for the amputee is apparent. The gait pattern has become more symmetric and physiological. The strong flexion moment shows that the patient is able to unload the contralateral side and to walk with a higher level of security and lower effort.

4. Conclusions

The possibilities to secure the stance phase and controlling knee flexion in the swing phase as well as the knee flexion under load are enormous. Amputees gain manifold benefit from such knees. Especially knee flexion under load allows them to unload the contralateral side and to walk with less effort. Furthermore they are able to walk ramps and descend stairs. This high level of security combined with sufficient dynamics is a great advantage of modern prostheses. The gait of amputees can nearly reach the symmetry of the normal gait of healthy persons.

References

1 Van de Veen P.G. *Above-knee Prothesis Technology*, P.G. van de Veen Consultancy, Enschede 2001.
2 Scherer H.W., Milde L *Orthopädie-Technik* **47**, pp 531-536, 1996.
3 Blumentritt *Orthopädie-Technik* **55** , pp 508-521, 2004.
4 Kaphingst W.: *Orthopädie-Technik* **45**, pp 18-25,1994.
5 Pawlik R. *Med. Orth. Tech*. **2**, pp 118-124, 2002.

Spinal-Load Analysis of Patient-Transfer Activities

Matthias Jäger, Claus Jordan, Andreas Theilmeier, Alwin Luttmann and the DOLLY Group*

Institut für Arbeitsphysiologie an der Universität Dortmund - *IfADo*, Ardeystr. 67, 44139 Dortmund, Germany
E-mail: mjaeger@ifado.de

* Members of the Dortmund Lumbar Load Study Group (besides authors): J. Metzler, H. Mujih, U. Öztürk, R. Göllner, M. Konhoff, K. Lukaszewski, J. Mattern, M. Schmitz, R. Smolka, J. Voß, F. Ziolkewicz

Abstract. Selected care-activities with patient transfers, which are classified as "definitely being endangering" with respect to the corresponding German occupational disease, were analyzed regarding the corresponding (bio-)mechanical load on the lumbar spine. In a laboratory study, the postural data of a health-care worker were recorded opto-electronically and via video documentation, the nurse's action-forces were captured via force sensors at a specifically modified bed, chair, or floor. The analyses of about 100 transfers show that patient transfers result in intensive lumbar load, which may exceed lumbar-load limits recommended for work design. Application of optimized transfer techniques resulted in diminished biomechanical load for the low-back.

1. Introduction

The transfer of patients may lead to high load on the spine, to acute low-back pain, and may accelerate the development of degenerative disc-related diseases in the long run of occupational life. Based on quantified (bio-)mechanical load on the lumbar section of the spine of health-care workers during patient transfers, the risk of overloading the spinal structures can be evaluated, and overload risk can be reduced by the derivation of adequate workplace design measures or applying optimized transfer techniques.

The so-called *Dortmund Lumbar Load Study 3* "*DOLLY 3"* [1-3] represents a 7-year research project on the determination of lumbar load in selected care-activities with patient transfers (cf. *DOLLY*: whole-shift lumbar-load monitoring for deriving adequate cumulative load indices [4], *DOLLY 2:* lumbar-load register for a large variety of materials handling tasks [5]). The *DOLLY 3* patient-transfer activities are classified by the Statutory Accident and Health Insurance Institution for Health Services and Welfare Care as "definitely being endangering" in the sense of the occupational disease "Intervertebral disc-related diseases of the lumbar spine caused by long-term lifting or carrying of heavy objects or caused by long-term activities in extremely trunk-flexed postures". In cases of this kind

of disease, specified criteria on disease as well as on work content have to be fulfilled if an individual must be compensated for.

2. Biomechanical Modelling

Applying simulation and evaluation software developed previously, but modified and extended for this study (*The Dortmunder* [6]), lumbar load was determined by model calculations. This tool, based on a 3-D multi-segmental dynamic validated biomechanical model, permits the quantification of several low-back load indicators considering inertial effects of the body and a handled object, the effects of asymmetry of posture and force exertion, as well as the effects of intra-abdominal pressure in supporting the trunk during forward-inclined positions.

In this computerized simulation tool, the human skeletal structure is represented by 30 body segments. These segments are, from the mechanical point of view, considered as rigid bodies, which are supported in 27 punctiform joints in total. Each body segment, supposing a cylindrical shape, is characterized by its length, radius, distance between centre of gravity and adjacent joint, weight as well as moment of inertia. The intervertebral discs within the trunk up to shoulder height – i.e. five lumbar discs and the lower ten out of the twelve thoracic discs - are considered as joints. Hence, sagittal and lateral bending, twisting, as well as the superposition of bending and twisting can be simulated realistically. For both sides of the body, foot, shank and thigh, shoulder, upper and forearm and hand were concerned. Ankle, knee, hip, shoulder, elbow and wrist joints represent the corresponding connecting points bilaterally. Besides a head-neck segment and the pelvis representing the trunk, 14 relatively flat cylindrical trunk segments were considered, the latter resulting from parallel cuts according to the location of intervertebral discs. Implementation of two object segments in the model, applied at the hands as arm's elongation, would allow studying the effect of tool usage on lumbar load.

The muscular structure in the lower trunk region which, in particular, is spread over the lumbar discs, is simulated by the effect of 14 muscles or muscle cords at the back and the abdominal wall. The back musculature is summarized in the Erector Spinae muscle group. Its two main muscle cords – the Longissimus muscle with its lumbar part and the Iliocostalis muscle with its medial part – are implemented each on both sides of the body. In addition to back muscles, medial-part muscle cords of the anatomically fan-like shaped Abdominal Obliques are considered. The internal and external parts of opposite sides are connected via a tendinous network, which particularly enable twisting the trunk. The lateral-part muscle cords of the Abdominal Obliques are also considered in the model; these muscles are located near the skin, are discriminated into internal and external parts, and are mainly activated during side bending postures. The two cords of the Rectus Abdominal muscle are located beneath the tendinous texture mentioned above and running parallel near the mid-sagittal plane. This muscle is not necessarily responsible for side bending, is more active in postures leaning backwards, and is therefore simulated in the model by a single muscle-force vector only, operating along the midline of the body. In contrast, the other muscle cords are represented in the model

by two muscle equivalents on the two body sides. In total, 9 equivalent force vectors for the analysis of lumbar load during manual materials handling and, in particular, during patient-transfer-activities are considered.

3. Experimental Methods

The examinations could not be performed in a hospital due to applying a measurement-assisted methodology for posture-and-force capturing. Figure 1 gives an impression of lab and equipment. Information about the nurse's postures was gathered via a combination of video-analysis and opto-electronic measurements [7]: One camera, installed beside the nurse at the lab's sidewall, documented preferably the trunk's forward inclination and spinal curvature, the 2nd camera – mounted above her at the ceiling - recorded bending and turning. A 3rd camera documented patient's posture, whereas a 4th one gave a spatial view of the scene. With a 3-D opto-electronic motion capturing system, small infrared markers attached to the subject were tracked. Two "position sensors" consisting each of three infrared cameras, were mounted at opposite walls of the lab. Markers at shoulders, hands, hips, heels and, for reference, the bed frame were tracked as 3-D coordinates' time courses. The nurse's movements were imitated in an iterative procedure applying a new whole-body stick figure animation system.

Nurse's forces during transfers in the bed (e.g. moving the patient towards the bed's head or shoving the bed-pan) were determined with regard to magnitude, direction and bilateral distribution by using a newly developed "measuring bed" [8]. Therefore, a common hospital bed was equipped with an additional framework, which was inserted between the bedstead and - via tri-axial force sensors at the four corners - the bedspring frame. So, nurse's forces were measured "indirectly" in all three components (vertical, forward, sideward); from bed-forces' distribution, the point of application of the resultant hand-force was derived. Leaning against the bed was considered via an additional sensor-equipped bar at the bed's side. Two force platforms were used for ground-reaction force recording at the floor in cases when the patient was leaving the bed.

A "measuring chair" and a "measuring floor", constructed analogously, enabled the analysis of transfers such as placing the patient in a chair or raising a lying patient from floor. For example, in order to examine transfer activities at a chair, e.g. "placing a patient from sitting at bed's edge in a chair and vice versa", the measuring system "chair" was developed on the basis of a commonly used patient-chair. Due to its dimensions and characteristics (e.g. lowerable arm rests or material of the upholstered seat), it was possible to reproduce many situations used in the care-sector with high authenticity. For gathering the action forces of the health-care worker, a force platform with four 3-D force sensors was used. The four rolls of the chair were replaced by a construction with several tie bars in order to ensure safe conditions of the chair on the platform. The height of the measuring chair could be adapted to the respective requirements. Furthermore, footstep-bridges were positioned above the platform in order to prevent a contact of the health-care worker

with the measuring system and to seperate patient-induced ground-reaction forces from nurse's action forces.

Throughout the research project, two professionally experienced health-care workers act as subjects, i.e. alternately as a patient or a nurse. They are both highly qualified in applying different performance conditions, in particular, conventional and optimized transfer techniques.

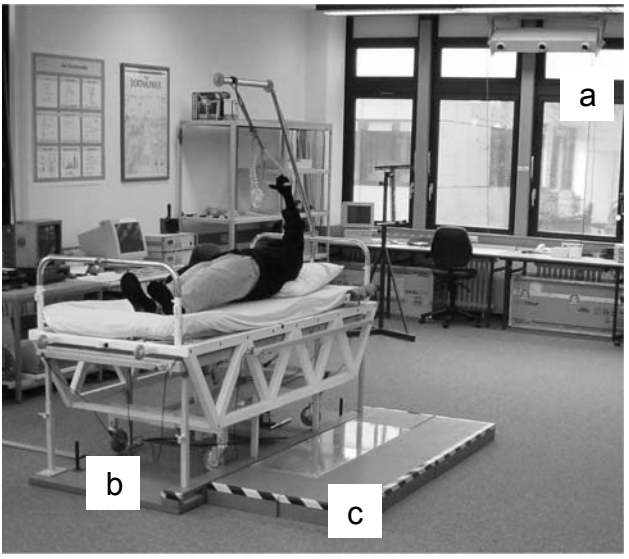

Fig. 1. Recording of nurse's postural data via opto-electronic position sensors (a), of action-forces via a "measuring bed" (b), and of ground-reaction forces at nurse's feet (c) in the Biodynamics Laboratory at the *IfADo*

4. Results

For several patient transfer activities within the bed, between the bed and a chair, and on the floor, various lumbar-load indicators - such as compressive and shear forces as well as bending and twisting moments of force with respect to the "lumbosacral disc L5-S1" between the 5th lumbar vertebra and the upper part of the sacrum - were determined. The time courses for the three force components at the reference disc during lifting a leg of the patient and the return action are exemplarily shown in Figure 2. A typical part of the activity - with acceleration and deceleration phases - is demonstrated in the 2nd section (nurse bends her trunk down to the patient): The disc compressive force falls briefly under the initial upright-posture value (0.8 kN), rises then up to a maximum (nearly 3 kN) and drops down to about 2 kN. During the "lifting phase", disc compression rises up to 4 kN, during holding it remains at about 3 kN. The two sections "lowering the patient's leg" and

"straighten up" essentially correspond reversely to "lifting" and "bending". The shear forces' time courses follow roughly the compressive force - however with clearly smaller values. In total, the highest force values are adopted during the lifting and lowering phases, when disadvantageous postures are superimposed by inertial effects. In the motion-induced sections of forward bending and straightening up and by the holding-the-leg phase, lower values resulted.

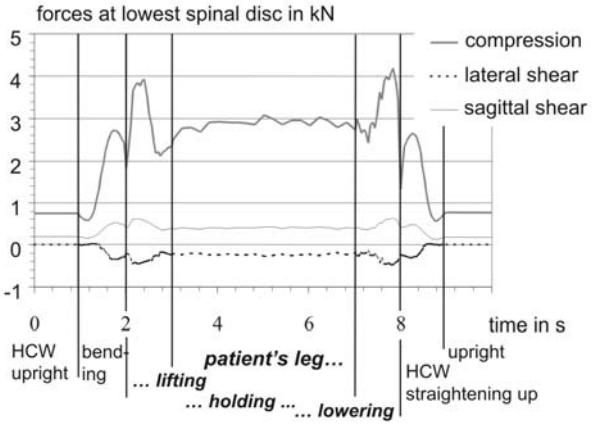

Fig. 2. Time courses for adequate indicators of lumbar-load, i.e. of the forces transferred via the lowest intervertebral disc of the spine ("L5-S1"), for an exemplary patient-transfer activity of a health-care worker (HCW): "lifting and lowering a patient's leg"

5. Discussion and Conclusions

Lumbar load strongly depends on nurse's posture and action forces, their temporal behaviour and the patient's support relating to her or his mobility and capacity, as the analyses of nearly 100 transfers studied in *DOLLY 3* has shown. Patient transfer activities may result in intensive lumbar load for the health-care workers, which in many cases exceed recommended lumbar-load limits (e.g. *Action Limit* [9], *Dortmund Recommendations* [10]). In summary, the obtained data are aimed to support work evaluation and the derivation of preventive measures for work design. Optimized transfer techniques resulted in considerably lower lumbar load in many cases. Exemplary testing of small auxiliaries (e.g. sliding board or mat) shows that lumbar load can furthermore be lowered in order to achieve health prevention in the everyday working life of health-care workers.

Previous biomechanically oriented studies into nurses' low-back load [11-15] can serve as a reference under restriction only, in spite of their undoubtless merits with other aspects in scientific analysis and prevention. For example, other types of patient transfers were analyzed than in *DOLLY 3*, or the transfers were limited to

"best-case scenarios" with low-weight patients or advantageous "palliating" postures and movements. Inertial effects due to patient-and-nurse movements or horizontal hand-forces were disregarded in other cases. In conclusion, this study demonstrates the necessity of a sophisticated postures-and-force capturing and biomechanical modelling, aiming an appropriate indication of lumbar load during patient transfer.

Acknowledgements. Berufsgenossenschaft für Gesundheitsdienst und Wohlfahrtspflege (Hamburg, Germany) for cooperation and financial funding as well as Barbara-Beate Beck and Beate Wiedmann (Forum fBB, Hamburg, Germany) for competent and helpful support.

References

1 M. Jäger, C. Jordan, A. Theilmeier, A. Luttmann, *Dortmunder Lumbalbelastungsstudie 3: Ermittlung der Belastung der Lendenwirbelsäule bei ausgewählten Pflegetätigkeiten mit Patiententransfer,* Shaker, Aachen 2005.
2 C. Jordan, A. Theilmeier, A. Luttmann, M. Jäger, and DOLLY Group, in *Meeting Diversity in Ergonomics,* Edited by R.N. Pikaar, E.A.P. Koningsveld, P.J.M Settels (CD-Rom paper), Elsevier, Amsterdam 2006.
3 A. Theilmeier, C. Jordan, N. Wortmann, S. Kuhn, A. Nienhaus, A. Luttmann, and M. Jäger, *Zbl. Arbeitsmed.* **56**, 228, 2006.
4 M. Jäger, C. Jordan, A. Luttmann, W. Laurig, and DOLLY Group, Int. J. Indust. Ergonomics **25**, 553, 2000.
5 M. Jäger, C. Jordan, A. Theilmeier, R. Göllner, and A. Luttmann, in *Handbuch der Arbeitsmedizin,* Edited by J. Konietzko, H. Dupuis, St. Letzel, Kap. IV-3.1, 36. Erg.-Lfg., Ecomed, Landsberg/Lech 2004.
6 M. Jäger, A. Luttmann, R. Göllner, and W. Laurig, in *SAE Digital Human Modeling Conf. Arlington VA,* Edited by Soc. Automotive Engineers (CD-Rom paper 201-01-2085), 2001.
7 C. Jordan, A. Theilmeier, A. Luttmann, and M. Jäger, in *Quality of Work and Products in Enterprises of the Future,* Edited by H. Strasser, K. Kluth, H. Rausch, H. Bubb, 1010, Ergonomia, Stuttgart 2003.
8 A. Theilmeier, C. Jordan, A. Luttmann, and M. Jäger, Z. Arbeitswiss. **59** 162, 2005.
9 National Institute for Occupational Safety and Health NIOSH, *Work Practices Guide for Manual Lifting,* Technical Report No. 81-122, DHHS, Cincinnati, 1981.
10 M. Jäger, A. Luttmann, and R. Göllner, Zbl. Arbeitsmed. **51**, 354, 2001.
11 W.S. Marras, K.G. Davis, B.C. Kirking, and P.K. Bertsche, Ergonomics **42**, 904, 1999.
12 M. Soyka, *Rückengerechter Patiententransfer in der Kranken- und Altenpflege*, Hans Huber, Bern 2000.
13 J. Skotte, M. Essendrop, A. Faber Hansen, and B. Schibye, J. Biomechanics **35**, 1357, 2002.
14 B. Schibye, A. Faber Hansen, C.T. Hye-Knudsen, M. Essendrop, M. Böcher, and J. Skotte, Appl. Ergonomics **34**, 115, 2003.
15 A. Garg, in *Meeting Diversity in Ergonomics,* Edited by R.N. Pikaar, E.A.P. Koningsveld, P.J.M Settels (CD-Rom paper), Elsevier, Amsterdam 2006.

Investigation of the Influence of Interbody Fusion on Biomechanics of the Cervical Spine Using a Computer Model

Stefan Lehner[1] and Ulrich Schreiber[2]

[1] Ingenieurbüro Stefan Lehner, Adolf-Kolping-Str. 2, 85737 Ismaning, Germany
E-mail: lehner.stefan@web.de
[2] Clinic of Orthopedics and Traumatology, Dept. of Biomechanics, University Hospital Rechts der Isar, Technical University, Connollystr. 32, 80809 Munich, Germany
E-mail: u.schreiber@tum.de

Abstract. Anterior cervical fusion alters the physiologic motion of the adjacent intervertebral joints. Using a computer model the changes in motion within the biological structures are investigated in dynamic loading situations. A multibody system of the cranial part of the upper spine (T3 to C1), clavicle, sternum, and cranium includes the exact geometry of the bony structures, the validated description of the material behavior of the passive soft tissue structures, and control elements simulating the active muscle structures.

1. Introduction

Since the mid 1950s anterior cervical fusion is a widely accepted method of treatment for cervical spine disease. Initially autogenous bone, typically harvested from the iliac crest, was used as interbody graft [1]. In the meantime alternative surgical techniques exist by using plates, cages, or spacers. The implants may consist of several materials, e.g. titanium, polyetheretherketone (PEEK), or carbon fiber reinforced plastics (CFRP) [4].

The main objectives for an anterior cervical fusion are: decompression of neural structures, reduction of deformity, immediate biomechanical support, restoration of foraminal height, maintainance of cervical lordosis, and creation of a conductive environment for optimal osteo-integration [2,3]. The clinical outcome of the fusion depends on multiple factors, such as the surgical technique and number of level fused. The success rate is reduced when multiple levels are fused than for single-level fusions [5].

Cervical interbody fusion results in a functional change of the spinal motion. Fusion may lead to an increased motion of the adjacent intervertebral joints. It is widely known that fusion of two or three vertebral segments lead to an accelerated degeneration of the next motion segments. Goal of this study was a detailed investigation of the biomechanical effects of single-level interbody fusion to the intersegmental motions of the adjacent joints and the change in the resulting forces in soft tissue structures. Dynamic loading situations were simulated using a three-dimensional multi-body system (MBS) computer model of cervical spine, neck, and head.

2. Experimental Methods

The development of physical material descriptions of soft tissue structures, like intervertebral discs or ligaments and tendons, and the three-dimensional motion of intervertebral joints are based on experimental data. This is inevitable for the verification of the functionality of the computer model.

Experimental Set-Up. The spine allows and restricts complex motion such as flexion-extension, lateral bending, axial rotation, and translation. The testing setup (Fig. 1, left) enabled movements in all 6 degrees of freedom. Depending on the alignment of the specimens within the setup, the applied force induced motion in the frontal (left/right lateral bending) or sagittal (flexion/extension) plane. Due to the lever arm (l = 375 mm), an alternating maximum load of M = ±7.5 Nm with an alternating axial component of F = ±20.0 N was implemented. The uniaxial load cell (F_{max} = 200 N, Burster, Germany) was placed coaxially to the cranio–caudal axis of the specimen at the end of the lever arm. As Yamamoto et al. found out, an axial load smaller than F = 150 N has no effect on the range of motion [7]. Left and right axial rotation (transversal plane) was realized by an electromechanical drive. Therefore, the specimens were loaded in their longitudinal axis with an alternating, maximum pure torsional moment of M = ±7.5 Nm and measured with a torque sensor (M_{max} = 100 Nm, Burster, Germany). According to literature, with these maximum loads, irreversible defects on the specimens could be ruled out [8,9,10]. For this biomechanical examination six human bisegmental specimen were used. At harvest the spines were dissected and the surrounding soft tissues were carefully removed to preserve the bony parts and spinal ligaments.

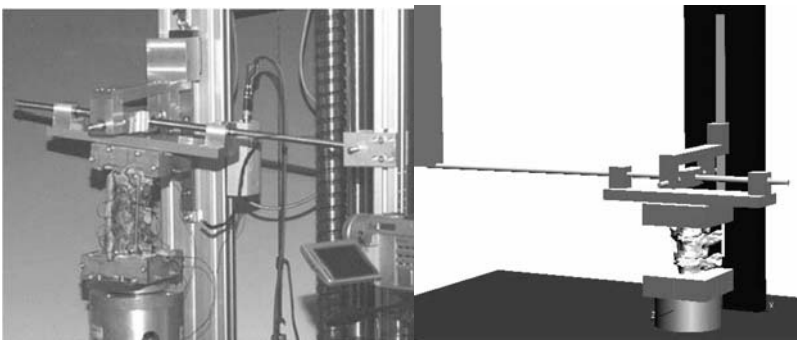

Fig. 1. Experimental set-up with bisegemental vertebra sections (left); MBS-model for validation of the computer model (right).

Computer Model. A multi body system (MBS) of the experimental set-up was developed to verify the description of the material behaviour of the intervertebral joints in the three main anatomical planes (frontal, sagittal, transversal) (Fig. 1, right).

With these verified descriptions a three-dimensional multi-body system (MBS) computer model of cervical spine, neck, and head was developed (Fig. 2). Based on computed tomography (CT) data of thoracic and cervical vertebras (T3 to C1), ribs, clavicle, sternum and cranium (without mandible) 3D surface models were created describing the exact bone geometries. Implementation of user routines allowed the modulation of force elements describing the material behaviour of human soft tissue structures, like ligaments, tendons, and cartilage layers. The viscoelastic behaviour of the ligaments was calculated depending on their cross-sectional areas, load-velocities, and the current strain situation. The force element was validated by tensile tests. The characteristic load/deformation curves (hystereses) of intervertebral joints were calculated depending on disc heights, pre-loads, rotational and translative velocities. Overall 25 muscles were modelled as control units. Depending on the physiological cross sectional areas and the resulting maximum forces each corresponding muscle takes part to execute specified motions of neck and head. The specified overall rotation, which was controlled by the muscles, was measured between vertebra T3 and Os cranium.

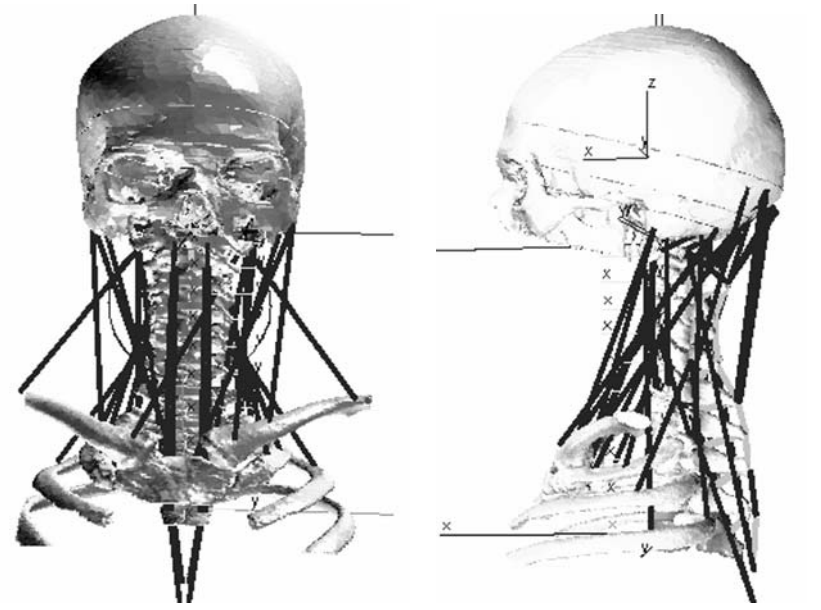

Fig. 2. Developed MBS-model with muscle elements; left: view from anterior, right: view from left side.

Loading Situations. Simulations were performed to compare the angle changes in the upper thoracic and the cervical spine with and without intervertebral fusion. Two loading situations were investigated:

a) To simulate a high dynamic loading situation a short impact was applied central at the Os frontale with a force peak of F_{max} = 1000 N during a period of time of t = 15 ms. After applied impact, the head moved backwards, followed by a muscle controlled return to initial position. Motion composition in intervertebral joints after fusion of C6-C7 was compared to the movement without fusion.

b) Comparison of motion composition in intervertebral joints after monosegmental (C6-C7) and bisegmental (C5-C7) fusion was investigated. An active muscle controlled flexion of the cranium related to vertebra T3 was applied to the model (rotation of α = 0.3 rad with a rotational velocity of v = 0.6 rad/s).

3. Results and Discussion

a) Motion composition in intervertebral joints after fusion of C6-C7 in extension of the head after impact

Comparison of the intervertebral angle change in the upper thoracic and the cervical spine with and without fusion (C6-C7) in the sagittal plane in high dynamic showed highest composition in the adjacent caudal joint C7-T1 (6.83 %) and an decrease of composition to the distant segments C2-C3 (5.63 %) and T2-T3 (2.93 %) (fig. 3).

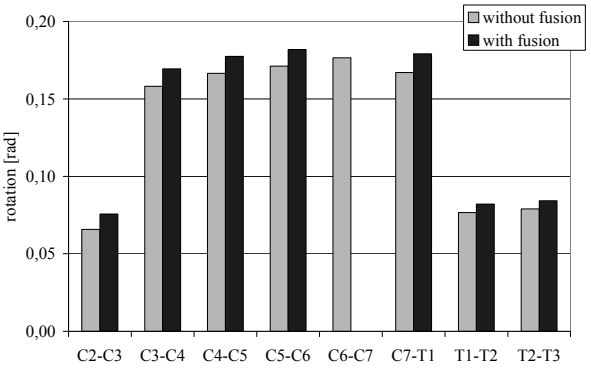

Fig. 3. Comparison of rotation in the intervertebral joints in extension with and without fusion in joint C6-C7.

The resulting forces in the Lig. longitudinale anterius increased by 4.5 % (mean), whereas the highest increase takes place in the next intervertebral joints (4.6 % in T1-C7, C6-C5, C5-C4) and the lowest increase in the upper cervical spine (4.2 %).

b) Motion composition in intervertebral joints after monosegmental (C6C7) and bisegmental (C5 to C7) fusion after active muscle controlled flexion of the head

Figure 4 shows the resulting motion composition in the intervertebral joints of the cervical and upper thoracic spine after monosegmental fusion at level C6C7 and bisegemental fusion at levels C5 to C7 compared to the motion of the spine without a fusion. As well in monosegmental and the bisegmental fusion a resulting higher increase of the rotation was investigated at all levels superior to the fusion level. Highest increase in both fusion techniques was calculated in the adjacent superior intervertebral joint with 19.7% in joint C5C6 within the simulation with the monosegmental fusion at level C6C7 and 23.9% in joint C4C5 within the simulation with the bisegmental fusion at levels C5C6 and C6C7. The greatest change in motion composition between the monosegmental and the bisegmental fusion case was seen in the adjacent joint superior to the fusion at intervertebral joint C7T1 (from 9.4% to 14.8%).

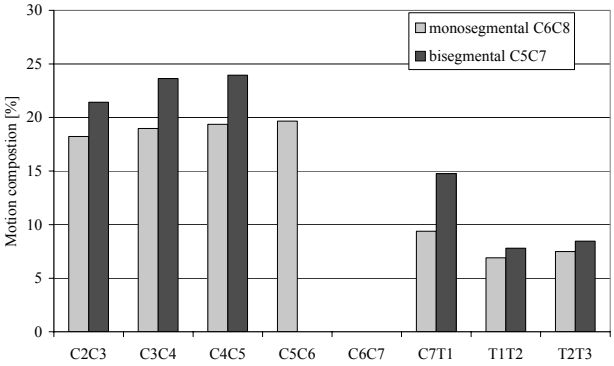

Fig. 4. Motion composition in the intervertebral joints during a muscle controlled flexion of the head: Comparison of monosegmental (level C6C7) and bisegmental (level C5C7) fusion.

Schwab et al. [6] observed significant differences of the motion at the levels immediately above and below the fusion at level C6-C7. In accordance to the results in this study, greater compensation occurred at the inferior segments than the superior segments for the lower level fusion C6-C7. In difference to the simulation these experimental tests were performed with a slow rotational velocity of 0.035 °/s and only with passive soft tissue structures (no muscles).

4. Conclusions

Anterior cervical discectomy and interbody fusion is a common treatment for the management of degenerative or traumatic instability of the cervical spine. Comparison of biomechanics (load effects and motion pattern) of the upper region of the human spine with or without an interbody fusion is very complex and comprises individual differences. Motion composition in extension for lower level fusion of the cervical spine at level C6C7 occurred at segments immediately adjacent to a single-level fusion, with greater composition below the fusion.

Comparison of monosegemental and bisegmental fusion showed greatest change in the adjacent joint superior to the fusion at intervertebral joint C7T1.

The developed computer model, with its implemented and experimentally validated force elements describing soft tissue structures, is an excellent tool for the simulation of the different loading and motion situations. In difference to cadaveric studies with experimental set-ups computer models allows the simulation of high dynamic loading situations.

References

1 D. S. Baskin, P. Ryan, V. Sonntag, R. Westmark and M. A. Widmayer, in *Spine*, Edited by J. N. Weinstein, Vol. 28(12), 1219, 2003.
2 L. Mastronardi, A. Ducati, L. Ferrante, in *Acta Neurochiru (Wien)*, Edited by J. A. Jane, Vol. 148, 307, 2006.
3 D. S. Brodke, P. Klimo, K. N. Bachus, and J. T. Braun, in *J Bone Joint Surg Am*, Edited by J. D. Heckman, Vol. 88(7), 1566, 2006.
4 H.-J. Früh, A. Liebetrau, and R. Bertagnoli, in *Orthopäde*, Edited by V. Ewerbeck, C.-J. Wirth, Vol. 31, 454, 2002.
5 T. H. Lanman and T. J. Hopkins, in *Neurosrug Focus*, Edited by J. A. Jane, Vol. 16(3), 1, 2004.
6 J. S. Schwab, D. J. DiAngelo, and T. Foley, in *Spine*, Edited by J. N. Weinstein, Vol. 31(21), 1439, 2006.
7 I. Yamamoto, M. M. Panjabi, T. Crisco, T. Oxland, in *Spine*, Edited by J. N. Weinstein, Vol. 14, 1256, 1989.
8 C. Knop, U. Lange, L. Bastian, and M. Blauth, in *Unfallchirurg*, Edited by C. Krettek, W. Mutschler, D. C. Nast-Kolb, Vol. 104(10), 984, 2001.
9 U. Schreiber, T. Bence, T. Grupp, E. Steinhauser, T. Muckley, W. Mittelmeier, and R. Beisse, in *Euro Spine J*, Edited by M. Aebi, Vol. 14, 197, 2005.
10 H. J. Wilke, V. Kemmerich, L. E. Cleas, and M. Arand, in *J Bone Joint Surg Br*, Edited by C. Krettek, W. Mutschler, D. C. Nast-Kolb, Vol. 83, 609, 2001.

Design and Testing of an Autonomous Computer Controlled Loading Device to Study Tissue Adaptation around Immediately Loaded Implants in the Reindeer Antler

Alireza Rahimi[1,2,3], Marcus Abboud[2], Gerhard Wahl[2], Ludger Keilig[1,3,4], Ingo Hensch[2,3] and Christoph Bourauel[3]

[1] Department of Orthodontics, Dental School, University of Bonn, Welschnonnenstr. 17, 53111 Bonn, Germany
E-mail: rahimi@uni-bonn.de
[2] Department of Oral Surgery, Dental School, University of Bonn, Welschnonnenstr. 17, 53111 Bonn, Germany
E-mail: g.wahl@uni-bonn.de
[3] Endowed Chair of Oral Technology, Dental School, University of Bonn, Welschnonnenstr. 17, 53111 Bonn, Germany
E-mail: bourauel@uni-bonn.de
[4] Department of Preclinical Education and Dental Research, Dental School, University of Bonn, Welschnonnenstr. 17, Germany
E-mail: ludger.keilig@uni-bonn.de

Abstract. The investigation of bone remodeling phenomena around immediately loaded dental implants with regard to clinical, histological and biomechanical aspects is of great importance. The main interest is directed towards the time-dependant behavior of the bone around the implants. The aim of this work was to develop an autonomous loading device that has the ability to load any inserted implant with a defined force for predetermined time slices. For the execution of the experimental studies a novel animal model will be established. For this task, the reindeer antler will be used as a reference model for bone remodeling processes as implant bed. For loading the implants, an autonomic simulator for the application of occlusal forces has been developed. The mechanical part of this device can be attached to the antler and it is capable of cyclically loading the implant with forces of up to 100 N. The loading device was subsequently tested with a biomechanical measuring system. The calibration of devices such as using a force/torque transducer with a range of 80N was done. This exhibit A logarithmic force/current relationship.

1. Introduction

The use of dental implants did broaden the alternatives of therapy after loss of teeth. Integration of implant anchored or implant supported reconstructions of the masticatory apparatus is a good approximation to the ideal of a functional 'Restutio ad integrum'. It is of particular interest to deal with the magnitude of intraoral forces under physiological loading (mastication, swallowing, and so on), the temporal distribution of these events, and the interdependencies of loading, implant healing and bone deformation. The stability of the implant/bone interface

was determined using different experimental and numerical methods as well. Clinical and animal experimental studies could prove that the bony tissue functionally adapts to a changed mechanical environment [1]. Within certain physiologic limits, bone has the ability to react to a change in the mechanical loading with a change in its structure. This ability to adapt to a changed environment is strongly dependent from the tissue and cell deformation in the microenvironment of the loaded bone. The investigation of bone remodelling phenomena around immediately loaded dental implants in animal experiments causes an enormous stress due to repeated anesthetization of the animals in order to realise a controlled loading protocol. It was the aim of this study to reduce this stress significantly by implementing a novel animal model using the reindeer antler as implant bed. From the biomechanical point of view, the material parameters of cortical bone and trabecular bone are of highest relevance and have an impact on the results of numerical simulations. Studies performed by Currey [2] and by Vashishth et al. [3, 4, 5] on reindeer antlers showed that the elastic and the fracture behaviour are analogous to that of bone. A prototype of an autonomous loading simulator was designed, that can be fixed to the antler and manages the cyclic loading of the implants over a predefined time span.

2. Experimental Methods

A prototype of an autonomous loading simulator was designed and constructed. The basic principle of the construction is shown in figure 1. The loading device consists of a mechanical and an electronical part. These are described in the following chapters.

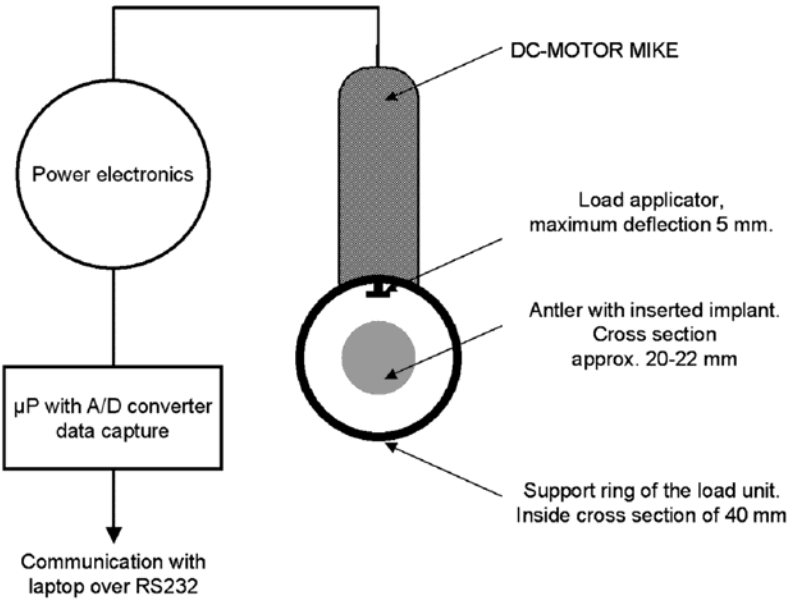

Fig. 1. Basic principle of the loading device.

Construction of the Mechanical Part. The mechanical part is manufactured from a commercial linear motor (DC Motor Mike, Lot-Oriel, Germany) and a customised motor chassis (figure 2). The chassis can be fixed to the antler on top of an inserted implant using corticalis screws (see figure 2a). The linear induction motor serves as loading unit which is connected to the motor chassis. Power supply of the motor is realised with a common 9 V battery block. The maximum load that can be applied with that motor and the battery reached 70 N.

Construction of the Electronical Part. The motor is controlled and driven by a control unit (figure 3), which allows to define different loading protocols. The control unit consists of a motor driver circuit and a matchbox-sized microcontroller board with integrated 12-bit analog/digital converter (µMODUL-8051LP, Phytec, Germany). The motor driver circuit (figure 3a) handles the microprocessor (µP) signals for moving the motor up and down, conditions data from the motor current for force calibration and transfers it to the µP. An especially developed software running on the µP board enables to define different loading protocols, measures the motor current, and counts the loading cycles, applied. The control unit can be connected via a serial port to a host-PC.

Power supply of the µP board is realised with a set of three 1.2 V accumulators. The microcontroller is equipped with an external battery buffer to back-up the data contents in the RAM and provide power for a Wake-Up logic of the board when it is in the OFF-Mode. This OFF-Mode offers extraordinary power saving capabilities: Operating in this mode, the power supply of the module is shut off and only essential board components are supplied via the battery buffer. The respective battery has a life span of 2 years.

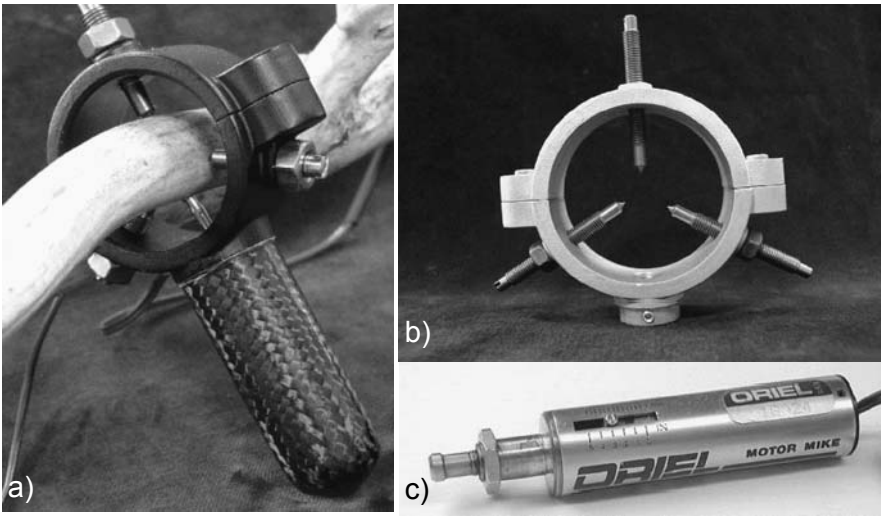

Fig. 2. Integrated loading device on a shedded antler (a), main chassis (b) and Motor Mike (b).

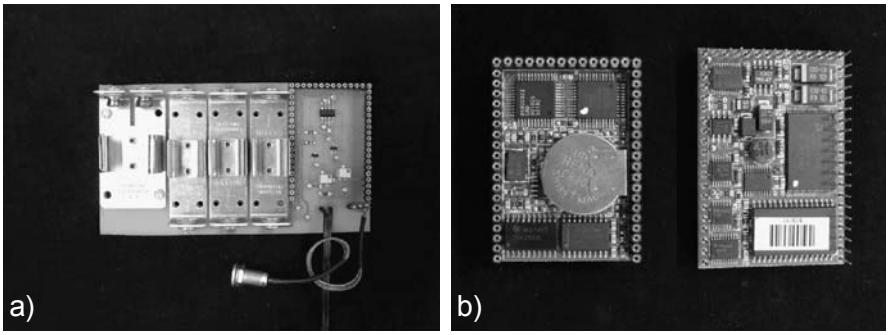

Fig. 3. Driver circuit and power supply board (a) and microprocessor module (b).

The control programme was realised such that the µP wakes up only for the loading cycles. During the remaining time, the µP is in the OFF-Mode. By doing so, the chosen accumulators with capacities of 2600 mAh ensure an autonomous operating time of up to 60 days.

The control unit can be connected over a wireless Data Communications Module to a host-PC. The communication is implemented using a 868.35 MHz Transceiver Module with a data transmission rate of 19.2 kbps. Hereby the device provides a wireless coverage of 300 meter.

Calibration and Measurements. The loading device was calibrated and tested using the biomechanical set-up He xapod Measurement System (HexMeS, figure 4, [6]). The HexMeS is equipped with a calibrated 6-component force/torque transducer with a range of 120N/12Nm (FT130/10, Schunck Spann- und Greiftechnik, Germany). The device was adjusted such that the loading tip was placed exactly on top of the lever arm of the force/torque transducer of the HexMeS (arrow in figure 4, right). The control programme of the µP regulated and measured the motor current. By increasing the motor current the force of the device was increased and measured by the HexMeS transducer. This procedure delivered a force/current relationship that can be used to define the forces in the loading protocols.

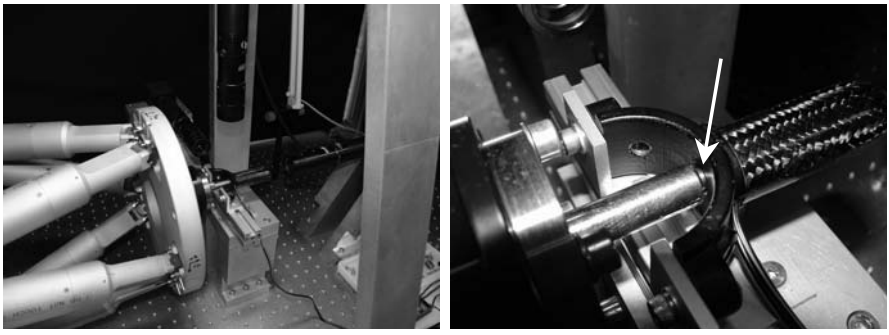

Fig. 4. Calibration of the loading device using a force/torque sensor.

3. Results and Discussion

Figure 5 shows the measured calibration curve of the device. As the power supply of the motor was realised with a common 9 V battery, the maximum motor current was limited to approximately 70 mA which allowed a vertical load of up to 70 N. As the maximum motor current is around 120 mA, forces up to 100 N can be realised by adapting the power supply. The calibration curve of the device displayed a logarithmic relationship between force and current (figure 5). This relationship was integrated into the control programme and is used to directly control the force of the device via a feedback loop.

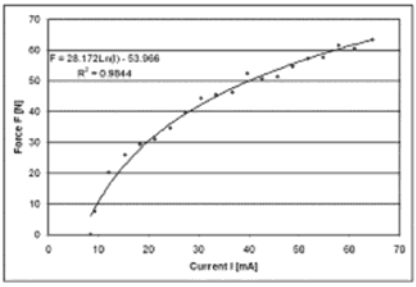

Fig. 5. The calibration reflects a logarithmic force/current relationship.

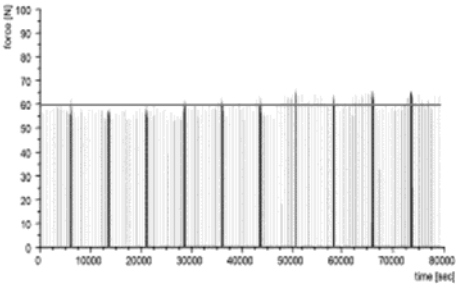

Fig. 6. Simulated loading protocol over one day with a predefined force of 58 N.

On the basis of a realistic loading protocol, a permanent loading test over 24 hours was performed (figure 6). The loading protocol comprised four loading cycles every ten minutes and 100 loading cycles every two hours. The maximum force was adjusted to 58 N. The thin needles in figure 6 represent the four loading cycles every ten minutes, the thicker needles the 100 loading cycles. Comparing the tips of the needles with the predefined force (red line), it is obvious that the force of the device can be controlled with an accuracy of approximately ±10 per cent.

Figure 7 shows a first test for adaption and positioning of the device on the antler. The animal was not anaesthetised for this test, holding of the animal by a keeper was sufficient.

4. Conclusions

Calibration of the loading device proved that the mechanical design and the selected motor are appropriate to apply vertical loads of up to 70 N with motor currents of a maximum of 70 mA. The maximum loading frequency is about 1 Hz, the maximum autonomous operating time around 60 days. With these parameters and the control programme it is possible to simulate complex loading protocols with idle periods and simulated chewing and swallowing processes in this new animal experiment employing the reindeer antler as an implant bed.

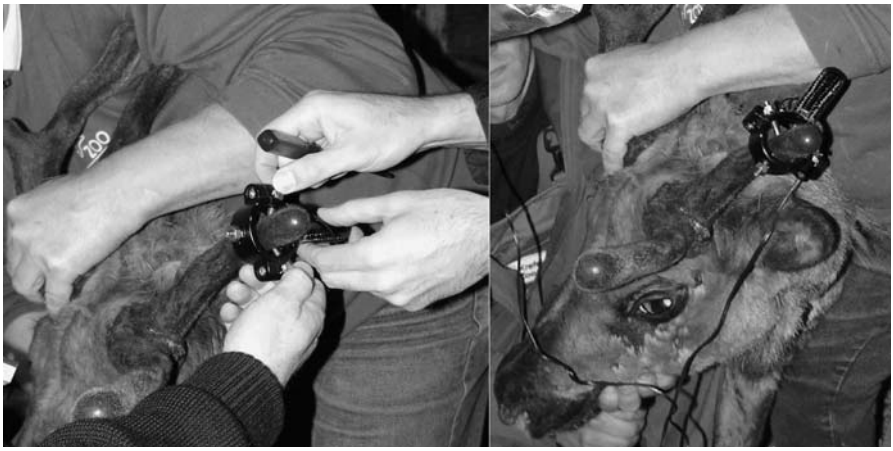

Fig. 7. Fixation of the device to the antler of a reindeer in Duisburg zoo. The animal stayed calm without any anaesthesia.

Decisive and important benefits of this animal model and the loading device are that the animals must not be sacrificed after experimentation, the load on the implant can be applied and controlled without repeated anaesthetisation and specimens of antler tissue can be prepared for biomechanical and histological studies from antler segments either after shedding or before that point by cutting segments out of the antler with an osteotomy saw. Finally, reindeers are very tame and easy to keep. This fact facilitates animal experimentation and first complex laoding protocols will start very soon.

Acknowledgements. The authors wish to thank Dentsply Friadent for financial support.

References

1 L. Lanyon, Journal of Bone Mineralisation Research **7**, 369, 1983.
2 J. D. Currey, Journal of Biomechanics **22**, 469, 1989.
3 D. Vashishth, K. E. Behiri, W. Bonfield, Journal of Biomechanics **30**, 763 (1997).
4 D. Vashishth, K. E. Tanner, W. Bonfield, Journal of Biomechanics **33**, 1169, 2000.
5 D. Vashishth, K. E. Tanner, W. Bonfield, Journal of Biomechanics **36**, 121, 2003.
6 L. Keilig, C. Bourauel, M. Grüner, S. Bayer, R. Hültenschmidt, K. H. Utz, H. Stark, Biomedizinische Technik **49**, 208 2004.

Numerical Simulation of the Biomechanical Properties of a Prefabricated Attachment System for Use in Prosthetic Dentistry

Susanne Reimann[1,2], Christoph Bourauel[1], Ludger Keilig[1,2,3], Andreas Jäger[2], Helmut Stark[3] and Mathias Strazza[4]

[1] Endowed Chair of Oral Technology, Dental School, University of Bonn, Welschnonnenstr. 17, 53111 Bonn, Germany
E-mail: bourauel@uni-bonn.de
[2] Department of Orthodontics, Dental School, University of Bonn, Welschnonnenstr. 17, 53111 Bonn, Germany
E-mail: susanne.reimann@uni-bonn.de
[3] Department of Preclinical Education and Dental Research, Dental School, University of Bonn, Welschnonnenstr. 17, 53111 Bonn, Germany
E-mail: ludger.Keilig@uni-bonn.de
[4] Cendres & Métaux SA, Rue de Boujean 122, 2501 Biel-Bienne, Switzerland

Abstract. In prosthetic dentistry many different prefabricated attachments are used for non-permanent fixation of dentures. A numerical model to evaluate the loading behavior of such a system in a realistic environment under different typical clinical loading situations was developed using Finite Element Analysis (FEA). The model was used to investigate the mechanical properties of one selected attachment system.

1. Introduction

Due to an increased average expectation of life in the population there is a growing need for prosthetic devices in dentistry. One method for the non-permanent fixation of partial dentures to the remaining teeth are prefabricated attachment systems [1, 2]. Currently there are lots of different attachment systems using various techniques in clinical practice. There is a large number of different systems, which gives rise to the question of the differences between the attachments. During clinical use all the different systems are exposed to mechanical loading, for example during chewing or swallowing. In order to investigate the differences in the loading behavior of such systems in clinical use, a FE model of the lower jaw including a partial denture held in place by such a system has been developed. The model development was based on the clinical situation of a lower jaw with six remaining teeth (31 to 33 and 41 to 43) and a partial denture over the remaining teeth 34 to 37 and 44 to 47. The mechanical behavior of these structures, the attachment itself as well as the surrounding soft and hard tissue, during typical clinical loads was investigated with the help of FEA.

As the jaw model should be applicable to investigate a large range of different attachment systems in order to compare them, modeling should include the relevant anatomical structures, which especially involves the soft tissue, i.e. mucosa

and periodontal ligament (PDL). Moreover, the size of the resulting model should allow an acceptable calculation time for the simulations.

2. Materials and Method

FE Model of the Lower Jaw. It was the aim of this study to determine the loading behavior of different attachment systems in clinical practice with a special regard to the biomechanical suspension of the attachment, the denture and the teeth including the surrounding soft tissues. Reduction of the model size was achieved by assuming symmetry and only modeling the left half of the jaw.

The FE model of the lower jaw was based on the surface data set 'teeth with roots and gums' by Digimation Corp., Louisiana, USA (see fig. 1a) containing a fully toothed lower jaw. As the alveolae were not present in the model, they were reconstructed using the geometry of the roots of the teeth. The molars and premolars were not required and removed from the model. The mucosa surface in the molar region was modified to represent the bone reduction following tooth loss (fig. 1b). Based on this mucosa surface the bone was modeled. The periodontal ligament plays an important role in the mobility of the teeth. It was modeled at the tooth/bone interface assuming a constant thickness of 0.2 mm. The resulting FE model consisted of approximately 187.000 tetrahedral elements and 36.000 nodes (fig. 1c).

Denture and Attachment System. The inner surface of the denture base followed the mucosa surface, representing a "perfect fit" denture. Surface data taken from the original jaw model was used to model the occlusal side of the denture.

The commercially available attachment system Mini-SG-PLUS (Cendres & Métaux SA, Switzerland, see fig. 2a) was chosen as the first system to be investigated. The FE models (approximately 47.000 nodes and 82.000 4- and 10-noded tetrahedral elements) were based on CAD data of the attachments. CAD data as well as material parameters of the involved materials were supplied by the manufacturer. Connecting the attachment to the canine, first the canine´s crown was reduced corresponding to clinical practice and restored with a dental gold alloy. Subsequently, the female part of the attachment was connected to this restored crown.

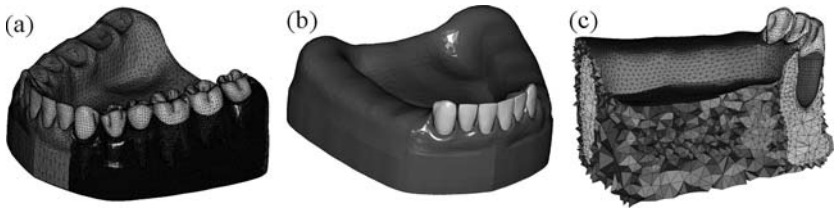

Fig. 1. (a) Surface model of the lower jaw with incorrect modeled alveolae and fully modeled teeth. (b) Surface model of the jaw after removing all molars and premolars and modeling the effect of an atrophy. (c) Resulting FE model of the left half of the jaw, including bone and periodontal ligament.

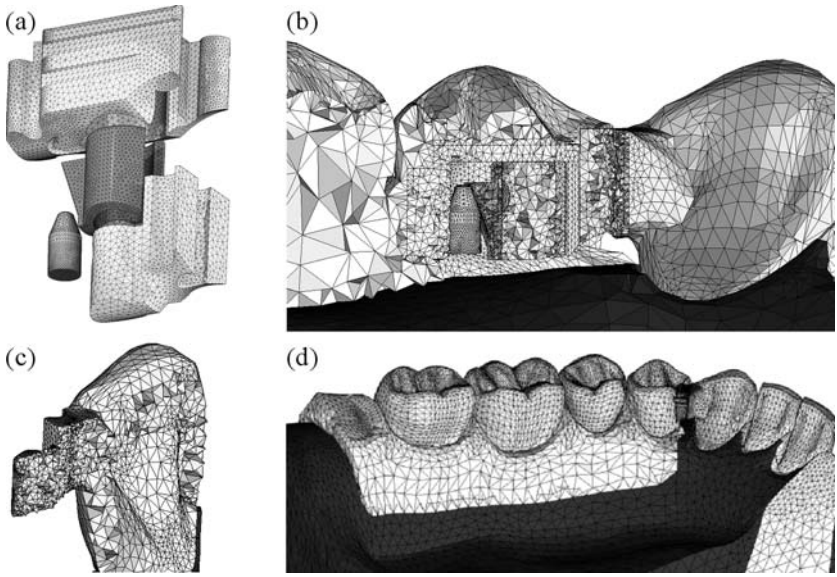

Fig. 2. (a) Attachment system Mini-SG-PLUS, consisting of the male and the female part, retention element and activation screw, which was idealized in the FE model. (b) Cut through the combined model. (c) Cut through the male part of the attachment connected to the canine tooth. (d) Overview over the complete model.

Simulated Load Cases. To investigate the loading behavior of the attachment and the surrounding tissue, three different load cases were considered (see fig. 3): In the load case 'single', load was applied directly onto the attachment without surrounding tissue. This load case can be compared with standard common materials tests of such devices. The base of the female part was fixed. As a tipping motion of the male part may occur depending on the exact location of the point of load incidence, this case was subdivided in one with excessive tipping and one without tipping (fig. 3a). The load cases 'indirect' and 'direct' corresponded to the clinical situation (see fig. 3b). In the load case 'indirect', force was applied in the posterior region of the denture at center of the tooth 36. In the load case 'direct', load

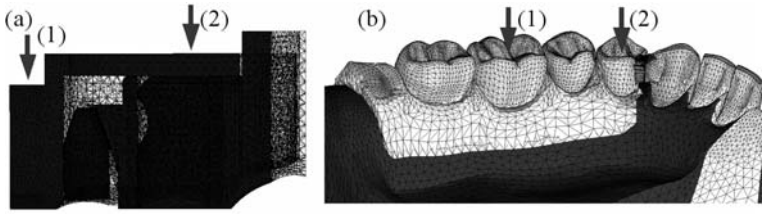

Fig. 3. Points of force application in the different load cases: (a1) 'single with tipping', (a2) 'single without tipping', (b1) 'indirect' and (b2) 'direct'.

was applied in the anterior region of the denture, directly above the male part of the attachment. In all three load cases two different loads (100 N and 200 N) from coronal direction (global z axis) were applied. These forces correspond to the values given in literature for typical mean clinical loads [3 – 6]. All FE simulations were preformed with the FE package MSC.Marc/Mentat 2005r2.

3. Results

In all simulations the highest loads within the attachment system could be found in the male part. Thus the following will focus mainly on this component. Highest stresses in these components were located in all cases at the connection (the 'neck') between the guidance and the base of the male part (see fig. 4). In the load case 'single with tipping' values of approximately 750 MPa were calculated in this area for a load of 200 N, which was clearly above the yield limit of the corresponding material (dental gold alloy 'Ceramicor', Cendres & Métaux SA). This stress would result in a plastic deformation of the male part and might induce a failure of the attachment. The forced tipping motion induced an additional location of high stresses at the top of the guidance as well as at the base (see fig. 4a, b). In both clinical load cases a slight tipping motion could be observed, which caused stresses at the top of the guidance (fig. 4c, d). Only minor additional stresses could be observed at the base. These stresses were clearly below the yield limit of Ceramicor, and consequently no plastic deformations are to be expected. In load case 'direct' the calculated stresses of approximately 250 MPa at a load of 100 N were twice as high as in the load case 'indirect'.

A comparison of the calculated stresses in the different load cases shows that stresses were highest for the load case 'single with tipping', while being lowest for the load case 'indirect' (fig. 4). Nonetheless the location of the peak stresses was identical in all simulations. High stresses were seen in the neck of the male part, and a tipping motion induced additional stresses at the top of the guidance.

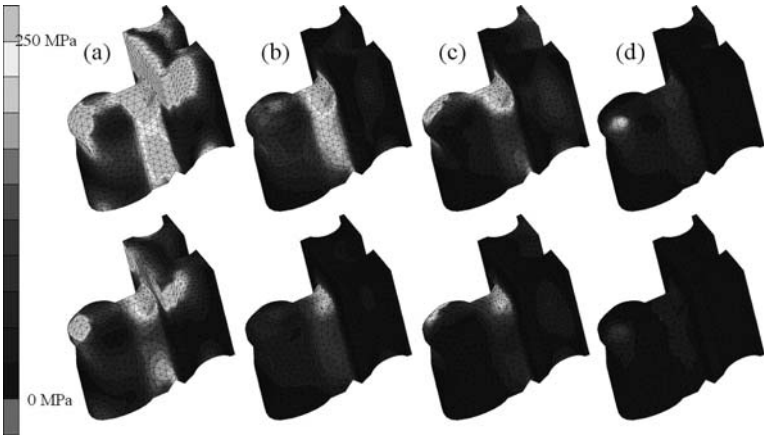

Fig. 4. Stress distribution in load case 'single with tipping' (a), 'single without tipping' (b), 'direct' (c) and 'indirect' (d) at a force of 200 N (upper row) and 100 N (lower row) .

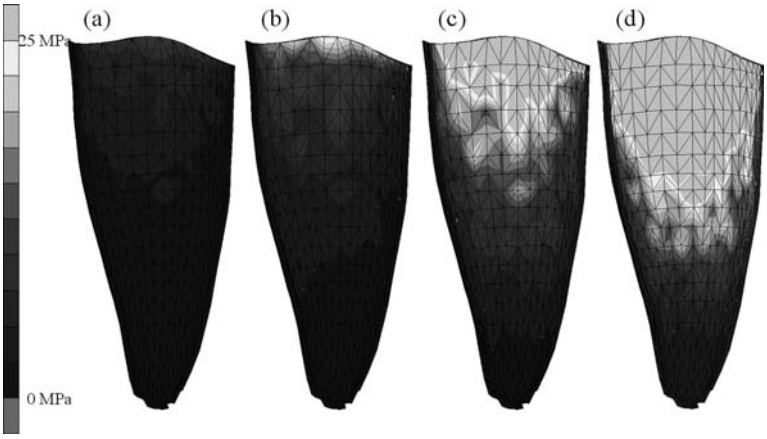

Fig. 5. Stress distribution in the PDL for the load case 'indirect' at a load of 100 N (a) and 200 N (b) and for the load case 'direct' at a load of 100 N (c) and 200 N (d).

The ratio between the stresses at the top of the guidance and the stresses at the neck in the clinical load cases showed, that neither the load case 'single with tipping' nor the load case 'single without tipping' can completely reflect the clinical situation. However this ratio can be approximated by comparing the two 'single' load cases, while the maximum stresses in the single load cases are clearly higher.

Loading of the denture in all the simulations resulted in a movement of the canine consisting mainly of a translation in z direction. This movement was caused by force transmission to the tooth via the male part. Forces at the male part were at 20 N and 37 N for the load case 'indirect' with 100 N and 200 N, respectively. In the load case 'direct', forces were at 73 N and 148 N for a load of 100 N and 200 N, respectively. The stresses within the PDL resulting from these forces are shown in fig. 5. For indirect loading these stresses were below 25 MPa. As the corresponding forces on the tooth are below typical loads given in literature, these stresses are in a secure range. For direct loading stresses below 50 MPa were calculated. As the corresponding forces on the tooth were in the same range as values given in literature these stresses should be acceptable.

4. Discussion

FE Model of the Lower Jaw. The simulations performed showed that the FE model developed for this study is suitable for the given tasks. The model can easily be adapted for further extra-coronal attachment systems, as only the connection between crown and male part and the interface to the denture have to be changed. The differences between the load cases with and without surrounding tissue showed that these structures must not be neglected. Currently the size of the model leads to extreme computation times of up to two weeks for one simulation. Optimisation has to be done especially with respect to the contact problems.

Loading Behavior of the Attachment and the Anatomical Structures. The analysis of the loading behaviour of the Mini SG-PLUS was successful, as the distribution of stresses and strains within the FE model of the Mini SG-PLUS helped to identify regions of excessive stresses beyond the yield limit of the corresponding materials. This information has already been used for design optimisations to reduce the risk of material failure.

The comparison of the results of the clinical load cases 'indirect' and 'direct' with the materials test load case 'single' can help to transfer data gained during materials tests to the clinical situation. However it could be seen that the load case 'single' seems to be acceptable to locate the possible weak points, while it is clearly not sufficient to evaluate the loading limits. Comparison of the loading of the PDL with typical forces showed that it was well below the normal loads during chewing for the clinical most relevant load case 'indirect', while being in the same range as normal loads for 'direct'.

5. Outlook

Currently the FE model of the jaw is used to evaluate different design variations of the presented attachment system as well as different materials. Further modifications of the model will allow the investigation of intra-coronal attachment systems. This will allow the study and the comparison of the loading behaviour of a large variety of attachment systems. Further modifications can extend the application area to dentures supported by telescopic crowns or implants.

Acknowledgements. The authors wish to thank Cendres & Métaux SA, Switzerland for financial support.

References

1 G. Becerra and M. MacEntee, Journal of Prosthetic Dentistry **58**, 322, 1987.
2 J. F. McCord, N. J. Grey, R. B. Winstanley, and A. Johnson, Dental Update **29**, 474, 2002.
3 T. R. Morneburg and P. A. Proschel, International Journal of Prosthodontics **15**, 20, 2002.
4 T. R. Morneburg and P. A. Proschel, International Journal of Prosthodontics **16**, 481, 2003.
5 J. Zivko-Babic, J. Panduric, V. Jerolimov, M. Mioc, L. Pizeta, and M. Jakovac, Collections of Antropology **26**, 293, 2002.
6 E. J. Richter, International Journal of Oral & Maxillofacial Implants **10**, 99, 1995.

Experimental and Numerical Analysis of the Mobility of Immediately Loaded Dental Implants Using a Pig Model

Alex Meier[1], Alireza Rahimi[2], Christoph Bourauel[2], Thorsten M. Buzug[3], Susanne Reimann[2] and Dennis Giantoro[2]

[1] RheinAhrCampus Remagen, Department of Mathematics and Technology,
E-mail: ameier@rheinahrcampus.de
[2] Department of Oral Surgery, University of Bonn, Germany
E-mail: bourauel@uni-bonn.de
[3] Institute of Medical Engineering, University of Luebeck, Germany

Abstract. The aim of this study was to model a system of implant and bone using the finite elements analysis (FEA). For this purpose immediately loaded dental implants were used. In an experimental analysis of preparations from pig jaws the force-displacement behaviour was measured using a self development set-up. With the aid of a micro computer tomograph (μCT) three dimensional surface models were reconstructed. These surface models were imported into the finite elements (FE) software package Marc/Mentat. Then the three dimensional surface models were transformed into FE-models, that mirror the geometry of implant and bone in detail. Comparison of the experimental achieved data and the numerical calculated data showed the magnitude of relative movements between implant and bone.

1. Introduction

Immediately loaded implants have been introduced to clinical practice in the last years. An immediate prosthodontics care takes place without prior healing phase. The mode of healing initially relies on the biomechanical stress of the bone surrounding the implant and especially on the specific quality of this bone and the geometry of the implant. Our aim was to construct a relation between the distortion of the bone and the reaction of the surrounding tissue. This relation can then be used to numerically simulate and predict the rebuilding processes of the bone itself.

2. Experimental Methods

In total three implant of the ANKYLOS® type (Dentsply-Friadent) were used for implantation into pig jaw segments. The dimensions of these implants were A11, A14 (diameter of 3.5mm, length of 11 and 14mm) and B14 (diameter of 4.5mm) respectively. In a high resolution opto-mechanical set-up the samples were loaded with up to 70 N axial and the implant deflection was measured. Afterwards the

implants were scanned using a micro-ct (Skyscan 1072). The scanned data were transferred to a self developed software (ADOR3D) to reconstruct the three dimensional geometry. The geometry was then converted to FE-models. Figure 1 shows three dimensional surface models of Ankylos implants in pig bone segments (size A11 and A14, respectively).

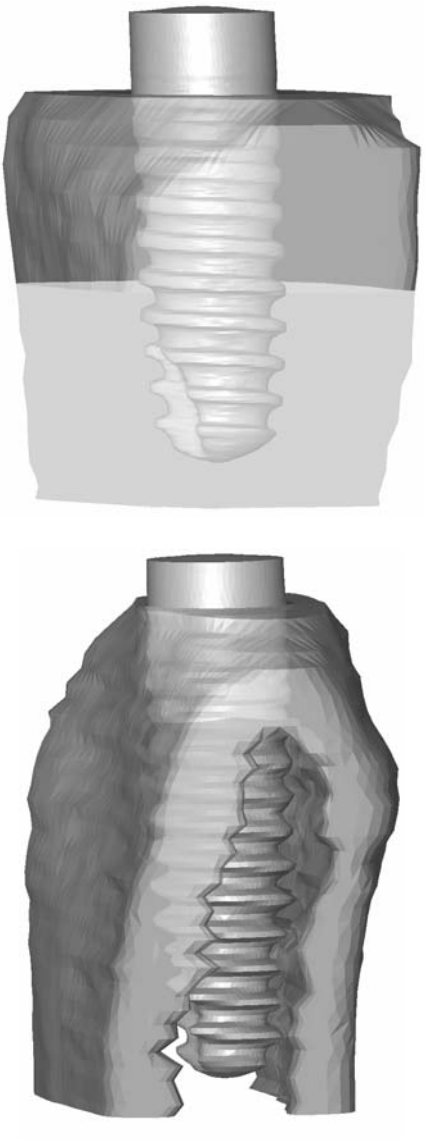

Fig. 1. Three dimensional surface model of chosen specimen.

FE-Calculations were conducted using the software modules MSC.Marc/Mentat 2005 with the following material parameters: spongious bone 20-500 MPa, cortical bone 10-16 GPa, implant 110 GPa, Poisson's ratio 0,3. Volume models were set together using an average of 180000 tetrahedron elements. Simulation of non-osseointegrated state was conducted using so-called contact analysis, were the surface of the implant in relation to the implant bed within the alveolar bone receives mobility The osseointegrated state is simulated by a fix implant-bone surface connection. Figure 2 shows FE-models of implants A11 and A14.

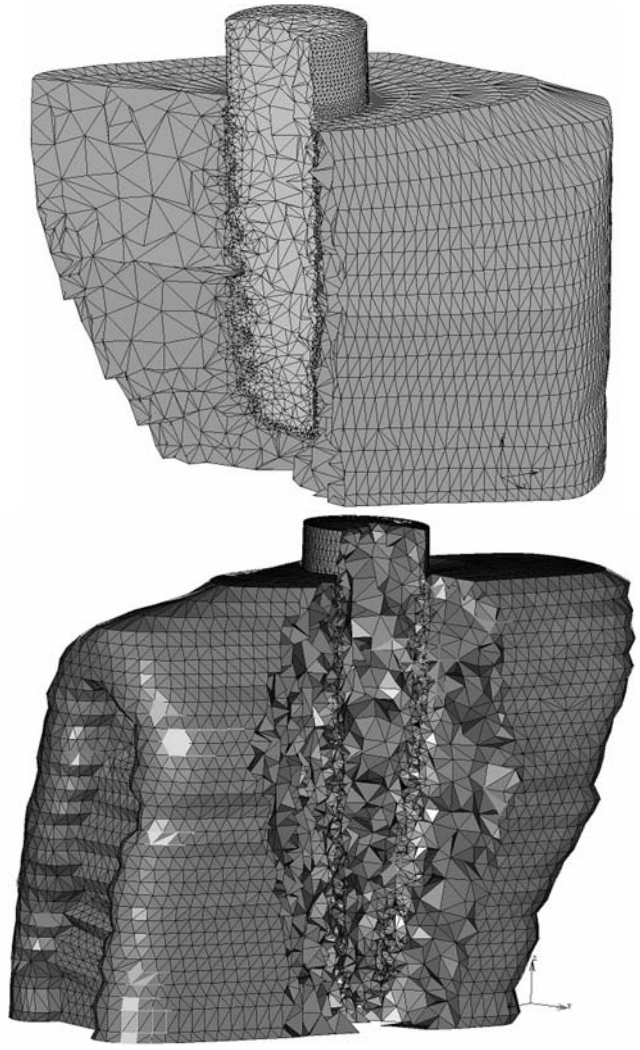

Fig. 2. Tetrahedron volume models with submodels showing cortical bone, spongious bone and implant.

3. Results and Discussion

The measured deflections of the implants were between 60 and 120 µm for the different sizes using a force of up to 70 N. These data were reproduced in the FE-Calculations by varying both the spongious bone and the cortical bone E-Modules and contact parameters. Calculated relative movements between implant and bone are shown in Figure 3, clearly depicting that implant surfaces were detached from the bone in the FE-Simulations. We conclude that a non-osseointegrated simulation based on contact analysis was conducted. The results of simulations using contact analysis and variation of material parameters were comparable to the experimental data.

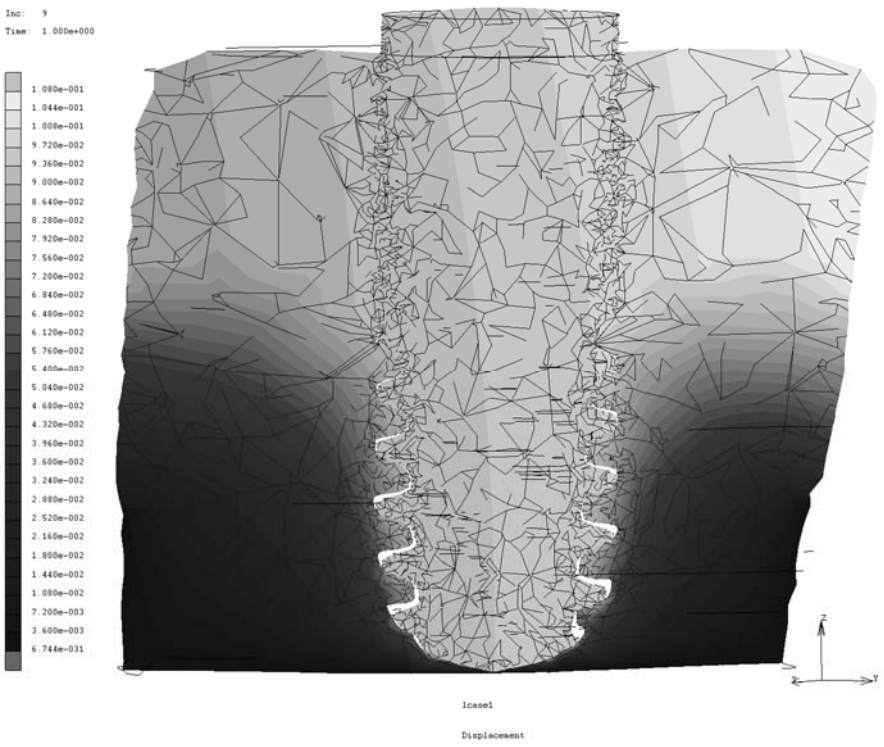

Fig. 3. Section through FE-Model of implant B14 with colour coded representation of the simulated displacements.

Simulating the loading of the implant without osseointegration shows that the bone detaches from the implant surface (figure 3, white areas). The osseointegrated state is simulated by a fix connection of implant and bone surface.

Using contact analysis the influence of the healing process around dental implant can be simulated. The implants are mainly supported by spongious bone in the initial healing process.

4. Conclusions

With the use of the finite elements analysis the biomechanical behaviour of dental single-tooth-implants in pig bone segments with full immediate loading was simulated. Systematic analysis using different material parameters and adaptive calculations can lead to optimised results for materials and contact parameters in the future.

Acknowledgements. A. M. would like to thank the study group in Bonn.

References

1 T. M. Buzug, *Einführung in die Computertomographie*, Springer-Verlag, Berlin/Heidelberg, 2004.
2 A. Rahimi, L. Keilig, G. Bendels, R. Klein, T. M. Buzug, I. Abdelgader, M. Abboud and C. Bourauel, *3D Reconstruction of Dental Specimens from 2D Histological Images and μCT-Scans*, Journal of Computer Methods in Biomechanics and Biomedical Engineering **8** (2005) pp. 167-176.
3 A. Meinken, *Finite Elemente in der Praxis*, Expert-Verlag, 2001.
4 P. M. Cattaneo, *Orthodontic Aspects of Bone Mechanics and Bone Remodelling*, University of Aarhus, Aarhus, Denmark, 2003.
5 L. Keilig, C. Bourauel, M. Grüner, R. Hültenschmidt, S. Bayer, K.H. Utz und H. Stark, *Aufbau und Erprobung eines neuartigen Meßsystems für die dentale Biomechanik - Messprinzip und Beispielmessungen des Hexapod-Meß-Systems*, Biomedizinische Technik 2004, 49:208-215.
6 MC, Software GmbH München, *MSC-Marc/Mentat Handbücher*, Software okumentation 2003, Version 2005.
7 H.M. Frost, *Bone mass and the mechanostat, a proposal*, The Anatomical Record 1987, 219:1-9.

Measuring System for the Comparative Ergonomic Study of Office Chairs

Rolf Ellegast[1], Rene Hamburger[1], Kathrin Keller[1] and Helmut Berger[2]

[1] BG Institute for Occupational Safety (BGIA), Alte Heerstrasse 111,
53757 Sankt Augustin
E-mail: bgia@hvbg.de
[2] BG for Administration (VBG), Bezirksverwaltung Bielefeld, Nikolaus Dürkopp-Strasse 8,
33602 Bielefeld
E-mail: bv.Bielefeld@vbg.de

Abstract. Working in static sitting postures at office workstations can cause musculoskeletal disorders (MSD). In the paper a measuring system for the comparative ergonomic study of office chairs is presented. With the system different concepts of dynamic office chairs that promote dynamic sitting and therefore prevent MSD, can be analyzed. Exemplary results of a laboratory study with different office chairs are described.

1. Introduction

Working frequently and continuously in static sitting postures at office workstations and visual display terminals (VDTs) can cause muscular tension and musculoskeletal disorders. Static strain of the musculature and particularly of the shoulder and neck can occur as well as functional under use of certain muscle groups, such as the back and abdominal muscles [1]. In the development of office chairs, the concept of dynamic sitting has therefore been encouraged in the last few years. By introducing structural elements that give the seat a dynamic mounting or active rotation of its own, some manufacturers of office chairs have created special chair characteristics that promote dynamic sitting with the aim of preventing musculoskeletal disorders at office and monitor workstations.

Various measurement methods for the quantification of the musculoskeletal load situation during seated activities at office workplaces and VDTs have been described in the literature. One example of this is stadiometry, in which the decrease in body height over the course of a day is adopted as the parameter for spinal loading [2, 3]. Other methods include electromyography (EMG), in which the muscle activity, e.g. of the back muscles, is taken as a measure of muscular stressing [4], or the measurement of body posture and movement as a means of quantifying spinal postures in particular [5, 6].

In the context of the study presented here, a measuring system has been created that combines existing measuring methods in such a way that the load situation during seated office work can be ergonomically analysed in both laboratory and real-life environments. The measuring system developed has been tested in the following in ergonomic analyses of special dynamic office chairs in comparison

with a conventional office chair during standardized office and VDT activities in the laboratory.

2. Experimental Methods

The measuring system consists essentially of three components and is derived from the CUELA measuring system developed at the BGIA [7].

Body postures and movements are measured with 3D acceleration sensors. From the measured signals, the following body/joint angles are calculated: Head inclination (sagittal and lateral), flexion/extension and lateral flexion of the spine in the thoracic (Th 3) and lumbar spinal regions (L1 and transition to L5/S1), trunk inclination and the spatial position of the upper and lower legs (right and left).

Surface electromyography (EMG) is used for measuring the muscle activity of the trapezius muscle (right/left) and erector spinae muscle (right/left). To assess the EMG signals, the RMS value is calculated from the raw EMG data. To standardize the RMS values, reference activities are performed at the beginning and end of measurement so that all muscle activities stand in relation to a reference voluntary contraction (% RVC).

To measure the setting of the office chair, acceleration sensors are used for 2D measurement of the backrest and seat inclination. With FSR (Force Sensing Resistors) pressure sensors (six each on the seat and backrest and three each on the armrests), the temporal and spatial extent of seat, armrest and backrest use are recorded.

All the measured data are synchronously recorded with a sampling rate of 50 Hz in a data logger of the CUELA measuring system. They can be depicted with the CUELA WIDAAN software together with the digitalized video recording of the workplace situation and are amenable to statistical evaluation (see Figure 1.).

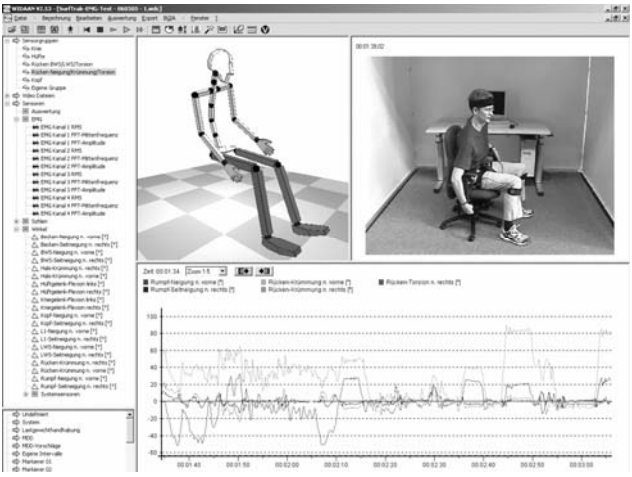

Fig. 1. Depiction of the measurement data with the CUELA software.

Figure 1 shows the graphic representation both of joint angle/time curves as well as a 3D computer depiction of the postures and the corresponding work situation in the video.

To check the function of the measuring system, a near-realistic office and VDT workstation was set up in the laboratory. 10 test subjects (5 men and 5 women) took part in the laboratory tests. The mean ages were 35.4 years (SD 12.1 years) for the men and 34.8 (SD 12.7) for the women. Body heights ranged from 1.75 to 1.86 m for the men and from 1.62 to 1.68 m for the women. Body weights varied from 76 to 100 kg for the men and from 47 to 78 kg for the women. Each subject tested a total of five office chairs (4 particularly dynamic ones and 1 reference office chair) during the performance of the standardized tasks listed in Table 1.

Table 1. Standardized office tasks with their task code and duration (min)

Task Code	Description of standardized tasks	Task duration (min)
A	Reading and correcting	10
B	Word processing	20
C	Intensive mouse use	20
D	Reading and correcting (2^{nd} part)	10
E	Word processing (2^{nd} part)	20
F	Sorting files	10
G	Phoning	10

Before and after measurement, the subjects were asked for their subjective assessment of comfort.

3. Results and Discussion

In the following exemplary results of the ongoing study are presented. Figure 2. shows exemplary frequency distributions of the RMS values of the erector spinae muscle (left and right) for one subject and one dynamic chair for all standardized tasks (A-G).

The frequency distributions are depicted as box-plot diagrams. The boundaries of the box are defined by the 25th and 75th percentile of the measured body angle distribution. The median (50th percentile value) of the distribution is given as the central value in the box. The edge values of the distributions (5th and 95th percentile values) are marked with whiskers.

Figure 2. shows clearly that the RMS values of the erector spinae muscle in %RVC are not high for all office tasks. Only for the more dynamic task F (sorting files) the RMS values for the erector spinae muscle left are 30% RVC (75th percentile) and 50%RVC (95th percentile).

The RMS values of the trapezius muscle are higher and much more dependant on the task performed (see Figure 3.). The static mouse task (task code C) yield to low RMS values of 5%RVC (50th percentile) to 10%RVC (75th percentile), whereas for the dynamic task F (sorting files) high RMS values of 140% RVC

(75th percentile, trapezius right) to 210%RVC (95th percentile, trapezius right) are measured.

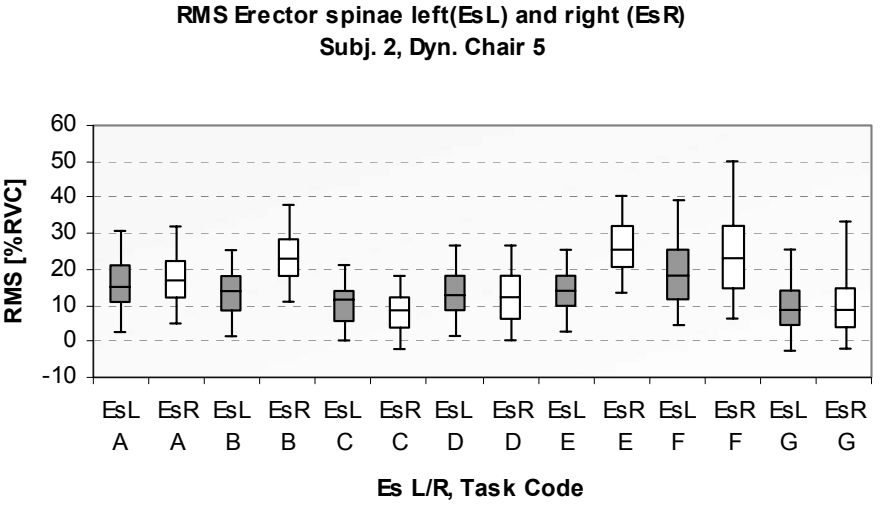

Fig. 2. Exemplary box-plot diagrams for the RMS values [in %RVC] of the erector spinae muscle left (EsL) and right (EsR) for subject 2, dynamic chair 5 and all tasks (A-G).

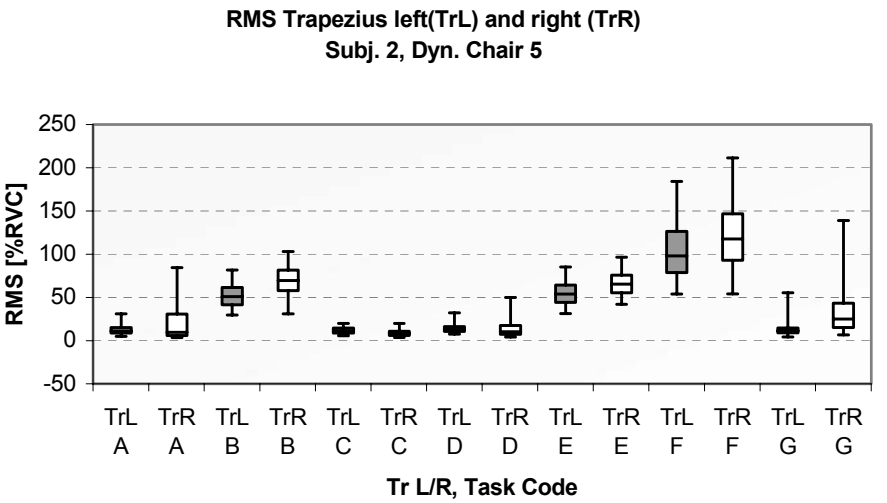

Fig. 3. Exemplary box-plot diagrams for the RMS values [in %RVC] of the trapezius muscle left (TrL) and right (TrR) for subject 2, dynamic chair 5 and all tasks (A-G).

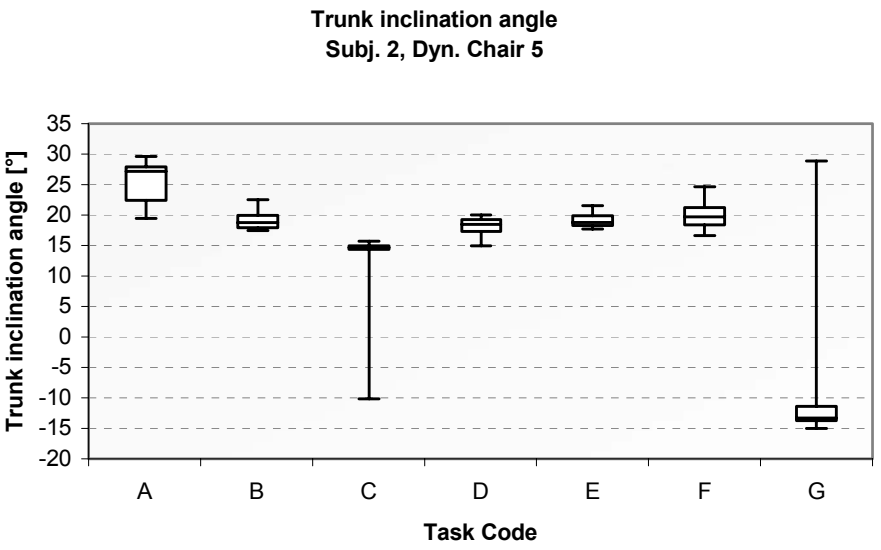

Fig. 4. Exemplary box-plot diagrams for the trunk inclination angle [in °] for subject 2, dynamic chair 5 and all tasks (A-G).

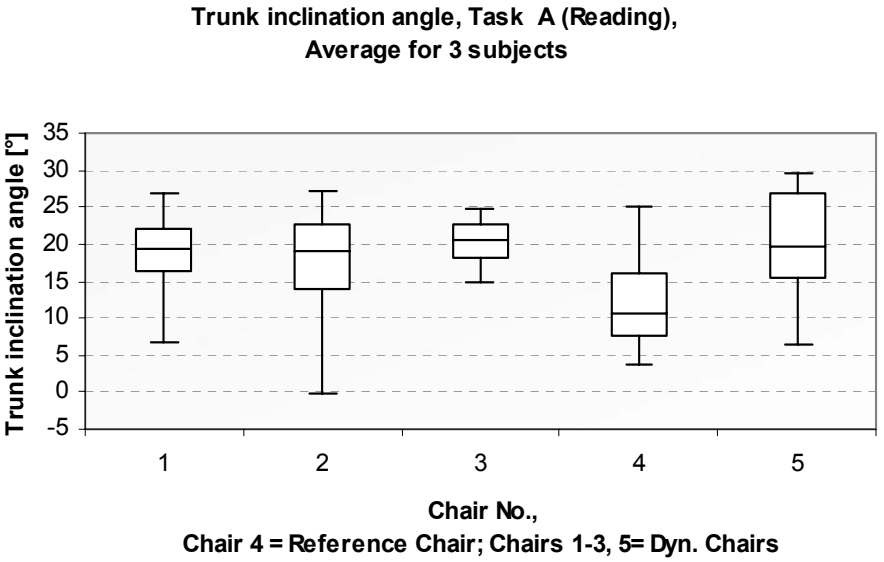

Fig. 5. Exemplary box-plot diagrams for the trunk inclination angle [in °] averaged for three subjects, task A (reading) for all chairs 1-5 (chair 4 = reference chair).

Figure 4. shows exemplary results for the trunk inclination angle for one subject and one dynamic office chair for all standardized tasks (A-G). Most of the tasks are performed in a static posture with the trunk inclined forward (exception: phoning task G, here the back rest was used intensively).

Figure 5. shows exemplary box-plot diagrams of the trunk inclination angles for task A (reading) averaged over three subjects for all chairs (chair 4 marks the reference chair and chairs 1-3, 5 indicate the dynamic chairs). The frequency distribution of the trunk inclination angle of chair 3 seems to be more static with a trunk inclination angle of 21° (50th percentile) in comparison to the reference chair 4 and the other dynamic chairs.

4. Conclusions

The measuring system developed permits the synchronous capture of different musculoskeletal load parameters. With the aid of the CUELA WIDAAN software, it is then possible to obtain, among other things, a very good general impression of muscle activity, body posture and movement, and the use of seat, backrest and armrest for each test subject in relation to standardized tasks and different chair types. An initial evaluation of the ongoing study suggests that the load situation depends more on the tasks performed than on the use of a particular type of office chair. This still has to be proved by statistical analysis.

References

1 W. Diebschlag and F. Heidinger, in *Arbeitsmed.Sozialmed.Präventivmed (ASP)*, Ergonomische Sitzgestaltung zur Prävention sitzhaltungsbedingter Wirbelsäulenschädigungen, 25, 123-126, 1990.

2 J.A.E. Eklund and E.N. Corlett, in *Spine*, Shrinkage as a measure of the effect of load on the spine, 9, 189-194, 1984.

3 I. Althoff, P. Brinckmann, W. Frobin, J. Sandover and K. Burton, in *Technical Report Bundesanstalt für Arbeitsschutz und Arbeitsmedizin (BAuA)*, Die Bestimmung der Belastung der Wirbelsäule mit Hilfe einer Präzisionsmessung der Körpergröße, Edited by BAuA, Berlin, 1993.

4 D.L. Bennet, D.K. Gillis, L.G. Portney, M. Romanow, A.S. Sanchez, in *Phys Ther*, 69, 902-913, 1989.

5 M. Adams and W.C. Hutton, in *Clin. Biomech.*, An electronic inclinometer technique for measuring lumbar curvature, 1, 130-134, 1986.

6 K.M. Black, P. McClure and M. Polansky, in *Spine*, The influence of different sitting positions on cervical and lumbar posture, 21, 65-70, 1996.

7 R.P. Ellegast RP and J. Kupfer, in *Ergonomic software tools in product and workplace design*, Edited by K. Landau, 47-54, Stuttgart, 2000.

3-Dimensional Foot Geometry and Pressure Distribution Analysis of the Human Foot. Visualization and Analysis of two Independent Foot Quantities for Clinical Applications

Ann-Kathrin Hömme[1,2], Ewald M. Hennig[2] and Ulrich Hartmann[1]

[1] RheinAhrCampus Remagen, Department of Mathematics and Technology, Germany
[2] Biomechaniklabor, Universität Duisburg-Essen, Deutschland
E-Mail: Ann_Kathrin_Hoemme@web.de

Abstract. The purpose of this research was to visualize three dimensional foot scan data simultaneously with pressure distribution information under the foot. Furthermore, simplified pressure distribution analysis software was developed. 382 school children were measured with a 3D - foot laser scanner and a pressure distribution platform during one-legged standing. A visualization program to combine foot geometry with plantar pressure distribution in a single graphical representation (*PressoMorph 1.0*) was developed using MATLAB. The two different data sets from the foot scanner and the pressure distribution device were imported into *PressoMorph 1.0* and matched in orientation, position and size. A positioning of the virtual three-dimensional foot onto the pressure matrix image resulted in a visual combination of both data as a wire-frame image with colour coded pressure isobarographs. Program options include rotations of the image along the three axes and provide a cursor value readout possibility for a user friendly program interface. The combination of 3D foot geometry and plantar pressure distribution data in only a single graphical representation guarantees a fast and easy judgement of foot shape and mechanical foot characteristics in a clinical setting.

1. Introduction

The description of structure and function of human movement is a complex task and can only be accomplished by a combination of various measurement techniques. Cinematographic and kinetic analyses of human gait and sports movements allow an insight in internal and external loads on the body during various phases of a given movement. It is, however, often difficult to draw conclusions from two independent data sets. Especially for clinical applications a fast and easy way to analyze and judge pathologies in patients is desirable. The primary task of this research was to visualize three-dimensional foot scan data simultaneously with pressure distribution information under the foot. Furthermore, simplified pressure distribution analysis software was developed for fast evaluation of important foot loading variables.

The visual combination of surface data and air pressure information is commonly used for weather forecast applications. Such analyses provide information about the state and the temporal development of air pressures in different regions on earth. With the visual combination of pressure and

topographic information it is easy for users, to judge current conditions and understand the development of weather events. The prediction of storms is a good example for the usefulness of such analyses.

2. Experimental Methods

The right foot of 382 school children between the ages of 6 and 10 were scanned with a three-dimensional foot laser scanner (Scanner INFOOT; IWL Inc.; Minoh City, Osaka, Japan). The INFOOT device is an active scanner, which emits laser beams and detects reflections from the object by eight cameras. This scanner contains four semiconductor lasers of the class 2M (CW 650 nm) with a maximum power of 3 mW. It has eight CCD cameras providing a maximum resolution of 1 mm [1].

For all school children the pressure distribution under their right foot was also measured with a pressure distribution platform (Emed ST; Novel Inc.; Munich, Germany). The company Novel uses 2736 capacitive sensors in a matrix arrangement [2, 3]. The sensor field has a size of 36 cm x 19 cm with a spatial resolution of 4 sensor/cm². The measuring frequency is 50 Hz and maximum pressures of up to 1.27 MPa can be recorded. The accuracy of the pressure transducers +/- 5 % with a hysteresis of < 3 % [2].

The pressures were recorded during one-legged standing. A visualization program to combine foot geometry as well as plantar pressure distribution in a single graphical representation (*PressoMorph 1.0*) was developed using MATLAB (Mathworks, Inc., Natick, Massachusetts, USA).

3. Results

Using the software packages from the scanner and pressure distribution devices, the data sets were exported as DXF and ASCII files. The data sets from both measuring systems have to be adjusted and synchronized to allow a combination of both information in a single graphical representation. The scanned feet normally do not have the same position and orientation in the scanner coordinate system as compared to the pressure distribution coordinates. First, the scanner data were prepared for the combination. The topographic reconstruction of the foot was adjusted to the origin of the scanner-coordinate-system. The imported point-cloud of the foot was moved into the origin of the scanner-coordinate-system. The coordinates of virtual reconstruction of the foot have in each case a X-, Y- and Z-component. The X-component describes the coordinates along the longitudinal-axis, the Y-component describes the coordinates along the width-axis and the Z-component describes the coordinates along the height-axis of the foot.

Consequently, a shift of the point-cloud into the origin of the scanner-coordinate-system refers only to a shift of the X- and Y- components of each point. The Z-coordinates are not changed.

The adaptation of the pressure data is the next step. After importing the data into the program the orientation of the pressure picture is not identical with the orientation of the digitalized foot. The pressure matrix has to be rotated to match

the three-dimensional scan data. First of all the transposed of the pressure matrix is formed. Then a turn in the second dimension and further a turn in the first dimension of the matrix follow. The transformations include a vertical and then horizontal reflection.

The position and orientation of the two data sets towards each other were accomplished by the above procedures. Because the spatial resolution of the two measuring systems is different, scaling has to be performed. The spatial resolution of the scanner data is 10 times higher than for the pressure data in the X and the Y directions. Therefore, scanner data were scaled to match the size of the pressure-platform foot image.

The foot morphology represents the basis for the data combination. Through the transformations both datasets now match in orientation, position and size. Thus, the program positions the virtual three-dimensional foot on the pressure matrix image, as if a foot would stand on a pressure-platform. The three-dimensional scanner data are located in the pressure-coordinate-system. Because the pressure data have a much lower resolution than the three-dimensional data, a great number of points always fit into a single sensor area. The visualization of pressure magnitude is realized through colour coding.

For pressure value adjustment to each point of the scan data a bilinear interpolation was performed. With the algorithm of the bilinear interpolation the tristimulus values of any pixels can be determined at arbitrary positions. At a given location the four colour components of the four pixel neighbourhood are determined for the point P [Fig. 1]. Through the sum of the four colour sections one receives the required tristimulus value for the point P (1). This procedure is used for all points. In this case the bilinear interpolation provides a smooth colour transition in the visualization. The interpolation results in a colour coded isobarograph below the virtual 3-D foot image.

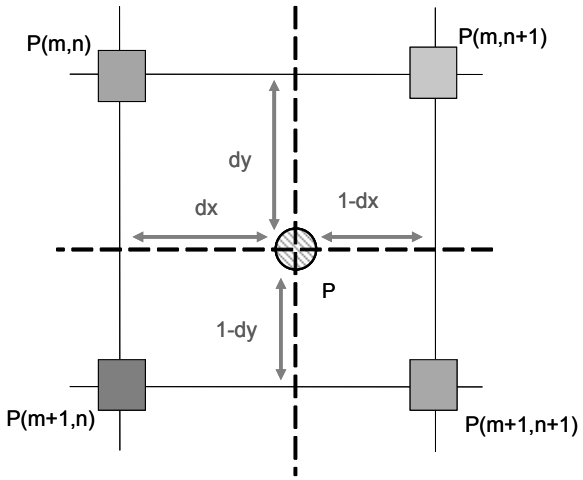

Fig. 1. Schematic diagram of bilinear interpolation

$$
\begin{aligned}
&Colour1 = [(1-dx)\cdot(1-dy)]\cdot P(m,n);\\
&Colour2 = [(dx)\cdot(1-dy)]\cdot P(m,n+1);\\
&Colour3 = [(1-dx)\cdot(dy)]\cdot P(m+1,n);\\
&Colour4 = [(dx)\cdot(dy)]\cdot P(m+1,n+1);\\
&P = Colour1 + Colour2 + Colour3 + Colour4
\end{aligned}
\tag{1}
$$

The main purpose of *PressoMorph 1.0* is the combination of the morphology and pressure data in one image. The user interface of the program for the visualization was intended to be user friendly. It was attempted to design a user interface which contains a clear structure with various functions and sub functions.

Furthermore, the user has different tools for the observation and analysis of the three dimensional graphs. *PressoMorph 1.0* has a Rotation Tool which enables the user to rotate the image in three dimensions. Additionally, the user can read out the coordinates of special locations on the foot with the Cursor Tool. Special regions can be observed more closely with the Zoom Tool. In addition, the current view on the screen can be saved as a picture in the JPEG-format with a Save Picture Button [Fig. 2].

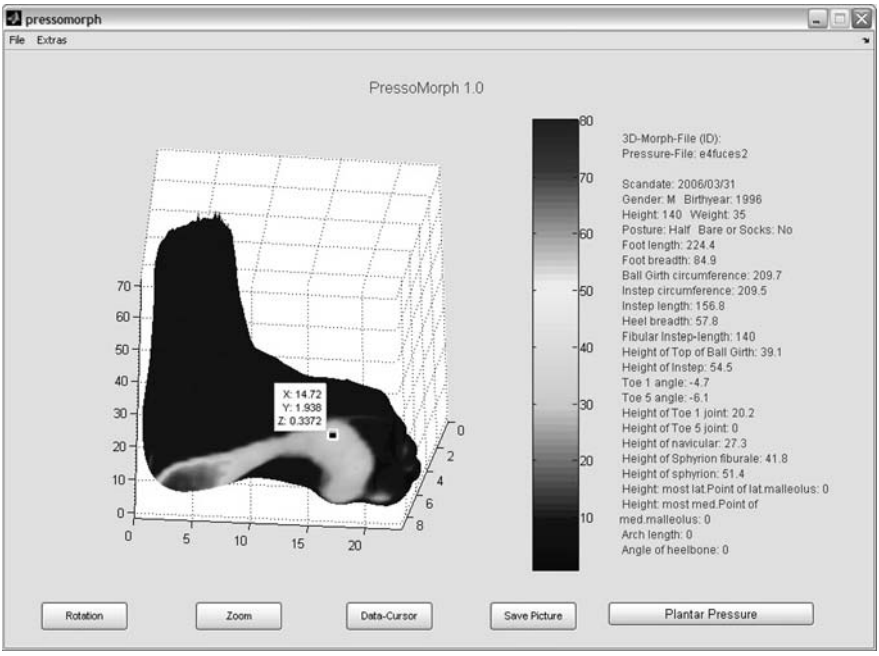

Fig. 2. User interface of PressoMorph 1.0

Furthermore, the quantitative information from the already existing programs, the scanner- and the pressure system software, should also be available in one program. This was achieved in *PressoMorph 1.0p*.

PressoMorph 1.0p was developed to supplement *PressoMorph 1*.0. For this purpose a user interface was designed for *PressoMorph 1.0p.* In contrast to *PressoMorph 1.0 PressoMorph 1.0p* mainly deals with the analysis of plantar-pressure-distribution measurements. The pressure-data-analysis enables the user to obtain detailed information about the plantar pressure distribution of the investigated subject. Furthermore, *PressoMorph 1.0p* saves the results in ASCII format. This simplifies the import of the calculated data into various statistic programs.

After importing the data into the program, information is gained from the pressure data. For the pressure data analysis the effort to calculate interesting parameters in *PressoMorph 1.0p* was smaller than importing the various parameters from the Novel pressure system software. Therefore, all parameters, including geometric as well as pressure variables, were calculated in *PressoMorph 1.0p* independently.

From the imported pressure data the sensor size of the pressure-platform is known. This information is used for all geometrical parameters to convert their size into cm. Furthermore the structure of the pressure data in form of a matrix is used to calculate additional geometrical parameters.

The first parameters which are calculated in *PressoMorph 1.0p* are foot length and foot width. *Foot length* and foot width are calculated on the basis of loaded pressure sensors in the transducer matrix. According to the definitions, as they are used in the Novel system evaluation software, the foot was divided into 7 anatomical regions (masks). Geometric information as well as pressure variables for each of these masks (Table 1.) were extracted from the imported ASCII files. The results were identical to those obtained from the Novel software.

Table 1. Listing of calculated parameters in PressoMorph 1.0p

Geometric parameters	**Pressure specific parameters**
Size of the pressure-matrix in rows and columns	Maximum pressure value of MPP (*)
Foot length (+)	Minimum pressure value of MPP (*)
Foot width (+)	Maximum pressure value of MVP (*)
Distance between heel and midfoot (+)	Minimum pressure value of MVP (*)
Distance between midfoot and forefoot (+)	Maximum pressure value of every mask (*)
Heel width (+)	Minimum pressure value of every mask (*)
Forefoot width (+)	Sum of all pressure values in each mask
Angle1 and Angle2 of the long plantar angle	

MPP = Maximum Pressure Picture
MVP = Mean Value Picture
* with coordinate information
+ in sensor size and cm

4. Conclusions

A program was developed to facilitate the evaluation of foot biomechanics during standing. The combination of 3D foot geometry and plantar pressure distribution data in only a single graphical representation guarantees a fast and easy judgement of foot shape and mechanical foot characteristics in a clinical setting. Additional quantitative data supplement the visual information and allow a statistical evaluation of relationships between morphological and foot pressure data.

An extension of PressoMorph 1.0 can be the development of new analysis functions which enable the user to measure self defined distances and areas in the visualization. Additionally, PressoMorph 1.0p can be complemented by further parameters which are useful for pressure distribution analyses.

References

1 Manual, I-ware Laboratory, http://www.iwl.jp
2 Manual, Novel Inc., http://www.novel.de
3 Nicol, K. and Hennig, E.M. (1978) Measurement of pressure Distribution by means of flexible, large-surface mat. in E. Asmussen & K. Jorgensen (Eds.) Biomechanics VIA (pp.374-380), Baltimore: University Park Pres

Assessment of Ambulatory Activity of Diabetic Patients: A Reliability Test

J. Baumeister[1], R. Ellegast[2], B. Drerup[1], A. Koller[1] and H. H. Wetz[1]

[1] Klinik und Poliklinik für Technische Orthopädie, Universitätsklinikum Münster
[2] BG Institute for occupational safety and health, Sankt Augustin

Abstract. In preventing the development of foot ulcerations in diabetic patients exposition to excessive plantar pressure is realized as a major risk. Therefore, ambulatory activity is important to know when assessing the risk of ulcerations.

1. Introduction

There are different systems available for the quantitative assessment of ambulatory activities which are be worn by the patients. They range from simple, easy to use devices to high-end systems. Systems are rare which combine a plantar pressure distribution measurement with a high-accuracy measurement of knee and hip angles outside of the lab, featuring a maintenance period of several hours. The CUELA system - originally designed for application in the domain of occupational safety - provides for the monitoring of movements and plantar loadings of a worker in his work place at a sampling rate of 50 Hz.

In a modified version, hardware and software are tailored to the requirements of activity monitoring of diabetic patients. It can be worn by the patient and measures simultaneously lower limb movements and plantar pressure. The software assesses automatically different kinds of ambulatory and stationary activities like sitting or standing.

By comparison with video films taken synchronously on a test course with various tasks like standing, sitting, walking, stair climbing in 10 diabetic patients the reliability of the automatic evaluation has been assessed. This is described in the following.

2. Experimental Methods

Subjects. Ten patients with diabetes mellitus were tested who visited the foot ambulance of a diabetics clinic. The mean age was 64 years ranging from 39 to 84 years; the mean body mass index was 26.8 ranging between 21 and 35.

Measurement System. The system used to assess activities is part of the CUELA measurement system originally designed for applications in occupational ergonomics research. For this application not the whole system is used, but a selection of components consisting of a gyroscope and inclinometers for an

inclination and a lateral tilt of the pelvis, potentiometric sensors for movements of the knee and hip joints in the sagittal plane and *Parotec* plantar pressure insoles.

The pelvic sensors are attached to the pelvis by means of a belt. The hip and knee sensors are fitted to the limbs by means of moulded pads and are fixed with elastic straps. The insoles are provided by Paromed Medizintechnik, (Neubeuern, Germany). Each insole features 24 isolated hydro-cells with piezoelectric sensors that measure the hydrostatic pressure.

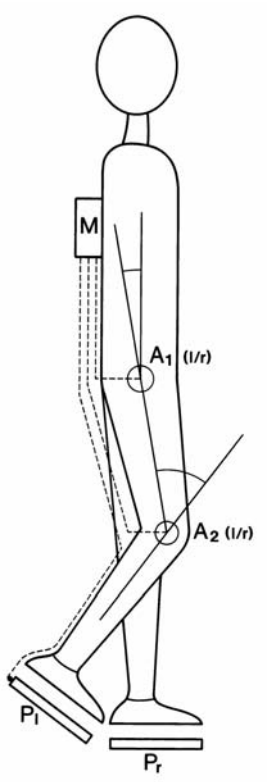

Fig. 1. Schematic of the modified CUELA-System used for activity monitoring. Plantar pressure is measured under both feet by pressure insoles (P_l and P_r). Hip-angle (A_1) and knee angle (A_2) are measured by potentiometric angle transducers. All measurement values are stored in the power supply and memory unit (M).

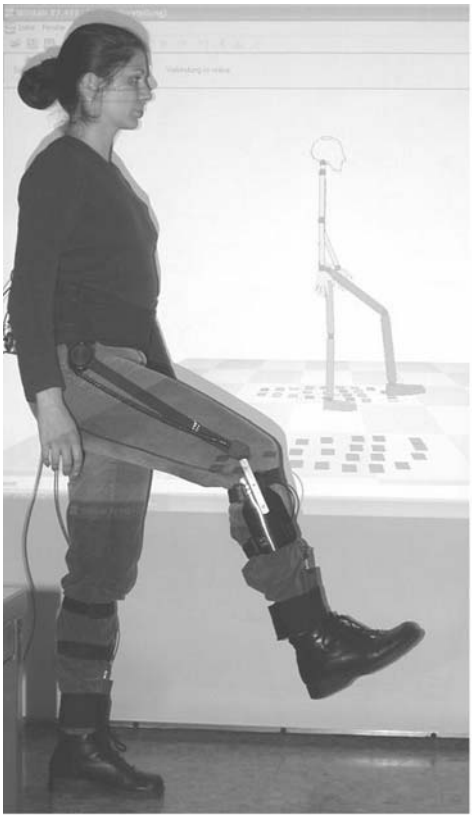

Fig. 2. Online display of the measured data: In the foreground subject with pressure insoles and angle encoders. On the screen behind: Visualization of the measured angle and pressure data using an animated figure and pressure distribution arrays

In total the measurement system comprises 54 sensors which are transferred in intervals of 20 msec to a data logger. A flash memory is used for off-line storage of the data. The capacity of the system (memory and batteries) is designed for 8 hours and it allows to process up to 102 sensors. To enable visual control of the measurements synchronized video recording is enabled

Data Analysis. At the end of a measurement the data are transferred to a computer for further analysis. The system comprises the WIDAAN software which - among other things - allows the automatic detection of different activities like: standing, walking and sitting and the automatic assessment of the duration of the activity.

For each activity, a data filter which is specific to the respective activity is configured effecting an analysis of several recorded sensor signals in parallel by

searching for specific patterns. After the automatic evaluation a second interactive run through the data is performed to eliminate or reinterpret interrupting signals, which falsely interrupt continuous periods of activities.

The analysis then automatically provides:

- a start/stop-list of the activities
- the cumulated duration of activities for individual activities and each type of activity the cumulated plantar pressure on individual sensors, foot regions and the whole foot
- the number of steps on level ground and/or stairs (both per activity period and in total)
- the step length and the walking velocity (mean and specified values for each walking period)
- the walking velocity (mean and specified)
- the step length (mean and specified)

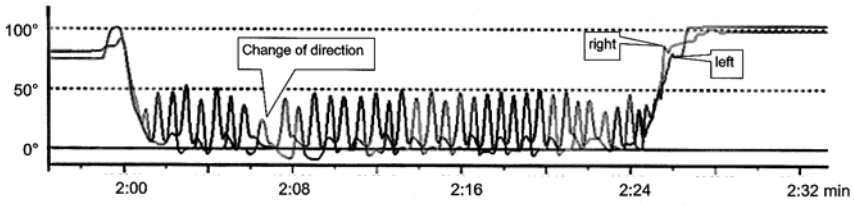

Fig. 3. Diagram - display of left (dark) and right (light) knee angle. Different phases can be easily recognized: Until 2:00 minutes sitting with flexed knees. Then walking until 2:24 minutes. During this period – at 2:06 minutes – change of direction.

The Test Course. On the floor and the stairway of the clinic a course of 114 m comprising 12 activity phases was set out. The phases were in detail: walking, standing on the left then on the right leg, walking, sitting with flexed knees and afterwards stretching the left and right knee alternatively, walking, sitting with alternative flexing of the knees, ascending stairs by taking 2 x 4 steps, sitting, descending stairs, standing, walking slowly and finally walking fast. Typically, the course took 5 minutes to complete.

The patients walked along the course with the activity monitor equipment being activated. They were accompanied by a physician and an assistant who recorded the activities videographically for subsequent comparison with the computer-generated analysis.

Evaluation of the Course. The different activities were classified in only 3 main activities: sitting, standing and walking. Two parallel time lists were compiled for comparison of the video analysis and the computer analysis. Each list specified in

respect of each activity the beginning and the end and - in the case of walking - the number of steps. The comparison was focussed on the questions, 1) whether the computer analysis detected the activities at all, 2) which interactive corrections were necessary and 3) within which accuracy limits the resulting durations of activities and gait parameters like step number, mean cycle period were in accordance with the video observation.

3. Results and Discussion

- Utilizing an interactive procedure the activities exercised by the patients are recognized correctly in 96.4%.
- Assessment of activity duration improves by interaction from 89% to 97%.
- The automatically counted number of steps differs from video-analysis by 4.7%
- The automatically assessed step length differs from video-analysis by 2%.

4. Conclusions

The CUELA measurement system together with the WIDAAN Software provides a reliable means to assess in diabetic patients activities of daily life during a whole day. It assesses and cumulates different loading situations of the foot to achieve a better understanding of the development of pressure ulcerations.

References

1 Bouten, CVC; Koekkoek, KTM; Verduin, M; Kodde, R; Janssen, JD (1997): A triaxial accelerometer and portable data processing unit for the assessment of daily physical activity, IEEE Trans. Biomed. Eng. 44, 136-147

2 Bussmann, JBJ; Martens, WLJ; Tulen, JHM; Schasfoort, FC; van den Berg-Emons, HJG; Stam, HJ (2001): Measuring daily behavior using ambulatory accelerometry: The activity monitor, Behav. Res. Methods Instrum. Comput. 33, 349-356

3 Foerster, F; Smeja, M; Fahrenberg, J (1999): Detection of posture and motion by accelerometry: a validation study in ambulatory monitoring, Computers in human behaviour, 15: 571-583

4 Mathie, MJ; Coster, ACF; Lovell, NH; Celler, BG (2004): Accelerometry: providing an integrated, practical method for long-term, ambulatory monitoring of human movement, Physiological measurement, 25, R1-R20

MBS-Modeling for Estimation of Stress and Strain in Human Body

Sabine Juchem[1], Lucas Pfaffmann[1, 2], Franziska Eckhardt[2], Dirk Thomsen[2], Stefan Lehner[1], Thorsten M. Buzug[3] and Karin Gruber[1]

[1] Institute of Sports Science, University of Koblenz-Landau, Campus Koblenz, Germany
[2] RheinAhrCampus Remagen, Department of Mathematics and Technology, Germany
[3] Institute of Medical Engineering, University of Luebeck, Germany

Abstract. Herniated and degenerated intervertebral disk is a painful disease which decreases the patient's quality of life. Because of the enormous pain every movement of the body is avoided and comprised the risk of clumping nerve cords. While the number of patients increases still no proper method is known to measure forces, pressure and torques in transmitted structures of the spine, especially during motion. The only accurate possibility for measurement is to place a sensor directly into the intervertebral disk, which leads beside the normal risk of surgery also to the risk of paraplegia and dangerous infections. Therefore, a new non-invasive method is developed to estimate the mentioned parameters in spine. This method is based on a computer generated model of the human lumbar spine which reflects geometry, surface and biomechanical features in an accurate way.

1. Introduction

Pressure, stress and strain are significant parameters to evaluate the load in the lumbar spine. These quantities are also interesting for spine surgery. Moreover, they can help to preplan surgeries and evaluate the result of them. The only accurate method to estimate biomechanical parameters is to insert a sensor directly in the lumbar spine. Caused by surgery and the implied risk this seems to be an unpractical way. Therefore, a new parameter estimation procedure is required. The idea is to create an accurate model of the lumbar spine with connected muscles and band structures by extracting the information from CT and MRI datasets and the mechanical behavior of the soft tissue structure. Based on such information an individual **M**ulti-**B**ody-**S**ystem (MBS)-Model [1] can be created which represents the spine features of a selected patient. Once the model is built it is possible to estimate the entire stress and strain on arbitrary position on the lumbar spine. For the modeling process first some image processing steps are required which are explained in the following sections. First preliminary results are presented and will be discussed before the conclusions are drawn.

2. Experimental Methods

In a first step, as already mentioned in the introduction, it is necessary to extract the required information from the imaging datasets. In our first approach we use two CT datasets of a human lumbar spine. One dataset includes the disconnected

vertebral bodies of the lumbar spine. In the second dataset the entire lumbar spine including the surrounded soft tissue is represented. This is necessary because in the dataset of the entire spine it is hard to segment where one vertebral body ends and the other begins. Especially a very sensitive region which requires sophisticated treatment in modeling are the facet joints of the vertebral bodies. It turns out that in the CT images a separation of the different vertebral bodies in the region of the facet joint is not recognizable anymore. For a realistic modeling of the lumbar spine datasets of clearly separated vertebral bodies are required. Therefore, a simple threshold method is used in order to create a mask for each vertebral body (Fig. 1).

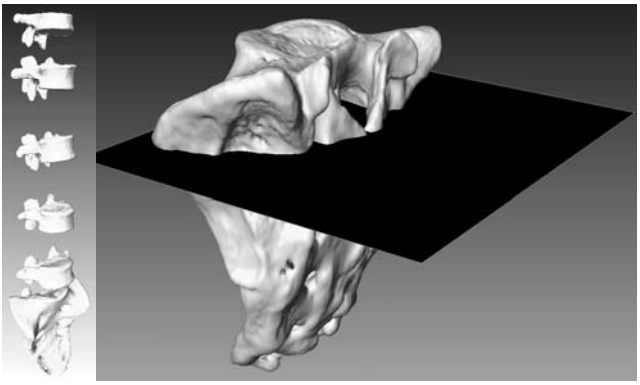

Fig. 1. Based on the disconnected vertebral body dataset it is possible to segment all bodies and store them for later usage in several masks.

The following registration algorithm is realized in three steps. First every mask is shifted over the other dataset to find out on which position the highest overlay can be found (see Fig. 2).

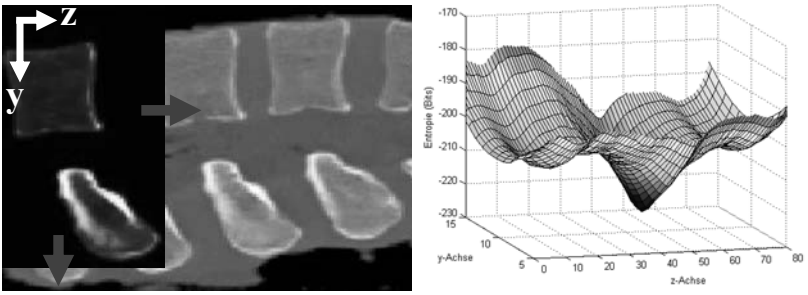

Fig. 2. On left hand-side a schematic registration procedure is displayed. The smaller mask of a vertebral body is shifted over the second dataset. When the translation is finished a new promising position is found. The mask is rotated around the directions in space to find a better matching. The best result is found by looking at the entropy (right image side). A small entropy value represents a high matching position.

For the evaluating process the entropy is used as a matching criteria [2]. Once a promising position is found the mask is rotated around the three directions in space to get a better fit. Due to the three-dimensional image space more additional translation steps are required. Afterwards the data information of the disconnected vertebral body is transferred to the complete dataset, which is known as model based segmentation.

The resulting datasets are used as input for the MBS-model. There each model segment is placed and connected correctly to its surrounding elements. With the help of the MBS-lumbar-spine model on one hand the simulation of various movements and on the other hand the calculation of stress and strain at defined places is possible. Furthermore for each element individual characteristics i.e. like mass, moment of inertia and center of mass can be defined. The results of the calculation by the model can be displayed by simulation of the movement and by plots of the time history of all interesting quantities like transmitted forces and torques between the different vertebral structures.

Fig. 3. A section of the Multi-Body-System, in this case without the intervertebral disks, is displayed. The change of color is used to distinguish adjacent vertebral bodies.

3. Results and Discussion

Starting from CT and MRI datasets many steps are required to create a MBS-model of the human lumbar spine. With the help of such a model it is possible to transfer the biomechanical features to many situations and to different movements.

Figure 4 shows the sacrum and the following vertebral body connected by a alternative model of the intervertebral disk. By defining the joint features it is also possible to define the agility of the multi-body-system.

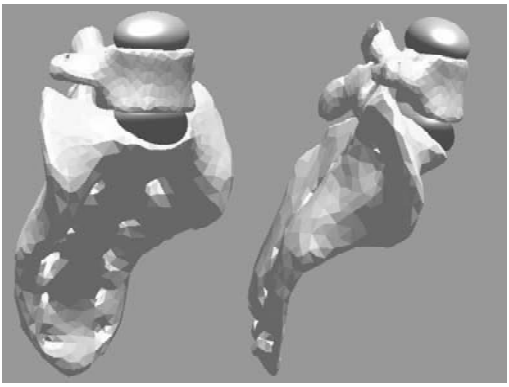

Fig. 4. A part of the model of the human lumbar spine with a substitution of the intervertebral disks is shown. Such a model can be used to measure stress and strain during motion of the human lumbar spine.

4. Conclusions

Estimating stress and strain at several positions in the human lumbar spine during motion is very complex. Like it is shown above many different and individual parameters affects the simulation. By reducing the number of unknown parameters it is possible to get a proper simulation result. For validation of the model a comparison study with sophisticated finite element models is planned. Additional results from in-vitro experiments found in literature can be used to make a final judgment of the accuracy. The future scope of this study is to create a full body model of the spine to compute stress and strain in the human spine during all-day movements like e.g. running, walking and sitting.

References

1. K. Gruber, H. Ruder, J. Denoth and K. Schneider, *A comparative study of impact dynamics: wobbling mass versus rigid body models*, Journal of Biomechanics (1998) 439.
2. T. M. Buzug und J. Weese, *Improving DSA images with an automatic algorithm based on template matching and an entropy measure*, Computer Assisted Radiology (CAR‘96), edt. H. U. Lemke et al. (Elsevier, Amsterdam, 1996) 145.
3. T. M. Buzug und J. Weese, *Image registration for DSA quality enhancement*, Journal of Computerized Medical Imaging and Graphics **22** (1998) 103.

A Bicycle Simulator Based on a Motion Platform in a Virtual Reality Environment – FIVIS Project

O. Schulzyk[1], J. Bongartz[1], T. Bildhauer[1] , U. Hartmann[1], B. Goebel[2], R. Herpers[2,3] and D. Reinert[4]

[1] RheinAhrCampus Remagen, Department of Mathematics and Technology, Südallee 2, 53424 Remagen, Germany
[2] Department of Computer Science, University of Applied Sciences Bonn-Rhein-Sieg, 53754 Sankt Augustin, Germany
[3] Department of Computer Science and Engineering, York University, 4700 Keele St. Toronto, Ontario, Canada,
[4] BG-Institute for Occupational Safety and Health - BGIA, Alte Heerstraße 111, 53757 Sankt Augustin, Germany

Abstract. The objective of this project is to develop a real bicycle simulator with the ability to represent real life traffic situations as a virtual scenario within an immersive environment. The bicycle will be fixed onto a motion platform to enable a close to reality simulation of turns and balance situations. The platform is fed with real forces and accelerations that have been logged by a mobile data acquisition system during real bicycle test drives. Thus, using a feedback system makes the movements of the platform match to the virtual environment and the reaction of the driver (e.g. steering angle, step rate).

1. Introduction

For almost all modern means of transportation (car, train, airplane) driving simulators exist that provide realistic models of complex traffic situations under defined laboratory conditions. For many years, these simulators have been successfully used for drivers' training and education and as a consequence have considerably contributed to the overall road safety. Unfortunately, there is no such advanced system for the bicycle, although the number of bike accidents has been increasing against the common trend (Source: Federal Statistical Office). Hence the objective of this project is to design a real bicycle simulator that virtually creates traffic situations within an immersive environment. For this purpose the bike is mounted onto a motion platform with six degrees of freedom (DOF) that enables a semi-realistic simulation of riding turns, of different track surfaces and additional external forces acting on the bike [1,2]. Test drives with a bike equipped with different sensors will provide the necessary data for the simulation. In addition, different basic visual stimuli can be specifically added to such a visual simulation setting, offering the possibility to examine the impact of visual perception on physical and mental performance under controlled basic conditions. Within the scope of this research project the correlation between the visually perceived motion and the physically generated motion will be studied for the first

time. Furthermore, a ergonomic model is created for the investigation of attention and concentration during labour. The simulation surrounding enables the stimulation of cognitive performance, as it is found in real work situations. Until recently, simulations under labour have been examined without the influence of additional cognitive strain. Thus, it is expected that investigation in such a simulation environment will provide closer to reality prediction of concentrativeness under labour. This system will facilitate a range of completely new applications in the field of safety at work,, in the research of occupational health and safety and in road safety education. To conclude; a prototype is developed that should serve for road safety education, for prevention purposes, and for specific simulations of visual information under simultaneous physical exercise.

2. Simulation Environment

Simple bicycle simulators or rather ergometers consist of a base plate and a support frame for the bike [3,4,5]. The rear wheel passes over an electronically controlled braking device, which simulates roll and air drag as well as the resistance while driving uphill. All bicycle simulators in the market share the common disadvantage of the bike being rigidly attached to the ground. This prevents a realistic simulation of certain riding situations. Realizing the dynamics of a close to reality bicycle ride is only possible by using a motion platform (Fig.1) with integrated force feedback control.

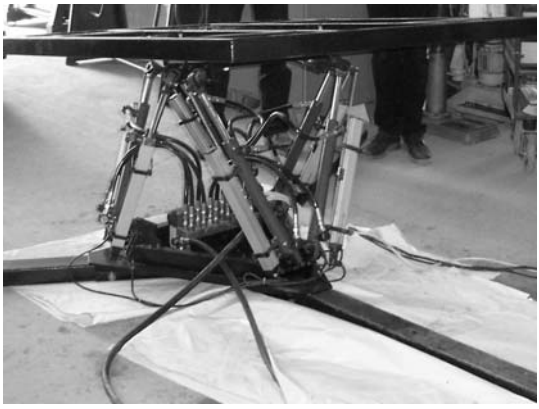

Fig. 1. Pragolet s.r.o. - Motion platform with six degrees of freedom.

Six DOF Motion Platform. The realization of this technology is one of the major objectives of this project. In order to reach this goal the acquisition of a 6 DOF motion platform is necessary. The design of the platform is known as a Hexapod or Stewart Platform. This base is designed as a synergistic system and has six identical hydraulic servo-actuators. The platform consists of a lower and upper

triangle frame. The actuators connect both frames. The bike is directly mounted on top of the upper frame. The platform performs the dynamics shown in Table 1.

Table 1. Technical data and dynamics of the Pragolet s.r.o. 6-DOF platform.

Max. Payload	2500 kg
Range of travel vertical	-277/+305 mm
Range of travel longitudinal	+/-531mm
Range of travel lateral	+/- 408 mm
Angle of pitch excursion	+/- 230mm
Angle of roll excursion	+/- 24o mm
Angle of yaw excursion	+/- 350 mm
Max. translation velocity	+/-0.65 m/s
Max. rotation velocity	+/- 30 °/s
Max. translation acceleration	+/-5.0 m/s2
Max. rotation acceleration	+/-100 °/s2
Actuator piston diameter	45 mm
Actuator piston rod diameter	28 mm
Actuator stroke	480 mm

Data Recording System for Bicycles. Logging of the mobile measurement data is currently organised with a mobile data recording system for bicycles [6]. The idea is to detect what kind of stress occurs on itemised components, for instance on the frame, the fork or on the handle bar while riding the bike. For this purpose diverse sensors are attached to a mountain bike with suspension fork. A displacement transducer at the suspension fork measures the swept volume. By means of these measurement data it is possible to assert whether or not the provided travel of the fork is ideally used. Furthermore it is interesting to know to what extent different adjustments of the suspension fork (spring stiffness, attenuation) affect the characteristic curve of the spring. Strain gauges on the handle bar and front end capture forces during a ride. An acceleration sensor synchronically measures the vertical acceleration of the frame. In the FIVIS-project this information is used to verify if the movements modelled by the motion platform conform to a real bicycle-ride. In order to record as much data as possible a standard Compact Flash Card is used as storage medium. As the achieved data is stored in a binary file, the evaluation of the data can be done by common software packages. The entire electronic measurement equipment and the storage battery are located inside a splash-proof box of acrylic glass that is fixed within the triangle of the bike frame (Fig.2.). Furthermore, the bike is furnished with a power measuring device, which by the use of torsion sensors, captures the forces that are applied to the pedals.

Immersive Visualisation Environment. Smart software components have to be developed to create a as realistic as possible situation of traffic (simulation of virtual road users) within an educational scenario, but when modelling a training mission, they can also present a competitor on the immersive visualisation screens. For the visual simulation of the riding ambiance, an immersive effect is

created. Therefore, it is mandatory to take care that the complete visual field is surrounded

Fig. 2. Data-Recording-System attached to the bike frame.

by projections. Three perfectly fitting projection screens are installed with an angle of 135° to each other. The computer-generated data is projected with three back screen projection units, which are hidden behind the screens. For the visual simulation the Immersion Square technology [7,8] is used. It was developed in a joint venture by the project partners, the Square Vision AG and the Univerity of Applied Sciences Bonn-Rhein-Sieg (see Fig. 3).

Fig. 3. Realisation of a car race in the Immersion Square.

3. Software Specifications

The essential software components for the bicycle simulator are:

The Input-Interface. The sensors attached to the bike platform need to collect various input data, which is required for the control of the virtual bike. The frequency and force of pedalling must be registered just like the position of the handle bar and the inclination of the whole bicycle frame.

Output-Interface (force feedback)
Forces calculated by the simulator need to be transferred (and presented audio-visually) to realistic forces which influence the motion platform and the bike (force feedback). Movement along the lateral axis of the bike frame is necessary to give the impression of going downhill and can further, if applied skilfully, serve for the simulation of acceleration and delay forces. With short crushes or vibrations on the bike's suspension, different road surface can be imitated. Finally, for an effective training, it is particularly necessary to adjust the pedalling resistance by software.

Physical Simulation. Within the simulated virtual world especially the forces that act on the operators' bike as well as on the simulated vehicles, need to be represented in a realistic way. This applies to accelerations and delays, as well as to the effects that appear while climbing up or going downhill.

Mathematical Simulation. A mathematical model of the dynamics of the bike is set up. The mechanics of the bike is transformed into a piece of modelling software that solves the underlying differential equations on the computer. One result will be the definition of stationary states of the bike providing important information for the setup of the motion platform. The computer bike model is generated on the basis of the research of Franke et al. [9].

Logics of Training. The logics of training affect and control the simulation in terms of a fitness scenario. Its role is to challenge the user as far as possible and as much as wanted. Besides, the logics of training should be able to influence the relation between the users expected speed and the visually simulated velocity, in a way that a motivational effect arises. In addition, further parameters, like nature and condition of the run could be changed as well as feedback forces and step resistance. Finally the users' motivation is raised by modelling competitive situations with virtual bikers. For the implementation the use of self-governed software agents [10] is intended. The entire logics will be configurable corresponding to the level of request and the type of implementation.

Means of Road Safety Education. For the means of road safety education the simulation of different types of road users is necessary to create every-day traffic situations. The virtual road users must orientate themselves in the virtual environment and need to act according to the traffic rules. In doing so, different categories of road users have to obey to different rules. They have to respond to each other as well as to the user. Finally, selected entities have to offend against

certain traffic rules, so that a dangerous situation is generated and the user needs to learn how to react appropriately. To provide an optimal educational programme, it should be possible to manually and randomly trigger such dangerous situations.

User Interface. A user interface shall grant access to all intrinsic system parameters. Thereby the handling should be as intuitive as possible. This is particularly important for the use in a fitness scenario.

Acknowledgements. We gratefully acknowledge the financial support of the Federal Ministry of Education and Research (BMBF) FIVIS project grant: 1736A05 and 5151736B05.

References

1 D.E.H. Jones, The stability of the bicycle, Physics Today 23(4) 1970, 34-40
2 R. Pawlik, Biomechanik des Radfahrens, Dissertation U Wien 1995
3 http://www.fahrradsimulator.de/galerie.php
4 http://www.simco-event.de/fahrrad.htm
5 http://www.simutech.de/verkehrserziehung.htm
6 T. Bildhauer, O. Schulzyk, U. Hartmann (2005) Zur Mechanik des Fahrradfahrens, in Aktuelle Methoden der Laser- und Medizinphysik, VDE-Verlag Berlin
7 F. Hetmann, R. Herpers und W. Heiden (2002) The Immersion Square - Immersive VR with standard components, Proc. of Virtual Environment on PC, Russia, ISBN 5-88835-011-7, 23-32,
8 R. Herpers, F. Hetmann, A. Hau, and W. Heiden (2005) The Immersion Square – A mobile platform for immersive visualizations, in Aktuelle Methoden der Laser- und Medizinphysik, VDE-Verlag Berlin
9 G. Franke, W. Suhr, F. Rieß (1990) An advanced model of bicycle dynamics, in: European Journal of Physics 11, 116-121
10 Caglayan/Harrison, Intelligente Software-Agenten, ISBN 3-446-19269-7, 1998

Inverse Dynamics in Cycling Performance

Malte Wangerin[1], Syn Schmitt[2], Björn Stapelfeldt[2] and Albert Gollhofer[2]

[1] RheinAhrCampus Remagen, Department of Mathematics and Technology, Germany
[2] Department of Sport and Sport Science, Radlabor, University of Freiburg, Germany

Abstract. Joint reaction forces and moments are of great interest for cyclists, coaches, therapists and medics because they give information about muscular effort and therefore cycling technique. The objective of this study is to examine the influence of pedalling rate and power on joint moments. An own mechanical construction was used to measure pedal forces, kinematic data was recorded and joint moment calculations were solved on a computer for ankle, knee and hip with help of a link segment model. Results show an increase of moments with increase of power and decrease of pedal rate.

1. Introduction

Professional and non-professional cyclists alike try to maximize their cycling performance as much as possible. The perfect interaction of athlete and bicycle is a main assumption of being successful. Therefore the calculation of joint reaction forces and joint moments could be of great interest for professional and non-professional cyclists, coaches, therapists and medics. Nevertheless there is little research dealing with the calculation of joint reaction forces and joint moments during cycling performance. Although Inverse Dynamics is a well known technique in biomechanical analysis as regards walking or running, it has hardly been applied to cycling. The difference between gait and cycling analysis in this means is the force measuring technique. While a fixed force plate is used in gait analysis a force measuring device which is connected to the rotating system of the pedal is needed in cycling analysis.

A review of the literature shows few studies working with different solutions to measure pedal forces which are needed for the calculation of joint reaction forces and moments. Gregor et al. (1985) [1] developed dynamometric pedals with strain gauges to measure pedal forces using an infra-red LED switch to identify the top dead centre (TDC) of the left pedal. The foot in the pedal was merely held in place with a toe clip. A clipless pedal system which is nowadays commonly used by cyclists was not applied. On the market are many different clipless pedal systems available but important is the combination of shoe and pedal which have to fit together. The aim of Gregor *et al.* was an integrated description using EMG, kinematic and kinetic data, for the lower limb during bicycle riding. Hull and Jorge (1985) [2] operated with a pedal dynamometer where the force transducers were applied to a pedal with toe clips and cycling shoes were equipped with cleats. In their paper Hull and Jorge wanted to focus on the determination of the functional roles of muscles which participate in pedalling [2]. In another study of Redfield and Hull (1986) [3] the same pedal dynamometer as in Hull's and Jorge's experiment was used to calculate joint moments and joint forces from

pedal forces. Redfield and Hull focused on the influence of cadence on joint moments while pedalling with constant power. According to Redfield and Hull pedalling rate, seat height, length of the crank arm and distance from spindle to the ankle do affect joint moments [3].

This brief review of the literature shows that athletes participating in these studies were restricted to certain pedal and therefore shoe or cleat systems the force measurement devices were constructed from. A study using a clipless pedal system is not known. In this study an own mechanical construction is used to measure pedal forces. This system allows every clipless pedal system to be attached and is therefore realistic and comfortable for athletes. The objectives of this study are to examine influence of pedalling rate at constant power and power at constant pedalling rate on joint moments with a MatLAB® based inverse model.

2. Experimental Methods

The Inverse Dynamics technique consists of four main assumptions. These include anthropometric data, a link segment model of the human body, kinematic data and external force measurement. For the calculation of segment mass, centre of mass locations and moments of inertia the anthropometric model presented by *Clauser et al.* [4] was used. A link segment model was developed to simplify the complex anatomy of the human body. Therefore joints are replaced by hinge joints and segments by masses and moments of inertia located at each segment's centre of mass. In addition a so called "free body diagram", where each segment is "broken" at the joint, helps to point out forces and moments that acts on each joint. For the entire model the body segments were assumed to be rigid bodies.

Two digital video cameras (50Hz) were used to record left and right side of each subject rectangular to the sagittal plane during the different measurements. Retro-reflective markers were applied to the lower extremities of the body. For kinematic measurements markers were positioned at great trochanter, knee joint centre, lateral malleolus and metatarsal on left and right side of the body. Two spot lights were positioned next to the cameras to guarantee best feasible visibility of the retro-reflective markers. A static measurement for each subject was carried out with the subject standing on the ground. For this, markers on heel and longest toe were added. The software Simi Motion® was used for the recording of the kinematic data. Cameras were calibrated with every knew subject..

Pedal forces were measured using the Powerforce® system and recorded with Simi Motion®. Whereas almost every other device used in cycling analysis is implemented in the pedal the Powertec® system is an own mechanical construction which is mounted between crank and pedal [5]. In contrast to most of the other measuring systems it allows every pedal system to be attached. *"The instrument is based on two sensor systems which determine the magnetic field variations (Hall-Effect) as a result of the displacement of a small sensor in respect to a magnet"* [5]. As soon as a load is applied to the circular construction of the Powerforce® system the corresponding sensor moves in respect to the opponent magnet. Because of two sensors being located orthogonal to each other the resulting force can be divided into a radial (extension of the crank arm with its

derivation in the pedal axis) and a tangential force (perpendicular to the pedal axis). To locate the position of the crank arm a light barrier was mounted near to the crank of the ergometer which was digitally counting the tooth of the big front chain ring (accuracy of 6.8°). The calculations for all data described above were treated in a Matlab® code. Therefore coordinates of all markers and the analogue data was imported from Simi Motion® into the programme code. Reaction forces and moments were calculated using the following equations of motion based on the conventional Newtonian mechanics:

$$F_x = m \times a_x \tag{1}$$

$$F_y = m \times a_y \tag{2}$$

$$M = I \times \alpha \tag{3}$$

where Fx = horizontal force on the segment, Fy = vertical force on the segment, m = mass, ax = acceleration in x direction, ay = acceleration in y direction, M = moment, I = moment of inertia about the proximal end of the segment and α = angular acceleration.

Two female (height = 1,60m/1.70m, weight = 50kg/57kg) and two male (height = 1.80m/1.79m, weight = 70kg/72.7kg) subjects (aged between 23 and 31) with one of each sex being a professional cyclist and the other a recreational cyclist participated in this experiment. The subjects were asked to cycle on a SRM® *(Schoberer Rad Messtechnik)* ergometer with varying power output (100W, 250W and 350W for women/400 W for men) and cadence (60 and 90 rpm). This was controlled by a computer connected to the ergometer and equipped with the SRM software. Kinematic data was recorded for ten seconds when the athlete cycled with constant power and pedal rate as mentioned before. The seat position on the ergometer was identical with that of each subjects own bicycle.

3. Results and Discussion

Mean joint moments with standard deviations are exemplarily displayed in Fig.1 for the left body side of a female test subject (1). The test person was pedalling with a constant power of 350 W and a pedal rate of 90 rpm. Moment curves are shown as functions of the crank angle. The results are briefly analysed in this chapter.

Ankle moments were found to be negative (plantar flexor) for the first 200° and remained close to zero for the rest of the cycle. A peak moment of -27 Nm (Table 1) was reached at approximately 90° of crank arm angle with a power output of 100 W and a pedal rate of 90 rpm. The positive peak (around 270°) decreased with higher load (350 W) from 16 Nm to 4 Nm. In contrast to the positive peak, negative peak moment rose significantly (-73 Nm) with a higher load. Furthermore negative peak increased when cadence was lowered to 60 rpm with constant load (250 W) from around -55 Nm to -79 Nm.

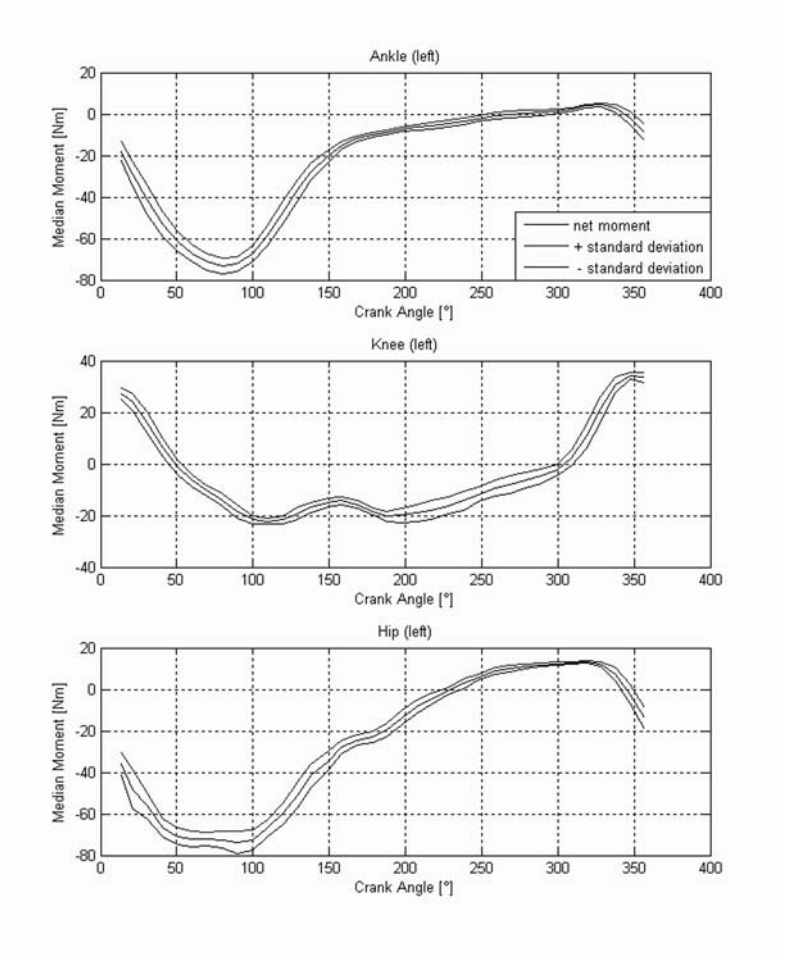

Fig. 1. Mean joint moments with standard deviations about left ankle, knee and hip for a 23 year old female professional cyclist (subject 1) of 50 kg weight and 1,60m height. Power output was 350 W and pedal rate 90 rpm.

With increase of power the athlete starts pulling on the pedal in the last phase of crank arm revolution. This thesis is supported by reaction forces in y-direction which are much higher (close to zero) in the last phase (beginning after 180°) of cycle. Changing the pedal rate (60 rpm) results in higher (negative) moments because higher forces are necessary to produce same power output with lower angular velocity.

Table 1: Moment peak change for variation of power and pedal rates. Values are exemplarily displayed for test subject 1.

	100W 90rpm [Nm]	250W 90rpm [Nm]	350W 90rpm [Nm]	250W 60rpm [Nm]
Ankle pos peak	16	6	4	4
Ankle neg peak	-27	-55	-73	-79
Knee pos peak	25	25	34	43
Knee neg peak	-5	-15	-22	-31
Hip pos peak	19	13	13	16
Hip neg peak	-18	-49	-74	-82

Knee moments were found out to be positive in the first phase (crank angle varies with power and cadence), being negative in the mid part and getting positive again in the end of the cycle. Therefore knee moments have a positive and negative peak. At 100 W positive peak is 25 Nm whereas negative peak is -5 Nm. With a higher load (350 W) an increase to 34 Nm and to -20 Nm was recorded for the positive and negative peak respectively. Pedalling with a lower cadence (60 rpm) showed an significant increase to 43 Nm for the positive peak compared to 25 Nm while cycling with a power of 250 W. Negative peak also increased to -31 Nm. Positive knee moments were found out to be extensor while negative moments are flexor. This seems feasible in the first phase of the cycle because the distance from greater trochanter to pedal is getting higher. Afterwards a flexor moment is recognized that means angle between shank and leg decreases. In the last cycle phase again an extensor moment is found because knee joint straightening, which is described after passing the TDC, is already prepared by the muscles. Significant differences in peak moments were found with a lower pedal rate (60 rpm), again the higher moments are to explain with the need of higher forces to produce same power. For this reason especially in the beginning of the cycle moments are higher because here the highest forces during one revolution are determined (around 90°).

Hip moments were found to be negative (extensor) for most of the time (until approx. 220°). While negative peak moments appeared close to 100° its magnitude at a power of 100 W is -18 Nm. The maximum negative moment rose to around -74 Nm with an increase of power to 350 W. With change of pedal rate (60 rpm) and a constant power of 250 W peak moments were even higher compared to those of 350 W and 90 rpm. The rest of the cycle (positive part, beginning after 200°) remained close to zero with a maximum of 19 Nm at a power output of 100 W. As expected and recognized at the ankle joint, negative moments (extensor) increase with an increase of power and with lower pedal rate (compared to same power output 250 W). Significant differences in the last phase of cycle were not visible.

4. Conclusions

Similar data was recorded for joint moments of ankle, knee and hip for four subjects. This study applies latest technology by using a specialised pedal force

measuring device, common pedal systems, the SRM® ergometer and professional cyclists. All in all the results which are in line with the literature [1,2] show that the tool which was developed for this study offers feasible output data. With help of this tool detailed technical analysis and improvement of cycling performance will be possible in the future and will present new evidence concerning the stress of joints. Further studies will have to be carried out to explore the ratio between seating position on the bike and lowest stress factor for the joints. Ideally further studies ought to integrate muscle activity (EMG).

Acknowledgements. The authors would like to thank the German Federal Ministry of Education and Research (BMBF) and the European Social Fund (ESF) for supporting this work with the programme EXIST-SEED (Grant No. 03ESFBW027).

References

1 R. J. Gregor, P. R. Cavanagh and M. Lafortune in *Knee Flexor Moments During Propulsion in Cycling - A Creative Solution to Lombard's Paradox*, J Biom, Vol. 18, No. 5, 307-316, 1985.

2 M. L. Hull and M. Jorge in *A Method for Biomechanical Analysis of Bicycle Pedalling*, J Biom, Vol. 18, No. 9, 631-644, 1985.

3 R. Redfield and M.L. Hull in *On the Relation between Joint Moments and Pedalling Rates at Constant Power in Bicycling*, J Biom, Vol. 19, No. 4, 317-329, 1986

4 C. Clauser, J. T. McConville and J.W. Young in *Weight, Volume, and Center of Mass of Segments of the Human Body*, AMRL-TR-69-70 (AD-710 622), Aerospace Medical Research Laboratory, Aerospace Medical Division, Air Force Systems Command, Wright-Patterson Air Force Base, 1969

5 B. Stapelfeldt, R. Morniuex, R. Oberheim, A. Belli and A. Gollhofer in *Developement and Evaluation of a New Bicycle Instrument for Measurements of Pedal Forces and Power Output in Cycling*, Int J Sp Med , in press

6 D. A. Winter in *Biomechanics and Motor Control of Human Movement*, second edition. John Wiley & Sons, Canada, 1990

Part V

Biomedical Optics

Determination of Alveolar Geometry by Optical Coherence Tomography to Develop a Numerical Model of the Fluid Dynamics in the Pulmonary Acinus

Sven Meißner[1], Alexander Krüger[1], Martina Wendel[2], Lilla Knels[2], Axel Heller[2], Thea Koch[2] and Edmund Koch[1]

[1] Klinisches Sensoring und Monitoring, Medizinische Fakultät der TU Dresden, Fetscherstr. 74, 01307 Dresden
[2] Klinik und Poliklinik für Anästhesiologie und Intensivmedizin, Universitätsklinikum Dresden, Fetscherstr. 74, 01307 Dresden

Abstract. In this feasibility study a Fourier domain optical coherence tomography (FD-OCT) system was used for 3D imaging of sub pleural lung parenchyma in the ventilated and perfused isolated rabbit lung. A series of 3D OCT images during a stepwise increase of pulmonary airway pressure was acquired. Refocusing and repositioning of the OCT scanner head allowed follow the volume changes of a single partial acinus of the lung.

1. Introduction

In intensive care mechanical ventilation is necessary to ensure sufficient oxygen supply of the patient, but might also contribute to the development of a lung injury or worsen an existing one [1-3]. One reason for ventilator induced injury is the mechanical stress put on the epithelial layer inside the alveoli. In order to develop new protective artificial ventilation strategies, it is necessary to quantify the mechanical stress to the epithelium cell layer. In order to develop and carry out appropriate numerical calculations of the mechanical stress it is primarily necessary to obtain reliable information about alveolar geometry and the alveolar deformations during artificial ventilation.

Because there is no non-invasive image modality which provides the necessary 3D resolution and acquisition speed for *in vivo* investigations, geometry data is usually obtained from fixated lungs and dynamic measurements are performed in animal models with 2D light microscopy of subpleural alveoli through a prepared window in the thorax [4].

Optical coherence tomography, an interferometric imaging technique developed by J. Fujimoto, uses backscattered infrared light to obtain depth information from subsurface structures in scattering tissue [5-6]. Recently, the application of 2D optical coherence tomography on imaging lung parenchyma has been shown to provide sufficient resolution and measurement depth to identify individual alveoli in cross sectional images of the perfused and ventilated rabbit lung [8]. In order to quantify volume changes and deformations of individual

acini's during the tidal volume uptake of the lung the full 3D information has to be acquired.

2. Experimental Methods

OCT is based on the principle of interferometry of short-coherent near-infrared light. The penetration of near-infrared light into biological tissue is larger than the penetration of visible light. Figure 1 shows the setup of the used Fourier-Domain-OCT-System.

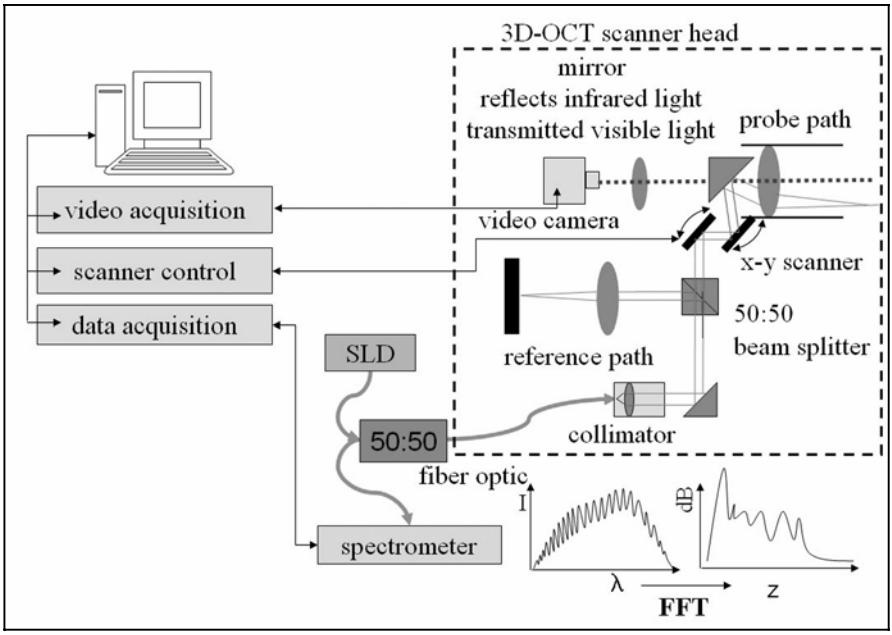

Fig. 1. Setup of used Fourier-Domain-OCT-System; Abbreviation: SLD: superluminescent diode, I: intensity, λ: wavelength, dB: Fourier amplitude in decibel, z: probe depth related to reference arm length, FFT: fast Fourier transformation

The resulting interference spectrum is detected with a photodiode line and changed into a depth profile by a Fast Fourier transformation. The single components of the interferometer are integrated into the scanner head.

For three-dimensional imaging a scanner head with two crossed electric controlled galvanometer scanners was designed to deflect the measurement beam in both lateral directions. The near-infrared light beam is splitted into reference and measurement beam by a beam splitter cube. Also a video camera is integrated for a better selection of the analyzed area on the probe surface.

Although OCT allows *in vivo* imaging of lung tissue, the model of the isolated, perfused and ventilated lung has some advantages compared to *in vivo* measurement, for example free access for OCT imaging to all regions of the lung surface.

As a result of blood-free perfusion of the isolated lung the scattering of near-infrared light, caused by erythrocytes in the blood vessels, is eliminated and so the measurement depth into biological tissue is increased. Figure 2 shows the setup of the isolated perfused and ventilated lung model.

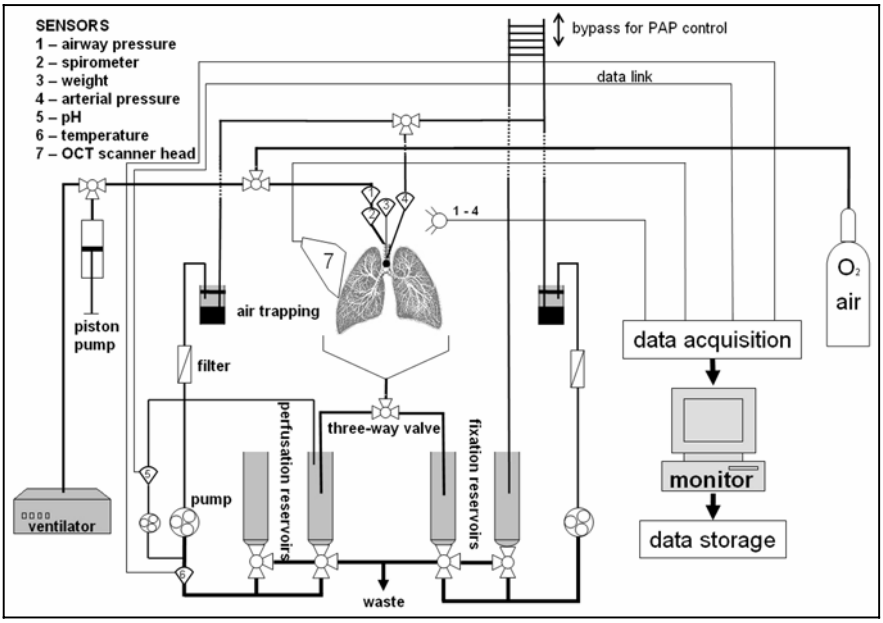

Fig. 2. Setup of isolated perfused and ventilated rabbit lung. The OCT scanner head is described in figure 1 in detail. Measurement signals (1 – 7) are acquired and monitored by a PC.

The preparation of the isolated, perfused and ventilated rabbit lung model has been described in detail by our group elsewhere [9]. The perfusat is pumped from the perfusat reservoir through a particle filter and an air trapping and through the arteria pulmonalis into the lung. The venous perfusat is returned to the perfusat reservoir. In the next step the lung is fixated with glutaraldehyde at different continuous pulmonary air pressure (CPAP) levels. Therefore a second circulation (fixation circulation) is integrated to avoid a contamination of the perfusation circulation by toxic glutaraldehyde. The ventilation of the lung was carried out by a small animal ventilator KTR-4 (Harvard Apparatus). For monitoring the volume-controlled ventilation a spirometer is integrated. The positive end-expiratory pressure (PEEP) is controlled by an external PEEP valve. The integrated piston pump is necessary to generate the dynamic and quasi-static pressure-volume-charts (pv-charts) of the isolated lung. To define the several CPAP levels an optional external oxygen and compressed air supply is available.

3. Results and Discussion

Quasi-static and dynamic pv-charts were acquired after isolating the lung, to define the lower point of inflection and the total lung capacity. For the quasi-static pv-chart the volume was increased in steps of 3 ml until reaching a pulmonary pressure of 30 mbar. Typical quasi-static and dynamic pv-charts are shown in Figure 3. A typical point of lower inflection was detected at 5 mbar and a total capacity at 25 mbar, by analyzing the lung pv-charts of different rabbits. After isolation the lung was recruited with the pressure which corresponds to the total lung capacity (defined by pv-chart).

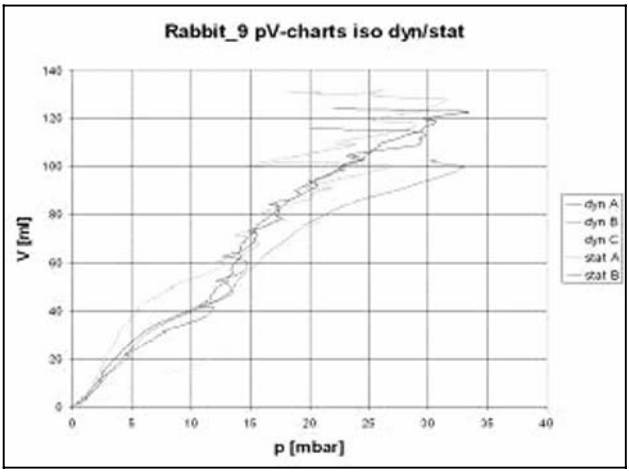

Fig. 3. Typical quasi-static and dynamic pressure-volume charts for isolated rabbit lung

Fig. 4. Isolated perfused and ventilated rabbit lung, on the left side the OCT 3D scanner head can be seen

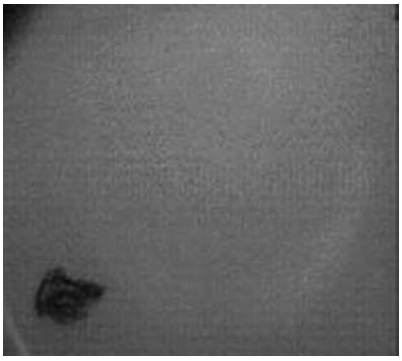

Fig. 5. Area of lung surface that was chosen for OCT measurement, the scanner head was positioned in such a way that the black marking was always at the same position in the camera image

To obtain information about alveolar volume or geometry changes during mechanical ventilation the following CPAP levels (25/20/15/10/5 mbar) were set with the help of the external compressed air supply and the PEEP valve. For each level a marked lung surface area (app. 2 x 2 x 0.5 mm) was documented by 3D-OCT imaging, to analyze the alveolar geometry changes at several CPAP levels.

The isolated, ventilated and perfused rabbit lung was ventilated with the following parameters: tidal volume of 20 ml; PEEP of 3 mbar; end-inspiratory pressure limit (EIP-limit) of 15 mbar. The lung was perfused with 50 ml per minute and the pulmonale arterial pressure (PAP) was approx. 4 mbar. Figure 6 shows sub pleural alveoli at different CPAP levels.

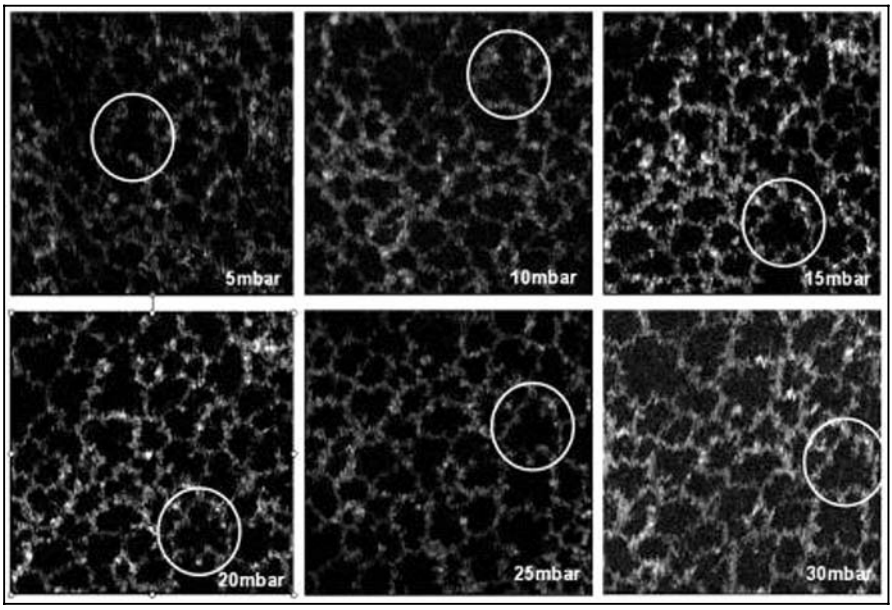

Fig. 6. Sub pleural alveoli at different CPAP levels, the same area was marked in all images

In all OCT images the same alveolar acini can be detected and a typical structure in the image is indicated by the circle. With this study we have proven that it is possible to detect alveoli at different CPAP-levels in the model of the isolated lung.

Acknowledgements. This project was supported by the DFG-Grant KO 1814/6-1

References

1 International consensus conferences in intensive care medicine: Ventilator-associated lung injury in ARDS, American Thoracic Society, European Society of Intensive Care Medicine, Societe de Reanimation Langue Francaise, Intensive Care Medicine 25 (1999) S. 1444-1452.

2 J. A. Frank and M. A. Matthay: Science review: Mechanisms of ventilator-induced injury, Critical Care 7 (2003) S. 233-241.

3 D. Carney, J. DiRocco, and G. Nieman: Dynamic alveolar mechanics and ventilator-induced lung injury," Critical Care Medicine 33 (2005) S. 122-128.

4 B. D. Daly, G. E. Parks, C. H. Edmonds, C. W. Hibbs, and J. C. Norman: Dynamic alveolar mechanics as studied by video microscopy, Respiratory Physiology 24 (1975) S. 217-232.

5 D. Huang, E. A. Swanson, C. P. Lin, J. S. Schuman, W. G. Stinson, W. Chang, M. R. Hee, T. Flotte, K. Gregory, C. A. Puliafito, and J. G. Fujimoto: Optical coherence tomography, Science 254 (1991) S. 1178-1181.

6 N. Hanna, D. Saltzman, D. Mukai, Z. Chen, S. Sasse, J. Milliken, S. Guo, W. Jung, H. Colt, and M. Brenner: Two-dimensional and 3-dimensional optical coherence tomographic imaging of the airway, lung, and pleura, Journal of Thoracial Cardiovascular Surgery 129 (2005) 615-622.

7 G. Häusler and M. W. Lindner: Coherence Radar and Spectral Radar - New Tools for Dermatological Diagnosis, Journal of Biomedical Optics 3 (1998) S. 21-31.

8 Popp, A., Wendel, M., Knels, L., Koch, T., and Koch, E. “Imaging or the Three-Dimensional Alveolar Structure and the Alveolar Mechanics of a Ventilated and Perfused Isolated Rabbit Lung with Fourier Transform Optical Coherence Tomography,” J Biomed Opt 11 (1), 14015, (2006)

9 G. de Abreu, M. Heintz, A. Heller, R. Szechenyi, D. M. Albrecht, and T. Koch: One-lung ventilation with high tidal volumes and zero positive end-expiratory pressure is injurious in the isolated rabbit lung model, Anesth. Analg. 96 (2003) S. 220-228.

Combining Optical Coherence Tomography (OCT) with an Operating Microscope

Eva Lankenau[1], David Klinger[1], Christian Winter[1], Asim Malik[1], Heike Hedwig Müller[2], Stefan Oelckers[2], Hans-Wilhelm Pau[3], Timo Just[3] and Gereon Hüttmann[1]

[1] Institute of Biomedical Optics, University of Lübeck, Germany
E-mail: huettmann@mll.mu-luebeck.de
[2] Möller-Wedel GmbH, Wedel, Germany
E-mail: s.oelckers@moeller-wedel.com
[3] ENT-Department, Medical School, University of Rostock, Germany
E-mail: hans-wilhelm.pau@med.uni-rostock.de

Abstract. Optical coherence tomography (OCT) is an emerging biomedical imaging technology which gives high-resolution sectional images of light scattering tissue down to a depth of a few millimeter. The objective of this work is to combine OCT with an operation microscope. A spectral domain OCT was adapted via a specially designed scanning optics to the camera port of an operation microscope. This enables a non-contact on-line OCT during different medical applications. Hidden tissue structures were visualized with a resolution below 30 µm. As a first example for an application in otolaryngology we demonstrated that the OCT operation microscope is basically able to reveal parts of the cochlear morphology without opening its enveloping membranes. Thus it may serve as a helpful guide for the surgeon to exactly localize the scala tympani before opening the fluid-filled inner ear for inserting the electrode array of cochlear implants.

1. Introduction

Optical coherence tomography (OCT) [1] is an emerging biomedical imaging technology that has been applied to a wide range of biological, medical, and material investigations. Similar to B-mode ultrasound imaging, reflections of near-infrared light are detected, which offers a non-contact real-time in vivo imaging of solid tissues. Depending on the scattering characteristics tissue structures 0.5 to 1.5 mm below tissue surface can be seen. Typically, a spatial resolution of 6-15µm is obtained. Recent developments in retinal imaging have demonstrated a resolution of 3 µm permitting the differentiation of individual retinal layers in vivo [2]. First medical applications of OCT were found in ophthalmology where imaging can be performed on transparent media of the anterior eye and the retina [3,4,5]. OCT using optical sources at longer wavelengths has enabled imaging in highly scattering soft tissues, which now includes applications to cardiology [6], gastroenterology [7,8], urology [9,10], dermatology [11,12], dentistry [13], and the central nervous system [14,15,16]. There are different developments to perform OCT measurements through an

colposcope [17], fiber-optic catheters and endoscopes [18, 19], and hand-held probes [12].

Here, we describe the combination of spectral domain optical coherence tomography (SD-OCT) with an operation microscope, which promises new medical applications for OCT.

2. Experimental Methods

SD-OCT is a coherent imaging method. Infrared light with a short coherence length is split by an interferometer into two parts, a probe and a reference light, which are either directed to the tissue or to a reference mirror, respectively. The light collected form the sample and the reference light are superposed at the output of the interferometer. The modulation of the cross correlation spectrum contains the distances of the light scattering structures in the tissue with respect to the reference distance. A Fourier transform of the measured spectra reveals the OCT A-scan of the depths resolved backscattering intensity. OCT B-scans are produced by scanning the probe in lateral direction and converting the A-scan amplitudes to logarithmic gray scales [21].

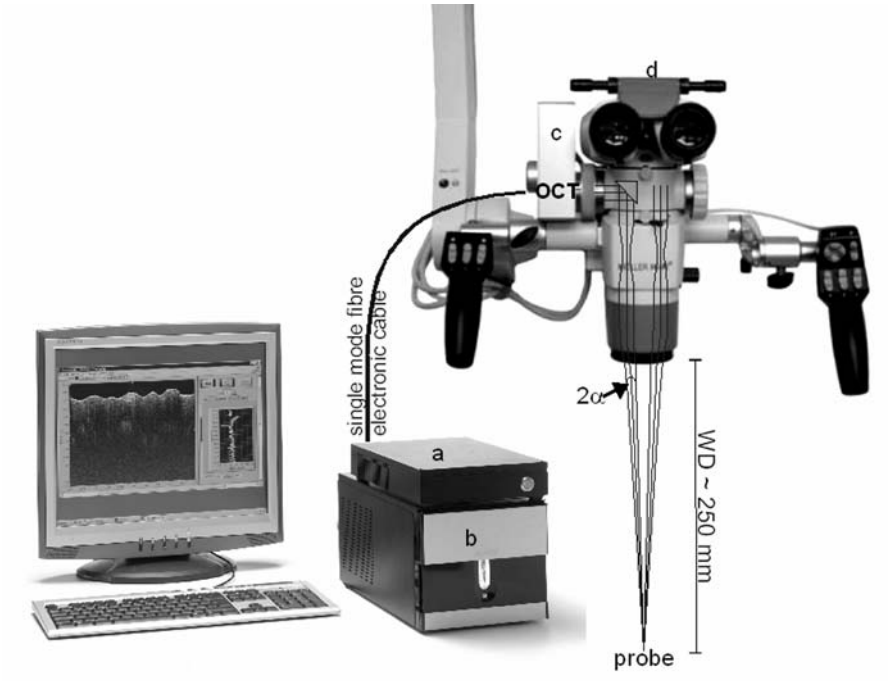

Fig. 1. OCT operating microscope with a working distance (WD) of about 250 mm : a) spectral domain OCT device, b) PC with Labview software, c) OCT adapter, d) OP-microscope.

A spectral domain optical coherence tomography (SD-OCT) device which was developed at the Institute of Biomedical Optics, University of Luebeck, and manufactured by the Thorlabs HL AG (Luebeck, Germany), was coupled to the camera port of an OP-microscope (HiRes1000, Möller-Wedel, Wedel, Germany), thereby using the same optics for OCT and conventional imaging (Fig.1). The scan range changed as the field of view was altered and the OCT system could adapt for changes of the working distance in the range from 232 mm to 290 mm by a motor control of reference mirror. A one axis scanner was implemented in the adapting optics which gives horizontal OCT section of the tissue in the center of imaging field.

The SD-OCT system consisted of a superluminescence diode at a central wavelenth of 840 nm and achieved an axial resolution of 11 µm in air. SD-OCT in the configuration used here produced a B-scan image with 3,6 mm imaging depth. The data were acquired at a rate of 1220 A-scans/second, digitized with 16 bits resolution, and transformed to A-scans on-line on the host computer. Data acquisition software was written in Labview.

3. Results and Discussion

For easily locating areas of interest overview images are necessary. For a high quality OCT images a high magnification is advised. The build-in zoom function of the HiRes1000 allowed to change the image magnification by a factor of six. Correspondingly the scan range changed from 4 mm to 24 mm. Figure 2 shows the image of a finger nail with two different imaging fields at a working distance of 232 mm.

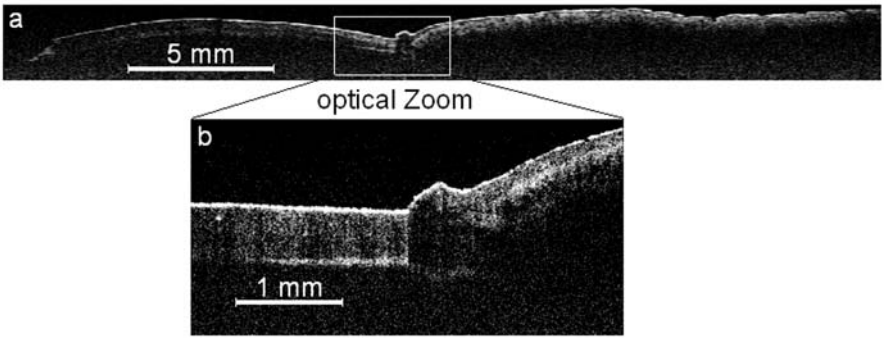

Fig. 2. Image of finger nail together with adjacent skin with the OCT operation microscope at a) lowest and. b) highest magnification.

The lateral resolution was nearly diffraction limited and depended on the magnification of the conventional image and the actual working distance of the microscope. Depth resolution was limited by the spectral width of the light source to 11 µm in air. In OCT images the speckle noise usually limits the resolution. The average diameter d of the speckle is essentially the diffraction limited resolution [22], which depends on the wavelength λ and the numerical aperture NA

$$d = 0.61\frac{\lambda}{NA} \tag{1}$$

Accordingly the lateral speckle size varied from 23 µm to 47 µm for the different magnifications and working distances (Table 1). The speckle size was larger than what is usually used in OCT because of the large working distance.

Table 1. Calculated speckle sizes for different magnifications and working distances

working distance	232 mm, highest mag.	232 mm, lowest mag.	290 mm, highest mag.	290 mm, lowest mag.
lateral scan size	4 mm	24 mm	4,8 mm	28 mm
calculates speckle diameter d	23 µm	39 µm	26 µm	47 µm

Due to the binocular design the NA of an operation microscope is limited to values of 0.02 or smaller, if the normal imaging path is used. To judge the degradation of the image quality due to this limited, NA tissues were measured with different diametes of the imaging lens. Figure 3 shows OCT B-scan of an mouse brain tissue, which was acquired with $NA = 0.06$, and $NA = 0.02$. As expected, small details of the tissue structure disappear under the speckles for the lower NA images. The imaging depth was not significantly decreased, although less light was detected.

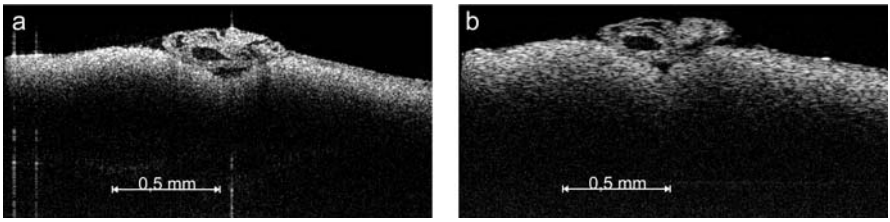

Fig. 3. Ex-vivo OCT images of mouse brain measured at nearly the same position with a numerical aperture of 0.06 (a) and 0.02(b).

An alternative approach to integrate OCT is the use the whole diameter of the front lens of the operation microscope. This would have needed significant changes in the optics or an increase of the size of the instrument which causes problems for some clinical applications. Therefore a complete integration of the OCT system into the operation microscope via the camera port was chosen though it sacrifices lateral resolution.

Speckle noise is reduced a factor of $\sqrt{N}$ by averaging images with N statistically independent speckle patterns. Imaging of the same structure under slightly varying angles causes statistically uncorrelated speckle patterns. Averaging several of these images therefore is expected to decrease speckle noise significantly. Increases in the A-scan rate and a motor control of the different axis of the operation microscope shall make this scheme feasible in a clinical environment.

For a possible application of an OCT operation microscope during ear surgery is was tested whether the device is able to reveal parts of the cochlear morphology without opening its enveloping membranes. Fresh tissue samples were imaged after removal of the out bone of the cochlear. Through the exposed but not yet opened membranous cochlear wall (lig.spirale) adjacent inner ear structures (scala tympani, scala vestibuli) could be visualized (Fig. 4).

Thus OCT may serve as a helpful guide for the surgeon to exactly localize the scala tympani before opening the fluid-filled inner ear when inserting the electrode array of a cochlear implant. In the past there was no imperative for an exact placement of the electrodes, since they were inserted into completely deaf cochleas, which were more or less considered just a sheath for the electrodes. Though there was always the demand to insert the array into the scala tympani, in recent studies [23] Aschendorff et al. could demonstrate by rotational tomography that in many cases the electrode finally was in the "wrong" scala, without the surgeon having noticed this malposition. In recent years the indication for cochlear implantation was extended, and surgery was carried out even on patients, who still had significant residual hearing [24]. In such cases it is essential to strictly fulfilling the demand of inserting the electrode array into the "right" scala tympani. The question for a specific landmarks, which may be provided by OCT, then becomes very important.

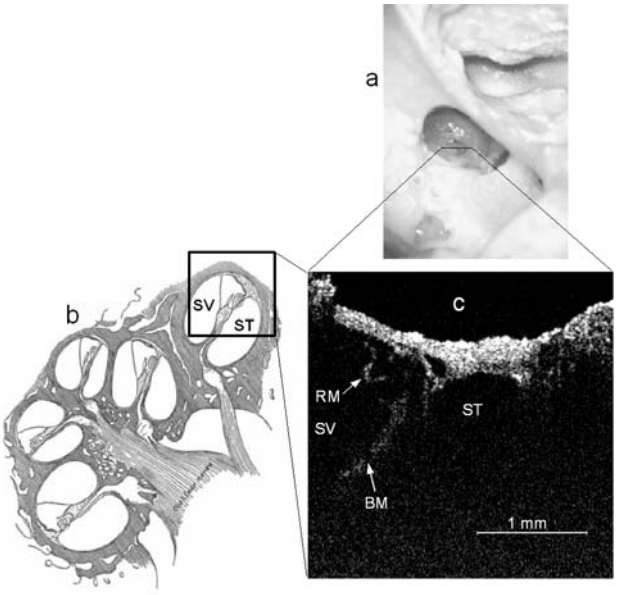

Fig. 4. Ex vivo measurement of the cochlear with the OCT operating microscope. a) Schematic image of the cochlear. b) Photo of the exposed cochlear in a fresh temporal bone. c) OCT scan of the lateral part of the exposed cochlear: besides the projections of the scalas some fine structures within the cochlear can be identified: the triangular cross section of the scala media with the Reissner membrane (SV = scala vestibule, ST = scala tympani, RM = Reissner membrane, BM = Basilar membrane).

4 Conclusions

Optical coherence tomography can be successfully integrated into a commercially available operation microscopy without compromising it's function. Hidden subsurface tissue structure can be visualized during surgery with a resolution of a few tens of a micrometer. Clinical applications of the new system may range from brain surgery [16], over ophthalmology [25] to ear surgery. OCT might contribute significantly to the safety of cochlear implant surgery.

Acknowledgements. This work was financially supported by Schleswig-Holstein (HWT 2004-12) and the Möller-Wedel GmbH.

References

1 D. Huang et al., in *Science* **254**, 1178, 1991
2 W. Drexler in *Invest Ophthalmol Vis Sci* **42**, 1993, 2001.
3 M. R. Hee et al., in *Arch Ophthalmol* **113**, 325, 1995.
4 M. R. Hee et al., in *Ophthalmology* **102**, 217, 1995.
5 C. A. Puliafito et al., in *J Biomed Opt* **9**, 47, 2004.
6 I. K. Jang et al., in *J Am Coll Cardiol* **39**, 604, 2002
7 B. E. Bouma et al. in *Gastrointestinal Endoscopy* **51**, 467, 2000
8 G. J. Tearney et al., in *Am J Gastroenterol* **92**, 1800, 1997
9 D. Daniltchenko et al. in *Radiologe* DOI 10.1007/s00117-005-1250-x, 2006;
10 E. V. Zagaynova et al., in *J Urol* **167**, 1492, 2002
11 J. M. Schmitt, M. J. Yadlowsky, R. F. Bonner, in *Dermatology* **191**, 93, 1995.
12 J. Welzel et al., in *Br J Dermatol* **150**, 220, 2004
13 B. W. Colston et al., in *Appl Opt* **37**, 3582, 1998
14 S. A.Boppart et al., in *Neurosurgery* **43**, 834, 1998
15 S. A. Boppart, in *Psychophysiology* **40**, 529, 2003
16 H. J. Böhringer et al., in *Lasers Surg Med* **38**, 588, 2006
17 M. Löning et al., in *Geburtsh Frauenheilk* **63**, 1158, 2003
18 G. J. Tearney et al., in *Science* **276**, 2037, 1997
19 T. Xie et al., in *Appl Opt* **42**, 6422, 2003
20 E. Lankenau et al., in *Proc. SPIE*, **5316,** 172, 2004
21 B.E .Bouma, and G. J. Tearney, *Handbook of Optical Coherence Tomography* Marcel Dekker, NewYork, 2002.
22 J. W. Goodmann, *Speckle Phenomena in Optics: Theory and Applications*, Roberts&Company, Greenwood Village, 2006.
23 Aschendorff et al., in *Otol Neurotol* **26**, 34, 2005
24 C. von Ilberg et al., in *J Otorhinolaryngol Relat Spec* **61**, 334, 1999
25 G. Geerling et al., in *Arch Ophthalmol* **123**, 253, 2005

Measurement of the Epidermal Thickness with Fourier Domain Optical Coherence Tomography in an Occupational Health Study on Natural Sun Protection of the Human Skin

A. Krüger[1], T. Schwabe[2], M. Cuevas[1], P. Knuschke[3] and E. Koch[1]

[1] Klinisches Sensoring und Monitoring, Medizinische Fakultät der TU Dresden, Fetscherstr. 74, 01307 Dresden, Germany
[2] Institut für künstliche Intelligenz, Fakultät für Informatik TU Dresden, 01062 Dresden, Germany
[3] Abteilung Photobiologie, Klinik und Poliklinik für Dermatolgie der Universitätsklinik Dresden, Fetscherstr. 74, 01307 Dresden, Germany

Abstract. Fourier domain optical coherence tomography (FD-OCT) was used to take cross-sectional images of the skin at the forehead, back of hand and back of volunteers. The aim of the occupational health study was the investigation of the natural sun protection of outdoor workers and in particular the quantification of the UV induced epidermal thickening. A set of manually segmented OCT images was used as a gold standard to evaluate the performance of automatic algorithms for finding the epidermal thickness. The established A-scan averaging method and two newly developed automatic algorithms were compared. The first of the new methods is based on Markov random chains and the second new and best performing algorithm is based on a convolution filter with a trace finding routine with a quadratic cost function. Although the results of all algorithms differ in the absolute values for the epidermal thickness, they all show the same tendencies. There is a strong dependency of epidermal thickness on skin site, a weak dependency on the season of the year and a noticeable epidermal thickening 7 days of recovery after UV induced erythema.

1. Introduction

In order to establish well-balanced health prevention recommendations for outdoor workplaces, the natural skin protection against sun light has to be quantified in a study with volunteers. Epidermal thickening and absorption by melanin are the two components of natural skin protection against UV-light. The overall protection can be quantified by measuring the so called minimal erythema dose (MED) of UV radiation which causes a sun-burn. Measuring the epidermal thickness (ET) status by successive invasive biopsies would mean an ethically unacceptable burden to the volunteers.

Optical coherence tomography (OCT) has been proven to be a non-invasive alternative to biopsies for measuring ET after UV exposure [1-4]. One problem associated with the quantitative analysis of OCT cross-sectional images, however, is to find a robust image analysis algorithm to measure the ET at different sites of the skin. Apart from manual segmentation several automatic algorithms have been

suggested, which can be divided into two groups: Group (A) uses averaged depth profiles and takes the first pixel above a grey-value threshold as the air-skin interface and local maxima or minima as the dermal-epidermal junction (DEJ)[1,2,4] and group (B) uses a shapelet based image analysis [5]. We developed two new algorithms. The first one is based on the formalism of Markov chains using learned features of the grey-value distribution to detect the air-skin interface and to find the epidermal thickness. The second one is a straightforward linear filter approach which computes the convolution of the OCT image with a 2D step kernel function and finds the maxima in the filtered image.

2. Experimental Methods

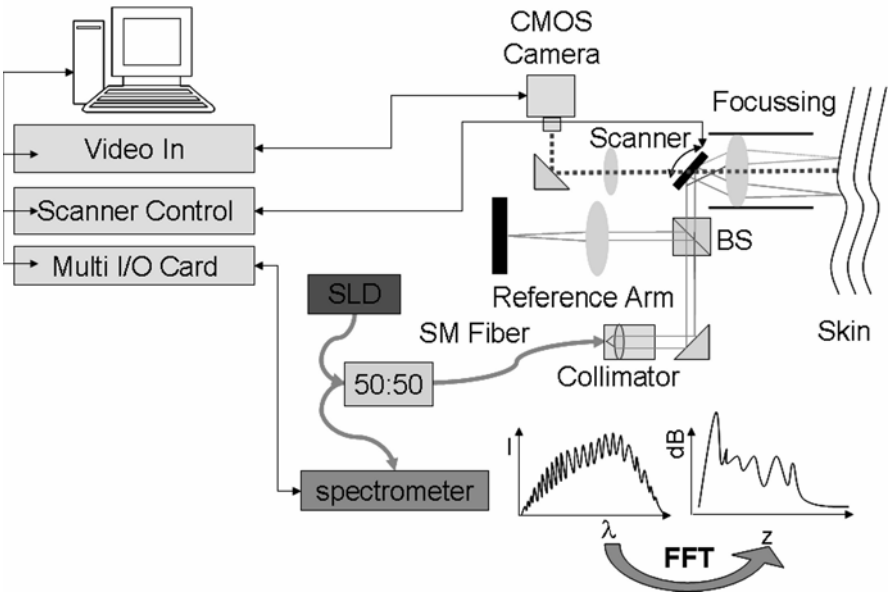

Fig. 1. Setup of the Fourier domain optical coherence tomograph; abbreviations: SLD: superluminescence diode, SM fiber: single mode optical fiber, BS: beam splitter cube, FFT: fast Fourier transformation, CMOS: Complementary Metal Oxide Semiconductor; Multi I/O Card: 16 bit 1.25 Ms/s analogue to digital converter and digital to analogue converter card; 50:50: fiber coupler with 1:1 splitting ratio.

The setup of the Fourier domain OCT system (see Figure 1.) we used for imaging is described in detail elsewhere [5]. In brief, a broadband superluminescence diode (50 nm spectral width, 840 nm central wavelength and 1 mW optical power) is coupled to a Michelson interferometer with reference and probe arm. The probe beam is deflected by a galvanometer mounted scanner mirror and focused moderately to a 9 μm spot size approximately 300 μm under the skin surface. The lateral scanning range of the probe beam is set to 6 mm in 600 equidistant steps. Probe

and reference reflections are superimposed and the resulting interference spectrum is analysed by a grating spectrometer with a line detector (1024 pixel).

After digitizing with 16 bit dynamic range and rescaling the spectra to wavenumber units they are Fourier transformed to obtain axial A-scans with 512 amplitudes spaced 4 μm (2.81 μm) in air (skin). The logarithmized amplitudes of the 600 A-scans of one lateral scan form one B-scan image, which is displayed online as an 8-bit grey scale image. The layered structure of the epidermis and upper dermis can be detected and marked in the image by trained persons.

A set of 84 FD-OCT images was acquired from 12 volunteers at three different skin sites: the forehead, the back of the hand and the back. The first 36 images were taken in March, the remaining 48 were taken in October containing an image of the skin on each back seven days of recovery after exposure to 1 MED (minimal erythema dose) of UV light. All images are associated to the group of outdoor workers.

The images were manually segmented by three trained experts. They look for differences in the appearance of the texture in the epidermal layer as compared to the dermal layer and drew a pixel trace at the borderline into the images. In the case of doubt they were allowed to leave out columns in the trace.

The Markov chain algorithm learned grey value histograms for the different skin layers and transition probabilities for the vertical pixel to pixel displacements of the borderlines from a training set of FD-OCT images which had been segmented manually. The skin surface line was found by assigning probabilities for being air or skin to each pixel, multiplying the probabilities to be air of all pixels above a position and the probabilities to be skin below the position. In this way a probability for each possible position in one A-Scan for being the air-skin transition was found. To calculate the estimated trace of the air-skin transition the position probabilities were multiplied with the transition probabilities to the neighbouring position (restricted to 15 possible transitions), forming a Markov random chain. Defining a quadratic cost function for the trace, the least costly choice turned out to be the expectation value of the joined probability for each position in each A-Scan.

The dermal-epidermal junction (DEJ) was found using the same formalism, but taking the gradient of the skewness of the grey value distribution as a binary probability. In addition a rejection condition was stated in such a way that if the variance of the expectation value exceeds an adjustable threshold value the found DEJ is omitted.

The convolution algorithm calculates the convolution between three 2D step function kernels of different size with the OCT image thus forming three new filtered images. The most distant (from the top of the image) absolute maximum value of the three filtered images along the y-direction is taken as the air-skin transition. The DEJ is found among the next prominent maxima under the skin surface by applying an empirically found threshold value. This algorithm is abbreviated by “Conv”. In addition a trace is computed along the three most prominent maxima, which minimizes a quadratic cost function for vertical transitions. This algorithm is termed “Conv+”.

In order to evaluate the performance of the algorithms the 3 expert traces in each of the 84 images were taken as a gold standard if all three coincided within a tolerance of ten pixels.

3. Results and Discussion

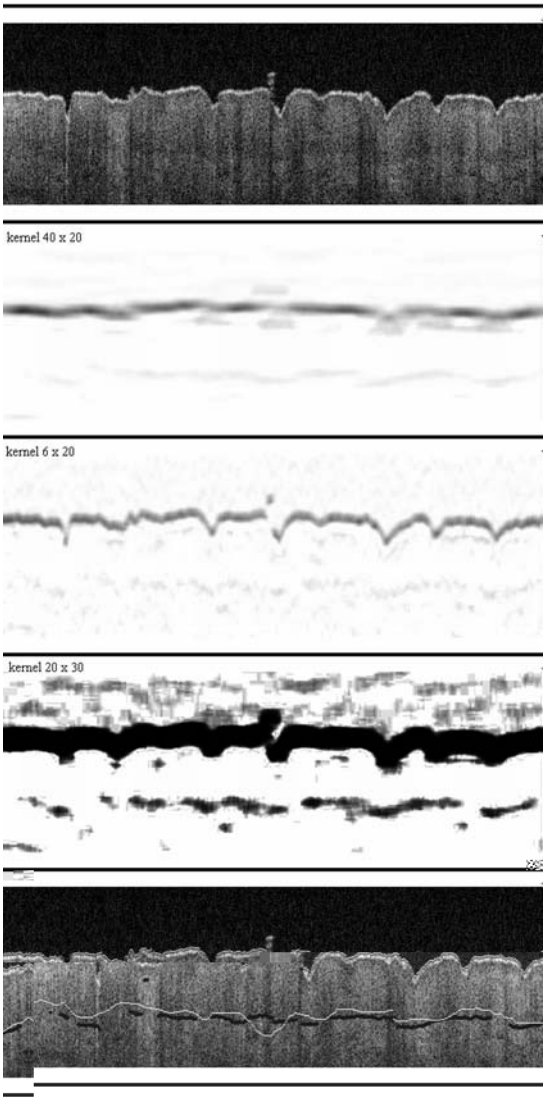

Fig. 2. Top: original OCT image; middle: 3 filtered images with different step function kernel sizes (40 x 20, 6 x 20, 20 x 30); bottom: computed air-skin interface (white), dermal epidermal junction (white: expert finding most differing from the trace of the algorithm, black: "Conv+"-algorithm). The 20 x 30 kernel filtered image has been gamma corrected to improve visibility of the DEJ.

Figure 2. (top) shows a B-scan OCT cross-sectional image of the skin at the back of a volunteer 7 days after exposure to 1 MED UV light. In the resulting segmented image (Figure 2, bottom) two traces for the dermal epidermal junction are drawn in the grey-scale image. The white trace corresponds to a manual segmentation of dermis and epidermis by a trained expert. The black trace indicates the finding of the step-convolution algorithm "conv+". As can be noticed in this example, the traces differ in detail but yield to a very similar mean epidermal thickness.

One problem in finding the air-skin transition is caused by hairs. In Figure 1. the first two filtered images show how to deal with the problem. The coarse filter with a 40 x 20 kernel equals out the hair, while the finer 6 x 20 kernel reproduces the wrinkles in a better way. The algorithm chooses the maximum intensity position either from the coarse filtered image or the fine filtered image according to which one of them is more distant from the top. This utilizes the fact, that wrinkles have their peaks downward while hairs stick out upward.

In order to evaluate the overall performance on the test set of 84 OCT images each one of the algorithms was tested against the 3 expert traces. The statistical variances of the experts' values divided by the variance of the experts' values plus the algorithm was taken as a quantitative index of performance. The mean of the performance indices of each method is listed in Table 1.

Table 1. Performance Indices of the algorithms

Performance Index = Variance (experts) / Variance (experts, algorithm)			
A-scan-aver.	Conv	Conv+	Markov
0.518524	0.629892	0.915359	0.753658

In order to find tendencies between images taken at different skin sites, different seasons of the year and different artificial UV exposure, the results were grouped according to these criteria in Table 2. All values are taken as the mean of the 12 volunteers. As expected from the performance indices the "Conv+" algorithm comes closest to the values and tendencies found by the experts.

The most striking difference in epidermal thickness is due to different skin sites, especially the back of the hand vs. the forehead shows a difference of $\Delta_{Epidermis} = 53$ µm. The next significant effect is caused by the exposure to a minimal erythema dose. The $\Delta_{Epidermis} = +15$ µm caused by the UV light can be attributed to a protective reaction of the skin rather than an inflammatory effect, because the skin had totally recovered from the erythema 7 days after the exposure. The light tendency towards thinner skin in October compared to skin in March is surprising, because one would expect an epidermal thickening caused by the natural sun exposure during summer in a group of people who predominately work outside.

Table 2. Epidermal thickness values (pixel) found by the algorithms

Epidermal Thickness / pixel (1 pixel = 2.81 µm with n=1.42)							
	Month	MED	Experts	A-aver	Conv	Conv+	Markov
back	3	-	35.11	32.42	33.09	34.98	34.70
	10	-	33.08	24.17	32.04	33.94	34.05
	10	1	38.33	29.83	37.05	39.06	37.12
fore-head	3	-	33.44	28.50	32.43	34.74	37.96
	10	-	31.12	26.67	30.70	32.89	34.31
hand	3	-	57.78	40.83	34.34	49.95	56.94
	10	-	49.91	39.58	36.96	52.07	54.07

4. Conclusions

The step kernel convolution algorithm plus a decision for a DEJ trace, which links the maxima in the filtered image with minimum vertical transition costs, has proven to be the best performing algorithm for finding the epidermal thickness. This holds true as long as one considers the experts' segmentations of the OCT images as the gold standard. In how far the found DEJ in the OCT image exactly corresponds to the basal membrane one would find in the histology of a biopsy is still an unclear issue. Since repetitive biopsies are not possible in a test group of volunteers the OCT measurement remains the preferable tool for performing routine measurements. The automatic algorithms will help to reduce time expenditure and costs for the analysis of the large number of images and will help to clarify the role of epidermal thickening in the natural sun protection of the human skin.

Acknowledgements. We acknowledge financial support by the Federal Institute for Occupational Safety and Health (project F 1986).

References

1 Welzel, J. et al.: Changes in function and morphology of normal human skin: evaluation using optical coherence tomography. Brit. J. Dermatol. 150, (2004), 220-225
2 Gambichler, T. et al.: UVA1 and UVB irradiated skin investigated by optical coherence tomography in vivo: a preliminary study. Clin. Exp. Dermatol. 30, (2005), 79-82
3 Knuschke P. et al.: Monitoring des natürlichen Lichtschutzes der Haut. Optische Strahlung - EU-Richtlinie und aktuelle Forschungsergebnisse, BAUA, (2005), 32-37
4 Gambichler, T. et al.: Comparison of histometric data obtained by optical coherence tomography and routine histology. J. Biomed. Opt. 10, (2005), 044008
5 Weissman, J. et al.: Optical coherence tomography of skin for measurement of epidermal thickness by shapelet-based image analysis. Optics Express 12, (2004), 5760-5769
6 Koch, P. et al.: Ultrahigh-resolution FDOCT system for dermatology. SPIE Proc. 5690, (2005), 24-30.

Multiscale Description of Light Propagation in Biological Tissue

Alwin Kienle, René Michels, Jan Schäfer, and Oliver Fugger

Institut für Lasertechnologien in der Medizin und Meßtechnik an der Universität Ulm, Helmoltzstraße 12, D-89081 Ulm, Germany
E-mail: alwin.kienle@ilm.uni-ulm.de

Abstract. A multiscale description of the light propagation in biological tissue is presented. The Maxwell's equations, the transport equation, and the diffusion equation are applied for the description on the microscopic, mesoscopic, and macroscopic scale, respectively. The *modus operandi* of the multiscale approach is illustrated for the case of tendon tissue. It is shown that the aligned microstructure of tendon strongly influences the light propagation in the tissue.

1. Introduction

Early diagnose of diseases is an important application of light in medicine. In order to exploit fully the potential of photonics in this field, it is necessary to understand the dependence of the light propagation on the microstructure of the considered tissues. For this aim a multiscale approach is necessary due to the finite resources of state-of-the-art computers or even high performance computers. For small volumes of the tissue we use analytical or numerical solutions of the Maxwell's equations, for large volumes the diffusion equation is solved and for intermediate volumes the transport theory is applied using the Monte Carlo method [1]. We discuss the different steps of this approach for the study of the light propagation in tendon tissue.

2. Microscopic Scale

For an exact description of the light propagation in biological tissue the Maxwell's equations have to be solved. Thus, the spatially resolved complex refractive index has to be known for the whole considered tissue volume, which is in many cases extremely difficult to obtain. However, often it is sufficient to identify the tissue's most important scatterers. For example, for the case of tendon the main scatterers are the collagen fibers, see Figure 1. The collagen fibers, for which we assumed a thickness of approximately 3µm, are aligned parallel to each other. In a first step we assumed that the collagen fibers can be considered as cylinders which lengths are much larger than their diameters. For this geometry it is possible to derive analytical formula for the angularly-resolved scattering (phase function), the scattering and the absorption cross sections from Maxwell's equations.

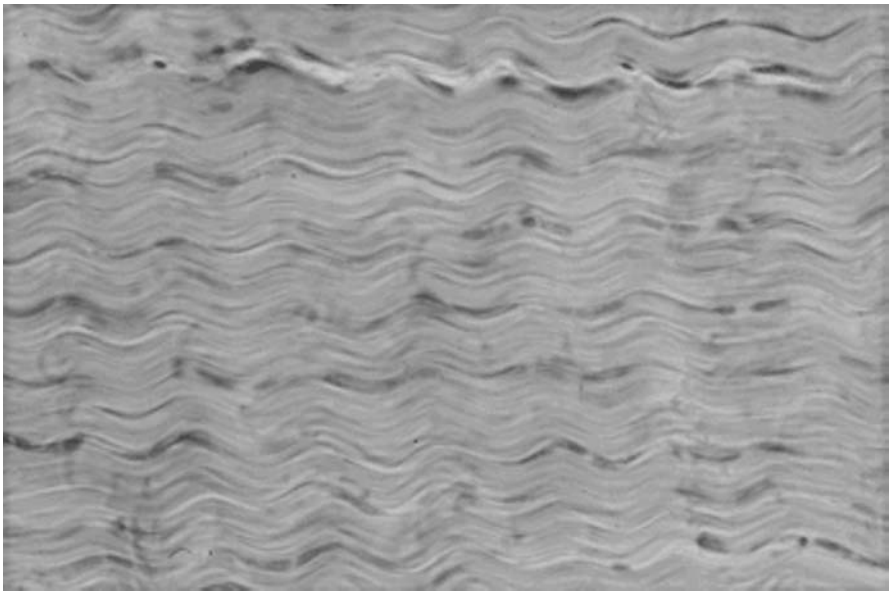

Fig. 1. Collagen fibers in tendon tissue.

Figure 2a) shows schematically the scattering of a plane wave by an infinite long cylinder. If the angle between the incident light and the cylinder is ξ, then the light is scattered within a cone having an opening angle of ξ. The probability distribution of the scattering versus ζ (that means within the cone) depends on the incident angle ξ and is given in Figure 2b) for the case of a collagen fiber.

Figure 2b) shows that the phase function depends not only on the scattering angle as was normally assumed in literature, but both on the scattered and on the incident directions. Also, the scattering coefficient depends on the incident direction. This leads to an anisotropic light propagation in such aligned tissues, see following section.

In a next step the wavy course of the fibers has to be considered. For this more complex geometry a numerical solution of the three-dimensional equations has to be used to calculate the phase function.

The accuracy of the model can be further enhanced considering the dependent scattering of the collagen fibers. The fibers are densely packed, compare Figure 1. Thus, it is likely that the fibers do not scatter independently from the adjacent fibers. We performed finite-difference time-domain simulations [2] to solve the Maxwell's equations for tissue containing different concentrations of collagen fibers, which showed that the scattering coefficient decreases due to dependent scattering effects.

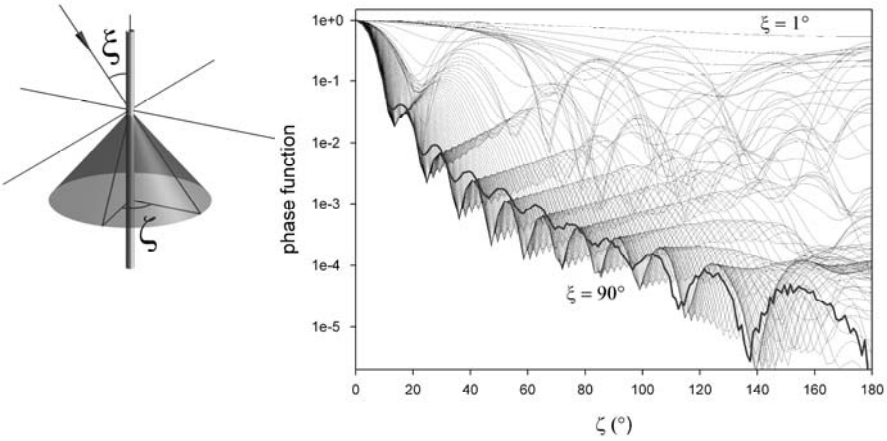

Fig. 2. a) Scheme of the scattering of a plane wave by a cylinder. b) Sattering probability versus ζ for different incident angles ξ for a collagen cylinder (refractive index 1.46 inside and 1.36 outside the cylinder having a diameter of 3μm).

The disadvantage of the numerical solution of the Maxwell's equations is that a large amount of processor and memory power is needed. Thus, it is only possible to consider relative small tissue volumes (<< 1mm^3).

3. Mesoscopic Scale

The mathematical description of the mesoscopic scale is given by the transport theory. It is an approximation of the Maxwell's equations and neglects, for example, interference effects. We solved the transport theory applying the Monte Carlo method. We used the phase function obtained from the solution of the Maxwell's equations as input for the Monte Carlo simulations. In this section we assume that the scattering by the collagen fibres is independent from each other. If this assumption is not valid, the phase function, the scattering and the absorption coefficients have to be modified accordingly, see section 2. The Monte Carlo simulations enable the calculations of much larger volumes as is possible with the solutions of the Maxwell's equations.

Figure 3a) and 3b) show the results of the spatially-resolved reflectance from a slab of tendon having a thickness of 10mm and 1mm, respectively. The tissue is illuminated by a pencil beam and the iso-intensity contour lines of the scattered and remitted light is calculated. The concentration of the collagen fibers was set to 6350mm^{-2}, which would result in a reduced scattering coefficient of 0.5mm^{-1}, if the fibers were isotropically distributed. In the simulations all fibers were directed along the *x*-direction. In addition to the fibers we assumed that all other scatterers in the tendon can be described by an isotropic reduced scattering coefficient of also 0.5mm^{-1}.

Both figures exhibit contour lines which are elongated perpendicular to the fibers' direction at small distances and parallel to it for large distances [3, 4]. Further it can be seen that the elongation of the contour lines at small distances (for example the $1e^{-2}$ contour line) is more pronounced for the slab having a thickness of 1mm compared to that with a thickness of 10mm. This is due to the smaller number of scatterings that the remitted photons experience at a given distance from the incident beam in the case of the 1mm thick tendon slab compared to the 10mm thick slab, because the probability of a photon to be transmitted from the slab (and thus the photon cannot be remitted anymore) is higher for the thinner slab. In general, the more scattering interactions a photon experience, the more diffuse (e.g. isotrop) is the angular distribution of the photons.

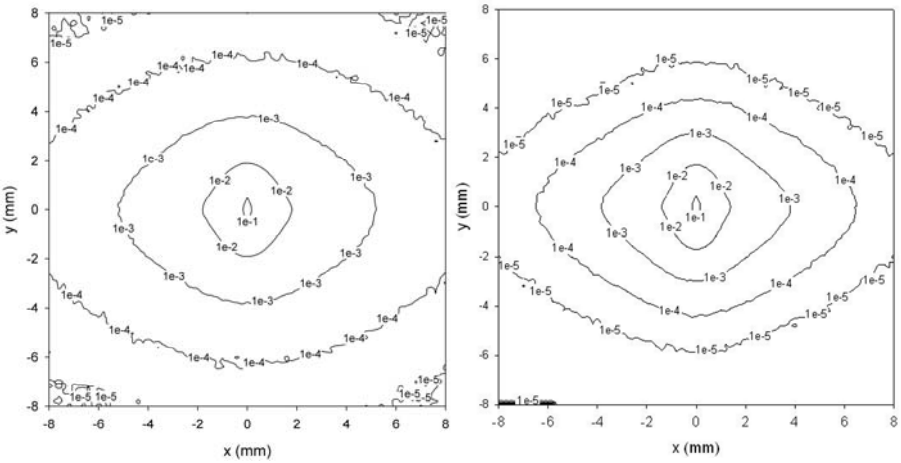

Fig. 3. Iso-intensity contour lines for the spatially-resolved reflectance from a tendon slab calculated with the Monte Carlo method. The thickness of the slab is a) 10mm and b) 1mm.

Figure 4 shows a measurement of the spatially-resolved reflectance from a bovine tendon having a thickness of 3mm using a CCD camera as detector and a HeNe laser as source. In principle, the same features of the remitted light can be seen as were obtained from the Monte Carlo simulations. Thus, the main components of the tendon microstructure were implemented in the theoretical model.

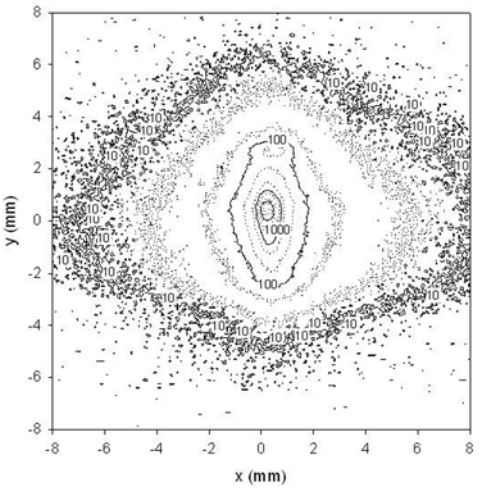

Fig. 4. Measurements of the spatially-resolved reflectance from tendon.

However, there are also differences, which can be probably explained by improving the theoretical model. For example, the incorporation of the wavy course of the tendon fibers in the model changes the form of the iso-intensity contour lines. In addition, inclusion of the dependent scattering effect into the model might modify the results.

4. Macroscopic Scale

For the description on the macroscopic scale we use solutions of the diffusion equation. In general, the diffusion equation is valid, if the photons were scattered many times so that their angular distribution is almost isotropic. The normally used isotropic diffusion equation, however, cannot be applied to describe the spatially-resolved reflectance from tendon tissue, because the iso-intensity contour lines are circles according to this equation. Recently, an anisotropic diffusion equation was developed which solutions exhibit elliptical iso-intensity contour lines [5]. Presently, we investigate if this solution can be used to describe the light propagation in tendon correctly for large distances from the source.

5. Conclusions

We showed that it is important to consider the microstructure of biological tissue to understand the light propagation in the tissue. For this purpose a multiscale approach has to be used due to the finite computer resources available today. Recently, several interesting effects have been explained with this approach, for example, light guiding [6] or optical magnification [7] in biological tissue. We

anticipate that the knowledge of the dependence of the light propagation in tissue on its microstructure will have a plethora of applications.

Acknowledgements. We acknowledge the support by the Deutsche Forschungsgemeinschaft.

References

1 A. Ishimaru, *Wave Propagation and Scattering in Random Media*, Academic Press, New York, 1978.
2 A. Taflove and S.C. Hagness, *Computional Electrodynamics: the Finite Difference Time Domain Method*, Artech House, Boston, 1995.
3 S. Nickell, M. Hermann, M. Essenpreis, T.J. Farrell, U. Krämer, and M.S. Patterson, Phys. Med. Biol. **45**, 2873, 2000.
4 A. Kienle, F.K. Forster, and R. Hibst, Opt. Lett. **29**, 2617, 2004.
5 P.M. Johnson, B.P.J. Bret, J.G. Rivas, J.J. Kelly, and Ad Lagendijk, Phys. Rev. Lett. **89**, 243901, 2002.
6 A. Kienle, and R. Hibst, Phys. Rev. Lett. **97**, 018104, 2006.
7 A. Kienle, R. Michels, and R. Hibst, J. Dent. Res. **85**, 955, 2006.

The Influence of Heterogeneous Optical Properties upon Fluorescence Diffusion Tomography of Small Animals

Saskia Bjoern[1,2], Sachin V. Patwardhan[1] and Joseph P. Culver[1]

[1] Department of Radiology, Washington University School of Medicine, St. Louis, MO, 63110, USA
[2] RheinAhrCampus Remagen, Department of Mathematics and Technology, Germany
E-mail: sbjoern@rheinahrcampus.de, culverj@wustl.edu

Abstract. We evaluated the influence of optical property maps on inversion of fluorescence data from mice. For highly absorbing regions (5x background) of sufficient size, heterogeneous optical property maps provide significant improvements over homogeneous maps.

1. Introduction

Recent advances in fluorescence tomography have demonstrated the potential for reporting optically based biological assays in three dimensions throughout the bodies of living mice [1, 2]. A critical aspect of fluorescence tomography has been the use of differential measurements involving the ratio of emitted fluorescence light intensity I_{emi} over the re-emitted excitation light intensity I_{exc}. Emission/excitation ratio data significantly reduce the influence of heterogeneous optical properties and path lengths. Thus far, small animal fluorescence tomography studies have therefore generally assumed homogeneous optical properties [1, 2]. However, measurements in mice show that light intensities at similar source-detector separations can vary by up to two orders of magnitude, indicating that mice have strongly heterogeneous optical properties. Considering the variation in the optical properties of different organs (e.g. lung vs. heart), this is not surprising. Previous studies that examined the influence of heterogeneous optical properties upon linear reconstructions of ratio data have come to different conclusions. Some studies have found the influence of moderately absorbing backgrounds on fluorescence reconstructions to be weak [3, 4], while other studies have found a more significant effect [5, 6]. These differences are due in part to the different optical property tests evaluated. Here, we examine a range of heterogeneous optical properties that reflect experimental light intensity measurements in small animals. We compare the image quality between reconstructions using homogeneous and heterogeneous optical property maps to determine the small animal imaging situations in which tissue heterogeneities become important.

2. Experimental Methods

For the fluorescence tomography forward model, we created sensitivity matrices A using an adjoint formulation [2]. Finite difference methods were used to calculate the Greens functions for predefined optical property maps [7]. Measurement data ($y=Ie_{mi}/I_{exc}$) was simulated for predefined fluorescent test objects x_{exact} using $y = A \cdot x_{exact} + e_{noise}$. Here the noise term was set at 0.5% additive Gaussian random noise—a value consistent with previous in vivo experimental data for fluorescence tubes with 100 nM concentrations of indocyanine green (ICG) and our fluorescence tomography system [2]. Reconstructions were performed with spatially variant regularization using direct inversion methods.

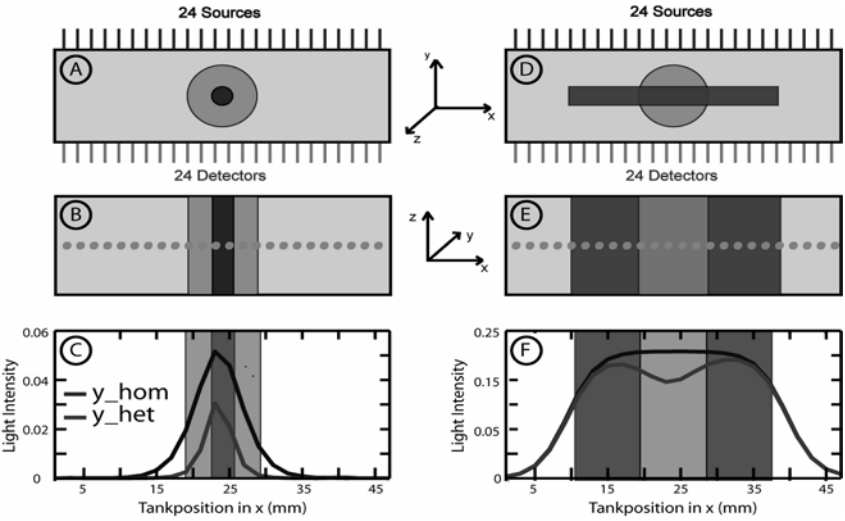

Fig. 1. (A) Top view of the tank. An absorbing tube (grey circle), surrounds a smaller fluorescent tube (red). Lines of 24 sources (red) and 24 detectors (blue) are on opposing sides of the imaging domain. In the side view (B), blue dots indicate the detector positions. (C) Simulated ratio data for opposing source and detectors are shown as a function of x position. Ratio data is ~40% smaller in magnitude for y_{het} compared to y_{hom}. Top (D) and side (E) views of the fluorescent sheet are also shown. (F) For the fluorescing slice object, the absorbing inclusion changes both the ratio data magnitude and shape.

To evaluate the influence of heterogeneous optical properties, we simulated fluorescence data for both heterogeneous and homogeneous optical property maps. Three types of images were reconstructed. A reference image was created by simulating measurement data y_{hom} for fluorescence inclusions using a homogeneous sensitivity matrix A_{hom} and inverting the measurement data using the same A_{hom}. This approach assumes the absorption of the fluorescence dye to be small relative to the background optical properties (e.g. 100 nM ICG, and typical optical properties, absorption μ_a=0.1 cm^{-1} and reduced scattering μ_s'=10 cm^{-1}). Ratio data representative of heterogeneous optical properties y_{het} were generated using a heterogeneous sensitivity matrix A_{het}. Reconstructions of y_{het}

with A_{hom} simulated the commonly used assumption of homogenous optical properties. The potential image quality improvements gained from knowledge of the optical properties maps are represented in the reconstructions of y_{het} with the correct A_{het}. We simulated a three-dimensional tank (x-direction: 48mm, y-direction: 15mm, z-direction: 16mm) filled with a matching fluid (μ_a=0.1 cm-1 and μ_s'=10 cm-1). In the middle of the tank, we placed a tube (r_a = 5mm, μ_a=1.0 cm-1 μ_s'=10 cm-1). The fluorescent object was either a tube (r_f = 1.5mm) or a slice (x-direction: 30mm, y-direction: 3mm, z-direction: 16mm) in the middle of the tank.

3. Results and Discussion

The influence of the optical properties on the fluorescence ratio metric data *y* is shown in Fig. 1. While data are used for all combinations of source and detector pairs, for illustrative purposes, only the data for directly opposing source and detector positions are shown. While the absorption of the inclusion (μ_a=1.0 cm^{-1}) is 10x greater than the surrounding media (μ_a=0.1 cm^{-1}), the magnitude of y_{het} is only 40% less than y_{hom}. This effect is due to the fact that the absorbing object reduces both the emission and excitation light intensities. The shapes of y_{hom} and y_{het} appear to be similar for the fluorescent tube object. On the other hand, the shapes are clearly different for the slice object with y_{het} dropping in magnitude near the position of the absorbing tube.

The quality of the reconstructed images of the fluorescent objects using A_{hom} and A_{het} are very different. In addition to the qualitative comparisons, we also analyzed the image error $\eta_x = \sum (x_{exact} - x_{recon})^2$. The reference image, y_{hom}, reconstructed with A_{hom} (green curve) has an image error of η_x=3.5 and peak value *max*=18 nM consistent with the expected broadening and partial volume effects. Reconstruction of the y_{het} with A_{hom} (blue curve, η_x =27) leads to increased ringing (Fig 2b) and surprisingly, a maximum *max*=36 nM greater than the reference image even though the data maximum is reduced. Reconstruction of y_{het} with A_{het} (green curve, η_x=2.7, *max*=19 nM) yields an image in good agreement with the reference image. For the fluorescent slice object, the A_{het} reconstruction (f, η_x=53) has dramatically improved image quality compared to reconstruction of y_{het} with A_{hom} (e, η_x=80). Alternate reconstructions that used *ART* for data inversion, both with and without positivity constraints, yielded similar results (not shown). While the positivity constraints eliminated the negative portions of the ringing (Fig 2b), other artifacts were introduced. The dependence of image error on the absorption properties of the slice (Fig. 2c) and cylindrical (Fig. 2c) objects shows that use of the correct optical property map can provide consistent image quality independent of the background absorption map, whereas use of the homogeneous forward model leads to increased error, particularly for absorbing objects more than 5x the surrounding optical properties.

4. Conclusions

Fluorescence tomography and bioluminescence tomography are gaining significant interest as methods for whole body imaging of biological activity. In principal, these methods can provide quantitative imaging assays. In this study, we have explored the influence of the assumption of homogeneous optical properties on fluorescence tomography reconstructions. We found that although the ratio data magnitudes do not change greatly in magnitude, the image quality can degrade more dramatically than analysis of the magnitude only would suggest. Furthermore, the use of the correct optical property map can largely regain the image quality obtained in the ideal case of homogeneous optical properties.

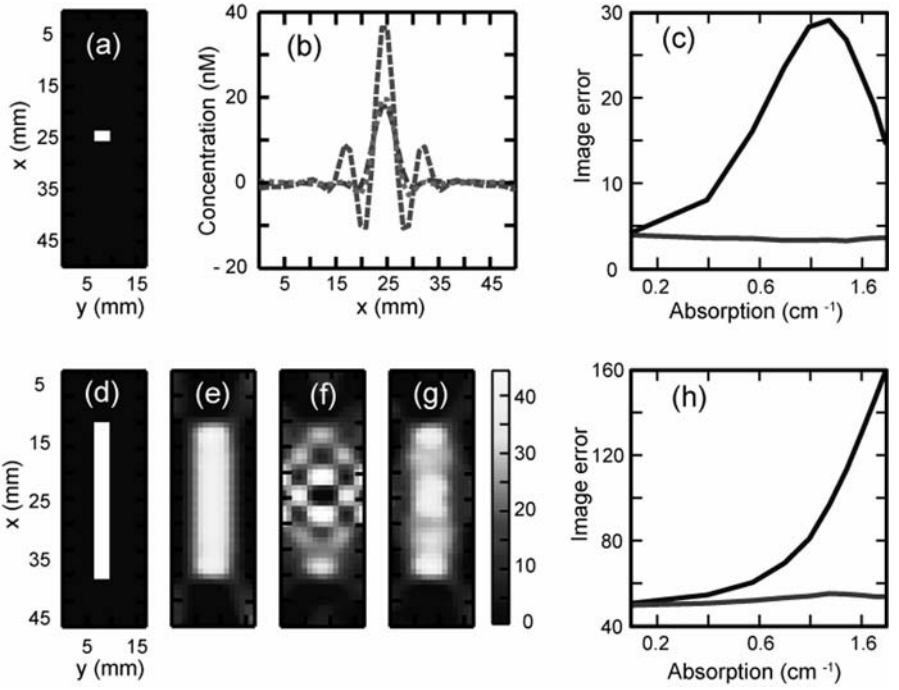

Fig. 2. The influence of heterogeneous optical properties on fluorescence tomography. (a) Test image of a fluorescing tube. (b) Comparisons of traces along the x-dimension in the center of the volume: y_{hom} reconstructed with A_{hom} (red solid), y_{het} reconstructed with A_{hom} (blue dashed) has enhanced ringing side lobes, while y_{hom} reconstructed with A_{het} (green dotted) more closely matches the original curve, y_{hom}/A_{hom} result. (c) Image error of the fluorescing image as a function of the absorption in the cylindrical tube. A slice object (d) was reconstructed using y_{hom} and A_{hom} (e). Reconstructions of y_{het} with A_{hom} (f) fail to capture the slice shape of the test object. In contrast reconstructions using A_{het} (g) are able to capture the general shape of the test image. (h) Image error of the fluorescing slice object as a function of cylindrical tube absorption.

In this study, we have assumed knowledge of the optical properties. These values could be obtained in practice through inversion of excitation data, potentially either continuous wave, frequency-domain, time-resolved, or multi-spectral data sets. In addition, optical property reconstructions may utilize *a priori* knowledge of tissue anatomy from co-registered magnetic resonance imaging (*MRI*), ultrasound, or computer tomography (*CT*) data.

We anticipate that as fluorescence tomography becomes more widely used, the development of methods to measure and incorporate heterogeneous optical property maps into fluorescence tomography reconstructions will become increasingly important.

Acknowledgements. I would like to thank Prof. Dr. Joseph P. Culver, Dr. Sachin V. Patwardhan, Prof. Dr. Samuel Achilefu and Prof. Dr. Matthias Kohl-Bareis

References

1 Ntziachristos, V., C.H. Tung, C. Bremer and R. Weissleder, *Fluorescence molecular tomography resolves protease activity in vivo.* Nat Med, 2002. **8**(7): p. 757-60.

2 Patwardhan, S.V., S.R. Bloch, S. Achilefu and J.P. Culver, *Time-dependent whole-body fluorescence tomography of probe bio-distributions in mice.* Optics Express, 2005. **13**(7): p. 2564 - 2577.

3 Soubret, A., J. Ripoll and V. Ntziachristos, *Accuracy of fluorescent tomography in the presence of heterogeneities: Study of the normalized born ratio.* Ieee Transactions on Medical Imaging, 2005. **24**(10): p. 1377-1386.

4 Eppstein, M.J., D.E. Dougherty, D.J. Hawrysz and E.M. Sevick-Muraca, *Three-dimensional Bayesian optical image reconstruction with domain decomposition.* Ieee Transactions on Medical Imaging, 2001. **20**(3): p. 147-163.

5 Gibson, A.P., J.C. Hebden, J. Riley, N. Everdell, M. Schweiger, S.R. Arridge and D.T. Delpy, *Linear and nonlinear reconstruction for optical tomography of phantoms with nonscattering regions.* Applied Optics, 2005. **44**(19): p. 3925-3936.

6 Cheng, X. and D.A. Boas, *Systematic diffuse optical image errors resulting from uncertainty in the background optical properties.* Optics Express, 1999. **4**: p. 299-307.

7 Culver, J.P., R. Choe, M.J. Holboke, L. Zubkov, T. Durduran, A. Slemp, V. Ntziachristos, B. Chance and A.G. Yodh, *Three-dimensional diffuse optical tomography in the parallel plane transmission geometry: evaluation of a hybrid frequency domain/continuous wave clinical system for breast imaging.* Med Phys, 2003. **30**(2): p. 235-47.

Cell Membrane Fluidity Determined by Fluorescence Lifetime and Polarization Screening

Thomas Bruns[1], Wolfgang S.L. Strauss[2] and Herbert Schneckenburger[1,2]

[1] Hochschule Aalen, Institut für Angewandte Forschung, Beethovenstr. 1,
73430 Aalen, Germany
E-mail: Thomas.Bruns@htw-aalen.de, Herbert.Schneckenburger@htw-aalen.de
[2] Institut für Lasertechnologien in der Medizin und Messtechnik an der Universität Ulm,
Helmholtzstr. 12, 89081 Ulm, Germany
E-mail: Wolfgang.Strauss@ilm.uni-ulm.de

Abstract. A novel setup for fluorescence measurements of surfaces of biological samples, in particular the plasma membrane of living cells, is described. The method is based on splitting of a laser beam and multiple total internal reflections (TIR) within the bottom of a microtiter plate, such that up to 96 individual samples are illuminated simultaneously by an evanescent electromagnetic field. In general, two different screening procedures (1) High Throughput Screening (HTS) and (2) High Content Screening (HCS) are distinguished, where in the first case a rapid measurement of large sample numbers, and in the second case a high information content from a single sample is achieved. In particular, a HCS system for the parameters fluorescence lifetime (Fluorescence Lifetime Screening, FLiS) and fluorescence anisotropy (Fluorescence Lifetime Polarization Screening, FLiPS) has been established and integrated into an existing HTS-system. While fluorescence lifetime represents a general measure for the interaction of a marker molecule with its molecular or cellular environment, fluorescence anisotropy corresponds to the time of rotation of this molecule from a position with defined orientation into a position with arbitrary orientation and reflects directly the viscosity of the environment and thus membrane fluidity. For fluorescence lifetime screening (FLiS) and fluorescence lifetime polarization screening (FLiPS) fluorescent membrane markers, intercalating into cell membranes, were applied to an established human glioblastoma cell line (U373-MG).

1. Introduction

For more than 20 years [1] total internal reflection (TIR) of laser light has been used to study cell-substrate interfaces in order to get more detailed information on cell membranes. When a light beam propagating through a medium of refractive index n_1 (e.g. glass) meets an interface with a second medium of refractive index $n_2 < n_1$ (e.g. cytoplasm), total internal reflection occurs at all angles of incidence Θ which are greater than a critical angle $\Theta_c = \arcsin(n_2/n_1)$. Despite being totally reflected, the incident beam establishes an evanescent electromagnetic field that penetrates into the second medium and decays exponentially with the distance z from the interface. According to the relation

$$d = (\lambda/4\pi)\cdot\left(n_1{}^2 \sin^2\Theta - n_2{}^2\right)^{-1/2} \quad (1)$$

penetration depths d between about 60 nm and more than 300 nm are attained depending on the wavelength λ and the angle of incidence Θ. Therefore, fluorophores located within or close to the plasma membrane can be examined almost selectively in living cells. So far, total internal reflection fluorescence microscopy (TIRFM) has been applied for measuring the topography of cell-substrate contacts [1,2], membrane [3] or protein [4] dynamics, membrane-proximal ion fluxes [5,6] as well as endocytosis or exocytosis [7,8].

Previously, membrane dynamics, i.e. membrane stiffness and fluidity of living cells, have been studied as a function of temperature, age and growth phase of the cells, as well as on the intracellular amount of cholesterol [3,9]. Changes of cholesterol amounts in cell membranes have been related to specific diseases [10-12] and may have some influence on the uptake of pharmaceutical agents. Following TIRFM measurements of membrane dynamics, screening of a larger number of samples appeared desirable, and a first fluorescence reader based on total internal reflection (TIR) of a laser beam on 96 samples of a microtiter plate (High Throughput Screening, HTS) was recently described [13]. However, in order to determine membrane stiffness and fluidity, further data of individual samples appeared necessary. Therefore, an optical setup for measurements of fluorescence lifetime and fluorescence anisotropy (High Content Screening, HCS) was developed and combined with the existing reader system. While fluorescence lifetime represents a general measure for the interaction of a marker molecule with its molecular or cellular environment, fluorescence anisotropy is related to the time of rotation of this molecule from a position with defined orientation into a position with arbitrary orientation and reflects directly the viscosity of the environment and thus membrane fluidity. For fluorescence lifetime screening (FLiS) and fluorescence lifetime polarization screening (FLiPS) the fluorescent membrane markers 22-(N-(7-nitrobenz-2-oxa-1,3-diazol-4-yl)amino)-23,24-bisnor-5-cholen-3beta-ol (NBD cholesterol) and 4-(4-(dihexadecylamino)styryl)-N-methylpyridinium iodide (DIA; 4-Di-16-ASP) – intercalating into cell membranes – were applied to an established human glioblastoma cell line (U373-MG).

2. Materials and Methods

U373-MG human glioblastoma cells obtained from the European Collection of Cell Cultures (ECACC No. 89081403) were routinely grown in RPMI 1640 culture medium supplemented with 10 % fetal calf serum (FCS), glutamine and gentamycin at 37°C and 5 % CO_2. After seeding of 500 cells/mm² within single cavities of a microtiter plate and a growth phase of 48 h (in order to obtain a subconfluent cell monolayer) cells were incubated with culture medium containing NBD cholesterol at a concentration of 2 µM for 60 min or DIA at concentrations of 5 - 20 µM for 30 min. At the end of the incubation time cells were washed in both cases with Earle's Balanced Salt Solution (EBSS) prior to fluorometric measurements. For fluorescence lifetime and anisotropy

measurements solutions of NBD cholesterol (5 μM) and DIA (5-20 μM) in medium and EBSS were used for calibration of the sensitivity of the photomultiplier tubes and for further comparison with the cell measurements.

As light source a picosecond laser diode (PDL 800-B with LDH-P-C-470, PicoQuant GmbH) operated at 470 nm with a repetition rate of 20 MHz as well as a pulse width of 70 ps was used. By a combination of 3 beam splitters and mirrors the laser light was divided into 8 beams of almost identical intensity to excite 8 rows of a microtiter plate using a glass rod of rectangular shape which was optically coupled (by immersion oil) to the glass bottom of the plate. As depicted in Figure 1, multiple total internal reflection occurs within the glass bottom, if the angle of incidence Θ is above the critical angle $\Theta_c = 64°$ (resulting from the refractive indices $n_1 = 1.525$ for the glass bottom and $n_2 = 1.37$ for the cells). In the present setup Θ can be calculated from the distance s = 9 mm between two wells of the plate and the thickness d = 2 mm of the glass bottom according to $\Theta = \arctan(s/2d) = 66°$. Therefore, the condition of total internal reflection is fulfilled for all wells, and a penetration depth of the evanescent wave of about 150 nm within the cells is calculated. The exciting laser light is coupled out of the glass bottom using a second glass rod of identical shape in order to avoid uncontrolled reflections.

For high content screening (Figure 1) fluorescence of individual wells is collected by a microscope objective lens with 10x magnification, an additional focusing lens (f=25mm) and a long pass filter for $\lambda \geq 515$ nm. After passing a polarizing beam splitter for fluorescence anisotropy measurements, fluorescence is detected by two photomultiplier tubes (H5783-01, Hamamatsu Photonics Deutschland GmbH) with respect to both polarizations parallel and perpendicular to the polarization of the exciting laser light. The signals from the multiplier tubes are collected by a router (NRT 400, PicoQuant GmbH), synchronized with the laser pulses and fed to a single photon counting device (TimeHarp 200, PicoQuant GmbH) for measurements of fluorescence lifetime and anisotropy. The whole equipment consisting of lenses, beam splitter and photomultipliers can be moved on a scanning table.

Unpolarized fluorescence decay curves F(t) were fitted as a sum of exponential terms corresponding to

$$F(t) = \sum_i \alpha_i \exp(-t/\tau_i) \tag{2}$$

with the fluorescence lifetimes τ_i and the preexponential factors α_i representing the fractional contributions of the components i. Moreover, fluorescence intensities were measured parallel [$I_{\parallel}(t)$] and perpendicular [$I_{\perp}(t)$] to the exciting electric field vector, and the anisotropy function r(t) was calculated as

$$r(t) = \frac{I_{\parallel}(t) - I_{\perp}(t)}{I_{\parallel}(t) + 2I_{\perp}(t)} \ . \tag{3}$$

r(t) was again fitted as a sum of exponential components according to

$$r(t) = r_0 \sum_i R_i \exp(-t/\tau_i) \quad (4)$$

where τ_i correspond to the rotational relaxation times (with respect to different molecular axes), R_i represent the preexponential factors and r_0 the anisotropy which would be observed in the absence of rotational diffusion.

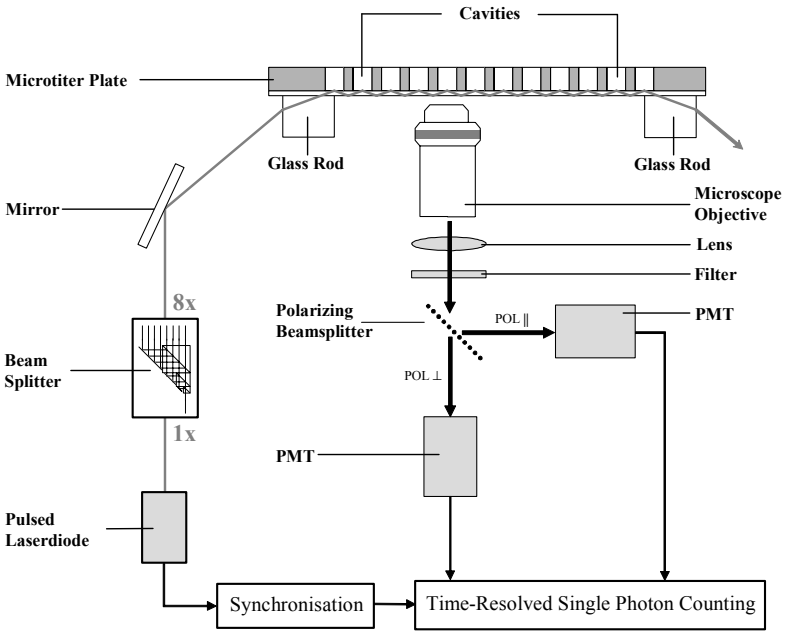

Figure 1. Experimental setup for fluorescence lifetime and anisotropy screening (FLiS, FLiPS)

3. Results

Fluorescence lifetime of individual samples was registered at $\lambda \geq 515$ nm in an unpolarized mode. Typical unpolarized fluorescence decay profiles $I_0(t)$ of DIA in U373-MG glioblastoma cells are depicted in Figure 2(a) and show a linear relation between concentration and amplitude of the membrane marker within the cell. The parameters obtained from biexponential fitting of the unpolarized fluorescence decay curve $I_0(t)$ upon application of 10 µM DIA shown in Figure 2(a) are depicted in Table 1 and compared with the parameters obtained from NBD cholesterol (2 µM). In comparison with DIA the fluorescence lifetimes are considerably larger for NBD cholesterol in the cellular environment.

Time-resolved fluorescence decay curves $I_{\parallel}(t)$, $I_{\perp}(t)$ of U373-MG glioblastoma cells incubated with NBD cholesterol were also recorded with polarization sensitivity. In contrast to the unpolarized decay curve $I_0(t)$, $I_{\parallel}(t)$ and $I_{\perp}(t)$ include both, fluorescence decay and rotational diffusion. This implies that $I_{\parallel}(t)$ decreases more rapidly than $I_0(t)$, and that the increase of $I_{\perp}(t)$ is slightly delayed in comparison to $I_0(t)$. The anisotropy function calculated from $I_{\parallel}(t)$ and $I_{\perp}(t)$ for NBD cholesterol is depicted in Figure 2(b). Similar to $I_0(t)$ for unpolarized decay profiles, r(t) proved to be fairly biexponential with the fitting parameters listed in Table 1. A fast rotational relaxation time of 0.23 ns was similar to NBD cholesterol in solution, whereas a long rotational relaxation time of about 28 ns was considerably larger than values found in solution.

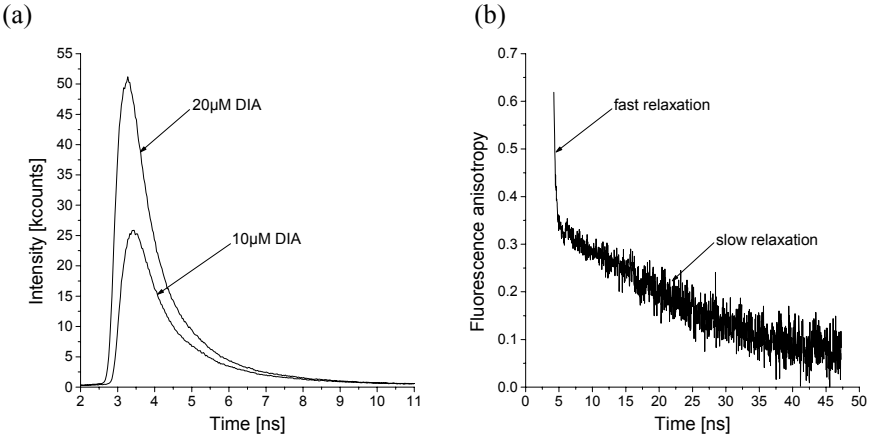

Figure 2. (a) Unpolarized time-resolved fluorescence intensity decays $I_0(t)$ of 10 and 20 µM DIA in U373-MG cells after incubation for 30 min; (b) Anisotropy lifetime decay r(t) for NBD cholesterol (2µM, 60 min) based on $I_{\parallel}(t)$ and $I_{\perp}(t)$

Table 1. Fluorescence lifetime (FLiS) and anisotropy lifetime (FLiPS) parameters of NBD cholesterol and DIA in cells (500 cells/mm^2) at excitation wavelength 470 nm.

	Parameter	in U373-MG cells
NBD	τ_1 [ns]	8.72 (± 0.1)
cholesterol	τ_2 [ns]	4.53 (± 0.11)
(2 µM, 60 min)		
	$\tau_{r,1}$ [ns]	27.95 (± 1.03)
	$\tau_{r,2}$ [ns]	0.23 (± 0.03)
DIA	τ_1 [ns]	2.18 (± 0.02)
(10 µM, 30 min)	τ_2 [ns]	0.78 (± 0.01)

4. Discussion

It has been shown that a HCS-system for the parameters fluorescence lifetime and fluorescence anisotropy could be integrated in an existing HTS-system using the TIR method. Therefore, membrane associated fluorescence can be measured simultaneously for a larger number of samples, before detailed information on fluorescence lifetime and polarization is acquired from individual samples. Switching from HTS to HCS only requires moving of appropriate detection optics to the sample of interest using an appropriate scanning table.

Fluorescence lifetime and fluorescence anisotropy are of particular interest for characterizing cell membranes. While fluorescence lifetime represents a general measure for the interaction of a marker molecule with its molecular or cellular environment, fluorescence anisotropy reflects the viscosity of the environment, and therefore is a measure of membrane fluidity. It is worth mentioning that the two rotational relaxation times obtained for NBD cholesterol in U373-MG cells, differ by more than a factor 100. This possibly results from a superposition of an almost free rotation along one axis of the molecule (in-plane rotation, similar to rotation in solution) and a strongly hindered rotation along a perpendicular axis (out-of-plane rotation) of the NBD cholesterol molecule. Fluorescence lifetime τ as well as rotational relaxation time τ_r appear rather sensitive parameters to measure changes of membrane stiffness or fluidity, e.g. in case of certain diseases.

Acknowledgements. This project was supported by the Ministerium für Wissenschaft, Forschung und Kunst Baden-Württemberg, Germany. Technical assistance by Claudia Hintze is gratefully acknowledged.

References

1. D. Axelrod in *Journal of Cell Biology* 89, 141-145 (1981).
2. K. Stock, R. Sailer, W.S.L. Strauss, M. Lyttek, R. Steiner and H. Schneckenburger in *Journal of Microscopy* 211, 19-29 (2003).
3. H. Schneckenburger, M. Wagner, M. Kretzschmar, W.S.L. Strauss and R. Sailer in *Photochemical and Photobioogical Sciences* 3, 817-822 (2004).
4. S.E. Sund and D. Axelrod in *Biophysical Journal* 79, 1655-1669 (2000).
5. G.M. Omann and D. Axelrod in *Biophysical Journal* 71, 2885-2891 (1996).
6. A. Demuro and I. Parker in *Biophysical Journal* 86, 3250-3259 (2004).
7. W.J. Betz, F. Mao and C.B. Smith in *Curr. Opin. Neurobiol.* 6, 365-371 (1996).
8. V. Beaumont in *Biochemical Society Transactions* 31, 819-823 (2003).
9. P. Weber, M. Wagner, H. Schneckenburger in *Cytometry* 69A 185-188 (2006).
10. G.P. Eckert, N.J. Cairns, A. Maras, W.F. Gattaz, W.E. Muller in *Dementia and Geriatric Cognitive Disorders* 11, 181-186 (2000).
11. S. Aozaki in *Gastroenterol Jpn.* 24, 246-254 (1989).
12. T. Koike, G. Ishida, M. Taniguchi, K. Higaki, Y. Ayaki, M. Saito, Y. Sakakihara, Y. Iwamori, K. Onno in *Biochimica et Biophysica Acta* 1406, 327-335 (1998).
13. T. Bruns, W.S.L. Strauss, R. Sailer, M. Wagner, H. Schneckenburger in *Journal of Biomedical Optics* 11(3), 34011 (2006).

Cholesterol Dependence of Cell Membrane Dynamics Proved by Fluorescence Spectroscopy and Imaging

Petra Weber[1], Michael Wagner[1], Wolfgang S. L. Strauss[2] and Herbert Schneckenburger[1,2]

[1] Hochschule Aalen, Institut für Angewandte Forschung, 73430 Aalen, Germany
E-mail: petra.weber@htw-aalen.de
[2] Institut für Lasertechnologien in der Medizin und Messtechnik an der Universität Ulm, Helmholzstr. 12, 89081 Ulm Germany

Abstract. Membrane dynamics –including membrane stiffness and fluidity- are important features of living cells. These parameters have a large impact on cellular uptake and release of metabolites or pharmaceutical agents and may be used for in vitro diagnostics. For assessment of these parameters we used a combination of conventional and total internal reflection fluorescence microscopy (TIRFM) as well as fluorescence decay kinetics. Laurdan, a polarity-sensitive fluorescent probe, whose electronic excitation energy is different in polar and non-polar environment proved to be useful for membrane studies, since its generalized polarization (GP, characterizing a spectral shift which depends on the phase of membrane lipids) and fluorescence lifetime (τ) revealed to be appropriate measures for membrane stiffness and fluidity. GP generally decreased with increasing temperatures and was always higher for the plasma membrane than for the intracellular membranes. Furthermore, GP appeared to increase during cell growth and upon aging of the cells. A specific role of cholesterol content on these findings was now examined using defined protocols of cholesterol depletion and enrichment. In addition to the decrease of GP with increasing temperature, the GP values showed a pronounced increase upon enrichment and a decrease upon depletion of cholesterol. Cholesterol content also had a large impact on fluorescence lifetime in the subnanosecond range. GP and τ were determined as integral values of single cells or small cell collectives and were also displayed as images with subnanosecond time resolution.

1. Introduction

Membrane dynamics – including membrane stiffness and fluidity – have a large impact on cellular uptake and release of various metabolites. Membrane dynamics have so far been deduced from measurements of fluorescence polarization [1] or fluorescence recovery after photobleaching (FRAP) [2] using specific membrane markers. In addition, polarity-sensitive probes, e.g. 6-dodecanoyl-2-dimethyl-amino naphthalene (laurdan), whose electronic excitation energy is different in polar and non-polar environments [3,4], proved to be useful for membrane studies. Once incorporated into cell membranes, the fluorescence of laurdan shows a spectral shift towards longer wavelengths when its molecules get into

contact with adjacent water molecules, e.g. when a phase transition from the tightly packed gel phase to the liquid crystalline phase of membrane lipids occurs. Fluorescence lifetime τ of laurdan has also been reported to depend on membrane dynamics [5], and also appears to be an appropriate measure. It is expected that spectral properties of laurdan mainly depend on mechanical stiffness whereas τ is affected by both parameters.

Fluorescence of laurdan arising from all kinds of cell membranes has so far been measured by conventional fluorescence microscopy, whereas an axial resolution has been obtained by confocal or two-photon laser scanning techniques [6]. In recent studies [7] fluorescence of the plasma membrane was detected selectively using the method of total internal reflection fluorescence microscopy (TIRFM), and compared with fluorescence arising from the whole cell. So far, membrane dynamics depended on temperature, age and growth phase of the cells. It is a purpose of our current research to correlate these findings with the intracellular amount of cholesterol using defined protocols of depletion or enrichment. Changes of cholesterol amounts in cell membranes have previously been related to specific diseases [8-11] and may have some influence on the uptake of pharmaceutical agents.

2. Experimental Methods

U373MG human glioblastoma cells were obtained from the European Collection of Cell Cultures (ECACC No. 89081403). Cells were routinely grown in RPMI 1640 medium supplemented with 10 % fetal calf serum and 1 % penicillin / streptomycin at 37°C and 5 % CO2. After seeding of 150 cells/mm², cells were grown on microscope object slides for 48 h prior to rinsing with Earl's balanced salt solution (EBSS) and incubation with either the membrane marker laurdan (8 µM) or co-incubation with laurdan (8 µM) and methyl-ß-cyclodextrine (MßCD; 1 mM or 4 mM) or co-incubation with laurdan (8 µM) and a MßCD:cholesterol complex (0.63 mM : 0.1 mM, final concentration 100 µM) diluted in culture medium without serum. Cholesterol depletion after application of MßCD as well as cholesterol enrichment after application of a MßCD:cholesterol complex are well documented in the literature [12]. After incubation for 60 min. in each case, cells were rinsed with EBSS and measured in an open aluminium chamber at variable temperatures ranging from 16°C to 40°C using a 63x/0.90 water immersion objective lens. The chamber (filled with a layer of 2-3 mm EBSS) contained a Peltier element for heating or cooling, as well as a calibrated thermocouple for temperature measurements in close vicinity to the measured part of the samples.

For fluorescence spectroscopy and microscopy a picosecond laser diode (LDH 400 with driver PDL 800-B, Picoquant, Berlin, Germany; wavelength: 391 nm; pulse energy: 12 pJ, pulse duration: 55 ps, repetition rate: 40 MHz; average power: 0.5 mW) was adapted to a fluorescence microscope (Axioplan 1, Carl Zeiss Jena, Germany) using a single mode fibre-optic system (kineFlex-p-3-S-395, Point Source, Southampton, UK) and a custom made dark field condenser unit [13]. This condenser permitted to use different angles of illumination below (Θ = 62°) or above (Θ = 66°) the critical angle Θ c of total internal reflection. In

the first case whole cells were illuminated, whereas in the second case only the plasma membrane and adjacent parts of the cytoplasm were illuminated by an evanescent electromagnetic wave with a penetration depth of about 150 nm. Conventional epi-illumination was used for some additional measurements of microscopic images. Fluorescence spectra of single cells were recorded using a long pass filter for $\lambda \geq 415$ nm, a custom made polychromator and an image intensifying detection unit (IMD 4562, Hamamatsu Photonics, Ichino-Cho, Japan) [14] fixed on top of the microscope. Fluorescence decay kinetics were measured using an image intensifying camera (Picostar HR 12; LaVision, Göttingen, Germany) by scanning a time gate of 200 ps over a time range of 10 ns.

3. Results

Fluorescence spectra of single U373MG cells incubated with laurdan are depicted in Figure 1 upon whole cell illumination at T = 24°C. The spectra show two overlapping emission bands with maxima around 440nm and 490 nm. Without any manipulation of the natural cholesterol content of U373MG cells similar fluorescence intensities were measured at 440 nm and 490 nm (lower curve). However, after enrichment of cholesterol, the 440 nm band appeared to be more pronounced (middle curve), whereas after depletion of cholesterol the 490 nm band was predominant (upper curve). This effect was quantified using the generalized polarization [15] $GP = (I_{440} - I_{490}) / (I_{440} + I_{490})$ with I_{440} corresponding to the fluorescence intensity at 440 nm and I_{490} to that at 490 nm. GP generally decreased with temperature between 16°C and 40°C and was always higher for the plasma membrane than for intracellular membranes (as deduced from whole cell measurements).

Fluorescence lifetimes of U373MG cells incubated either with laurdan (control) or with laurdan and MßCD (at 2 concentrations) or with laurdan and the MßCD:cholesterol complex upon illumination of whole cells at T = 24°C are depicted in Figure 2. Obviously, fluorescence lifetimes are longer after enrichment than after depletion of cholesterol. In all cases, short rise times of laurdan fluorescence (below 500 ps; not shown) and lifetimes of 3-5 ns were obtained from biexponential curve fitting. The fluorescence lifetime τ slightly increased from 4.5 ns (in control cells) to 4.8 ns after cholesterol enrichment, but decreased to 3.3 ns after cholesterol depletion (with 4 mM MßCD).

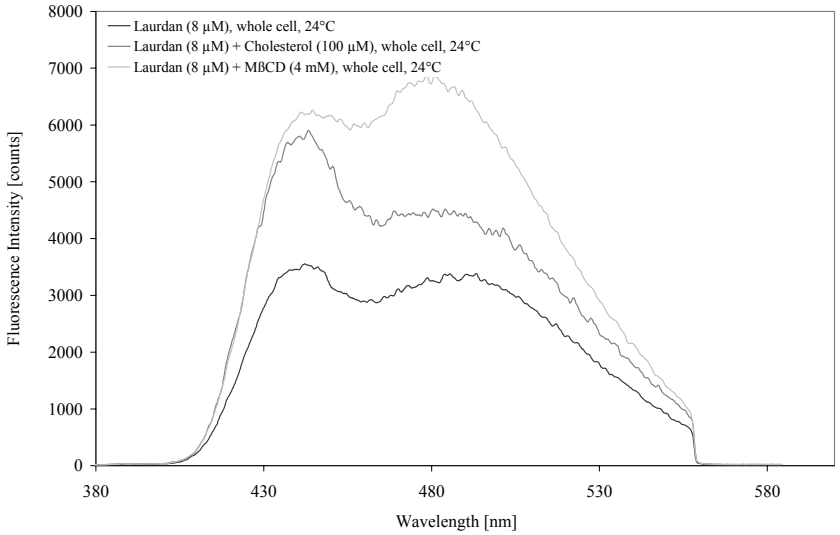

Fig. 1. Fluorescence spectra of single U373MG cells incubated for 60 min. with laurdan (lower curve) or co-incubated with laurdan and a MßCD:cholesterol complex (middle curve) or co-incubated with laurdan and MßCD (4 mM; upper curve) at T = 24°C upon whole cell illumination. Excitation wavelength: 391 nm.

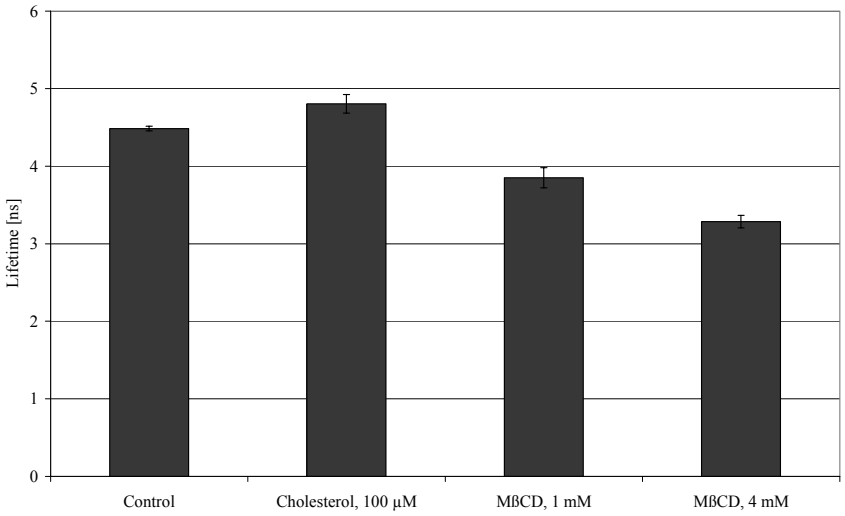

Fig. 2. Fluorescence lifetime of U373MG cells incubated with laurdan in U373MG cells after enrichment (by a MßCD:cholesterol complex) or depletion (by 1 mM or 4 mM MßCD) of cholesterol in comparison with control cells at T = 24°C upon whole cell illumination. Values represent median values and median absolute deviations (MAD's) of about 20 measurements in each case.

4. Conclusions

Previous measurements with Chinese hamster ovary (CHO) [7] cells showed a pronounced decrease of the general polarization (GP) with increasing temperature, and a larger GP value for the plasma membrane as compared with intracellular membranes. In addition, the fluorescence lifetime changed with temperature and upon aging of the cells. Changes of membrane dynamics during cell aging as well as the differences between the plasma membrane and intracellular membranes were supposed to depend on the content of cholesterol [7]. Assuming GP to be an appropriate measure of membrane stiffness, the present paper demonstrates that stiffness does not only decrease with increasing temperature, but also with decreasing cholesterol content. Intracellular membranes are more affected by cholesterol depletion with MßCD than the plasma membrane.

In addition to GP, the fluorescent lifetime τ was found to depend on cholesterol content. A high content of cholesterol may also account for effects of cell aging, as reported previously [7]. A correlation between membrane parameters and cholesterol content might further be useful to detect some specific diseases (with alteration of membrane properties) and to detect the influence of pharmaceutical agents on membrane properties. Inherent differences of membrane properties of different cell lines, however, should be considered. For a more quantitative evaluation biochemical measurements of the intracellular cholesterol content are presently combined with spectroscopic investigations.

Acknowledgements. This project was supported by the Ministerium für Wissenschaft, Forschung, und Kunst Baden-Württemberg (Zentrum für Angewandte Forschung und Landesschwerpunktthema "Funktionelle Nanoskopie") and by the Bundesministerium für Bildung und Forschung (BMBF; Grant No. 1701B04). Technical assistance by Claudia Hintze is gratefully acknowledged.

References

1. 1. J.R. Lakowicz, Principles of Fluorescence Spectroscopy, Plenum Press, New York - London, 1999.
2. N.L. Thompson, A.W. Drake, L. Chen, W.V. Broek, "Equilibrium, kinetics, diffusion and self-association of proteins at membrane surfaces: measurement by total internal reflection fluorescence microscopy", Photochem. Photobiol. 65, 39-46, 1997.
3. T. Parasassi, G. d0e Stasio, A. d'Ubaldo, E. Gratton, "Phase fluctuation in phospholipid membranes revealed by laurdan fluorescence", Biophys. J. 57, 1179-1186, 1990.
4. T. Parasassi, E.K. Krasnowska, L. Bagatolli, E. Gratton, "Laurdan and prodan as polarity-sensitive fluorescent membrane probes", J. Fluoresc. 4, 365-373, 1998.
5. L.A. Bagatolli, T. Parasassi, G.D. Fidelio and E. Gratton, A model for the interaction of 6-lauroyl-2-(N,N-dimethylamino) naphthalene with lipid

environments: implications for spectral properties, Photochem. Photobiol., 1999, 70, 557-564.
6. W. Yu, P.T.C. So, T. French, E. Gratton, Fluorescence generalized polarization of cell membranes: a two-photon scanning microscopy approach, Biophys. J. 70, 626–636, 1996.
7. H. Schneckenburger, M. Wagner, M. Kretzschmar, W.S.L. Strauss and R. Sailer: “Laser-assisted fluorescence microscopy for measuring cell membrane dynamics”, Photochem. Photobiol. Sci. 3 (2004) 817-822.
8. G.P. Eckert, N.J. Cairns, A. Maras, W.F. Gattaz, W.E. Muller (2000) Cholesterol modulates the membrane-disordering effects of beta-amloyid peptides in the hippocampus: specific changes in Alzheimer’s disease. Dement. Geriatr. Cogn. Disord. 11: 181-186.
9. S. Aozaki (1989) Decreased membrane fluidity in erythrocytes from patients with Crohn’s disease. Gastroenterol. Jpn. 24: 246-254.
10. T. Koike, G. Ishida, M. Taniguchi, K. Higaki, Y. Ayaki, M. Saito, Y. Sakakihara, Y. Iwamori, K. Onno (1998) Decreased membrane fluidity and unsaturated fatty acids in Niemann-Pick disease type C fibroblasts. Biochim. Biophys. Acta 1406: 327-335.
11. C. Pasternak, S. Wong, E.L. Elson (1995) Mechanical function of dystrophin in muscle cells. J. Cell. Biol. 128:355-361.
12. A.E. Christian, M.P. Haynes, M.C. Phillips, G.H. Rothblat, “Use of cyclodextrins for manipulating cellular cholesterol content”, J.Lipid Res. 38, 2264-72, 1997.
13. K. Stock, R. Sailer, W.S.L. Strauss, M. Lyttek, R. Steiner, H. Schneckenburger, “Variable-angle total internal reflection fluorescence microscopy (VA-TIRFM): realization and application of a compact illumination device“, J. Microsc. 211, pp. 19-29, 2003.
14. H. Schneckenburger, M.H. Gschwend, R. Sailer, H.-P. Mock, W.S.L. Strauss, “Time-gated fluorescence microscopy in molecular and cellular biology“, Cell. Mol. Biol. 44, 795–805, 1998.
15. T. Parasassi, G. de Stasio, G. Ravagnan, R.M. Rusch and E. Gratton, “Quantitation of lipid phases in phospholipid vesicles by the generalized polarization of laurdan fluorescence”, Biophys. J. 60, 179-189, 1991.

Fast and Objective Classification of Tumor Tissue by Optical Vibrational Spectroscopy

Gerald Steiner[1], Christoph Krafft[2], Claudia Beleites[2], Stephan Sobottka[3], Gabriele Schackert[3], Edmund Koch[1] and Reiner Salzer[2]

[1] Dresden University of Technology, Medical Faculty, Clinical Sensoring and Monitoring
[2] Dresden University of Technology, Institute for Analytical Chemistry
[3] Dresden University of Technology, Medical Faculty, Department for Neurosurgery

Abstract. Since optical vibrational spectroscopy is exquisitely sensitive to the biochemical composition of the sample and variations therein, it is possible to monitor metabolic processes and biochemical states in tissue and cells. The chances of identifying spectral indicators of diseases are much more favourable when spectroscopic imaging methods are used. Such images permit a direct correlation between the spectroscopic information and the sample histopathology. The spectroscopic imaging methods, which are barely ten years old at this point in time, become now a valuable technique for biomedical applications. In this contribution we illustrate the capability and versatility of spectroscopic imaging on the example of identification and visualization of brain tumors.

1. Introduction

In the past years optical methods of vibrational spectroscopy as Fourier Transform Infrared (FTIR) and Raman spectroscopy have been applied in many cases to the analysis of tissue, blood and other fluids. Since vibrational spectroscopy probes the molecular level, it is a potentially powerful tool for the early detection of diseases because many changes occur on the molecular level in tissue before a diseased state can be observed macroscopically. Technological developments in infrared and Raman microscopy imaging, in particular high sensitive array detectors, have extended the field of biomedical applications.

Both methods FTIR and Raman spectroscopy provide a wealth of information about the biochemical state of the sample under investigation. The spectrum contains structural information from all molecules. Consequently, the challenge consists in the extraction of relevant information in terms of the histological diagnosis. From the theoretical point of view, it is necessary to have as much independent spectra as possible. A milestone to overcome this limitation was therefore the introduction of imaging spectroscopy. The vast of spectral data generated from imaging spectroscopy permits sophisticated multivariate statistical analysis of data and enables to discern tissue regions where spectra signatures from pathological states differ from those of healthy tissue. In both methods the image contrast is provided solely by spatial variations in the sample intrinsic chemistry, the clinician can visualize a sample directly in terms of its biochemical features. Table 1 lists examples of tissue characterization by FTIR imaging spectroscopy.

Table 1. Characterization of tissue by FTIR imaging spectroscopy.

tissue	aim of the investigation	Ref.
bone	mineralization	[1, 2, 3]
bone	distribution of collagen	[4]
breast	identification tumor	[5, 6]
prostate	identification tumor	[7, 8]
oral cavity	identification tumor	[9]
skin	identification tumor	[10, 11, 12]
skin	exogenous molecules, distribution of molecules	[13, 14]
iliac	identification tumor	[15]
brain	identification tumor	[16, 17, 18]

Although in-vivo applications are desirable, currently developments are aimed to complement established methods for histology by FTIR imaging spectroscopy under in-vitro conditions as basis for future in-vivo applications. Here we summarize results of a long time study exploring the diagnostic potential of FTIR imaging spectroscopy of human brain tumors.

2. FTIR Imaging Spectroscopy

Spectroscopic images were capture by the Bruker Hyperion system (Fig. 1). The spectrometer itself is designed to operate in continuous scan modes. The microscope houses both a conventional single element MCT detector and a focal plane array detector for imaging measurements. The sample area captured for one image is 270 x 270 μm^2 under the microscope or 4 x 4 mm in the macro sample compartment. Computer-controlled x;y-stages permit sequential recording of images, which can be pooled in the subsequent evaluation procedure in order to render larger sample areas.

3. Spectroscopic Classification

The spectral classification procedure employed two algorithms in tandem. The first algorithm is a genetic optimal region selection routine. This program receives as input both the spectra of interest (training set) and their histopathological designations. The second algorithm employs linear discriminant analysis (LDA) to optimally partition the compressed spectra into groups. For present purposes, once this procedure had succeeded in reproducing the original histological designations, the recipe so derived was then employed as the basis to predict the histological status for test set spectra.

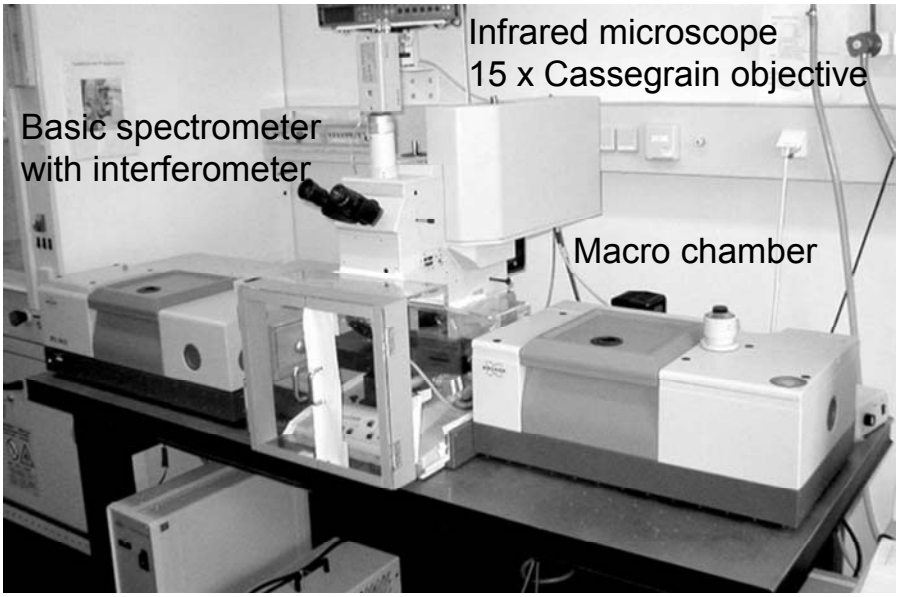

Fig. 1. FTIR imaging spectrometer Bruker Hyperion. The microscope hosts a focal plane array detector for imaging measurements. Larger samples can be measured in the macro sample chamber.

4. Sample Preparation

All experiments were carried out on control and tumor samples from human brain tissue. The experimental procedures were approved by the Human Ethics Committee of the Technical University of Dresden. Tumor specimens were obtained from adult patients undergoing surgery to remove brain tumors. Non-tumor tissue sections as control samples were obtained from individuals who had no clinical history of cognitive decline or central nervous system disease. Immediately following surgical removal, the tissue was snap frozen in liquid nitrogen until ready for use. A tissue section of 10 µm thickness was cut from the frozen tissue, transferred onto a 10 x 10 x 1 mm CaF_2 window. The sample area was typically between 0.25 and 0.5 cm^2. Parallel sections were mounted and stained in the conventional manner and histological diagnosis was made according to the WHO classification scheme. A training set for the classification algorithm was distilled from the spectra acquired for 41 patients

5. Results

The simplest starting point to seek and assess spectral differences between the tissue sections is to average all spectra within each diagnostic class. The class average spectra of glioblastomas grade IV, astrocytomas grade III, astrocytomas grade II and normal tissue are shown in Figure 2. All of these spectra illustrate

features common to soft tissue specimens, dominated by the amide I band at 1650 cm^{-1} and amide II band at 1530 cm^{-1}.

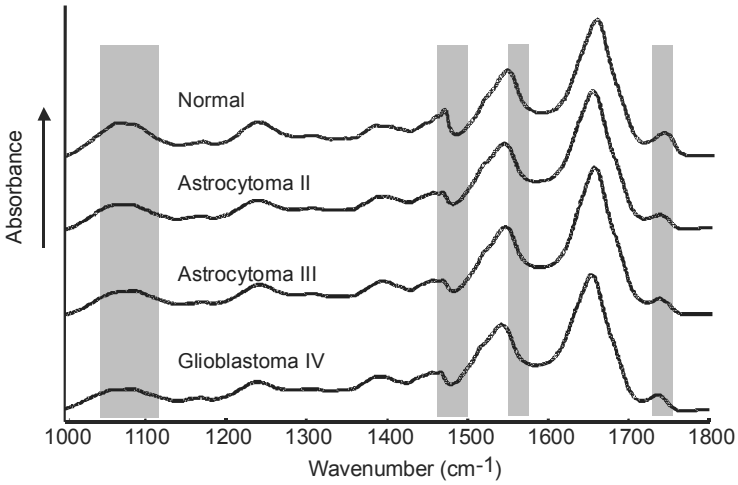

Fig. 2. Class average spectra of the four tissue classes. The highlighted regions are the spectral regions identified by the genetic selection algorithm for distinguishing the various classes.

Although some obvious differences occur among the class average spectra, a more sophisticated approach is required to successfully classify the individual spectra. The combined genetic algorithm/LDA as describe above approach was employed to identify diagnostic features optimally separating the spectra into the four histopathological groups of interest. The highlighted spectral regions in Fig. 2 encompass absorptions that are commonly ascribed to amide groups (amide II absorption, at ~1550 cm^{-1}), lipids (acyl CH_2 bends, at ~1450 cm^{-1}). The other two highlighted regions fall within the 1050-1100 cm^{-1} and the 1730-1760 cm^{-1} spectral windows. The first range is usually associated with the C-O stretching modes of sugars and complex carbohydrates whereas the second spectral range represents the C=O stretching modes lipid acids. These spectral regions correspond to gangliosides. Gangliosides are acidic glycosphingolipids, present in the cell membrane of all vertebrate cells and especially in the cells of the central nervous system [19]. Several studies have suggested a correlation of the ganglioside profile of human gliomas with the degree of malignancy [20]. It is known that with higher grades of malignancy, there is a loss of normal brain gangliosides and an increase in such called GD3 gangliosides. Fig. 3 summarizes pictorially the classifications predicted for three test tissue sections designated by histopathology as astrocytoma grade II, astrocytoma grade III and glioblastoma grade IV, respectively. These tissue sections were completely imaged as described above for the training set specimens, and a representative subset was used as test set. The 'brightfield' image is shown only to portray the shape of the tissue section; the intensity for each pixel is simply proportional to the integrated intensity (1000-1800 cm^{-1}) for the corresponding un-normalized spectrum. It is worth noting immediately that for each tissue sample not all spectra are assigned

to one grade of malignancy. While this may simply highlight errors in the spectroscopic-based method, it is more likely due to various malignancy grades appearing within a single sample.

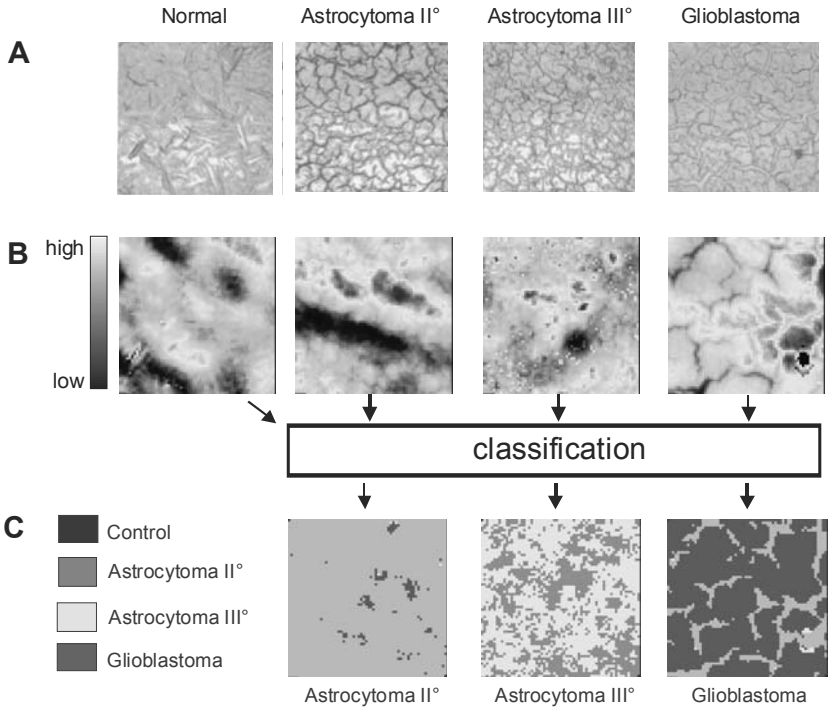

Fig. 3. A) Microscopic image of the tissue section (dimension 270x270 μm^2), B) Infrared spectroscopic brightfield image and C) distribution of the classified spectra for independent test set samples.

The accuracy of the classification was almost higher than 90%. Although the spectroscopic-based classifications were not entirely consistent with conventional histopathology in grading the tumors, the classifications showed no confusion between tumor and normal tissues. Furthermore, pathological assessment is often performed rapidly while surgery is ongoing without the use of involved immunochemical methods for diagnosis. It would seem quite reasonable to suggest that the classification results are not contradicting the histopathological diagnoses, but are simply revealing more details about the tissue properties and inhomogeneities based on the biochemical composition of the tissue.

6. Conclusion

On the example of spectroscopic-based classification of brain tumors it is demonstrated that vibrational spectroscopy is well suitable to identify and to grade

tumors. The spectroscopic classification is consistent with conventional histopathology. The results show no confusion between tumor and normal tissues. FTIR imaging spectroscopy and classification of tissue may yield diagnostic information that is not readily available via routine histopathology.

References

1 C. Marcott, R.C. Reeder, E.P. Paschhalis,D.N. Tatakis, A.L. Boskey and R. Mendelsohn, in *Cell. Mol. Bio*., Vol. 44, 109, 1998.

2 N.P. Camacho, P. West, P.A. Torzilli and R. Mendelsohn, in *Biopolymers*, Vol. 62, 1, 2001.

3 H. Ou-Yang, E.P. Paschalis,W.E Mayo, A.L. Boskey, and R. Mendelsohn, in *Bone Miner Res*., Vol. 16, 893, 2001.

4 E.P. Paschalis, K. Verdelis, S.B. Doty, A.L. Boskey, R. Mendelsohn and M. Yamauchi, in *Bone Min. Res*., Vol. 16, 1821, 2001.

5 L.H. Kidder, V.F. Kalasinsky, J.L. Luke, I.W. Levin and E.N. Lewis, in *Nature Med*., Vol. 3, 235, 1997.

6 L. Zhang, G.W. Small, A.S. Haka, L.H. Kidder and E.N. Lewis, in *Appl. Spectr*., Vol. 57, 14, 2003.

7 D.C. Fernandez, R. Bhargava, S.M. Hewitt and I.W. Levin, in *Nature Biotech*., Vol. 23, 469, 2005.

8 A.S. Haka, L.H. Kidder and E.N. Lewis, in *Proc. SPIE Biomarkers and Biological Spectra Imaging,* Vol. 4259, 47, 2001.

9 C. Conti, E. Giorgini, T. Pieramici, C. Rubini and G. Tosi, in *Mol. Structure*, Vol. 744-747, 187, 2005.

10 L.M. McIntosh, J.R. Mansfield, A.N. Crowson and H.H. Mantsch, in *Biospectr*., Vol. 5, 265, 1999.

11 L.M. McIntosh, J.R. Mansfield, A.N. Crowson, J.W.P. Toole, H.H. Mantsch and M. Jackson, in *Therapeutics and Systems*, Vol. 3907, 126, 2000.

12 M.E. Rerek, D.J. Moore, R. Mendelsohn and E.P. Paschalis, in *Biophysical J*., Vol. 78, 250A, 2000.

13 R. Mendelson, H.C. Chen, M.E. Rerek and D.J. Moore, in *Biomed. Optics*, Vol. 8, 185, 2003.

14 D. Moore and R Mendelsohn, in *J. Invest. Derm*., Vol. 114, 878, 2000.

15 R. Mendelsohn, E.P. Pschalis and A.L. Boskey, in *Biomed. Optics*, Vol. 4, 14, 1999.

16 G. Steiner, A. Shaw, L.-P. Choo-Smith, M.H. Abuid, G. Schackert, S. Sobottka, W. Steller, R. Salzer and H.H. Mantsch, in *Biospectroscopy Biopolymers*, Vol. 72, 464, 2003.

17 C. Beleites, G. Steiner, M. G. Sowa, R. Baumgartner, S. Sobottka, G. Schackert and R. Salzer, in *Vibr. Spectr*., Vol. 38, 143, 2005.

18 T. Richter, G. Steiner, M. H. Abu-Id, R. Salzer, R. Bergmann, H. Rodig and B. Johannsen, in *Vibr. Spec*tr., Vol. 28, 103, 2002.

19 R. Jennemann, H.-D. Mennel, B.L. Bauer and H. Wiegandt, in *Acta Neurochir*. Vol. 126, 170, 1994.

20 P. Lasch and D. Naumann, in *Cell. Mol. Biol.Vol.* 44, 189, 1998.

Algorithms for Muscle Oxygenation Monitoring Corrected for Adipose Tissue Thickness

Dmitri Geraskin[1], Petra Platen[2], Julia Franke[2] and Matthias Kohl-Bareis[1]

[1] RheinAhrCampus Remagen, Department of Mathematics and Technology, Suedallee 2, 53242 Remagen, Germany
E-mail: kohl-bareis@rheinahrcampus.de
[2] Ruhr University Bochum, Overbergstrasse 19, 44801 Bochum, Germany

Abstract. The measurement of skeletal muscle oxygenation by NIRS methods is obstructed by the subcutaneous adipose tissue which might vary between < 1 mm to more than 12 mm in thickness. A new algorithm is developed to minimize the effect of this lipid layer on the calculation of muscle haemoglobin / myoglobin concentrations. First, we demonstrate by comparison with ultrasound imaging that the optical lipid signal peaking at 930 nm is a good predictor of the adipose tissue thickness (ATT). Second, the algorithm is based on measurements of the wavelength dependence of the slope $\Delta A/\Delta\rho$ of attenuation A with respect to source detector distance ρ and Monte Carlo simulations which estimate the muscle absorption coefficient based on this slope and the additional information of the ATT. This method is tested on experimental data measured on the vastus lateralis muscle of volunteers during an incremental cycling exercise during normal and hypoxic conditions (corresponding to 0, 2000 and 4000 m altitude). The experimental setup uses broad band detection between 700 and 1000 nm at six source-detector distances. We demonstrate that the description of the experimental data is improved and the calculated changes in oxygen saturation are markedly different when the ATT correction is included.

1. Introduction

Near infrared spectroscopy (NIRS) is currently under development and scrutiny as a non-invasive monitoring tool for muscle oxygenation during exercise. Most instruments for monitoring are based on a small number of source-detector separations and the conversion of light intensities into concentration of the oxygenated and deoxygenated haemoglobin (and myoglobin) components (*oxy-Hb* and *deoxy-Hb*) as well as the oxygen saturation SO_2 *(=oxy-Hb/(oxy-Hb+deoxy-Hb)*).

Most current algorithms treat the tissue as homogeneous, which is clearly flawed for muscle where the subcutaneous fat might have a thickness of > 10 mm. The objective here is, first, to show that the optical lipid signal peaking at 930 nm is a good predictor of this adipose tissue thickness (ATT). Second, a new algorithm for the monitoring of muscle oxygenation including this lipid layer is introduced which is based on existing spatially-resolved spectroscopy [1, 2]. For this purpose the distortion of the attenuation spectra by the lipid layer is estimated from Monte Carlo simulations and the impact studied in data obtained during an incremental cycling exercise study under hypoxic conditions.

2. Methods

Spectroscopic Set-up. The spectroscopy system is based on a Peltier-cooled slow-scan CCD-camera (Spec-10, Roper Scientific Germany) with a 1340 x 400-detector array and 16 bit resolution in combination with a spectrometer (SP-150, Acton Research). Six light detecting fiber bundles of 1 mm diameter were arranged in a line separated by $\Delta\rho$ = 2.5 mm at a mean distance ρ = 35 mm from the light delivering bundle (5 mm diameter, halogen light source) resulting in six independent recorded spectra. Data acquisition and on-line analysis of the spectra was programmed in LabView 7.1 (National Instruments Inc.) and an additional off-line data evaluation in MATLAB (Version R14; Mathworks Inc., USA). Details of the setup are given elsewhere [3].

Measurement of Adipose Tissue Thickness. Adipose tissue thickness over the right vastus lateralis muscle was evaluated in 25 volunteers with a 10 MHz ultrasound imaging system. Adipose tissue has a strong absorption peak close to 930 nm, and the relative strength of this was estimated from the second derivative of the attenuation spectra with respect to the wavelength $\partial^2 A/\partial\lambda^2$. There is a strong correlation between these signals indicating that the optical measure is a good indicator for ATT (Fig. 1). The non-linearity of the correlation is explained by a Monte Carlo based estimate of the sensitivity for an upper layer of increasing thickness over a homogeneous sample.

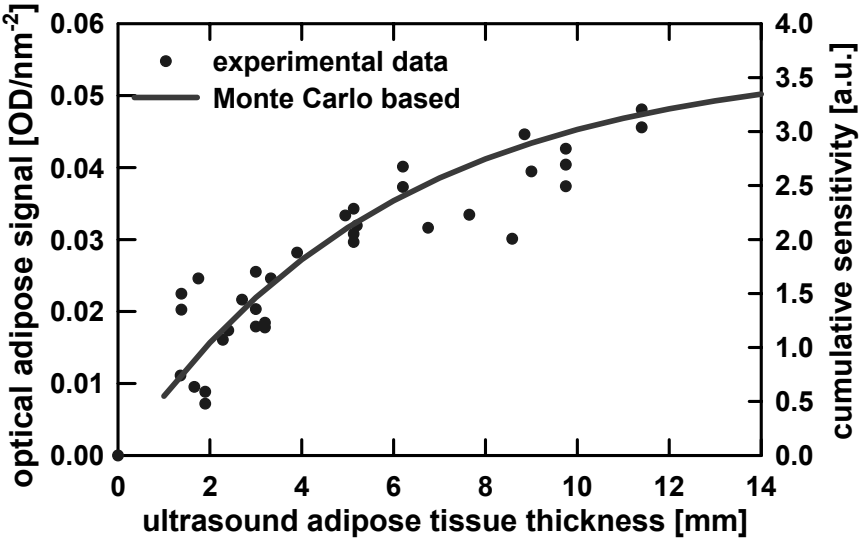

Fig. 1. Correlation of adipose tissue thickness measured with ultrasound and optical adipose signal derived from the second derivative $\partial^2 A/\partial\lambda^2$ of the attenuation spectra. The non-linear correlation is confirmed by a Monte Carlo estimation of the sensitivity as a function of lipid thickness.

Monte Carlo Based Algorithm. Monte Carlo code for a layered medium [4] was used to estimate the slope $\Delta A/\Delta\rho$ for a two layer medium where a lower layer represents the muscle and an upper layer the adipose tissue lipid. For the model tissue the transport scattering coefficient was assumed to be $\mu_s' = 1$ mm^{-1} and the absorption coefficient was varied between $\mu_{a,M} = 0.005$ and 0.04 mm^{-1} for muscle and $\mu_{a,L} = 0.0$ and 0.02 mm^{-1} for a lipid layer with a thickness between 0 mm ≤ ATT ≤ 14 mm. From ex-vivo measurements it is known that the lipid absorption is lower by a about a factor 3 - 6 than the muscle absorption for the wavelength range 700 – 900 nm [5]. Therefore $\mu_{a,L}$ was assumed to be zero. An example of the relationship of the slope $\Delta A/\Delta\rho$ versus $\mu_{a,M}$ for different values of ATT is shown in Fig. 2. Look-up tables were generated to derive $\mu_{a,M}$ from the experimental data $\Delta A/\Delta\rho$ and known ATT. Spectra of absorption coefficients were subsequently converted in absolute haemoglobin concentrations *oxy-Hb* and *deoxy-Hb* based on tabulated extinction spectra of the haemoglobin components and a standard linear least-square fitting routine.

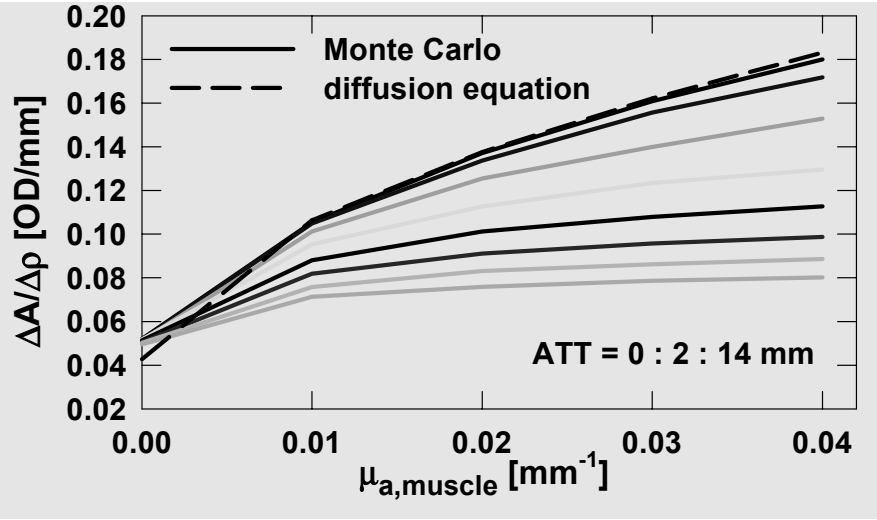

Fig. 2. Estimate of the slope $\Delta A/\Delta\rho$ from a two layer Monte Carlo model for adipose tissue thicknesses ATT between 0 and 14 mm. The analytical solution for a homogeneous model tissue is based on the diffusion approximation. The assumed properties are $\mu_s' = 1$ mm^{-1}, $\mu_{a,M} = 0.01$ mm^{-1} and $\mu_{a,L} = 0$ mm^{-1} , the source detector distance is $\rho = 30$ mm.

Protocol. Muscle oxygenation was measured in 8 volunteers on the right vastus lateralis muscle. The light guiding fibers were placed on the main body of the right vastus lateralis muscle. The volunteers performed an exercise protocol of 10 min rest sitting on a cycle ergometer (Ergoline GmbH, ergometrics 900), a stepwise (3 min, ΔP = 40 W) incremental exercise with automatic, cadence independent power control up to maximal power for each volunteer followed by a 10 min cycling period at 30 W.

3. Results and Discussion

In Figure 3 an example of the experimental $\Delta A/\Delta\rho$-spectra is shown. When no lipid layer is included, the description of the experimental data by fitting the haemoglobin spectra is rather poor. After inclusion of the ATT correction in the algorithm, the agreement of fitted and experimental spectra as judged by the residuum is much better.

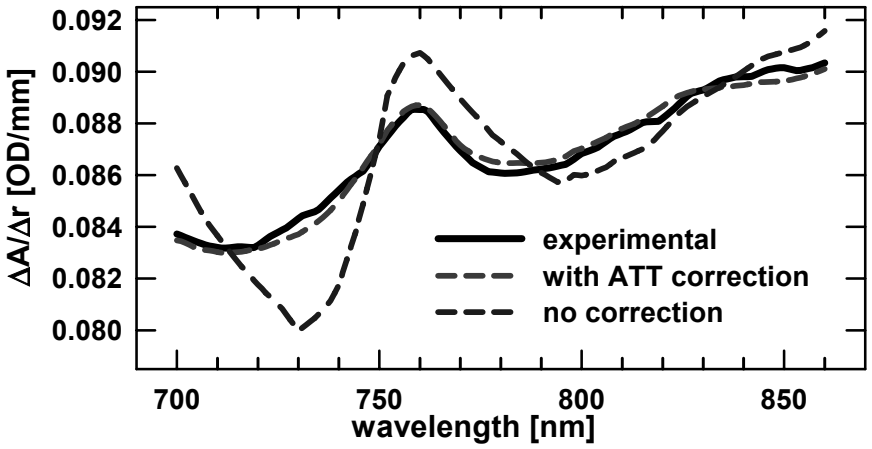

Fig. 3. Spectrum of $\Delta A/\Delta\rho$ measured on the vastus lateralis muscle of a volunteer with an *ATT* of 6.2 mm measured by ultrasound. When no correction of the ATT was included the residuum of the fitted spectrum is much larger as with the inclusion of the Monte Carlo based correction.

In Figure 4 the time course of the oxygen saturation and the mean of the residuum are shown for a male volunteer. When no ATT correction is used, the difference ΔSO_2 during the exercise condition is about -10% while it is about -30% when including the ATT correction. The residuum is better by about a factor 4 with ATT correction.

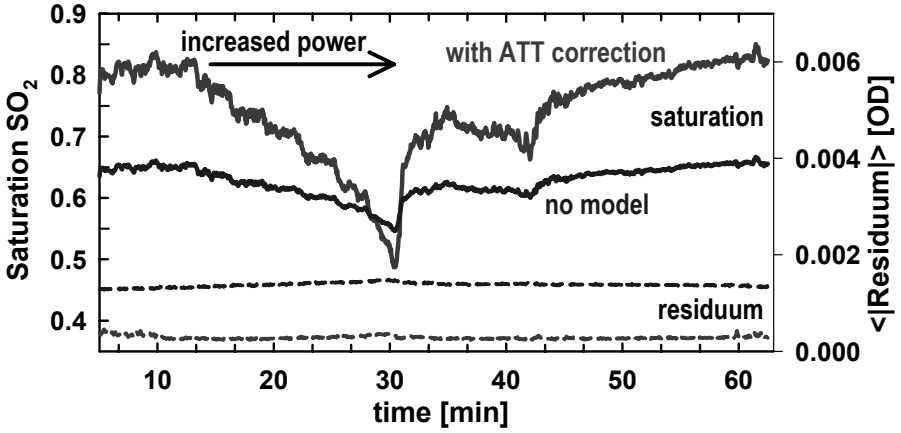

Fig. 4. Oxygen Saturation measured over the vastus lateralis muscle of a volunteer during an incremental cycling exercise with an ultrasound measured *ATT* of 6.2 mm based on an analysis with and without ATT correction (blue and red, respectively). The mean of the residuum is larger by a factor of about 4 when no model is used.

Similar data was obtained for most of the volunteers. The need for a lipid correction is substantial for *ATT* larger than a few mm. However, we still do have an unsatisfactory fit of the experimental spectra for smaller *ATT* values. Currently we elaborate the algorithm to include an upper melanin layer as well as a wavelength dependence of the scattering properties.

References

1 Matcher S J, Kirkpatrick P, Nahid K, Delpy D T (1993) Absolute quantification method in tissue near infrared spectroscopy *SPIE* ***2389***, 486 – 495

2 Suzuki S., Takasaki S., Ozaki T., Kobayashi Y. (1999) A tissue Oxygenation monitor using NIR spatially resolved spectroscopy. *SPIE* ***3597***, 582 – 592.

3 Geraskin D., Platen P., Franke J., Andre Ch., Bloch W., Kohl-Bareis M (2005) Muscle Oxygenation during exercise under hypoxic conditions assessed by spatial-resolved broad-band NIR spectroscopy *SPIE* ***5859****,* 58590L-01 - 06.

4 Wang L., Jacques S. Zheng L. (1995) MCML-Monte Carlo modelling of photon transport in multi-layered tissues, *Comput. Methods Prog. Biomed.* **47**, 131 – 146.

5 Simpson C. R., Kohl M., Essenpreis M., Cope M. (1998) Near-infrared optical properties of *ex vivo* human skin and subcutaneous tissues measured using the Monte Carlo inversion technique *Phys. Med. Biol*. **43** (1998) 2465–2478

Establishment of an Optical Imaging Device for Intraoperative Identification of Active Brain Areas

Tobias Meyer[1,2], Hans Dietrich[1], Falk Uhlemann[1,3], Stephan B. Sobottka[2], Matthias Kirsch[2], Alexander Krüger[4], Edmund Koch[4], Ralf Steinmeier[5], Gabriele Schackert[2] and Ute Morgenstern[1]

[1] Institut für Biomedizinische Technik, Technische Universität Dresden, Georg-Schumann-Straße 9, 01069 Dresden, Germany
[2] Klinik für Neurochirurgie, Medizinische Fakultät Carl Gustav Carus, Technische Universität Dresden, Fetscherstr. 74, 01307 Dresden, Germany
[3] Department of Computer Science, University of Auckland, New Zealand
[4] Klinisches Sensoring und Monitoring, Medizinische Fakultät Carl Gustav Carus, Technische Universität Dresden, Fetscherstraße 74, 01307 Dresden, Germany
[5] Klinikum Chemnitz gGmbH, Flemmingstraße 2, 09116 Chemnitz, Germany

Abstract. Intraoperative optical imaging in neurosurgery has the potential to reduce morbidity during tumour resection. This method for identifying active functional areas of the cortex has been tested experimentally. In this work an equipment configuration for intraoperative use of optical imaging was developed. On the basis of phantom tests parameters for intraoperative data acquisition were determined. First clinical tests during tumour resection show that it is possible to acquire significant information with high spatial resolution about the activation of cortical tissue.

1. Introduction

The identification of functionally important brain areas is vital to preserve brain function after tumour resection. Preoperative diagnostics like positron emission tomography (PET), functional magnetic resonance imaging (fMRI) and single photon emission computed tomography (SPECT) are able to detect these active areas. The data sets can be visualised during surgery using a navigation system. The surgeon is able to locate the tumour and the active areas with this navigation system and thus preserve the functional areas. However, during surgery local shift of the brain causes a misalignment with the preoperative acquired functional data sets. This can be compensated by intraoperatively acquired fMRI. However, the required equipment is bulky and expensive. A less expensive method is the measurement of evoked electrical potentials of the cortex with electro-physiological examinations. The spatial resolution of this method is limited by the location of a certain number of electrodes [1].

Optical imaging of cortical activity could be a new method to decrease morbidity caused by neurosurgical interventions. It combines a fast and contact free data acquisition with a high spatial resolution over the whole operation site. Costs for equipment and the required space within the OR are comparatively low.

For studies of animal physiology, brain mapping is established with very long averaging times of measured data. So far, for use in humans this technique is an experimental one [2] and should be adapted to clinical conditions. It is intended to integrate this method for detecting cortical activity into clinical routine in neurosurgery.

2. Experimental Methods

The main means of transport for oxygen and carbon dioxide in human body are the erythrocytes in the blood. About 98 % of the oxygen is chemically combined with the haemoglobin (Hb) in the erythrocytes. The rest is physically dissolved in the blood. Haemoglobin can be divided in oxygenated haemoglobin (OxHb), deoxygenated haemoglobin (DeHb), methaemoglobin and carboxyhaemoglobin. DeHb is transformed to OxHb by adding 4 oxygen molecules [1].

Haemoglobin influences the reflectance of brain tissue. With optical imaging methods the intensity of the light reflected by the cortical tissue is measured. The optical properties of the brain tissue change with neuronal and metabolic processes (intrinsic signals) in the brain. One process that affects the intrinsic signals is the expansion of the capillaries by an increased blood flow in the area of neuronal activity. The absorption of light at the wavelength around 570 nm is affected. Between the wavelengths of 400 to 600 nm the fractional change of the oxygenation affects the measured signal. The difference in the spectral absorption at a certain wavelength between oxygenated and deoxygenated haemoglobin is used to differentiate between activated and non-activated areas. Above 630 nm ion and water movements, intercellular changes, and neurotransmitter influence the intrinsic signals [3].

The equipment for intraoperative optical imaging consists of a high resolution CDD camera, a light source and a computer for controlling the data acquisition and data analysis. The camera and the light source were mounted to an operating microscope from Möller-Wedel GmbH. It is possible to cover the microscope with an aseptic drape. Another advantage is that the surgeon can easily position the microscope and use the integrated functions for zoom and focus adjustment.

For first clinical tests an electron bombarded CCD camera (EB-CCD) C7190-13W from Hamamatsu Photonics [4] was used. The principle of the electron bombardment is that a photocathode converts incident photons into electrons which are accelerated by high voltage towards the CCD sensor. Therefore these cameras have a very high photosensitivity. The main field of application is data acquisition over several minutes. One problem of this camera type is the so called “Ion-Feedback” which results in white pixels in the acquired image [1]. This is caused by x-ray generated during collision of accelerated electrons with the surface of the CCD sensor [5]. The sensor has a resolution of 512 x 512 pixels and a digital video pixel depth of 12 bit.

Further tests were made with the less photosensitive CCD Camera C4742-96-12G04 from Hamamatsu Photonics [6] because the high photosensitivity of the EB-CCD made it difficult to adjust the illumination of the operation site during surgery. The resolution of this camera is 1344 x 1024 pixels. The digitising is also 12 bit.

The activation of brain areas influences the optical properties at different wavelengths. One future goal is the acquisition of data at different wavelengths using various interference filters. The changes of the signal amplitude caused by an increased blood flow are measured with a 568 nm (FWHM 20 nm) wavelength filter. The estimated signal changes account for about 1 - 10 %. The changes caused by the difference in the absorption of light between OxHb and DeHb will be measured at 610 nm. The signal changes are expected to account for about 0.5 - 2 % [1].

Currently the filter is integrated in the co-observation port of the operating microscope so only one filter can be used for data acquisition on one patient. The filter with the transition maximum at 568 nm was used because at that wavelength higher signal amplitudes are expected. It is planned to integrate a filter wheel to allow for an easy filter change during the imaging procedure.

For illumination of the operation site a 250 W halogen white light source from Möller-Wedel GmbH with a stabilised power supply is used. Figure 1. shows the equipment for intraoperative optical imaging as it is used in the OR.

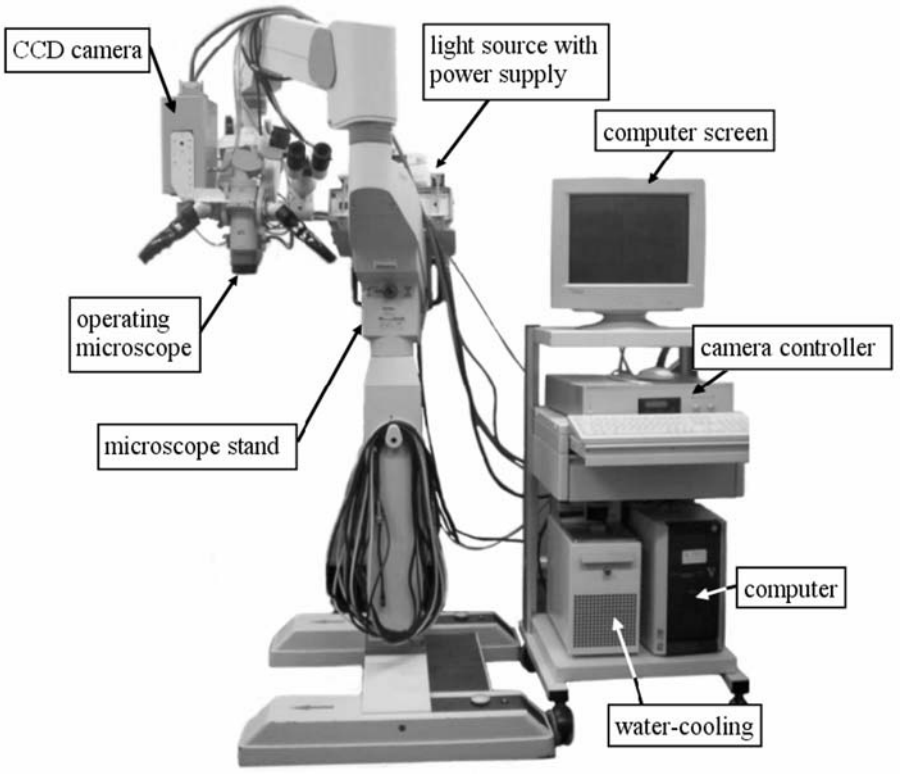

Fig. 1. Equipment configuration for intraoperative optical imaging

The duration to acquire one data set is 9 minutes with alternating 30 seconds without stimulation (baseline) and 30 seconds with stimulation.

The evaluation of the acquired data is done by a programme implemented in Matlab [7]. It calculates the average over all frames of rest and all frames of stimulation. The difference between these averaged frames is calculated and normalised by the intensity of the averaged frame of rest.

Different areas of the cortex were stimulated depending on the localisation of the operation site. Stimulations of the somatosensory cortex via the median nerve, trigeminal nerve or the tibial nerve were performed using an electrical stimulation. The visual cortex was stimulated with blinking LEDs and the acoustic cortex with sounds from headphones at a frequency of 250 Hz at 105 dB.

As a reference for the activation maps, evoked potentials of the cortex were derived right before optical imaging to localise the position of the activated area.

During data acquisition all other light sources in the OT were switched off to reduce disturbance.

3. Results and Discussion

All data analysis was performed postoperative. For each data set an activation map as well as frequency of the changes of the intensity in the image stream was computed. The position of the electrodes of the electrophysiological examination was projected onto the activation map for reference purpose.

In figure 2. a) the operation site of a tumour patient recorded with the C4742 CCD camera is shown. The cortical surface can be seen through the opening in the cranial bone. Figure 2. b) shows the activation map of this patient. The visual cortex was stimulated. The negative differences between rest and stimulation normalised to the averaged frame of rest is shown. The activation (right) can clearly be seen as the bright region. In both pictures the position of the electrodes used for electrophysiological examination are overlaid as white dots.

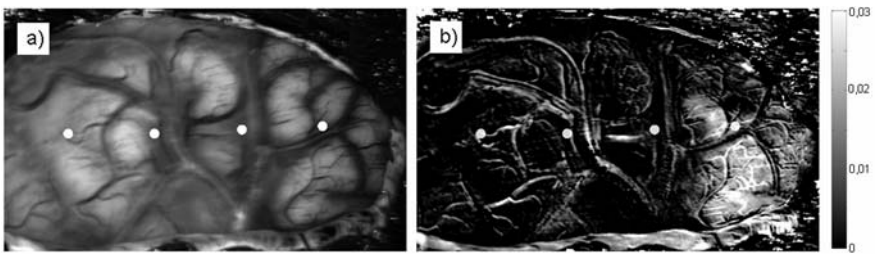

Fig. 2. a) Intraoperative site of a tumour patient overlaid with the position of the electrodes of the electrophysiological examination (white dots), b) activation map (stimulation of visual cortex)

The EB-CCD camera from Hamamatsu Photonics turned out to be unsuitable for intraoperative optical imaging due to its high photosensitivity and the resulting reflection highlights. The illumination levels had to be kept low in order not to

saturate the sensor. This resulted in a poor signal-to-noise ratio for reflectance changes within the limited integration time. The C4742 camera was more suitable, however, the exposure time per frame had to be increased which sometimes led to blurred images caused by the movement of the brain. Furthermore the C4742 camera is less bulky and heavy and therefore easier to handle for the surgeon.

The postoperative numerical analysis of the acquired image data sets showed the localised activation of cortical tissue. The calculated location and the size of the activated region corresponded to the results derived by electrophysiological examinations and confirmed the estimation of the neurosurgeons.

The advantage of optical imaging is the intraoperative high spatial resolution of surface activation compared to the selective measurement of activation at the electrode position using electrophysiological measuring principles.

4. Conclusions

Our data show that it is possible to achieve significant results about the localisation of activated cortical tissue at the wavelength of 568 nm. In addition, data acquisition with the 610 nm filter are going to be conducted to determine if signal changes caused by the difference in the absorption between OxHb and DeHb can be detected with the presented equipment configuration.

Furthermore, it was shown that it is possible to integrate the presented equipment configuration into clinical routine. The reliability of the system must be evaluated by further data acquisition.

Acknowledgements. We would like to thank Andreas Schöppe and the surgical staff.

References

1 H. Dietrich, *Optimierung der Bildaufnahmetechnik zur Identifikation funktionell aktiver Hirnareale bei neurochirurgischen Operationen mittels Phantomaufnahmen*, Diplomarbeit, Institut für Biomedizinische Technik, TU Dresden, 2005.

2 N. Pouratian; N. Sicotte; D. Rex et al., *Spatial/Temporal Correlation of BOLD and Optical Intrinsic Signals in Humans*, Magnetic Resonance in Medicine, Vol. 47, 766-776, 2002.

3 A.W. Toga; J.C. Mazziotta, *Brain Mapping - The Methods*, Academic Press, 1996.

4 Datasheet, *Electron Bombardment CCD Cameras C7190,* Hamamatsu Photonics K. K., 2003.

5 K. Weinbuch, *Technical Paper EB-CCD Camera*, Hamamatsu Photonics Deutschland GmbH, 2005.

6 Datasheet, *IEEE1394-Based Digital Camera ORCA-285*, Hamamatsu Photonics K. K., 2004.

7 *Matlab: The Language of Technical Computing*, The MathWorks, Inc., http://www.mathworks.com/products/matlab, 04.10.1984.

Parallel FDTD Simulation of the Scattering of Light in Media Containing Cylindrical Scatterers

Jan Schäfer[1], Alwin Kienle[1] and Alfred Strey[2]

[1] Institut für Lasertechnologien in der Medizin und Meßtechnik an der Universität Ulm (ILM), 89081 Ulm
E-mail: jan.schaefer@ilm.uni-ulm.de
[2] Universität Ulm, Abteilung Neuroinformatik, 89069 Ulm

Abstract. We have implemented a parallel two-dimensional finite difference time domain (FDTD) method to investigate the propagation of light in biological tissue. In particular we want to examine the dependence of the light propagation on the microstructure of tissue containing cylindrical scatterers. Therefore we performed simulations for a series of various tissue models of randomly distributed cylinders embedded in dielectric media with varying cylinder concentrations and tissue probe thickness.

1. Introduction

For the effective application of light in medical diagnosis and therapy an understanding of the interaction between the incident light and the biological tissue is essential. The knowledge achieved in experimental laboratories can be extended with the results from simulations using adequate computer models. Up to now in the majority of cases approximative equations, like the radiative transfer equation or the diffusion equation, are used for these calculations, even though they omit effects due to the wave nature of light. To include all effects in the computation a solution of the Maxwell equations is necessary.

The FDTD method is widely used for the calculation of the propagation of electromagnetic waves especially in the field of electrical engineering [1]. It is based on a numerical solution of the Maxwell equations using a finite difference approach leading to an explicit time-stepping scheme for a discretized problem space. The major caveat of the FDTD method is the high demand on computer memory and CPU resources. Otherwise the algorithm is highly capable for parallelization and vectorization, which allows to exploit the power of fast parallel computers [2]. For light impinging perpendicular on infinitely elongated structures a two-dimensional formulation of the FDTD method can be used.

One of our objects of interest is the human tooth. The tooth consists of the inner pulp surrounded by a dentin layer and the visible enamel. This study is focused on dentin, which is the largest part of the human tooth. Dentin is permeated by small cylindrical channels, the tubules. These channels run slightly curved from the pulp to the enamel. The diameter of the tubules is approximately 2µm at the pulp and decreases to 1.3µm at the border between the dentin and the enamel. The tubules density in dentin varies from 45000mm^{-2} near the pulp to 15000mm^{-2} close to the enamel. The refraction index of the tubules' core is 1.33, pure dentin has a

refraction index of approximately 1.52. Because of the cylindrical structures of the tubules and the nearly unidirectional orientation of the cylinders, we can use two-dimensional FDTD simulations for our investigations.

2. Implementation of the FDTD Method

Our program is suitable for 2D FDTD computations. At the boundaries of our problem space we use the perfectly matched layer (PML) absorbing boundary conditions in its split-field formulation to truncate outgoing waves [3]. As incident light we use gaussian pulses, which allow us to examine wide frequency ranges in one single simulation run. We employ the total-field scattered-field mechanism to introduce the pulse into the simulation area [4]. To calculate the far-field scattering parameters, like the phase function or the scattering coefficient, a near-field to far-field transformation has been implemented [1]. A parallel version of our code is available, offering the possibility of using fast parallel computers for our simulations. In Figure 1 a validation of our code is shown.

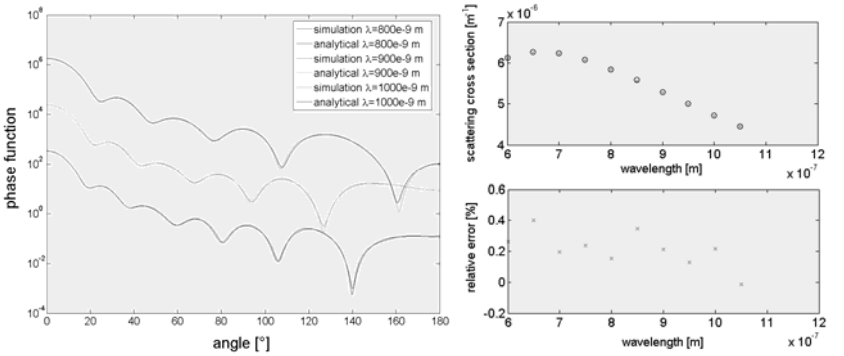

(a) (b)

Fig. 1. In (a) the simulated phase function of the scattering by an infinite cylinder (n=1.33, ø=2µm) in dentin (n=1.52) for various wavelengths is compared with the analytical solution found by solving the Maxwell equations. For the wavelengths 900 nm and 1000 nm the phase functions are multiplied by a factor of 100 and 10000 for better visibility. In (b) the scattering cross sections for various wavelengths and the relative errors are depicted.

3. The Two-Cylinder Problem

We are examining multiple light scattering by dentin. The simplest multiple scattering model consists of two cylinders embedded in a dielectric media. With the help of an analytical solution of the Maxwell equations for the two-cylinder problem [5] we investigated scattering of light (650nm) by two cylinders (ø = 2µm, n=1.33) in dentin (n=1.52) for various orientations. We consider the transverse magnetic (TM) polarization where the magnetic field lies in the scattering plane.

In the first case the connecting line between the cylinders is oriented perpendicular to the direction of the incident light. Figure 2 shows the scattering cross sections calculated for different distances between the cylinders. The scattering cross section oscillates around a value of about 2 times the cross section of one cylinder as the distance between the cylinders increases. The oscillations are due to interference effects.

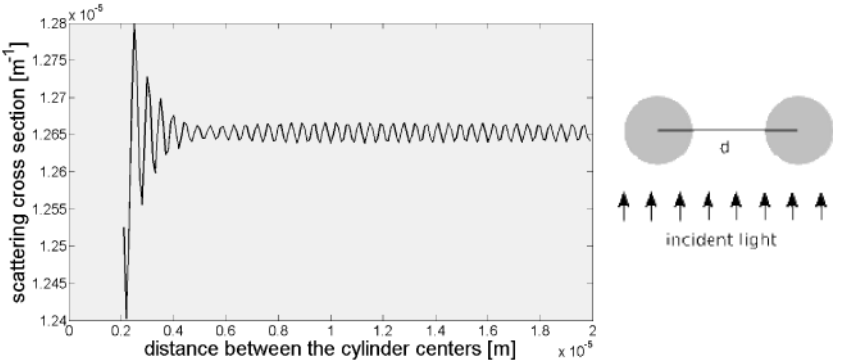

Fig. 2. The scattering cross section (TM) of two-cylinder systems with various distances d between the cylinder centers (connection line perpendicular to the direction of the incident light).

In the second case the connecting line between the cylinders is oriented parallel to the propagation direction of the incident light. The scattering cross section for various cylinder distances is shown in Figure 3. Though the cross section seems to converge against the twofold one-cylinder cross section as the distance increases, a perceptible reduction of scattering occurs at distances smaller than 100µm.

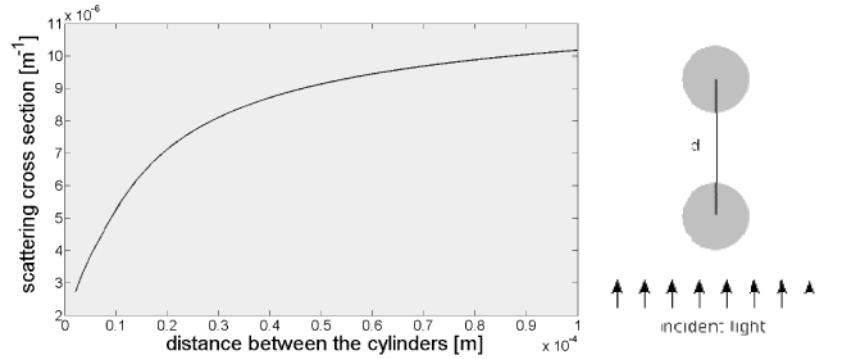

Fig. 3. The scattering cross section (TM) of two-cylinder systems with various distances d between the cylinder centers (connection line parallel to the direction of the incident light).

4. Simulation Results

We use our FDTD simulation software to analyse the impact of the effect of scattering reduction by two cylinders on multiple scatterer systems. In a first series of simulations we examined the effect of the cylinder density on scattering. Therefore, we simulated models of randomly distributed cylindrical scatterers (ø = 2µm) in an 10 x 10µm² area with various scatterer densities. For each density we performed 10 simulation runs and calculated the averaged parameters. The results of our simulations and the corresponding standard derivations are presented in Figure 4. Even for a few cylinders the increase of the scattering cross section differs from linearity as would be expected for independent scattering systems. For the case of 4 cylinders (which is approximately the tubule density of dentin) and more scatterers an even smaller increase of the scattering cross section can be seen. This is due to dependent scattering.

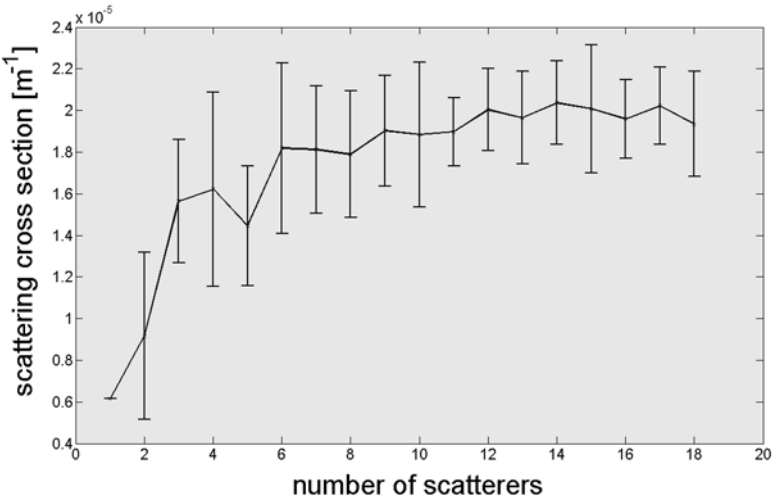

Fig. 4. The scattering cross section (TM) averaged over 10 runs for various numbers of randomly distributed scatterers. The bars show the standard derivations.

In a second step we investigated the dependence of the scattering cross section on tissue thickness. For a given cylinder concentration of 40000mm^{-2} and a tissue width of 10µm we performed a series of simulations with various tissue thicknesses. To acquire averaged results, five simulation runs with randomly distributed cylinders were made for each thickness. A decrease of the scattering cross section per scatterer can be seen, which decays for thick probes (see Figure 2). This behaviour is in conflict with Lambert-Beers law for small thicknesses, where no decrease of scattering cross section per scatterer is expected. Nevertheless for higher thicknesses the scattering cross section per scatterer seems to remain constant.

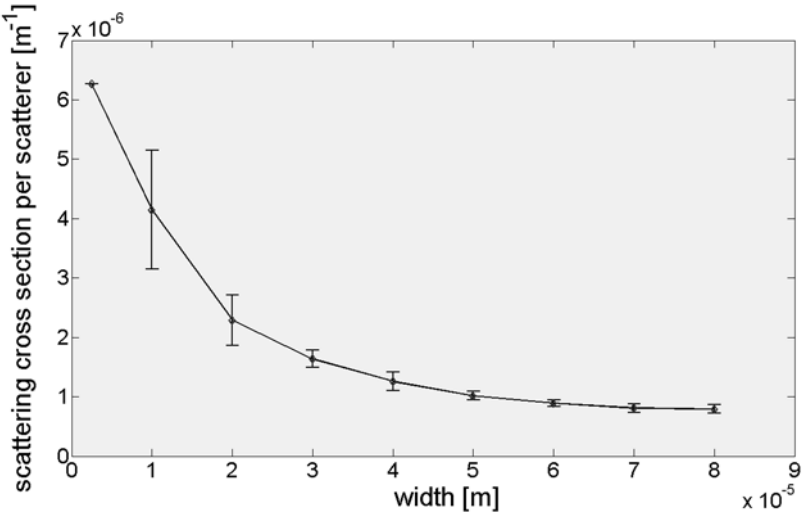

Fig. 5. The scattering cross section (TM) per scatterer averaged over 5 runs of different tissue models with various thicknesses. The bars show the standard derivations.

5. Conclusions

We showed an effect of scattering reduction in two-cylinder systems by calculating the analytical solution of the problem. With the help of our FDTD software we found effects due to dependent scattering in multiple-cylinder systems. When messuring light propagation in dentin for example in order to estimate the scattering coefficient of the tissue these effects have to be considered.

Acknowledgements. We greatfully acknowledge the Landesstiftung Baden-Württemberg gGmbH for supporting our work.

References

1 A. Taflove, *Advances in Computational Electrodynamics: The Finite-Difference Time-Domain Method*, Artech House, 1998.
2 R. S. Brock, X. Hu, P. Yang, and J. Q. Lu, Optics Express **13**, 5279, 2005.
3 J. P. Berenger, Journal of Computational Physics **114**, 185, 1994.
4 R. Drezek, A. Dunn, and R. Richards-Kortum, Optics Express **6**, 147, 2000.
5 H. A. Yousif, Computer Physics Communications **59**, 371, 1990.

Cerebral Oxygenation Monitoring during Cardiac Bypass Surgery in Babies with Broad Band Spatially Resolved Spectroscopy

Jan Soschinski[1], Dmitri Geraskin[1], Branislav Milosavljevic[1], Uwe Mehlhorn[2], Uwe Fischer[2], Gerardus Bennink[2] and Matthias Kohl-Bareis[1]

[1] RheinAhrCampus Remagen, Department of Mathematics and Technology, Suedallee 2, 53242 Remagen, Germany
E-mail: kohl-bareis@rheinahrcampus.de
[2] Pediatric Cardio-Thoracic Surgery, Cologne University Kerpener Strasse 62, 50924 Köln, Germany

Abstract. Neurological impairments following cardio-pulmonary bypass (CPB) during open heart surgery can result from microembolism and ischaemia. Here we present results from monitoring cerebral hemodynamics during CPB with near infrared spatially resolved spectroscopy. In particular, the study has the objective (a) to monitor oxy- and deoxy-hemoglobin concentrations (oxy-Hb, deoxy-Hb) and their changes during CPB surgery and (b) to develop and test algorithms for the calculation of these parameters from broad band spectroscopy. For this purpose a detection system was developed based on a lens imaging spectrograph designed to optimise sensitivity of recorded reflectance spectra for wavelengths between 600 and 1000 nm. Two independent detector channels for both cerebral hemispheres each with three source-detector distances are used. It is demonstrated that the system does record cerebral oxygenation parameters during CPB in infants with a significant decrease in oxygen saturation SO_2 during cardiac arrest. The methodological focus is on an error estimation of the haemoglobin concentrations and separation of cerebral from skin signals. The depth sensitivity profile of the set-up is estimated with a layered structure model of tissue and Monte Carlo methods for the description of the photon propagation.

1. Introduction

For some years near infrared spectroscopy (NIRS) is under development and scrutiny as a non-invasive monitoring tool for brain oxygenation which is of paramount importance during CPB. Currently, most instruments for monitoring the haemoglobin components (oxy-Hb, deoxy-Hb) are based on a small number of source-detector separations and the measurement at typically two to four wavelengths.

Our aim is to use broad band spectroscopy rather than a few wavelengths to allow for an inspection of the algorithms and their underlying assumptions of tissue geometry and optical parameters. For this purpose a lens imaging spectrometer with a high f/# = 1:1.2 was designed resulting in an improvement of light throughput by about one order of magnitude compared with standard systems. During the last years NIRS has been employed in a number of studies

with similar aims, here, however, we try to estimate the reliability and consistency of the methods by use of a broad-band spectroscopy system with 6 independent detectors. The analysis is based on spatially-resolved spectroscopy (SRS) [1 - 3] which measures the slope of light attenuation (A) with source detector distance (ρ), $\Delta A/\Delta\rho$ and an analytical solution for the conversion of this measurement into haemoglobin concentrations (oxy-Hb, deoxy-Hb) and oxygen saturation SO_2 (= oxy-Hb/(oxy-Hb + deoxy-Hb)). This has been validated in physiological and clinical trials [3, 4]. Registration between 600 – 1000 nm allows to focus on a comparison of near-infrared spectroscopy algorithms.

There is some disagreement in the literature about the best method and algorithm for the calculation of tissue haemoglobin parameters. While time and frequency domain is widely considered to be the best approach for the recovery of tissue absorption coefficients, only measurements at multi-wavelengths are capable to discern haemoglobin and other tissue chromophores like water and lipid and possibly cytochrome.

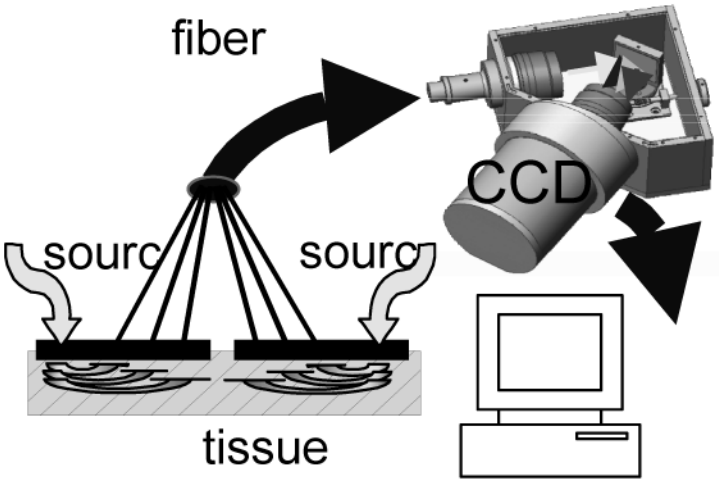

Fig. 1. Experimental set-up with a high f-number lens imaging spectrometer and a slow-scan CCD recording six independent reflectance spectra.

2. Experimental Methods

Spectroscopic Set-up. The spectroscopy system is based on a Peltier-cooled slow-scan CCD-camera (PIXIS, Roper Scientific) with a 512 x 512-detector array and 16 bit resolution in combination with an especially designed lens imaging spectrometer (f/# = 1:1.2; f = 58 mm) giving an improvement of light throughput of about one order of magnitude when compared with a standard mirror based

spectrometers (f/# = 1:4.0). With a 600 lines /mm grating, a wavelength range of about 300 nm is recorded. Two monitoring channels for both hemispheres of the head were used each with 3 light detecting fiber bundles of 1 mm diameter arranged in a line separated by $\Delta\rho = 2.5$ mm at a mean distance $\rho = 30$ mm from the light delivering bundle (3 mm diameter, halogen light source) resulting in six independent recorded spectra. Data acquisition and on-line analysis of the spectra was programmed in Labview 7.1 (National Instruments Inc.). The software stores both the calculated haemoglobin values as well as all raw intensity spectra to allow a separate off-line analysis. For easy transportation and use in the operation theatre the set-up is mounted in a case.

Recorded reflectance spectra were converted in attenuation ($A(\lambda)$) first, and tissue absorption spectra derived from the slope $\partial A/\partial\rho$ [1 – 3]:

$$\mu_a(\lambda) = \frac{1}{\mu_s'(\lambda)} \cdot \frac{1}{3} \cdot \left(\ln(10) \frac{\partial A(\lambda)}{\partial \rho} - \frac{2}{\rho} \right)^2 .$$

Here μ_s' is the transport scattering coefficient, which can be assumed to have a small wavelength dependence only [5]. Subsequently, μ_a – spectra were converted into haemoglobin concentrations with a linear fitting procedure based on the assumption that the dominant tissue chromphores are oxy-Hb, deoxy-Hb and water and the absorption coefficient is

$$\mu_a(\lambda) = \sum_i \varepsilon_i(\lambda) \cdot c_i ,$$

where c_i is the concentration of the chromophore with ε_i the corresponding extinction coefficient at wavelength λ.

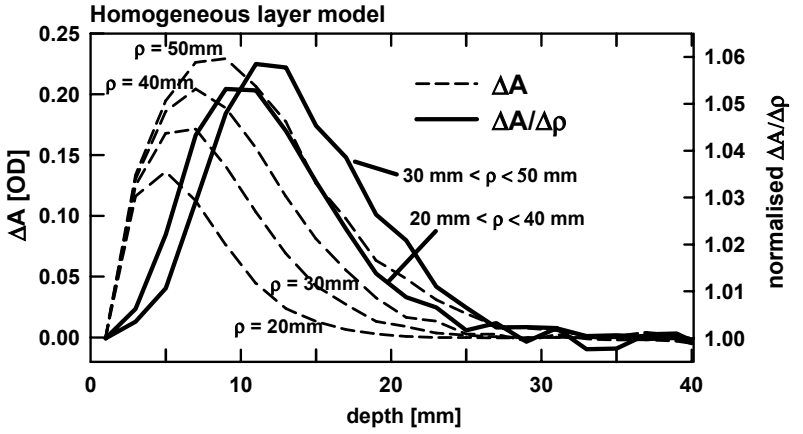

Fig. 2. Depth sensitivity calculated from Monte Carlo simulations for a homogeneous medium with $\mu s' = 1$ mm-1 and $\mu a = 0.01$ mm-1 for various source-detector distances ρ. The depth profile is compared for changes in attenuation ΔA and $\Delta A/\Delta\rho$.

The depth sensitivity of the method was estimated with Monte Carlo simulations for a layered tissue phantom [6]. In this mathematical model, 20 layers each of 2 mm thickness were stacked on a semi-infinite layer and all characterized by the refractive index and absorption and transport scattering coefficients μ_a and μ_s' in the range found for biological tissue. For a pencil like light source (typically $5 - 50 \cdot 10^6$ photons) the number of photons reflected from the upper layer were calculated as a function of distance and the optical properties. The depth sensitivity was estimated by varying the absorption coefficient for each layer and calculating the influence of this variation on attenuation (ΔA) or the slope of attenuation with distance ($\Delta A/\Delta\rho$).

3. Results and Discussion

The depth profile calculated for typical optical properties of tissue (see Fig. 2) indicate that deeper tissue is probed when the slope $\Delta A/\Delta\rho$ is used rather than changes in attenuation ΔA. When ρ is between 20 and 40 mm, the highest sensitivity is for a depth of 10 – 12 mm, with little signal from the upper layers (depth 0 < 6 mm). When ΔA is considered for source detector spacings of 30 and 40 mm, the highest sensitivity is for a depth between 6 and 7 mm with a much higher contribution from the upper few mm. Simulations for various optical properties as well as inhomogeneities due e.g. a melanin layer indicate that this finding is not altered significantly. This depth profile is significant as it indicates that there is less crosstalk from changes in the scalp and the skull when the slope $\Delta A/\Delta\rho$ is used. Furthermore, movement artefacts that might result in changes in the optical coupling between fibers and skin are limited as well as the influence of the skin colour.

In figure 3 the time course of cerebral haemoglobin concentrations (oxy-Hb, deoxy-Hb) and oxygen saturation SO_2 during CPB in an infant is shown with the main events marked. Cerebral SO_2 varies by about 35 % during the surgery with a large decrease during the phase of bypass of aorta and cardioplegia. During the cardiovascular arrest (around t = 4800 s for about 90 s) there is an immediate drop in SO_2 by about 20 %. Changes in blood flow and blood pressure set externally by the cardio pulmonary machine are readily mirrored in the SO_2 time trace. When the body temperature is reduced by cooling both the blood supplied by the CPM and the head externally, the SO_2 rises. SO_2 recovers to the initial values at the end of the operation.

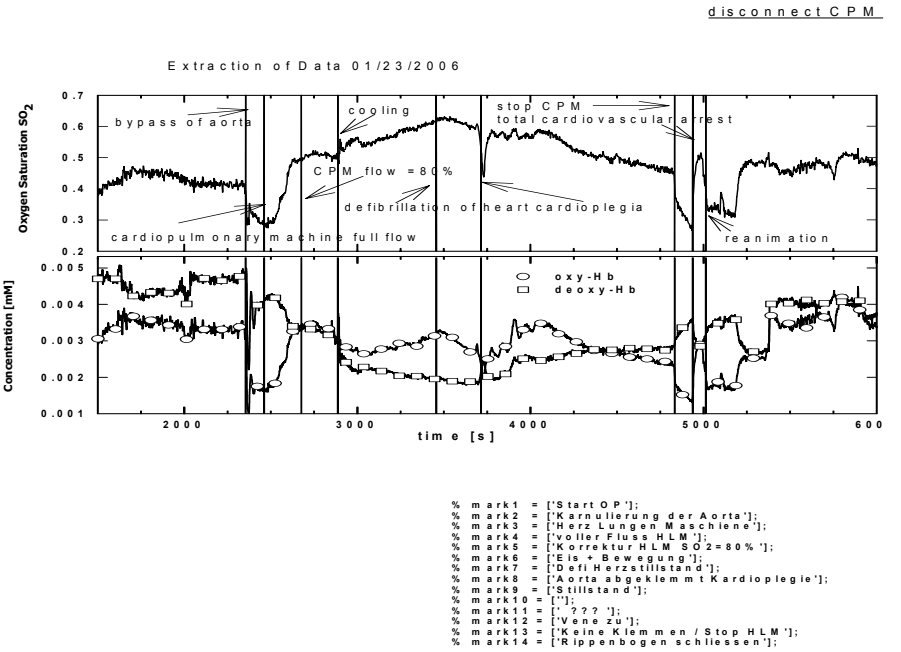

Fig. 3. Time course of cerebral oxygen saturation SO_2 and concentration in oxy-Hb and deoxy-Hb of an infant during cardiac bypass surgery. The main events during the operation are indicated with large swings in the oxygenation due to the cardio pulmonary machine (CPM) and a rapid drop in SO_2 during arrest.

4. Conclusions

The advantage of the high light throughput of the lens imaging spectrometer is that spectra can be recorded at larger source detector distances thus probing deeper tissue layers (compare with Fig. 2). Alternatively, a cheaper CCD detector would be sufficient which does reduce the cost of the set-up considerably. The depth sensitivity profile estimated by Monte Carlo simulations show that the SRS-method is advantageous to probe cortical tissue and to reduce the influence of extra-cerebral tissue like skin and skull. The main advantage of the broad band approach followed here is that the influence of the wavelength range for the calculation of the haemoglobin parameters can be tested. Furthermore, we are aiming at an independent monitoring of skin oxygenation via optical spectroscopy in the VIS band.

References

1. Matcher S J, Kirkpatrick P, Nahid K, Delpy D T (1993) Absolute quantification method in tissue near infrared spectroscopy *SPIE 2389*, 486-495
2. Suzuki S., Takasaki S., Ozaki T., Kobayashi Y. (1999) A tissue Oxygenation monitor using NIR spatially resolved spectroscopy. *SPIE 3597*, 582-592.
3. Geraskin D., Platen P., Franke J., Andre Ch., Bloch W., Kohl-Bareis M (2005) Muscle Oxygenation during exercise under hypoxic conditions assessed by spatial-resolved broad-band NIR spectroscopy *SPIE 5859,* 58590L-01-06.
4. Al-Rawi P., Smielewski P., Kirkpatrick P. J. (2001) Evaluation of a Near-Infrared Spectrometer (NIRO 300) for the Detection of Intracranial Oxygenation Changes in the Adult Head *Stroke*. 32, 2492 - 2500.
5. Matcher S. Appl. Opt. Matcher S J, Cope M, Delpy D T (1993) In vivo measurements of the wavelength dependence of tissue scattering coefficients between 760 and 900 nm measured with time resolved spectroscopy, *Applied Optics* **36**, 386- 396
6. Wang L., Jacques S. Zheng L. (1995) MCML-Monte Carlo modelling of photon transport in multi-layered tissues, *Comp. Methods Progr in Biomedicine* 47, 131 – 146.

Microspectrofluorometry and Polarisation Microscopy of Membrane Dynamics in Living Cells

Michael Wagner[1], Petra Weber[1] and Herbert Schneckenburger[1, 2]

[1] Hochschule Aalen, Institut für Angewandte Forschung, Beethovenstr. 1, 73430 Aalen, Germany
E-Mail: Michael.Wagner@htw-aalen
[2] Institut für Lasertechnologien in der Medizin und Messtechnik an der Universität Ulm, Helmholtzstr. 12, 89081 Ulm

Abstract. Organization and dynamics of cell membranes have a large impact on cellular uptake and release of various metabolites or pharmaceutical agents. Membranes of living cells are characterized using the membrane marker 6-dodecanoyl-2-dimethylamino naphthalene (Laurdan). Membranes are assessed by laser-assisted fluorescence microscopy, in particular a combination of microspectrofluorometry and total internal reflection fluorescence microscopy (TIRFM). Previously Membrane stiffness was related to spectral properties and expressed by the generalized polarization (GP), which depends on the phase of membrane lipids. GP generally decreased with temperature, and was always higher for the plasma membrane than for intracellular membranes. In addition, membrane fluidity was assessed by measurements of steady-state and time-resolved fluorescence anisotropy r(t), since with increasing viscosity, i. e. decreasing fluidity of the environment, the rotation of an excited molecule is impeded. The parallel and perpendicular components of the fluorescence emission from the sample were measured simultaneously using an imaging device with polarization sensitivity. In addition to GP, fluorescence anisotropy r(t) proved to be an independent measure for characterizing membrane dynamics. So far, membrane dynamics depended on temperature, growth phase as well as the on the intracellular amount of cholesterol.

1. Introduction

Time-resolved measurements of fluorescence anisotropy allow for analysis of membrane dynamics in cells. In contrast to free rotation in liquid media the motion of fluorophores in organized structures such as membranes is limited in angular range, since the surrounding architecture usually imposes certain restrictions on the orientation of the probe [1]. Membranes of living cells can be characterized using the membrane marker 6-dodecanoyl-2-dimethylamino naphthalene (laurdan) or 1,6 diphenyl-1,3,5 hexatriene (DPH) (Figure 1).

The fluorescence of laurdan shows a spectral shift towards longer wavelengths when its molecules get into contact with adjacent water molecules, e.g. when a phase transition from the tightly packed gel phase to the more fluid liquid crystalline phase of membrane lipids occurs [2]. In addition, its fluorescence lifetime t and fluorescence anisotropy r(t) depend on the lipid phase. Therefore,

the membrane marker laurdan appears appropriate for measuring membrane stiffness and fluidity [3].

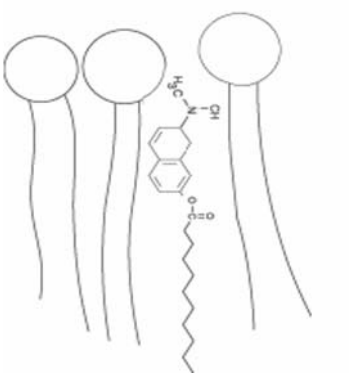

Fig. 1. The membrane marker 6-dodecanoyl-2-dimethylamino naphthalene (laurdan) is intercalating between the phosphor lipids.

The emission dipole moment of laurdan is oriented approximately along its long molecular axis. Rotation around these long axes of the molecule is expected to be considerably faster than rotation along perpendicular axes, but this fast rotation does not displace the emission dipole and hence does not depolarize the emission [4]. In recent studies fluorescence of the plasma membrane was detected selectively using the method of total internal reflection fluorescence microscopy (TIRFM), and compared with fluorescence arising from the whole cell. So far, membrane dynamics depended on temperature as well as on the intracellular amount of cholesterol [5], [6].

2. Experimental Methods

Cultivated U373-MG human glioblastoma cells (obtained from the European Collection of Cell Cultures (ECACC No. 89081403) were used as a model system for studies of membrane dynamics. Cells were routinely grown in RPMI 1640 medium supplemented with 10 % fetal calf serum and 1 % penicillin / streptomycin at 37°C and 5 % CO2. After seeding of 150 cells/mm², cells were grown on microscope object slides for 48 h prior to rinsing with Earl's balanced salt solution (EBSS) and incubation with the membrane marker laurdan (8 µM; 60 min.). After incubation cells were again rinsed with EBSS and measured in an open aluminium chamber at variable temperatures ranging from 16°C to 41°C using a 63x/0.90 water immersion objective lens. The chamber (filled with a layer of 2-3 mm buffer solution) contained a pair of high power thermoelectric elements for heating and for cooling, as well as a calibrated thermocouple for temperature measurements in close vicinity to the measured part of the samples.

For fluorescence spectroscopy and decay kinetics a picosecond laser diode (LDH 400 with driver PDL 800-B, Picoquant, Berlin, Germany; wavelength: 391

nm; pulse energy: 12 pJ, pulse duration: 55 ps, repetition rate: 40 MHz; average power: 0.5 mW) was used. This laser diode was adapted to a fluorescence microscope (Axioplan 1, Carl Zeiss Jena, Germany) using either a multimode or a single mode fibre-optic system (kineFlex-p-3-S-395, Point Source, Southampton, UK). For illumination a custom made dark field condenser unit was used [7]. This condenser permitted to use different angles of illumination below ($\theta = 62°$) or above ($\theta = 66°$) the critical angle θ_c of total internal reflection. In the first case whole cells were illuminated, whereas in the second case only the plasma membrane and adjacent parts of the cytoplasm were illuminated by the evanescent electromagnetic wave with a penetration depth around 150 nm (TIR illumination).

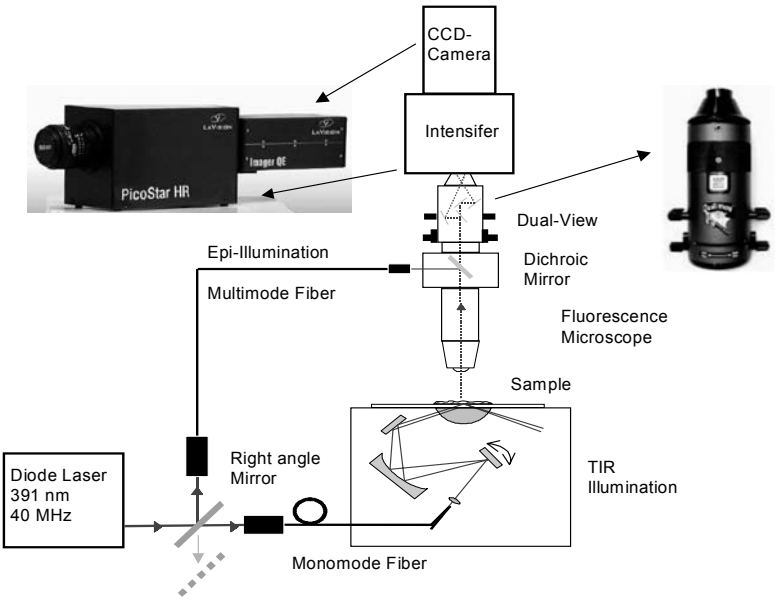

Fig. 1. Schematic set up of the fluorescence microscope using TIR or epiillumination as well as an image intensifying CCD-camera from LaVision.

Fluorescence spectra of single cells were recorded using a long pass filter for $\lambda \geq 415$ nm, a custom made polychromator and an image intensifying detection unit (IMD 4562, Hamamatsu Photonics, Ichino-Cho, Japan) fixed on top of the microscope [8]. Fluorescence decay kinetics and time-resolved fluorescence anisotropy were measured using an image intensifying camera (Picostar HR 12; LaVision, Göttingen, Germany) by scanning a time gate of 200 ps over a time range of 10 ns. Polarized fluorescence was detected simultaneously parallel and perpendicular to the plane of incidence using a dual beam imaging system (Dual View, Optical Insights, OR, USA).

3. Results

Spectral measurements of living cells as well as the evaluation of the generalized polarization (GP) as a measurement of membrane stiffness are described elsewhere [9]. Membrane stiffness decreased with increasing temperature and was always higher for the plasma membrane then for the intracellular membranes.
Measurements of fluorescence decay parallel [$I_{||}(t)$] and perpendicular [$I_{\perp}(t)$] to the plane of incidence are depicted in Figure 3. In addition, the anisotropy function r(t) is calculated according to

$$r(t) = [I_{||}(t) - I_{\perp}(t)] / [I_{||}(t) + 2I_{\perp}(t)] \quad (1)$$

Since in membranes the rotational motions of a fluorophore are hindered, the anisotropy function r(t) does not decay to zero, but to a limiting value r_{∞} (observed at times which are long compared with the fluorescence lifetime).

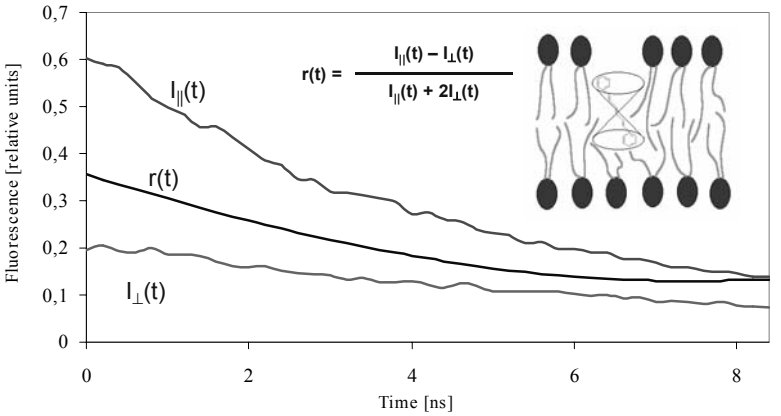

Fig. 3. Time course of fluorescence intensities of U373MG cells incubated with laurdan parallel and perpendicular to the exciting electrical field vector at T = 16°C; anisotropy function r(t); model for a restricted rotational motion of a fluorophore in a lipoid bilayer.

If one assumes that the decay from r_0 to r_{∞} occurs exponentially, time-resolved fluorescence anisotropy may be described by the equation

$$r(t) = (r_0 - r_{\infty})\, e^{-t/\tau r} + r_{\infty} \quad (2)$$

which can be used to calculate the rotational diffusion time τ_r. As depicted in Figure 4, this rotational diffusion time τ_r decreased with temperature from 3.14 ± 0.25 ns at T = 16°C to 2.30 ± 0.22 ns at T = 40°C, thus indicating a decrease of the environment's viscosity and possibly a phase transition of membrane lipids between 24°C and 32°C.

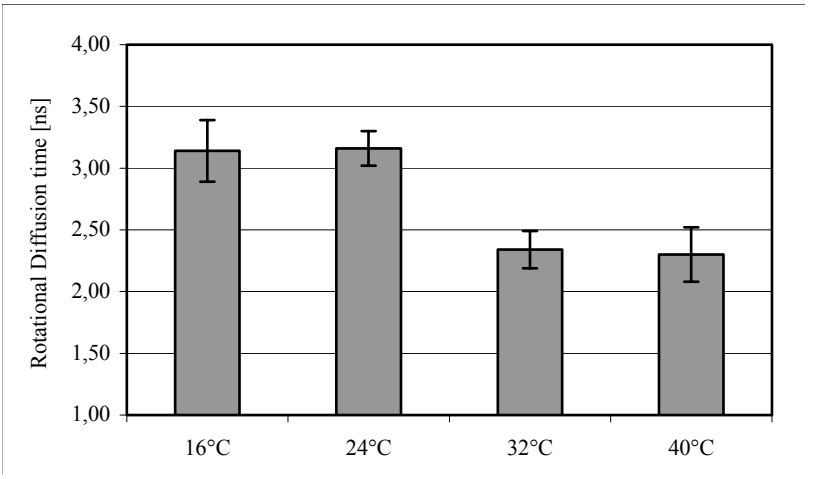

Fig 4. Temperature dependence of the rotational diffusion time τ_r of laurdan in U373MG cells under an angle of incidence θ= 62°. Values represent median values and median absolute derivatives (MAD's) of about 25 measurements in each case.

In all cases, a longer rotational diffusion time τr was measured for selective measurements of the plasma membrane.

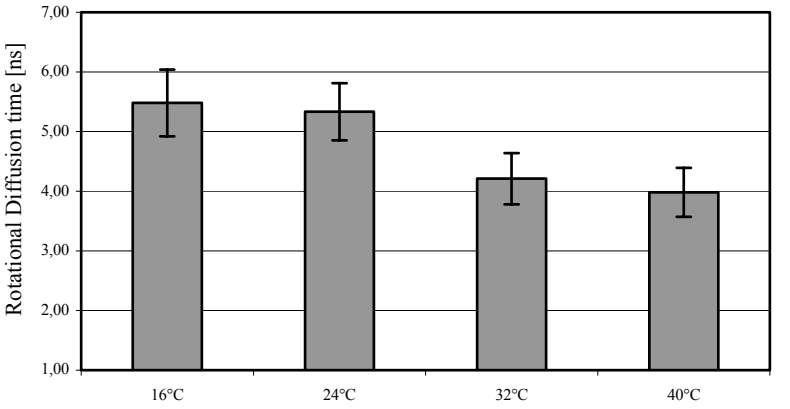

Fig 5. Temperature dependence of the rotational diffusion time τ_r of laurdan in U373MG cells under an angle of incidence θ= 66° (TIRFM condition). Values represent median values and median absolute derivatives (MAD's) of 20–30 measurements in each case.

4. Conclusions

Fluorescence anisotropy and general polarization (GP) of laurdan have been used as parameters of membrane fluidity and stiffness in living cells. GP as well as the time constant τ_r of rotational diffusion show a pronounced decrease with

temperature between 24°C and 32°C. This indicates that in this temperature range a phase transition of membrane lipids from the rather stiff gel phase to the more fluid liquid crystalline phase might occur. In addition, time constant τ_r of rotational diffusion of the plasma membrane was larger behaviour than for intracellular membranes, for all temperatures in the range of $16°C \leq T \leq 41°C$. This correlates with GP measurements and indicates that plasma membranes are stiffer and less fluid than intracellular membranes.

Acknowledgements. This project was supported by the Ministerium für Wissenschaft, Forschung, und Kunst Baden-Württemberg (Zentrum für Angewandte Forschung und Landesschwerpunktthema "Funktionelle Nanoskopie") and by the Bundesministerium für Bildung und Forschung (BMBF; Project No. 1701B04). Technical assistance by Claudia Hintze is gratefully acknowledged.

References

1 Kazuhiko Kinosita, Akira Ikegami, Suguru Kawato, *"On the wobbling-in-cone analysis of fluorescence anisotropy decay"*, Biophys. J. 37, 461-464, 1982.

2 T. Parasassi, E.K. Krasnowska, L. Bagatolli, E. Gratton, *"Laurdan and prodan as polarity-sensitive luorescent membrane probes"*, J. Fluoresc. 4, 365-373, 1998.

3 L.A. Bagatolli, T. Parasassi, G.D. Fidelio and E. Gratton, "*A model for the interaction of 6-lauroyl-2-(N,N-dimethylamino) naphthalene with lipid environments: implications for spectral properties"*, Photochem. Photobiol., 1999, 70, 557-564.

4 J.R. Lakowicz, *Principles of Fluorescence Spectroscopy*, Plenum Press, New York - London, 1999.

5 H. Schneckenburger, M. Wagner, M. Kretzschmar, W.S.L. Strauss and R. Sailer: *"Laser-assisted fluorescence microscopy for measuring cell membrane dynamics"*, Photochem. Photobiol. Sci. 3 (2004) 817-822.

6 D. Axelrod, *"Cell-substrate contacts illuminated by total internal reflection fluorescence"*, J. Cell Biol. 89, 141145, 1981.

7 K. Stock, R. Sailer, W.S.L. Strauss, M. Lyttek, R. Steiner, H. Schneckenburger, *"Variable-angle total internal reflection fluorescence microscopy (VA-TIRFM): realization and application of a compact illumination device"*, J. Microsc. 211, 1929, 2003.

8 H. Schneckenburger, M.H. Gschwend, R. Sailer, H.-P. Mock, W.S.L. Strauss, *"Time-gated fluorescence microscopy in molecular and cellular biology"*, Cell. Mol. Biol. 44, 795805, 1998.

9 P. Weber, M. Wagner, H. Schneckenburger, *"Microfluorometry of cell membrane dynamics"*, Cytometry 69A, 2006, in press.

Goniometrical Measurements of the Phase Function of Microstructured Tissue

René Michels and Alwin Kienle

Institut für Lasertechnologien in der Medizin und Meßtechnik, Helmholtzstr.12, D-89081 Ulm, Germany
E-Mail: Rene.Michels@gmx.de

Abstract. We present an experimental setup for the goniometric measurement of non rotational symmetric phase functions in the whole solid angle. These asymmetric phase functions are usually found in biological tissues with an aligned microstructure like muscle, skin, tooth and various other tissues. A method for the measurement of thin slabs of tissue samples was developed. We present goniometric measurements of pork muscle und compare them with microscopic images.

1. Introduction

Modern optics has produced countless applications of light in medicine. Beside therapeutically techniques, like in surgery, ophthalmology und dentistry, particularly diagnostic techniques have been established. Fundamental for both scopes is the proper understanding of light propagation in biological tissue. The understanding of light propagation in tissue enables to measure, noninvasively, medical relevant quantities like the oxygen and carbon dioxide amount of blood, muscle oxygenation [1], brain activity and cancer diagnosis. Also therapeutic techniques can be optimized to administer light, and therefore the energy, precisely to the target area [2]. In recent years, many improvements have been made, but still various questions are unsolved. The complexity of biological tissue accompanied with the immense demand on computational power impede the exact solution.

To calculate the light distribution in tissue normally the transport equation is solved [3]. The common solutions of the transport equation simplify the complexity of the media. A widely used approximation of the transport equation of light in scattering media is the (isotropic) diffusion theory. It approximates the media as a homogeneous distribution of rotationally symmetric scatterers. The optical properties of the tissue are reduced to the absorption coefficient and the reduced scattering coefficient. Indeed the numerical solutions of the transport equation additionally account for the phase function of the scattering particles. The Heyney-Greenstein phase function is widely used to calculate the angle dependent scattering for Monte-Carlo simulations. The Heyney-Greenstein function is based on astronomic observations and therefore has no deeper connection to biological tissue.

Using the Heyney-Greenstein phase function, the real microstructure of the tissue is not considered even though the microstructure is the basic reason for scattering in tissue. By taking these microstructures in account one can explain

astonishing phenomenas in biological tissue [4]. Furthermore it can be shown that the optical properties of biological tissue, acquired without taking respect to the microstructure, may have errors of more than 50% [5].

In long term it is not possible to calculate the exact solution of the light propagation in biological tissue for large tissue volumes. For microscopic small volumes < $100^3 \mu m^3$ this is possible with a numerical solution of the Maxwell's equations like the FDTD simulation but for larger areas approximations have to be made. With the substitution of the Heyney-Greenstein phase function with a physically correct phase function which is based on the real scattering properties of biological tissue it is possible to take into account the aligned microstructure many biological tissues have. Therefore, it is possible to calculate the light propagation of biological tissue for large areas utilizing a physically correct phase function and a Monte-Carlo simulation.

2. Methods and Materials

Specimen. For this study a microtome was utilized to produce slices of muscle tissue of various thicknesses reaching from 1 µm to 50 µm. The results which are presented here are measurements from porcine muscle tissue from the hip, which was obtained from the butcher. The tissue has been shock frozen in liquid carbon dioxide and then cut in slices in various directions in respect to the muscle fiber. The slices for the goniometric measurements and the microscopy images presented here have been 3µm thick.

Goniometer. A fully automated goniometrical system, which is capable of the measurement of the phase function in almost the whole solid angle, was developed. The goniometrical setup was presented elsewhere [6], a scheme is shown in Figure 1.

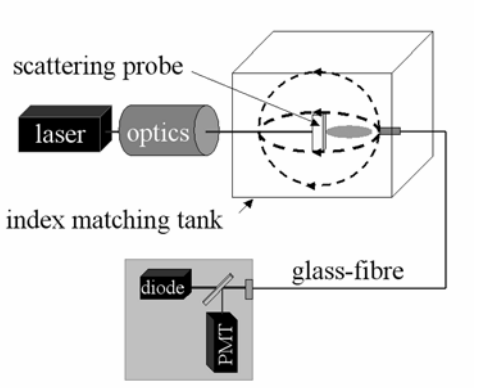

Fig. 1. Scheme of the goniometrical setup capable to measure the phase function in almost the whole solid angle.

The scattering specimen and the distal end of the measurement fiber are held in an index matching tank, filled with distilled water which refractive index is close to the refractive index of biological tissue. This reduces the distortion of phase function by refraction and, compared with using air, it shifts the critical angle of total internal reflection from 43° to 72°. Furthermore, water is inexpensive, almost not scattering and easy to handle.

The scattering specimen is held inside a cuvette built from cover glasses with 100 µm thickness. A He-Ne laser with its long coherence length would produce unpredictable interference effects inside the cuvette, which would frustrate a correction like explained in Section 2.3. Therefore, a temperature stabilized diode laser at 680 nm with a coherence length with less than 100 µm was employed as light source.

Cuvette Correction. In goniometric measurements of tissue slices the slab geometry of the specimen will inevitably distort the measurement. Tissue slices with a thickness of only a few microns additionally need to be clamped inside a cuvette which distorts the measurements even more.

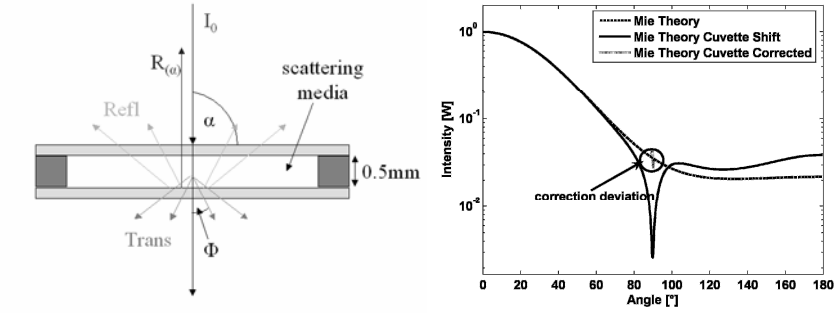

Fig. 2. (a) Scheme of the measurement cuvette illustrating geometrical optics effects that influence the measured phase function. (b) Example of forward and backward correction of the theoretical phase function of Intralipid.

In Figure 2 (a) the two most important effects, that will distort the measurement in a cuvette, are illustrated. Firstly, the incident Laser beam is reflected at the backplane of the cuvette, which produces apparent scattering in backwards direction. Secondly, an amount of the scattered light will also be reflected at the cuvette glasses.

In Figure 2 (b) an example for the resulting distortion of the phase function is shown for a cuvette filled with Intralipid. Mie theory was used to calculate the phase function of Intralipid. To demonstrate the effects of the cuvette we calculated the distortion by a cuvette model. Also the backward calculation is shown which restores the theoretical curve nearly completely.

Microscope. The microscopic images shown here are acquired with a Sony SSC-DC58 CCD Camera, which was mounted to a Zeiss Axiophot microscope. The microscope is equipped with a phase contrast unit. The tissue was not stained in order to not change its optical properties.

3. Results and Discussion

We present here goniometrical measurement of the phase function of muscle slices. The analysis of microscopy images yields explanations for the measured phase functions.

As you can see in Figure 3 (a), the goniometer is capable of measuring the phase function for the whole solid angle. Measurements for the whole solid angle with a good resolution can take up to 3 days. Because muscle tissue would show unpredictable side effects during that time period we have focused this study on measuring the phase function till 30° as is shown in Figure 3 (b). For the measurement of the muscle cut parallel to fiber direction, like shown here, the phase function is not rotational symmetric. The fiber direction of the Figure 3 (a, b), is from up to down the image. The scattering function of the muscle illuminated perpendicular to fiber direction, like it is plotted in here, has roughly an elliptical shape. This means that the scattering in fiber direction is weaker.

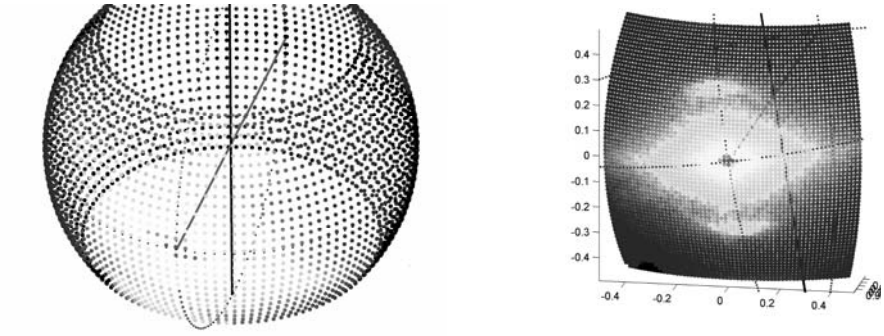

Fig. 3. Goniometric measurement of a 3µm muscle slice which was cut along with the fiber direction. On the left side, (a) the goniometric measurement of almost the whole solid angle is shown, on the left side, (b) the region till 30° is magnified.

Additionally 2 diffraction maxima can be seen at an angle of +/-16° alongside the fiber direction. This diffraction maxima are not caused by the fiber alone, like it can be observed in other tissues, for example tooth. Diffraction which is caused by regular ordered fibers would cause diffraction maxima lying perpendicular to the fiber direction. It is obvious that this diffraction is cased by the inner structure of the muscle fibers which is explained later on. The measurements of the muscle illuminated parallel to the fiber direction do not show this characteristics. Instead, a rotational symmetric scattering function was measured without special features. (A comparison of both is shown in Figure 5 (a).)

Figure 4 demonstrates what is causing the observed diffraction in the muscle tissue. In Figure 4 (b), the muscle is cut lengthwise to the fiber direction, fine ripples are observed which are orientated perpendicular to the fiber direction and which are not shown in Figure 4 (a) where the muscle is cut cross wise. These ripples arise through the inner structure of the sarcomeres, which build the muscle fibers. As is found in histology books, the sarcomeres consist of dark A-bands and

brighter I-bands. Within the I-bands a dark Z-line is located which is very sharp and not visible here. The A- and I–Bands should be roughly 1 µm long respectively. In Figure 4 (a) it can be seen that the length of a double line of one A and one I Band is 1.46µm.

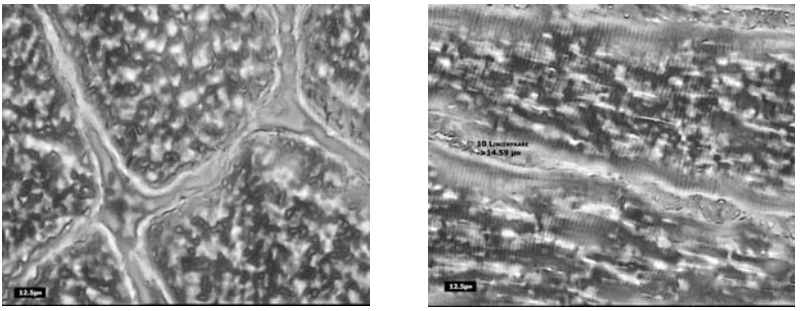

Fig. 4. Phase contrast microscopic images of muscle slices. On the left side, (a) the slice is cut perpendicular to the fiber direction. The image on the right (b) was cut parallel with the fiber direction.

In Figure 5 (a) the goniometrical measurements of muscle cut perpendicular to the fiber direction is compared to measurements which are cut parallel. The perpendicular measurement is rotational symmetric, the plot along the azimuthal angle is very similar to the plot along the polar angle. In comparison to this the measurement of the parallel cut muscle is not rotational symmetric. The polar angle plot shows higher intensity as the azimuth angle plots. The diffraction maximum is observed at 15.9°. Figure 5 (b) shows a calculation of the phase function. Basically the calculation considers the diffraction at the different structure sizes of an microscopic image of the muscle structures and builds up a theoretical phase function. The calculation predicts the maximum intensity of the parallel cut muscle also for 16.7° which is in good agreement with the experiment.

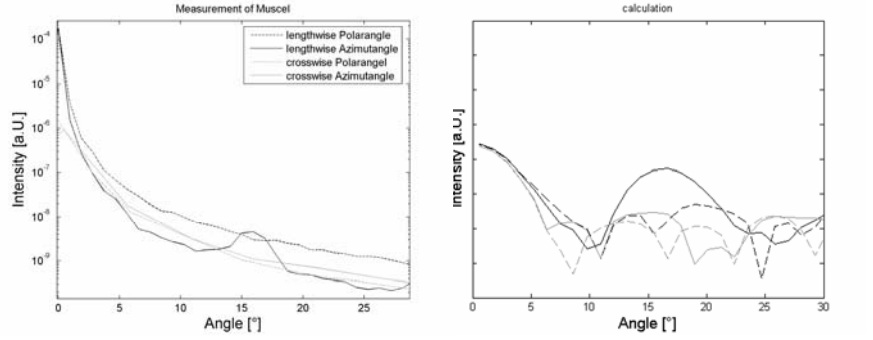

Fig. 5. (a) The measurement of the intensity vs. the angle is plotted for a sample which was cut parallel (black) and also for a sample which was cut perpendicular (gray) to the fiber direction. The scattering is not rotational symmetric, therefore both main directions, polar and azimuth angle, are plotted. (b) A calculation is shown which shows a phase function from a microscopic images of muscle tissue. The colors correspond to (a).

4. Conclusions

We presented measurements of the phase function of porcine muscle. The measured phase functions are complex and non rotational symmetric. We explained important features of these phase functions by a calculation which is based on microscopic images and therefore on the microstructure of the tissue.

Acknowledgements. We would like to thank the Deutsche Forschungsgemeinschaft.

References

1 D. Geraskin, P. Platen, J. Franke, C. Andre, W. Bloch, and M. Kohl-Bareis. Muscle oxygenation during exercise under hypoxic conditions assessed by spatially resolved broadband nir spectroscopy. *Proceedings of the SPIE*, 5859:83-88, 2005.

2 A. Kienle and R. Hibst. Optimal parameters for laser treatment of leg telangiectasia. *Lasers Surg. Med*., **20**:346-353, 1996.

3 A. Ishimaru. Wave propagation and scattering in random media. *Academic Press* New York, 1978.

4 A. Kienle, R. Michels, and R. Hibst. Magnification - a new look at a long-known optical property of dentin. *J. Dent. Res*., **85**:955-959, 2006.

5 J.R. Mourant, J. Boyer, A.H. Hielscher, and I. J. Bigio. Influence of the scattering phase function on light transport measurements in turbid media performed with small source-detector separations. *Opt. Lett*., **21**:546-548, 1996.

6 F.K. Forster, A. Kienle, R. Michels, and R. Hibst. Phase function measurements on nonspherical scatterers using a two-axis goniometer. *J. Biomedical Optics*, **11**:024018, 2006.

Part VI

Medical Laser Engineering

Comparison of Process Temperature during Laser and Mechanical Cutting of Compact Bone

Astrid Brendemühl[1], Martin Werner[2], Mikhail Ivanenko[2], Peter Hering[2,3] and Thorsten M. Buzug[4]

[1] RheinAhrCampus Remagen, Department of Mathematics and Technology,
E-mail: abrendem@rheinahrcampus.de
[2] Center of European Studies and Research (caesar), Bonn, Germany
[3] Institute of Laser Medicine, Heinrich-Heine-University Düsseldorf, Germany
[4] Institute of Medical Engineering, University of Lübeck, Germany

Abstract. Thermal side effects are the main problems concerning laser osteotomy. Data of the temperature increase in the vicinity of the laser cut for different irradiation conditions are important for understanding and optimisation of the laser ablation process. The first temperature measurements were done with an IR-camera (Flir SC 3000, spectral sensitivity 7.5 - 10 µm) from the back side of a bone plate (compact bone of bull femur) during drilling. The ablation is carried out with a TEA CO_2 laser (λ = 10.6 µm, pulse duration 1 µs and focus diameter 230 µm ($1/e^2$ level)). In another series of experiments the temperature was monitored during multi-pass cutting with the same laser. The temperature was investigated depending on the laser pulse energy, pulse repetition rate and beam scanning velocity and the settings of the cooling spray. Room temperature was amounted to 23 °C. The temperature during the laser drilling (50 Hz, 30 mJ) grows up to 400 °C (5 min, pressurised air jet cooling) respectively to 120 °C (3 min.) with a water spray cooling. During the laser multi-pass bone cutting with the use of a water spray and a scanning velocity of 2 mm/s the temperature reaches only 30 °C. These examinations emphasise that laser cutting is not dangerous for living bone cells under optimal conditions. The results of the temperature measurements during laser ablation are compared to the test results during mechanical abrasion. They underline that laser cutting of bones and mechanical abrasion show temperatures of an equal level. One strong advantage of laser cutting of bone is the nearly arbitrary cut geometry which could lead to an improvement in surgery.

1. Introduction

Nowadays osteotomy (cutting of bone) is performed by saw. This mechanical cutting causes vibrational traumata and deposition of metal abrasion particles within the bone. Against it, laser osteotomy is a non-contact ablation process. A prototype laser osteotome has been developed recently at the centre of European studies and research (caesar) in Bonn on the basis of a reliable short pulsed CO_2 laser system which emits at a wavelength of λ = 10.6 µm.

The laser ablation process can be divided into the following steps. First the laser radiation is strongly absorbed by the bone and evaporates the inner water. This leads to a micro-explosion in the thin absorption layer, which causes the tissue ablation [1]. One potential problem can be the temperature development

during the ablation process. Former trials e.g. [2] ended with thermal damage of the bone tissue. In caesar's developed system, which works with a pulsed CO_2-laser a water spray is directed at the bone that prevents dehydration, cools the tissue and disposes ablated material. After an ablation with water spray application the bone exhibits no visible thermal damage. Only very thin (~10µm) thermal damage zones were found in histological studies [3].

To investigate the heat distribution and development the ablation process was observed with an IR-camera (ThermaCAM SC 3000, Flir Systems) while varying the ablation parameters [4]. Of particular interest was a comparison of the heat development during the drilling and cutting with water spray and air jet application and a comparison of laser ablation and mechanical abrasion.

2. Temperature Measurements

The measurements were arranged from the reverse side of the irradiated thin bone sample. The rate of picture acquisition was 50 Hz. An optical filter (CaF_2, spectral transmission range: $\lambda < 10$ µm) protected the camera against the laser scattering. The influence of the filter optic can be balanced by the emissivity of the bone tissue in the camera software. The experimental setup is shown in the following figure.

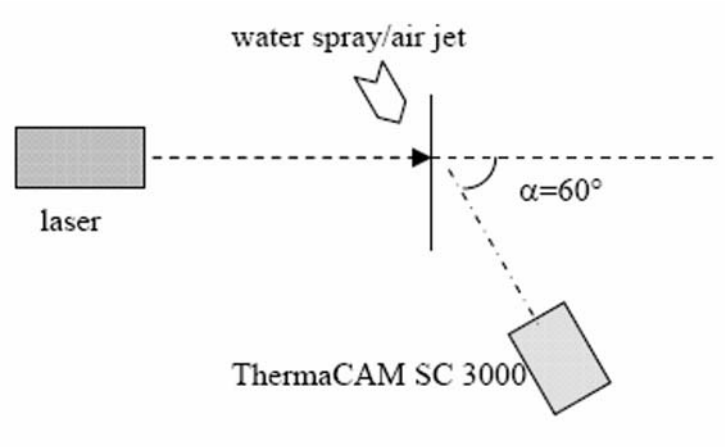

Fig. 1. Schematic experimental setup

The measurements compare the temperature development during laser ablation and mechanical abrasion of bone tissue. The laser ablation was carried out under the following conditions: Pulse repetition frequency f = 50 Hz, pulse energy E ≈ 30 mJ, thickness of bone tissue sample d = 1.25 mm.

Drilling. These measurements compare the temperatures during drilling of bones by laser and trephine. The laser drilling was done by spot irradiation (bore diameter ≈ beam diameter) and the mechanical drilling was done with a trephine with a diameter of 1.4 mm. The first investigation of mechanical bone removal was done during drilling by trephine with an air jet cooling.

This measurement results in a maximum temperature at breakthrough of 110 °C. The progression of temperature is shown below in Fig.2.

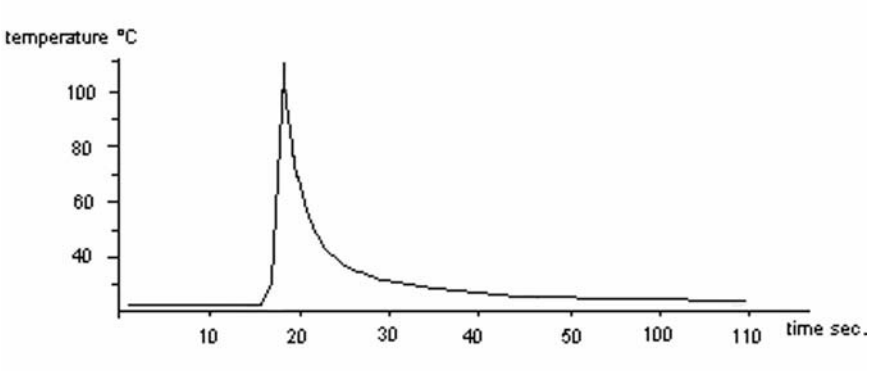

Fig. 2. Maximum temperature during drilling by trephine (air jet application)

Another measurement investigates the heat development during drilling with a trephine during water spray cooling. Drilling with a trephine at a rotation speed of 6000 min^{-1} causes temperatures of about 40 °C.

The laser drilling experiments are done with bone samples of the same thickness and also with air jet and afterwards with water spray application. At the time of material breakthrough during laser drilling with air jet application a maximal temperature of 400 °C is reached after 5 minutes ablation time.

The temperature development during laser drilling with water spray cooling is shown below in Fig. 3. At laser breakthrough after 3 min the temperature grows up to 120 °C.

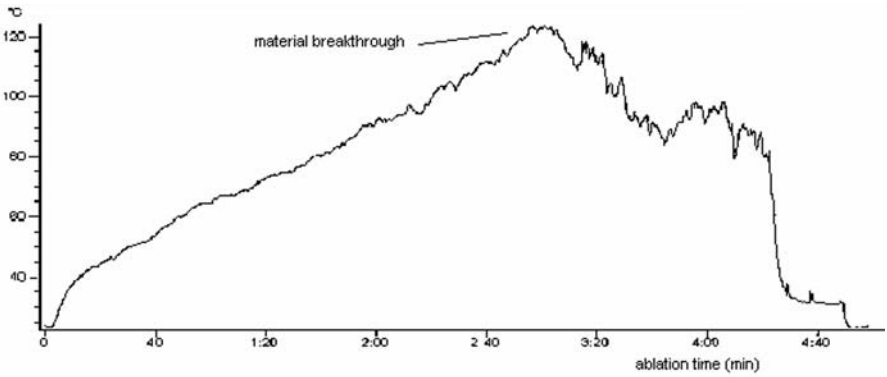

Fig. 3. Maximum temperature versus time (laser drilling with water spray application)

All measurements during drilling of bones show that laser drilling causes higher maximum temperatures compared to mechanical abrasion additionally the laser ablation takes longer with these specific irradiation parameters. However it has to be mentioned that the laser bores have much smaller diameters compared to the mechanical drilled holes. The excessive heat accumulation during laser drilling could possibly be reduced significantly by beam scanning in a certain pattern, which creates bores of larger diameter (1 – 2 mm).

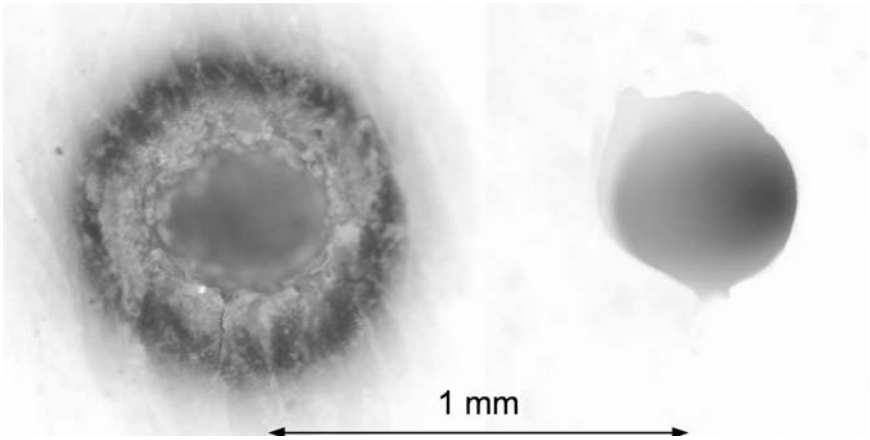

Fig. 4. Drilled hole by laser with air jet (left) and water spray application (right)

Cutting. For the measurement during cutting a similar setup was used. The bone tissue was aligned on a PC-controlled motorised linear drive stage which moves with a velocity of v = 2 mm/s through the laser beam. The IR-camera observes the backside of the thin bone tissue sample.

The laser ablation causes an average temperature of 25 °C except at the turning points of the bi-directional scanning line. In these points many laser pulses per time impinge on one spot which causes a temperature rise to ca. 45 °C. Temperatures above 45 °C are caused by burning of previously ablated bone tissue. The progression of the maximal temperature is shown in Fig.5.

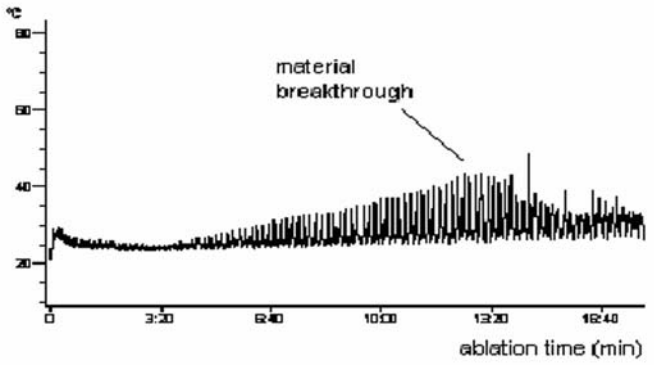

Fig. 5. Maximum temperature while cutting bone by laser

The result of the experiments shows that pulsed CO_2 lasers can be a biological compatible tool for bone processing (cutting or drilling) when used in combination with a water spray, a fast beam scanning technique and a suitable planning of the incision geometry. Especially geometries with many changes of direction with a small angle (triangle) or bi-directional scanning on small scales should be avoided or changed for example in circular geometries.

Fig. 6. Bone cut with laser with water spray application and beam scanning

The mechanical cutting was done with a circular saw using a water spray for cooling. At the time of breakthrough the temperature rises to 25 °C.

3. Conclusion

The results show that laser ablation with short pulsed CO_2 lasers is suitable for osteotomy, used in combination with the developed fast multi-pass beam scanning technique and the application of a water spray [1]. During the laser incision under optimal conditions the bone tissue achieves temperatures of only 25 °C (temperature rise of 2 K) which is comparable to the temperatures during mechanical sawing but the laser application causes no vibrational trauma and deposition of metal abrasion particles at all.

Another convenience of laser-osteotomy is an arbitrary cut geometry that would open up new vistas in many therapies for example specialized interventions at the skull base.

References

1 M. Ivanenko, M. Werner, M. Klasing, S. Afilal and P. Hering, *Ablation of hard bone tissue with pulsed CO_2-laser*, Med Las App **20**, 13, 2005.

2 S. D. Gertzbein, D. deDemeter, B. Cruickshank, A. Kapasouri, *The effect of laser osteotomy on bone healing*, Lasers in Surgery and Medicine **1**, 361, 1981.

3 M. Frentzen, W. Götz, M. Ivanenko, S. Afilal, M. Werner and P. Hering, *Osteotomy with 80-µs CO_2 laser pulses – histological results*, Laser Med Sci **18** 119, 2003.

4 A. Brendemühl, M. Werner, M. Ivanenko, P. Hering and T. M. Buzug, *Temperature Measuremrements with an IR Camera During Drilling and Cutting of Bone with a Pulsed CO2 Laser*, Biomedizinische Technik **50**, Suppl. Vol 1, 1264, 2005.

Spectral Analysis of the Acoustic Signal During Ablation of Biological Tissue with Pulsed CO_2-Lasers

Hendrik Steigerwald[1,3], Martin Werner[2], Manfred Klasing[1], Mikhail Ivanenko[1], Daniela Harbecke[2], Christian Wagner[1] and Peter Hering[2]

[1] center of advanced european studies and research (Caesar), Bonn, Germany
[2] caesar and Institute of Laser Medicine, University of Düsseldorf, Germany
[3] physics department, University of Bonn, Germany

Abstract. The advantages of laser osteotomy are free cut geometry and minimal thermal damage. Due to the lack of haptic feedback there is need for an alternate feedback method for accurate Laser Osteotomy. Based on the frequency analysis of the acoustic signal, generated by the ablation process, we are developing a feedback system to obtain in situ information on the ablation and for differentiation between different sorts of biological tissue. We used a pulsed slab CO_2-laser (wavelength 10.6 µm, pulse length 80 µs) and piezoelectric sensors for sound detection. We studied the correlation of the ablation signal of different kinds of tissue in the frequency domain.

1. Introduction

Today osteotomy, the transection of bone, is still performed with drills, oscillating saws and chisels. This procedure implies the danger of vibrational trauma, thermal damage and deposition of metal impurities in the bone tissue. In contrast, the non-contact treatment with a laser beam does not have these disadvantages but the advantage of free cutting and drilling geometry is given. CO_2 lasers are an adequate tool for ablation of bone tissue due to the good beam shape and their wavelength that is strongly absorbed in the mineral hydroxyapatite, 55-58 weight-percent [1] of which consist of the bone material.

The ablation process is generated by microexplosion. The laser pulse is absorbed by the hydroxyapatite and heats the bone matrix. The heat is transferred to the water, enclosed in the bone. The water is conveyed to an isochoric system; therefore a pressure build-up takes place. Above a certain threshold, the bone matrix bursts, the water evaporates almost instantaneously and a shock front is generated [2].

For accurate surgery the ablation process has to be stopped before the laser causes damage to the underlying soft tissue. The ablation process generates acoustic signals in the audible and the ultrasound regime. We analyzed the characteristic frequencies of this signal for different materials, since the varying concentration of water and the different tensile strength should influence the ablation process. The Comparison of the Fast Fourier Transformation (FFT) of signals of different materials with the current signal, using the correlation coefficient method, indicates in which material the current ablation process is

taking place. This method of tissue discrimination offers a reliable procedure to trigger the laser and to prevent damage to tissue that is not supposed to be ablated.

2. Experimental Methods

A schematic diagram of the experimental setup is shown in Figure 1. The laser beam is focused on the biological tissue by a scanner system, which is able to direct the laser beam with two mirrors along the programmed cutting or drilling path. The SC x 30 laser (Rofin Sinar) emits pulses with a length of 80 µs at a wavelength of 10.6 µm and a pulse energy of 80 mJ.

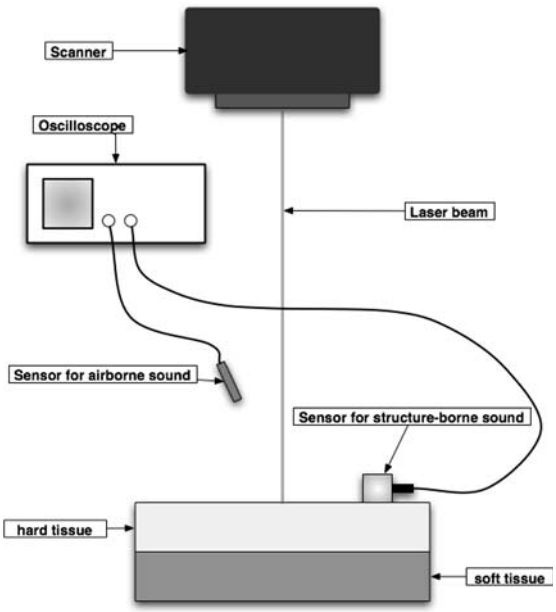

Fig. 1. Experimental setup for detection of acoustic signal generated by ablation of biological tissue with a pulsed CO_2-laser

For the acoustic signal that propagates through air, a piezoelectric pressure transducer, produced by the company PCB, with a bandwidth of 1 MHz, is positioned at a distance of 5 cm and at an angle of 15° with respect to the beam axis. This ensures that the higher frequencies, which have a smaller solid angle of emission and a higher damping in air, are still detectable [3]. Next to the ablation zone, at a distance of 3 cm, a sensor for structure-borne sound by the company Vallen-Systeme with a Bandwidth of 700 kHz is positioned.

Both sensors are connected to a LeCroy Waverunner 6051 Oscilloscope simultaneously. The structure-borne sound is used for level triggering, since it is located at a shorter distance than the sensor for the airborne sound and the signal

arrives first. The cutting or drilling process is performed with up to 200 Hz. After several cycles of ablation and some tissue removal, a single pulse is positioned on a reference point inside the ablation zone and the acoustic signal is stored. An FFT is performed and the resulting frequency spectra are compared with each other using the correlation coefficient. FFT yields the advantage of an absolute scale for the abscissa, so that the time shift between the signals, as a result of the variation of the trigger signal and the shift of the ablation zone, has not to be taken into account for the correlation coefficients. If the correlation coefficient of the current ablation signal and a reference signal drops below a certain threshold, the ablated material has changed and the laser can be switched off.

3. Results and Discussion

In Figures 2 and 3 oscillograms of the same ablation process, obtained by the two different sensors are shown. A typical characteristic of the acoustic signal is the bipolar structure. This is caused by the shock front generated by the micro explosion. The structure-borne sound signal contains high frequencies of higher amplitude than the airborne signal. This is caused by the fact that the impedance difference between bone material and air is high and therefore yields high reflection of the signal at the boundary layer [4]. The structure-borne signal amplitude has a larger time constant for damping, which is also caused by the high reflectivity, so that only a small fraction of the structure-borne signal is "coupled out".

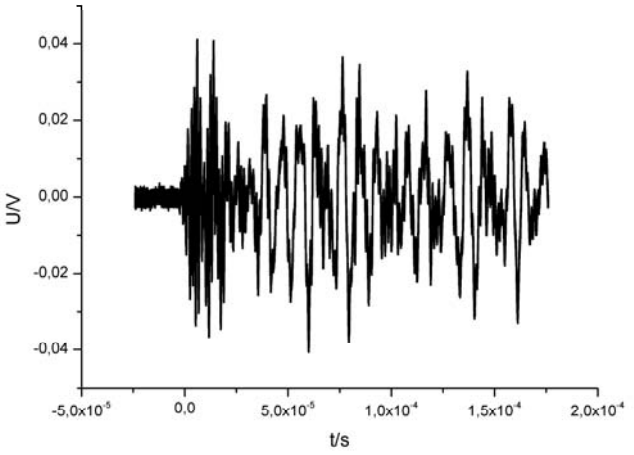

Fig. 2. Structure-borne signal obtained by the M58 Sensor of the company Synotech

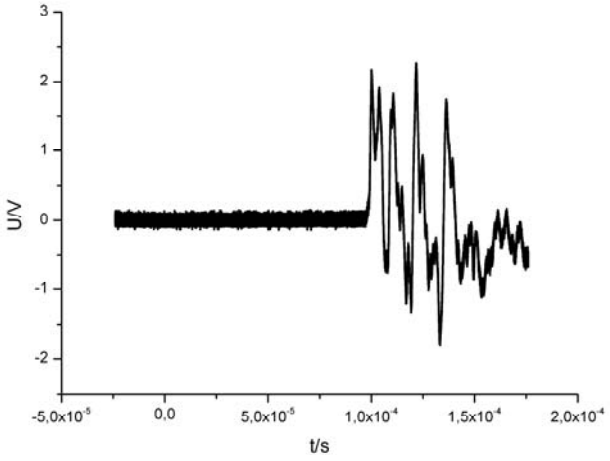

Fig. 3. Airborne sound obtained by the PCB Sensor

The signal analysis is performed in the frequency domain, since the signals can have an offset due to varying amplitude and the constant trigger level. The correlation of two signals in the time domain could be low, even though the signals are almost identical but phase shifted in regard to each other. Signals from the same sensor generated by different laser pulses are compared to one reference signal of known origin that has been stored in advance by the correlation coefficient. High correlation of successive pulses shows that the ablation process and therefore the ablated material are identical. A decreasing correlation coefficient indicates a changeover from one material to another, e. g. from hard tissue to soft tissue. Table 1 shows the correlation coefficients of a series of pulses that have been recorded during a cutting process in young bull femur. After one cutting cycle there was one pulse shot on a reference point inside the cutting region and the signal was stored. The FFT of the same signal detected by both sensors is shown in Figures 4 and 5.

The changeover from hard tissue to soft tissue takes place with signal 41. The signals from 36 to 40 have a high correlation in regard to each other. With signal 41 and 42 the dominating frequencies change and therefore the ablation process must have changed due to a different ablated material. During our experiments it became clear that the correlation coefficients, which were calculated with frequency spectra obtained with the Sensor for the airborne signal, are more significant those detected with the sensor for the structure-borne signal, even though the higher frequencies should have a better coupling to the structure-borne sound sensor. This could be the result of multiple internal reflections of the high frequencies, which would lead to background noise inside the bone caused by the high impedance difference.

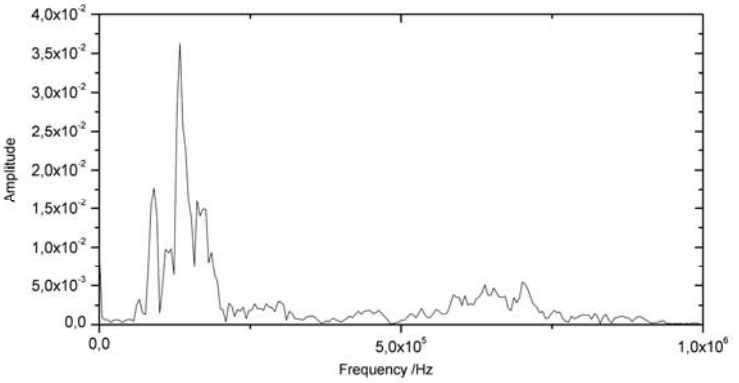

Fig. 4. FFT of the Structure-borne signal recorded with the AE-Sensor

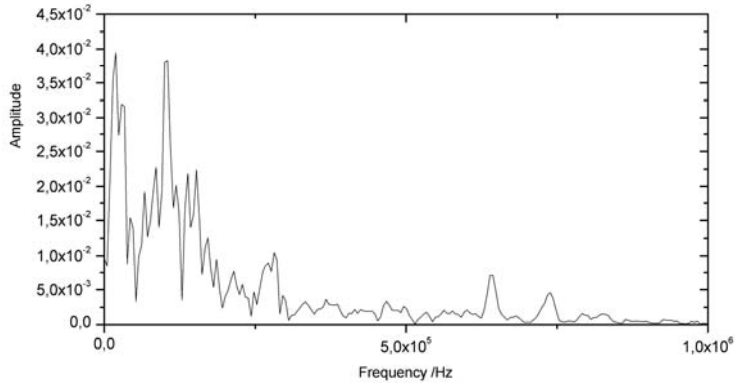

Fig. 5. Airborne signal recorded with the PCB-Sensor.

Table 1. Correlation coefficients of successive pulses during a cutting process in bone with underlying soft tissue detected with the PCB-Sensor

Pulse number	36	37	38	39	40	41	42
36	1.00						
37	0.86	1.00					
38	0.61	0.61	1.00				
39	0.78	0.79	0.72	1.00			
40	0.86	0.82	0.65	0.74	1.00		
41	-0.05	-0.07	-0.07	-0.06	-0.07	1.00	
42	0.04	0.05	0.02	0.06	0.00	-0.08	1.00

4. Conclusions

It has been shown that differentiation of biological tissue based on the frequency analysis of the ablation signal is possible. In the case of tissue changeover from hard to soft tissue in laser osteotomy, probing the soft tissue with several laser pulses does not cause much damage to the underlying tissue but offers a reliable differentiation procedure. The sensor for the airborne signal yields results of higher significance and is more appropriate for the usage in medical application, since it does not need direct contact to the ablated tissue.

Acknowledgements. I would like thank my work group at caesar for the very good and pleasant collaboration

References

1 F. A. Duck, in *Physical Properties of Tissue*, Academic Press, 1990.
2 M. Ivanenko, in *Medical Laser Ablation of hard bone tissue with pulsed CO_2lasers*, Medical Laser Ablation, Vol. 20, 13, 2005.
3 H. Kuttruff, in *Physik und Technik des Ultraschalls,* S. Hirzel Verlag Stuttgart, 1988.
4 V. A. Sutilov, in *Physik des Ultraschalls*, Springer Verlag Wien New York, 1984.

Laser-Scalpel for Kidney Resection Based on 1,94 µm Fibre Laser System

Dirk Theisen-Kunde[1], Söhnke Tedsen[2], Veit Danicke[1], Robert Keller[3] and Ralf Brinkmann[1]

[1] Institute of Biomedical Optics, University of Lübeck; Peter-Monnik-Weg, 23562 Lübeck, Germany, email: theisen@bmo.uni-luebeck.de
[2] Department of Urology, University Hospital Schleswig-Holstein, Campus Lübeck; Ratzeburger Alle 160, 23538 Lübeck, Germany
[3] Department of Surgery, University Hospital Schleswig-Holstein, Campus Lübeck; Ratzeburger Alle 160, 23538 Lübeck, Germany

Abstract A Laser-Scalpel system (StarMedTec, GmbH, Starnberg, Germany) emitting a wavelength at 1,94µm and a laser power at 16 W (cw mode) was used for partial resection of the porcine kidney in comparison to standard HF dissection device (Elektrotom 505, Berchtold, Tutlingen, Germany). Partial resection were performed on 6 kidneys, three with the Laser-Scalpel and three with the HF dissection device respectively. Blood lost was 11±10 ml with the Laser-Scalpel and 170±121 ml with the HF Dissector. Total resection time including haemostasis of the remaining tissue was 8,7±1,5 min with the Laser-Scalpel and 13,7±5,8 min with the HF dissection device. During resection with the Laser-Scalpel no occlusion of the blood supply of the kidney was needed compared to 6±2,2 min ischemic time by the use of the Elektrotom. In conclusion, the first experiments show that the 1,94 µm Laser-Scalpel is a very promising device for bloodless and fast kidney resection.

1. Introduction

In general surgery as well as in urology there is still a need for fast and precise dissection devices with reliable haemostasis of dissected blood vessels. The use of 1.94µm laser radiation for tissue dissection in surgery has two major advantages:

1. The high absorption coefficient of water (128 cm^{-1}) [1] at that wavelength yields to efficient water vaporisation in tissue and therefore to a precise tissue dissection with defined thermal damage.
2. The laser power can easily be transmitted via commercial available quartz fibre with core diameter of 200 µm. Newly developed fibre laser systems emitting in continuous wave mode (cw) at a wavelength of 1,94 µm are available with power up to 100 W.

Since 1999, in vitro investigations on different tissues are performed with cw solid state Thulium laser systems to investigate the potential of the continuous wave mode in combination with an emitted wavelength at 2µm for medical laser therapy [2-4]. Thulium fibre laser systems emitting at a wavelength at 1.9 µm are

currently investigated in vivo animal studies as dissection devices in urology with successfully results [5,6]. In this study a 1,94µm Laser-Scalpel is used for the first time in comparison to HF dissection for partial resection of porcine kidney in vivo.

2. Experimental Methods

Study design and animal experiments were approved by the Ministry of Environment, Nature Conservation and Agriculture of the Land Schleswig-Holstein, Germany, in accordance with the European convention on Animal care.

A Laser-Scalpel system (StarMedTec, Starnberg, Germany) emitting a wavelength at 1,94µm and a laser power at 16 W (cw mode) was used for partial resection of the kidney in comparison to standard HF dissection device (Elektrotom 505, Berchtold, Tutlingen, Germany). Laser power was transmitted via quartz fibre with a core diameter at 200µm with polished distal fibre tip which was held in a stainless steel tube (Fig.1).

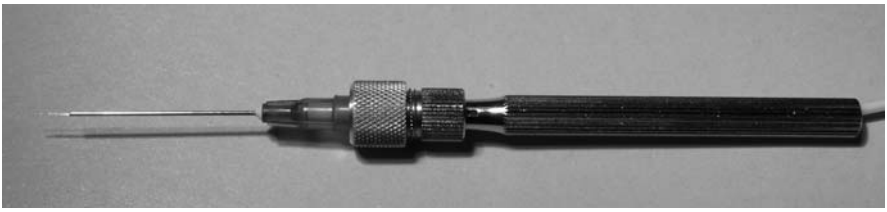

Fig. 1. Application tool for 200µm (core diameter) quartz fibre to transmit laser power to the tissue.

In three pigs general anaesthesia and a median laparotomy was performed to expose both kidneys. At each pig one kidney was dissected with the Laser-Scalpel and the other with the HF dissection device in a randomised way. The final evaluation data included

- total resection time to complete haemostasis at the remaining tissue
- blood loss
- mass of dissected tissue
- total ischemic time of the kidney

Each operation was executed as quickly as possible by an experienced Urologist.

3. Results and Discussion

No complications occurred during all operations, the weight of the animals were 32,3±10,1 kg.

Evaluated data was documented and is listed in table 1

Table 1. Evaluated data for partial porcine kidney resection performed by a 1,94µm Laser-Scalpel compared to standard HF dissection device. Data are presented as the mean value and the standard deviation

	1,94µm Laser-Scalpel	HF dissection device
Mass of dissected tissue	7,6 ± 4,5 g	11,4 ± 9,75 g
Blood lost	11 ± 10 ml	170 ± 121 ml
Total resection time	8,7 ± 1,5 min	13,7 ± 5,8 min
Ischemic time for the kidney	0 min	6 ± 2,2 min

In general the dissection with the 1,94 µm Laser-Scalpel was accompanied with simultaneous haemostasis of the dissected blood vessels. After resection of the kidney only a few (3-5) spots remain bleeding. Those bleeding were also stopped by exposure the spot with the laser light. Caused by the coagulation of the tissue haemostasis could be reached easily. The pure resection of the tissue with the HF dissection device was faster compared to the Laser-Scalpel but bleeding occurred all over the cutting edge. Therefore the blood supply of the kidney was temporally occluded and the vessels were closed by hand suture. This was accompanied with blood loss and time consuming haemostasis of single vessels.

4. Conclusions

In conclusion partial kidney resection could be easily and fast performed by the use of a 1,94µm Laser-Scalpel system. Haemostasis was highly sufficient so blood lost was negligible. The first results indicated that the 1,94µm Laser-Scalpel system is a very promising dissection device for urological surgery.

Acknowledgements. This work was supported by StarMedTec GmbH, Starnberg, Germany.

References

1 Maher, E. F. 29-90 (USAF School of Aerospace Medicine, Texas, 1978).

2 Pierce, M. C., Jackson, S. D., Dickinson, M. R. & King, T. A. Laser-Tissue Interaction with a high -power 2µm fiber Laser: Preliminary studies with soft tissue. in *Laser Med. Surg.* 25, 407-413 1999.

3 Theisen-Kunde, D., Ott, V., Ziegler, A., Brinkmann, R. & Keller, R. in *Proceedings of Annual Meeting of German Society for Biomedical Technology* 120-121 Ilmenau, 2004.

4 Theisen-Kunde, D., Ott, V., Brinkmann, R. & Keller, R. in *Proceedings of SPIE-OSA Biomedical Optics* G1-5 Munich, 2005.

5 Fried, N. M. Therapeutic applications of lasers in urology: an update. in *Expert Rev Med Devices* 3, 81-94 2006.

6 Fried, N. M. High-power laser vaporization of the canine prostate using a 110 W Thulium fiber laser at 1.91 micron. in *Lasers Surg Med* 36, 52-6 2005

Three-Dimensional Surface Measurement Using Digital Holography with Pulsed Lasers

Stephanie Heintz[1], Sven Hirsch[1, 2], Andrea Thelen[1] and Peter Hering[1, 3]

[1] Caesar foundation, Ludwig-Erhard-Allee 2, D-53175 Bonn
[2] Hightech Research Center of Cranio-Maxillofacial Surgery, University Hospital Basel, Schanzenstrasse 46, CH-4031 Basel
[3] Institute for laser medicine, University of Düsseldorf, Universitätsstraße 1, D-40225 Düsseldorf

Abstract. For medical application in the field of maxillofacial surgery, a highly resolved 3D digital representation of the human face is needed. Especially moving objects, i.e. infant patients are hard to capture with conventional systems. We eliminated moveable artifacts systematically by using eye safe holographic recording with short pulsed lasers (Nd:YLF laser, 526.5 nm wavelength). With a single pulse (35 ns, 1,4 J energy), surface data are recorded. Our conventional system uses an analogue process, where the hologram is reconstructed optically and digitized slice-by-slice.
We explored the possibility for a complete digital process. The conventional analogue recording material is replaced by a CCD-sensor with significantly lower pulse energy (0.1 mJ) for exposure. Numerical reconstruction of the real image is performed on a computer using appropriate algorithms. Surface calculations can follow immediately. Using this digital holographic approach to measure 3D surfaces means, that processing time, costs and effort can be reduced. However, in terms of resolution, digital technology lags behind the capabilities of our current analogue method for 3D surface detection. This involves inherent limitations at the current technological state of sensor technology. Nevertheless first applications are already possible.

1. Introduction

The analogue method of pulsed holographic topometry proved to be highly effective for facial topometry, mainly due to the systematic elimination of movement artifacts [1]. In a current effort we aim for recording and storing 3d surface information by the use of digital sensors. This demands a sufficient resolution, not only axial, but especially lateral for detection of the third dimension. Nonetheless this approach will offer new opportunities in metrology with its possibilities for recording time series of moving objects.

2. Principles of Digital Holography

In a hologram, three dimensional information of a wavefront is stored. By recording the interference pattern of light reflected from an object (object wave)

with non deformed light from the same source (reference wave) the object surface data is captured with intensity and phase information [2].

For digital holography – as in photography – a light sensitive chip (CCD or CMOS) is used to record the intensity information of the interference pattern. The intensity for the interference of complex amplitudes in the local area $A(x,y,z)=a \exp(i\varphi)$ is described as [3]:

$$I = \left|A_R + A_O\right|^2 = a_R{}^2 + a_O{}^2 + 2a_R a_O \cos(\varphi_R \varphi_O) \tag{1}$$

The first two terms represent the undiffracted object and reference wave; the last term stands for their interference.

The resolution of the recording material defines the quality with witch the object can be recorded. The difference between analogue hologram plates with at most 0,1 µm and CCD-sensors with at least 5 µm pixel size introduces a factor of about 50-100 in resolution. The sampling theorem delivers the maximal fringe spacing for the recordable pattern to be reconstructed unambiguously [4].

$$f_{\max} = \frac{1}{2\Delta x} \tag{2}$$

This affects the maximal recording angle under which the object information is still ascertainable, as the interference pattern of a point is getting finer to its outwards. The maximal recording angle is defined by:

$$\theta_{\max} = 2\arcsin(\frac{\lambda}{4\Delta x}) \approx \frac{\lambda}{2\Delta x} \tag{3}$$

Each recorded point experiences a sharpness progression throughout its reconstruction in different distances to the hologram. Maximum sharpness is achieved in the area of the points' real positioning (Figure 3) and will culminate in a minimal beam waist. The axial extend of this waist which limits the accuracy of the z-positioning of the reconstructed point is called focal length.

$$z_R \approx \frac{4\lambda d_{obj}^2}{\pi(np)^2} \tag{4}$$

An exact determination of the surface point position is necessary for a correct reconstruction of the object surface. The resolution can be improved by using a larger recording area (np^2) or by selecting a shorter recording distance (d_{obj}), which in turn limits the maximally recordable object extend.

3. Experimental Setup

In our setup a short pulsed (35 ns) Nd:YLF laser with 526.5 nm wavelength and a coherence length of more than 3 m is used (GP-2J, www.geola.com). With up to 2 J pulse energy it's suited to record analogue holograms, where the emulsion on the film needs enough energy to react during the short pulse. The sensitivity of a CCD-sensor allows to hologram capture with unamplified pulses of 0,5 mJ, which is nearly 5000 times lower than for plates. High repetition rates are easily

achievable and only technically limited by camera data throughput of 2 Images/s. That means that serial motion recordings are easily possible.

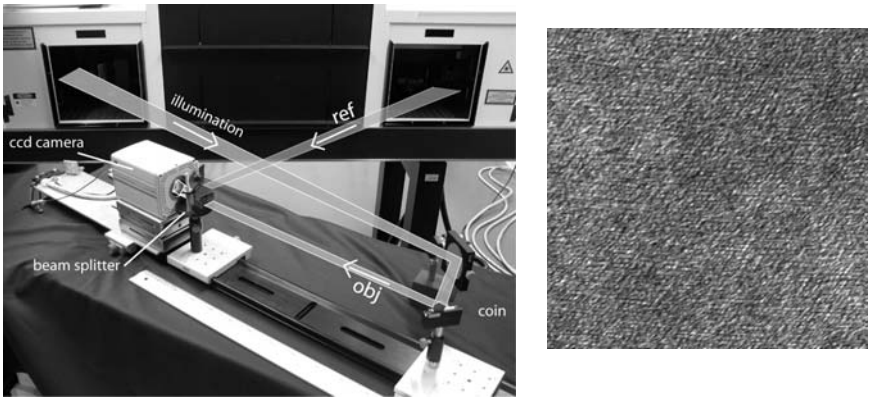

Fig. 1. Left: Photo of the experimental setup for recording of digital holograms with reference, illumination and object beam; right: 256 x 256 pixel, 8 bit, clipping of a digitally recorded hologram (2k*2k pixels) from the depicted setup.

The laser beam from the source – we use a spherical wavefront – is split into two parts. The reference beam is directly conducted towards the beam splitter in front of the camera and onto the sensor. The illumination beam is directed towards the object. The reflected object beam passes the beam splitter as well to interfere with the reference beam in a slightly off-axis alignment. Both light paths should have a similar path length, to make use of the full coherence length.

For recording we use a Kodak Megaplus ES 4.0 camera which inherits a interline CCD-chip with 2048 x 2048 pixels of 7,4 µm size with 60% fill factor, a bit depth of 12 bits and 0,08 µJ/cm² sensitivity. Figure 1 shows an example digital hologram. The camera is synchronized with the laser system to record the laser beam pulses in a time window of approximately 1 ms.

4. Reconstruction

The calculation of the diffracted light field is described by the well known Fresnel-Kirchoff integral. The calculation can be simplified in several ways; we identified the Fresnel approximation [3] of the common reconstruction methods as appropriate and quick. Its calculation – with h being the hologram data, E_R the reference wave and f an additional factor including the object distance d_{obj} – is basically described by the following formula:

$$\Gamma(\xi,\eta) = iFFT\{h(x,y)E_R^*(x,y)f\} \tag{5}$$

Whereas the reconstruction pixel size is fixed to:

$$\Delta x' = \frac{d_{obj}\lambda}{N\Delta\xi} \tag{6}$$

Together with filter methods like highpass filtering and mean-value subtraction to dispose of the undiffracted parts of object and reference waves which cover the reconstruction by a white square in size of the CCD-chip, we achieved our best results so far.

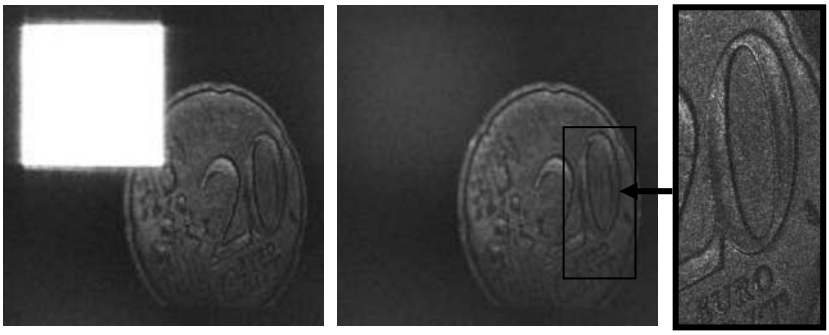

Fig. 2. Reconstruction of a 20 cent coin in 40 cm distance with the Fresnel approximation. On the left the unfiltered image with the bright square of undiffracted light; in the middle the result by using the filter methods highpass and mean-value subtraction; on the right an enlarged region.

Reconstructing the object for different distances a sharpness progression is visual, having the surface parts sharp which are located in the current distance.

Fig. 3. Reconstruction of a 20 cent coin recorded in a distance of about 40 cm. Reconstructed from left to write in 39,7 cm, 41,1 cm and 43,6 cm distance.

Detecting the sharp areas in each image with contrast based methods [5] will lead to the objects surface data.

As described above, a larger recording area (number of pixels) is responsible for a more accurate reconstruction result. So far we have used a chip of 2048 x 2048 pixel size, but further extensions are planed. By applying the Fresnel approximation, which is a quite effective reconstruction method, each pixel is multiplied with a phase factor and a iFFT (inverse Fast Fourier Transform) is applied. Especially the use of the iFFT results for pictures of the named size in a high compute expense of $N \log_2 N$. That is why we tested different approaches for computing the iFFT. At first we implemented the method using the Java Plugin FFTJ for ImageJ, an open source graphics program we are working with. It turned out to be highly beaten by the strongly optimized FFTW algorithm, a library based on C++. Best performances were achieved by using the GPUFFT library, again based on C++. Here the calculation isn't done on the CPU (Central Processing Unit) like normal, but on the GPU (Graphics Processing Unit) of the graphis board [6]. A total overview of the time results for different picture sizes gives Figure 4. The calculation was done on a PC with 2x Dual Core AMD operators (64-bit) with both 2.2 GHz, 16 GByte memory and the graphic card QuadroFX 4500 PCIExpress with 512 Mbyte memory.

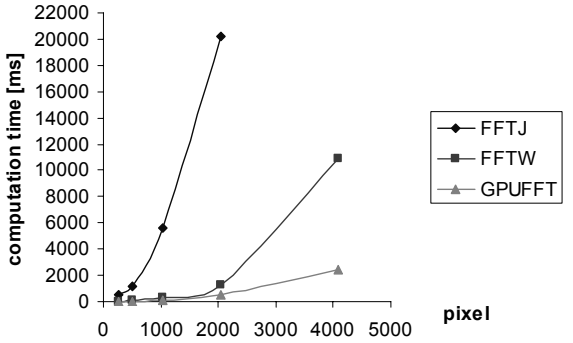

Fig. 4. Computation time for the use of the inverse FFT used for the Fresnel approximation for different picture sizes, testing three different FFT libraries.

Especially for multiple reconstructions, as needed for surface detection, a fast computation is of importance. It showed that the computation time of the iFFT can be improved enormously. Currently we are optimizing the complex multiplication with the phase factor which is the second contribution to the computation cost.

5. Results and Discussion

In the previous chapter the reconstruction of a 20 cent coin has been shown already. Moreover we made successful experimental recordings of non-reflecting objects [7]. The achieved lateral resolution of around 0,2 mm could be detected by recording a Siemens star target (Figure 5, left). The depth profile of the reconstructed stack shows the focal progression of the image (Figure 5, right). For

a recording in 30-40 cm distance, a focal length of around 1-2 mm can be achieved. This turned out to be sufficient for a first rough surface reconstruction of a recorded coin.

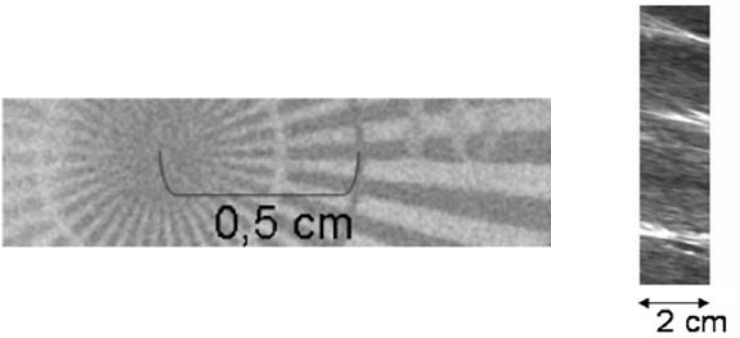

Fig. 5. Reconstructions showing the achieved lateral and axial resolution. Left hand a Siemens star target in a distance of 60 cm. Right hand a depth profile of a reconstructed coin in about 30 cm distance with a step width of 1 mm.

6. Conclusions

In terms of quality, digital technology lags behind current analogue processes for 3D surface detection, but first application areas can be seen already. In addition, further development in this area can be expected for the future. Using this digital holographic method to measure 3D surfaces, time, money and effort can be saved.

References

1 J. Bongartz, in *Hochauflösende dreidimensionale Gesichtsprofilvermessung mit kurzgepulster Holographie*, PhD thesis, Mathematische Naturwissenschaftliche Fakultät der Heinrich-Heine-Universität Düsseldorf, 2002.
2 P. Heiß, in *Holographie-Fibel*, Wittig Fachbuchverlag, 1995.
3 U. Schnars and W. Jueptner, in *Digital Holography – Digital Hologram Recording, Numerical Reconstruction, and Related Techniques*, Springer, 2005.
4 B. Jähne, in *Digitale Bildverarbeitung*, Springer-Verlag, 2002.
5 A. Thelen, in *Optimized surface extraction from holographic data*, PhD thesis, Mathematische Naturwissenschaftliche Fakultät der Heinrich-Heine-Universität Düsseldorf, 2006.
6 T. Jansen, B. von Rymon-Lipinski, N. Hanssen and E. Keeve, in *Fourier Volume Rendering on the GPU Using a Plit-Stream-FFT*, Stanford, USA, 666, 2004.
7 S. Heintz, in *Einsatz der digitalen Holographie im Verfahren für die 3d Oberflächenerfassung*, diploma thesis, Fachbereich Digitale Medien der Hochschule Furtwangen, 2006.

Laser Spectroscopic Online Monitoring of Volatile Diseasemarkers in Human Breath

Manfred Mürtz, Sven Thelen, Thomas Fritsch and Peter Hering

University of Düsseldorf, Institute for Laser Medicine, D-40225 Düsseldorf, Germany
E-mail: muertz@uni-duesseldorf.de

Abstract. We present an overview of the recent progress on spectroscopic online monitoring of exhaled breath with mid-infrared coherent sources. The current detection limits of laser spectroscopic approaches are in the picomolar to nanomolar range, depending on the molecular compound. The time resolution of the measurements is down to the sub-second range. This very high sensitivity and time resolution open up exciting perspectives for novel analytical tasks in biomedical research and clinical diagnosis.

1. Introduction

Modern infrared lasers get more and more useful for analytical tasks in biomedical research. In the past decade, an increasing number of publications dealt with the investigation of biogenic trace gases. In particular, the role of volatile disease markers released by the human body has gained growing interest [1]. The quantitative trace analysis of exhaled breath provides important information about the health status of a living subject. Besides the major components, like carbon dioxide and water, exhaled human breath contains several hundred volatile compounds of endogenous origin. Most of them are present in volume fractions on the order of part per billion (ppb, $1{:}10^9$) or even below. A few years ago, it has been found that small molecules like nitric oxide, carbon monoxide and volatile hydrocarbons are formed in the human organism. Some of these exhaled compounds are considered to be disease markers [2]. For example, ethane and pentane are potential markers of lipid peroxidation, whereas nitric oxide is considered to be an important marker for inflammations in the respiratory tract.

In the past 15 years, the performance of laser spectroscopic methods for analytical purposes has made significant progress [3]. A major advantage of laser spectroscopic breath analysis is the capability of online measurements [4]. Online measurement means, that the exhaled breath is analyzed during exhalation in real-time whereas with offline techniques the breath is collected in a bag or a sorbent trap. The potential problems of off-line methods, like reproducibility of breath sample collection, contamination during sample storage and the inability to allow for instantaneous feedback, can be avoided with online methods.

Most laser spectroscopic techniques are based on the principle of absorption spectroscopy. The gas sample of interest is transferred into an absorption cell and the wavelength-dependent attenuation of the laser light which passes the cell is measured. Spectroscopy in the mid-infrared spectral region is most advantageous

since most of the gaseous compounds of biomedical interest are molecular gases that have characteristic, strong ro-vibrational absorption bands in this spectral region.

In our laboratory, two different approaches for extremely sensitive, specific and fast analysis of biogenic trace gases are pursued: Faraday Modulation Spectroscopy (FAMOS) based upon magneto-optic rotation [5], and Cavity Leak-Out Spectroscopy (CALOS), which boosts sensitivity by using an external optical resonator [6,7,8]. Whereas the FAMOS approach is limited to open-shell molecules (like nitric oxide), the CALOS technique also enables rapid analysis of many other volatile compounds (hydrocarbons, carbon monoxide, etc.) on the picomolar level; this corresponds to fractions in the parts-per-trillion range (ppt, $1{:}10^{12}$). In the following, we describe recent progress on laser-based online monitoring of exhaled biomarkers.

2. Experimental

Cavity leak-out spectroscopy (CALOS) is based upon the optical excitation of a high-finesse cavity which encloses the gas sample to be analyzed. The absorption measurement is carried out via monitoring the decay rate of the light leaking through one of the cavity mirrors. Due to the large effective absorption pathlengths (typ. several kilometers), this technique offers considerably better detection limits than is obtainable in conventional absorption spectroscopy.

Our spectrometer is based on a high-finesse cavity of 50 cm length which provides an optical absorption pathlength of several kilometers. The compact laser system is based on difference-frequency mixing in periodically poled $LiNbO_3$ (PPLN); with the present set-up, we observe a maximum mid-infrared power (idler) of about 280 μW near 3.3 μm. More detailed information can be found in [9]. For the CALOS work in the 5 μm wavelength region, a laboratory-bound CO sideband laser, based on a liquid-nitrogen-cooled gain tube, is used. The CO laser beam is sent to a CdTe electro-optical modulator (EOM) operating at microwave frequencies for the generation of tunable sidebands. More details have been reported in [10]

For the trace gas measurements, the laser power is periodically injected into the ring-down cell. After determination of the empty cavity decay time τ_0, and the decay time of the cell filled with the sample τ, the absorption coefficient, can be directly determined via

$$\alpha(\lambda) = \frac{1}{c} \cdot \left(\frac{1}{\tau(\lambda)} - \frac{1}{\tau_0} \right), \tag{1}$$

where α is the absorption coefficient, λ is the wavelength, and c is the speed of light.

For online measurements, direct exhalations into a mouthpiece are continuously analyzed in real time. A schematic of the gas set-up for online analysis of breath ethane is shown in Fig. 1. The breath sampling is performed by means of a modified mouthpiece, which is used to supply the breath sample to the

analyzer. Two gas supplies supply lines at the mouthpiece are used to continuously extract portions of the breath into the CALOS analyzer and into a capnograph; the latter is used for monitoring the exhalation flow rate, the CO_2 and O_2 concentrations. The gas sample is dehumidified by means of a Nafion tube and fed through a cooling trap at a temperature of about 160 K to eliminate interfering molecules. The pressure inside the cell is kept constant near 50 mbar independently of the flow.

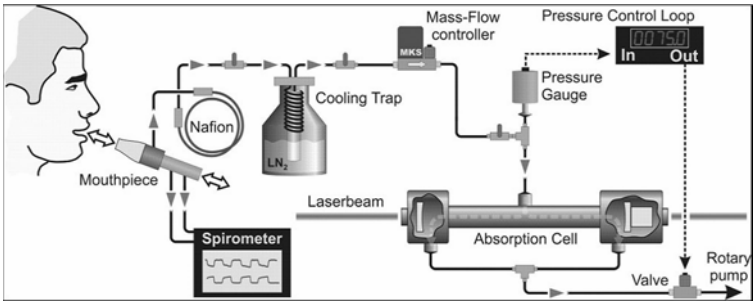

Fig. 1. Schematic of the gas set-up. A part of the exhaled breath is directed into the CALOS absorption cell via a Nafion tube and a cooling trap, which are used to dehumidify and clean the gas sample.

3. Results

Online Monitoring of Ethane with DFG. The difference frequency of our set-up covers the spectral region between 2650 cm^{-1} and 3100 cm^{-1} via tuning of the pump laser wavelength. Additionally, a suitable PPLN grating period and temperature has to be selected. Each grating covers about 100 cm^{-1} for temperatures between 20 and 120 °C. The maximum DFG power achieved was 280 µW near 3.35 µm.

In order to determine the minimum detectable absorption, the leak-out cell was flushed with grade 5.0 nitrogen. For an observation time of 180 s the 1σ-uncertainty of the measured absorption is 5.6×10^{-10} cm^{-1}, corresponding to a noise equivalent absorption of 8×10^{-9} cm^{-1} $Hz^{-1/2}$. This corresponds to a noise equivalent ethane concentration of 270 ppt $Hz^{-1/2}$.

The ethane molecule has a characteristic fingerprint spectrum in the wavelength region near 2983 cm^{-1}. For online measurements, direct exhalations into a mouthpiece are continuously analyzed in real time. To achieve high time resolution, no wavelength scan is made; only single-frequency measurements on an ethane absorption peak near 2983.38 cm^{-1} were made. Online breath measurements need a time resolution on the order of 1 s. The time resolution is given by the T90 time. This is the time interval needed for an increase in observed concentration from 10% to 90%, which results from an instantaneous increase of the concentration from 0% to 100%. Basically, the time resolution is determined by both the exchange time of the gas set-up and the averaging time (integration time) of the data processing. The T90 time determined is *(*1.1 ± 0.1*)* s, which is limited by the gas-exchange time. With regard to flow, pressure, and volume, the

system has a theoretical gas exchange time of 850 ms. A representative example of an online recording is shown in Fig. 2. Here, the ethane concentration is plotted over the exhaled volume (expirogram).

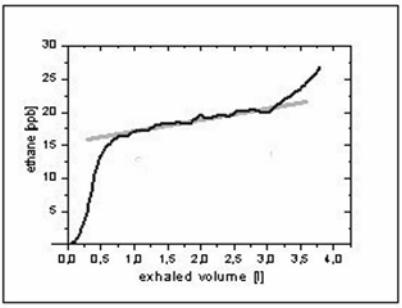

Fig. 2. Measurement of a single-exhalation expirogram for ethane. Exhalation flow rate: 10 l/min.

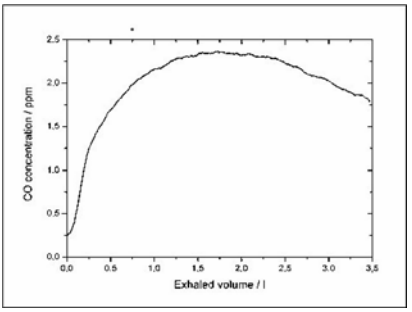

Fig. 3. Measurement of a single-exhalation expirogram for CO. Exhalation flow rate: 4 l/min.

Online Monitoring of Carbon Monoxide with a CO Sideband Laser. Recently, the CALOS technique has also been used to investigate exhaled carbon monoxide (CO). CO appears to be an important signalling molecule which may be useful for the assessment of different diseases, in a similar way like. This molecule exhibits strong absorption lines in the 5 µm spectral region. However, it is essential to choose a spectral window which is not overlapped too much by absorption lines from carbon dioxide and water. A typical online recording of exhaled carbon monoxide at low exhalation flow rate (4 l/min) is shown in Fig. 3. The breath sampling for the CO measurements was essentially the same as described above. The detection limit of CO in exhaled breath is 24 ppb, (1 s averaging time), far below the average exhaled CO concentration of 1 to 10 ppm. It is worth noting that the alveolar plateau exhibits a negative slope for breath flow rates below 10 l/min. We speculate that this course of concentration reflects the sequential emptying of the different compartments in the lungs in combination with localized production of CO within the tissue of the region which is emptied in the beginning of the exhalation.

Online Monitoring of NO Isotopologues. Nitric oxide is known to be a central mediator in biological systems and the research on NO production and signalling pathways is still ongoing. Next to the well-known enzymatic production pathway, there is a non-enzymatic way of NO production, occurring for example in human sweat when the skin is exposed to UV radiation from the sun [11].

A particular advantage of laser-based NO analysis is the capability to distinguish between different isotopologues, for example ^{14}NO and ^{15}NO. In medical research, the use of labelled NO (or labelled precursors) is essential to be able to distinguish between endogenous and exogenous sources and sinks of nitric oxide. By monitoring the increase of metabolites that contain an isotopic label one can draw conclusions about the metabolic reaction rate etc. Such investigations are called tracer investigations.

We have recently investigated the simultaneous online detection of ^{14}NO and ^{15}NO with CALOS. Our measurements were performed with the CO sideband laser in the wavelength region around λ = 5µm. The spectrum near 1875 cm^{-1} exhibits characteristic absorption lines of ^{15}NO and of ^{14}NO with comparable absorption at natural isotope ratio. Measuring at the maximum of absorption near 1875 cm^{-1} the noise-equivalent concentrations are 800 ppt ^{14}NO and 40 ppt ^{15}NO, respectively.

Fig. 4A shows the ^{14}NO (black) and ^{15}NO (grey) concentrations during the chemical reduction of nitrite (NO_2^-) with potassium iodine (0.1 M KI in 0.1 M HCl). Nitrite is a constituent of sweat in the low micromolar range. The vertical scale unit is ppm for ^{14}NO and ppb for ^{15}NO. The resulting isotope ratio can be calculated in two different ways. One approach is to determine the amount of released NO during the reaction. The area beneath the curve gives the total amount of (383.5 ± 0.5) nmol ^{14}NO and (1071 ± 9) pmol ^{15}NO which gives $\delta^{15}N$ = (-240.4 ± 6.5)‰. Another approach is to calculate the isotope ratio from the measured concentrations vs. time shown in Fig. 4B. More details on this work can be found in [10].

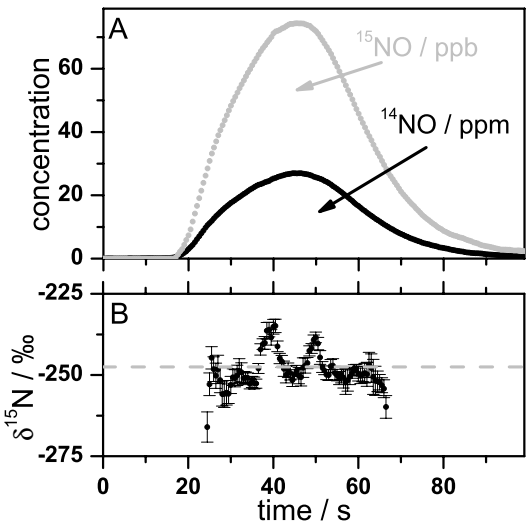

Fig. 4 A. Time resolved measurement of ^{14}NO (black) and ^{15}NO (grey) concentrations during a reduction of nitrite with potassium iodine. **B.** $\delta^{15}N$ vs. time.

4. Conclusions

It is obvious that the analysis of breath metabolites opens new diagnostic windows in clinical medicine. Breath analysis is very attractive because this is a literally non-invasive way to monitor a patient's physiological status. However, the clinical value of exhaled biomarkers will depend on the availability of reliable and

inexpensive analyzers. Since the exhaled concentrations are extremely low, the technical problems of breath testing are still severe.

Laser-based breath analysis is an exciting way to improve this situation. Laser spectroscopy is currently the only technique that allows for single-breath resolved real-time measurements of exhaled traces gases with picomolar sensitivity. For example, the sensitivity and specificity for breath ethane monitoring is unprecedented. Laser spectroscopic online monitoring of breath ethane could become a promising approach for non-invasive acquisition of the oxidative stress status in various pathophysiological situations.

Future progress in this field will depend on the availability of tunable, room-temperature MIR laser sources that are compact, cheap, and robust. The most promising candidates for this purpose are semiconductor lasers and direct solid-state lasers. In combination with the spectroscopic techniques that have been discussed in this chapter, portable real-time breath analyzers seem feasible in the near to mid-range future. Advances in optical technologies will definitely result very soon in smaller devices that are cheaper and easier to use. In particular, the use of optical fiber technology will lead to more compact and finally portable analyzers.

Acknowledgements. We gratefully acknowledge contributions of Daniel Halmer to this work. Moreover, we acknowledge financial support by the Deutsche Forschungsgemeinschaft and the European Commission (Sixth Framework Programme).

References

1. M. Phillips, in *Breath Analysis for Clinical Diagnosis and Therapeutic Monitoring*, Edited by A. Amann and D. Smith, World Scientific, Singapore, 293, 2005.
2. T.H. Risby, in *Disease Markers in Exhaled Breath*, Edited by N. Marczin and M. H. Yacoub, IOS Press, Amsterdam, 113, 2002.
3. M. Mürtz and P. Hering, in *Laser in Environmental and Life Sciences,* Edited by P. Hering, J. P. Lay, S. Stry , Springer, New York, 247, 2004.
4. M. Mürtz, Breath Diagnostics Using Laser Spectroscopy, Optics & Photonics News **16**, 30, 2005.
5. H. Ganser, M. Horstjann, C.V. Suschek, P. Hering, and M. Mürtz, Appl. Phys. B **8**, 513, 2004.
6. M. Mürtz, B. Frech, W. Urban¸ Appl. Phys. B **68**, 243, 1999.
7. G. von Basum, H. Dahnke, D. Halmer, P. Hering, M. Mürtz, J. Appl. Physiol. **95** 2583, 2003.
8. D. Halmer, G. von Basum, P. Hering, M. Mürtz, Opt. Lett. **30**, 2314, 2005.
9. D. Halmer, S. Thelen, P. Hering, M. Mürtz, Appl. Phys. B **85**, 437, 2006.
10. D. Halmer, G. von Basum, M. Horstjann, P. Hering, M. Mürtz, Isotop. Environ. Health Stud. **41**, 303, 2005.
11. A.N. Paunel, A. Dejam, S. Thelen, M. Kirsch, M. Horstjann, P. Gharini, M. Mürtz, M. Kelm, H. de Groot, V. Kolb-Bachofen and C.V. Suschek, Free Radic. Biol. Med., **38**, 606, 2005.

Design and Technical Concept of a Tm Laser Scalpel for Clinical Investigation Based on a 60W, 1.92 µm Tm Fiber Laser System

Sebastian Wenk[1], Stephan Fürst[1], Veit Danicke[2] and Dirk Theisen Kunde[2]

[1] Medical Laser Center Luebeck , Peter-Monnik Weg 4, 23562 Luebeck, wenk@bmo.uni-luebeck.de
[2] Institute of Biomedical Optics, University of Luebeck, Peter-Monnik Weg 4, 23562 Luebeck, theisen@mll.mu-luebeck.de

Abstract. This article shows the development of a concept for a Thulium (Tm) laser scalpel at the emitting wavelength of 1.92 µm with a maximum output power of 60 W. The system is currently developed at the Medical Laser Center in Luebeck for a clinical investigation in minimal invasive surgery, e. g. to be used on liver and kidney. The concept includes technical construction as well as the design and usability referring to standards in medical engineering. The required documentation, design and the software were part of two diploma theses at the Institute of Biomedical Optics/University of Luebeck, Germany.

1. Introduction

There are currently several different tissue dissection technologies for general and laparoscopic surgery on the market. They are based on radiofrequency, ultrasonic, water jet or laser radiation techniques [1, 2].

All of these devices aim at an efficient and bloodless tissue dissection with negligible damage to the surrounding tissue. The application of a 2 µm laser scalpel has several advantages concerning the common techniques as it has a better cutting efficiency and at the same time seals the vessels with less blood loss [1, 2].

Therefore the Medical Laser Center Luebeck in cooperation with the Institute of Biomedical Optics, University of Luebeck, realized a Tm laser scalpel based on a 60 W, 1.92 µm Tm fibre laser system to be used in a clinical investigation.

In the near future the laser system could be used especially for the minimal invasive surgery, e.g. for cutting liver and kidney.

2. Methods

The assembling and the design of the Tm laser scalpel should be able to meet the essential requirements of the directive for medical devices MDD 93/42 EWG, Annex VIII. The Tm laser scalpel was developed for the use in a clinical investigation. The system is called, in order to the EC directive MDD 93/42 EWG, Annex VIII a device for special purposes.

The manufacturer has the obligation to verify that the clinical research is in accordance with the latest scientific and technical knowledge. Therefore, it is necessary to fulfill the standards and to pre-estimate between the intended risks for the patient compared to the intended advantage.

To meet the requirements of the specification sheet and the requirements for medical devices for special purpose, it was necessary to consider national standards:

The standards that had to be mentioned were:

DIN EN 60601: standards for medical electrical equipment, for example the general requirements for safety; usability of medical products
DIN EN 60825: particular requirements for the safety and essential performance of laser equipment and safety of laser products
DIN EN ISO 14971: risk analysis

For the software development the following standards were mentioned:

DIN EN 60825: particular requirements for the safety and essential performance of laser equipment and safety of laser products
DIN EN 60601-1-6: General requirements for safety - Collateral standard: Usability (IEC 60601-1-6:2004)
DIN EN 60601-2-22: particular requirements for the safety of diagnostic and therapeutic laser equipment (IEC 60601-2-22:1995)

Evaluation of the design has been realized by reviews and walkthroughs.

3. Results and Discussion

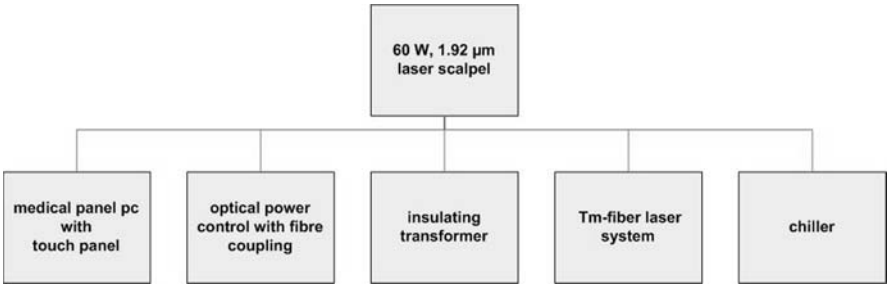

Fig. 1. Schematic configuration of the Tm laser system

The Tm laser scalpel consists of several stand alone parts [Fig. 1] and is based on a 70 W Tm fiber laser (IPG Photonics, Burbach, Germany) with a wavelength of 1.92 µm, which has high water absorption and therefore has a big advantage in cutting tissue.

The system is controlled by a medical panel pc (Penta GmbH, Puchheim, Germany) with a touch panel on top of the system which was chosen because of its medical accreditation. The control is based on the software LabVIEW™ 8.0 (National Instruments, USA) that is running on a Windows XP system. The insulating transformer (Schmidbauer, Hebertsfelden, Germany) has a medical approval and makes sure that the leakage current of each part of the system meets the standards of medical products.

The chiller (Termotek, Rastatt, Germany) ensures that the laser system is cooled down to operating temperature.

Safety Concept. To coordinate all components and to implement the needed safety features, a program based on LabVIEW™ 8.0 has been developed especially for this system.

High attention was put into the safety precautions to make the system as safe as possible for the patient. Therefore a watchdog is implemented which monitors system functions and minimizes the risk caused by unpredictable complications of the pc system.

The laser power is permanently double checked with the internal power control of the laser and an additional detector due to safety precautions, as shown in Fig. 2. Another point that needed to be included is footswitch surveillance which checks on a second channel if it is active [3].

An uninterruptible power supply monitors the power supply and protects the panel pc from power loss. As an effect of complications the emission would be cut off to avoid damage to the patient.

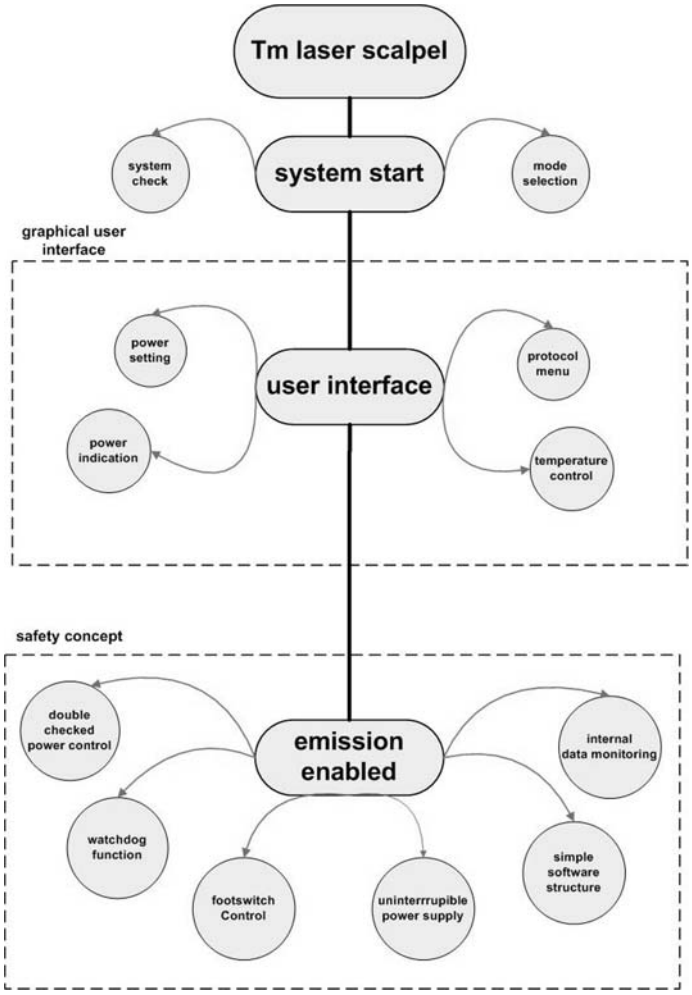

Fig. 2. Laser concept block diagram

User Interface. The graphical user interface (GUI) was designed to meet the newest requirements for ergonomics, workflow and usability. It was designed to be used intuitively and, as far as possible, to avoid user errors. The user surface is designed to meet the requirements to be used with a minimum of application training.

The front panel includes all controls for the system. The controls are grouped into controls and displays and zoned from each other so that they can be clearly differentiated.

Another important feature of the system is that there is no further electronics in the system. It is completely controlled and monitored by panel pc and software.

The background colour was kept dark to enhance contrast to signal colours like red or green and to make the controls come to the foreground [4]. The overall number of used colours is minimized to avoid irritation.

The buttons also act as indicators to keep the numbers of elements on the panel as low as possible. Displays show different background colours to show their current status to set alert parameters.

Buttons on the panel have a 3-dimensional shape so that they can clearly be identified as input elements, symbols on the buttons enhance the recognition value. It was tried to keep the buttons simple but clearly understandable, shown in Fig. 3.

As there is no input device connected, an onscreen keyboard helps the user to enter patient data for example.

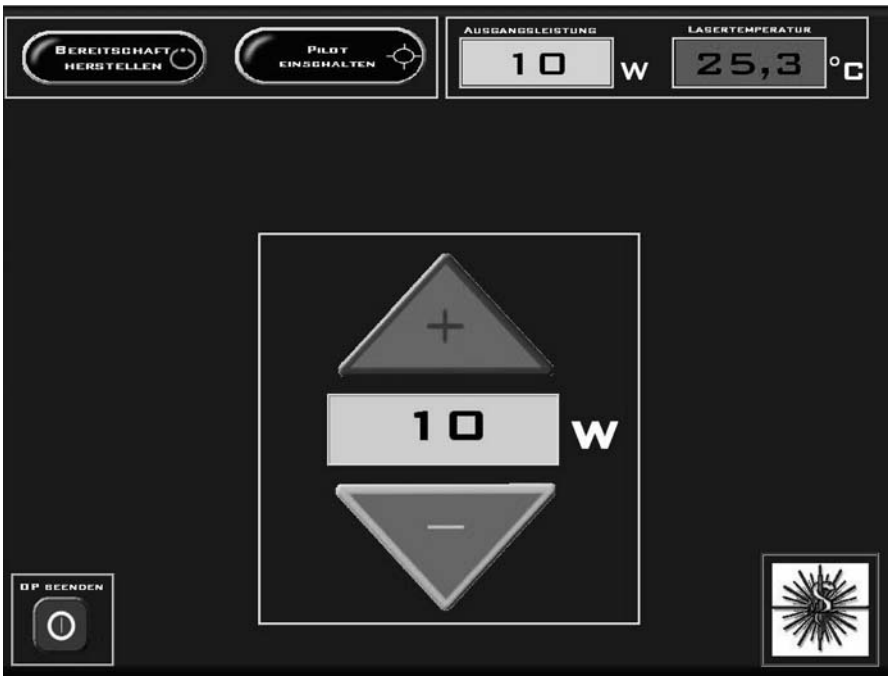

Fig. 3. Front panel of the laser control

4. Conclusions

Recapitulatory is to be determined that the Tm laser scalpel accomplishes the requirements for clinical evaluation. Both diploma theses pointed out clearly the implementation of the requirements and the emphasis in the development for an accreditation for the clinical investigation. The emphasis for the development is

the safe and simple usability for the user in consideration with the required standards.

References

1. Theisen-Kunde, D., Ott, V., Brinkmann, R & Keller, R. in Proceedings of Annual Meeting of German Society for Biomedical Technology 120-121 (Illmenau, 2004)
2. Theisen-Kunde, D., Ott, V., Brinkmann, R. & Keller, R. in Proceedings of SPIE-OSA Biomedical Optics G1-5 (Munich, 2005)
3. DIN EN 60601-2-22: particular requirements for the safety of diagnostic and therapeutic laser equipment (IEC 60601-2-22:1995)
4. Bürgel, M., Screen Design und visuelle Kommunikation- Gestaltung interaktiver Oberflächen, Heidelberg, Hüthig, 2001

Laser Osteotomy with Pulsed CO_2 Lasers

Martin Werner[1,2], Mikhail Ivanenko[1], Daniela Harbecke[1,2], Manfred Klasing[1], Hendrik Steigerwald[1,3] and Peter Hering[1,2]

[1] Center of Advanced European Studies and Research, caesar, Bonn Germany
E-mail: werner@caesar.de
[2] Institut für Lasermedizin, Heinrich-Heine-Universität, Düsseldorf, Germany
[3] Physikalisches Institut, Rheinische Friedrich-Wilhelms-Universität, Bonn, Germany

Abstract. Non-contact laser osteotomy offers new opportunities in various surgical fields, since it allows very precise pre-programmed incisions with completely free geometry. However laser osteotomy is a demanding task, because bone is a tough composite material, which is at the same time a living tissue and sensitive to temperature increases. Besides thermal side effects, practical laser applicability was limited until now because of very low cutting rates and limited incision depths. We discuss how to overcome these disadvantages by means of an optimal arrangement of thermo-mechanical ablation with a pulsed CO_2 laser and with a water-spray as an assisting media. To this arrangement belong optimal pulse duration, irradiance and radiant exposure of the laser pulses, as well as multi-pass cutting procedures. Effective ablation of hard bone tissue with minimal thermal damage is possible with relatively long CO_2 laser pulses of 80 µs duration and an average laser power of up to 40 W. To overcome the depth limitation special scanning techniques, which allow deep incisions even in thick multi-layer bones in feasible irradiation times, were developed in our group.

1. Introduction

Laser osteotomy offers multiple advantages in comparison to conventional mechanical tools as saws and trephines. However until now thermal damage to the surrounding tissue induced by the laser interaction [e.g.1] or extremely low cut rates [e.g. 2] prohibited practical application of this technique in medicine.

Short pulsed CO_2 lasers applied in an especially developed fast multi-pass scanning technique in combination with a fine water spray provide an effective and biologically compliant way to process hard biological tissues for medical purposes [3, 4]. To achieve fast and deep in-vivo incisions with minimal thermal side-effects a precise understanding of the ablation process is necessary. Moreover special irradiation techniques have to be developed. The ablation process of bone tissue with CO_2 lasers (as well as Er:YAG lasers) are of thermo-mechanical nature [3, 5] and based on the fast evaporation of the liquid (mainly water) enclosed in the bone matrix in a very thin absorption layer. This results in a strong internal pressure build-up. If the pressure rise time is shorter than the thermal relaxation time of the tissue, the pressure finally exceeds the ultimate tensile strength of bone tissue (approximately 100MPa [6]) and the tissue tears apart in a so-called micro-explosion. With the ablation products excessive heat is

removed from the tissue thus thermal damage to the surrounding tissue can be minimized. CO_2 lasers are chosen because their wavelength is strongly absorbed in the mineral component (hydroxyapatite) of bone tissue and so a small tissue volume can be heated extremely fast.

When using optimal scanning parameters excessive heat accumulation in the tissue can be avoided creating a clean cut with minimal thermal damage to the surrounding bone tissue.

An in depth overview of the ablation mechanism and the physical conditions necessary for effective and "clean" ablation is given in a recent publication of our group [4]. The above stated considerations lead to a threshold for the minimal theoretically necessary radiant exposure (J/cm^2) Φ_{th} to reach a pressure build-up which is sufficient to induce a micro explosion in the bone of 0.54 J/cm^2 for a laser wavelength of 9.6 µm (CO_2 laser) and 0.8 J/cm^2 for a wavelength of 10.6 µm (CO_2 laser). These values fit quite well to experimental data yielded in our group [4]. To accumulate the necessary energy in the absorption layer to reach this energy threshold, the energy has to be accumulated fast enough to compensate losses from thermal diffusion. As a result a second threshold I_{th} applies to the laser peak irradiance I (W/cm^2).

$$I_{th} = \Phi_{th} / \tau_T \tag{1}$$

The thermal relaxation time τ_T in (1) characterizes the time scale of the heat dissipation and can be defined in different forms, depending on the model considered. We estimate τ_T to around 20 µs for 9.6 µm and to around 45 µs for 10.6 µm. For further details see [4] and the relevant references there.

Our experiments show that even under optimal irradiation conditions with $\Phi_{laser} >> \Phi_{th}$ and $I_{laser} >> I_{th}$ prolonged laser irradiation on the same spot will induce thermal damage and ultimately carbonization of the bone tissue if additional measures are not taken. The thermal damage happens due to heating of the cut border with the sub-ablative wings of the Gaussian beam profile in the focus and the accumulation of rest heat in the tissue. This leads to parching of the heated tissue, which makes the continuation of the thermo mechanical ablation process impossible because of absence of water in the ablation region. An effective way to prevent dehydration of the bone tissue is the application of a fine water spray to the irradiated bone area to compensate the water loss and provide additional cooling. For medical applications isotonic NaCl solution can be used. Due to the fine spraying of the fluid light energy loss of the laser from absorption can be kept under 5 %.

Although the water spray is an essential component of the laser osteotomy technique it cannot completely prevent negative thermal side effects at laser repetition rates of several tenth of Hz or higher. Temperature measurements with a fast IR camera [7] have shown that even at laser repetition rates of 50 Hz with a short pulsed TEA CO_2 laser ($\tau_{laser} < 1\mu s$) temperatures of around 120°C are reached at the border of the ablation crater during spot irradiation (E_{laser}=30 mJ/pulse; D_{focus}=0.23 mm (@1/e^2 level); 2 ml/min water spray flow). This heat accumulation can be avoided by scanning of the laser beam over the bone. The rest heat is evenly distributed along the incision and the tissue can cool down between the beam pass cycles. In the example above we have not detected

any significant temperature increase when the laser beam was scanned with a velocity of only 2 mm/s.

Based on these findings a prototype laser osteotome was developed in our group. In this prototype system a fast and precisely repeated motion of the focused laser beam along a planned cut trajectory is realised with computer controlled fast galvanic beam scanner. This technique allows the use of powerful "relatively" long 80 µs laser pulses of a reliable CO_2 slab laser at pulse repetition rates between 100 – 400 Hz for "clean" incisions in bone tissue with average powers of up to 40 W [8]. For focus diameters D_f of 0.2 to 0.4 mm ($1/e^2$ level) the scan velocity is usually chosen in a way that the distance the laser beam is moved between two pulses is about $D_f/2$. On in-vitro irradiated bone samples measurements of ablation rate [4, 8], histological [9] and SEM [10] analysis as well as animal experiments [11] have proven, that good results can be achieved with the described technique.

2. Experimental Methods

With the described laser osteotomy technique narrow cuts of down to 0.2 mm width (depending on the focussing optic) are created. With these narrow cuts incision depths of up to about 7 mm can be created efficiently and fast. However deeper incisions require unproportional longer irradiation times and may be accompanied with not controllable thermal damage in the deeper parts of the incisions. The phenomenon of decreasing cut efficiency with increasing incision depth is well known for laser material processing in general and described for medical applications in [12]. With the observed wedge-shaped cut cross-section less and less laser energy reaches the lower section of the cut as its depth grows. The energy is lost due to absorption at the incision sidewalls and increasing heat flow normally to the sidewall surface [12]. It is also lost due to light absorption in the ablation debris and vapor, which is confined in the deep cut. The positioning of the laser beam focus slightly beneath the bone surface can bring some improvement. However this is not sufficient for osteotomies of thick multi-layer bones, as e.g. mandibles. The delivery of laser energy to the lower parts of the incision can be improved with special techniques, developed in our group, to artificially dilate the incision [4, 13]. The cut dilatation can be done in different ways. An effective technical solution, which can easily implemented with a suitable galvanic beam scanner, is to superimpose the main incision trajectory with a small circular beam motion ("wobble"). With correct matching of the "wobble" amplitude and frequency to the linear scanning velocity and laser repetition rate and the laser beam focus diameter, much deeper incisions than with the simple line cutting procedure can be reached. Generally one can say that the "wobble" amplitude (i.e. the incision width) has to be increased with rising desired cut depth.

Experiments with a Rofin Sinar SC x 30 slab CO_2 laser in combination with an Arges Elefant 20 galvanic laser beam scanner are described in the next section. The experimental parameters used, were 80 µs pulse duration (FWHM), pulse repetition rate 200 Hz, pulse energy 70 mJ/pulse (average power 14 W), focus diameter 0.160 mm and linear scan velocity 40 mm/s. The wobble parameters

were chosen to D_{wobble}= 0.8 mm and f_{wobble}=135 Hz. For the widened wobble cuts the laser beam focus was positioned 5 mm below the bone tissue surface for optimal results. For the narrow line cuts the focus position was on the bone surface.

3. Results and Discussion

The results of the comparative measurements of narrow line cuts and dilated wobble cuts are presented in Figure 1., where the cut rate R (in µm^2/pulse) is shown, plotted against the incision depth D. The cut rate is the product of cut length L_{cut} and incision depth D divided by the number of applied pulses N_{pulse}.

$$R=(D \cdot L_{cut})/N_{pulse} \quad (2)$$

The cut rate R is a measure for the cut efficiency which is independent from the incision width and can be used for the comparison of cuts of very different widths as in this case.

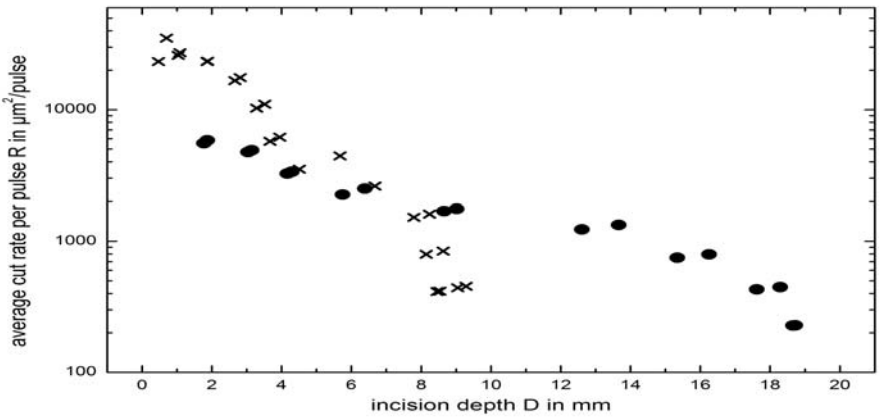

Fig. 1. Average cut rate R in µm^2/pulse against incision depth D in mm for wobble cuts (●) and narrow line cuts (×) (parameters see text)

In Figure 1. is visible, that the maximal achievable cut depth can be increased significantly from 9 mm (narrow line cuts) to 19 mm (wobble cuts D_{wobble}=0.8 mm) by dilating the incision width artificially. Lager wobble diameters could create even deeper incisions in cortical bone tissue. For incision depths below 5 - 6 mm the narrow line cuts are more efficient, but with increasing depth the dilated wobble cuts are getting increasingly more efficient and can reach cut depths which are not achievable with the narrow line cut technique.

Lager wobble diameters could create even deeper incisions in bone tissue. Special scanning algorithms with additional progressive focus shifts during the laser irradiation and matching of the wobble diameter to the current cut depth even yield improved results.

4. Conclusions

With the laser osteotomy technique, introduced by our group, using pulsed CO_2 lasers with additional water spray and fast multi-pass beam scanning techniques combined with cut dilation deep and clean incisions even in thick multilayer bones as e.g. the mandible are possible. So for the first time a practical medical application of laser osteotomy is possible and already successfully demonstrated in animal experiments [11]. An applicable prototype laser osteotome system utilising the described laser osteotomy technique was developed and tested by our group. Laser osteotomy can now offer new surgical approaches in several fields of medicine e.g. for ENT surgeries at the skull base or maxillofacial interventions at the mandible.

References

1 S.D. Gertzbein, D. deDemeter, B. Cruickshank, A. Kapasouri, in *Lasers in Surgery and Medicine*, 1, 361, 1981.

2 A.K. Murray, M.R. Dickinson, in *Lasers in Medical Science*, 19, 127, 2004.

3 M.M. Ivanenko, P. Hering, in *Applied Physics B*, 67, 395, 1998.

4 M. Ivanenko, M. Werner , S. Afilal., M. Klasing, P. Hering, in *Medical Laser Application*, 20, 13, 2005.

5 M. Forrer , M. Frenz, V. Romano, H.J. Altermatt, H.P. Weber, A. Silenok, M. Istomyn, V.I. Konov, in *Applied Physics B*,56, 104, 1993.

6 F.A. Duck, Physical Properties of Tissue, Academic Press, San Diego, 1990.

7 A. Brendemühl, M. Werner, M. Ivanenko, P. Hering, T. Buzug, in *Biomedizinische Technik; 50 Suppl. Vol.1, Part*, 1264, 2005.

8 S. Afilal, M. Ivanenko, M. Werner, P. Hering, in *Fortschritt-Berichte VDI, 17. Biotechnik / Medizintechnik 231*, 164, 2003.

9 M. Frentzen, W. Götz, M. Ivanenko, S. Afilal, M. Werner, P. Hering, in *Lasers in Medical Science*, 18; 119, 2003.

10 M. Werner, S. Afilal, M. Ivanenko, M. Klasing, P. Hering, in *Aktuelle Methoden der Laser- und Medizintechnik, Berlin, VDE*, 275, 2005.

11 M. Ivanenko, R. Sader, S. Afilal, M. Werner, M. Hartstock, C. von Hänisch, S. Milz, W. Erhardt, H.-F. Zeilhofer, P. Hering, in *Lasers in Surgery and Medicine*, 37; 144, 2005

12 M. Ivanenko, T. Mitra, P. Hering, in *SPIE Proc. Optical Biopsy and Tissue Optics 4161*, 46, 2000.

13 P. Hering, T. Mitra, M. Ivanenko, *Patent DE 10133341A1 "Laserschneiden"*, 2001.

T-Scan: First Experiences with Acquisition of Cleft Morphology

K. Schwenzer-Zimmerer [1,2], B.-I. Boerner [1,2], A.A. Müller [1,2], P. Jürgens [1,2], A. Ringenbach [3] and E. Schkommodau [3]

[1] Hightech Research Center of Cranio-Maxillofacial Surgery, University Basel, Spitalstr.21 CH 4031 Basel, Switzerland
E-mail: schwenzerk@uhbs.ch
[2] Dept. of Cranio-Maxillofacial Surgery, University Hospital Basel, Spitalstr.21 CH 4031 Basel, Switzerland
[3] Institut für Medizinal- und Analysetechnik, FHNW, Gründenstrasse 40 4132 Muttenz, Switzerland

Abstract. For capturing facial surfaces, different commercial systems are available. These conventional systems can be mainly divided into white-light-scanners, linear laser scanners and photogrammetric devices. The latest developments are based on holographic image acquisition. With all these devices shadowing effects will occur. These effects might be avoided by the use of a hand-held laser scanner with simultaneous registration. The T-Scan (Fa. Steinbichler, Germany [1]) is such a tracked scanning device. To assess the suitability of this scanner, a total of 16 scans (two infants with a lip-alveolus-palate cleft) were acquired by the same surgeon. Data sets with an accuracy of less than a millimetre were acquired.

1. Introduction

Throughout the last years the three dimensional capturing of body surfaces became more and more important. In different medical subspecialties, parts of the body are scanned. It is necessary to gain an as precise as possible documentation of the initial situation and of the different treatment results. Different devices for the capturing and digitising of the facial surface are commercially available and suitable for compliant persons. Examples are white-light-scanners, linear laser-scanners and also photogrammetric devices [1, 2]. The latest image acquiring procedure is the holographic facial measurement technique. All these systems are fundamental for the three dimensional acquisition of the human face. The cases we present deal with the capturing of baby facial surfaces with cleft lip and palate. In Western Europe the incidence of this facial malformation is about one in 500 births. The characteristic of the cleft lip and palate deformity differ individually from one patient to another. Therefore an adequate pre- and postoperative documentation is important. In our department, the correction of this mal-formation normally will be proceeded when the infant is at least three months old and the body weight is at least about 5 kilograms. Especially these very young patients need an optimal pre-operative documentation because they are still

growing and changing very much. In addition the data gained by scanning can be used for pre-operative, computer based 3D planning and navigation systems as well as for an objective monitoring of the chosen treatment. To receive an optimal data quality (with harmless application) the following requirements have to be fulfilled: The method has to be biocompatible, especially because children who are not asleep will open the eyes unknowingly. A contact free acquirement is needed otherwise the soft tissue is displaced and an accurate reproducibility is not possible. A high resolution (in the range of sub millimetre) is necessary and also a technical system which can be used by technical inexperienced staff (e.g. in the operation theatre).

The T-Scan® (Fa. Steinbichler, Neubeuern, Germany) meets all of these criteria. Through the last years the T-Scan® was developed and used for industrial purpose (e.g. car surface and finish control or product engineering). The laser source is classified as a laser class two and therefore no special safety precautions are necessary. By moving the scanner, the patient facial surface can be captured completely .In contrast to other methods undercut regions are accessible due to the hand-held use of the T-Scan® and simultaneous registration.

2. Material and Method

The facial surface is captured by a visible laser beam (670 nm, laser class 2) and measured with high scanning frequencies. The laser beam is linearly orientated by a polygon mirror. The measurement distance is calculated using the triangulation principle. The exact position of the scanner is detected in six degrees of freedom (three spatial coordinates and three tilting angles). This is possible due to 29 infrared markers. Three of these markers have to be determined for the exact spatial position using an optical tracking system. The correct scanning distance can be kept by paying attention to a pilotbeam and LED`s on the back side of the scanner.

The technical data of the T-Scans® are following ones: measuring depth: 75mm, scan width: 90 mm, mean measuring distance: 83 mm, scan frequency: 10-140 Hz, sampling rate of distance measurement: 10kHz, resolution of distance measurement: 1 µm, accuracy of distance measurement: +/- 30 µm, point density in scan direction: 0.14-1.96 mm, sensor weight: <1500g, sensor dimensions: 185x199x145 mm, standard cable length scanner-PC: 9 m, lateral resolution: 0,1 mm, laser type: diode, wavelength 670 nm, laserclass: 2. The used Optotrak System has an approx. weight of 19 kg and a dimension of 1126x200x161 mm. [1].

For the assessment of the T-Scans® two infants in the age of three months one with an unilateral cleft lip and palate and one with a bilateral cleft lip and palate were captured. They received in general anaesthesia two scans before the surgical procedure, two scans straight after the operation and another two scans 7 days later when the sutures were removed. Combined intra- and extraoral plaster casts (Figure 1) [4] of the infant's face were also produced for determination of the

reliability of the scanner using the comparable morphology without movement. Two scans from each of these masks were also preformed. All of the 16 scans were acquired by the same surgeon to guarantee the same use of the scanning system (Figure 2).

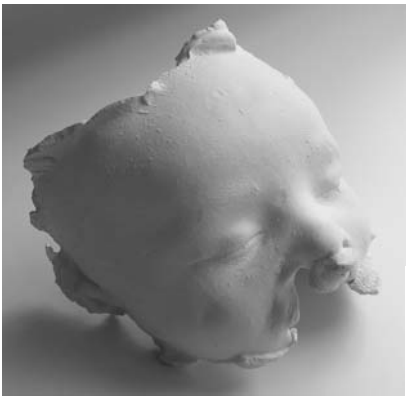

Fig. 1. Intra-extraoral plaster cast

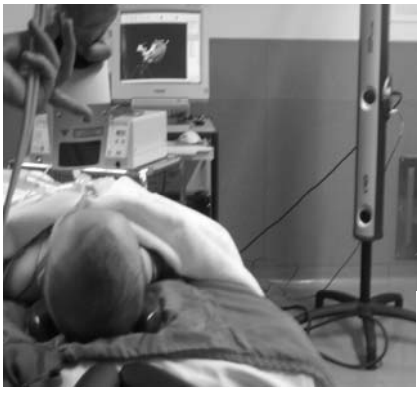

Fig. 2. The T-Scan set up in the operation theatre

A feature of the T-Scan system is the possibility to scan the same surface several times. Thereby multiple layers occur which are combined with each other. To generate surface data post proceeding (matching, reduction, filtering, etc.) is essential. The above mentioned scans were done twice to test the reproducibility of the measurement data. The two datasets were optimized, registered and statistically evaluated without the Iterative-Closets-Point method as a post proceeding feature. The variance was taken as a measurement feature for the accuracy.

3. Results

Datasets in the range of less than a millimetre were acquired (Figures 3, 4, 5) The mean accuracy of the plaster masks were 0.04 mm, the standard deviation was 0.03 mm and the maximal deviation was 0.14 mm. The scans from the children (in general anaesthesia) showed a mean accuracy of 0.08 mm, a standard deviation of 0.12 mm and a maximal deviation of 0.22 mm.

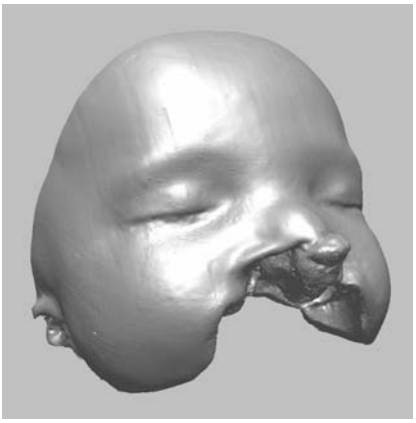

Fig. 3. Reconstructed T-Scan data set

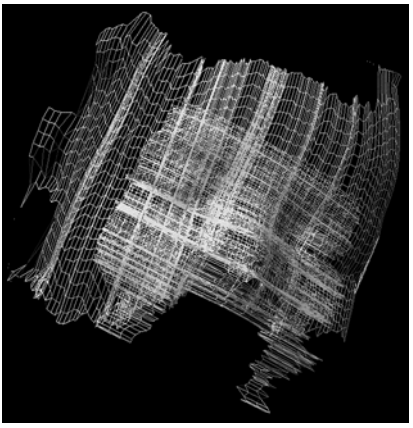

Fig. 4. Layers of one T-Scan-Image

The time period for one complete scan differed between 10 and 30 sec. These differences were due to the speed the user moved the T-scan device from the right to left side and from the top of the face to the beginning of the neck.

The scanning device was fairly good to handle in the operation theatre. The plaster cast could be captured without lost of data. The children had to be scanned a few times in complex areas (cleft lip alveolus and palate, ear) to gain a complete facial surface.

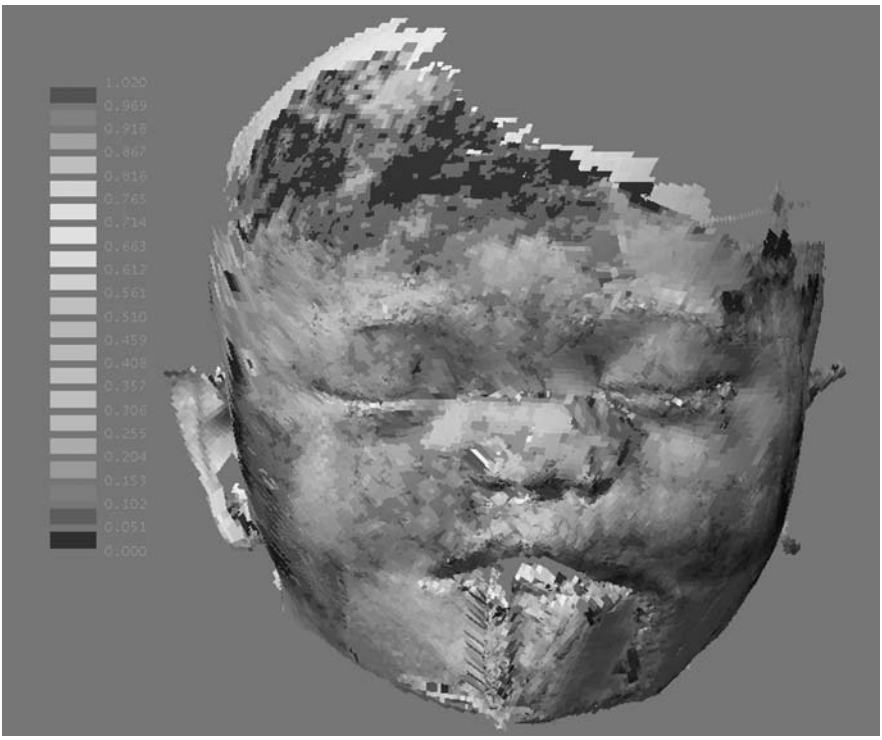

Fig. 5. The absolute deviation of two data sets presented with pseudo-colours (scale: red 1 mm, green 0.5 mm und blue 0 mm).

4. Discussion and Conclusions

The feasibility of a handheld triangulation scanner offers a new opportunity in the operation theatre and therefore it is also well useable as a follow-up tool. The capturing of three dimensional datasets in the range of less than a millimetre was possible in aggravating circumstances (breathing patient, small operation theatre). However the relative long input time and therefore motion artefacts will result in wider deviations when using this system for scanning awake patients. Compared with other scanning devices a major advantage is the possibility to scan undercut complex regions in detail. When the same surface was scanned several times regions were shadowing artefacts normally occurred were captured without

artefacts. In our cleft lip and palate baby patients the lip and nose region as well as the complete ears were acquired in a very precise way. The input time for acquiring a complete precise image in a lifely patient is long. In comparison with the intra operation used plaster cast method (which takes about 20 min.) to get similar documentation - but with tremendous soft tissue deformation - it is very fast. For the intraoral part due to the wet surface inside the mouth, the scanning of the intra-oral region is not possible. There we still combine the facial scanning method with the acquisition of intraoral impressions.

In terms of the flexibility and mobility, a lighter and smaller scanner would be preferable. The handling of the scanner is possible for laymen in minutes. In our cases the images gained with the T-Scan will be used for follow-up and growth studies. We use the T-scan for different procedures. One perspectives for the use of the T-scanning device is the three dimensional cephalometry. [5] Another one is the use as data base for rapid-prototyping models. Ear and nose facial prosthesis would be examples for rapid prototyping models in the field of maxillofacial surgery were the base might show shadowing artefacts with lasers scanning systems which can't be moved and rotated. Another aim is to use the T-Scan for soft tissue navigation during surgical procedures. To minimise movement artefacts the corrections of the patient movements can be relativated by patients tracking. An exclusion of minimal facial muscle movements won't be possible at the moment.

Acknowledgements. These investigations were done with support of the Swiss National Funds, Co-Me, NCCR.

References

1 www.Steinbichler.com.
2 K. Schwenzer, C. Holberg, J. Willer, G. Mast, M. Ehrenfeld: 3-D imaging of the facial surface by topometry using projected white light strips. Mund Kiefer Gesichtschir;2 (Suppl 1):130-4, 1998
3 M. Krimmel, M. Bacher, C.P. Cornelius, S. Schubert, G. Göz, and S. Reinert: 3-dimensionale Bildakquisition zur Analyse der primären spaltbedingten Gesichtsdeformität mit optoelektronischem Oberflächenscanner. Mund Kiefer Gesichtschir. 6:157-16, 2002
4 M. Bacher, G. Göz, T. Pham, U. Bacher, O. Werner, P. Buchner et al.: Three-dimensional analysis of cleft palate topology in newborn infants with reference to the cranial skeleton. Cleft Palate Craniofac J;35(5):379-95, 1998
5 K. Schwenzer, C. Holberg, C. Hagenmaier, M. Bacher, B. Kunz, C. P. Cornelius, N. Schwenzer, M. Ehrenfeld: Positioning of the premaxilla in cases of bilateral cleft lip, alveolus and palate using Lathams appliance. Mund Kiefer Gesichtschir;Jan, 7(1):25-30, 2003

Part VII

Clinical Post-Deadline Papers

Accuracy of Translation and Rotation Measurements in Navigated ACL Reconstruction

D. Kendoff, M. Citak, R. Meller, P. Bretin, J. Geerling, C. Krettek and T. Hüfner

Unfallchirurgische Klinik, Medizinische Hochschule Hannover, Trauma Department, Hannover Medical School, Germany, Carl-Neuberg-Str.1, 30625 Hannover
E-mail: kendoff.daniel@mh-hannover.de

Abstract. An accurate tool for a combined pre-, intra-, and postoperative stability measurment for rotation and translation after ACL reconstruction of the tibia is still not in clinical use, although these measurments provide important stability parameters. Navigation has been introduced a few years ago for the evaluation of impingement problems or the drill canal for ACL replacement but the measurement of the tibial translation and rotation is only available for a short time and only available with a few navigation modules. The navigated accuracy is 1 mm/°. In this study navigated measurement of tibial rotation and translation were evaluated with a new developed mechanical device and directly compared with a c-arm based navigation modul.

Material and Methods. Accuracy of navigation was compared with the KT1000 for the anterior-posterior (AP) translation and to a new developed goniometer tool concerning the rotational range of motion. Comparative tests included plastic whole leg models and specimens. Tests were repeated with intact and dissected ACL´s. A conventional navigation system (Vector Vision, Brainlab, Heimstetten, Germany) was used in all cases. This included software developed for fluoroscopy based navigated ACL reconstruction. The following knee kinematics were detectable with the navigation system: Flexion/Extension degrees of the knee joint (°); AP translation of the tibia in relation to the femur (mm); Axial tibial rotation relative to the femur (°). At first neutral tibial rotation was defined and marked in the knee joint in neutral position. All rotational measurements were done with a new developed goniometer tool and compared to the navigated technique. Then the knee was rotated externally until 45° (maximum) and internally 45° (maximum), by single 2.5° steps. These measurements were repeated in 0°, 30°, 60° and 80° knee flexion. All tests were repeated three times and performed by 3 different observers. A total of 1296 measurements were done. Measurements of the tibial translation were compared with the KT 1000 for the specimen testings.

Results. Results revealed: accurate navigated measurement of tibial rotation in plastic and specimen models; variation of absolute AP translation values between KT1000 and navigation; variation of the AP translation corresponding to the ACL condition; increased range of total tibial rotation after dissecting the ACL compared to the intact ligament. General adequate use of the navigation system in combination with the c-arm registration of the articulating knee joint.

Discussion. Aim of an ACL reconstruction is also to restore the rotational stability and limiting of the AP translation. Intraoperative measurments of these important parameters are not available as a navigated system. Our study shows that navigation is an accurate technique to measure the AP translation and rotation of the knee with intact and disected ACL´s under laboratory conditions. It might be used intraoperative and further clinical studys should improve our results.

Stability of Different Attachment Arrays of Reference Bases Against Mechanical Stress

M. Citak, D. Kendoff, P. Bretin, J. Geerling, C. Krettek and T. Hüfner

Unfallchirurgische Klinik, Medizinische Hochschule Hannover, Trauma Department, Hannover Medical School, Germany, Carl-Neuberg-Str.1, 30625 Hannover
E-mail: citak.musa@mh-hannover.de

Abstract. An invasive, rugged fixation of the reference bases is necessary to execute a save and precise navigated operation. In case of dislocation of the reference bases the operation must be stopped and the system must be calibrated again, because already small dislocations mean severe impreciseness during the operation. Aims of that study were to test the stability of some of the reference bases especially how much power is needed to remove them.

Material and Method. The developement of a measuring unit, which detects the power by using resistance strain gauges, was managed in our university, also the conversion to torque (Nm).The fowolling reference bases have been tested: Singular pin fixation systems (Schanz`screw, BrainLab MIRA system and Stryker adjustment system). The tear-out-forces have been tested for the following anatomic structures: shaft of femur, distal femur, head of tibia, shaft of tibia, crista iliac, SIAS and talus. At tibia and femur the tear out power was detected for mono- and bicortical abjusments of the RS wich were mentioned in the text before.The tested Synbone Models were fixed in cement, the reference base were placed at the bone and the experiment set up was connected to the measuring unit. A torque produced by a lever was put on the reference base up to its dislocation or breakout of the whole system. The powers were detected and saved.

Results. From the tested adjustment systems the BrainLab Mira (6,36Nm) was the firmest followed by Stryker (2,66Nm) and the conventional Schanz' screw (1.38 Nm). The smallest torque for the dislocation of the monocortical mounting of the Schanz' screw was determined on the proximal tibia in our series (0.23. Nm). The maximally needed strength was required for the dislocation of the BrainLab Mira on the femur bicortically fixed (6.36 Nm). The monocortical adjustment was in this study only possible with the BrainLab (femur: 5, 9 Nm; tibia: 6.0 Nm) und Schanz' screw (femur: 0.43 Nm; tibia: 0.23 Nm).

Discussion. The biomechanical charakteristics of the different types of RS systems were evaluated for the first time by this study. As our machine is limited to tourques, powers like bends or torsion have not been tested. In the future all the differnt RS systems on the world wide market should be tested and compared. The monocortical fixation showed it definitive advantage in intramedullary nail osteosynthesis.

Problems of the Pre- and Postoperativ Determination of the Antetorsionangle of the Femur by Navigation and CT

M. Citak, D. Kendoff, P. Bretin, J. Geerling, C. Krettek and T. Hüfner

Unfallchirurgische Klinik, Medizinische Hochschule Hannover, Trauma Department, Hannover Medical School, Germany, Carl-Neuberg-Str.1, 30625 Hannover
E-mail: citak.musa@mh-hannover.de

Abstract. One Problem of the intramedullary nail osteosynthesis are clinical relevant errors in the torsion of the femur. It can hardly be noticed during the surgery, and often it cannot be avoided. It is necessary to know the antetorsion and the length of the healthful femur in a navigated operation, although there are preoperative CT analysis. There is no way to use invasive reference bases on a healthful extremity, but good working non-invasive technologys are not available at this point of time. Thats why the reference base is placed on the operation table and the leg must be fixed in a good position and may not be moved during the operation. More time is needed, also a high dose x-ray. This study tried to determine the antetorsionangel and the tolerable Differences in a.p.and lateral view of 15 human femurs by using the Brainlab Navigation System and the CT.

Material and Methods. Compared to references data, which was measured by the department for radiology with CT scan, the antetorsionangle of 15 human femurs was determined by flouroscopy-based navigation procedure.The systems of Brainlab and Traumapplikation Version 2.50 were used. The procedure was repeated 3 times for every radiologic view, the median was computed. For the first setting we chose a difference of 90° between the a.p. and the lateral view.For the following settings the difference was reduced to 75°, 60°, and last 50°.

Results. For the difference of 90° we found a minimal abberance of 0° and a maximal aberarance of 4.33°, median 2 °.For 60° difference the minimal abberance was 0° and maximal 3.2°,median ca 2°. For the difference of 50° the median abberance was bigger than 5°.

Discussion. The study shows reproducible effects. The minimal abberance between the a.p. and the lateral view could be determined. Intraoperative the picture acquisition should not take place as Inlet and Outlet admission. A non-invasive reference base would improve data, but own attempts have showed that the technology is not available at this point of time.

3D-Analyses and Libraries for the Construction of Individual Craniomaxillofacial Alloplastic Implants

Th. Hierl[1], J. Hendricks[2], G. Wollny[2], F. P. Schulze[3], E. Scholz[3], G. Berti[4], J. G. Schmidt[4] and Th. Schulz[5]

[1] Department of Oral & Maxillofacial Plastic Surgery, Leipzig University
[2] MPI for Evolutionary Anthropology, Leipzig
[3] University of Applied Sciences, Leipzig
[4] C & C Research Laboratories NEC Europe, St. Augustin
[5] Department of Diagnostic Radiology, Leipzig University, Germany
E-mail: hiet@medizin.uni-leipzig.de

Abstract. Alloplastic CAM-CAM manufactured implants are regularly used to cover bony defects of the skull in craniomaxillofacial surgery. Regarding unilateral "simple" deficiencies, mirroring procedures can be successfully employed for construction. In cases of complex and bilateral defects resp. syndromic malformations, planning can only be performed according to the esthetic understanding of the engineer-doctor team. Especially in the facial region with its high esthetic impact this situation is less preferable. Therefore a study was planned to allow planning of CAD-CAM implants on the basis of reliable data.

Material and Methods. As a planning guide for alloplastic implant construction, two investigations were performed. In a first step a library of bony facial segments (mandible with chin and mandibular angle, zygoma, and nasoethmoidal-frontal region) were to be segmented from CT-scans of unaffected patients. Segmetation was done in VWorks® on the original CT-data sets. These segments were then exported in stl-format. In a second step, CT sets were analyzed in a 3D-cephalometric software tool using 86 anatomical landmarks. Only data sets of acceptable accuracy (slice thickness and spacing less than 2 mm) were chosen.

Results. Out of 117 CT data-sets 399 bony segments could be segmented for a future craniofacial library. Modules included left and right zygoma, naso-ethmoidal-frontal region, chin, and both mandibular angles. After export into stl-format these were labeled according to gender, age and 3D-cephalometric data. 3D-cephalometric analysis of 120 non-pathologic data-sets showed that not all anatomical landmarks could be regularly identified and reproduced.

Discussion. In combination with the 3D-cephalometric data, planning of complex alloplastic implants should be possible utilizing our library. According to individual patient data, a fitting bony segment can be taken from the library as a basis for CAD-CAM implant production. By now several individual titanium implants could be successfully incorporated using the above described procedure.

Evaluation of Various Ceramic Implants after Immediate Loading

J. Neugebauer[1], B. Nolte[1], T. M. Buzug[2], M. Weinländer[3], V. Lecovic[4], F. Vizethum[3], C. Khoury[5] and J. E. Zöller[1]

[1] Interdisciplinary Dept. of Oral Surgery and Implantology, University of Cologne
[2] Institute of Medical Engineering, University of Luebeck, Germany
[3] Private Dental Practice for Implantology and Periodontology, Vienna
[4] Department of Periodontology, University of Belgrade
[5] School of Dentistry, University of Beirut
E-mail: joerg.neugebauer@uk-koeln.de

Abstract. Ceramic implants showed in the past a very nice soft tissue behavior but the clinical success was compromised due to lack of osseointegration in the early stage and mechanical complication like fracture in the long term run. New material like Yttrium stabilized Zirconia ceramics promise a higher mechanical stability. While mechanical stability can be proven by in-vitro-testing the course of osseointegration had to be determined by in-vivo condition. A pilot study on four mongrel dogs was performed to compare the course of osseointegration of root-form and parallel walled one-piece ZrO-ceramic implants in comparison to titanium implants.

Material and Methods. A total of 64 implants were placed. The root form ceramic implants (White Sky, Bredent Medical, Senden, Germany) had machined (CM), grid-blasted (CG) and a collagen-coated (CC) surface. The control implants were cylindrical ceramic implants (CZ) (Z-Lock, Z-Systems, Konstanz, Germany) and titanium root form implants (TG) (Sky, Bredent Medical, Senden, Germany). The bone-to-implant contact were evaluted by flourocence and thin grinding histological sections and the 3d-evaluation of μ-computertomography.

Results. The root form implants showed always a higher insertion torque than the cylindrical implants. If an insertion torque above 50 Ncm occurred the implant sides received additional preparation to avoid over-compression of the peri-implant bone. After removal of the premolar a healing period of 8 weeks was applied. In each quadrant four implants with the various surfaces were placed and immediate restoration with a resin bridge was performed. After 3 month of loading the animals were sacrificed and radiological and histological investigations were performed. Two implants with machined surface showed now osseointegration. All other implants were stable. The bone to implant contact was improved in the following order CM < ZC < CG < TG < CC. The preliminary result of the histomorphometric evaluation shows a woven structure at the peri-implant bone for the conical implants. The cylindrical implants showed a concentric formation of the peri-implant bone remodelling

Discussion. The use of ceramic implants is possible if a high primary stability could be achieved and a stabilization of the implants within one bridge is possible. Due to the one piece design special clinical consideration should be performed to achieve a high clinical success. Conical implants with a standardized undersized implant cavity inducing micro-fractures show a earlier bone remodelling in comparison to cylindrical implants.

Author Index

SPRINGER PROCEEDINGS IN PHYSICS

67 **Nonlinearity with Disorder**
Editors: F. Abdullaev, A.R. Bishop, and S. Pnevmatikos

68 **Time-Resolved Vibrational Spectroscopy V**
Editor: H. Takahashi

69 **Evolution of Dynamical Structures in Complex Systems**
Editors: R. Friedrich and A. Wunderlin

70 **Computational Approaches in Condensed-Matter Physics**
Editors: S. Miyashita, M. Imada, and H. Takayama

71 **Amorphous and Crystalline Silicon Carbide IV**
Editors: C.Y. Yang, M.M. Rahman, and G.L. Harris

72 **Computer Simulation Studies in Condensed-Matter Physics IV**
Editors: D.P. Landau, K.K. Mon, and H.-B. Schüttler

73 **Surface Science**
Principles and Applications
Editors: R.F. Howe, R.N: Lamb, and K. Wandelt

74 **Time-Resolved Vibrational Spectroscopy VI**
Editors: A. Lau, F. Siebert, and W. Werncke

75 **Computer Simulation Studies in Condensed-Matter Physics V**
Editors: D.P. Landau, K.K. Mon, and H.-B. Schüttler

76 **Computer Simulation Studies in Condensed-Matter Physics VI**
Editors: D.P. Landau, K.K. Mon, and H.-B. Schüttler

77 **Quantum Optics VI**
Editors: D.F. Walls and J.D. Harvey

78 **Computer Simulation Studies in Condensed-Matter Physics VII**
Editors: D.P. Landau, K.K. Mon, and H.-B. Schüttler

79 **Nonlinear Dynamics and Pattern Formation in Semiconductors and Devices**
Editor: F.-J. Niedernostheide

80 **Computer Simulation Studies in Condensed-Matter Physics VIII**
Editors: D.P. Landau, K.K. Mon, and H.-B. Schüttler

81 **Materials and Measurements in Molecular Electronics**
Editors: K. Kajimura and S. Kuroda

82 **Computer Simulation Studies in Condensed-Matter Physics IX**
Editors: D.P. Landau, K.K. Mon, and H.-B. Schüttler

83 **Computer Simulation Studies in Condensed-Matter Physics X**
Editors: D.P. Landau, K.K. Mon, and H.-B. Schüttler

84 **Computer Simulation Studies in Condensed-Matter Physics XI**
Editors: D.P. Landau and H.-B. Schüttler

85 **Computer Simulation Studies in Condensed-Matter Physics XII**
Editors: D.P. Landau, S.P. Lewis, and H.-B. Schüttler

86 **Computer Simulation Studies in Condensed-Matter Physics XIII**
Editors: D.P. Landau, S.P. Lewis, and H.-B. Schüttler

87 **Proceedings of the 25th International Conference on the Physics of Semiconductors**
Editors: N. Miura and T. Ando

88 **Starburst Galaxies**
Near and Far
Editors: L. Tacconi and D. Lutz

89 **Computer Simulation Studies in Condensed-Matter Physics XIV**
Editors: D.P. Landau, S.P. Lewis, and H.-B. Schüttler

90 **Computer Simulation Studies in Condensed-Matter Physics XV**
Editors: D.P. Landau, S.P. Lewis, and H.-B. Schüttler

91 **The Dense Interstellar Medium in Galaxies**
Editors: S. Pfalzner, C. Kramer, C. Straubmeier, and A. Heithausen